

ภาคผนวก ก

Contents lists available at [SciVerse ScienceDirect](http://www.sciencedirect.com)

Journal of Asian Earth Sciences

journal homepage: www.elsevier.com/locate/jseas

Morphology of the Andaman outer shelf and upper slope of the Thai exclusive economic zone

Pachoenchoke Jintasaerane^{a,c,*}, Wilhelm Weinrebe^a, Ingo Klaucke^a, Anond Snidvongs^{b,d}, Ernst R. Flueh^a^a Leibniz Institute of Marine Sciences at Kiel University (IFM-GEOMAR), Dienstgebäude Ostufer, Wischhofstr. 1-3, 24148 Kiel, Germany^b Southeast Asia START Regional Center, Chulawich 1 Building, 5th Floor, Chulalongkorn University, Henri Dunant Road, Bangkok 10330, Thailand^c Department of Aquatic Science, Faculty of Science, Burapha University, 169 Long-Hard Bangsaen Road, Mueang, Chonburi 20131, Thailand^d Department of Marine Science, Faculty of Science, Chulalongkorn University, 254 Phayathai Road, Patumwan, Bangkok 10330, Thailand

ARTICLE INFO

Article history:

Received 21 June 2010

Received in revised form 2 November 2011

Accepted 2 November 2011

Available online xxxx

Keywords:

Andaman Sea

Submarine landslides

Tsunami

Bathymetry

Sounding

ABSTRACT

Following the devastating 2004 tsunami that hit the southwestern coast of Thailand, the need for detailed bathymetric data of the Andaman Sea outer shelf became evident in order to better predict tsunami wave propagation and coastal impact. Bathymetric data and subbottom profiler records covering the outer shelf and upper slope of the Thai exclusive economic zone (EEZ) were collected onboard Thai RV Chakratong Tongyai in 2006 and 2007. The data cover an area of approximately 3000 km² between 500 and 1600 m water depth. The soundings allowed generating a final bathymetric grid with 50 m grid cell spacing. The outer shelf is rather smooth and slightly inclined southward, while the upper slope is strongly dissected by gullies. Several previously unknown features are identified including mud-domes, pockmarks, three large plateaus surrounded by moats, gas-charged sediment on subbottom profiler records, and only few indications for small submarine landslides on the upper slope. The largest of these possibly translational submarine landslides involved 2.2×10^7 m³ of sediment. This slide would have generated a tsunami wave of less than 0.12 m wave height. Considering the entire data, there is no evidence that landslides have been the source of tsunami waves in recent geological time.

© 2011 Elsevier Ltd. All rights reserved.

1. Introduction

On December 26, 2004 tsunami waves triggered by the Sumatra–Andaman earthquake of magnitude 9.3 (Lay et al., 2005) struck the southwestern coast of Thailand, causing considerable damage and killing thousands of people (Choowong et al., 2008). Subsequently, the impact of the tsunami on various field elements has been documented (Velmurugan et al., 2006; Choowong et al., 2008) including buildings, infrastructure (Ghobarah et al., 2006) and coastal ecosystems (Cochard et al., 2008). Different models for predicting future tsunamis, their travel times and potential impact on the Andaman coast have been developed (Kowalik et al., 2005; Geist et al., 2007; Kietpawpan et al., 2008). In order to deliver reliable results, these models require detailed knowledge of the bathymetry of the Thai shelf beyond the accuracy of existing GEBCO bathymetry or satellite derived altimetry data (Smith and Sandwell, 1997).

In addition, tsunamis are not only triggered by large earthquakes but can also be generated by large submarine landslides (Hampton et al., 1996; McAdoo and Watts, 2004; McMurtry et al., 2004; Smith et al., 2004; López-Venegas et al., 2008). Considering the bathymetry of the Andaman Sea outer shelf break and

slope with gradients up to 4.5° (IOC, IHO and BODC, 2003), the Andaman Sea slope has the potential for generating landslides (Hampton et al., 1996). In order to detect and characterize possible submarine landslides on the continental slope, detailed bathymetric data are required. At present such data are only available for the Central Basin of the Andaman Sea (Raju et al., 2004) and the southern part of the basin including parts of Mergui Ridge and Mergui Basin (Krabbenhoef et al., 2010).

In this paper, we present for the first time the multibeam bathymetric data covering approximately 3000 km² on the outer shelf and upper slope of the Thai EEZ between 500 and 1600 m water depth. These data have been acquired using a portable Seabeam 1050 system installed on Thai RV Chakratong Tongyai during two cruises in 2006 and 2007. The resulting detailed bathymetry reveals a number of previously unknown seafloor features including three large plateaus and several indications for fluid escape on the seafloor, but no clear indications for recent large submarine landslides.

2. Geological setting of the Andaman Sea

The Andaman Sea is an active backarc basin resulting from the subduction of the Indo-Australian Plate under the Asian Plate. The distribution of earthquakes indicates rather unequal longitudinal compression and relative oblique movement of different segments

* Corresponding author. Tel.: +49 431 600 2415; fax: +49 431 600 2922.

E-mail address: pjintasaerane@ifm-geomar.de (P. Jintasaerane).

along the subduction zone (Eguchi et al., 1979; Kumar, 1981; Curray, 2005). The oblique convergence of the plates causes bending of the Sunda Arc and therefore forms an extension of the plate between the subduction zone and right-lateral faults. An increasing of the rate of strike-slip motion caused the opening of the Mergui Basin and separating the East Andaman Basin starting at about 32 Ma ago (Curray, 2005).

The East Basin (Fig. 1) probably represents a right lateral compressive segment affected by pull-apart extension faults occurring in the Central Basin (Raju et al., 2004) and many strike-slip faults in the vicinity of the outer shelf. The Central Basin is underlain by oceanic crust and seafloor spreading probably started about 4 Ma ago (Curray, 2005) with initial rates of about 1.6 cm/yr increasing to roughly 3.8 cm/yr at present (Raju et al., 2004). In Myanmar and Thailand, many longitudinal strike-slip faults were studied, especially the Shan Scarp Fault. The faults are almost oriented in a N-S direction (Mitchell, 1992; Richter et al., 1993; Bertrand and Rangan, 2003), but their seaward extension into the East Basin is not exactly known (Curray, 2005). In addition, the Mergui Faults could have cut off the southern ends of the Ranong and the Klong Marui Fault and may have crossed the Mergui Ridge. The faults are oriented in a NW-SE direction and lie on the complex strike-slip faults zone between the Mergui Ridge and the Ranong Ridge. Nevertheless, their positions in the basin are not accurately known (Polachan and Racey, 1993). These faults possibly also generate pathways for fluids. The Mergui Ridge was probably part of the original volcanic arc, and four mud-volcanoes were reported on the ridge (Curray, 2005).

The sediment blanket in the East Basin consists of sand and foraminiferal ooze (Rodolfo, 1969; Saidova, 2008) or sandstone and coral-algal reef limestone (Polachan and Racey, 1993). The East Basin has a section of flat lying-sediments of at least 4.6 km in thickness (Curray, 2005). The main sediment source of the

Andaman Sea is fluvial input from the Irrawaddy River (Rodolfo, 1969) with a large sediment influx over 360 million tons/yr (Rao et al., 2005). Over 70% of the sediment accumulated on the inner shelf and in the Gulf of Martaban, whereas the rest settled offshore near the edge of the continental shelf (Ramaswamy et al., 2008). The average primary productivity of the Andaman Sea is presently rather low with approximately 6×10^7 tons of C/yr (Qasim, 1977). However, the biogenic productivity at about 10–8 Ma ago was higher than at present (Gupta et al., 2004).

3. Method and depth accuracy testing

Bathymetric data of the Thai EEZ on the outer shelf and upper slope of the Andaman Sea were collected during two cruises of Thai RV Chakratong Tongyai in November–December 2006 and October–November 2007 using a pole-mounted Seabeam 1050 system with 50 kHz transducers. The investigated area comprises water depths ranging between 500 and 1600 m. During the first cruise in 2006 some of the staves of the multibeam transducers were damaged so that several beams did not provide useful data. In addition, vibrations of the pole supporting the multibeam transducers limited the range of the multibeam system to generally less than 1500 m water depth. The multibeam data were processed using MB-System (Caress and Chayes, 2004) and displayed using Generic Mapping Tool-GMT (Wessel and Smith, 1998). In addition to multibeam data, 4–12 kHz subbottom profiler records were obtained with an INNOMAR SES2000 medium system. The records were processed and analyzed by using the traditional SES software and subsequently imported into KINGDOM Suite. However, the sandy sediments of the Andaman Sea prevented good penetration of the parametric signal.

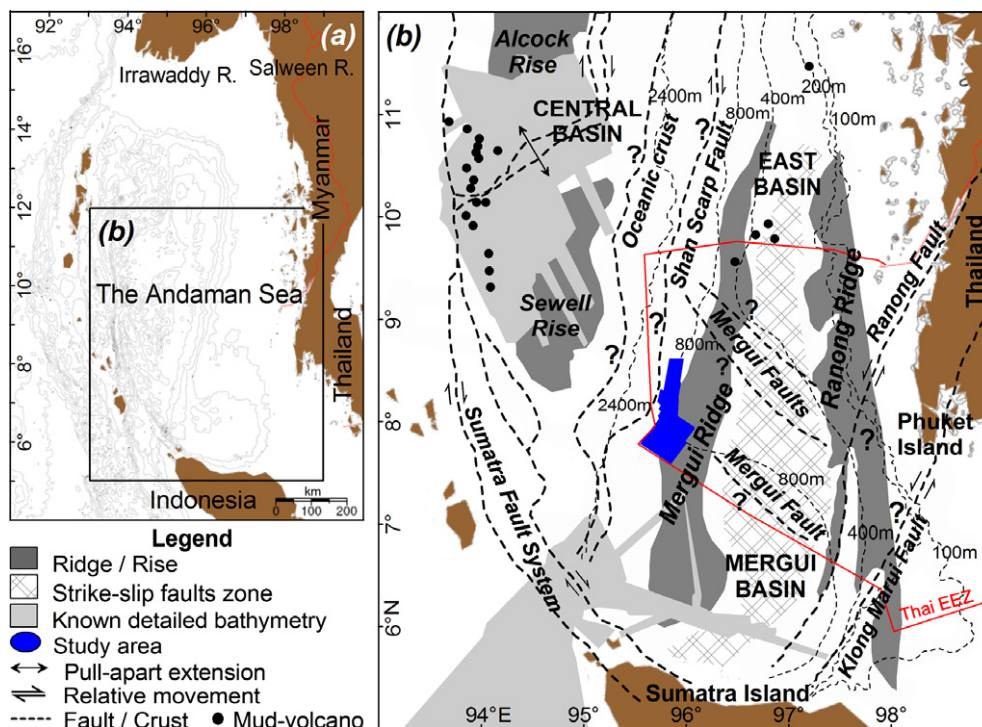


Fig. 1. (a) Location of study area in the Andaman Sea of the northeastern Indian Ocean. (b) Synthesis tectonic map of the East Andaman Basin redrawn from Curray (2005) showing pull-apart extension fault in the Central Basin (Raju et al., 2004), strike slip faults with their approximate positions such as the Shan Scarp Fault and the Mergui Faults in the East Basin, strike-slip faults zone between Mergui Ridge and Ranong Ridge, the Ranong and the Klong Marui Fault (Richter et al., 1993; Polachan and Racey, 1993; Curray, 2005), and known detailed bathymetry (Raju et al., 2004; Krabbenhoft et al., 2010). Boundary of Thai EEZ is shown by red line. (For interpretation of the references to color in this figure legend, the reader is referred to the web version of this article.)

The depth accuracy tests revealed that 95% of the processed grids obtained values equal or better than 1% of water depth, which is acceptable for the generation of a final grid (Beyer et al., 2003, 2005; de Alteriis et al., 2003) when grid resolution has been set to 50 m (Fig. 2). The depth accuracy of the instrument can also be linked to the standard deviation, thus the values should vary between 5 and 16 m height. This test reveals that 95% of the grid cells obtained standard deviations better than 16 m height.

4. Results

The bathymetry and subbottom profiles allow the characterization of gradients of the upper slope and reveal several previously unknown prominent features (Fig. 3). On N–S profiles (Fig. 4a), the outer shelf, lying in 500–600 m water depth, is rather smooth and slightly inclined southward with a gradient of less than 0.08° . In contrast, the upper slope comprises several escarpments and gullies or possible heads of submarine canyons. Slope inclination angles on E–W profiles (Fig. 4b) allow dividing the slope into two zones; the upper slope and the middle slope. The upper slope comprises the area on the southern end of the investigated area where the gradient is approximately 1° at 700–1200 m water

depth, and the northern part of the shelf where gradients range between 1.5° and 2.2° at 600–900 m. The middle slope covers the area where gradients vary from 3° along the southern part at 900–1300 m water depth to 4.8° further north.

Several prominent features are observed in the study area. These include; fault traces, an area comprising small slumps, various indications of gases and fluids in the shallow sub-surface, various escarpments and gullies on the continental slope (Fig. 3), a possible submarine landslide (Fig. 5), a possible mud-dome (Fig. 7), three large plateaus protruding more than 50 m above the ocean floor on the smooth outer shelf and a possible giant pockmark (Fig. 8).

4.1. Submarine landslides and slope failures

At location $8^\circ 12.94'N$ and $95^\circ 48.80'E$ the bathymetric data show evidence for a possible submarine landslide occurring on the slope at a water depth of roughly 945 m. The trapezoid-like slide scar is oriented in an E–W direction and incises as much as 25 m into the underlying sediments (Fig. 5a). Surface extent of the failure is approximately 1100 m width and 800 m length (Fig. 5b) resulting in a volume of roughly $2.2 \times 10^7 \text{ m}^3$ of failed

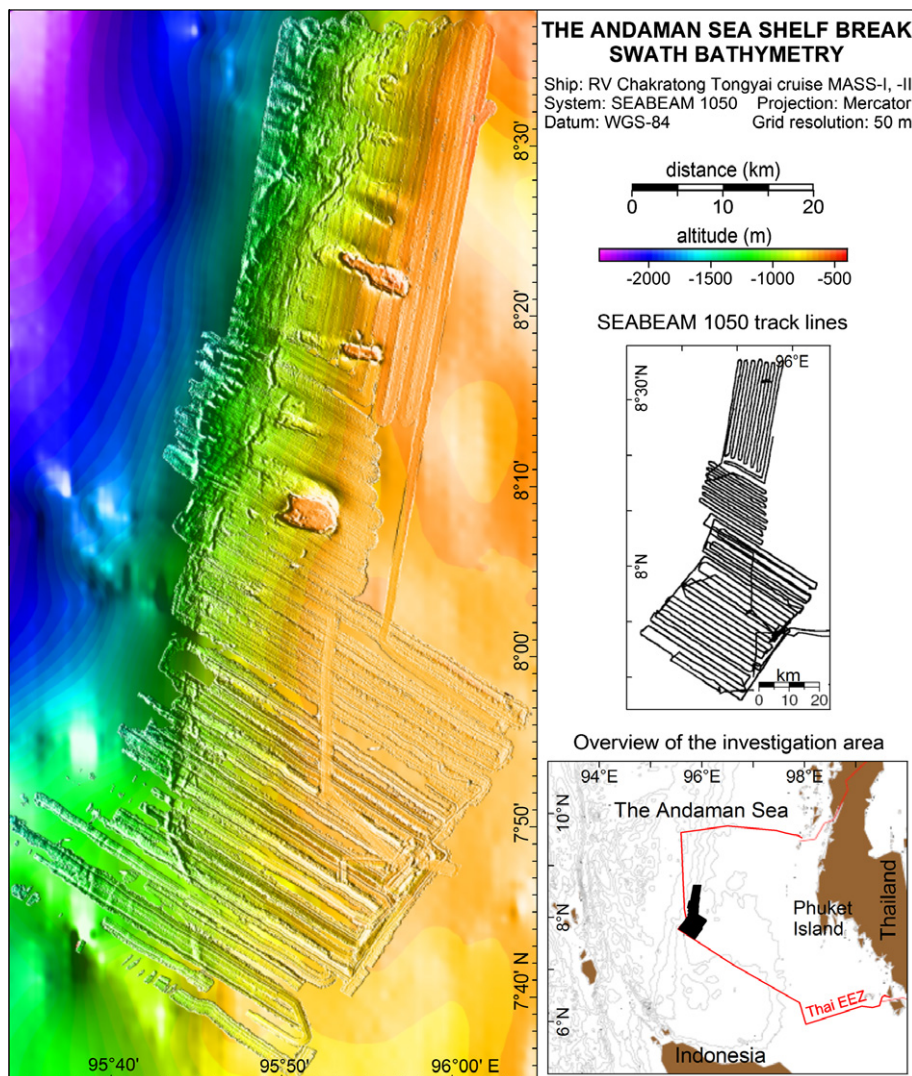


Fig. 2. Detailed bathymetry of the upper slope of the Andaman Sea outer shelf overlain on GEBCO 30 arc-second (The GEBCO_08 Grid, 2009) is shown by color-shaded relief map.

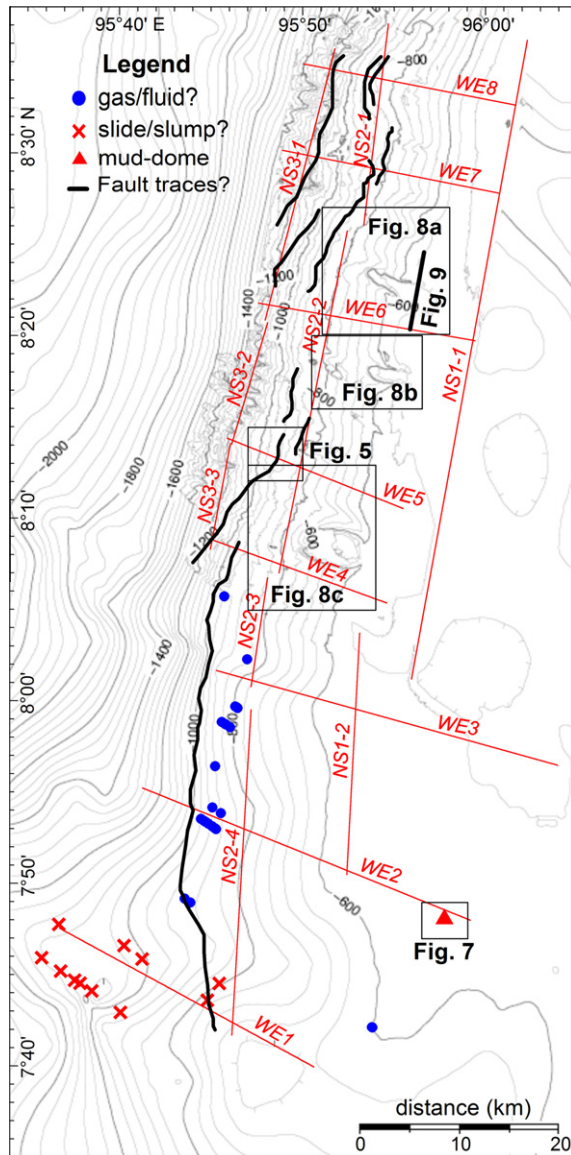


Fig. 3. Interpretation of the bathymetry and subbottom profiles showing prominent features including a mud-dome, a possible slide, three large plateaus, drawn lines of escarpments, and an area comprising gaseous sediments or fluids and slumps. Contour interval is 40 m.

sediment. A subbottom profile across the area (Fig. 5c) indicates different phases of failure processes. The first slide scar is about 13 m height, followed by a second slide scar of 10 m height. About 2.5 km downslope of the main scarp, convex-upward slope profiles probably correspond to the deposits from this sediment failure. The echo-character of these deposits (Fig. 5c) shows weak, transparent subbottom reflections that could represent sediment flows and their deposits (Pratson and Laine, 1989).

In addition, eleven other locations of possible small slides/slumps are observed on subbottom profiler records from the southwestern end of the study area (Fig. 3) where slope gradients are approximately 1° . Although the area is rather smooth, slides occurring on similar slopes have been reviewed (Hampton et al., 1996). Their sizes vary between 500 and 1000 m long and 10–20 m high. Distributions of the slides/slumps cover an area of approximately 200 km². The echo character is a distinct, continuous, steeply dipping bottom echo with dipping subbottom reflectors. The echo type is classified as quiescent hemipelagic sedimentation by combined processes and/or slump deposited by mass wasting (Pratson and Laine, 1989).

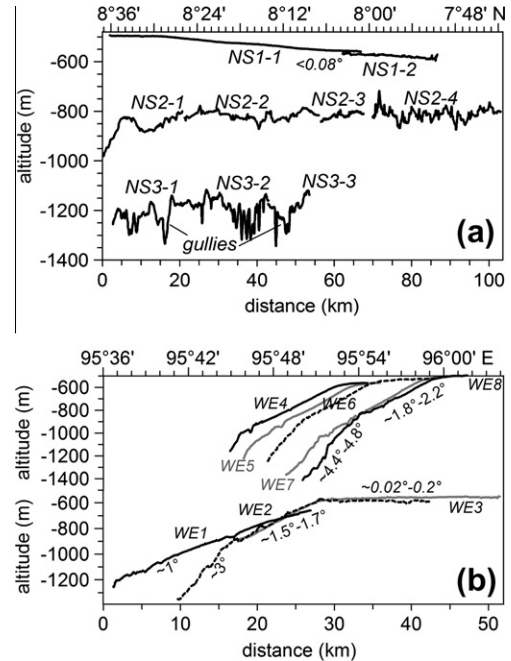


Fig. 4. (a) Latitudinal (NS1-1 to NS3-3) and (b) longitudinal profiles (WE1 to WE8) show the general morphological trends of the Andaman Sea outer shelf and upper slope. For profile locations refer to Fig. 3.

4.2. Fault traces

On the outer shelf and upper slope, longitudinal escarpments generally stretching N–S are observed (Fig. 3). The escarpments are contour parallel and occur in water depths between 600 and 1300 m. The escarpments are not uniform in height and continuous, but separated into various sizes of escarpments. Their sizes vary from few kilometers to more than twenty kilometers in length with a height of tens of meters. Although available data do not allow clear identification of the nature of these features, they most likely represent the seafloor expression of normal or strike-slip faults related to the opening of the Andaman Basin.

4.3. Fluid flow features

At least 24 locations show evidence of possible gas or fluid accumulation below the seafloor in the southwestern part of the study area (Fig. 3) in water depths of about 950 m. Anomalous features such as dome-shaped structures beneath the seafloor (Fig. 6a) are visible on subbottom profiler records. The domes have at least 10 m relief height and 200 m width, but could be much larger, as the deeper structure is not resolved with the present subbottom profiler data. On top of the domes, negative polarity reflections are shown in blue, while bottom reflections and subbottom reflectors are shown in red, point to the presence of gas or fluid beneath seafloor (Fig. 6b).

A sub-circular mound-like feature is observed at $7^\circ48.04'N$ and $95^\circ57.80'E$ in a water depth of about 500 m (Fig. 7a). Surface profiles traced over the dome with a dimension of about 900 m length (profile aa'), 40 m height (profile bb'), and 400 m width (profile cc') reveal that the dome is not a complete circle, but stretched in a NE–SW direction (Fig. 7b). In addition at $7^\circ48.19'N$ and $95^\circ57.75'E$, one subbottom profile showed another tiny dome north of the actual mound. The size of this dome is approximately 20 m height and 400 m length. Strong subbottom echoes and echoes in the water column suggest that sediments are gas-charged in the vicinity of

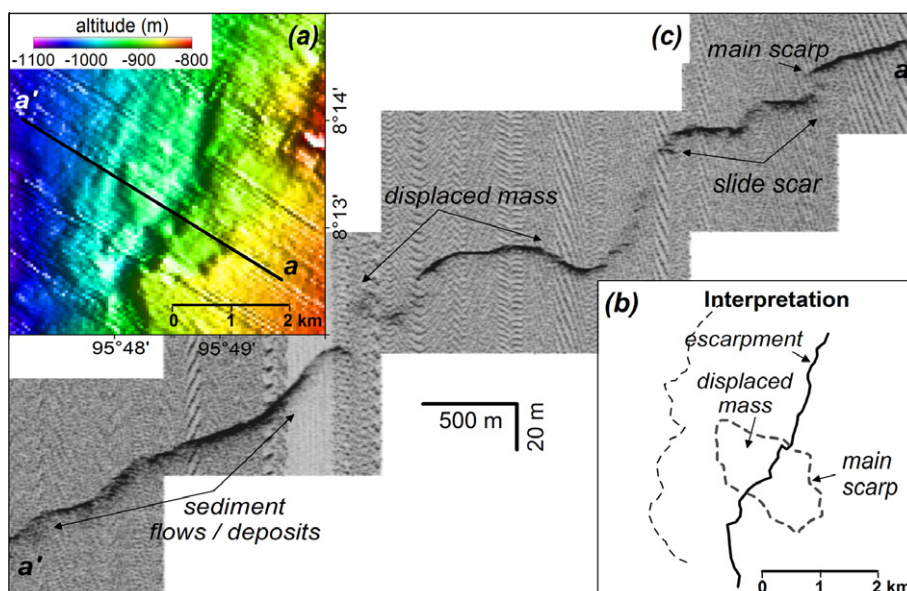


Fig. 5. (a) Color-coded shaded relief map and (b) interpretation showing a possible submarine landslide. (c) Subbottom profiler records along profile aa' show slide scar and convex-upward slopes that could represent displaced mass and slide deposits.

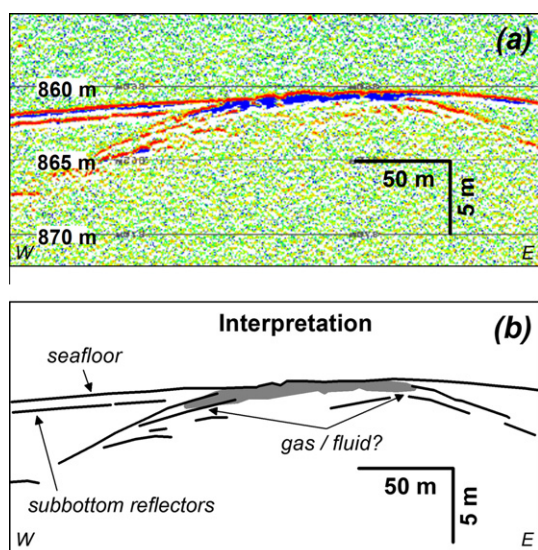


Fig. 6. (a) Subbottom profiler records at location 7°58.6'N and 95°45.97'E and (b) interpretation of possible gas or fluid occurrence.

the mound and that gas may even escape into the water column (Fig. 7c).

4.4. Plateaus

The most striking features that were discovered by the new, detailed bathymetry are three plateau-like structures between 8°07' to 8°24'E and 95°50' to 95°57'N (Fig. 8). The northernmost plateau (Fig. 8a) has an elliptical shape and covers an area of approximately 2×8 km. The middle plateau (Fig. 8b) is about 2×4 km in dimension, and the southern oval-like plateau (Fig. 8c) covers an area of approximately 4×6 km. The plateaus have an almost flat top, but are slightly inclined westward. The edges of the plateaus are bounded by rather steep vertical slopes with relief heights of about 50 m towards the shelf and exceed more than 200 m towards the

slope, i.e. at their western end. Although the three plateaus have many features in common, there are distinct differences. All plateaus show the presence of cracks around their edges and deep moats surrounding them. The moat is actually much wider and more pronounced for the southern plateau. This plateau also shows the smoothest surface except for the southwestern quadrant that displays the presence of several sub-rounded depressions (Fig. 8c). The middle and northern plateaus show a rather smooth surface on their western half while the eastern half is more irregular (Figs. 8a and 8b). These two plateaus also show an irregular, hummocky surface at the western down-dip slope in the continuation of the plateaus that could represent slump deposits from disintegration of part of the plateaus. However, unequivocal interpretation of the observed features is not possible with the current data set. Finally, a possible pockmark is recognized just north of the middle plateau at 8°18.90'N and 95°54.64'E (Fig. 8b). This giant pockmark covers an area on approximate of 1×0.3 km and incises to a depth of 30 m.

5. Discussions

The relatively steep slope of the Andaman Sea outer shelf and upper slope within the Thai EEZ presents many features that are prerequisites for the generation of large submarine landslides (Hampton et al., 1996; Mulder and Cochonat, 1996). These features include rapid sedimentation originating from the Irrawaddy River, the expulsion of gases and fluids, and the occurrence of large earthquakes at close distance. However, close analysis of the detailed bathymetric data presented in this paper, shows only one distinct submarine landslide located at 8°12.94'N and 95°48.80'E (Fig. 5), and even this potential submarine landslide only involved 2.2×10^7 m³ of sediment. Based on the morphology of the mass failure, the Skempton ratio between the depth ($H = 85$ m) and the length ($L = 2240$ m) of the slide, together with the character of the slump or slide, is generally used for the classification of the mass failures. The ratio which is estimated from subbottom profiler records is $H/L = 0.04$, suggesting that the mass failure corresponds to a translational submarine landslide (Mulder and

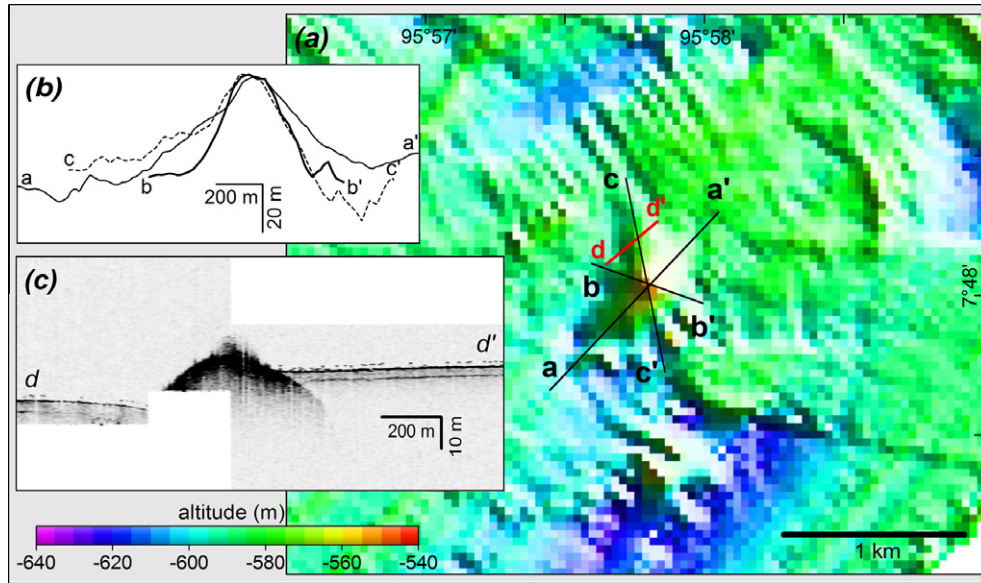


Fig. 7. (a) Bathymetry of a mound shown by color-shaded relief map and (b) three surface profiles aa', bb', cc'. (c) Subbottom profiler records along profile dd' of a possible mud-dome.

Cochonat, 1996). Could such the landslide generate a tsunami wave?

The theoretical tsunami wave length and maximum amplitude directly over the slope failure generated by disintegrative submarine landslides can be calculated by the semi empirical equations proposed by Watts et al. (2003) and McAdoo and Watts (2004), but the formulae do not include tsunami propagation and run-up along shore.

$$\lambda_l = 3.87(bd/\sin\theta)^{0.5} \quad (1)$$

$$A_l = 0.224T[w/(w+\lambda)][(\sin\theta)^{1.29} - 0.746(\sin\theta)^{0.29} + 0.170(\sin\theta)^{3.29}](b/d)^{1.25} \quad (2)$$

where b is the initial length of the failure perpendicular to the margin, w the initial width of failure parallel to the margin, θ the mean slope of the failure scar, T the maximum initial thickness of the failure normal to the slope and d the initial water depth at the center of the failure. The landslide is assumed as thin, linear slides with no basal friction and strong fluid dynamic drag. Intrinsic amplitude accuracy regarding the equation is $\pm 5.3\%$. The results show that the observed landslide would have generated a tsunami wave of about 4450 m wave length and with a maximum wave height of about 0.12 m. These initial wave characteristics could be input criteria for tsunami propagation models (Synolakis et al., 2002; Brune et al., 2009) in order to calculate wave propagation and potential onshore run-up. However, the small initial wave height already indicates that the observed submarine landslide could not generate a devastating tsunami on the coast. It is consequently unlikely that submarine sliding has contributed to the tsunami hazard along the Andaman Sea coast in the recent geological past. Similar conclusions have been drawn by Brune et al. (2009) who also found only small landslides offshore West Sumatra. However, the presence of the landslide indicates the existence of upper slope instability. The reason for the absence of large, tsunami-generating landslides might be found in the nature of the sediments at the Andaman Sea outer shelf and upper slope. Both subbottom profiler records (Fig. 5c) and published data from Rodolfo (1969) suggest the presence of sandy deposits that would be well drained precluding the build-up of overpressure.

Another point that needs to be discussed is the nature of the three prominent plateaus on the outer Andaman shelf. Morphologically, the plateaus resemble guyots, i.e. drowned coral atolls. However, irregular surfaces on the eastern part of the middle and northern plateaus are not consistent with this interpretation. Sub-bottom profiler records over the plateaus (Fig. 9) show prolonged echoes of about 10 m of thickness with no subbottom reflectors. This echo type could be interpreted as coarse-grained sediment cover on top of the plateau similar to echo-type defined by Damuth (1980) for 3.5 kHz echograms. Sediments covering the Mergui Ridge consist of sand and foraminiferal ooze or sandstone and coral reef limestone (Rodolfo, 1969; Polachan and Racey, 1993; Saidova, 2008). Consequently, we interpret the plateaus as old coral structures or atolls that are blanketed by sediment deposits. The edges of the plateaus show numerous signs of disintegration of already consolidated deposits. Additional data are clearly required in order to clarify the nature and evolution of these structures.

6. Conclusions

New detailed bathymetric data of the Andaman Sea outer shelf and upper slope of the Thai EEZ derived from multibeam swath mapping allow generating a final grid with 50 m grid cell spacing. The new map allowed the identification of several previously unknown features such as mud-domes, three large plateaus that most likely represent oceanic guyots, and allowed the characterization of potential submarine landslides. In addition, the new bathymetry will help improving tsunami wave propagation models and impact assessment.

One possible translational submarine landslide of 1100 m length, 800 m width and 25 m height is identified on the upper slope. Based on the geometry of the failed mass, a tsunami wave length of about 4450 m and a maximum tsunami wave height of about 0.12 m directly above the slide are computed following semi empirical equations. The Andaman Sea upper slope consequently does not show evidence for potential recent submarine landslides that could have been the source for generating tsunamis. However, the presence of submarine landslide suggested widespread instability of the upper slope.

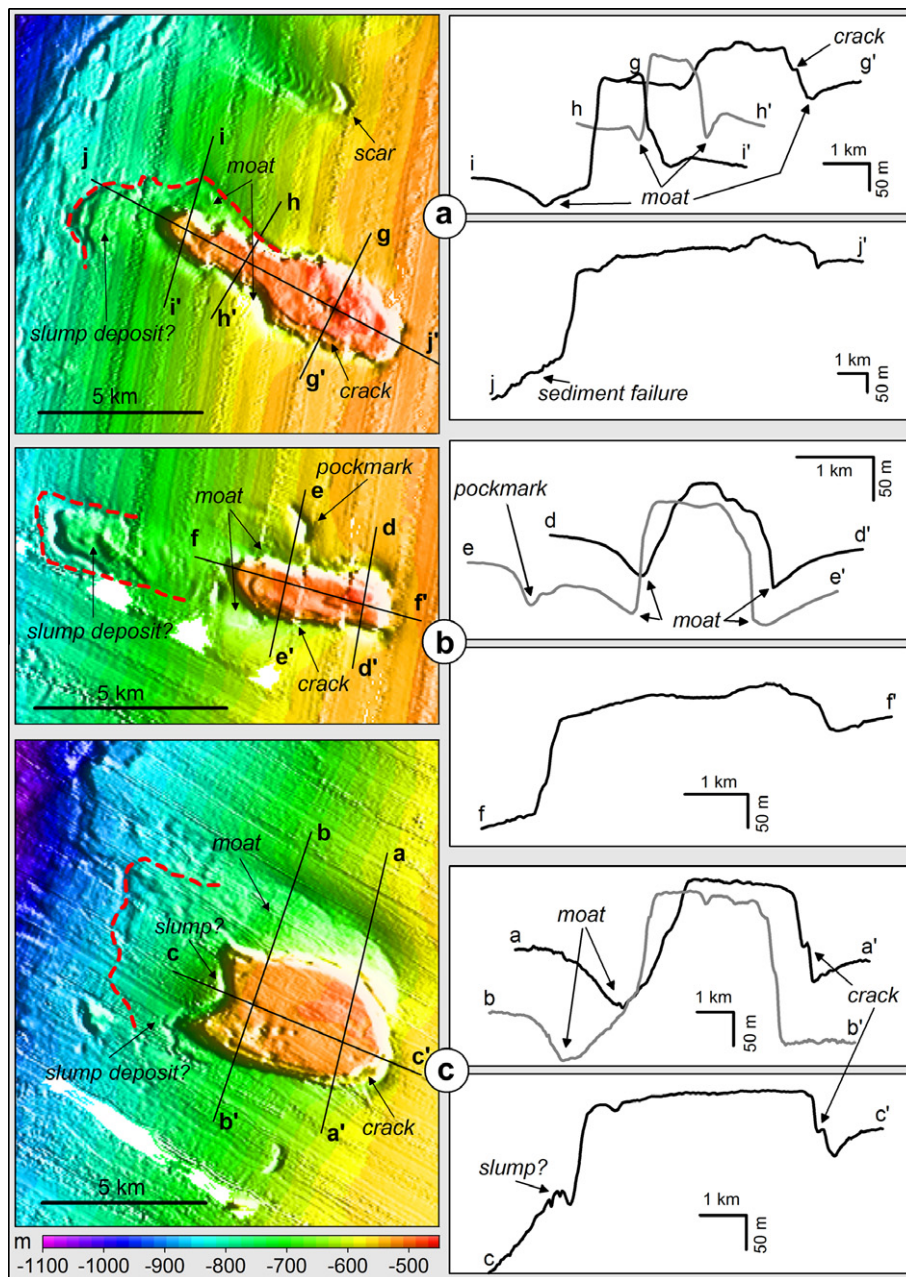


Fig. 8. (a) Morphology of the northern plateau, (b) the middle plateau, (c) and the southern plateau are shown by bathymetry and their surface profiles. The boundaries of possible sediment failure deposits are marked by red dots. (For interpretation of the references to color in this figure legend, the reader is referred to the web version of this article.)

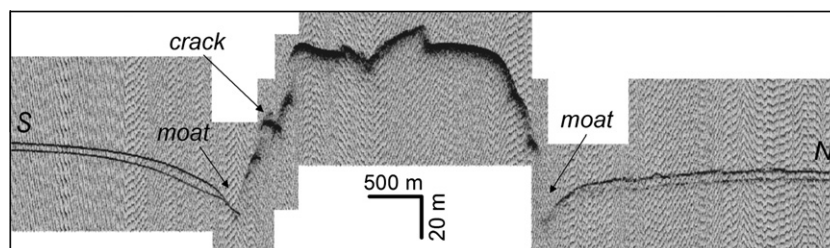


Fig. 9. Subbottom profiler records over the northern plateau shows possible coarse-grained sediment covering on top of the northern plateau. For profile locations refer to Fig. 3.

The exact nature of many of the observed features could not be clarified with the existing data set. Additional data including high-resolution seismic data are required to decipher the history of the Andaman Sea outer shelf region.

Acknowledgements

The authors would gratefully acknowledge financial support jointly by the German Research Foundation (DFG) and the National Research Council of Thailand (NRCT). The United Nations University, Institute for Environment and Human Security (UNU-EHS) for providing a PhD scholarship to the first author. Warner Brückmann, Christian Hensen, Suratta Bunsomboonsakul, Capt. Chonwat Singnu and his crews are thanked for their help in making the cruises a success.

References

- Bertrand, G., Rangin, C., 2003. Tectonics of the western margin of the Shan plateau (central Myanmar): implication for India-Indochina oblique convergence since the Oligocene. *Journal of Asian Earth Sciences* 21, 1139–1157.
- Beyer, A., Schenke, H.W., Klenke, M., Niederjaspert, F., 2003. High resolution bathymetry of the eastern slope of the Porcupine Seabight. *Marine Geology* 198, 27–54.
- Beyer, A., Rathlau, R., Schenke, H.W., 2005. Multibeam bathymetry of the Håkon Mosby mud volcano. *Marine Geophysical Researches* 26, 61–75.
- Brune, S., Ladage, S., Babeyko, A.Y., Müller, C., Kopp, H., Sobolev, S.V., 2009. Submarine landslide at the eastern Sunda margin: observations and tsunami impact assessment. *Natural Hazards and Earth System Sciences* 54 (2), 547–562.
- Caress, D.W., Chayes, D.N., 2004. MB-System Version 5 Open source software distributed at <<http://www.ldeo.columbia.edu/MB-System/>> and <<http://www.mbari.org/data/mbsystem/>>.
- Choochong, M., Murakoshi, N., Hisada, Ken-ichiro, Charusiri, P., Charoentitirat, T., Chutakositkanon, V., Jankaew, K., Kanjanapayont, P., Phantuwongraj, S., 2008. 2004 Indian Ocean tsunami inflow and outflow at Phuket, Thailand. *Marine Geology* 248, 179–192.
- Cochard, R., Ranamukhaarachchi, S.L., Shivakoti, G.P., Shipin, O.V., Edwards, P.J., Seeland, K.T., 2008. The 2004 tsunami in Aceh and Southern Thailand: a review on coastal ecosystems, wave hazards and vulnerability. *Perspectives in Plant Ecology, Evolution and Systematics* 10, 3–40.
- Curry, J.R., 2005. Tectonics and history of the Andaman Sea region. *Journal of Asian Earth Sciences* 25, 187–232.
- Damuth, J.E., 1980. Use of high-frequency (3.5–12 kHz) echograms in the study of near-bottom sedimentation processes in the deep-sea: a review. *Marine Geology* 38, 51–75.
- de Alteriis, G., Passaro, S., Tonielli, R., 2003. New, high resolution swath bathymetry of Gettysburg and Ormonde seamounts (Corring Bank, eastern Atlantic) and first geological results. *Marine Geophysical Researches* 24, 223–244.
- Eguchi, T., Uyeda, S., Maki, T., 1979. Seismotectonics and tectonic history of the Andaman Sea. *Tectonophysics* 57, 35–51.
- Geist, E.L., Titov, V.V., Arcas, D., Pollitz, F.F., Bilek, S.L., 2007. Implications of the 26 December 2004 Sumatra–Andaman Earthquake on tsunami forecast and assessment models for great subduction-zone earthquakes. *Bulletin of the Seismological Society of America* 97 (1A), 249–270.
- Ghobarah, A., Saatcioglu, M., Nistor, I., 2006. The impact of the 26 December 2004 earthquake and tsunami on structures and Infrastructure. *Engineering Structures* 28, 312–326.
- Gupta, A.K., Singh, R.K., Joseph, S., Thomas, E., 2004. Indian Ocean high-productivity event (10–8 Ma): linked to global cooling or to the initiation of the Indian Monsoon? *Geology* 32, 753–756.
- Hampton, M.A., Lee, H.J., Locat, J., 1996. Submarine landslides. *Reviews of Geophysics* 34 (1), 33–59.
- IOC, IHO and BODC, 2003. Centenary Edition of the GEBCO Digital Atlas, published on CD-ROM on behalf of the Intergovernmental Oceanographic Commission and the International Hydrographic Organization as part of the General Bathymetric Chart of the Oceans. British Oceanographic Data Centre, Liverpool, U.K. See <<http://www.bodc.ac.uk/projects/gebco/>> and <<http://www.ngdc.noaa.gov/mgg/gebco/gebco.html>>.
- Kietpawpan, M., Visuthimajarn, P., Tanavud, C., Robson, M.G., 2008. Method of calculating tsunami travel times in the Andaman Sea region. *Natural Hazards* 46, 89–106.
- Kowalik, Z., Knight, W., Logan, T., Whitmore, P., 2005. Numerical modeling of the global tsunami: Indonesian tsunami of 26 December 2004. *Science of Tsunami Hazards* 23 (1), 40–56.
- Krabbenhoft, A., Weinrebe, R.W., Kopp, H., Flueh, E.R., Ladage, S., Papenberg, C., Planert, L., Djajadihardja, Y., 2010. Bathymetry of the Indonesian Sunda margin-relating morphological features of the upper plate slopes to the location and extent of the seismogenic zone. *Natural Hazards and Earth System Sciences* 10, 1899–1911.
- Kumar, S., 1981. Geodynamics of Burma and Andaman–Nicobar region, on the basis of tectonic stresses and regional seismicity. *Tectonophysics* 79, 75–95.
- Lay, T., Kanamori, H., Ammon, C.J., Nettles, M., Ward, S.N., Aster, R.C., Beck, S.L., Bilek, S.L., Brudzinski, M.R., Butler, R., DeShon, H.R., Ekstroem, G., Satake, K., Sipkin, S., 2005. The Great Sumatra–Andaman Earthquake of 26 December, 2004. *Science* 308, 1127–1133.
- López-Venegas, A.M., ten Brink, U.S., Geist, E.L., 2008. Submarine landslide as the source for the October 11, 1918 Mona Passage tsunami: observations and modelling. *Marine Geology* 254, 35–46.
- McAdoo, B.G., Watts, P., 2004. Tsunami hazard from submarine landslides on the Oregon continental slope. *Marine Geology* 203, 235–245.
- McMurtry, G.M., Watts, P., Fryer, G.J., Smith, J.R., Imamura, F., 2004. Giant landslides, mega-tsunamis, and paleo-sea level in the Hawaiian Islands. *Marine Geology* 203, 219–233.
- Mitchell, A.H.G., 1992. Late Permian–Mesozoic events and the Mergui Group Nappe in Myanmar and Thailand. *Journal of Southeast Asian Earth Sciences* 7 (2/3), 165–178.
- Mulder, T., Cochonat, P., 1996. Classification of offshore mass movements. *Journal of Sedimentary Research* 66 (1), 43–57.
- Polachan, S., Racey, A., 1993. Lower Miocene larger foraminifera and petroleum potential of the Tai Formation, Mergui Group, Andaman Sea. *Journal of Southeast Asian Earth Sciences* 8 (1–4), 487–496.
- Pratson, L.F., Laine, E.P., 1989. The relative importance of gravity-induced versus current-controlled sedimentation during the Quaternary along the Mideast US outer continental margin revealed by 3.5 kHz echo character. *Marine Geology* 89, 87–126.
- Qasim, S.Z., 1977. Biological productivity of the Indian Ocean. *Indian Journal of Marine Science* 6, 122–137.
- Raju, K.A.K., Ramprasad, T., Rao, P.S., Rao, B.R., Varghese, J., 2004. New insights into the tectonic evolution of the Andaman basin, northeast Indian Ocean. *Earth and Planetary Science Letters* 221, 145–162.
- Ramaswamy, V., Gaye, B., Shirolkar, P.V., Rao, P.S., Chivas, A.R., Wheeler, D., Thwin, S., 2008. Distribution and sources of organic carbon, nitrogen and their isotopic signatures in sediments from the Ayeyarwady (Irrawaddy) continental shelf, northern Andaman Sea. *Marine Chemistry* 111, 137–150.
- Rao, P.S., Ramaswamy, V., Thwin, S., 2005. Sediment texture, distribution and transport on the Ayeyarwady continental shelf, Andaman Sea. *Marine Geology* 216, 239–247.
- Richter, B., Fuller, M., Schmidtke, E., Myint, U.T., Ngwe, U.T., Win, U.M., Bunopas, S., 1993. Paleomagnetic results from Thailand and Myanmar: implications for the interpretation of tectonic rotations in Southeast Asia. *Journal of Southeast Asian Earth Sciences* 8 (1–4), 247–255.
- Rodolfo, K.S., 1969. Sediments of the Andaman Basin, Northeastern Indian Ocean. *Marine Geology* 7, 371–402.
- Saidova, Kh.M., 2008. Benthic Foraminifera Communities of the Andaman Sea (Indian Ocean). *Oceanology* 48 (4), 517–523.
- Smith, W.H.F., Sandwell, D.T., 1997. Global sea floor topography from satellite altimetry and ship depth soundings. *Science* 277, 1956–1962.
- Smith, D.E., Shi, S., Cullingford, R.A., Dawson, A.G., Dawson, S., Firth, C.R., Foster, I.D.L., Fretwell, P.T., Haggart, B.A., Holloway, L.K., Long, D., 2004. The Holocene Storegga Slide tsunami in the United Kingdom. *Quaternary Science Reviews* 23, 2291–2321.
- Synolakis, C.E., Bardet, J.P., Borrero, J.C., Davies, H.L., Okal, E.A., Silver, E.A., Sweet, S., Tappin, D.R., 2002. The slump origin of the 1998 Papua New Guinea Tsunami. *Proceedings of the Royal Society A* 458, 763–789.
- The GEBCO_08 Grid, 2009. The GEBCO_08 Grid version 20090202. <<http://www.gebco.net>>.
- Velmurugan, A., Swarnam, T.P., Ravisankar, N., 2006. Assessment of tsunami impact in south Andaman using remote sensing and GIS. *Journal of the Indian Society of Remote Sensing* 34 (2), 193–202.
- Watts, P., Grilli, S.T., Kirby, J.T., Fryer, G.J., Tappin, D.R., 2003. Landslide tsunami case study using a Boussinesq model and a fully nonlinear tsunami generation model. *Natural Hazards and Earth System Sciences* 3, 391–402.
- Wessel, P., Smith, W.H.F., 1998. New improved version of generic mapping tools release. *EOS Transactions American Geophysical Union* 79 (47), 579.



Submarine mass wasting and associated tsunami risk offshore western Thailand, Andaman Sea, Indian Ocean

J. M. Schwab¹, S. Krastel¹, M. Grün¹, F. Gross¹, P. Pananont², P. Jintasaeranee³, S. Bunsomboonsakul⁴, W. Weinrebe¹, and D. Winkelmann¹

¹GEOMAR | Helmholtz Centre for Ocean Research Kiel, Germany

²Department of Earth Sciences, Faculty of Science, Kasetsart University, Bangkok, Thailand

³Department of Aquatic Science, Burapha University, Chonburi, Thailand

⁴Thailand Southeast Asia START Regional Center, Chulalongkorn University, Bangkok, Thailand

Correspondence to: J. M. Schwab (jschwab@geomar.de)

Received: 23 March 2012 – Revised: 30 June 2012 – Accepted: 23 July 2012 – Published: 17 August 2012

Abstract. 2-D seismic data from the top and the western slope of Mergui Ridge in water depths between 300 and 2200 m off the Thai west coast have been investigated in order to identify mass transport deposits (MTDs) and evaluate the tsunamigenic potential of submarine landslides in this outer shelf area. Based on our newly collected data, 17 mass transport deposits have been identified. Minimum volumes of individual MTDs range between 0.3 km³ and 14 km³. Landslide deposits have been identified in three different settings: (i) stacked MTDs within disturbed and faulted basin sediments at the transition of the East Andaman Basin to the Mergui Ridge; (ii) MTDs within a pile of drift sediments at the basin-ridge transition; and (iii) MTDs near the edge of/on top of Mergui Ridge in relatively shallow water depths (< 1000 m). Our data indicate that the Mergui Ridge slope area seems to have been generally unstable with repeated occurrence of slide events. We find that the most likely causes for slope instabilities may be the presence of unstable drift sediments, excess pore pressure, and active tectonics. Most MTDs are located in large water depths (> 1000 m) and/or comprise small volumes suggesting a small tsunami potential. Moreover, the recurrence rates of failure events seem to be low. Some MTDs with tsunami potential, however, have been identified on top of Mergui Ridge. Mass-wasting events that may occur in the future at similar locations may trigger tsunamis if they comprise sufficient volumes. Landslide tsunamis, emerging from slope failures in the working area and affecting western Thailand coastal areas therefore cannot be excluded, though the probability is very small compared to the probability of earthquake-triggered tsunamis, arising from the Sunda Trench.

1 Introduction

The extremely catastrophic tsunamis of December 2004 in the SE Indian Ocean and March 2011 in Japan, as well as many other incidents (NGDC/WDC Global Tsunami Event Database, 2012), show that tsunamis pose a major threat to low-lying coastal areas. Ocean-wide tsunamis are predominantly triggered by earthquakes, but submarine landslides are also known for their potential to trigger regional tsunamis of significant wave heights (Ward, 2001; Harbitz et al., 2006). A well-studied prehistoric example of a landslide-triggered tsunami is the Storegga Slide offshore Norway (Jansen et al., 1987; Dawson et al., 1988; Bondevik et al., 1997, 2005). Tsunami deposits associated with the Storegga Slide were reported from Iceland, Norway, Scotland and the Shetland Islands with run-up heights exceeding 20 m in places (Bondevik et al., 2003). Moreover, several recent examples for locally destructive tsunami hazards were associated with submarine landslides, such as the Grand Banks tsunami (1929, Canada) that killed 28 people (Hasegawa and Kanamori, 1987; Piper et al., 1999; Fine et al., 2005), a tsunami at Skagway Harbor (1994, Alaska) with one casualty (Kulikov et al., 1996) and the Sissano or Aitape tsunami (1998, Papua New Guinea) causing about 2000 fatalities (Tappin, 1999; Tappin et al., 2001; Matsumoto and Tappin, 2003). Extensive research and modeling of landslide tsunami generation has been undertaken (Ward, 2001; Harbitz et al., 2006; Grilli et al., 2009; Weiss et al., 2009). However, early warning of landslide tsunami hazards is difficult due to the fact that seismological (Lomax et al., 2007) or GPS (Blewitt et al., 2006; Sobolev et al., 2007) techniques,

applicable to earthquake induced tsunamis, are not useful to detect landslide-generated tsunamis due to the comparably small amount of seismic energy release and long-period-signal of submarine landslides (Brune et al., 2009, 2010). Moreover, the time lag between sediment failure and tsunami arrival at the coast in the near field of a submarine landslide might be too small to forewarn and evacuate endangered regions (Biscontin et al., 2004).

It is therefore important to gain thorough knowledge on current stability of the continental slope for individual areas, in order to estimate frequencies and dimensions of failures and rate probability of future failures. This in turn can be used to assess tsunami risk and preparedness for corresponding coastal areas, such as the Thai Andaman Sea coast. The vicinity of this coast to the seismically highly active Sunda Trench (NGDC, Global Significant Earthquake Database, 2012) makes the area vulnerable to tsunamis. The geological record reveals recurrent tsunami events of destructive dimensions that struck the Thai west coast (Jankaew et al., 2008; Fujino et al., 2009). A potentially unstable continental slope off the Thai coast may pose an additional risk from submarine landslides, whether co-seismically triggered or triggered by other factors, provided that these failures would be of tsunamigenic dimensions. Assessing this risk is the central task of the MASS-project (Morphodynamics and Slope Stability of the Andaman Sea Shelf Break) in the frame of the Thai-German cooperation TRIAS (Tracing Tsunami impacts on- and offshore in the Andaman Sea Region).

Bathymetric and sub-bottom profiler data were obtained during the first project phases MASS I and MASS II. Jintasaerane et al. (2012) identified possible slumping areas, though these landslides are considered to be too small for having triggered a significant tsunami in the recent past. Jintasaerane et al. (2012), however, did not investigate older slope failures. New seismic data were collected during the MASS III research cruise in January 2011. These data are used in this study to trace landslide-related features in the subsurface in order to (1) identify areas that show indications of previous slope failure, (2) estimate volumes/dimensions of slides, (3) determine pre-conditioning and trigger mechanisms, and (4) assess the tsunamigenic potential of the detected landslides. The terms “landslide” and/or “mass transport deposit (MTD)” are used in this paper in a broad sense, denoting all types of gravitational mass wasting products, irrespective of the process.

2 Regional setting

The study area is situated at the western outer Sunda shelf in the southeastern part of the Andaman Sea backarc-basin, about 250 km off Phuket (Fig. 1). A basement high, the Mergui Ridge, forms the outer shelf break, where water depths increase from 300 to 2200 m in the working area. The Mergui Ridge separates two adjacent basins, the East Andaman

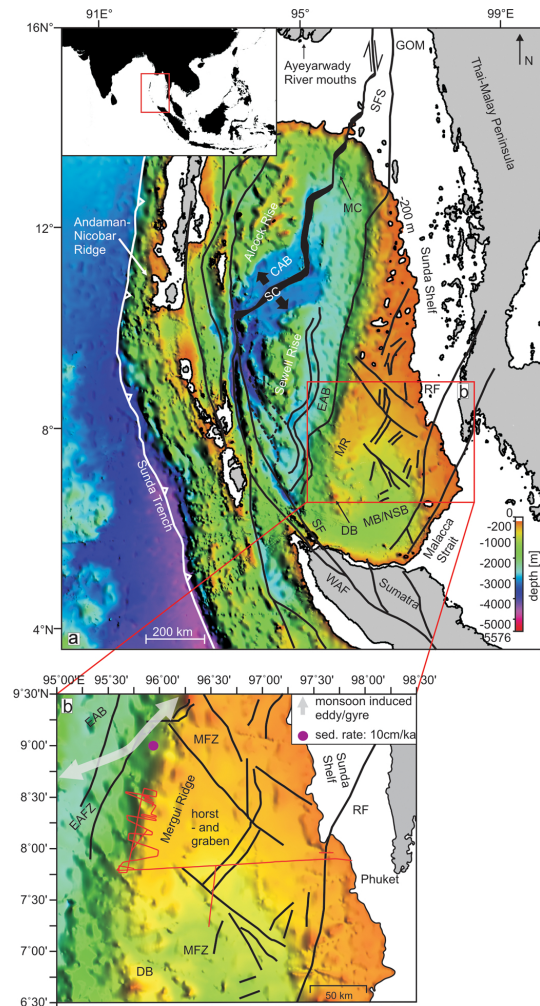


Fig. 1. (a) Bathymetric map and structural framework of the Andaman Sea area. The structural elements are modified from Curray (2005). Black continuous lines mark fault traces of the main fault systems: SFS: Sagaing Fault System; WAF: West Andaman Fault; RF: Ranong Fault; SF: Sumatra Fault System; GOM: Gulf of Martaban; MC: Martaban Canyon; SC: Modern spreading centre; CAB: Central Andaman Basin; EAB: East Andaman Basin; MR: Mergui Ridge; MB/NSB: Mergui Basin/North Sumatra Basin; DB: Dreadnought Bank. The bathymetry has been reproduced from GEBCO. (b) Close-up of the working area, situated in the western flank of Mergui Ridge. The red lines mark seismic lines of MASS III cruise. The black lines denote fault systems, modified after Curray (2005), Morley et al. (2011) and Polachan (1988). MFZ: Mergui Fault Zone (modified after Curray, 2005 and Morley et al., 2011). EAFZ: East Andaman Fault Zone (from Polachan, 1988). DB: Dreadnought Bank. EAB: East Andaman Basin. The grey arrow shows the approximate position of a monsoonal gyre that induces currents in deeper parts of the water column (modified after Varkey et al., 1996). The purple dot shows the position of a sediment core discussed by Rodolfo (1969). The bathymetry has been reproduced from SRTM30 PLUS (Becker et al., 2009).

Basin in the west and the Mergui Basin in the east and southeast (Fig. 1). The East Andaman Basin and the Mergui Basin are elongated, approximately NNE–SSW trending, sediment filled sub-basins of the Andaman Sea, located southwest of the Central Andaman Basin (Fig. 1, Curray, 2005). They have been described as rift basins (Hall and Morley, 2004; Jha et al., 2010), like numerous other Cenozoic basins across Sundaland (Polachan et al., 1991; Morley et al., 2001; Morley, 2002; Hall and Morley, 2004; Doust and Noble, 2008) and accordingly comprise a sedimentation history that is linked to typical rift stages (Doust and Noble, 2007; Doust and Sumner, 2008; Jha et al., 2010). The formation of the East Andaman Basin and the Mergui Basin results from backarc-related extensional tectonics, active throughout the area (Chakraborty and Khan, 2009; Curray, 2005). For the development of the Andaman Sea basins multi-stage models have been suggested (Kamesh Raju et al., 2004; Curray, 2005; Kamesh Raju, 2005; Chakraborty and Khan, 2009). The area of rifting moved from the Mergui Basin over the East Andaman Basin to its current position (Fig. 1) during Oligocene to Pliocene, due to increasingly oblique plate motions and changing convergence rates of Indian and Sundaland plates (Curray, 2005). In the Central Andaman Basin active sea floor spreading has occurred since 4 Ma (Kamesh Raju et al., 2004; Kamesh Raju, 2005; Khan and Chakraborty, 2009). This modern spreading center links a group of N–S striking dextral strike-slip faults (Sagaing Fault, West Andaman Fault and Sumatra Fault, Fig. 1a). This system is described to accommodate the oblique convergence of the Indian and Sundaland plates (Michel et al., 2001; Nielsen et al., 2004a; Curray, 2005; Socquet et al., 2006; Chakraborty and Khan, 2009).

The East Andaman Basin has been influenced by extensional and also strike-slip faulting. Kishore et al. (2010) described NE–SW trending extensional faults, truncated by N–S trending strike slip faults. W–NW facing listric block faulting at the western flank of Mergui Ridge was reported by Curray (2005). The general trend of main strike-slip faults in the East Andaman Basin area is N–S to NE–SW (Morley et al., 2011). The East Andaman Basin is bounded towards the Mergui Basin by the East Andaman Fault Zone (EAFZ, Fig. 1b), interpreted as a branch of the Sagaing Fault System (Polachan and Racey, 1994; Jha et al., 2010). North of the working area, the NW–SE trending strike-slip Mergui Fault is cutting across Mergui Ridge (Fig. 1b). Recent reactivation at this fault has been observed (Polachan and Racey, 1994).

The establishment of the Pliocene spreading center has been given as a reason for thermal subsidence of the area (Morley et al., 2011), which is still ongoing today (Lin et al., 2010). Moreover, right lateral movement along strike slip faults in the East Andaman Basin, such as the EAFZ, took place during the Late Miocene and caused subsidence and the development of mass wasting complexes west of the Mergui Ridge (Jha et al., 2010).

Today, the East Andaman Basin comprises a total sedimentary thickness of 4600 m (Curray, 2005). It is under a shallow- to deep- water regime since the Middle to Late Miocene (Curray, 2005; Jha, 2011) and post-rift sediments up to 2500 m thick have been deposited in this environment since the Middle Miocene (Jha et al., 2010). Presently, the main source for fine grained terrigenous sediment in the Andaman Sea is the Ayeyarwady-Salween river-system (Fig. 1a, Rodolfo, 1969; Colin et al., 1999). An enormous quantity of sediment is shed into the Andaman Sea (364 MT a^{-1} , Robinson et al., 2007), and a fraction of it reaches the deeper basins of the Andaman Sea via the Martaban Canyon (Fig. 1; Rao et al., 2005; Ramaswamy et al., 2004). An additional source of terrigenous input in the southern part of the Andaman Sea is the Malacca Strait (Fig. 1), delivering fine grained terrigenous detritus to the deeper parts of the Andaman Sea basins (Keller and Richards, 1967). Transport or deposition of terrigenous sediments on the outer shelf areas along Myanmar and the Thai-Malay peninsula (Sunda shelf, Fig. 1a), between the Ayeyarwady mouth and Mergui Ridge (Fig. 1a), is not important; these areas are described to be sediment starved (Rao et al., 2005; Ramaswamy et al., 2004; Panchang et al., 2008; Rodolfo, 1969), whereas the adjacent East Andaman Basin is one of the main depocenters in the Andaman Sea (Morley et al., 2011).

The recent hydrographic regime of the Andaman Sea is dominated by the Asian Monsoon, leading to seasonal reversal of upper ocean circulation directions (Wyrтки, 1961). During Northeast Monsoon (December–March) the circulation is cyclonic, whereas during Southwestern Monsoon (June–September) anticyclonic circulation prevails (Rao et al., 2005). Seasonal upwelling (Wyrтки, 1961; Buranapratheprat et al., 2010) and lowered salinity in the surface waters due to freshwater discharge during SW Monsoon (Wyrтки, 1961) are consequences of the monsoonal influence on the area. Circulation in greater water depths is affected as well. A steady, seasonal gyre is reported (Varkey et al., 1996) to be located slightly northwest of the working area (Fig. 1b). Lateral exchange with Indian Ocean water masses occurs at sills in the Andaman-Nicobar Ridge (Fig. 1, Wyrтки, 1961). They comprise maximum depths of around 1800 m. Below 1800 m exchange is restricted (Rodolfo, 1969; Dutta et al., 2007). However, a very uniform well mixed water mass is present in the deepest parts throughout the Andaman Sea (Varkey et al., 1996; Dutta et al., 2007). This implies vigorous vertical mixing (Dutta et al., 2007) with renewal times of about 6 yr (Okubo et al., 2004). Dutta et al. (2007) suggest that internal waves, creating turbulence over irregular topography, may be responsible for this mixing process. Large amplitude internal waves have indeed been reported to occur repeatedly in the Andaman Sea (Osborne and Burch, 1980; Nielsen et al., 2004b; Hyder et al., 2005; Vlasenko and Alpers, 2005). They are described to be created by tidal currents near the shallow sills of the Andaman and Nicobar island arc from where they travel eastward across the Andaman sea, propagating at

Table 1. Measured properties of identified MTDs in the working area.

MTD	Interpolated areal extent (km ²)	Maximum thickness of MTD (m)	Approx volume of MTD (km ³)	Depth of shallowest point from surface (m)
A1	70	56	1.3	1130
A2	27	36	0.3	1280
A3	33	55	0.8	1350
A4	69	166	3.0	1210
B1	24	91	1.0	1850
B2	10	46	0.3	1950
B3	43	135	3.0	1570
B4	53	150	3.4	1710
B5	27	125	1.5	2020
C1	23	76	0.7	1480
C2	46	89	2.6	1420
C3	45	90	2.1	1550
C4	32	62	1.0	1530
C5	22	72	1.0	1560
D1	40	75	0.9	880
D2	33	234	4.0	830
D3	585	62	14.0	640

density interfaces (Vlasenko and Alpers, 2005); over shallowing ground they may break and form turbulence (Osbourne and Burch, 1980; Hyder et al., 2005; Vlasenko and Stashuk, 2007). Scattering of an internal wave and creation of secondary internal waves has been reported from the southern tip of Mergui Ridge (Dreadnought Bank, Vlasenko and Alpers, 2005).

3 Dataset and methods

A total of 39 seismic reflection lines were collected at the transition Mergui Basin-Mergui Ridge-East Andaman Basin within the Thai exclusive economic zone in ESE–WNW and N–S directions during cruise MASS III from 11 January 2011 to 24 January 2011 (Fig. 1b). The total length of acquired seismic lines is about 630 km and the investigated area comprises approximately 5000 km². High resolution seismic reflection data were acquired using a micro GI-Gun (2×0.1 l) and a 150 m-long 96-channel digital Geometrics GeoEel streamer. The gun was operated at 120 bars and shot every 5 s resulting in a shotpoint distance of 10 m at vessel speeds of 4 knots. The main frequency used was 200 Hz. The streamer consisted of 12 sections with 8 channels each. The channel distance was 1.56 m. The signals were digitized at 4 kHz and converted into SEG-Y format for further processing.

Standard processing steps were performed with Vista Seismic Data Processing (GEDCO). After setup of the geometry, common midpoint sorting and normal moveout corrections were applied as well as bandpass frequency filtering for frequency contents of 25/50–600/1200 kHz, stacking and time-

migration (using a constant velocity of 1500 m s⁻¹). IHS Kingdom Suite was used for interpretation and volumetric calculations.

The bathymetry data set analysed in this study was obtained during previous cruises MASS I and MASS II in 2006 and 2007, using a portable Seabeam 1050 multibeam echo sounder. The system uses a frequency of 50 kHz, 126 individual beams and a swath width of up to 153° (Jintasaerane et al., 2012). Resolution of the processed bathymetric grid is 50 m.

The general architecture of the background sedimentary units and the distributions and dimensions of mass transport deposits (MTDs) were deduced from the seismic dataset. MTDs were interpreted according to their external geometries and internal reflector characteristics. Examples of acoustic facies characteristics are given in Fig. 2. Lens- or wedge-shaped bodies showing a chaotic to transparent seismic facies were classified as MTDs. Precise measurements of volumes and areal extents of MTDs were not possible from our dataset, as spacing between profiles is relatively large, ranging between about 1 km and 7 km. Therefore, the geometries of the MTDs had to be interpolated over long distances of up to 7 km. An isopach grid was calculated, based on interpreted horizons of top and base for each MTD, using a constant sound velocity of 1500 m s⁻¹. Subsequently, volume and areal extent was deduced from the isopach grid. Values are summarized in Table 1. The values in Table 1, however, have to be regarded only as rough estimations due to the uncertainties mentioned above and due to the fact that the lateral boundaries of the MTDs are not present in our dataset, except for one MTD close to the sea floor, where boundaries

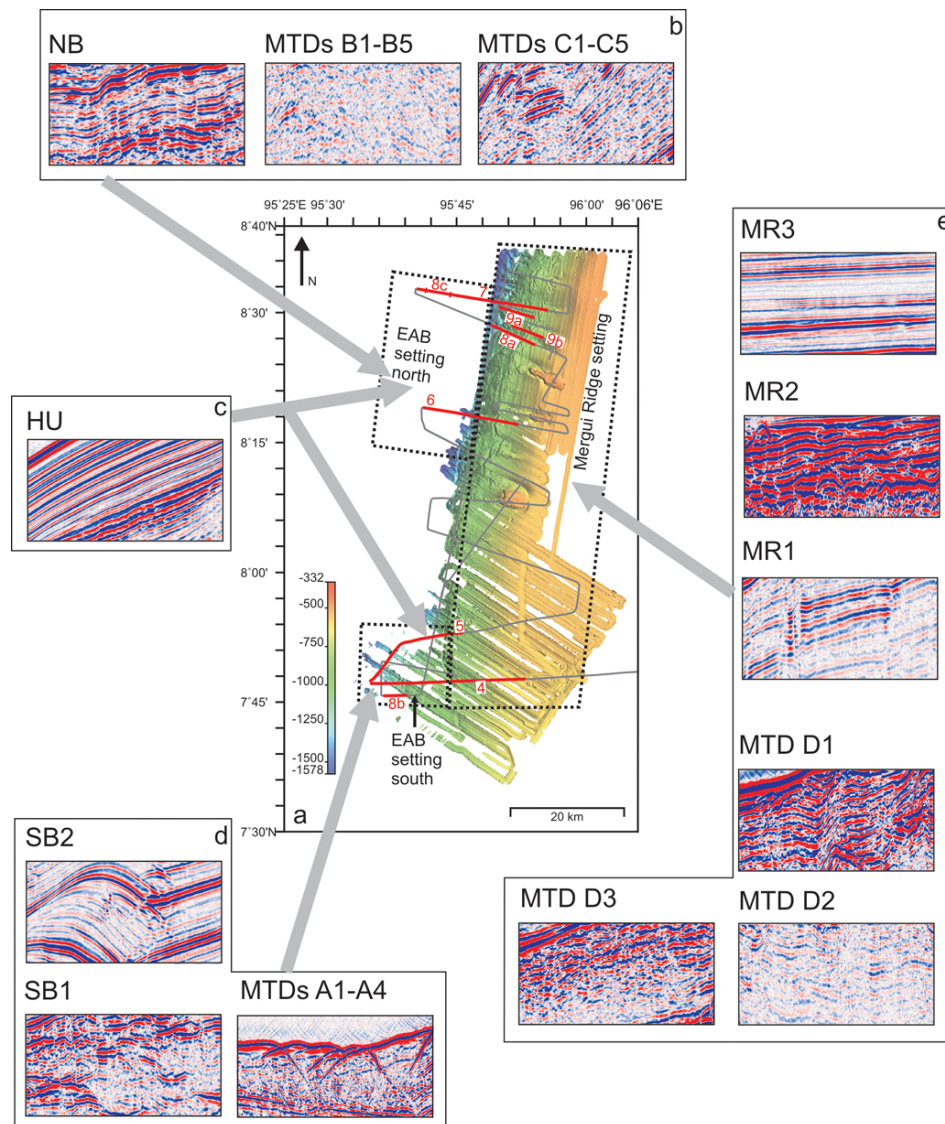


Fig. 2. (a) Bathymetric map of the working area modified after Jintasaerane et al. (2012). The stippled black lines mark the three defined settings in the working area: Mergui Ridge, East Andaman Basin north and East Andaman Basin south. (b) Examples of the acoustic facies that were identified in the subsurface sediments of the northern working area, which are background sedimentary unit NB and MTDs B1–B5 and C1–C5. (c) Example of the acoustic facies of the surficial sedimentary unit HU identified throughout the East Andaman Basin area. (d) Examples of acoustic facies identified in the subsurface sediments of the southern working area, which are background sedimentary units SB1 and SB2 and MTDs A1–A4. (e) Examples of the acoustic facies identified in the Mergui Ridge setting, which are subsurface sedimentary units MR1 and MR2, surficial unit MR3 and MTDs D1–D3.

could be deduced from the bathymetry. Therefore, the values represent minimum estimates of individual MTDs, and actual volumes might be larger than mapped in this study. For a simple estimation of thickness of undisturbed sediment between the individual failure events, we calculated the thickness between the top and base horizon isopach grids of consecutive MTDs. For calculation of time intervals between the MTDs we used a sedimentation rate of 10 cm ka^{-1} . This sedimentation rate was established by Rodolfo (1969) from a sediment core about 50 km north of our working area (Fig. 1b, approx-

imately $9^{\circ}00' \text{ N}$, $95^{\circ}57' \text{ E}$). The results of the calculations are given in Table 2.

4 Results

The investigated area is located at the transition from the Mergui Ridge/outer shelf area to the deep sea environment of the East Andaman Basin, and seismic profiles used in this study run across this basin-ridge transition (Figs. 1b, 2a and 3). Water depths are increasing from east (Mergui Ridge)

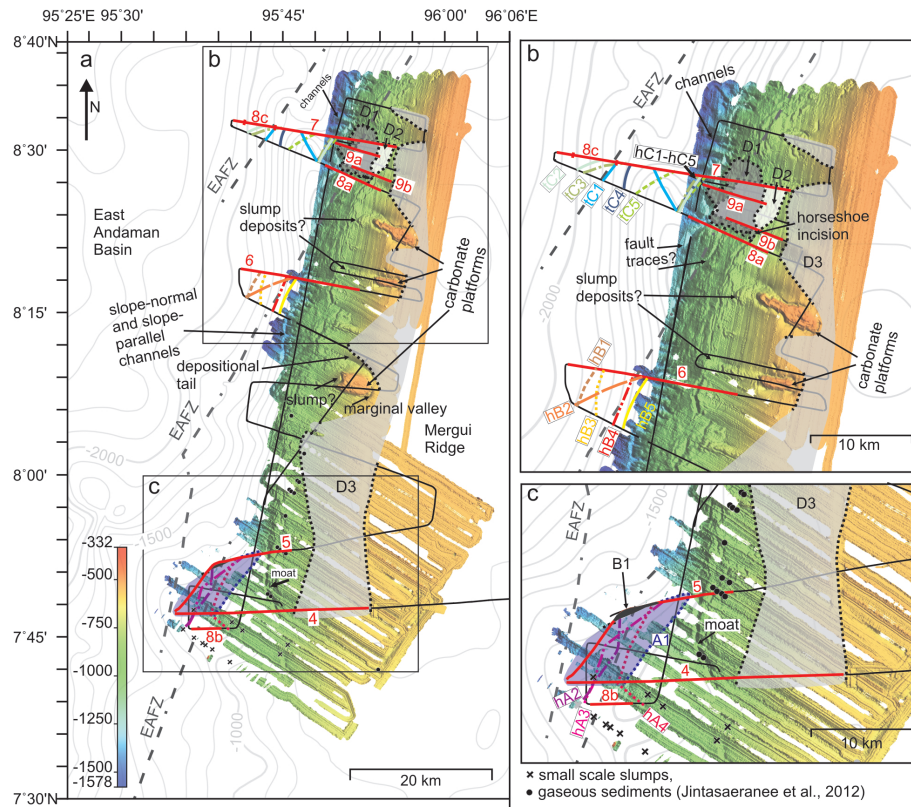


Fig. 3. (a) Bathymetric map of the working area (from Jintasearane et al., 2012) with contour lines from SRTM30.PLUS (Becker et al., 2009). The interpretation of several morphological features, carbonate platforms, slump deposits, fault traces, as well as the positions of small scale slumps and gas-bearing sediment are taken from Jintasearane et al. (2012) as well. The black continuous lines show the cruise track and the red lines indicate the seismic profiles shown in this study. The grey shaded areas on the Mergui Ridge mark the areal extents of MTDs D1–D3, the black stippled lines show the slide margins where they were interpolated. The grey dotted lines indicate positions of branches of the EAFZ (from Polachan, 1988). (b) Close-up of the northern working area. The coloured dotted lines indicate heads (hB1–hB5 and hC1–hC5) and toes (tC1–tC5) of individual MTDs, as mapped from the seismic data. The grey shaded areas show the extents of the Mergui Ridge-MTDs D1–D3. (c) Close-up of the southern working area. The purple shaded area indicates the areal extent of MTD A1. The purple dotted line indicates the slide margins where they were interpolated. The dark grey block indicates the position of a potential in-situ block (B1, see also Fig. 5) or the slide margin north of A1. The coloured dotted lines denote the interpolated heads of MTDs A2–A4 (hA2–hA4).

to west (East Andaman Basin) from about 300 m to about 2200 m (Fig. 3). The western flank of Mergui Ridge forms the slope of the East Andaman Basin. Slope gradients of the basin–ridge transition are generally lower in the southern working area with values of about 1.5° (Figs. 4 and 5). Towards the north, slope angles at the edge of the Mergui Ridge are considerably higher, and reach, for example on Profile 14, values around 12° (Fig. 6). Downslope of the flank of the Mergui Ridge, the basin area is deepening towards the north (Fig. 3).

The bathymetric dataset reveals a very smooth seafloor on Mergui Ridge in the eastern part of the working area, except for three pronounced morphological highs that are pinching out from the flat top of Mergui Ridge (Fig. 3). In contrast, the sea-floor morphology is generally rough towards the western edge of the ridge. Several slope normal channels cut the edge of Mergui Ridge, and numerous elongated depressions run

approximately N–S to NNE–SSW (Fig. 3). Bathymetric features that have been examined in more detail by Jintasearane et al. (2012) are marked on Fig. 3. Seismic data reveal a smooth relief further down the slope, where sediments of the East Andaman Basin are deposited (Figs. 6 and 7).

4.1 Background sedimentary units and their architecture

Based on the architecture of the basin–ridge transition, we differentiated three settings in the working area: (1) Mergui Ridge in the western part of the working area; (2) Basin sediments of the East Andaman Basin in the southern working area; (3) Basin sediments of the East Andaman Basin in the northern working area. The location of these three settings and an overview on the acoustic facies of the seismic units identified are given in Fig. 2.

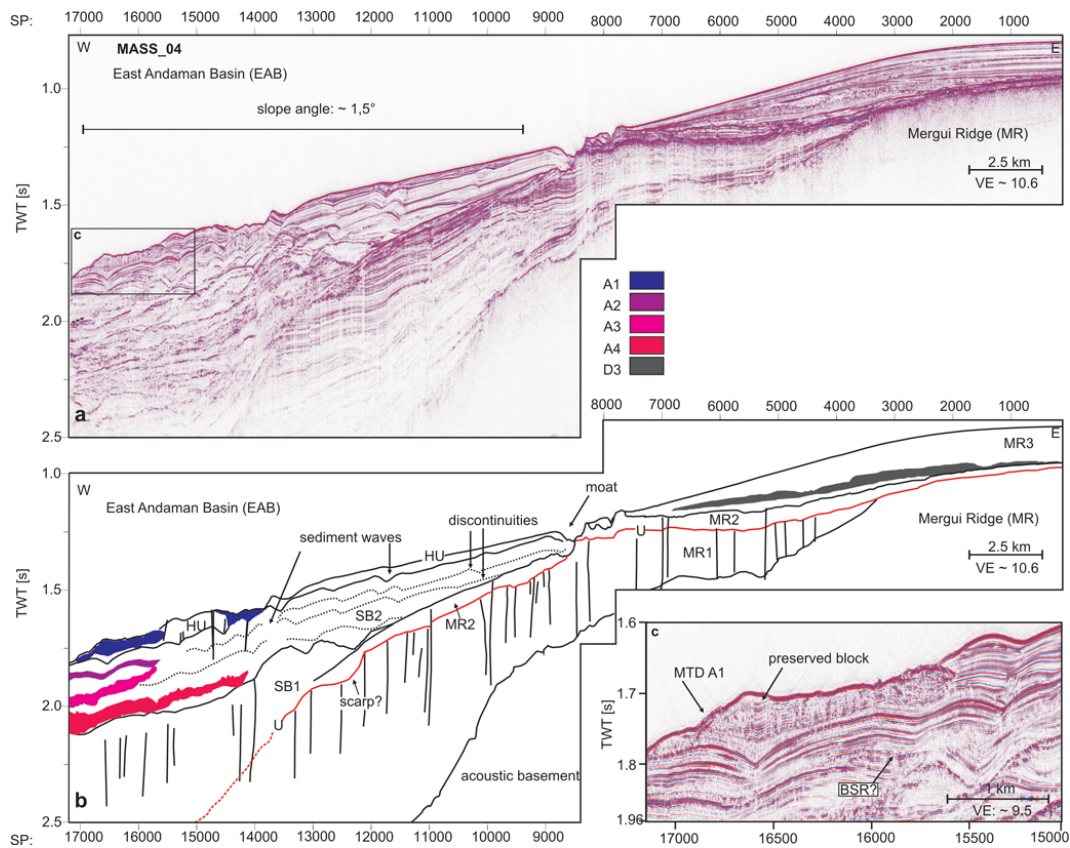


Fig. 4. (a) Seismic profile MASS_04 across the basin-ridge transition Mergui Ridge-East Andaman Basin in the southern working area. (b) Interpretation of the seismic profile showing the seismic units of Mergui Ridge in the east (MR1–MR3) and those of the southern East Andaman Basin area to the west. Faults are marked as black vertical lines. Black lines mark boundaries of seismic units. The black dashed lines mark the positions of possible discontinuities within SB2. The red line denotes the position of the unconformity *U*. The colored areas mark the position of the MTDs A1–A4. See Figs. 2 and 3 for location of profile. (c) Blowup of the superficial MTD A1, showing blocky structure of the deposit. The label BSR indicates the location of a potential bottom simulating reflector. See text for further explanations. See Figs. 2 and 3 for location of the profile.

Table 2. Calculated minimum time intervals between slide events, based on constant sedimentation rates of 10 cm ka^{-1} (from Rodolfo, 1969).

Interval between MTDs	Maximum thickness of undisturbed sediment between MTDs (m)	Calculated time interval (ka)
A1–A2	94	940
A2–A3	91	910
A3–A4	119	1190
B1–B2	39	390
B2–B3	22	220
B3–B4	96	960
B4–B5	147	1470
C1–C2	47	470
C2–C3	95	950
C3–C4	37	370
C4–C5	48	480

4.1.1 Mergui Ridge

The seismic units identified in the Mergui Ridge setting are laterally traceable on all profiles. We separated them into three seismic units: MR1 shows continuous parallel reflectors of variable amplitude (Fig. 2), and in the northern part towards its top a reflection pattern of transparent patches, alternating with chaotic high amplitude areas (Figs. 6 and 7); MR2 comprises high-amplitude, subparallel reflectors (Fig. 2); MR3 is characterized by parallel reflectors of variable amplitude with good lateral continuity (Fig. 2).

MR1 is overlying the acoustic basement at the western flank of Mergui Ridge (Fig. 4). It has a wedge-shaped geometry. The thinning of this unit towards the east and its reflector characteristics indicate deposition in a hemipelagic environment (Figs. 4 and 5). Deformation of MR1 is caused by numerous faults throughout the working area (Figs. 4–7). In the north, a section of MR1 sediments is exposed to the seafloor (Fig. 8a), indicating a recent erosive or non-depositional

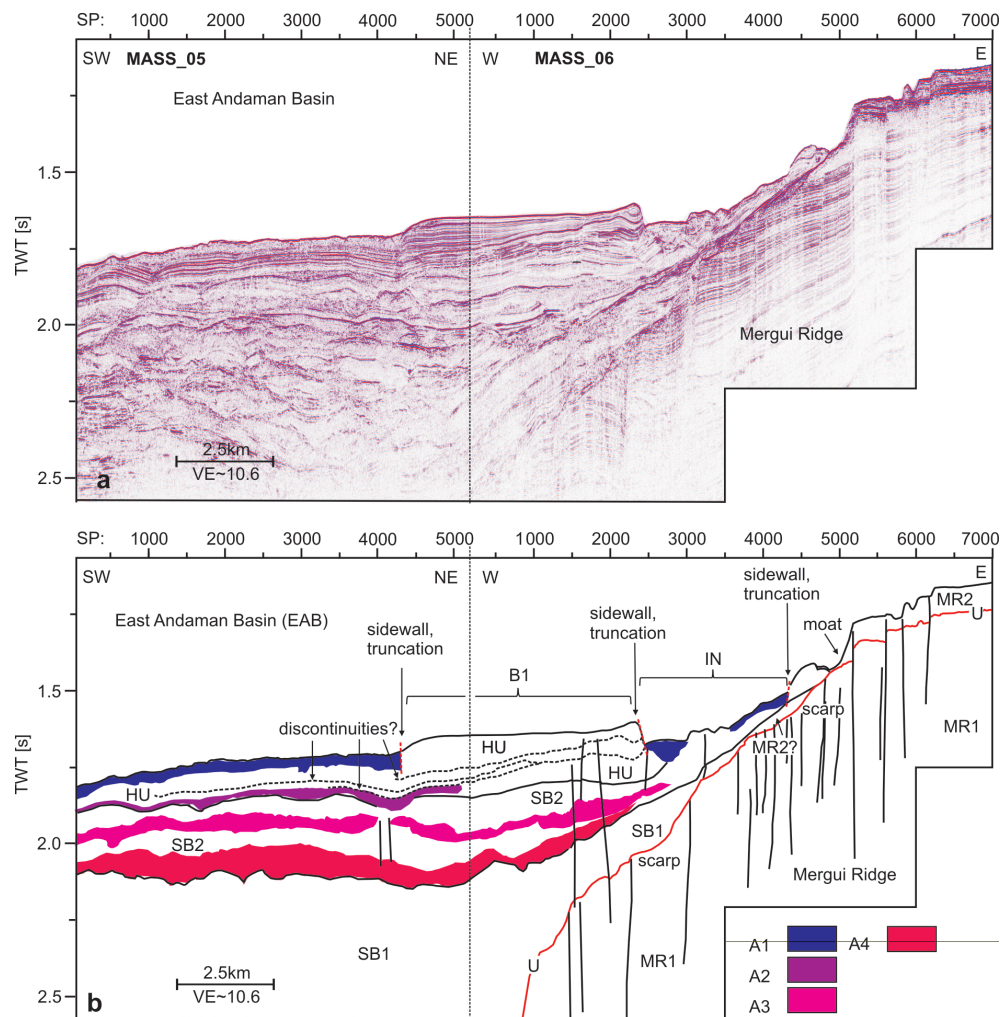


Fig. 5. (a) Seismic profiles MASS_05 and MASS_06, from the southern working area. (b) Interpretation of the profile, showing Mergui Ridge seismic units MR1 and MR2 in the east and basin sedimentary units SB1, SB2 and HU in the SE. The black lines mark boundaries of seismic units. The red line denotes the position of unconformity *U*. The vertical lines mark the positions of faults. The colored areas denote the position of MTDs within the basin sediments. The black dashed line marks discontinuities within the upper unit HU, indicative of drift deposits. B1 marks a stable block/slide margin, confined by steep sidewalls, and bordered by disturbed sediment bodies of superficial deposit MTD A1; "IN" indicates an incision in the sedimentary column. See Figs. 2 and 3 for the location of the profiles and text for further explanations.

environment at the western edge of Mergui Ridge. In this area, individual blocks have been displaced and faults are cutting through the surface. A smaller block is situated basinward of these deformed MR1 sediments. A pronounced erosive unconformity (*U*) bounds unit MR1 at its top. The unconformity is traceable on top of the Mergui Ridge (Figs. 4–7). In the southern working area, unconformity *U* can be traced westward into the East Andaman Basin (Figs. 4 and 5). To the north, where MR1 exhibits a more transparent/chaotic reflection pattern in its upper part, unconformity *U* is difficult to trace to the East Andaman Basin (Figs. 6 and 7). We interpret the chaotic reflection pattern of the upper part of MR1 as depositions of slope channels as such channels are visible in the bathymetric data of this area (Fig. 3). However, these

depositions do not extend across the edge of Mergui Ridge. In addition, large-scale buried slope parallel channel incisions, reaching incision depths of up to ca. 200 m are identified in places within MR1 (Figs. 6 and 7). Such slope-parallel channels are identifiable from the bathymetry as well (Fig. 3).

Seismic unit MR2 is overlying the acoustic basement and unit MR1 on top of Mergui Ridge with a maximum thickness of around 100 m (Fig. 4). In places, it has an eroded irregular top with truncated reflectors (Fig. 5). This indicates an erosive phase between deposition of MR2 and the unit on top. MR2 is exposed to the seafloor at the edge of Mergui Ridge, forming an irregular topography (Figs. 5 and 6). Downslope of the edge of Mergui Ridge, eroded packages of MR2 seem

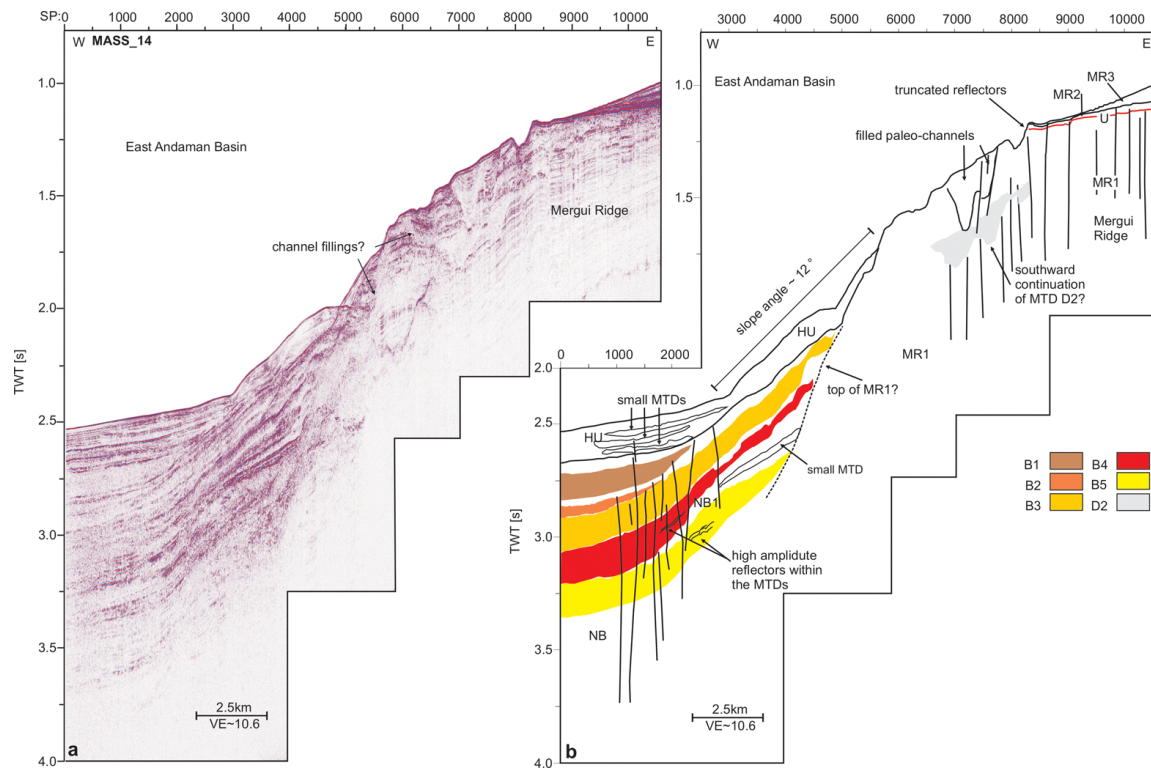


Fig. 6. (a) Seismic profile MASS_14, running across the basin-ridge transition in the northern working area, with channel-fillings indicated at the edge of Mergui Ridge. (b) Interpreted profile showing Mergui Ridge units MR1–MR3 in the east and basin sediments NB and HU in the west. The black lines mark boundaries between the seismic units. The red line denotes the position of unconformity *U*. The black stippled line marks the possible upper boundary of MR1. Channel fillings are present in the upper part of MR1. The reflectors of the upper Mergui Ridge units (MR2 and MR3) are truncated at the edge of the ridge. At the edge of the ridge a U-shaped structure is present, indicating an approximate slope parallel paleo-channel. The coloured areas mark the position of the stacked MTDs B1–B5 and a possible southward continuation of MTD D2. See text for further explanations and Figs. 2 and 3 for location of the profile.

to be present partially on top of the basinward continuation of unconformity *U* (Fig. 4).

Seismic unit MR3 is the youngest of the Mergui Ridge units. It is deposited on top of MR2. The thickness of this unit varies between about 120 m and 40 m; it is tapering out towards its seaward edge. Marginal valleys and mounded structures are present at the surface within MTD3 around the morphological highs on top of Mergui Ridge (Fig. 3).

4.1.2 East Andaman Basin South

Directly west of the Mergui Ridge lies the East Andaman Basin, which comprises water depths between 900 m and 2200 m. Sediments, infilling the East Andaman Basin, are resolved in the dataset to a subsurface depth of up to about 900 m. In the southern working area, we differentiate three seismic units within these basin sediments. SB1 is the oldest basin fill unit. It exhibits a disturbed acoustic character with reflectors of varying amplitude and continuity (Fig. 2). Towards its landward termination, the oldest basin fill unit SB1 is directly overlying MR1/MR2 sediments (Figs. 4 and 5).

SB1 is overlain by SB2. SB2 shows packages of well stratified, continuous to sub-continuous parallel reflectors of weak-to-moderate amplitudes, separated by pronounced reflectors of high amplitude (Fig. 2). Towards its upslope edge, SB1 onlaps against MR1/MR2 and it is confined by a moat (Figs. 4 and 5). Sediment waves are a characteristic feature of this up to 300 m thick unit (Fig. 4). Narrow vertical zones of low amplitude, crossing several reflectors, are evident within SB2 (Fig. 8b). These features may represent fluid migration pathways. At one location, a possible bottom simulating reflector (BSR) has been identified at subsurface depths around 80 m (Fig. 4c). The youngest unit HU, deposited on top of SB2, shows very regular, parallel, high-amplitude reflectors, with amplitude strengths increasing towards the seafloor (Fig. 2). Based on its reflector characteristics, it is interpreted as a hemipelagic deposit, which is undisturbed in most parts. Sediment waves have a topographic expression in this unit (Fig. 4). Towards the surface, a few zones with small scale faulting are evident within HU (Fig. 8b).

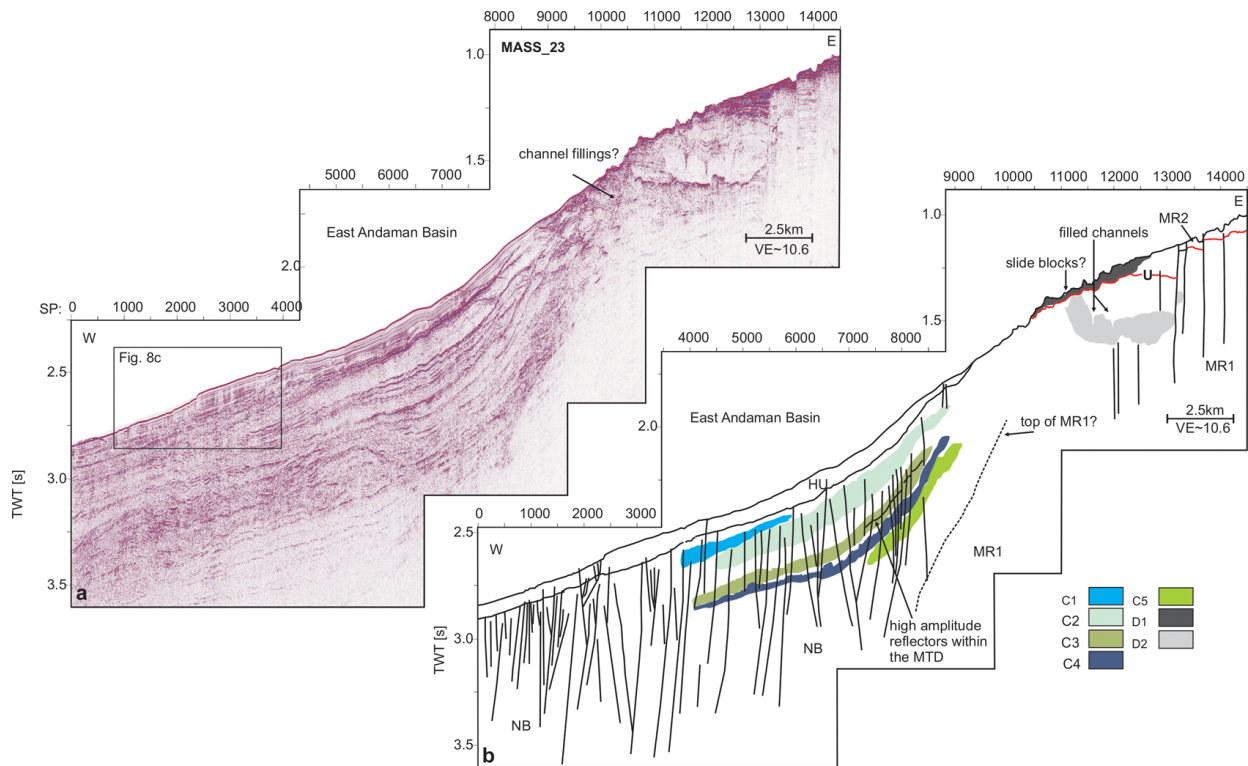


Fig. 7. (a) Slope normal seismic line MASS_23 from the basin ridge transition in the northern working area with channel fillings indicated at the edge of Mergui Ridge (b) Interpreted profile, showing seismic units of Mergui Ridge in the east (MR1, MR2) and seismic units of basin sediments in the west (HU, NB). The black lines indicate boundaries between units. The red line marks the position of unconformity *U*. The black dashed line marks a possible top boundary of MR1 towards the basin. The vertical lines indicate fault positions. The colored areas mark the stacked MTDs C1–C5 in the basin area and MTDs D1 and D2 on Mergui Ridge. See Figs. 2 and 3 for location of profile and text for further explanation.

4.1.3 East Andaman Basin North

We differentiated two seismic units within the northern basin sediments. The lower unit (NB) onlaps the Mergui Ridge unit MR1. Several bodies, characterized by transparent/low amplitude chaotic reflections are alternating with sediments imaged as high-amplitude reflections within NB (Figs. 6 and 7). Deformation of NB sediments is evident from numerous normal faults, dissecting the entire basin fill into blocks and leading to a rather disturbed appearance of NB (Fig. 7).

We did not correlate the lower units in the northern working area (SB1, SB2) and the lower unit in the north (NB). No seismic lines for direct lateral correlation are available. Although these units show similar characteristics, such as high amplitude reflectors alternating with low-amplitude packages, a clear correlation is not possible due to the disturbed character of NB and the lack of an internal boundary within NB, corresponding to the boundary between SB1 and SB2.

The older NB basin sediments in the north are overlain by an up to 200 m-thick hemipelagic unit characterized by parallel and fairly continuous/sub-continuous reflectors. The seismic character of this unit is very similar to the southern unit HU. Hence, we assume that this unit is the same and it is

also labeled as HU (Figs. 6 and 7). HU is quite undisturbed, in contrast to the unit NB below it. However, some faults are cutting through HU to the surface. Along one of these faults, the seafloor is displaced by about 20 m (Fig. 8c). Seaward of this fault, the sediments show a wavy pattern (Fig. 8c). Vertical transparent zones, interpreted as potential fluid migration pathways, are present in the seismic unit HU (Fig. 8c)

4.2 Distribution and dimensions of mass transport deposits

Seventeen individual mass transport deposits (MTDs) were identified in the three different environments described above. Four MTDs are located in the southern basin area (MTD A1–A4), ten MTDs in the northern part (MTD B1–B5 and MTD C1–C5), and three MTDs on Mergui Ridge (MTD D1–D3). The positions of the MTDs, their boundaries and minimum areal extents, as far as they were traceable on the dataset, are illustrated on Fig. 3. The MTDs identified within the basin sediments (A1–A4, B1–B5, C1–C5) are generally characterized as lens- or wedge-shaped bodies, partially with a hummocky surface. They reveal

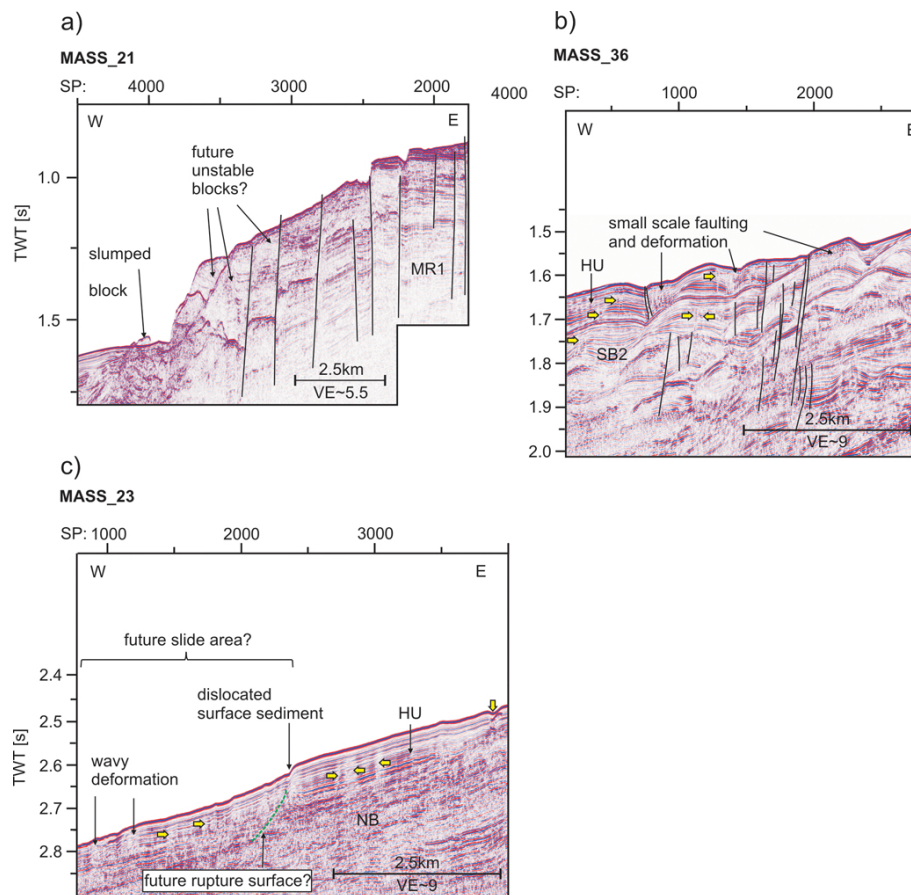


Fig. 8. Possible locations of future slope failures from the Mergui Ridge setting (MASS_23), the East Andaman Basin in the southern working area (MASS_36) and the East Andaman Basin in the northern working area. **(a)** Seismic profile from the edge of Mergui Ridge located slightly south of MTDs D1 and D2. Several faults, marked by black lines, cut to the surface and indicate recent deformation and dislocation of blocks. A small slumped block may indicate that some failure already occurred. **(b)** Profile MASS_36 shows drift sediments from the southern working area. Fluid migration pathways are imaged in these sediments as transparent narrow vertical zones (yellow arrows). Small scale faulting and deformation of the upper sedimentary layers may indicate future failure of the drift deposits. **(c)** Seismic profile MASS_23 reveals numerous vertical transparent features interpreted as pathways for fluids (yellow arrows), and a fault dislocating the sea floor (green dotted line), that might act as future rupture surface. Wavy deformation of the surficial sediments downslope of this fault may indicate remobilization of the sediment. See Figs. 2 and 3 for location of profiles, and text for further explanations.

internal chaotic to transparent reflector characteristics (see Fig. 2 for examples of acoustic facies).

4.2.1 MTDs in the southern working area (A1–A4)

Four MTDs have been identified within basin sediments of unit SB2 and HU (A1–A4, Figs. 4 and 5) on the flank of the East Andaman Basin in the southern working area (see Fig. 2 for location). Estimated minimum volumes of these deposits range between 0.3 km^3 and 3 km^3 (Table 1).

At or close to the seafloor (Figs. 3, 4 and 5) we identified several bodies with disturbed internal structure, interpreted as MTDs. From our dataset we cannot clearly identify if these bodies are interconnected. As they occur in close proximity to each other and in the same stratigraphic depth, we interpreted them to belong to one failure event. There-

fore, we include them all in MTD A1 for the volume estimation. Being situated at or very close to the seafloor, MTD A1 is likely one of the youngest mapped slide deposits. Within the MTD A1, partially sub-parallel reflections are preserved, indicating that movement of slide bodies caused only limited internal deformation (Fig. 4c). Individual bodies/lobes of MTD A1 are found east and southwest of an un-mobilized sediment block (B1 on Fig. 5). This block shows an undisturbed internal structure characteristic for units HU/SB2. It is truncated by steep, about 65 m-high sidewalls. Depending on the motion direction of the slides, B1 may represent a stable in-situ block within the slide area of MTD A1, or the margin of the slide (Fig. 3). Northeast of B1, a 700 m wide and up to 65 m deep incision, marked as IN in Fig. 5, is confined by truncated sidewalls at its eastern and western boundaries, which indicate erosion and removal of sediment.

This structure is interpreted as an evacuated area, which was most likely created during the failure of MTD A1. Disturbed small sediment bodies interpreted to belong to the MTD A1 are located inside the evacuated area. Volumes of MTD A1 deposits are estimated to be $\sim 1.3 \text{ km}^3$, which then is a minimum estimate for MTD A1.

MTD A2, A3 and A4 are buried mass transport deposits (Figs. 4 and 5) within seismic units HU and SB2. They are characterized by transparent to chaotic internal structures and hummocky tops. The boundaries of the individual MTDs are not easily detectable because of the overall low amplitude reflectors of the surrounding background sediment. MTD A4 is the largest slide body identified in the southern working area with an estimated volume of 3.0 km^3 (Figs. 4 and 5, Table 1).

4.2.2 MTDs in the northern working area (B1–B5 and C1–C5)

In the northern working area (see Fig. 2 for location), mass transport deposits were identified in two locations within seismic unit NB (Figs. 3, 6 and 7). In both settings, several stacked MTDs are located at the basin-slope transition (B1–B5 and C1–C5). Figure 3 shows positions and extents of the deposits as mapped out based on the available data set. Figure 2 gives examples of the acoustic characteristics of these bodies.

The seismic profile in Fig. 6 shows at least five stacked slide deposits (B1–B5), originating at or near the slope of Mergui Ridge within background sediments of unit NB. The volumes of the mapped parts of these deposits range from 0.3 km^3 to 3.4 km^3 (Table 1). The mapped slide bodies contain patches of higher amplitude reflections (Fig. 6). These reflections possibly result from un-deformed blocks within the MTDs. An alternative explanation for these higher amplitude reflections may be multiple failure events. The high amplitude reflectors may then represent boundaries between individual events. Several smaller MTDs are present in the vicinity of Mergui Ridge, predominantly in unit HU, but also in the deeper parts of the basin sedimentary succession (Fig. 6).

The MTDs C1–C5 (Fig. 7) are located within the same basin-slope transition setting as MTDs B1–B5 and they are also stacked slide deposits, but their thicknesses are smaller than those of B1–B5 (Table 1). It is also difficult to determine individual slide bodies at this location, because the background sediment in this part of the basin is generally disturbed and exhibits widespread irregular reflector characteristics. Hence, only chaotic to transparent areas without traceable reflectors were mapped as slide bodies. Volumes and depths are listed in Table 1.

4.2.3 MTDs on Mergui Ridge (D1–D3)

Estimated volumes of the MTDs identified in the Mergui Ridge setting (see Fig. 2 for location of setting and Fig. 3

for location of MTDs) range between 0.9 km^3 and 14 km^3 (Table 1). The individual MTDs exhibit very different characteristics in terms of external and internal structures.

MTD D1 consists of displaced sediment blocks with disturbed internal structure (Fig. 9). These blocks are located near the seafloor at the western edge of Mergui Ridge. The high amplitude reflectors inside these blocks show characteristics similar to those of MR2 sediments. This suggests that MTD D1 consists of remobilised MR2 sediment. The partly preserved stratification of the blocks implies that deformation was probably not strong and the blocks have not moved very far. As MTD D1 is situated close to the seafloor, its boundaries are deducible from seafloor morphology. The possible extent of MTD D1 therefore was deduced from the bathymetric dataset (Fig. 3).

MTD D2 is found within seismic unit MR1 (Figs. 7 and 9). Compared to the other MTDs, it shows a large maximum thickness of up to 230 m. The body of MTD D2 comprises blocks ranging from acoustic transparency to some weak internal sub-parallel layering. Its top is eroded (Figs. 7 and 9) and its slide toe is deformed (Fig. 9a). A possible rupture surface is located at the base of MTD D2 (Fig. 9). A steep depression in the seafloor morphology is located upslope of the head area of MTD D2 (Fig. 9b). This 75 m-deep incision is characterized by slope angles of up to 13.5° . The incision can also be identified on the bathymetry, where it shows an amphitheatric shape, typical for a landslide headwall (Fig. 3). The southern boundary of MTD D2 is not very clearly identifiable in the seismic dataset (Fig. 6); the MTD may therefore actually be larger than mapped.

MTD D3 is situated on the flat top of Mergui Ridge, interbedded in the strata of MR3 (Fig. 4). Due to its internal chaotic structure, we categorize it as a MTD, although no headwall or other indicators typical of slide deposits are observed. MTD D3 is traceable over a large part of the working area (about 580 km^2). Despite its large areal extent, it has a maximum thickness of about 60 m. MTD D3 comprises the largest volume of all identified MTDs (about 14 km^3). Erosive structures and channel fills at the top of MTD D3 imply that its original thickness may have been larger. Moreover, its eastward maximum extent may not be covered by our dataset, which also implies a larger original volume of the deposit.

4.3 Recurrence of failure events

Approximate time intervals between individual slide events (A1–A4, B1–B5, C1–C5) have been established for the MTDs in the southern and northern East Andaman Sea settings (see Fig. 3 for locations) following the approach described in Sect. 3. For the southern working area (A1–A4) they range between 940 ka and 1.19 Ma; for the northern working area between 220 ka and 1.47 Ma (B1–B5) and 370 and 950 ka (C1–C5), respectively (Table 2). For the MTDs on Mergui Ridge (D1–D3), no calculation of recurrence intervals have been established as information on sedimentation

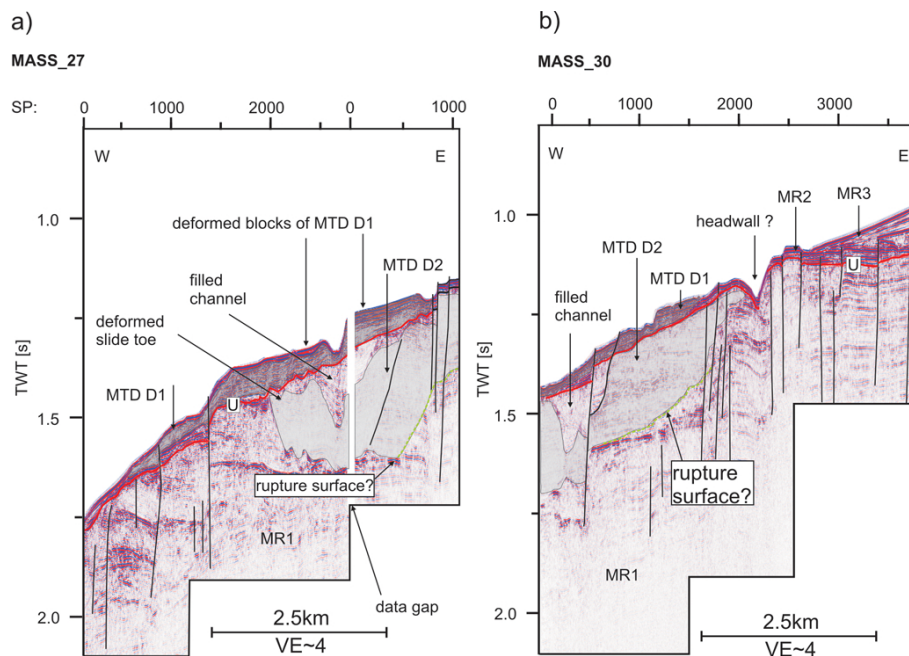


Fig. 9. Seismic profiles showing the edge of Mergui Ridge. The vertical lines indicate positions of faults. The red line marks unconformity *U*. **(a)** Deformed toe of MTD D2 (coloured in light grey). **(b)** Head area of D2 (coloured in light grey) with a steep scarp at its upper part, which may represent the modified head wall (see text for details). The green dotted line indicates the location of a possible rupture surface of D2. See Figs. 2 and 3 for the location of the profiles.

rates was not available. The subsurface depths of the uppermost MTDs in the northern working area range between 100 and 150 m for B1 and between 40 and 120 m for C1.

5 Discussion

5.1 General development and influences on background sedimentary units

5.1.1 Hemipelagic sedimentation

The reflector characteristics of the youngest seismic units HU and MR3 indicate recent hemipelagic sedimentation in the working area (Figs. 4–7). Main sedimentary components in the working area are derived from terrestrial detritus and biogenic production (Keller and Richards, 1967; Rodolfo, 1969; Colin et al., 1999). Regarding sediment type and sedimentation rates, there are differences between the area on top of Mergui Ridge and the downslope basin area of the East Andaman Basin. Whereas on top of the ridge, sediments mainly consist of foraminiferal oozes, silty clays prevail in the adjacent basin area (Keller and Richards, 1967; Rodolfo, 1969). The outer shelf of the Thai-Malay peninsula is described as sediment starved (Rodolfo, 1969; Andreason et al., 1997; Panchang et al., 2008). Rodolfo (1969) described relict foraminifera and relict corals in modern sediments of the Mergui area, implying that sedimentation rates on the Mergui Ridge are generally low and/or mainly related to biogenic

input (Rodolfo, 1969). Left lateral movement along Ranong Fault (Fig. 1) is described as the cause for diversion of river systems towards the Gulf of Thailand and subsequently reduced riverine input from the Thai-Malay Peninsula since the Miocene (Andreason et al., 1997). Recent sediment starvation along the western outer shelf of the Thai-Malay peninsula is explained by Rao et al. (2005) to be due to the trapping of the Ayerawaddy riverine input in the Gulf of Martaban, and direct transfer into the deeper parts of the Andaman Sea by submarine canyons. Detritus delivered by via the Malacca Strait is also deposited only in the deeper parts of the Andaman Sea (Keller and Richards, 1967). Therefore, input of terrigenous material is largely restricted to the areas off the ridge, and sedimentation rates on top of the Mergui Ridge are low, whereas they are moderately high in the off-ridge part of the working area (around 10 cm ka^{-1} , Rodolfo, 1969, Fig. 1).

5.1.2 Sediments of Mergui Ridge

Comparison of our data set with data from the Mergui Basin (Fig. 1) east of Mergui Ridge (Polachan, 1988) suggests an approximate age of Lower Miocene for unit MR2, a large hiatus between units MR2 and MR3 and a Plio-Pleistocene age of unit MR3. MR1 reveals faulting at the western edge of Mergui Ridge (Fig. 4). Extensive faulting along the western flank of Mergui Ridge is explained by several authors by extension due to basin formation processes all over the Andaman Sea (Polachan et al., 1991; Curray, 2005; Jha et

al., 2010; Kishore et al., 2010; Morley et al., 2011). According to Morley et al. (2011), rifted sequences are deposited at the western flank of Mergui Ridge as a result of this extension. These late syn-rift deposits west of Mergui Ridge were probably deposited during formation of the East Andaman Basin in Late Oligocene/Early Miocene in an open-marine environment (Jha et al., 2010). As the deposition of MR1 clearly predates the Lower Miocene unit MR2, and its reflector characteristics indicate that the sediments are deposited in a hemipelagic environment, we speculate that the sediments of unit MR1 correspond to these synrift sequences and form an older eroded slope of Late Oligocene/Early Miocene age deposited in the marine environment that was prevailing in the area since Early Miocene (Jha et al., 2010). Younger sediments on top of Mergui Ridge (MR2/MR3) are not tectonically deformed.

5.1.3 Drift deposits in the East Andaman Basin and on top of the Mergui Ridge

Jha et al. (2011) described a post-rift sedimentary succession in the region directly west of our working area. They identified a lower sequence containing a chaotic seismic facies interpreted as mass flow complexes, and an upper sequence characterized by pelagic sedimentation since Late Miocene. This upper sequence is described to exhibit mass flow deposits in places and to be influenced by contour currents. Jha et al. (2011) attribute the mass flows within their lower sequence to subsidence in the East Andaman Basin caused by rifting in the Central Andaman Basin since Late Miocene. The presence of mass flows in their upper unit is attributed to disturbances due to modern sea-floor spreading in the Central Andaman Basin since Late Plio-Pleistocene. The sedimentary succession in the southern working area (SB1 and SB2, see Fig. 2 for location) reveals a pattern similar to that described by Jha et al. (2011). Seismic unit SB1, situated on top of the assumed synrift sediments of MR1, reveals largely disturbed sediments, possibly attributable to an older mass flow complex and correlatable to the mass flow unit described by Jha et al. (2011).

The unit SB2 comprises distinct low amplitude packages, separated by high amplitude reflectors. Sediment waves are present (Fig. 4). Rebesco and Stow (2001) described characteristics of elongated plastered drift deposits. Typical features are erosive moats at their boundaries and fields of migrating sediment waves within the deposits. Seismic characteristics of drift deposits comprise uniform low-to medium amplitude patterns (Nielsen et al., 2008). Moreover, discontinuities within drifts, marked by high amplitude reflectors, are common (Faugères et al., 1999). These criteria are met by seismic unit SB2 and we therefore interpret it as bottom current controlled sedimentary unit. SB2 may correlate to the upper, bottom current influenced unit of Jha et al. (2011). The approximate age of SB2 would then be Plio-Pleistocene.

Hernández-Molina et al. (2008) give examples of typical geometries of sediments deposits that develop around obstacles when bottom currents rework sediments. Regarding the current direction, a characteristic marginal valley may persist on the stoss side and a depositional tail on the lee side of the obstacle. Such structures have developed around the carbonate platforms in our working area, reworking sediments of unit MR3 (Fig. 3). We therefore conclude that bottom currents may act over a large part of the working area and influence the sediments on Mergui Ridge as well. In this context, the rugged morphology at the edge of the ridge may be attributed to erosive processes induced by bottom currents.

The presence of reversal currents in the Andaman Sea area is explained to be monsoon controlled (Wirtky, 1961). Such wind driven currents can extend to the bottom and induce sediment reworking (Hollister and McCave, 1984; Shanmugan, 2008). Northwest of our working area (Fig. 1b), a stable, monsoon-induced eddy/gyre is described by Varkey et al. (1996). Measurements revealed currents speeds of 12 m s^{-1} at 500 m and 10 m s^{-1} at 1000 m water depth (Varkey et al., 1996). In addition, internal waves and tides are able to influence deep-water bottom currents and their deposits (Shanmugan, 2008). Large amplitude internal waves have repeatedly been observed in the working area (Osburne and Burch, 1980; Nielsen et al., 2004b; Vlasenko and Alpers, 2005). They can affect the water column in the working area as deep as several hundred meters below the surface (Osburne and Burch, 1980; Nielsen et al., 2004b). Vlasenko and Alpers (2005) report in depths of up to 241 m interaction of internal waves with the Dreadnought Bank (see Fig. 1b for location). Such internal waves may be able to rework sediment (Pomar et al., 2012).

Although we do not have direct information on bottom currents, we suggest that the two processes described above may induce or influence bottom currents in our working area in the East Andaman Basin. Therefore, we interpret the character of units SB2 and HU in the southern working area and unit MR3 on top of Mergui Ridge as formed by reworking and deposition of currents.

5.1.4 Tectonically deformed sediments in the East Andaman Basin

The EAFZ is a strike slip fault zone west of the Mergui Ridge (Polachan et al., 1988; Polachan and Racey, 1994; Morley et al., 2011). Polachan (1988) reported branches of the EAFZ cutting through our working area (Fig. 3). Recent fault reactivation has been reported from the Mergui Fault north of the working area (Morley et al., 2011). Jintasearane et al. (2012) interpreted steep NNE–SSW striking scarps in the bathymetry of our working as fault traces exposed at the sea floor. These observations let us infer that tectonic deformation in the working area is ongoing. The East Andaman Basin sediments in the northern working area (see Fig. 2 for location), especially the older deposits of seismic unit NB,

exhibit features of tectonic movement, such as the presence of numerous faults. Although the youngest basin unit HU exhibits an overall undisturbed character, a few faults cut through this unit in the northern working area (Figs. 7b and 8c). This pattern is in agreement with the description of recent deformation due to activity of fault zones near the working area, such as EAFZ and Mergui Fault.

5.2 Causes for slope instability

Causes for slope failures are manifold and may include (i) sedimentary processes, such as sedimentation at very high rates and resulting excess pore pressures, margin oversteepening, and the deposition/formation of weak layers; (ii) the presence of fluids and resulting overpressure; (iii) tectonic processes, such as fault activity and tectonic steepening; and (iv) cyclic loading by earthquakes (Hampton et al., 1996; Canals et al., 2004; Masson et al., 2006; Yamada et al., 2012 and references therein). The factors relevant for the survey area are discussed below.

5.2.1 Influence of sedimentation on slope stability

Slope channels can act as a sediment conduit from the shelf to the deep sea (Stow and Mayall, 2000). Erosion and oversteepening may also cause slope failure within canyons (Arzola et al., 2008). In our data, channels are mainly evident from the northern area and only directly at the edge of the Mergui Ridge (Figs. 3, 6 and 7). As sedimentation rates are low in the Mergui Ridge area and erosion takes place on the edge of Mergui Ridge (see above), we hypothesize that input of sediments by slope channels into the East Andaman basin may result from erosion of older sediments (MR1). The channels, however, seem to be restricted to the edge of the ridge, and no continuation of them has been detected in the basin sediments further downslope. Hence, we consider their influence on basin sedimentation and slope stability as small, but better data coverage of the basin would be needed to be confident about the distribution of canyons and their influences on slope stability. As sediment transport from the Mergui Ridge into the East Andaman Basin seems to be of minor importance and mainly results from erosion of older Mergui Ridge sediments, rapid sediment load and associated oversteepening and/or development of overpressure may play a role only in the deeper parts of the working area, basinward below the edge of Mergui Ridge (MTDs A1–C5). For the destabilization of sediments on top of Mergui Ridge (MTDs D1–D3) other preconditioning factors must be more important.

5.2.2 Tectonic influence: subsidence and fault controlled failures

Tilting of the slope due to subsidence of a margin can act as a preconditioning factor for slope failure (Masson et al., 2010). The Mergui Ridge has undergone subsidence since the onset of rifting in the Central Andaman Basin in Late Miocene

(Kamesh Raju, 2005) due to dextral movement along EAFZ in Late Miocene (Jha et al., 2010) and/or due to thermal contraction (Morley et al., 2011). Jha et al. (2010) described large scale subsidence as a cause for the formation of mass flows west of our working area. These deposits may be correlatable to our seismic unit SB1 (see above). Recent subsidence rates from the shelf area of the Malacca Strait are in the range of 0.25 mm a^{-1} (Lin et al. (2010)). This value is relatively small compared to areas with recent extension, for example the Corinth Basin with a subsidence rate of 1 mm a^{-1} (Lykousis et al., 2007). In addition, subsidence rates tend to decrease after termination of rifting (Prosser, 1993). Therefore, subsidence and steepening may still play a role for slope stability but its influence became probably smaller since the onset of rifting that created the large mass flows described by Jha et al. (2010).

The presence of faults has been suggested to act as controlling or preconditioning factor for slope failures (Dillon, 1993; Hampton, 1996; Anasetti et al., 2012). Except for the top unit HU, large parts of the basin fill sediments in the northern working area (unit NB, see Fig. 2 for location) are tectonically deformed. The MTDs C1–C5 and B1–B5 are located in this environment and we consider fault activity as one of the main reasons for slope failures in our working area. Episodic slope failure due to episodic fault activity has been described by Reicherter et al. (2011) to result in slide deposits interbedded in well stratified layers. A similar pattern can be observed for the MTDs in the northern working area (B1–B5 and C1–C5) (Figs. 6 and 7). Moreover, the MTDs B1–B5 seem to occur in stratigraphic depths similar to those of C1–C5. This would imply laterally contemporaneous failures in the northern working area. We therefore suggest that episodic fault activity was important for weakening the sediments along the slope.

Tectonic deformation may also play a role in development of MTDs on top of/at the edge of the Mergui Ridge (D1–D3), where sedimentation rates are low and oversteepening probably is not a preconditioning factor for slope failure. Surficial MTD D1 and buried MTD D2 are both located at the edge of the Mergui Ridge. Tectonic deformation of the top parts of unit MR1 may have caused the development of unstable blocks that were subsequently dislocated. Internal structures of these blocks are still preserved; therefore, run out distances of blocks seem to be small.

In conclusion, weakening of the sediments due to tectonic activity is considered as a main pre-conditioning factor for slope failure, especially at the basin-ridge transition.

5.2.3 Instable drift deposits

Drift deposits are present in the southern working area (see Fig. 2 for location). Laberg and Camerlenghi (2008) show an interrelation between contourite features and slope instabilities: Drifts generally tend to be prone to liquefaction during seismic loading due to good sorting of their particles and

resulting high porosity. High sedimentation rates in drift deposits may result in rapid loading and development of excess pore pressure. The development of excess pore pressure is further facilitated by gas migration, fueled by high organic matter input from productive water masses along continental margins. (Laberg and Camerlenghi, 2008). All these factors increase the susceptibility of drift sediments for failure (Laberg and Camerlenghi, 2008). Migrating fluids can especially cause build-up of excess pore pressure in upper sediment layers, a process which is well known to be capable for destabilizing slope sediments (Vorren et al., 1998; Stigall and Dugan, 2010). Sediments that build drift deposits in the southern working area contain terrigenous material from the Ayeyawady River and/or the Malacca Strait, whereas sediment input from the Mergui Ridge seems unlikely (see above). Off the ridge, sedimentation rates are high (10 cm ka^{-1} , Rodolfo, 1969). An unusually high content of terrestrial organic carbon has been reported for these sediments (Keller and Richards, 1967; Colin et al., 1999; Bird et al., 2008; Ramaswamy et al., 2008), which may be favorable of formation of gas within the drift deposits. Jintasaerane et al. (2012) reported gas-charged sediment at the Mergui Ridge slope area from subbottom profiler data (Fig. 3). Several possible gas migration pathways are imaged on our seismic data as vertical zones of acoustic transparency (see Fig. 8). A possible bottom simulating reflector (BSR) was identified in the southern working area (Fig. 4c). Therefore, we consider that build-up of excess pore-pressure due to migrating fluids and instability of drift deposits was an important pre-conditioning factor for the failure events in the southern working area (MTDs A1–A4).

5.2.4 Final trigger mechanism

An important factor for the formation and recurrence of submarine landslides is the presence of a final trigger leading to the failure of potentially unstable sediments (e.g. Masson et al., 2006). Seismic activity is common along the Sunda trench and also within the Andaman Sea (Lay et al., 2005; Ornthammarath et al., 2011; Khan, 2012; NGDC, Global Significant Earthquake Database, 2012). Neotectonic activities have been reported from many structures in the Andaman Sea, such as the modern spreading centre (Kamesh Raju et al., 2004), the Sagaing Fault (Wang et al., 2011), the Andaman Arc (Radhakrishna et al., 2008), or the West Andaman Fault (Kamesh Raju et al., 2007). Ongoing tectonic activity is also documented in our data as faults reaching the surface. Therefore, earthquakes are likely final triggers for slope failures.

In summary, several concurring factors have contributed to past slope failures. We consider migrating fluids, instability of drift sediments and tectonic activity as most important preconditioning factors. Regular earthquakes may act as final trigger for slope failure.

5.3 Recurrence of mass transport deposits

In the East Andaman Basin, several MTDs were detected at different stratigraphic depths at the basin-ridge transition. The stacking of MTDs in the East Andaman Basin sediments implies recurrent slide events. The ages and hence the recurrence rates for the slides in the working area are difficult to estimate. No age data are published; hence, direct age determinations are not possible. The thickness of undisturbed sediments between individual slide events can be used to estimate the recurrence rates of landslides if accumulation rates are known. However, information on accumulation rates in or close to the working area are sparse. The most reliable value is given by Rodolfo (1969), who suggested an average sedimentation rate of 10 cm ka^{-1} for the basin sediments west of Mergui Ridge. Using this accumulation rate and the mapped sediment thickness between individual slide deposits, calculations of recurrence rates result in values around 100 ka. We would like to point out that the estimates for landslide recurrence intervals contain very large error bars. This simple calculation, however, shows that recurrence rates are several 10 000 to 100 000 yr and not 100 to 1000 yr.

The values are similar for the different settings of the basin sediments. Only one slide in the basin area (MTD A1) is found close to or at the seafloor, while all other slides are deeply buried. However, the presence of several MTDs throughout the working area lets us deduce that landslides occurred repeatedly and that the slope area has been generally unstable and prone to failure.

5.4 Estimation of tsunamigenic potential and indicators for failure susceptibility

5.4.1 Past failures and likelihood of tsunamis

Important criteria that control the tsunamigenic potential of a landslide are volume, stiffness/cohesiveness of the slide material, water depth, and initial acceleration of the landslide (Løvholt et al., 2005; Haugen et al., 2005; Grilli and Watts, 2005; Ward, 2001; Greene et al., 2006). We have no knowledge on the initial acceleration and only sparse information on sediment properties, but we can analyse water depths and volumes of the identified MTDs leading to a qualitative assessment of the likelihood of tsunami generation in the past. Generally, the critical water depth for tsunami generation is given as maximum 1000 m, while the minimum volume sufficient to create a tsunami from a submarine landslide is $\sim 2 \text{ km}^3$ (Greene et al., 2006). We would like to point out these values can only be used as guidelines; large landslides in water depths deeper than 1000 m (Tappin et al., 2001) and small landslides ($< 2 \text{ km}^3$) in very shallow water (Rahiman et al., 2007) have triggered tsunamis in the past.

The volumes of the MTDs detected in our working area ($0.3\text{--}14 \text{ km}^3$, Table 1) are small compared to giant landslides on active and passive margins, which may reach volumes

of several hundreds of cubic kilometers (Hühnerbach et al., 2004; Geersen et al., 2011; Krastel et al., 2012).

In the southern working area (see Fig. 2 for location), only one MTD (A4) comprises a volume $> 2 \text{ km}^3$ (Table 1), while the others are less than 2 km^3 . The presence of discontinuities within background unit SB2 indicates erosive events. Such erosive events are common in drift deposits, due to short term changes of boundary conditions (Faugères et al., 1999). This implies that MTDs identified within SB2 may originally have been larger.

All MTDs in the southern area are located at water depths deeper than 1000 m. Subsidence in the working area is ongoing, but rates have been moderate since cessation of rifting, and therefore the water depth at the time of failure was most likely below 1000 m.

The situation is different for superficial MTD A1. Its source area (see depth of evacuated area IN, Fig. 5) is located at water depths around 1000 m. The mapped volume of MTD A1 is smaller than 2 km^3 (Table 1). However, the true extent of this MTD is not known and might be larger than 2 km^3 . Therefore, MTD A1 may fall in the range of tsunamigenic landslides. In the northern working area, four slide deposits with volumes greater than 2 km^3 were found, but none of these MTDs shows a volume of more than 3.5 km^3 (MTDs B3, B4, C2 and C3, Table 1). As all of these slides are situated in water depths significantly deeper than 1000 m, it seems unlikely that the relatively small MTDs B3, B4, C2 or C3 triggered a tsunami.

On top of Mergui Ridge all detected MTDs (D1, D2 and D3) are located above/near 1000 m water depth, and MTD D2 and MTD D3 comprise volumes $> 2 \text{ km}^3$, whereas MTD D1 which is located near the surface, has a volume below 2 km^3 and therefore it has probably not been a tsunamigenic landslide.

MTD D2 comprises a volume of 4 km^3 . Its toe region is deformed. Similar structures have been described by Frey-Martinez et al. (2006) to occur near the frontal ramp of slides that do not leave the scarp area and are frontally confined. A horseshoe incision is located on the landward side of this deposit (Fig. 3b). In contrast to most landslide scarps, this feature is more similar to an incision than a morphological step (Fig. 9b). The landward flank of the incision, however, is significantly higher than the seaward side. Such shapes of landslide scarps are reported from other areas. Krastel et al. (2011) suggest that such scarps were modified by post-failure processes, especially strong bottom currents. This seems plausible, as bottom currents are acting in the working area. Hence, we interpret the incision as headwall of MTD D2. This headwall is the location of slide initiation and located at around 830 m water depth. Therefore, D2 potentially falls in the range of tsunamigenic slides.

MTD D3 shows the largest (mapped) volume of the slides detected in our working area (14 km^3 , Table 1). MTD D3 has a somewhat outstanding position among the MTDs on Mergui Ridge. It is located within the tectonically undisturbed

bottom current influenced unit MR3. A possible source area is not evident from our dataset. Although the conditions for slide initiation and evolution cannot be reconstructed, we can infer that this slide definitely falls in the range of tsunamigenic landslides.

5.4.2 Possible locations of future slope failures and their tsunamigenic potential

Three locations of possible future slope failures were identified in our data set. Slightly south of the location of MTD D2 (see Fig. 3 for location), faults cut through the seafloor (Fig. 8a). As fault reactivation and deformation in the region seems plausible, these deformed back rotated blocks may fail in the future. Moreover, a slumped block is located basinward of this deformed area, which may indicate, that some disintegration and failure already occurred. Masson et al. (2006) suggest that thick slide blocks with a steep headwall (rotational slides) might be particularly effective in tsunami generation even without large displacements. Therefore, future slope failures at this location in relatively shallow water depths between 700 m and 1100 m may definitively be tsunamigenic. Regarding MTD D3 that is also located on Mergui Ridge, we cannot reconstruct initiation or evolution of this MTD, as outlined above. However, we can infer that a potential future failure of the same dimensions at the same water depths of about 500–700 m definitely falls in the range of tsunamigenic landslides.

An area in water depths near 1000 m close to MTD A1 in the southern working area may be prone to future failures (Fig. 8b). Widespread sediment waves in combination with small scale faulting and indications for fluid migration pathways suggest a potentially unstable slope. Jintasaerane et al. (2012) described numerous small scale failures in this area. Therefore, we conclude that future failures in this area are likely. A failure of significant volume of this part of the slope may be tsunamigenic. However, the area comprises large structural complexity and ongoing tectonic activity. Slope failures from areas with regular seismic activities are expected to be small in size, due to frequent triggers in the form of earthquakes, subsequently, not leaving sufficient time to accumulate large amounts of material for voluminous slides (Völker et al., 2009). Therefore, we would rather expect several small failures of individual sediment packages instead of voluminous failures. Hence, we consider the tsunami hazard emerging from this area as low.

Figure 8c shows an enlargement of the topmost sediment layers of profile MASS_23 in the northern working area. A listric fault cuts and dislocates parts of the superficial sediment of unit HU. This fault may be interpreted as possible future failure surface. Downslope of the surface expression of the fault, the sediment is deformed and destabilization may be indicated by the wavy deformation patterns visible on the seismic data. Migrating fluids may further contribute to future slope instability. However, within the northern working

area, all MTDs as well as the area of potential future slope failure are situated well below 1000 m water depth. Consequently, future slides in the northern part of the East Andaman Basin area may occur but probably do not pose a tsunami hazard.

In summary, the same settings that induced slope failures in the past may also lead to slope failure in the future, but only a few slides show volume and depth values typical for tsunamigenic slides. However, it has to be taken into account that our volume estimations are minimum values, as the lateral boundaries of the MTDs in most cases are not covered by the seismic dataset. Moreover, we cannot exclude a correlation between the stacked MTDs (B1–B5 and C1–C5) in the northern working area, as the settings where they occur show great similarity regarding characteristics, amount and architecture of the MTDs. This implies that more slides than outlined above may have triggered tsunamis in the past. However, even then their number would be small as suggested by the time intervals between the slides.

5.5 Recurrence of landslide tsunamis compared to earthquake tsunamis in the Andaman Sea

The Mergui Ridge–East Andaman Basin transition seems to be unstable and slides seem to occur repeatedly. Most of the identified slides are relatively small ($\sim 2 \text{ km}^3$) and occur at relatively large water depths ($> 1000 \text{ m}$); hence, it is unlikely that these slides triggered significant tsunamis. Though numerous slides were found throughout the working area, their recurrence rate is definitely very long, exceeding 100 ka.

The recurrence rates of major tsunamigenic earthquakes occurring in the Sumatra–Andaman area, which triggered tsunamis also affecting the coast off Thailand, were estimated by Monecke et al. (2008). These authors analysed a 1000-yr sediment record off Northern Sumatra. They identified two older extensive sand sheets with similar sediment characteristics as the sand sheet deposited by the 2004 tsunami and concluded that the 2004 Indian Ocean tsunami is separated from its youngest full predecessor by $\sim 600 \text{ yr}$. Similar values for major tsunamis are reported by Jankaew et al. (2008) for the Andaman Sea coast in Thailand suggesting recurrence rates of major earthquake tsunamis in the range of 400–600 yr for the Thai coast. Our estimations of time intervals between individual MTDs suggest that they are in the hundred ka to Ma range and only four potential tsunamigenic landslides were identified in the sedimentary record. Hence, the risk of submarine landslide tsunamis is negligible compared to earthquake-generated tsunamis. Landslide-triggered tsunamis, however, would hit the coast with almost no warning time.

6 Conclusions

We investigated the top and the western slope of Mergui Ridge and the Andaman Basin and found that older background sediments in the working area show clear indications for tectonic deformation and rifting processes, leading to extension and faulting. Younger sediments in the East Andaman Basin and on top of Mergui Ridge are mainly shaped by bottom currents.

Special attention was drawn to the occurrence of MTDs and the related tsunami hazard. Several MTDs as well as potential future slope failure locations were identified within sediments of the Mergui Ridge and East Andaman Basin. Generally, the slope area seems to be unstable and landslides occur repeatedly, mainly because of occurrence of potentially unstable drift sediments, the presence of fluids, and ongoing tectonic activity that produces deformation and generates earthquakes that are most likely the final trigger for the destabilization of the sediments.

Tsunami generation in the past by most of these slope failures is unlikely due to their relatively small size and their occurrence at large water depths. Recurrence rate of (tsunamigenic) landslides is small compared to the frequency of tsunamigenic earthquakes in the area. Hence, we consider the risk of landslide-generated tsunamis for the Thai west coast as very low. Triggering of tsunamis by submarine landslides, however, cannot be excluded, especially for slope instabilities at the edge of or on top of Mergui Ridge, and such a tsunami would hit the Thai coast almost without warning time.

Acknowledgements. We thank the scientists and crew of MASS III cruise for their help in collecting the data. Logistic support by the Phuket Marine Biological Center and the Thailand Southeast Asia START Regional Center is greatly appreciated. We thank Deniz Cukur for his support during seismic data analysis. Constructive reviews by Aggeliki Georgiopolou and an anonymous reviewer significantly improved the quality of the manuscript. Our work is funded in the frame of German–Thai TRIAS-project funded by the Deutsche Forschungsgemeinschaft (Grant KR2222-8) and the National Research Council of Thailand (NRCT).

The service charges for this open access publication have been covered by a Research Centre of the Helmholtz Association.

Edited by: K. Schwarzer

Reviewed by: A. Georgiopolou and one anonymous referee

References

- Anasetti, A., Winkelmann, D., Krastel, S., Bialas, J., and Brückmann, W.: The BGR slide off Costa Rica: Preconditioning factors, trigger, and slide dynamics, in: Submarine mass movements and their consequences, edited by: Yamada, Y., Kawamura, K., Ikehara, K., Ogawa, Y., Urgeles, R., Mosher, D., Chaytor, J., and Strasser, M., Advances in natural and technological hazards research, Springer, Netherlands, 289–299, 2012.
- Andreasson, W. M., Mudford, B., and Onge, E. S. J.: Geologic evolution and petroleum system of the Thailand Andaman Sea basins, in: Indonesian Petroleum Association Proceedings of the Petroleum System of SE Asia and Australasia Conference, May 1997, 337–350, 1997.
- Arzola, R. G., Wynn, R. B., Lastras, G., Masson, D. G., and Weaver, P. P. E.: Sedimentary features and processes in the Nazaré and Setúbal submarine canyons, west Iberian margin, *Mar. Geol.*, 250, 64–88, doi:10.1016/j.margeo.2007.12.006, 2008.
- Becker, J. J., Sandwell, D. T., Smith, W. H. F., Braud, J., Binder, B., Depner, J., Fabre, D., Factor, J., Ingalls, S., Kim, S.-H., Ladner, R., Marks, K., Nelson, S., Pharaoh, A., Trimmer, R., Von Rosenberg, J., Wallace, G., and Weatherall, P.: Global Bathymetry and Elevation Data at 30 Arc Seconds Resolution: SRTM30 PLUS, *Mar. Geod.*, 32, 4, 355–371, doi:10.1080/01490410903297766, 2009.
- Bird, M. I., Robinson, R. A. J., Win Oo, N., Maung Aye, M., Lu, X. X., Higgitt, D. L., Swe, A., Tun, T., Lhaing Win, S., Sandar Aye, K., Mi Mi Win, K., and Hoey, T. B.: A preliminary estimate of organic carbon transport by the Ayeyarwady (Irrawaddy) and Thanlwin (Salween) rivers of Myanmar, *Quaternary Int.*, 186, 113–122, doi:10.1016/j.quaint.2007.08.003, 2008.
- Biscontin, G., Pestana, J. M., and Nadim, F.: Seismic triggering of submarine slides in soft cohesive soil deposits, *Mar. Geol.*, 203, 341–354, doi:10.1016/S0025-3227(03)00314-1, 2004.
- Blewitt, G., Kreemer, C., Hammond, W. C., Plag, H.-P., Stein, S., and Okal, E.: Rapid determination of earthquake magnitude using GPS for tsunami warning systems, *Geophys. Res. Lett.*, 33, L11309, doi:10.1029/2006gl026145, 2006.
- Bondevik, S., Svendsen, J. I., and Mangerud, J.: Tsunami sedimentary facies deposited by the Storegga tsunami in shallow marine basins and coastal lakes, western Norway, *Sedimentology*, 44, 1115–1131, doi:10.1046/j.1365-3091.1997.d01-63.x, 1997.
- Bondevik, S., Mangerud, J., Dawson, S., Dawson, A. G., and Lohne, O.: Record-breaking height for 8000-year-old tsunami in the North Atlantic, *EOS, Transactions American Geophysical Union*, 84, 289–293, 2003.
- Bondevik, S., Løvholt, F., Harbitz, C., Mangerud, J., Dawson, A., and Inge Svendsen, J.: The Storegga slide tsunami—comparing field observations with numerical simulations, *Mar. Petrol. Geol.*, 22, 195–208, 2005.
- Brune, S., Babeyko, A. Y., and Sobolev, S. V.: Are tilt measurements useful in detecting tsunamigenic submarine landslides?, *Geochem. Geophys. Geosy.*, 10, Q06002, doi:10.1029/2009gc002491, 2009.
- Brune, S., Babeyko, A., Gaedicke, C., and Ladage, S.: Hazard assessment of underwater landslide-generated tsunamis: A case study in the Padang region, Indonesia, *Nat. Hazards*, 53, 205–218, doi:10.1007/s11069-009-9424-x, 2010.
- Buranapraphat, A., Laongmanee, P., Sukramongkol, N., Prommas, R., Promjinda, S., and Yanagi, T.: Upwelling induced by meso-scale cyclonic eddies in the Andaman Sea, *Coast. Mar. Sci.*, 34, 68–73, 2010.
- Canals, M., Lastras, G., Urgeles, R., Casamor, J. L., Mienert, J., Cattaneo, A., De Batist, M., Haffidason, H., Imbo, Y., Laberg, J. S., Locat, J., Long, D., Longva, O., Masson, D. G., Sultan, N., Trincardi, F., and Bryn, P.: Slope failure dynamics and impacts from seafloor and shallow sub-seafloor geophysical data: Case studies from the COSTA project, *Mar. Geol.*, 213, 9–72, 2004.
- Chakraborty, P. P. and Khan, P. K.: Cenozoic geodynamic evolution of the Andaman–Sumatra subduction margin: Current understanding, *Isl. Arc*, 18, 184–200, doi:10.1111/j.1440-1738.2008.00643.x, 2009.
- Colin, C., Turpin, L., Bertaux, J., Desprairies, A., and Kissel, C.: Erosional history of the Himalayan and Burman ranges during the last two glacial-interglacial cycles, *Earth Planet. Sc. Lett.*, 171, 647–660, 1999.
- Curray, J. R.: Tectonics and history of the Andaman Sea region, *J. Asian Earth Sci.*, 25, 187–232, 2005.
- Dawson, A. G., Long, D., and Smith, D. E.: The Storegga slides: Evidence from eastern Scotland for a possible tsunami, *Mar. Geol.*, 82, 271–276, 1988.
- Dillon, W. P., Risch, J. S., Scanlon, K. M., Valentine, P. C., and Huggett, Q. J.: Ancient crustal fractures control the location and size of collapsed blocks at the Blake escarpment, east of Florida, in: Submarine landslides: Selected Studies in the U.S. Exclusive Economic Zone, edited by: Schwab, W. C., Lee, H. J., and Twichell, D. C., US Geological Survey Bulletin, 54–59, 1993.
- Doust, H. and Noble, R. A.: Petroleum systems of Indonesia, *Mar. Petrol. Geol.*, 25, 103–129, doi:10.1016/j.marpetgeo.2007.05.007, 2008.
- Doust, H. and Sumner, H. S.: Petroleum systems in rift basins – a collective approach in southeast Asian basins, *Petrol. Geosci.*, 13, 127–144, doi:10.1144/1354-079307-746, 2007.
- Dutta, K., Bhushan, R., and Somayajulu, B. L. K.: Rapid vertical mixing rates in deep waters of the Andaman Basin, *Sci. Total Environ.*, 384, 401–408, doi:10.1016/j.scitotenv.2007.04.041, 2007.
- Faugères, J.-C., Stow, D. A. V., Imbert, P., and Viana, A.: Seismic features diagnostic of contourite drifts, *Mar. Geol.*, 162, 1–38, doi:10.1016/S0025-3227(99)00068-7, 1999.
- Fine, I. V., Rabinovich, A. B., Bornhold, B. D., Thomson, R. E., and Kulikov, E. A.: The Grand Banks landslide-generated tsunami of November 18, 1929: Preliminary analysis and numerical modeling, *Mar. Geol.*, 215, 45–57, 2005.
- Frey-Martínez, J., Cartwright, J., and James, D.: Frontally confined versus frontally emergent submarine landslides: A 3D seismic characterisation, *Mar. Petrol. Geol.*, 23, 585–604, doi:10.1016/j.marpetgeo.2006.04.002, 2006.
- Fujino, S., Naruse, H., Matsumoto, D., Jarupongsakul, T., Sphawajraksakul, A., and Sakakura, N.: Stratigraphic evidence for pre-2004 tsunamis in southwestern Thailand, *Mar. Geol.*, 262, 25–28, 2009.
- GEBCO 2008: General Bathymetric Chart of the Oceans (GEBCO), available at: <http://www.bodc.ac.uk/data/onlineDelivery/gebco/>, last access: 28 June 2012.
- Geersen, J., Völker, D., Behrmann, J. H., Reichert, C., and Krastel, S.: Pleistocene giant slope failures offshore Arauco peninsula, southern Chile, *J. Geol. Soc. London*, 168, 1237–1248, doi:10.1144/0016-76492011-027, 2011.

- Greene, H. G., Murai, L. Y., Watts, P., Maher, N. A., Fisher, M. A., Paull, C. E., and Eichhubl, P.: Submarine landslides in the Santa Barbara Channel as potential tsunami sources, *Nat. Hazards Earth Syst. Sci.*, 6, 63–88, doi:10.5194/nhess-6-63-2006, 2006.
- Grilli, S. T. and Watts, P.: Tsunami generation by submarine mass failure, I: Modeling, experimental validation, and sensitivity analyses, *J. Waterw. Port C.-ASCE*, 131, 283–297, 2005.
- Grilli, S. T., Taylor, O.-D. S., Baxter, C. D. P., and Marezki, S.: A probabilistic approach for determining submarine landslide tsunami hazard along the upper east coast of the United States, *Mar. Geol.*, 264, 74–97, 2009.
- Hall, R. and Morley, C. K.: Sundaland basins, in: *Continent-Ocean Interactions within the East Asian Marginal Seas*, edited by: Clift, P., Wang, P., Kuhnt, W., and Hayes, D., American Geophysical Union, Geophysical Monograph, 149, Washington DC, 55–85, 2004.
- Hampton, M. A., Lee, H. J., and Locat, J.: Submarine landslides, *Rev. Geophys.*, 34, 33–59, doi:10.1029/95rg03287, 1996.
- Harbitz, C. B., Lovholt, F., Pedersen, G., and Masson, D. G.: Mechanisms of tsunami generation by submarine landslides: A short review, *Norw. J. Geol.*, 86, 255–264, 2006.
- Hasegawa, H. S. and Kanamori, H.: Source mechanism of the magnitude 7.2 Grand Banks earthquake of November 1929: Double couple or submarine landslide?, *B. Seismol. Soc. Am.*, 77, 1984–2004, 1987.
- Haugen, K. B., Løvholt, F., and Harbitz, C. B.: Fundamental mechanisms for tsunami generation by submarine mass flows in idealised geometries, *Mar. Petrol. Geol.*, 22, 209–217, 2005.
- Hernández-Molina, F. J., Maldonado, A., and Stow, D. A. V.: Abyssal plain contourites, in: *Contourites, Developments in Sedimentology*, edited by: Rebesco, M. and Camerlenghi, A., Elsevier, Amsterdam, Netherlands, 345–378, 2008.
- Hollister, C. D. and McCave, I. N.: Sedimentation under deep-sea storms, *Nature*, 309, 220–225, 1984.
- Hühnerbach, V. and Masson, D. G.: Landslides in the North Atlantic and its adjacent seas: An analysis of their morphology, setting and behaviour, *Mar. Geol.*, 213, 343–362, doi:10.1016/j.margeo.2004.10.013, 2004.
- Hyder, P., Jeans, D. R. G., Cauquil, E., and Nerzic, R.: Observations and predictability of internal solitons in the northern Andaman Sea, *Appl. Ocean Res.*, 27, 1–11, doi:10.1016/j.apor.2005.07.001, 2005.
- Jankaew, K., Atwater, B. F., Sawai, Y., Choowong, M., Charoentitrat, T., Martin, M. E., and Prendergast, A.: Medieval forewarning of the 2004 Indian Ocean tsunami in Thailand, *Nature*, 455, 1228–1231, 2008.
- Jansen, E., Befring, S., Bugge, T., Eidvin, T., Holtedahl, H., and Sejrup, H. P.: Large submarine slides on the norwegian continental margin: Sediments, transport and timing, *Mar. Geol.*, 78, 77–107, doi:10.1016/0025-3227(87)90069-7, 1987.
- Jha, P., Ros, D., degli Alessandrini, A., and Kishore, M.: Speculative petroleum system and play model of East Andaman Basin from regional geology and basin evolution concepts: Addressing the exploration challenges of an extreme frontier area, 8th Biennial International Conference and Exposition on Petroleum Geophysics, Hyderabad, India, P-261, 2010.
- Jha, P., Ros, D., and Kishore, M.: Seismic and sequence stratigraphic framework and depositional architecture of shallow and deepwater postrift sediments in East Andaman Basin: An overview, *GeoIndia 2011*, Greater Noida, New Delhi, India, 12–14 January, 2011.
- Jintasaerane, P., Weinrebe, W., Klauke, I., Snidvongs, A., and Flueh, E. R.: Morphology of the Andaman outer shelf and upper slope of the Thai exclusive economic zone, *J. Asian Earth Sci.*, 46, 78–85, doi:10.1016/j.jseas.2011.11.003, 2012.
- Kamesh Raju, K. A.: Three-phase tectonic evolution of the Andaman Backarc Basin, *Curr. Sci. India*, 89, 1932–1937, <http://drs.nio.org/drs/handle/2264/339>, 2005.
- Kamesh Raju, K. A., Ramprasad, T., Rao, P. S., Ramalingeswara Rao, B., and Varghese, J.: New insights into the tectonic evolution of the Andaman Basin, northeast Indian Ocean, *Earth Planet. Sc. Lett.*, 221, 145–162, 2004.
- Kamesh Raju, K. A., Murty, G. P. S., Amarnath, D., and Kumar, M. L. M.: The West Andaman Fault and its influence on the aftershock pattern of the recent megathrust earthquakes in the Andaman-Sumatra region, *Geophys. Res. Lett.*, 34, L03305, doi:10.1029/2006gl028730, 2007.
- Keller, G. H. and Richards, A. F.: Sediments of the Malacca Strait, Southeast Asia, *J. Sediment. Res.*, 37, 102–127, doi:10.1306/74d7166d-2b21-11d7-8648000102c1865d, 1967.
- Khan, A.: Seismogenic sources in the bay of bengal vis-à-vis potential for tsunami generation and its impact in the northern bay of bengal coast, *Nat. Hazards*, 61, 1127–1141, doi:10.1007/s11069-011-9970-x, 2012.
- Kishore, M., Jha, P., and Ros, D.: Structural modeling and seismic attributes analysis of synrift sequences in East Andaman Basin: A qualitative approach towards fault seal analysis in a frontier exploration area, 8th Biennial International Conference and Exposition on Petroleum Geophysics, Hyderabad, India, P-262, 2010.
- Krastel, S., Wefer, G., Hanebuth, T., Antobreh, A., Freudenthal, T., Preu, B., Schwenk, T., Strasser, M., Violante, R., Winkelmann, D., and M78/3 shipboard scientific party: Sediment dynamics and geohazards off Uruguay and the de la Plata River region (northern Argentina and Uruguay), *Geo-Mar. Lett.*, 31, 271–283, doi:10.1007/s00367-011-0232-4, 2011.
- Krastel, S., Wynn, R. B., Georgiopolou, A., Geersen, J., Henrich, R., Meyer, M., and Schwenk, T.: Large-scale mass wasting on the Northwest African continental margin: Some general implications for mass wasting on passive continental margins, in: *Submarine mass movements and their consequences*, edited by: Yamada, Y., Kawamura, K., Ikehara, K., Ogawa, Y., Urgeles, R., Mosher, D., Chaytor, J., and Strasser, M., Advances in natural and technological hazards research, Springer, Netherlands, 189–199, 2012.
- Kulikov, E. A., Rabinovich, A. B., Thomson, R. E., and Bornhold, B. D.: The landslide tsunami of November 3, 1994, Skagway Harbor, Alaska, *J. Geophys. Res.*, 101, 6609–6615, doi:10.1029/95jc03562, 1996.
- Laberg, J. S. and Camerlenghi, A.: The significance of contourites for submarine slope stability, in: *Contourites, Developments in sedimentology*, edited by: Rebesco, M., and Camerlenghi, A., Elsevier, Amsterdam, Netherlands, 537–556, 2008.
- Lay, T., Kanamori, H., Ammon, C. J., Nettles, M., Ward, S. N., Aster, R. C., Beck, S. L., Bilek, S. L., Brudzinski, M. R., Butler, R., DeShon, H. R., Ekström, G., Satake, K., and Sipkin, S.: The great Sumatra-Andaman earthquake of 26 December 2004, *Science*, 308, 1127–1133, doi:10.1126/science.1112250, 2005.

- Lin, Y.-n. N., Sieh, K., and Stock, J.: Submarine landslides along the Malacca Strait-Mergui Basin shelf margin: Insights from sequence-stratigraphic analysis, *J. Geophys. Res.*, 115, B12102, doi:10.1029/2009jb007050, 2010.
- Lomax, A., Michélini, A., and Piatanesi, A.: An energy-duration procedure for rapid determination of earthquake magnitude and tsunamigenic potential, *Geophys. J. Int.*, 170, 1195–1209, doi:10.1111/j.1365-246X.2007.03469.x, 2007.
- Løvholt, F., Harbitz, C. B., and Haugen, K. B.: A parametric study of tsunamis generated by submarine slides in the Ormen Lange/Storegga area off western Norway, *Mar. Petrol. Geol.*, 22, 219–231, doi:10.1016/j.marpetgeo.2004.10.017, 2005.
- Lykousis, V., Sakellariou, D., Moretti, I., and Kaberi, H.: Late Quaternary basin evolution of the Gulf of Corinth: Sequence stratigraphy, sedimentation, fault-slip and subsidence rates, *Tectonophysics*, 440, 29–51, doi:10.1016/j.tecto.2006.11.007, 2007.
- Masson, D. G., Harbitz, C. B., Wynn, R. B., Pedersen, G., and Lovholt, F.: Submarine landslides: Processes, triggers and hazard prediction, *Philos. T. R. Soc. A*, 364, 2009–2039, doi:10.1098/rsta.2006.1810, 2006.
- Masson, D. G., Wynn, R. B., and Talling, P. J.: Large landslides on passive continental margins: Processes, hypotheses and outstanding questions, in: *Submarine mass movements and their consequences*, edited by: Mosher, D. C., Moscardelli, L., Baxter, C. D. P., Urgeles, R., Shipp, R. C., Chaytor, J. D., and Lee, H. J., *Advances in natural and technological hazards research*, Springer, Netherlands, 153–165, 2010.
- Matsumoto, T. and Tappin, D. R.: Possible coseismic large-scale landslide off the northern coast of Papua New Guinea in July 1998: Geophysical and geological results from SOS cruises, *Pure Appl. Geophys.*, 160, 1923–1943, 2003.
- Michel, G. W., Yu, Y. Q., Zhu, S. Y., Reigber, C., Becker, M., Reinhardt, E., Simons, W., Ambrosius, B., Vigny, C., Chamot-Rooke, N., Le Pichon, X., Morgan, P., and Matheussen, S.: Crustal motion and block behaviour in SE-Asia from GPS measurements, *Earth Planet. Sc. Lett.*, 187, 239–244, doi:10.1016/s0012-821x(01)00298-9, 2001.
- Monecke, K., Finger, W., Klarer, D., Kongko, W., McAdoo, B. G., Moore, A. L., and Sudrajat, S. U.: A 1,000-year sediment record of tsunami recurrence in northern Sumatra, *Nature*, 455, 1232–1234, doi:10.1038/nature07374, 2008.
- Morley, C. K.: A tectonic model for the Tertiary evolution of strike-slip faults and rift basins in SE Asia, *Tectonophysics*, 347, 189–215, doi:10.1016/s0040-1951(02)00061-6, 2002.
- Morley, C. K., Woganan, N., Sankumarn, N., Hoon, T. B., Alief, A., and Simmons, M.: Late Oligocene-recent stress evolution in rift basins of northern and central Thailand: Implications for escape tectonics, *Tectonophysics*, 334, 115–150, doi:10.1016/s0040-1951(00)00300-0, 2001.
- Morley, C. K., Charusiri, P., and Watkinson, I.: Structural geology of Thailand during the Cenozoic, in: *The geology of Thailand*, edited by: Barber, A. J. and Ridd, F. D., Geological Society of London, London, United Kingdom, 539–571, 2011.
- National Geophysical Data Center/World Data Center (NGDC/WDC), Significant Earthquake Database, Boulder, CO, USA, available at: <http://www.ngdc.noaa.gov/nndc/struts/form?t=101650&s=1&d=1>, last access: 28 June 2012.
- National Geophysical Data Center/World Data Center (NGDC/WDC), Global Historical Tsunami Database, Boulder, CO, USA, available at: http://www.ngdc.noaa.gov/hazard/tsu_db.shtml, last access: 28 June 2012.
- Nielsen, C., Chamot-Rooke, N., and Rangin, C.: From partial to full strain partitioning along the Indo-Burmese hyper-oblique subduction, *Mar. Geol.*, 209, 303–327, doi:10.1016/j.margeo.2004.05.001, 2004a.
- Nielsen, T. G., Bjørnsen, P. K., Boonruang, P., Fryd, M., Hansen, P. J., Janekarn, V., Limtrakulvong, V., Munk, P., Hansen, O. S., Satapoomin, S., Sawangrerruks, S., Thomsen, H. A., and Østergaard, J. B.: Hydrography, bacteria and protist communities across the continental shelf and shelf slope of the Andaman Sea (NE Indian Ocean), *Mar. Ecol. Prog. Ser.*, 274, 69–86, doi:10.3354/meps274069, 2004b.
- Nielsen, T., Knutz, P. C., and Kuijpers, A.: Seismic expression of contourite depositional systems, in: *Contourites, Developments in sedimentology*, edited by: Rebesco, M. and Camerlenghi, A., Elsevier, Amsterdam, Netherlands, 301–321, 2008.
- Okubo, A., Obata, H., Nozaki, Y., Yamamoto, Y., and Minami, H.: 230th in the Andaman Sea: Rapid deep-sea renewal, *Geophys. Res. Lett.*, 31, L22306, doi:10.1029/2004gl020226, 2004.
- Ornthammarath, T., Warnitchai, P., Worakanchana, K., Zaman, S., Sigbjörnsson, R., and Lai, C.: Probabilistic seismic hazard assessment for Thailand, *B. Earthq. Eng.*, 9, 367–394, doi:10.1007/s10518-010-9197-3, 2011.
- Osborne, A. R. and Burch, T. L.: Internal solitons in the Andaman Sea, *Science*, 208, 451–460, doi:10.1126/science.208.4443.451, 1980.
- Panchang, R., Nigam, R., Raviprasad, G. V., Rajagopalan, G., Ray, D. K., and Hla, U. K. Y.: Relict faunal testimony for sea-level fluctuations off Myanmar (Burma), *J. Palaeon. Soc. India*, 53, 185–195, 2008.
- Piper, D. J. W., Cochonat, P., and Morrison, M. L.: The sequence of events around the epicentre of the 1929 Grand Banks earthquake: Initiation of debris flows and turbidity current inferred from sidescan sonar, *Sedimentology*, 46, 79–97, 1999.
- Polachan, S.: The geological evolution of the Mergui Basin SE Andaman area, Thailand, Ph.D thesis, University of London, London, 218 pp., 1988.
- Polachan, S. and Racey, A.: Stratigraphy of the Mergui Basin, Andaman Sea: Implications for petroleum exploration, *J. Petrol. Geol.*, 17, 373–406, doi:10.1111/j.1747-5457.1994.tb00147.x, 1994.
- Polachan, S., Praditjan, S., Tongtaow, C., Janmaha, S., Intarawijit, K., and Sangsuwan, C.: Development of cenozoic basins in thailand, *Mar. Petrol. Geology*, 8, 84–97, doi:10.1016/0264-8172(91)90047-5, 1991.
- Pomar, L., Morsilli, M., Hallock, P., and Bádenas, B.: Internal waves, an under-explored source of turbulence events in the sedimentary record, *Earth-Sci. Rev.*, 111, 56–81, doi:10.1016/j.earscirev.2011.12.005, 2012.
- Prosser, S.: Rift-related linked depositional systems and their seismic expression, Geological Society, London, Special Publications, 71, 35–66, doi:10.1144/gsl.sp.1993.071.01.03, 1993.
- Radhakrishna, M., Lasitha, S., and Mukhopadhyay, M.: Seismicity, gravity anomalies and lithospheric structure of the Andaman Arc, NE Indian Ocean, *Tectonophysics*, 460, 248–262, doi:10.1016/j.tecto.2008.08.021, 2008.
- Rahiman, T. I. H., Pettinga, J. R., and Watts, P.: The source mechanism and numerical modelling of the 1953 Suva tsunami,

- Fiji, *Mar. Geol.*, 237, 55–70, doi:10.1016/j.margeo.2006.10.036, 2007.
- Ramaswamy, V., Rao, P. S., Rao, K. H., Thwin, S., Rao, N. S., and Raiker, V.: Tidal influence on suspended sediment distribution and dispersal in the northern Andaman Sea and Gulf of Martaban, *Mar. Geol.*, 208, 33–42, doi:10.1016/j.margeo.2004.04.019, 2004.
- Rao, P. S., Ramaswamy, V., and Thwin, S.: Sediment texture, distribution and transport on the Ayeyarwady continental shelf, Andaman Sea, *Mar. Geol.*, 216, 239–247, doi:10.1016/j.margeo.2005.02.016, 2005.
- Rebesco, M. and Stow, D.: Seismic expression of contourites and related deposits: A preface, *Mar. Geophys. Res.*, 22, 303–308, 2001.
- Reicherter, K., Hoffmann, N., Lindhorst, K., Krastel, S., Fernández-Steeger, T., Grützner, C., and Wiater, T.: Active basins and neotectonics: Morphotectonics of the Lake Ohrid Basin (FYROM and Albania), *Z. Dtsch Ges. Geowiss.*, 162, 217–234, 2011.
- Robinson, R., Bird, M., Oo, N., Hoey, T., Aye, M., Higgitt, D., Lu, X., Swe, A., Tun, T., and Win, S.: The Irrawaddy river sediment flux to the Indian Ocean: The original nineteenth-century data revisited, *J. Geol.*, 115, 629–640, 2007.
- Rodolfo, K. S.: Sediments of the Andaman Basin, northeastern Indian Ocean, *Mar. Geol.*, 7, 371–402, 1969.
- Shanmugam, G.: Deep-water bottom currents and their deposits, in: *Contourites, Developments in sedimentology*, edited by: Rebesco, M., and Camerlenghi, A., Elsevier, Amsterdam, Netherlands, 59–81, 2008.
- Sobolev, S. V., Babeyko, A. Y., Wang, R., Hoechner, A., Galas, R., Rothacher, M., Sein, D. V., Schröter, J., Lauterjung, J., and Subarya, C.: Tsunami early warning using GPS-shield arrays, *J. Geophys. Res.*, 112, B08415, doi:10.1029/2006jb004640, 2007.
- Socquet, A., Vigny, C., Chamot-Rooke, N., Simons, W., Rangin, C., and Ambrosius, B.: India and Sunda plates motion and deformation along their boundary in Myanmar determined by GPS, *J. Geophys. Res.*, 111, B05406, doi:10.1029/2005jb003877, 2006.
- Stigall, J. and Dugan, B.: Overpressure and earthquake initiated slope failure in the Ursa region, northern Gulf of Mexico, *J. Geophys. Res.*, 115, B04101, doi:10.1029/2009jb006848, 2010.
- Stow, D. A. V. and Mayall, M.: Deep-water sedimentary systems: New models for the 21st century, *Mar. Petrol. Geol.*, 17, 125–135, 2000.
- Tappin, D. R.: Sediment slump likely caused Papua New Guinea tsunami, *EOS Transactions American Geophysical Union*, 80, 1999.
- Tappin, D. R., Watts, P., McMurtry, G. M., Lafoy, Y., and Matsumoto, T.: The Sissano, Papua New Guinea tsunami of July 1998 – offshore evidence on the source mechanism, *Mar. Geol.*, 175, 1–23, 2001.
- Varkey, M. J., Murty, V. S. N., and Suryanarayana, A.: Physical oceanography of the Bay of Bengal and Andaman Sea, *Oceanography and Marine Biology: An Ann. Rev.*, 34, 1–70, 1996.
- Vlasenko, V. and Alpers, W.: Generation of secondary internal waves by the interaction of an internal solitary wave with an underwater bank, *J. Geophys. Res.*, 110, C02019, doi:10.1029/2004jc002467, 2005.
- Vlasenko, V. and Stashchuk, N.: Three-dimensional shoaling of large-amplitude internal waves, *J. Geophys. Res.*, 112, C11018, doi:10.1029/2007jc004107, 2007.
- Völker, D., Weinrebe, W., Behrmann, J. H., Bialas, J., and Klaeschen, D.: Mass wasting at the base of the south central Chilean continental margin: The Reloca slide, *Adv. Geosci.*, 22, 155–167, doi:10.5194/adgeo-22-155-2009, 2009.
- Vorren, T. O., Laberg, J. S., Blaume, F., Dowdeswell, J. A., Kenyon, N. H., Mienert, J., Rumohr, J. A. N., and Werner, F.: The Norwegian–Greenland sea continental margins: Morphology and late Quaternary sedimentary processes and environment, *Quaternary Sci. Rev.*, 17, 273–302, doi:10.1016/s0277-3791(97)00072-3, 1998.
- Wang, Y., Sieh, K., Aung, T., Min, S., Khaing, S. N., and Tun, S. T.: Earthquakes and slip rate of the southern Sagaing Fault: Insights from an offset ancient fort wall, lower Burma (Myanmar), *Geophys. J. Int.*, 185, 49–64, doi:10.1111/j.1365-246X.2010.04918.x, 2011.
- Ward, S. N.: Landslide tsunami, *J. Geophys. Res.-Sol. Ea.*, 106, 11201–11215, 2001.
- Weiss, R., Fritz, H. M., and Wünnemann, K.: Hybrid modeling of the mega-tsunami runup in Lituya Bay after half a century, *Geophys. Res. Lett.*, 36, L09602, doi:10.1029/2009gl037814, 2009.
- Wyrtki, K.: Physical oceanography of the southeast Asian waters, NAGA Report, Volume 2, Scientific Results of Marine Investigations of the South China Sea and the Gulf of Thailand 1959–1961, The University of California, Scripps Institution of Oceanography, La Jolla, California, 195 pp., 1961.
- Yamada, Y., Kawamura, K., Ikehara, K., Ogawa, Y., Urgeles, R., Mosher, D., Chaytor, J., and Strasser, M. (Eds.): Submarine mass movements and their consequences, *Advances in natural and technological hazards research*, Springer, Dordrecht, Netherlands, 2012.

Jintasaeranee, P., Weinrebe, W., Flueh, E.R. (Leibniz Institute of Marine Sciences (IFM-GEOMAR), Kiel, Germany), Snidvongs, A. (Department of Marine Science, Faculty of Science, Chulalongkorn University, Bangkok, Thailand)

Morphodynamics of the Andaman Sea Shelf Break, Thai EEZ

The primary aim of the project Morphodynamics and Slope Stability of the Andaman Sea Shelf Break is the in situ characterization of the slope of the Andaman Shelf in Thai EEZ with special emphasis on previous slope failures and a possible tendency to fail in the future. The first cruise of the project was conducted in November-December 2006, the second cruise in October-November 2007 using the RV Chakratong Tongyai. Both cruises were devoted to hydroacoustic mapping of the shelf break and the slope. A multibeam bathymetric echosounder (MB) and a parametric sediment echosounder (sub-bottom profiler; SBP) were used to map the bathymetry and the thickness and structure of the uppermost sedimentary layer of hitherto unexplored parts of the shelf break in the Andaman Sea. An area of more than 3,000 km² in the southwestern corner of the Thai EEZ in the Andaman Sea was successfully mapped. The data cover the upper shelf break from about 500 m down to about 1,400 m water depth. Three especially interesting slope areas and three plateaus are seen in the bathymetric map. In addition, one mud volcano and more than 10 mounds in the mud volcano area have been identified. The processing of the SBP data is still ongoing, so far 34 locations that had distinct morphologic and/or unusual sediment seismic features in this survey area were studied. Most of these (30) anomalous features were attributed to areas with possible occurrence of low-density fluids or gases in the shallow sediment layers. Almost all of these fluid or gas deposits were in lower slope areas with water depth greater than 900 m. In addition, several manifestations of fluid venting were also mapped on the upper shelf edge at water depths of about 600 m. Some of these shallower vents could form mounds with diameters of up to 500 m and heights of up to 50 m. Diffuse reflections in the vicinity of the mounds and strong signals not related to seafloor reflections indicate the presence of uprising bubbles or gas flares.

Contact person

Name: Mr. Pachoenchoke Jintasaeranee
Leibniz-Institut für Meereswissenschaften an der universität Kiel (IFM-GEOMAR)
Address: Dienstgebäude Ostufer Wischhofstr. 1-3, 24148 KIEL, GERMANY.
Telephone:
Telefax:
email: pjintasaeranee@ifm-geomar.de

Contribution

Title: Morphodynamics of the Andaman Sea Shelf Break, Thai EEZ
Presentation type: Oral
Session: MG Marine Geophysics
Keywords: Andaman Sea, Bathymetry, Multibeam echosounder
Key Topic(s): S 1 Marine Geophysics
Info WWW:
Info email:
Special devices:



69. Jahrestagung der
Deutschen Geophysikalischen
Gesellschaft
23.3. - 26.3.2009



IFM-GEOMAR
Leibniz-Institut für Meereswissenschaften
an der Universität Kiel



IFM-GEOMAR
Leibniz-Institut für Meereswissenschaften
an der Universität Kiel

**Southeast Asia
START**
IHDP · IGBP · WCRP
Regional Center



**UNITED NATIONS
UNIVERSITY
UNU-EHS**
Institute for Environment
and Human Security



Morphodynamics of the Andaman Sea Shelf Break, Thai EEZ

The high resolution bathymetry

Pachoenchoke Jintasaeranee^{1,2,5}, Wilhelm Weinrebe², Ernst Flueh², Anond Snidvongs^{3,4}, Ingo Klaucke², and Daniel Winkelmann²

Outline

1. Tectonic provinces of the Andaman Sea
2. Instruments (swath bathymetry & sediment echosounder)
3. Results
 - accuracy assessment of echodata
 - prominent morphological features
 - comparison of the high resolution bathymetry to digital global bathymetric data set
4. Summary



¹ The United Nations University, Institute for Environment and Human Security (UNU-EHS), Bonn, Germany.

² Leibniz-Institut für Meereswissenschaften an der Universität Kiel (IFM-GEOMAR), Kiel, Germany.

³ Southeast Asia START Regional Center, Chulalongkorn University (START), Bangkok, Thailand.

⁴ Department of Marine Science, Faculty of Science, Chulalongkorn University, Bangkok, Thailand.

⁵ Department of Aquatic Science, Faculty of Science, Burapha University, Chonburi, Thailand.

Tectonic provinces of the Andaman Sea

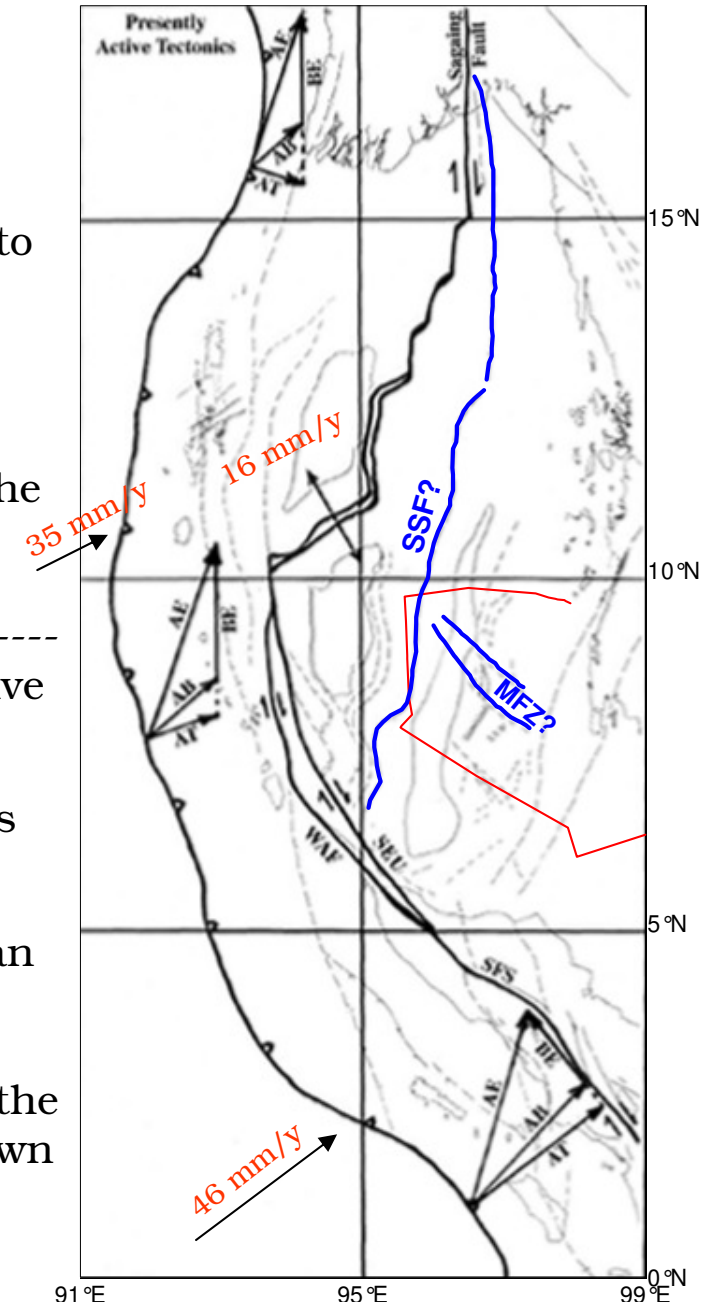
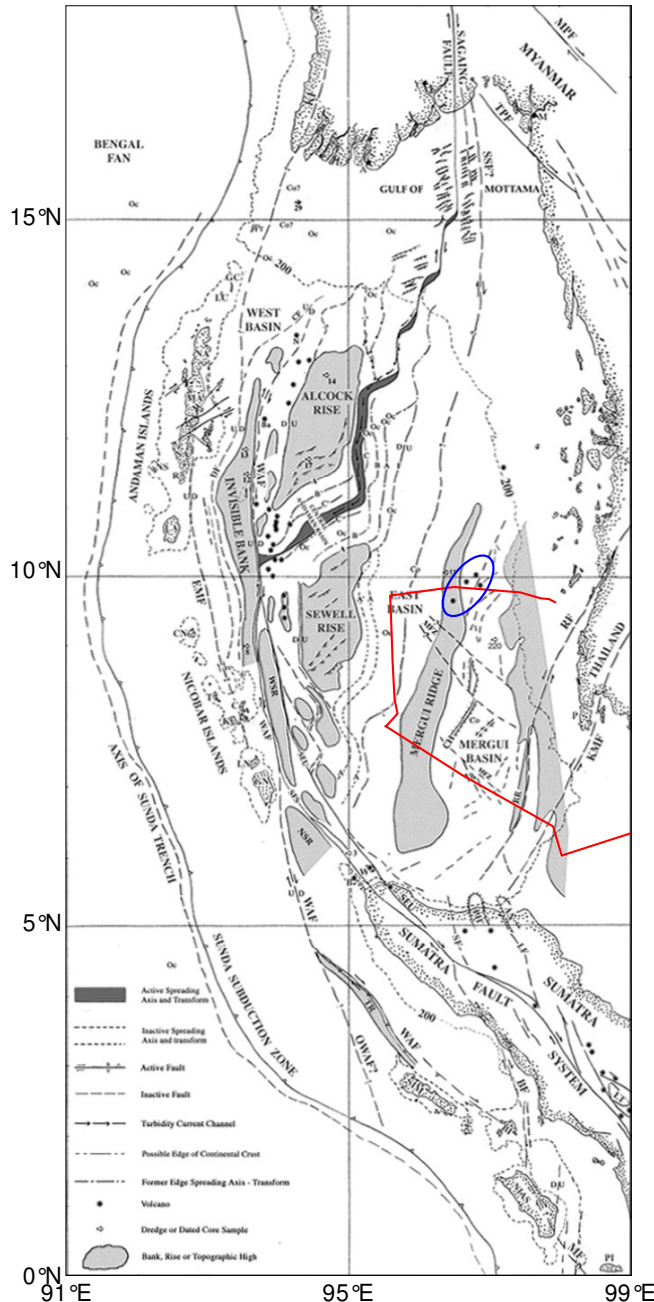
The Andaman basin is divided into three provinces (Curry, 2005).

1. A forearc basin includes West Basin.
2. The magmatic arc corresponds to Barren-Narcondam volcanic islands
3. The backarc region includes Alcock and Sewell Rises, East Basin, the shelf and basins to the north and east and the Central Andaman Basin.

The Andaman sea is an oblique active backarc basin (Curry, 2005).

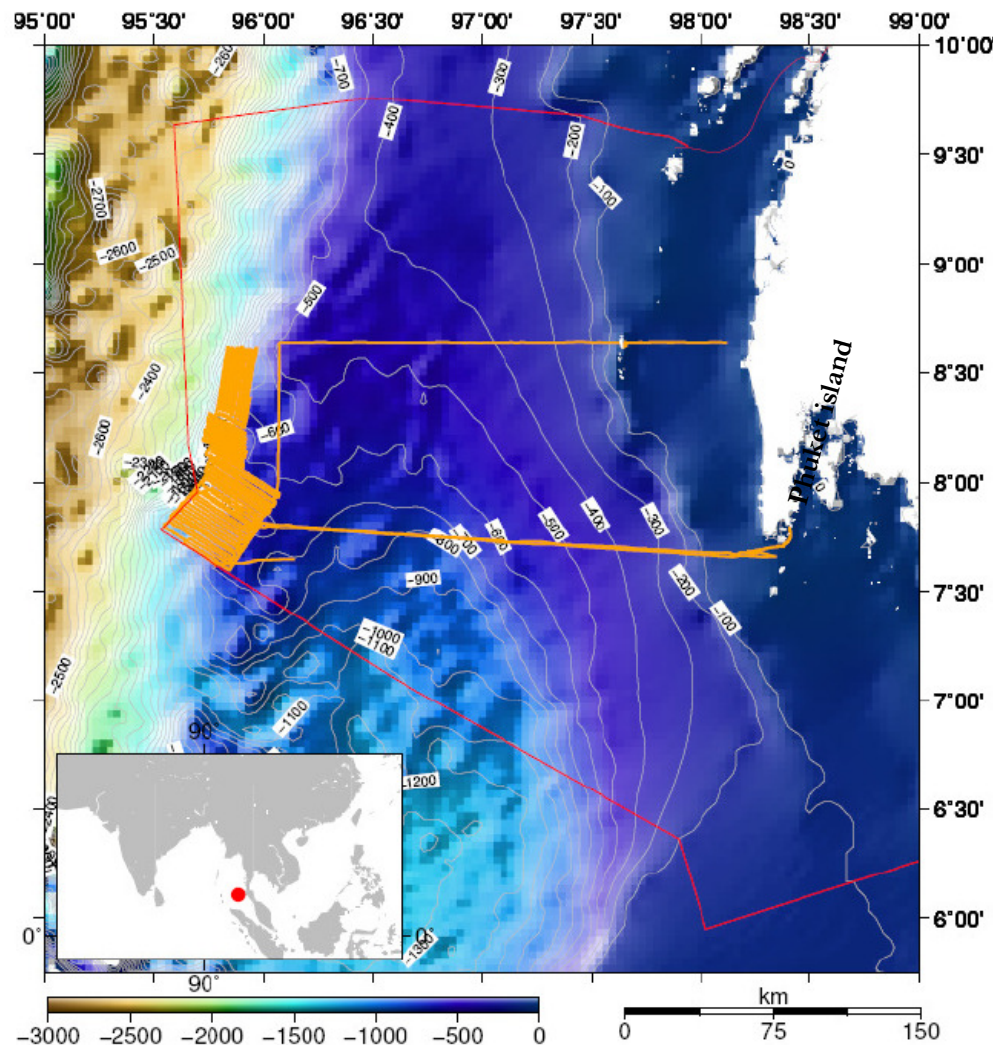
An extension of the central fault has been surveyed (Raju et al., 2004).

The position of strike-slip fault, Shan Scarp Fault (**SSF?**) and Mergui fault (**MFZ?**), in vicinity of the Andaman Sea shelf break near the Mergui Ridge is not exactly known (Richter, et al., 1993; Polachan and Racey, 1993; Curry, 2005).



MASS project

- The 2004 tsunami hit the coast and kill many people.
- The NRCT-DFG cooperation research which is “Morphodynamic and slope stability of the Andaman Sea Shelf break” is commenced in 2006 (MASS project)



Objectives

- To map a new bathymetry which is derived from multibeam echosounder.
- To characterized the morphology of the western slope of Mergui Ridge.

Field surveys

- MASS-I, 1st-cruise : 20 November-6 December 2006
- MASS-II, 2nd-cruise : 6-15 November 2007
- An area ~3000 km² has been mapped.

Research vessel

R.V. Chakratong Tongyai. (PMBC)



Survey Instruments

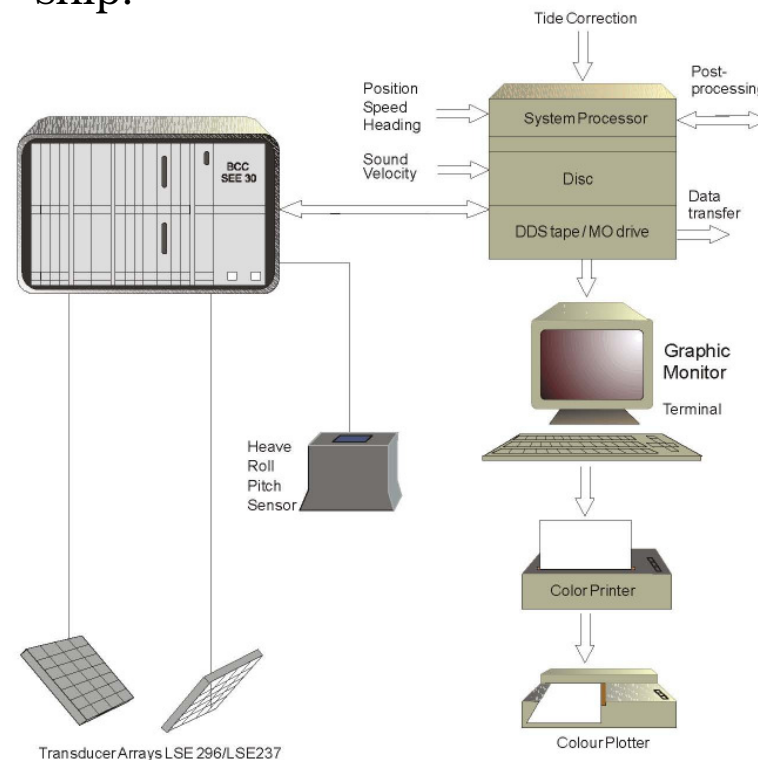
- An INNOMAR SES 2000

Parametric sediment echosounder system
was mounted at starboard side of the vessel.



- The IXSEA OCTANS 1000
Motion Sensor recorded the ship
roll, pitch and heave data

- A GARMIN 152 GPS recorded
position, speed and heading of the
ship.



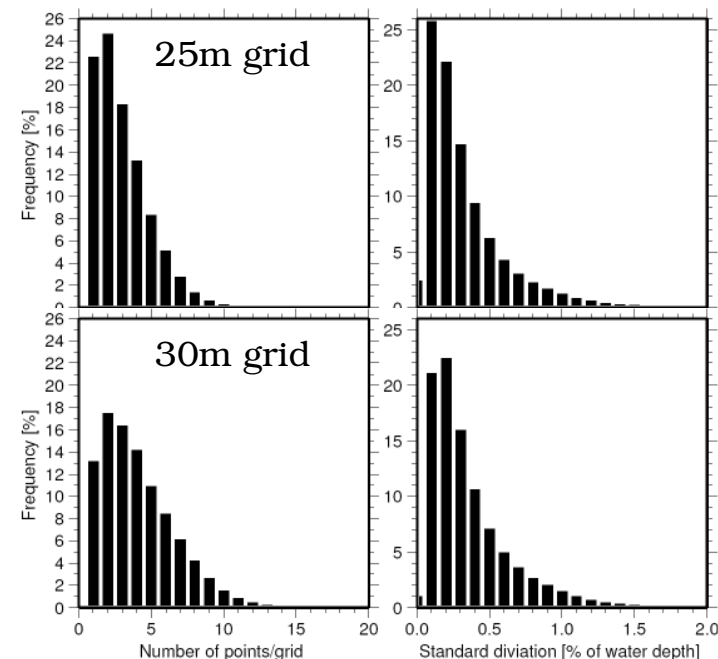
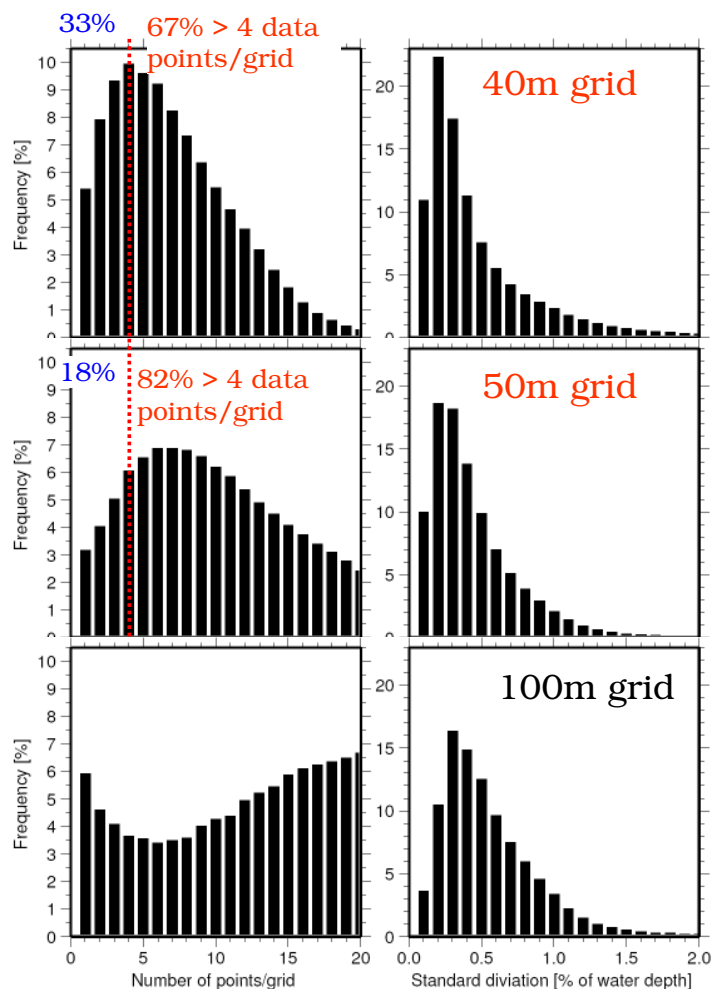
- A SEA BEAM 1050

Multibeam echosounder system
was mounted at the port side.



Accuracy assessment of terrain model

	MASS-I leg1	MASS-I leg2	MASS-II
Num. of good beams	79.82 %	69.03 %	72.44 %
Num. of zero beam	4.80 %	12.76 %	5.65 %
Num. of flagged beams	15.38 %	18.21 %	21.91 %

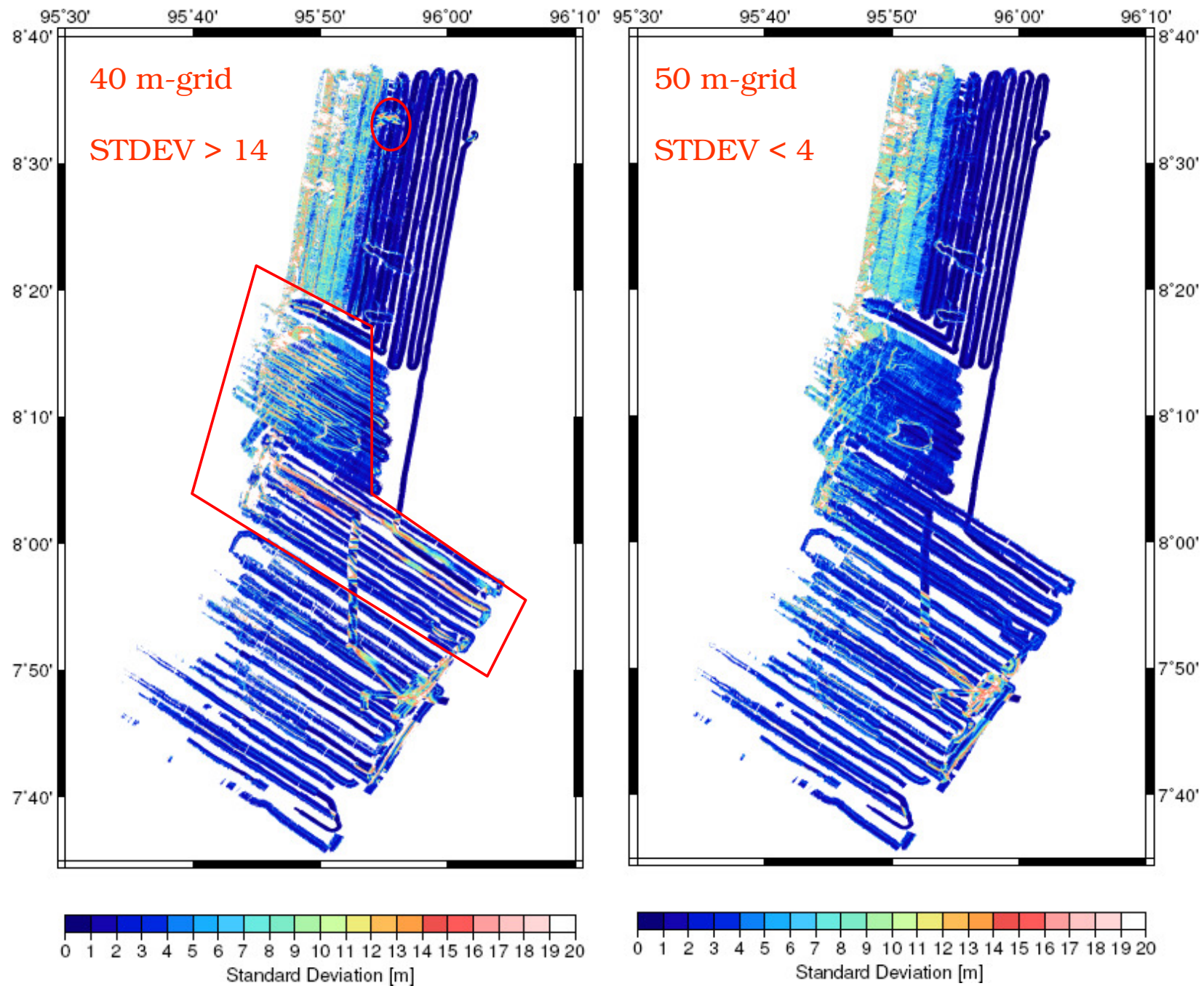


-A number of data points per grid and a standard deviation are used for assessment an accuracy of various grid qualities (Beyer, Rathlau, and Schenke, 2005b).

-The bathymetry can be presented by a 40 m-grid and/or a 50 m-grid resolution.

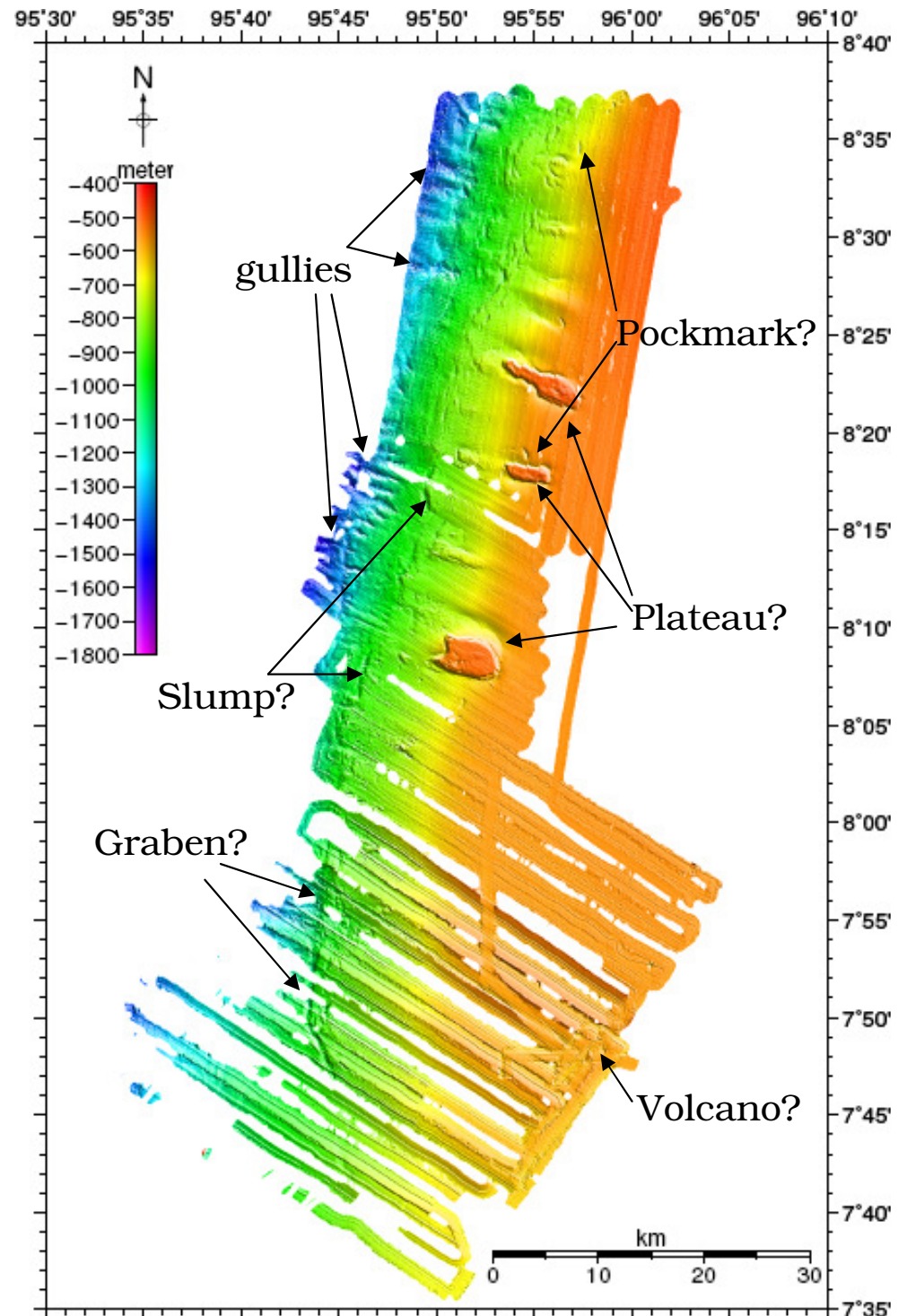
Grid resolution	25 m	30 m	40 m	50 m
data points/grid (average)	2.29	3.29	5.86	9.15
data points/grid (median)	~1-2	~2-3	~3-5 67% > 4 33% < 4	~6-8 82% > 4 18% < 4
Median standard deviation (% of water depth)	>0.1	>0.2	>0.2	>0.2

Accuracy assessment of terrain model



Prominent morphological features

- The bathymetry could be generated by a 50 m-grid resolution. It is called “**MASS50**” in this presentation.
- Ten positions of mound-like feature and two positions of volcano-like feature are observed in a volcano area at 500-950 m depth.
- Three positions of flat-top plateau-like feature that protrude high above the ocean floor and two positions of pockmark-like feature are observed at 500-700 m depth.
- Two possible slumps and more than ten gullies are identified in a slope area below 700 m depth

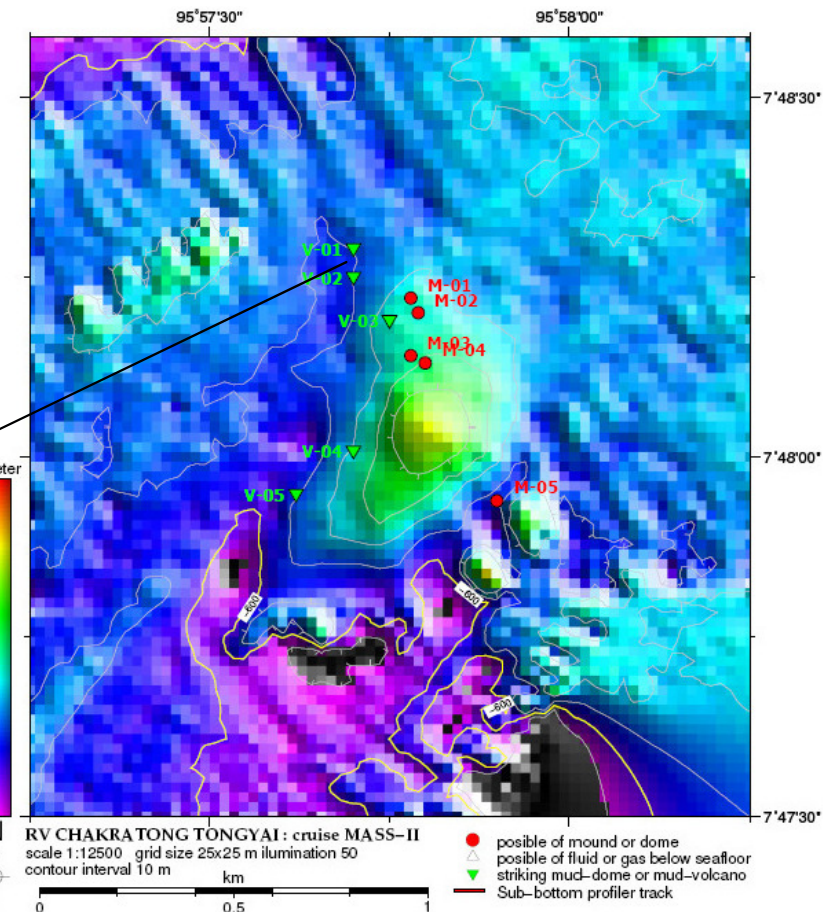
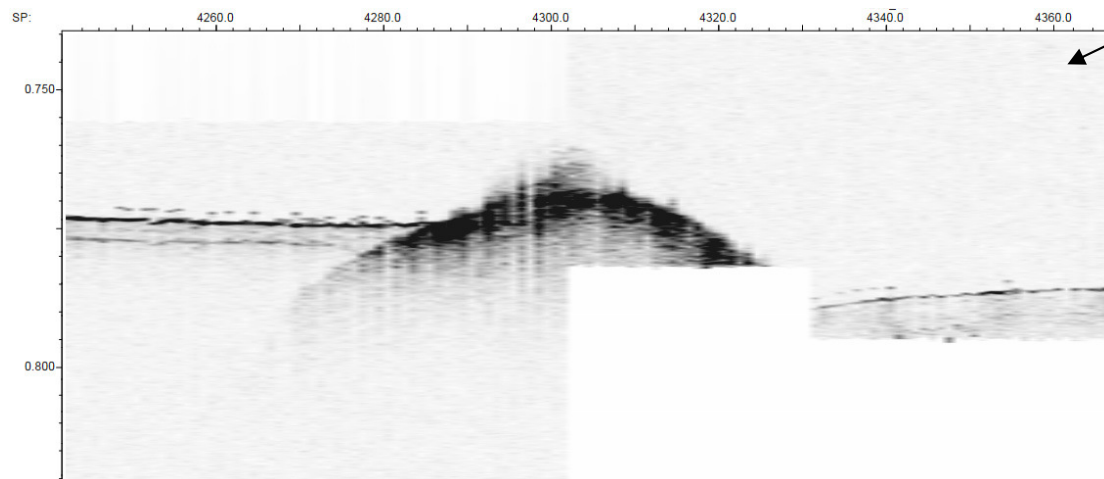
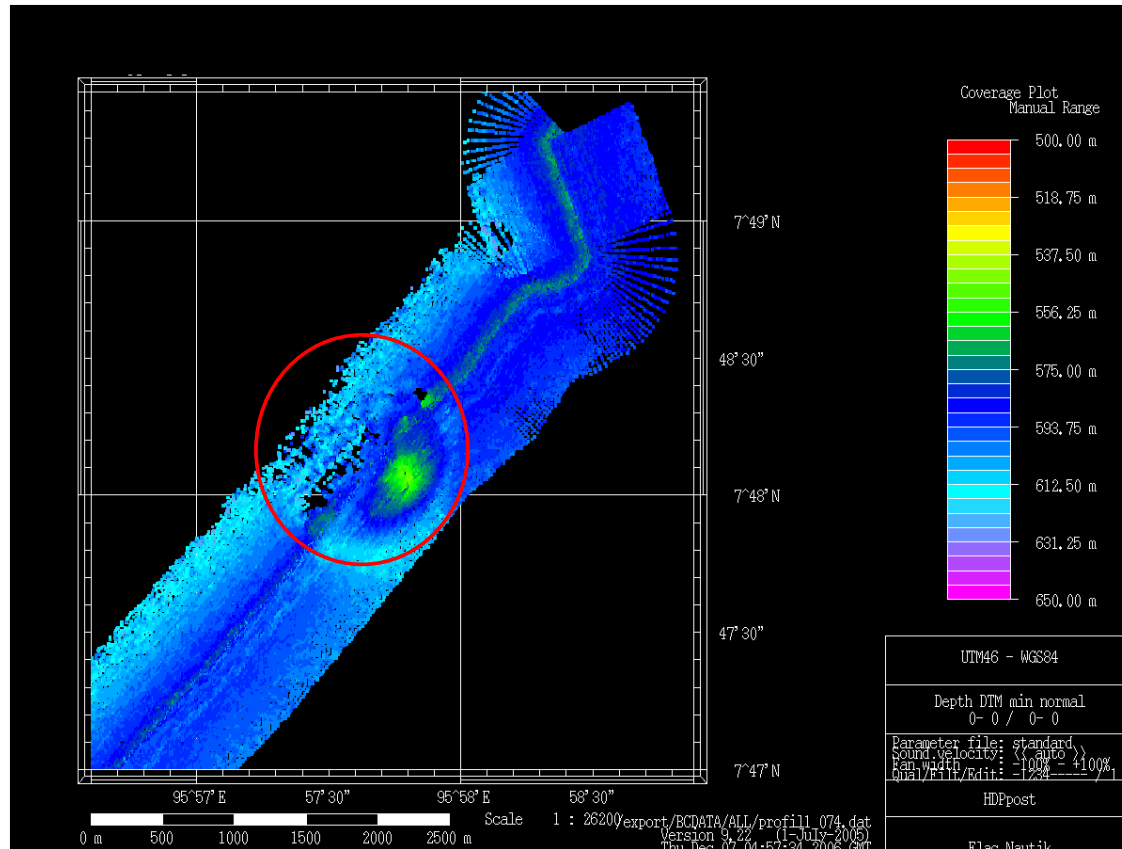


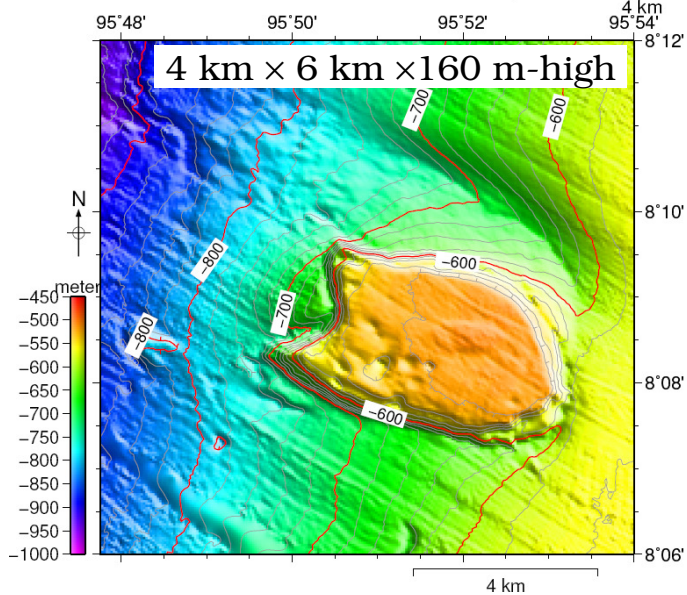
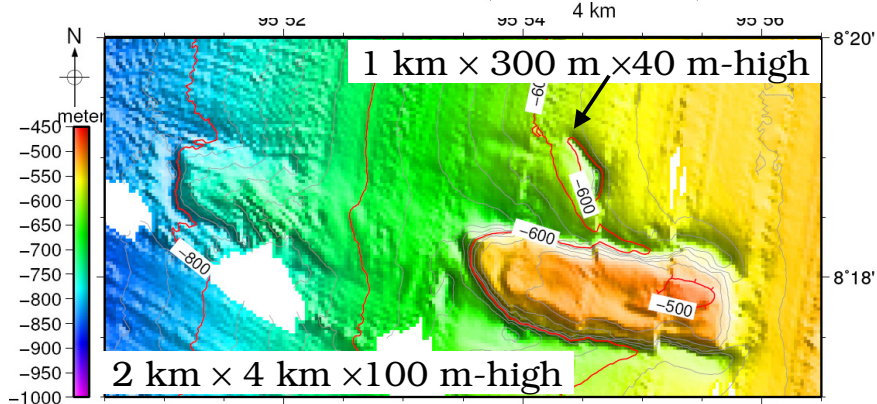
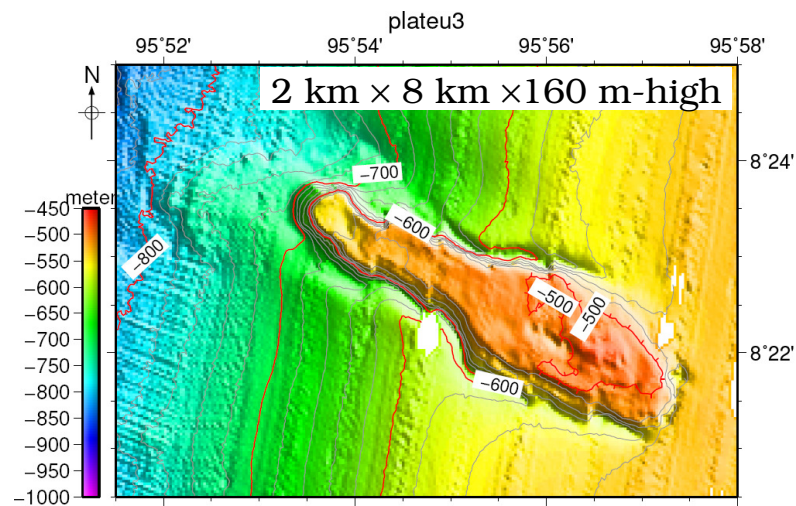
Prominent morphological features

- A circular domal uplift of about 35 m high with a diameter of about 500 m.

- Strong signals not related to the seafloor reflection appear in the vicinity of volcano-like feature.

- Negative polarity signals indicate the present of escape fluid/gas on top of the dome.





Plateau-like

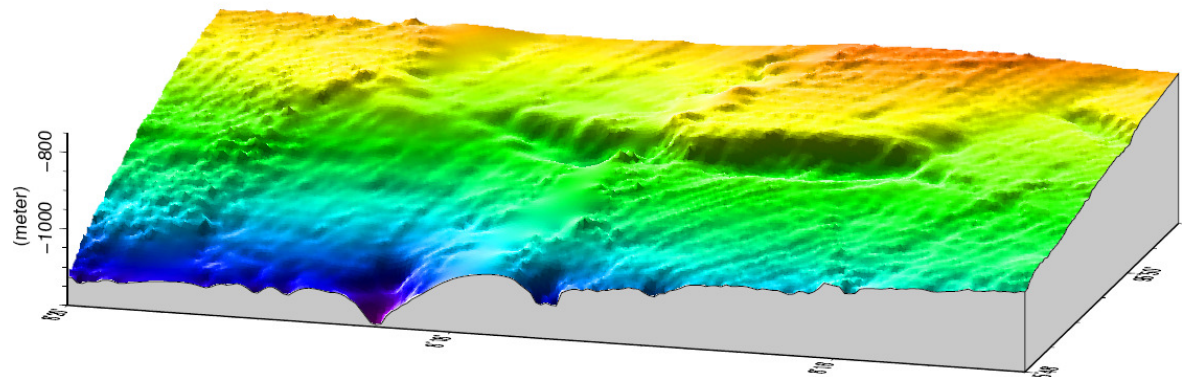
- Moat appear around the features.
- Sediment texture in the eastern of Mergui Ridge consists of sand/Foraminiferal ooze ([Rodolfo, 1969](#)) or sandstone/coral-agal reef limestone ([Polachan and Racey, 1993](#)).
- Deepwater corals/Old coral fragments?

Pockmark-like

- Two carter-shape are priliminary identified as pockmark-like features ?.
- Pockmarks are important sedimentary features as they indicate possible fluid/gas supporting to deepwater environment ([Sumida, et al., 2004](#)).

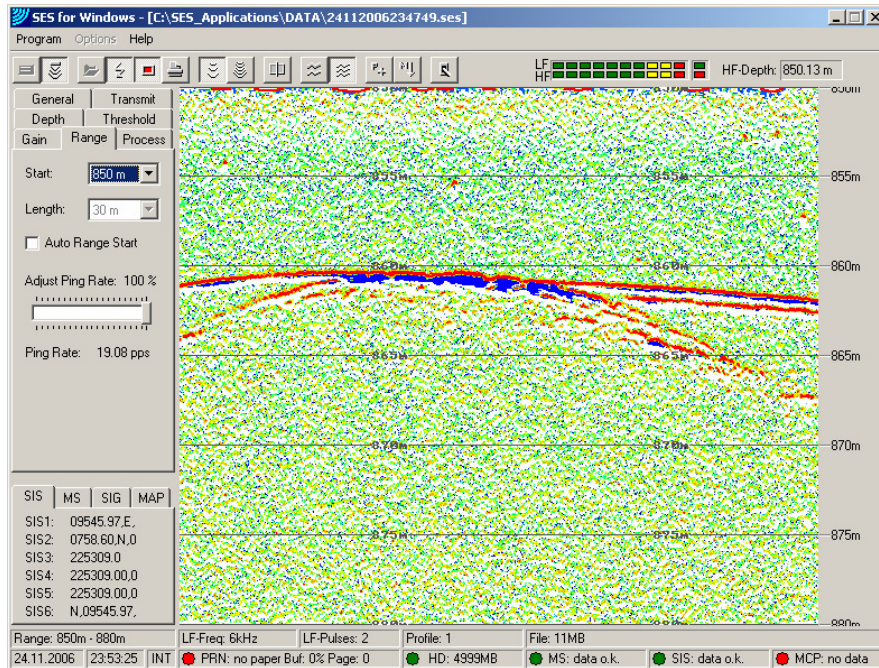
Slump

A large slump was found downward of the middle plateau with a dimension about 5 km long and 70 m height.



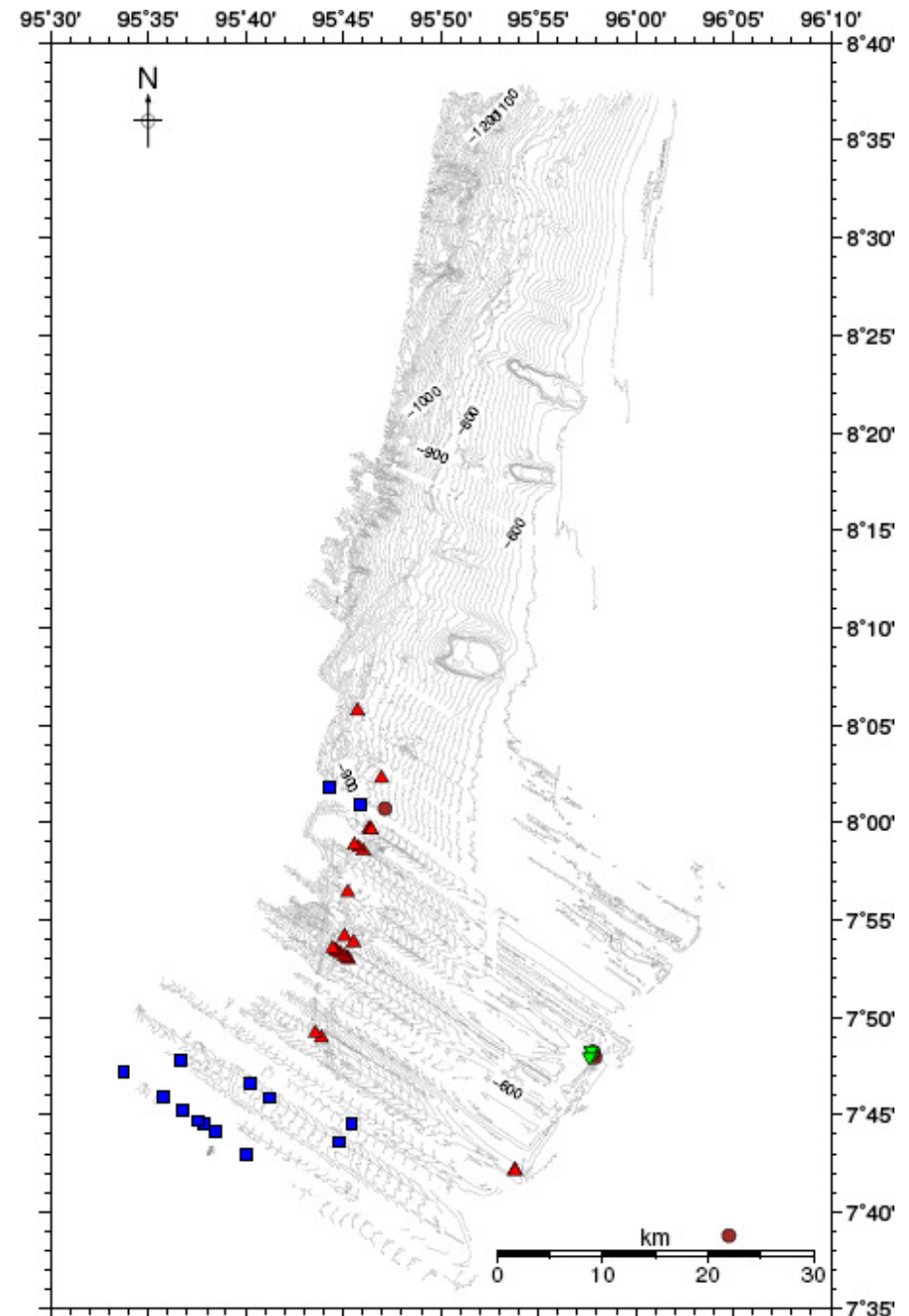
Morphology (prominent features)

Negative polarity indicated reflection from layers with less density than water (**red triangle**) 11 positions have been observed at the depth range of 850-950 m. Shallow gas?

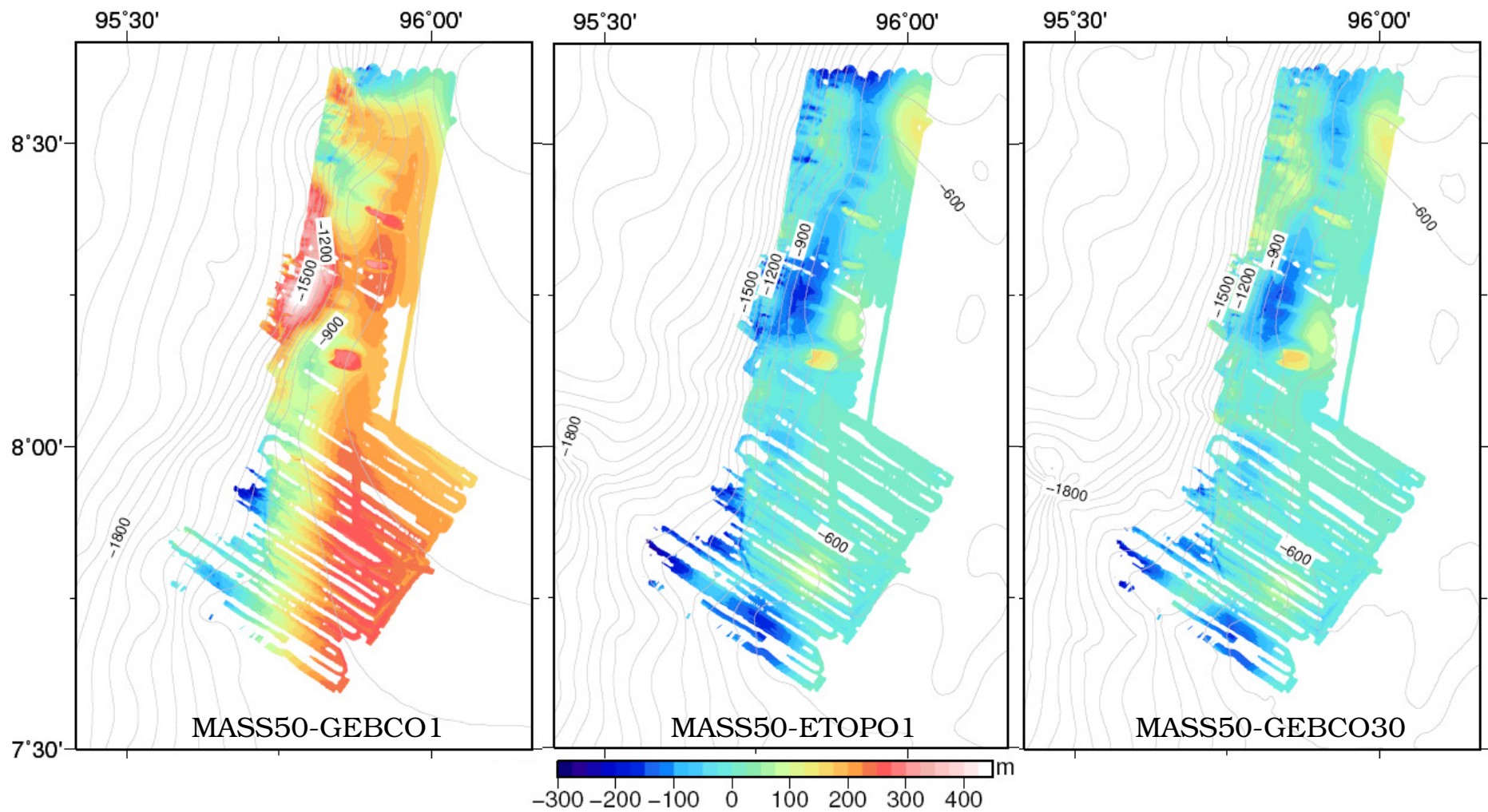


Possible slumps (**blue square**) have been observed at 14 positions in the depth range of 850-950 meters. The thickness of these slump was about 10 m.

Possible mound-like at 9 positions (**brown circle**) and possible mud volcanoes at 3 positions (**green triangle**) have been observed in the depth range of 850-950 m.



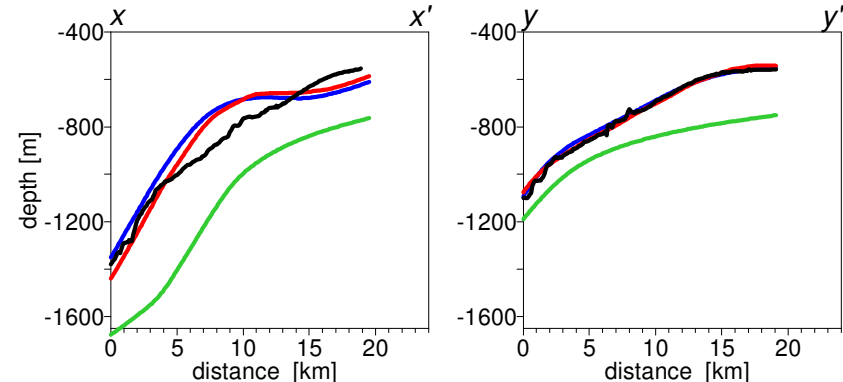
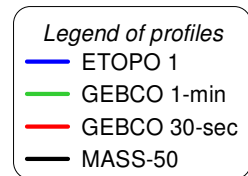
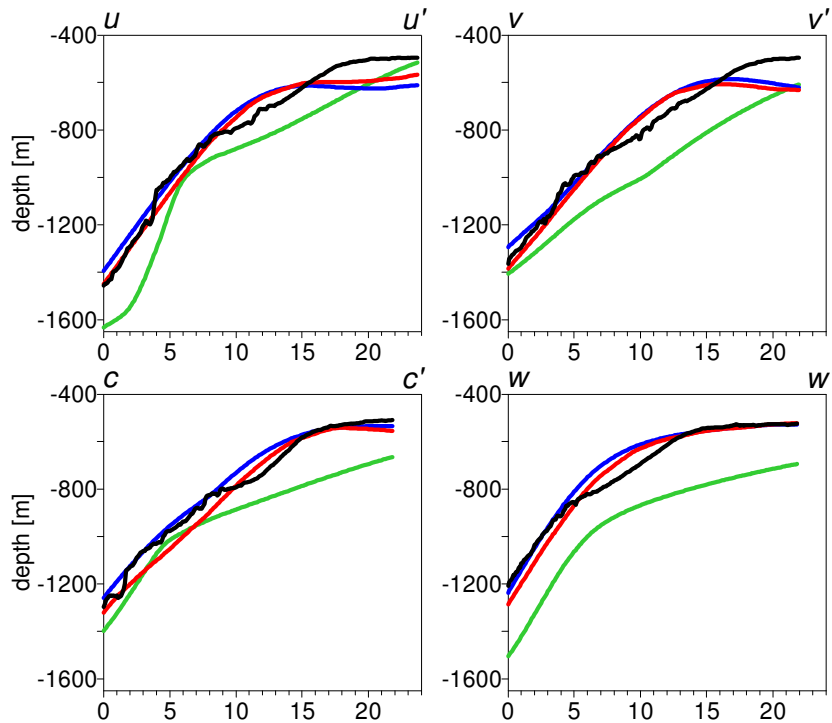
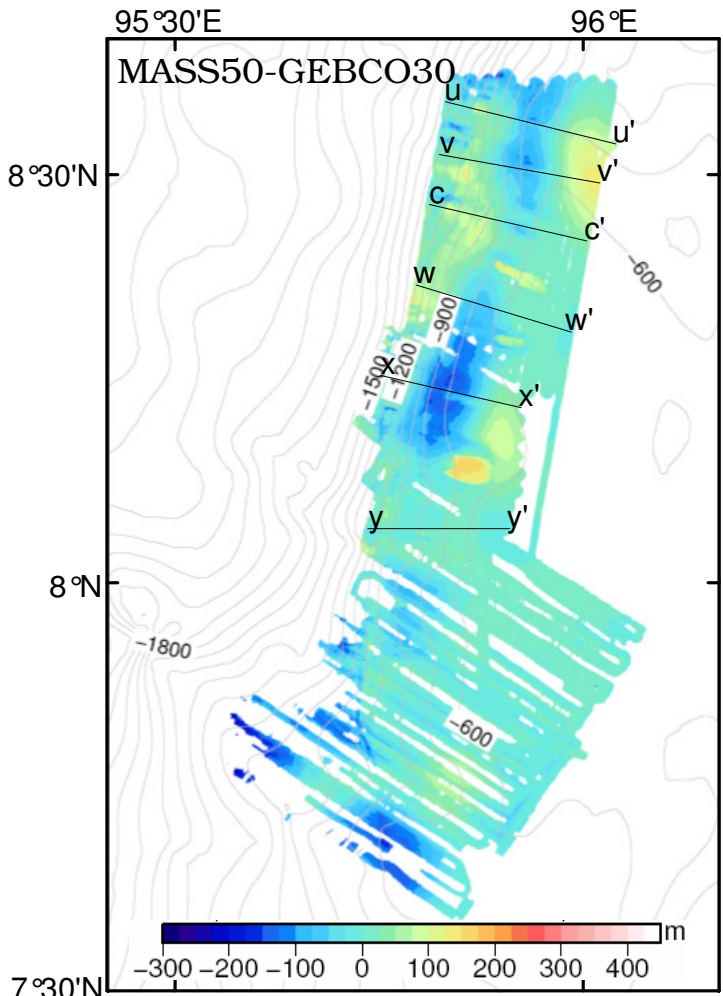
comparision of the high resolution bathymetry to global bathymetric data set



	MASS50-GEBCO1	MASS50-ETOPO1	MASS50-GEBCO30
R²	33 %	92 %	95 %
RMSE	188	63	51

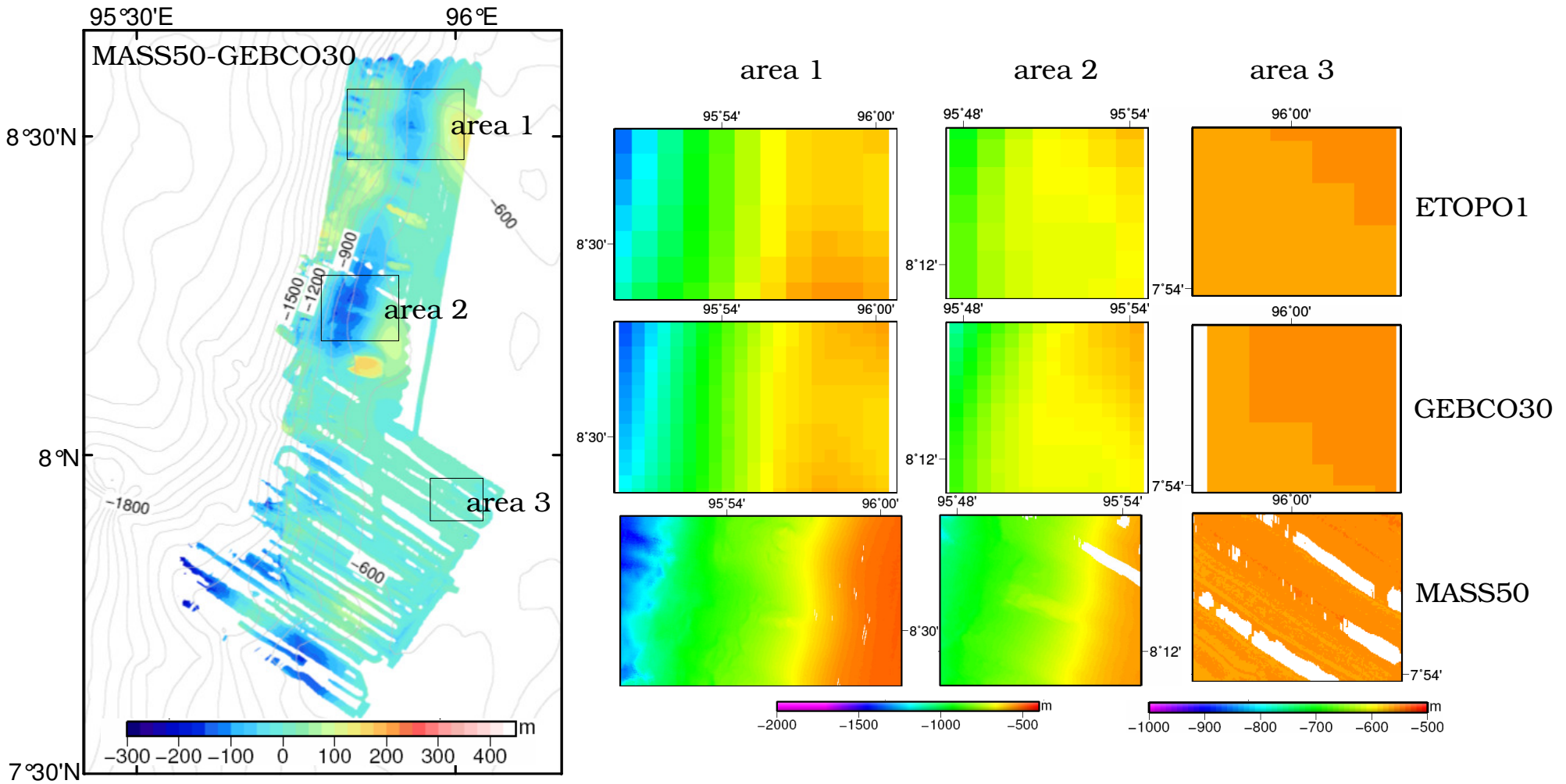
MASS50 : Number of data = 1,085,639 points; Mean -762.25 m

comparision of the high resolution bathymetry to global bathymetric data set



Profile-No.	ETOPO1	GEBCO30
uu' (239)	93 %	96 %
vv' (221)	95 %	93 %
cc' (220)	97 %	96 %
ww' (220)	94 %	95 %
xx' (193)	87 %	91 %
yy' (192)	99 %	99 %
Average R ²	94 %	95 %
RMSE	14-85	11-68

comparision of the high resolution bathymetry to global bathymetric data set



	area 1		area 2		area 3	
	R ²	RMSE	R ²	RMSE	R ²	RMSE
MASS50-ETOPO1	93 %	63	53 %	98	88 %	7
MASS50-GEBCO30	94 %	60	65 %	85	97 %	4

Summary

An area $\sim 3,000 \text{ km}^2$ in the southwestern corner of Mergui Ridge was successfully mapped. The map covered the upper shelf break from approximate 500 m down to the shelf edge at approximate 1,700 m depth.

A new bathymetric chart derived from a high resolution swath bathymetry can be generated with respect to 50 m grid resolution with sufficient data in each grid to be of significance.

Three plateau-like features, two pockmark-like features, one volcano-like feature and ten mounds-like features are identified in the smooth area above 700 m depth. Two possible slumps and more than 10 gullies are identified in a slope area below 700 m depth. All prominent features need more documents to verify.

Sediment echodata are on going process, however, eleven anomalous features with possible occurrence of low-density fluids or gases in the shallow sediment layers are indentified. Almost all of these fluid or gas deposits were in lower slope areas with water depths greater than 900 m.

The quality of fit between the high resolution bathymetry and global bathymetry data sets, GEBCO 30 arc second, in term of Pearson's correlation show a value 97% for smooth area and 65% for distinguished area of prominent features, whereas a root mean square error (RMSE) show 4 and 85 respectively. The values indicate an accuracy of the global digital terrain model.

The author would gratefully acknowledge a finance support jointly by the National Research Council of Thailand (NRCT) and the German Research Foundation (DFG) for a cooperation research which is MASS project-“A Morphodynamic and slope stability of the Andaman Sea Shelf break”.

The Leibniz-Institut für Meereswissenschaften an der Universität Kiel (IFM-GEOMAR) and Southeast Asia START Regional Center for cooperation research between Thai and German scientists.

The United Nations University, Institute for Environment and Human Security (UNU-EHS) for support a PhD Scholarship (GITEWS-3).

Dr. Warner Brueckmann, Dr. Christian Hensen, Miss Suratta Bunsomboonsakul, capt. Chonwat Singnu and his crews who make the cruises successful.

Thank you for your attention.



Morphodynamics of the Andaman Sea Shelf Break, Thai EEZ

P. Jintasaerane (1,2,5), W. Weinrebe (2), E.R. Flueh (2), A. Snidvongs (3,4)

(1) PhD researcher The United Nations University, Institute for Environment and Human Security (UNU-EHS), UN Campus, Bonn, Germany., (2) Leibniz-Institut für Meereswissenschaften an der Universität Kiel (IFM-GEOMAR), Kiel, Germany., (3) Southeast Asia START Regional Center, Chulalongkorn University, Bangkok, Thailand., (4) Department of Marine Science, Faculty of Science, Chulalongkorn University, Bangkok, Thailand., (5) Department of Aquatic Science, Faculty of Science, Burapha University, Chonburi, Thailand.

The primary aim of the project “Morphodynamics and Slope Stability of the Andaman Sea Shelf Break” is the in situ characterization of the slope of the Andaman Shelf in Thai EEZ with special emphasis on previous slope failures and a possible tendency to fail in the future. The first cruise of the project was conducted in November-December 2006, the second cruise in October-November 2007 using the RV Chakratong Tongyai. Both cruises were devoted to hydroacoustic mapping of the shelf break and the slope. A multibeam bathymetric echosounder (MB) and a parametric sediment echosounder (sub-bottom profiler; SBP) were used to map the bathymetry and the thickness and structure of the uppermost sedimentary layer of hitherto unexplored parts of the shelf break in the Andaman Sea.

An area of more than 3,000 km² in the southwestern corner of the Thai EEZ in the Andaman Sea was successfully mapped. The data cover the upper shelf break from about 500 m down to about 1,400 m water depth. Three especially interesting slope areas and three plateaus are seen in the bathymetric map. In addition, one mud volcano and more than 10 mounds in the mud volcano area have been identified. The processing of the SBP data is still ongoing, so far 34 locations that had distinct morphologic and/or unusual sediment seismic features in this survey area were studied. Most of these (30) anomalous features were attributed to areas with possible occurrence of low-density fluids or gases in the shallow sediment layers. Almost all of these fluid or gas deposits were in lower slope areas with water depth greater than 900 m. In addition, several manifestations of fluid venting were also mapped on the upper shelf edge at water depths of about 600 m. Some of these shallower vents could form mounds with diameters of up to 500 m and heights of up to 50 m. Diffuse reflections in the vicinity of the mounds and strong signals not related to seafloor reflections indicate the presence of uprising bubbles or gas flares.



XY647 (EGU2009-2650)

Morphodynamics of the Andaman Sea Shelf Break, Thai EEZ

The high resolution bathymetry



P. Jintasacra^{1,3,5}, W. Weinrebe¹, E.R. Flueh¹, A. Snidvongs^{2,4}, I. Klaucke¹, and D. Winkelmann¹



Figure 1. The Thai research vessel RV Chakratong Tongyai of Phuket Marine Biological Center, Thailand (PMBC).

Figure 2. A color relief bathymetry of the Andaman sea and Mergui ridge generated from GEBCO 1-min (IOC, IHO and BODC, 2003). The Thai EEZ (The Royal Gazette, 1988) is shown by the red lines. Ship tracks surveys are shown by the orange lines.

1. Introduction

A devastating tsunami waves had destroyed constructions in large areas along the Andaman Sea coast of Thailand and killed many peoples since December 26, 2004. To predict the next tsunami in near future and to assess potential of slope failure occurring in the area, a reliable bathymetric chart to be available is a major demand for scientific community.

“A Morphodynamic and slope stability of the Andaman Sea Shelf break”-MASS project is commenced in 2006. Primary aim of the project is to map a high resolution bathymetry of Andaman Sea in Thai EEZ and to determine morphodynamic and tectonic state of the area. The bathymetry is successfully utilized for further visual planning of investigation and measurements.

2. Instruments and Field surveys

Equipments used in the surveys consist of two hydroacoustic survey systems which are the SEA BEAM 1050 multibeam echosounder system, and the INNOMAR SES 2000 parametric sediment echosounder system.

Bathymetry was obtained on board RV Chakratong Tongyai (fig.1) at water depth ranging from 500-1,700 m. The first cruise was separated into two legs, leg 1 covered 20-27 November 2006 and leg2 covered 29 November-6 December 2006. The second cruise was conducted 5-15 November 2007 (fig.2).

Detailed information can be found at www.ifm-geomar.de/index.php?id=4222&L=1

Deutsche Forschungsgemeinschaft
DFG

IFM-GEOMAR
Leibniz-Institut für Meereswissenschaften
an der Universität Kiel

GITEWS

Acknowledgement

Gratefully acknowledge a finance support jointly by the German Research Foundation (DFG) and the National Research Council of Thailand (NRCT). The Leibniz Institute of Marine Sciences (IFM-GEOMAR), the Southeast Asia START Regional Center, Chulalongkorn University and Burapha University for cooperation research between German and Thai scientists. The United Nations University, Institute for Environment and Human Security (UNU-EHS) for support a PhD Scholarship (GITEWS-3).

Southeast Asia
START
Regional Center

UNITED NATIONS
UNIVERSITY
UNU-EHS
Institute for Environment
and Human Security

¹ Leibniz Institute of Marine Sciences (IFM-GEOMAR), Kiel, Germany.
² Southeast Asia START Regional Center, Chulalongkorn University, Bangkok, Thailand.
³ United Nations University-Institute for Environment and Human Security (UNU-EHS), Bonn, Germany.
⁴ Department of Marine Science, Faculty of Science, Chulalongkorn University, Bangkok, Thailand.
⁵ Department of Aquatic Science, Faculty of Science, Burapha University, Chonburi, Thailand.

3. Results

An area of about 3,000 km² in the southwestern corner of Mergui Ridge was successfully mapped. The map covered the upper shelf break from approximate 500 m down to the shelf edge at approximate 1,700 m depth.

3.1 The high resolution bathymetry : Histogram plots of a 50 m grid of a number of data points per grid and percent frequency show 82% obtained data higher 4 points per grid and show 60% of those grids obtained a standard deviation in percent of water depth better than 0.4 (fig.3). Regarding to the statistic computed, A new high resolution bathymetry of the Andaman Sea, Thai EEZ can be generated by 50 m grid resolution with sufficient data in each grid to be of significance.

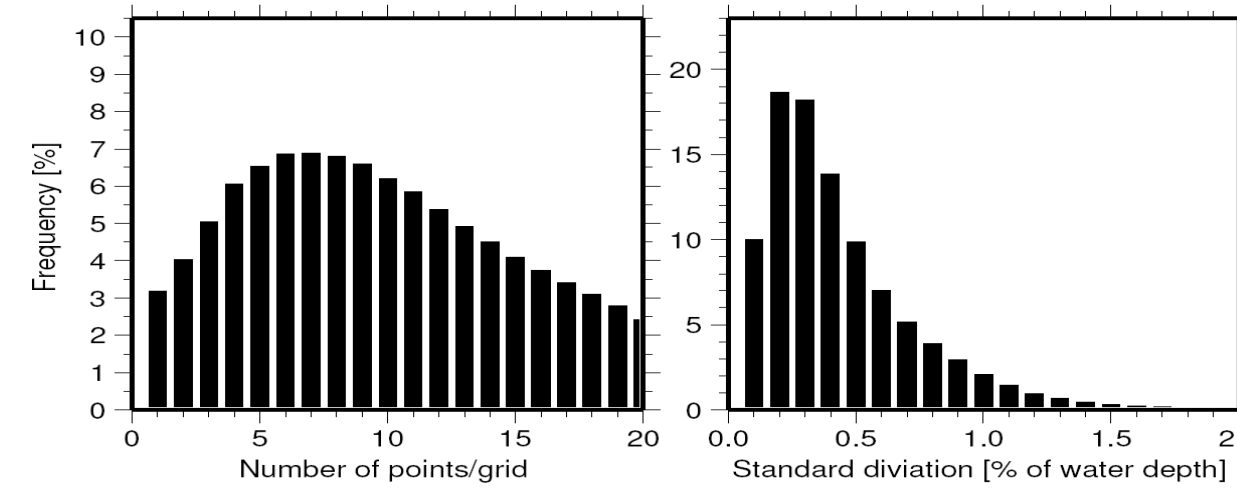
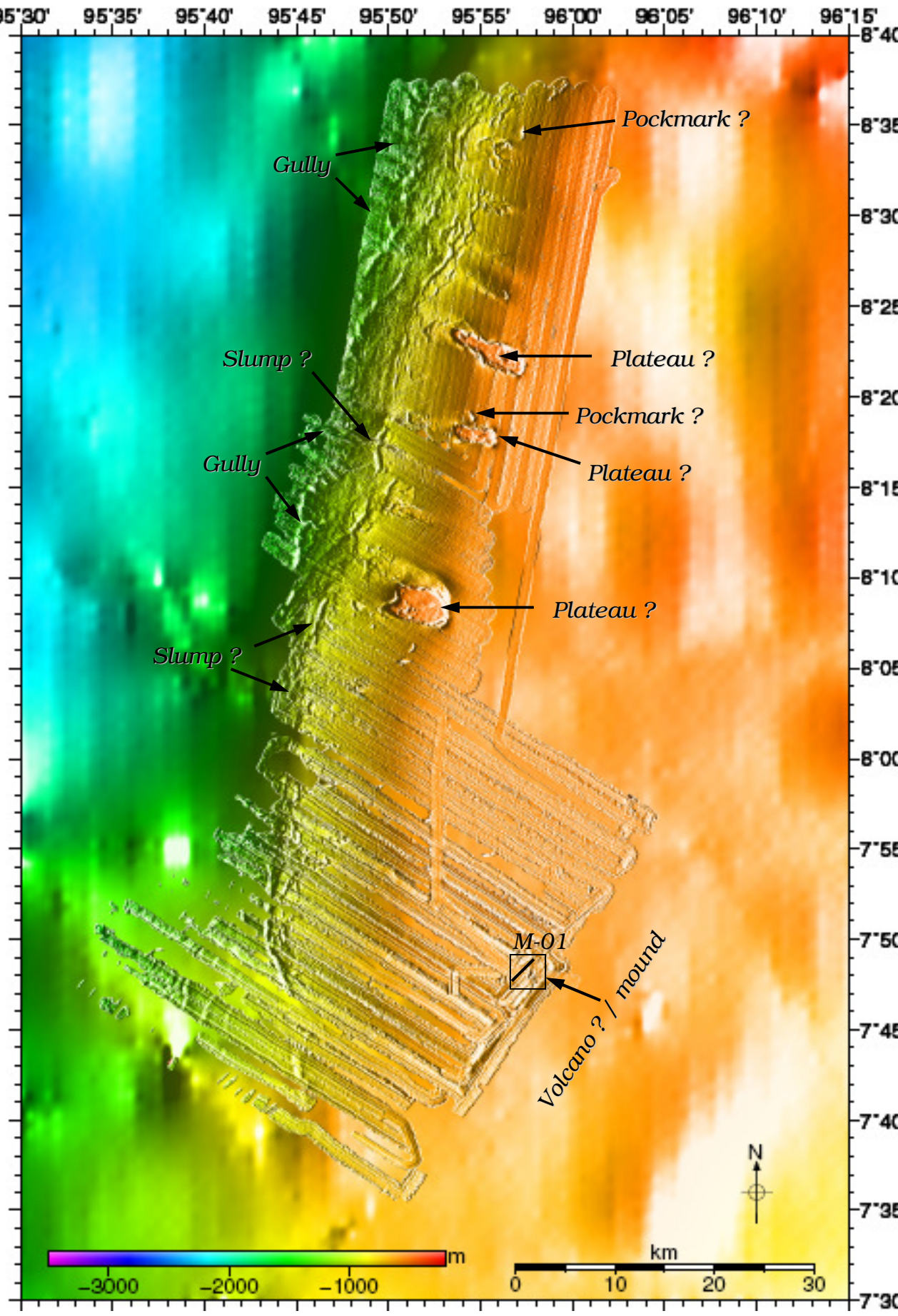
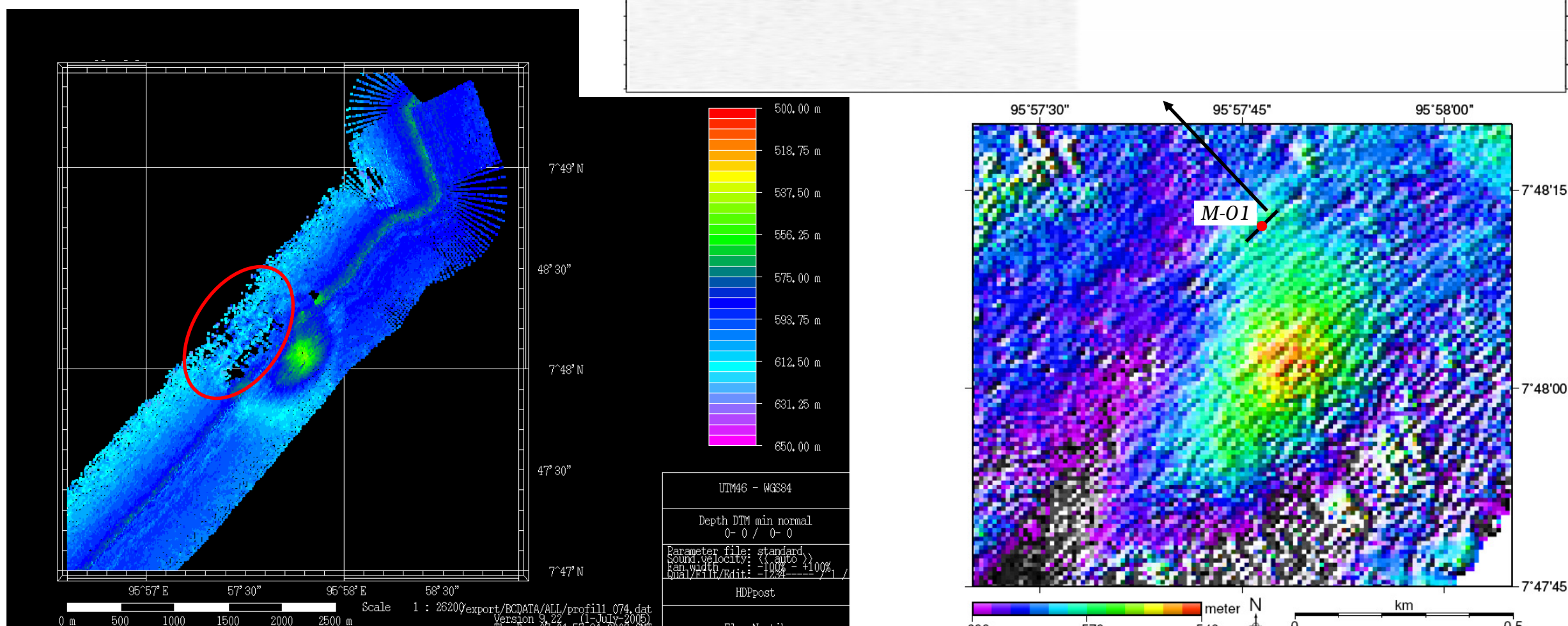


Figure 3. Histogram plots of 50 m-grid resolution show dense data points per grid and their standard deviation (left). A shade relief of 50 m-grid resolution bathymetry of the Andaman Sea in Thai EEZ overlaid on GEBCO 30-arc second (The GEBCO_08 Grid, 2009) (right).

3.2 Mounds/Volcanoes : An average inclination angle in the area which are computed from many cross section profiles indicates a smooth topography. A flat top area is characterized on the upper most area of Mergui Ridge with approximate 500-700 m depth. Most of area has no large distinct topographic features on its top. An embankment can be observed at 95°57.8' E and 7°48' N. Shape of the feature is nearly to a circular form with dimension of about 35 m high and 500 m in diameter (fig.4).

Figure 4. A swath bathymetry cover a volcano-like structure show bad signal at starboard side close to an embankment (left). A shade relief 10 m-grid resolution bathymetry of the embankment (lower-right). A parametric profile M-01 (upper-right).



3.4 Two features which can probably be characterized as pockmark can be remarked at situation 95°54'35" E and 8°18'45" N, and 95°57'10" E and 8°35' N. Dimension of them are about 1km × 0.25km × 40m (fig.5).

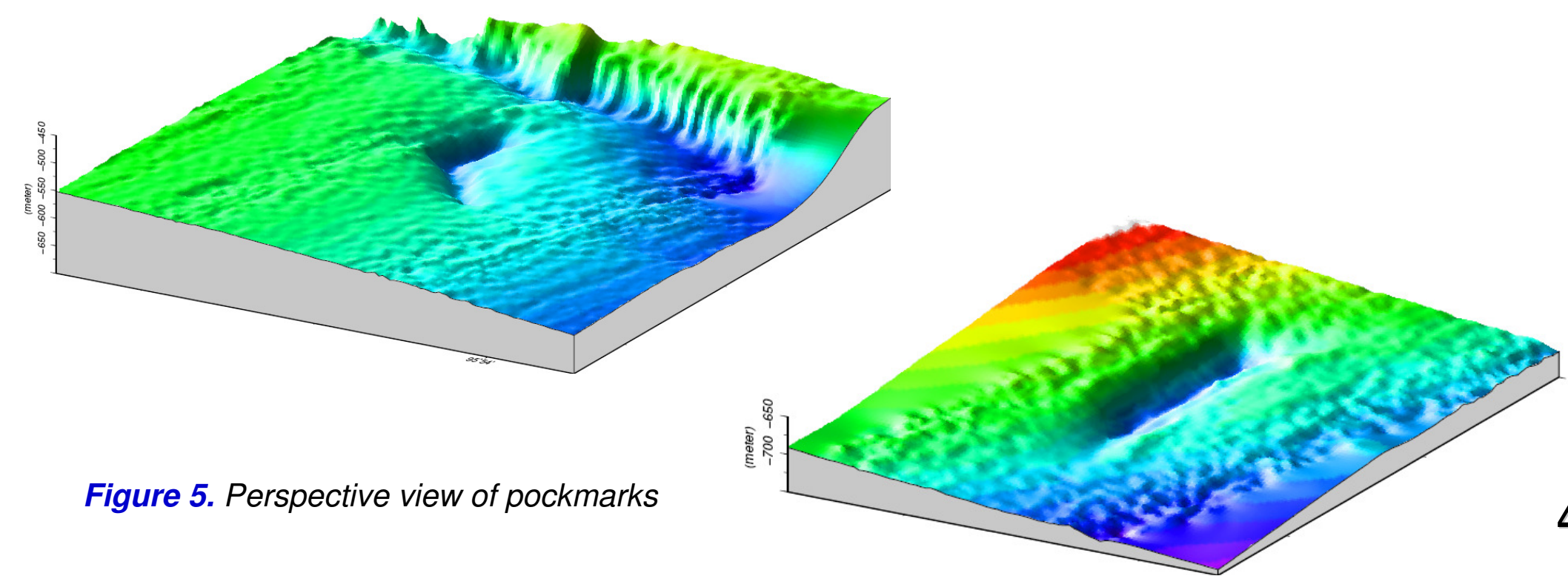


Figure 5. Perspective view of pockmarks

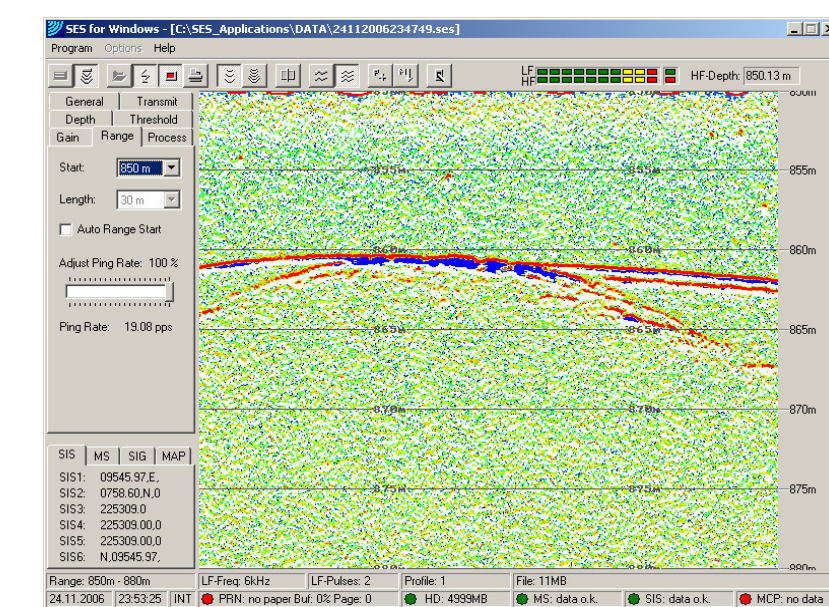
Summary

The primary aim of the project “Morphodynamics and Slope Stability of the Andaman Sea Shelf Break” is the in situ characterization of the slope of the Andaman Shelf in Thai EEZ with special emphasis on previous slope failures and a possible tendency to fail in the future. The first cruise of the project was conducted in November-December 2006, the second cruise in October-November 2007 using the RV Chakratong Tongyai. A multibeam bathymetric echosounder (MB) and a parametric sediment echosounder (sub-bottom profiler; SBP) were used to map the bathymetry and the thickness and structure of the uppermost sedimentary layer of hitherto unexplored parts of the shelf break in the Andaman Sea.

An area of more than 3,000 km² in the southwestern corner of the Thai EEZ in the Andaman Sea was successfully mapped. The data cover the upper shelf break from about 500 m down to about 1,700 m water depth. Three possible slope areas and three plateaus-like structures are observed in the bathymetric map. In addition, one mud volcano and more than 10 mounds in the mud volcano area have been identified. The processing of the SBP data is still ongoing, so far 34 locations that had distinct morphologic and/or unusual sediment seismic features in this survey area were studied. Most of these anomalous features were attributed to areas with possible occurrence of low-density fluids or gases in the shallow sediment layers. Almost all of these fluid or gas deposits were in lower slope areas with water depth greater than 900 m. In addition, several manifestations of fluid venting were also mapped on the upper shelf edge at water depths of about 600 m. Some of these shallower vents could form mounds with diameters of up to 500 m and heights of up to 50 m.

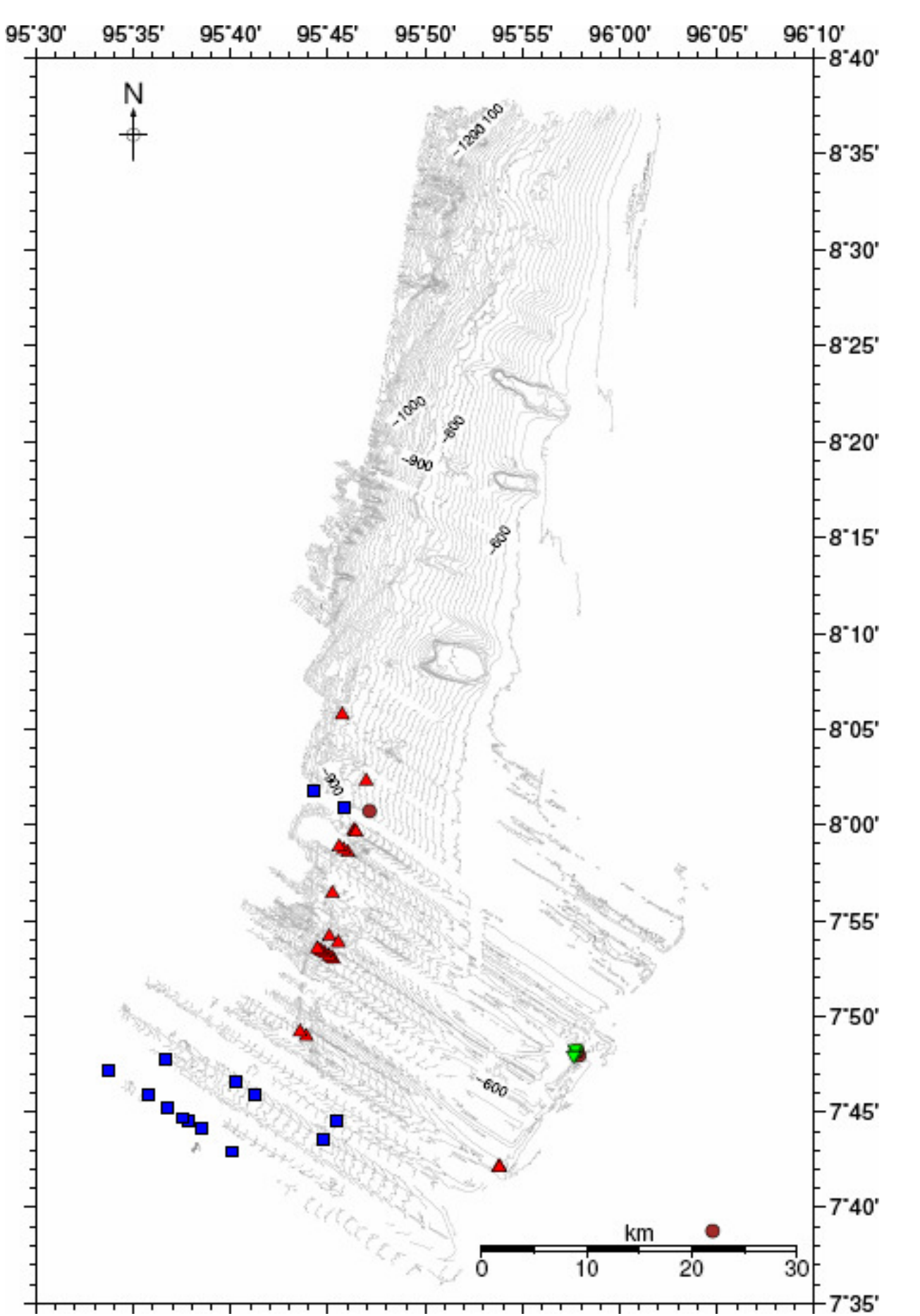
3.3 Three conspicuous feature shaped so-called plateaus? are observed at water depth about 550 meters. The dimension of them are varied between 4-8 km in diameter and 100-160 m high. Moat appear around the features. Sediment texture in the eastern of Mergui Ridge consists of sand/Foraminiferal ooze (Rodolfo, 1969) or sandstone/coral-agal reef limestone (Polachan and Racey, 1993). With respect to these informations, the features can possible be deepwater corals/old coral fragments? However, there features can not be proven without sediment samplings.

3.5 Eleven anomalous features with possible occurrence of low-density fluids or gases in the shallow sediment layers. Parametric profile show negative polarity which indicated reflection from layers with less density than water (red triangle) in the slope areas with water depths greater than 900 m.



Fourteen positions of possible slumps (blue square) are observed at water depth ranging about 850-950 meters.

Nine positions of possible mounds (red circle) are observed at water depth vary about 850-950 meters.



4. Reference

Curray, J.R. (2005). "Tectonics and history of the Andaman Sea region", *Journal of Asian Earth Science*, Vol.25. 187- 232.
IOC, IHO and BODC. (2003). Centenary Edition of the GEBCO Digital Atlas, published on CD-ROM on behalf of the Intergovernmental Oceanographic Commission and the International Hydrographic Organization as part of the General Bathymetric Chart of the Oceans, British Oceanographic Data Centre, Liverpool, U.K.
Polachan, S., and A. Racey. (1993). "Lower Miocene larger foraminifera and petroleum potential of the Tai Formation, Mergui Group, Andaman Sea", *Journal of Southeast Asian Earth Science*, Vol. 8. 487-496.
Rodolfo, K.S. (1969). "Sediments of the Andaman Basin, Northeastern Indian Ocean", *Marine Geology*, Vol. 7. 371-402.
The GEBCO_08 Grid. (2009). version 20090202, <http://www.gebco.net>.
The Royal Gazette (1988). The EEZ Claims of Thailand according to The Royal Gazette. V. 105(120), 231-234 (26 July 1988).

The high resolution bathymetry of the Andaman Sea shelf break

P. Jintasaeranee^{1,2,5}, W. Weinrebe², E.R. Flueh², A. Snidvongs^{3,4}, I. Klaucke², and D. Winkelmann²



UNITED NATIONS
UNIVERSITY
UNU-EHS
Institute for Environment
and Human Security

Deutsche
Forschungsgemeinschaft
DFG



IFM-GEOMAR
Leibniz-Institut für Meereswissenschaften
an der Universität Kiel

Southeast Asia
START
Regional Center



¹ United Nations University-Institute for Environment and Human Security (UNU-EHS), Bonn, Germany.

² Leibniz Institute of Marine Sciences (IFM-GEOMAR), Kiel, Germany.

³ Southeast Asia START Regional Center, Chulalongkorn University, Bangkok, Thailand.

⁴ Department of Marine Science, Faculty of Science, Chulalongkorn University, Bangkok, Thailand.

⁵ Department of Aquatic Science, Faculty of Science, Burapha University, Chonburi, Thailand.

1. Introduction

2004 tsunami waves triggered by the Sumatra-Andaman earthquake had destroyed constructions and killed many peoples along the Andaman Sea coast of Thailand. Besides the earthquake, submarine slumping could be a potential for landslide-generated tsunami hazards [3]. To assess potential of slope failure occurring in the area, a reliable bathymetric chart is a major demand for scientific community.

By a tectonic point of view, the Andaman Sea is an active backarc basin which lies above and behind the Sunda subduction zone where convergence between the overriding Southeast Asian plate and the subducting Australian plate is highly oblique [1].

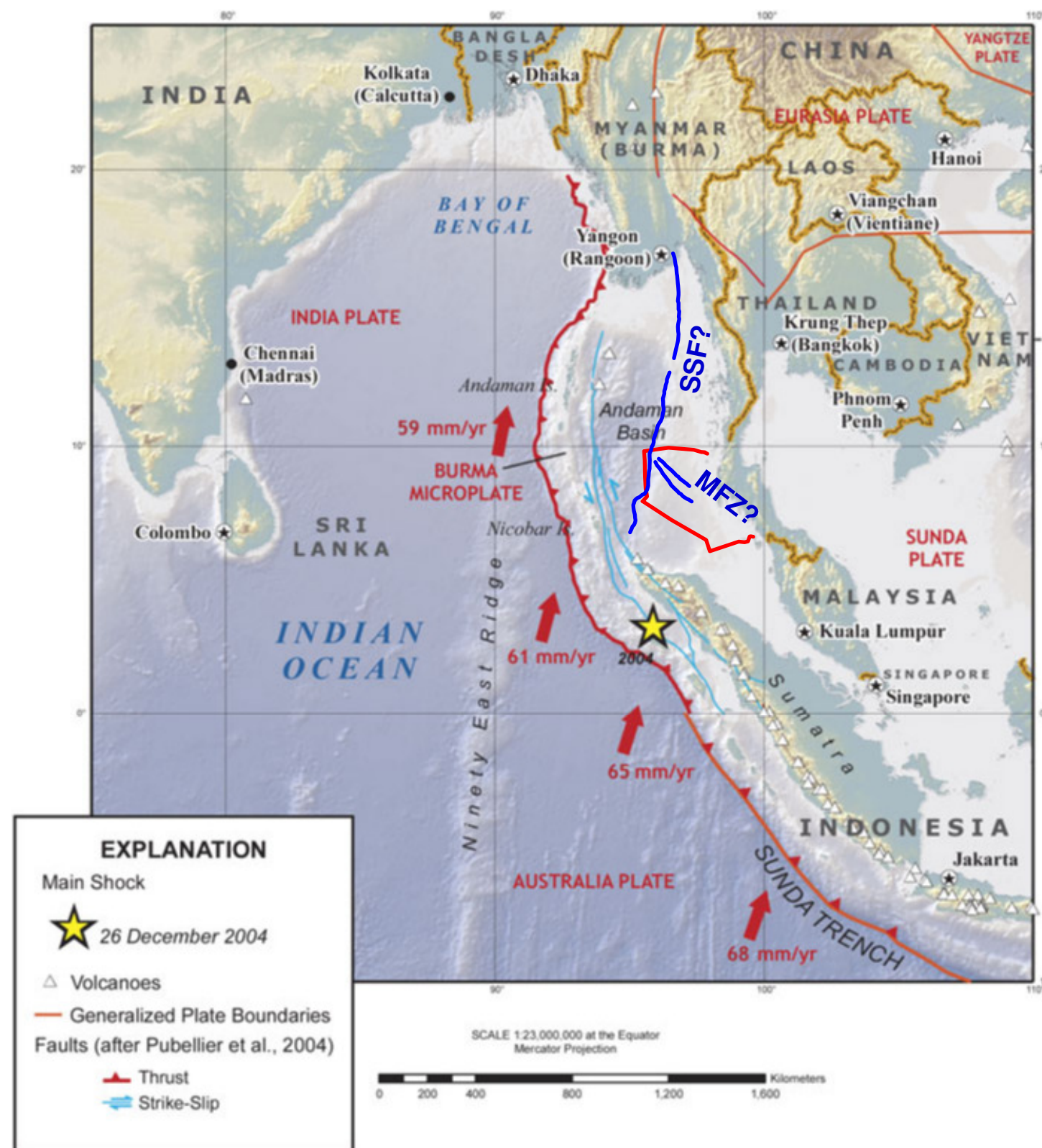


Figure 1. shows a tectonic map of the Andaman basin (<http://enviweb.gov.in/>). Approximate situations of Shan Scarp Fault (SSF?) and Mergui Fault (MFZ?) [1] show by solid blue lines. A boundary claim of Thai EEZ [8] shows by a solid red line.

“Morphodynamics and slope stability of the Andaman Sea Shelf break”-MASS project was commenced in 2006. Primary aim of the project is to map a high resolution bathymetry of Andaman Sea in Thai EEZ and to determine morphodynamic and tectonic state of the area. The bathymetry is utilized for further visual planning of investigations and measurements.

2. Instruments and field surveys

Two hydroacoustic survey systems, the SEABEAM 1050 multibeam echosounder, and the INNOMAR SES 2000 “medium” parametric profiler, were used in two research cruises.

Echo data along ship-track surveys covering an area ~3,000 km² were obtained on board between November - December 2006 and November 2007 at water depth ranging from 500-1,700 m (Fig. 2).

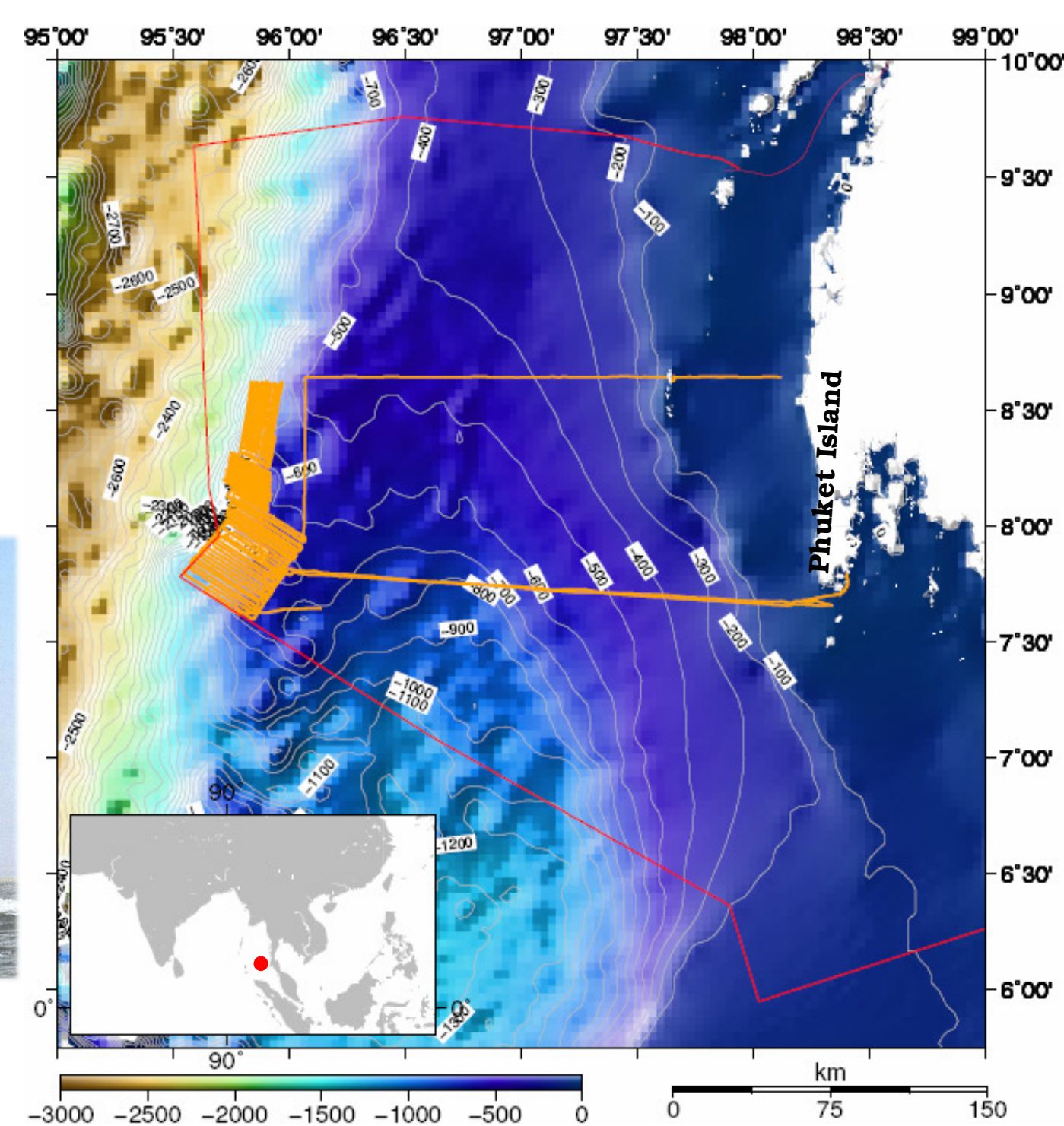


Figure 2. The Thai research vessel RV Chakratong Tongyai. A color relief bathymetry of Andaman sea and Mergui ridge generated from GEBCO 1-min [2]. The Thai EEZ [8] is shown by the red lines. All of ship-track surveys are shown by the orange lines.

Detailed information of the project can be found at :
www.ifm-geomar.de/index.php?id=4222&L=1

4. Summary

- The new reliable bathymetric chart covering ~3,000 km² derived from a high resolution swath bathymetry can be generated by 50 m grid resolution.
- Three plateau-like features, two pockmark-like features, one mud-volcano-like feature and ten mound-like features are identified in the smooth area above ~700 m depth. Two possible slumps and more than ten gullies are identified in a slope area below ~700 m depth.
- Sediment samples is very important which must be collected to verify the textures of the prominent features.
- Investigations are important for more understanding insight in the area.

References

- [1] Curry, J.R. (2005). *J. of Asian Earth Science*, 25:187-232.
- [2] IOC, IHO and BODC. (2003). Centenary Edition of the GEBCO Digital Atlas.
- [3] McAdoo, B.G., and P. Watts. (2004). *Marine Geology*, 235:245.
- [4] Polachan, S., and A. Racey. (1993). *J. of Southeast Asian Earth Science*, 8:487-496.
- [5] Richter, R., M. Fuller, E. Schmidtko, U.T. Myint, U.T. Ngwe, U.M. Win, and S. Bunopas. (1993). *J. of Southeast Asia Earth Science*, 8:247-255.
- [6] Rodolfo, K.S. (1969). *Marine Geology*, 7:371-402.
- [7] The GEBCO_08 Grid. (2009). version 20090202, <http://www.gebco.net>
- [8] The Royal Gazette (1988). 105(120):231- 234 (26 July 1988).

3. Results

3.1 Accuracy assessment

Histogram plots shows ~82% of those 50 m grid cells obtained data higher 4 points per grid and show ~60% obtained standard deviation better than 0.4 (Fig.3-left). Regarding to the statistic computed, the new high resolution bathymetry can be generated by 50 m grid resolution.

3.2 Inclination angle of Slope profiles

Inclination angles are computed from many cross section profiles. An average of inclination angle computed from ~500-700 m depth is ~0° indicates a smooth area on top of the ridge. West side of the ridge can possibly be divided into two provinces. The first ones is ~700-1,300 m depth with slopes ~1-1.7°. The second one is ~1,300-1,700 m depth with slope ~3.2°-4.6° indicates tendency of possible submarine land slide in the area.

3.3 Prominent features

Many prominent features are identified from visual interpretations which are escarpments, gullies, slump/slide, plateau-like features, pockmark-like features, and mud-volcano-like feature (Fig.3-right).

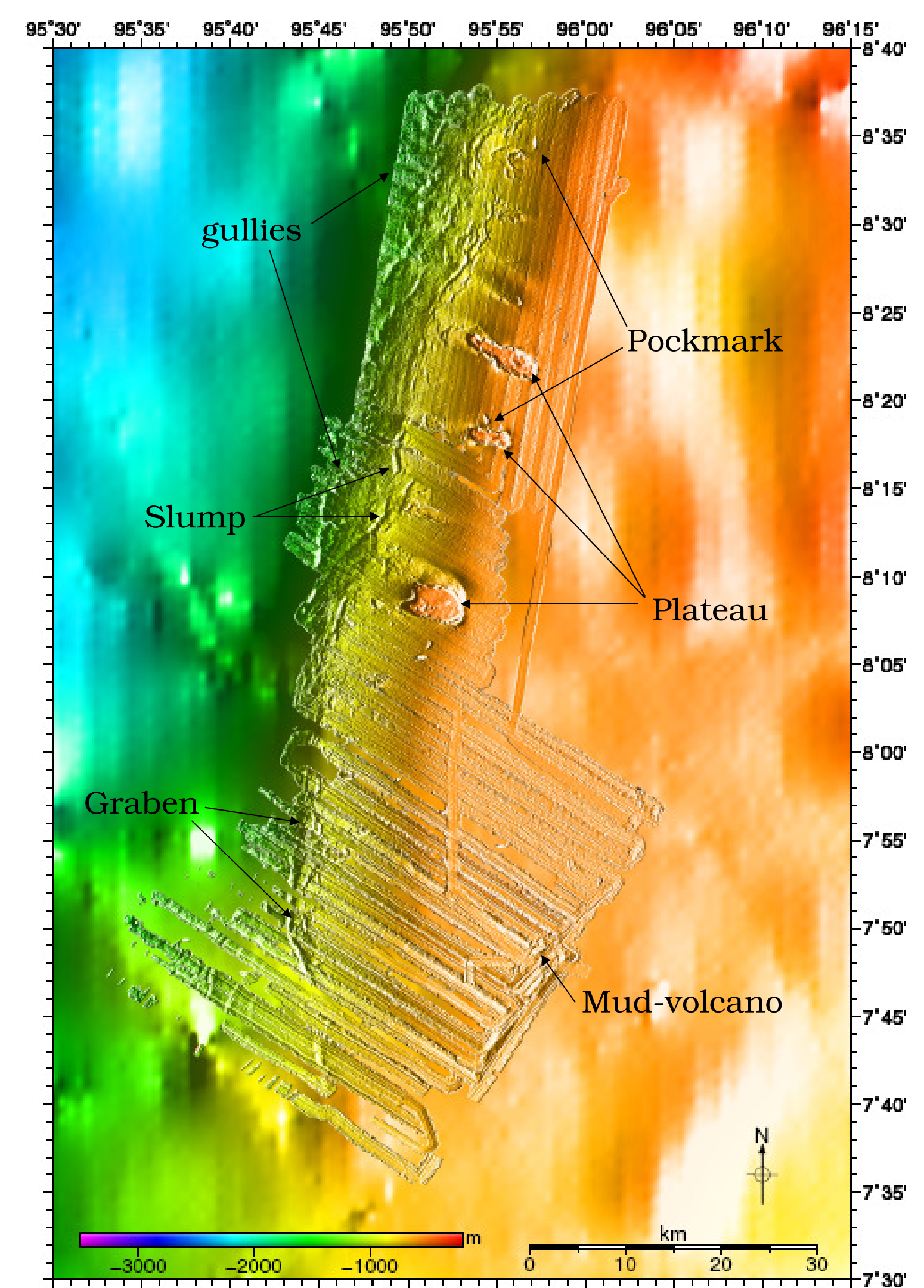
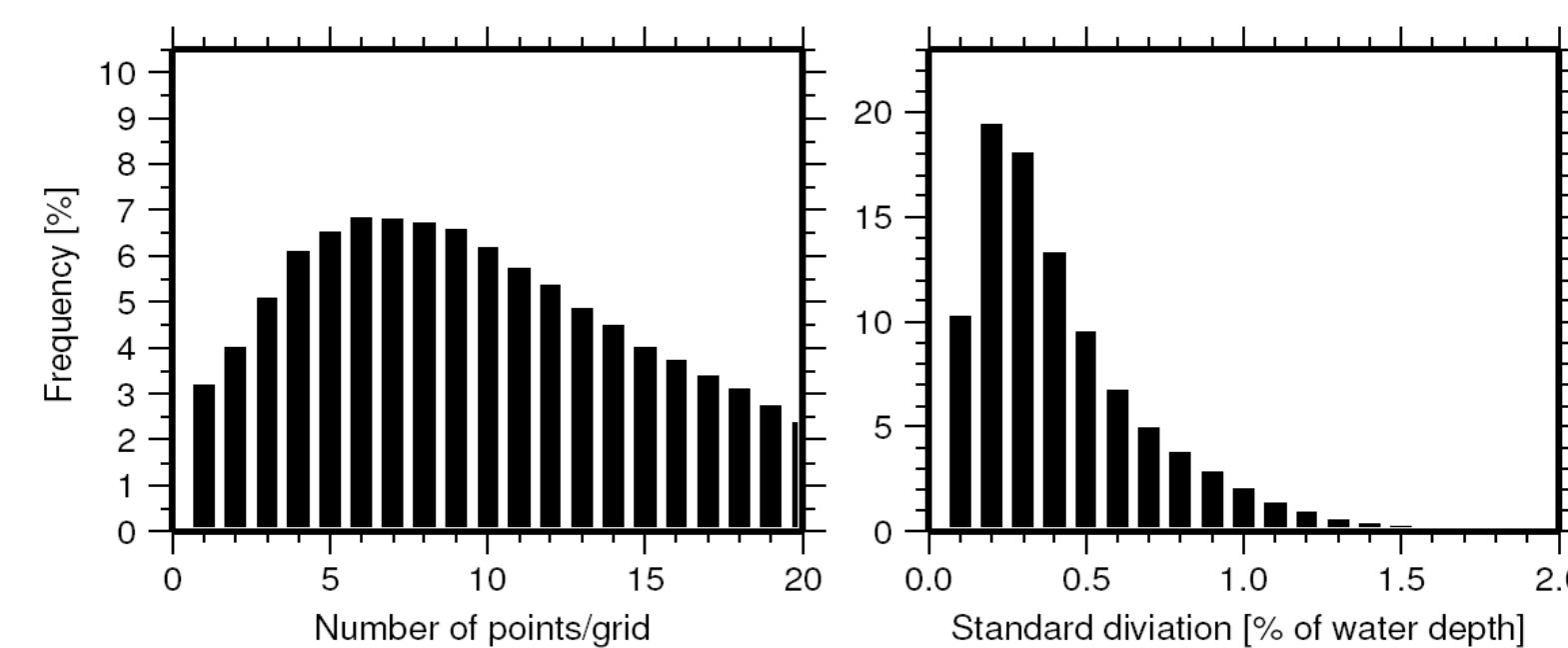


Figure 3. Histogram plots of 50 m-grid resolution show dense data points per grid and their standard deviation (left). A shade relief of 50 m-grid resolution bathymetry of the Andaman Sea in Thai EEZ overlaid on GEBCO 30-arc second [7] (right).

Plateau-like features

Three flat-top plateau-like features with 5-7 km in diameter that protrude high above the ocean floor and two prominent features like pockmark are observed at ~500-700 m depth.

A Multibeam backscatter plot shows low reflectivity on top of the plateau-like features and along slope area which could indicate high ability of material to absorb echo waves (Fig. 4).

Sediment texture in the eastern part of Mergui Ridge consists of sand and Foraminiferal ooze [6] or sandstone and coral-agal reef limestone [4]. Recently of an especial cruise of MASS investigation, a bone of coral and gravel were dredged from the area. The plateau-like features could possibly be identified as deepwater corals or old coral fragments. However, the texture can not be proven with out sediment sampling.

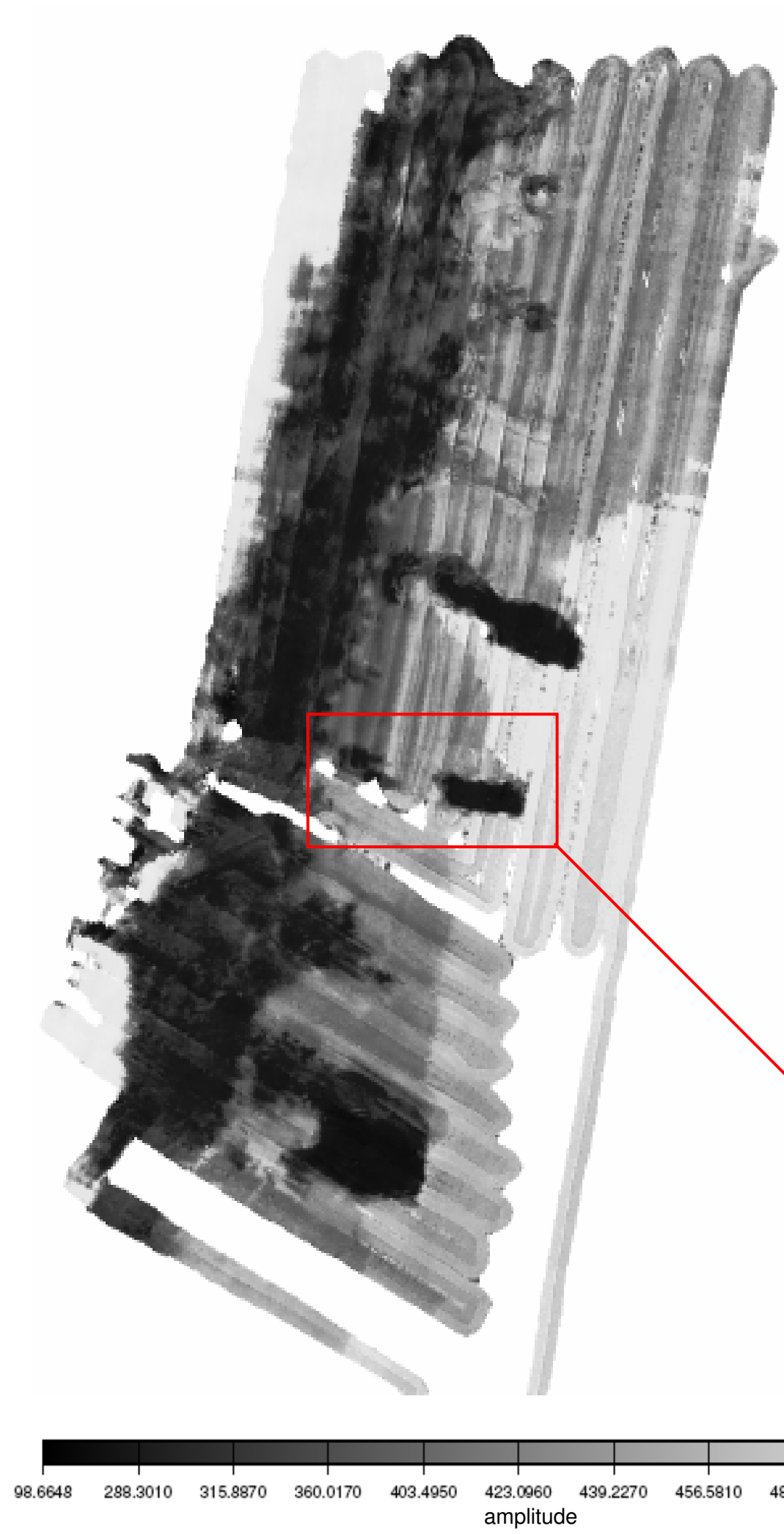


Figure 4. show a color-code multibeam back scatter plot of MASS-II (left) and a shade relief 50 m-grid resolution bathymetry of a plateau-like structure and a pockmark-like feature (right).

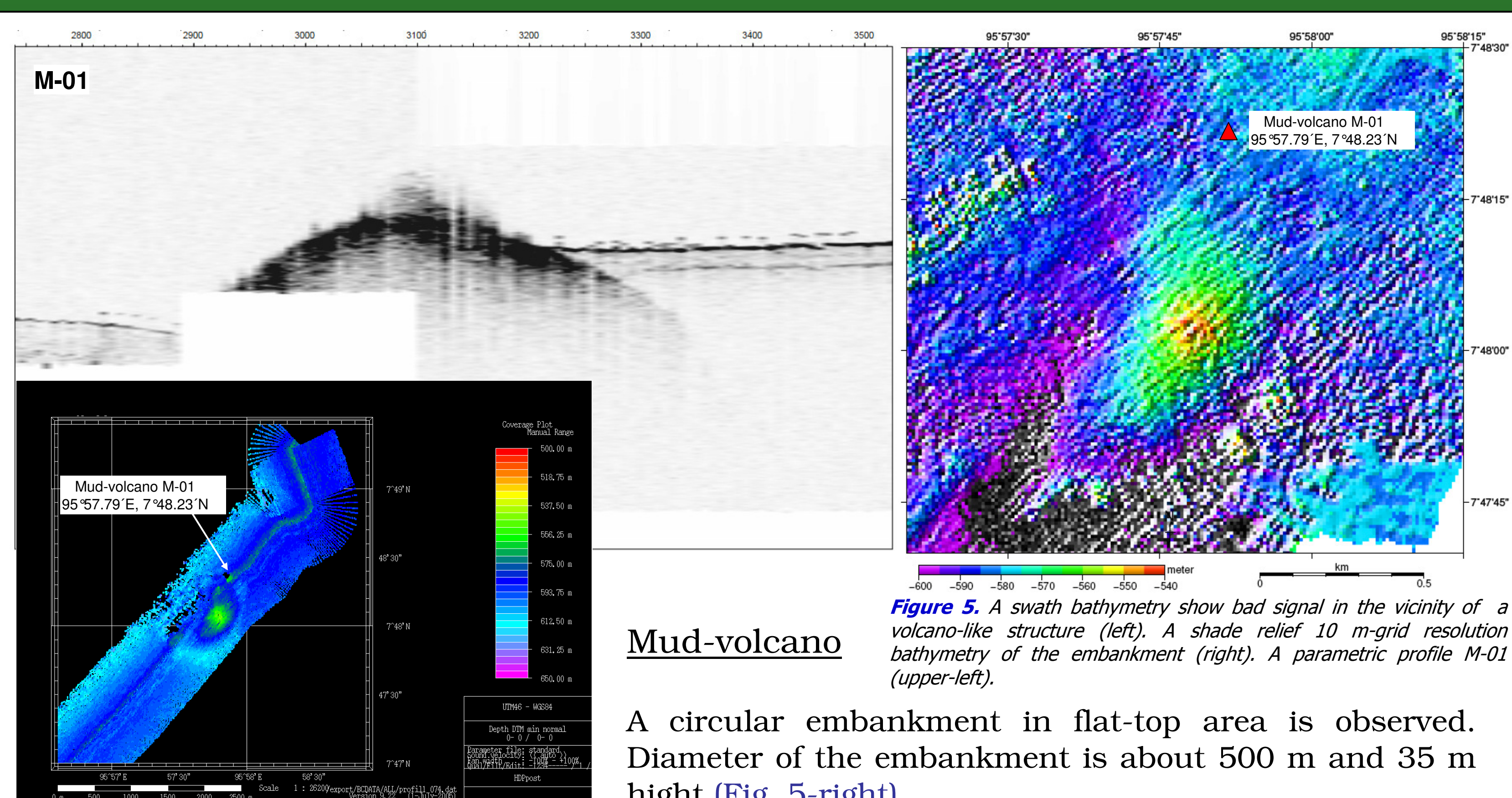
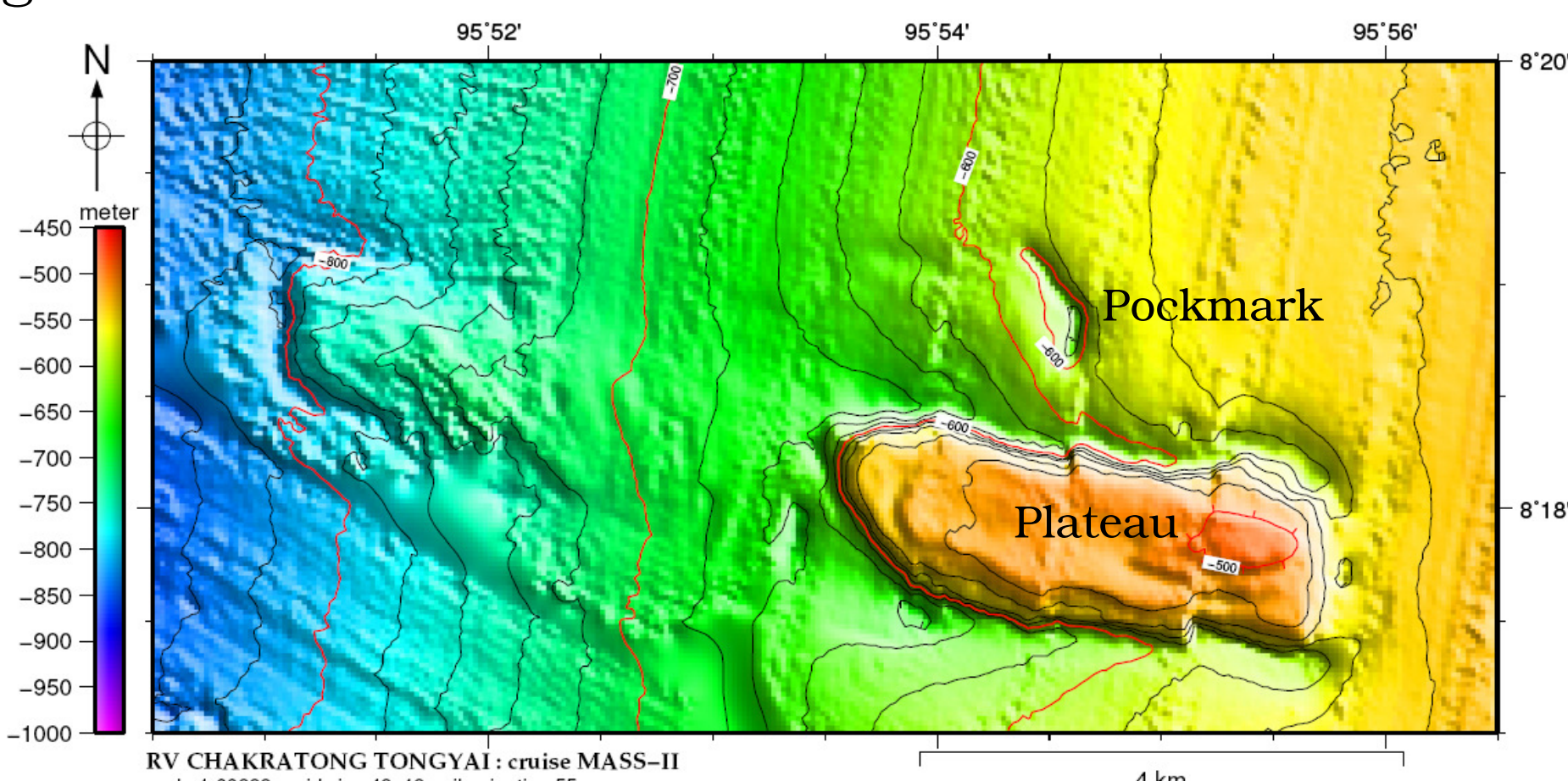


Figure 5. A swath bathymetry show bad signal in the vicinity of a volcano-like structure (left). A shade relief 10 m-grid resolution bathymetry of the embankment (right). A parametric profile M-01 (upper-left).

Mud-volcano

A circular embankment in flat-top area is observed. Diameter of the embankment is about 500 m and 35 m high (Fig. 5-right).

Strong signals not related to the seafloor reflection are observed in the vicinity of the mud-volcano-like feature (Fig. 5-left). In addition, negative polarity signals which are observed at position M-01 of sub-bottom profiler indicates the present of escape fluid or gas on top of the dome (Fig. 5-upperleft). The domal uplift could possibly be identified as submarine mud-volcano.

ภาคผนวก ข

การฝึกอบรมเชิงปฏิบัติการทางธรณีฟิสิกส์

“โครงการเสถียรภาพของชั้นตะกอนและการเกิดแผ่นดินถล่มใต้ทะเลบริเวณขอบไหล่ทวีปในทะเลอันดามัน”

ระหว่างวันที่ 22-26 สิงหาคม 2554

ณ ภาควิชาวิทยาศาสตร์พื้นพิภพ คณะวิทยาศาสตร์ มหาวิทยาลัยเกษตรศาสตร์

หลักการและเหตุผล

จากการที่สำนักงานคณะกรรมการวิจัยแห่งชาติ (วช.) และ Deutsche Forschungsgemeinschaft (DFG) ได้ร่วมกันให้การสนับสนุนกรอบความร่วมมือไทย-เยอรมันเพื่อการศึกษาวิจัยทะเลอันดามัน: ธรณีศาสตร์ นิเวศวิทยาและวิศวกรรมศาสตร์เพื่อการจัดการภัยพิบัติทางธรรมชาติและการใช้ทรัพยากรทางทะเลอย่างยั่งยืน (Thai-German Cooperative Research and Capacity Building: Ocean Geosciences, Marine Ecology and Natural Hazard Management) มาตั้งแต่ พ.ศ. 2549 โดยมีกรอบความร่วมมือมีโครงการที่กำลังดำเนินการโดยการสนับสนุนจาก วช. จำนวน 4 โครงการ และ จาก DFG จำนวน 6 โครงการ โดยแบ่งเป็น 6 กลุ่มวิจัย คือ

1. Morphodynamics and Slope Stability of the Andaman Sea Shelf Break
2. Tsunami Deposits in Nearshore and Coastal Waters
3. Tracing Tsunami Impacts in Coastal Geo- and Bio-Archives
4. Ocean-Reef Coupling and Dynamics
5. Tsunami Attenuation Performance of Coastal Forests
6. Tsunami Risks, Vulnerability and Resilience

ด้วยจุฬาลงกรณ์มหาวิทยาลัย โดยศูนย์เครื่องข่ายงานวิเคราะห์วิจัยและฝึกอบรมการเปลี่ยนแปลงของโลกแห่งภูมิภาคเอเชียตะวันออกเฉียงใต้ ได้รับการสนับสนุนงบประมาณการวิจัย โครงการวิจัยต่อเนื่องระยะเวลา 3 ปี เพื่อดำเนินโครงการ “เสถียรภาพของชั้นตะกอนและการเกิดแผ่นดินถล่มใต้ทะเลบริเวณขอบไหล่ทวีปในทะเลอันดามัน” ตามกลุ่มวิจัยที่ 1 ดังกล่าวข้างต้น บัดนี้โครงการฯ ได้ดำเนินจนถึงปีที่ 3 และมีความคืบหน้าและได้ข้อมูลทางวิชาการใหม่ๆ จากการสำรวจในปีที่ 1 และ 2 ของโครงการฯ โดยใช้เรือสำรวจวิจัยจักรทอง ทองใหญ่ ในปีพ.ศ.2549 พ.ศ.2550 และ พ.ศ.2554 เพื่อหยั่งความลึกพื้นทะเลด้วยคลื่นเสียงสะท้อนแบบหลายความถี่ (Multibeam bathymetric echo sounding), ศึกษาการเรียงตัวของชั้นตะกอนโดยใช้คลื่นเสียงทุติยภูมิ (Parametric sediment echo sounding) ในพื้นที่สำรวจกว่า 3,000 ตารางกิโลเมตร ภายในเขตเศรษฐกิจจำเพาะทะเลอันดามันของประเทศไทยด้านตะวันตกเฉียงใต้ ที่ความลึกของทะเลช่วง 500–1600 เมตร และเนื่องจากบุคลากรในประเทศไทยยังขาดประสบการณ์และความชำนาญในการวิเคราะห์ข้อมูลเชิงธรณีฟิสิกส์ ดังนั้นเพื่อให้การวิเคราะห์ข้อมูลและประมวลผลข้อมูลให้เป็นไปอย่างมีประสิทธิภาพ นักวิจัยทั้งสองฝ่ายจึงได้เห็นพ้องกันว่าควรจะจัดการฝึกอบรมเชิงปฏิบัติการทางธรณีฟิสิกส์ ของโครงการ “เสถียรภาพของชั้นตะกอนและการเกิดแผ่นดินถล่มใต้ทะเลบริเวณขอบไหล่ทวีปในทะเลอันดามัน” ณ กรุงเทพฯ โดยจัดที่ภาควิชาวิทยาศาสตร์พื้นพิภพ คณะวิทยาศาสตร์ มหาวิทยาลัยเกษตรศาสตร์ เนื่องจากมีข้อจำกัดเรื่องลิขสิทธิ์

ของโปรแกรมในการวิเคราะห์ข้อมูลและเครื่องคอมพิวเตอร์ที่มีความเฉพาะต่อการวิเคราะห์ข้อมูลทางธรณีฟิสิกส์ โดยนักวิจัยทั้งฝ่ายไทยและเยอรมันของโครงการฯ ร่วมเป็นวิทยากร ดังกำหนดการในเอกสารแนบ โดยมีวัตถุประสงค์เพื่อพัฒนานุเคราะห์ด้านการวิเคราะห์ข้อมูลการสำรวจชั้นตะกอนทะเลลึกทั้งทฤษฎีและภาคปฏิบัติให้มีประสิทธิภาพมากขึ้น และสอดคล้องกับยุทธศาสตร์การวิจัยของชาติ (พ.ศ. 2551- 2554) ในหัวข้อการสร้างศักยภาพและความสามารถในการพัฒนาทางวิทยาการและทรัพยากรบุคคล อีกด้วย

วัตถุประสงค์

1. การพัฒนานุเคราะห์ด้านการวิเคราะห์ข้อมูลการสำรวจชั้นตะกอนทะเลลึกทั้งทฤษฎีและภาคปฏิบัติ
2. เพื่อเผยแพร่ผลงานวิจัยภายใต้กรอบความร่วมมือทางวิชาการออกสู่กลุ่มผู้ใช้งานหรือกลุ่มเป้าหมาย เพื่อให้เกิดการประยุกต์ใช้งานจริง

กำหนดการประชุม

ระหว่างวันที่ 22 – 26 สิงหาคม 2554 ณ ภาควิชาวิทยาศาสตร์พื้นพิภพ คณะวิทยาศาสตร์ มหาวิทยาลัยเกษตรศาสตร์ กรุงเทพมหานคร (กำหนดการดังแสดงในเอกสารแนบ)

ผู้ร่วมการประชุม

ผู้เข้าร่วมจำนวน 20 คน ประกอบด้วย นักวิจัย นิสิต นักศึกษา และผู้แทนจากหน่วยงานที่เกี่ยวข้องและผู้เชี่ยวชาญอื่นๆ

รูปแบบการประชุม

1. การให้ความรู้ภาคทฤษฎีทั้งหมด 3 หัวข้อ
2. การปฏิบัติการทางธรณีฟิสิกส์ทั้งหมด 5 หัวข้อ

หน่วยงานสนับสนุนบุคลากรและ In Kind ต่างๆ เพื่อร่วมการประชุม

ฝ่ายไทย:

- จุฬาลงกรณ์มหาวิทยาลัย
- ศูนย์เครือข่ายงานวิเคราะห์วิจัยและฝึกอบรมการเปลี่ยนแปลงของโลกแห่งภูมิภาคเอเชียตะวันออกเฉียงใต้ จุฬาลงกรณ์มหาวิทยาลัย
- ภาควิชาวิทยาศาสตร์พื้นพิภพ คณะวิทยาศาสตร์ มหาวิทยาลัยเกษตรศาสตร์
- มหาวิทยาลัยบูรพา

ฝ่ายเยอรมัน:

- Leibniz Institute for Marine Sciences (IFM-GEOMAR), Kiel, Germany

ผู้รับผิดชอบในการจัดประชุม

ศูนย์เครือข่ายงานวิเคราะห์ วิจัย ฯ จุฬาลงกรณ์มหาวิทยาลัย

ติดต่อ: นางสาวสุรัตตา บุญสมบุรณ์สกุล email: suratta@start.or.th

โทรศัพท์ 0-2218-9465-67 โทรสาร 0-2251-9416



Agenda

Workshop of the bilateral, NRCT and DFG funded Project
“Morphodynamics and Slope Stability of the Andaman Sea Shelf Break (MASS)”
On Geophysics: acoustic and seismic imaging

Day 1, 22 August 2011

- 8.30-9.00 Registration
9.00-9.15 Opening of the workshop: MASS-Team

Morning: (include coffee break)

- 9.15-12.00 Introduction to hydroacoustic imaging: Principles and concepts,
Prof. Dr. Sebastian Krastel, *IFM-GEOMAR*

Afternoon: (include coffee break)

- 13.00-16.00 GMT Exercise I

Day 2, 23 August 2011

Morning: (include coffee break)

- 9.00-12.00 Bathymetric and sidescan sonar imaging,
Prof. Dr. Sebastian Krastel, *IFM-GEOMAR*
Mr. Pachoenchoke Jintasaeranee, *Burapha University*

Afternoon: (include coffee break)

- 13.00-16.00 GMT Exercise II and real multibeam data (MASS I&II)

Day 3, 24 August 2011

Morning: (include coffee break)

- 9.00-12.00 Seismic Imaging, some basic theory,
Prof. Dr. Sebastian Krastel, *IFM-GEOMAR*
Dr. Passakorn Pananont, *Kasetsart University*

Afternoon: (include coffee break)

- 13.00-16.00 Seismic exercise I

Day 4, 25 August 2011

Morning: (include coffee break)

- 9.00-12.00 Seismic Processing

Afternoon: (include coffee break)

- 13.00-16.00 Seismic exercise II

Day 5, 26 August 2011

Morning: (include coffee break)

- 9.00-12.00 Integrated data interpretation including exercise with KINGDOM

Afternoon: (include coffee break)

- 13.00-15.00 cont. Integrated data interpretation including exercise with KINGDOM
15.00-16.00 Conclusion and Discussion
16.00 Closing



future ocean
KIEL MARINE SCIENCES

Acoustic Imaging

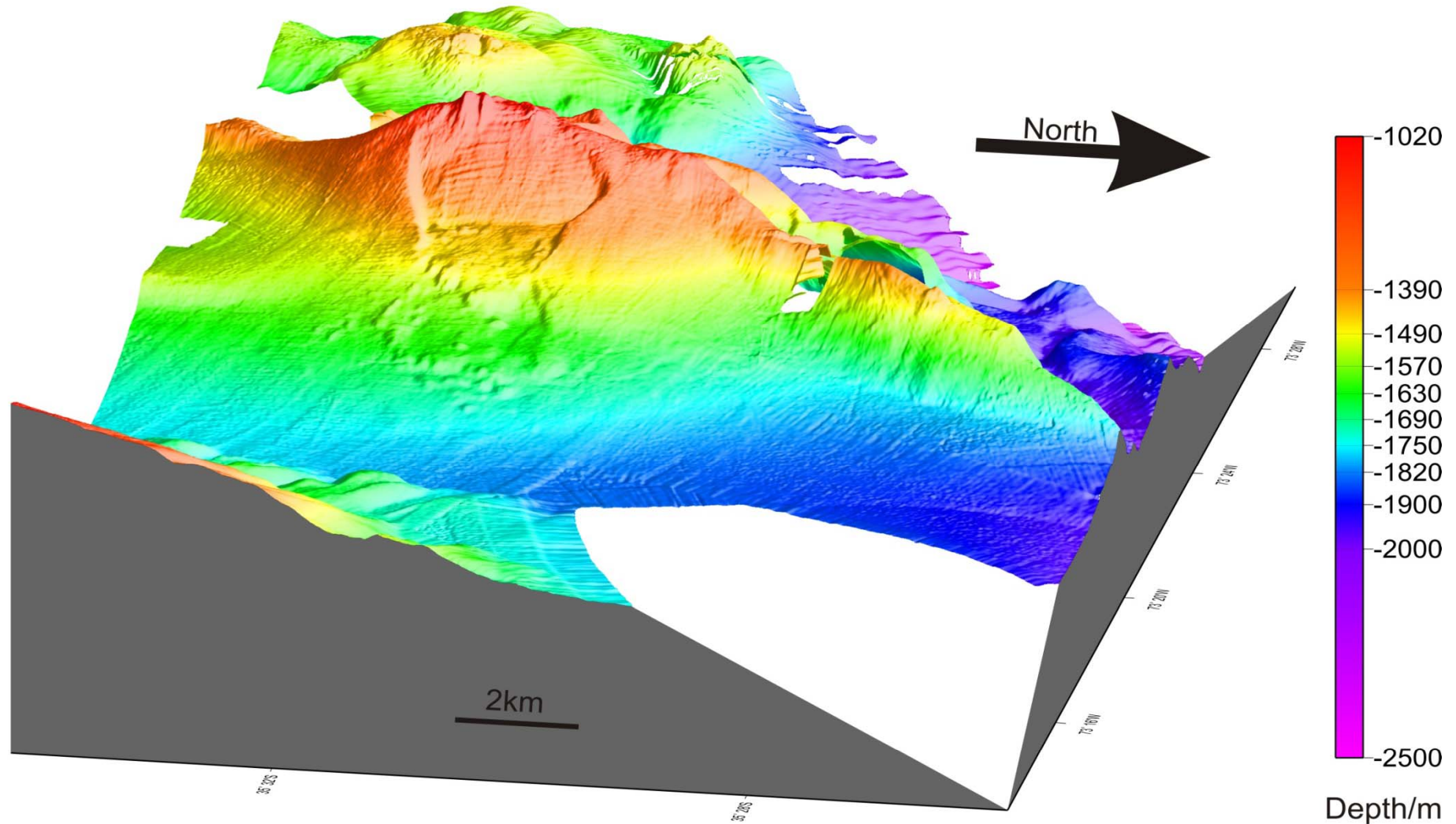
Introduction



IFM-GEOMAR
Leibniz-Institut für Meereswissenschaften
an der Universität Kiel

Submarine Mapping (Techniques and Exercises)

Sebastian Krastel



Bangkok, 22. – 26.08.11



The Leibniz Institute of Marine Sciences at the University of Kiel (IFM-GEOMAR) was founded in January 2004 through the merger of the Institut für Meereskunde (IfM) and the Research Center for Marine Geosciences (GEOMAR). The institute is a member of the Leibniz Association and employs more than 750 scientific and technical staff.

The institutes' mandate is the interdisciplinary investigation of all relevant aspects of modern marine sciences, from sea floor geology to marine meteorology. Research is conducted worldwide in all oceans.

The mission of the institute is:

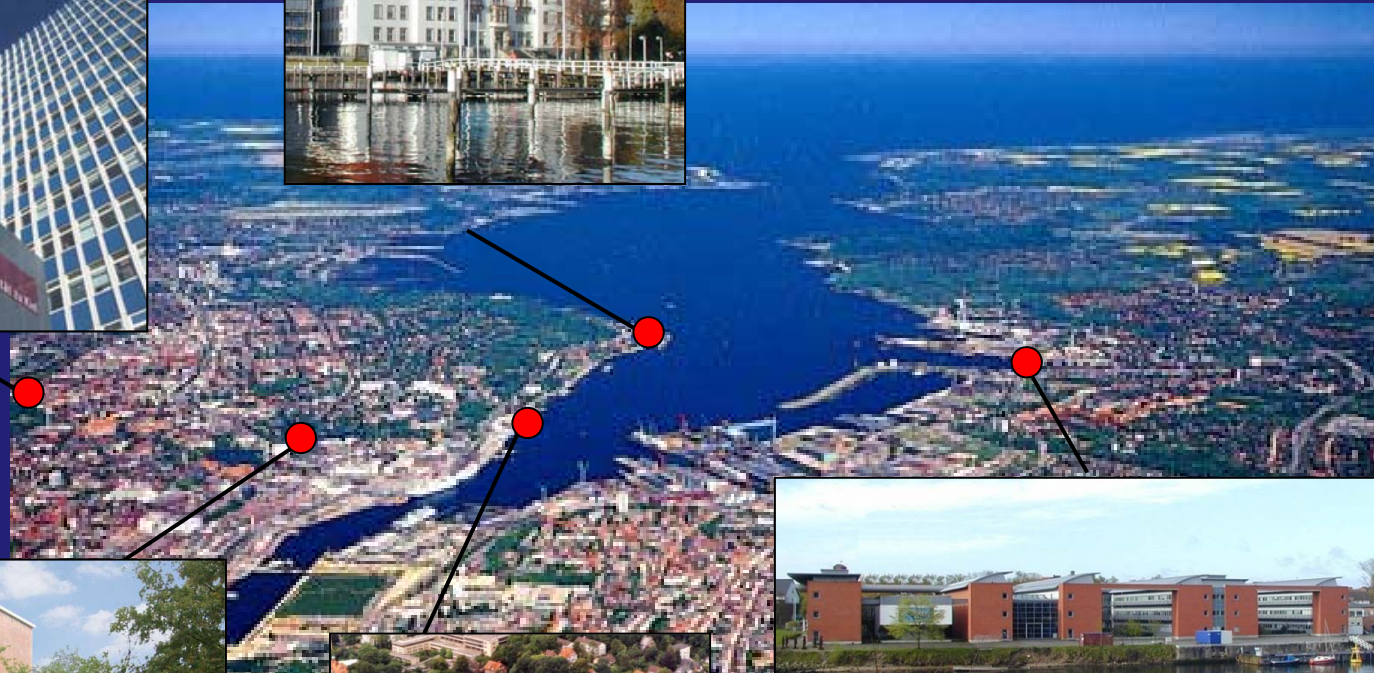
To investigate the physical, chemical, biological, and geological processes in the ocean and their interaction with the seafloor and the atmosphere.

„Network of Kiel Marine Sciences“

Faculties of the
Christian Albrechts University



Kiel Institute
for the World Economy



MUTHESIUS
Academy of Fine Arts



IFM-GEOMAR



muthesius
kunsthochschule



Massholmer Vorträge, 28.07.2008

Structure

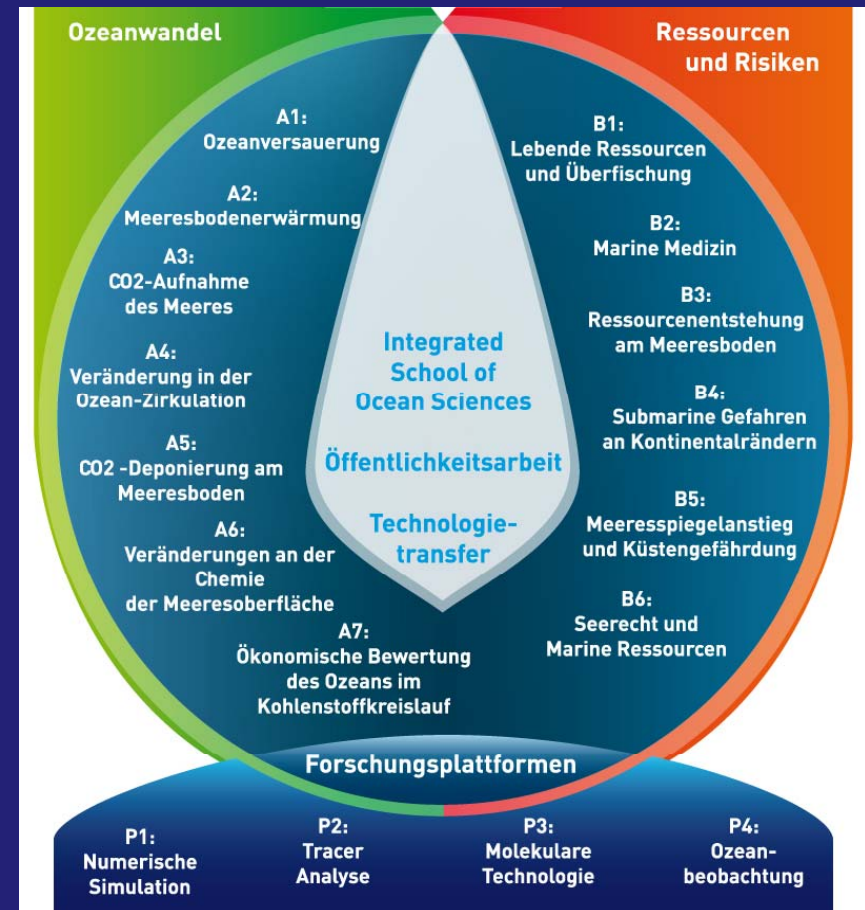
The network

200 scientists from five faculties and 26 institutes at Kiel University, as well as the Kiel Leibniz Institute of Marine Sciences (IFM-GEOMAR), the Kiel Institute for the World Economy (IfW) and the Muthesius Academy of Fine Arts.

Unique in Germany

Oceanographers, Geoscientists, Economists, Jurists, and , medics, mathematicians, and social scientists are investigating ocean change, resources and risks.

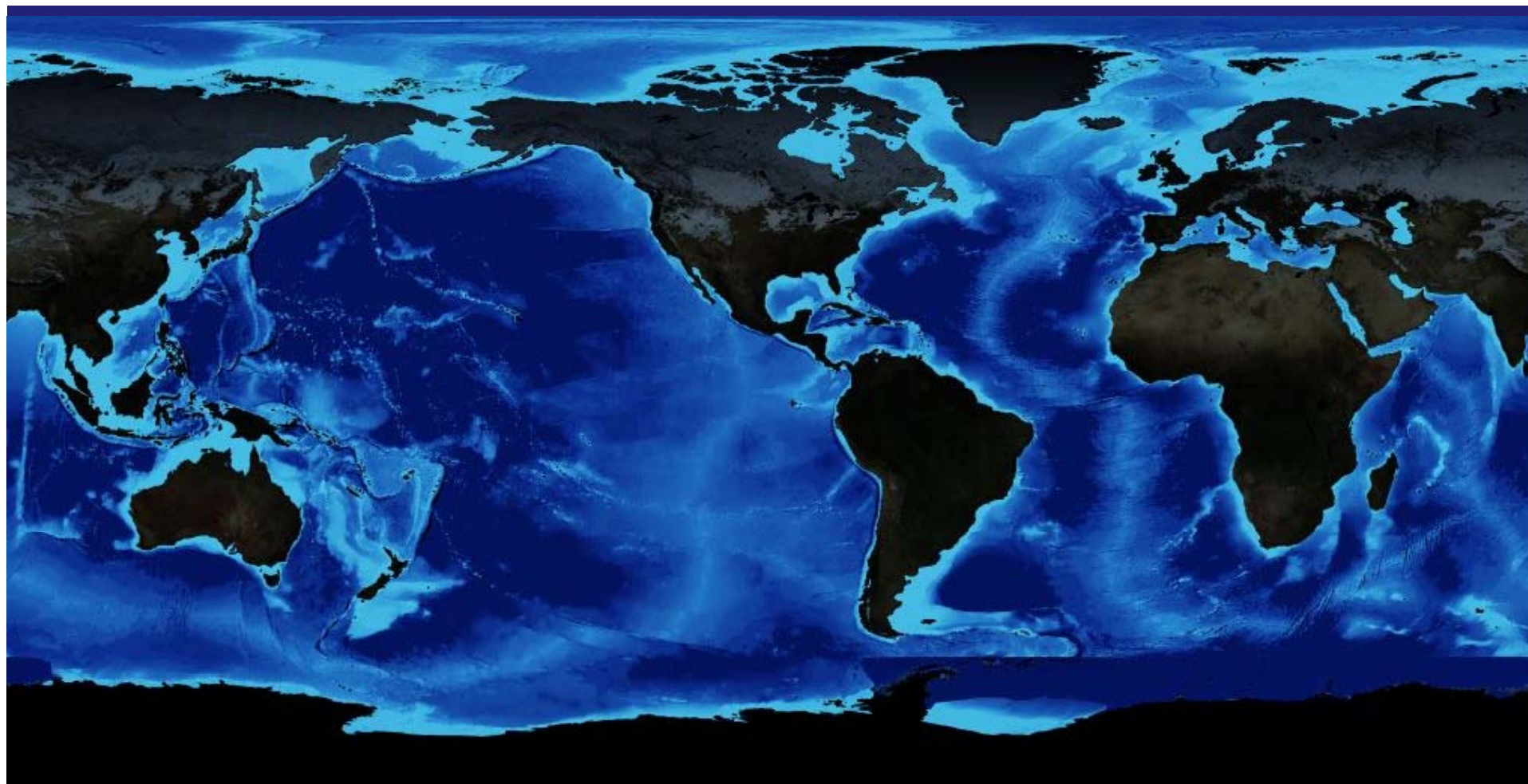
13 new groups in Kiel investigating the 'Future Ocean'





future ocean
KIEL MARINE SCIENCES

„ Understanding the ocean — sustaining our future“



C | A | U

Christian-Albrechts-Universität zu Kiel



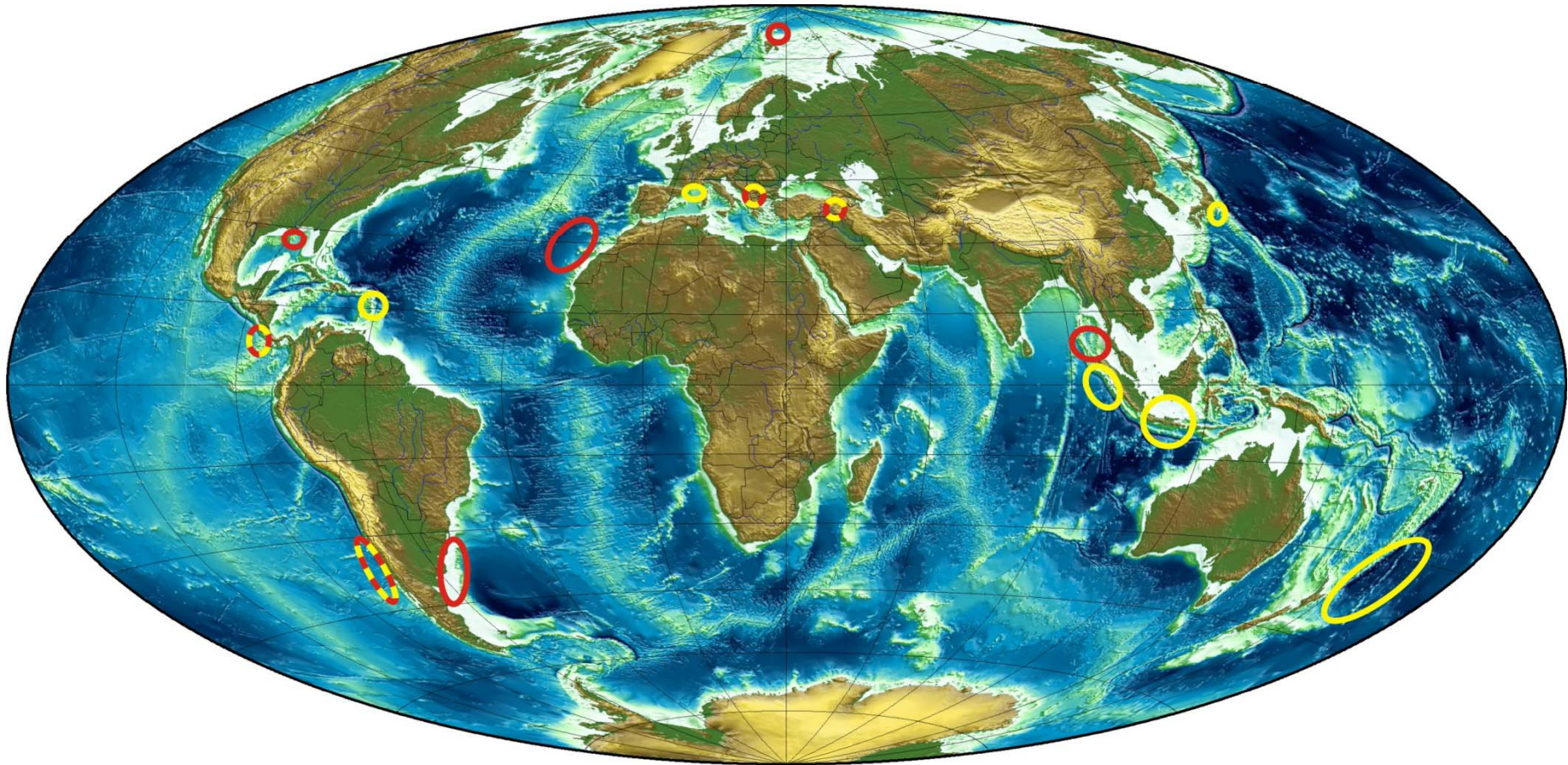
muthesius
kunsthochschule

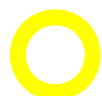



IFM-GEOMAR

Massholmer Vorträge, 28.07.2008

Submarine Hazards at Continental Margins



-  Research Topic 'Assessment of the Link between the Structure and Dynamics of Subduction Zones and the Mega-Earthquake Cycle'
-  Research Topic 'Slope Stability at Continental margins'



Thai - German Cooperation

Tracing Tsunami Impacts On- and Offshore in the Andaman Sea Region

„TRIAS“

MASS - Morphodynamics and slope stability of the Andaman Sea Shelf Break

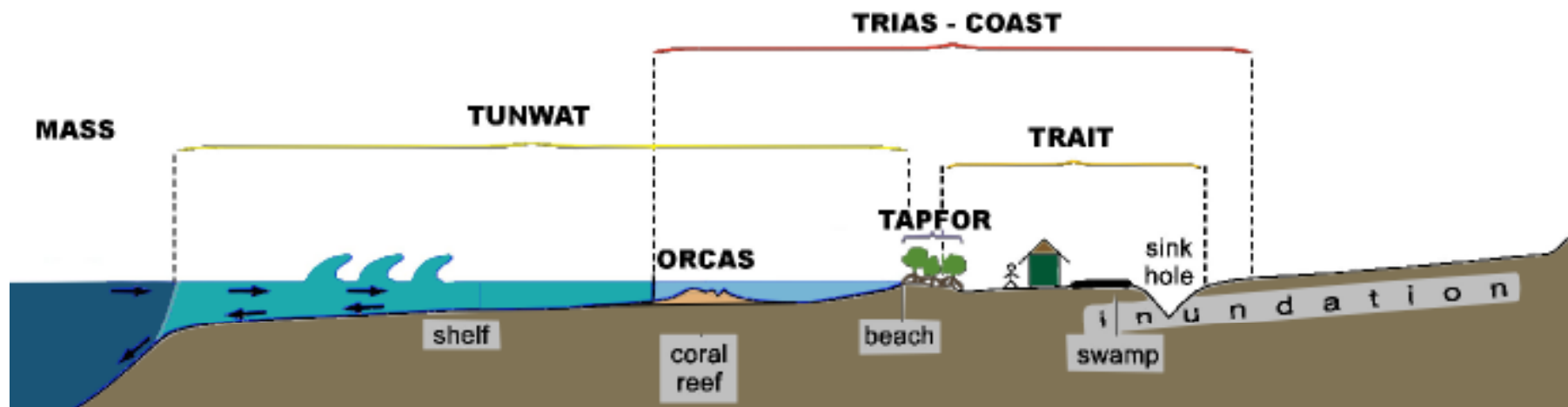
ORCAS - Pelagic-benthic coupling near Andaman Sea Coral Reefs

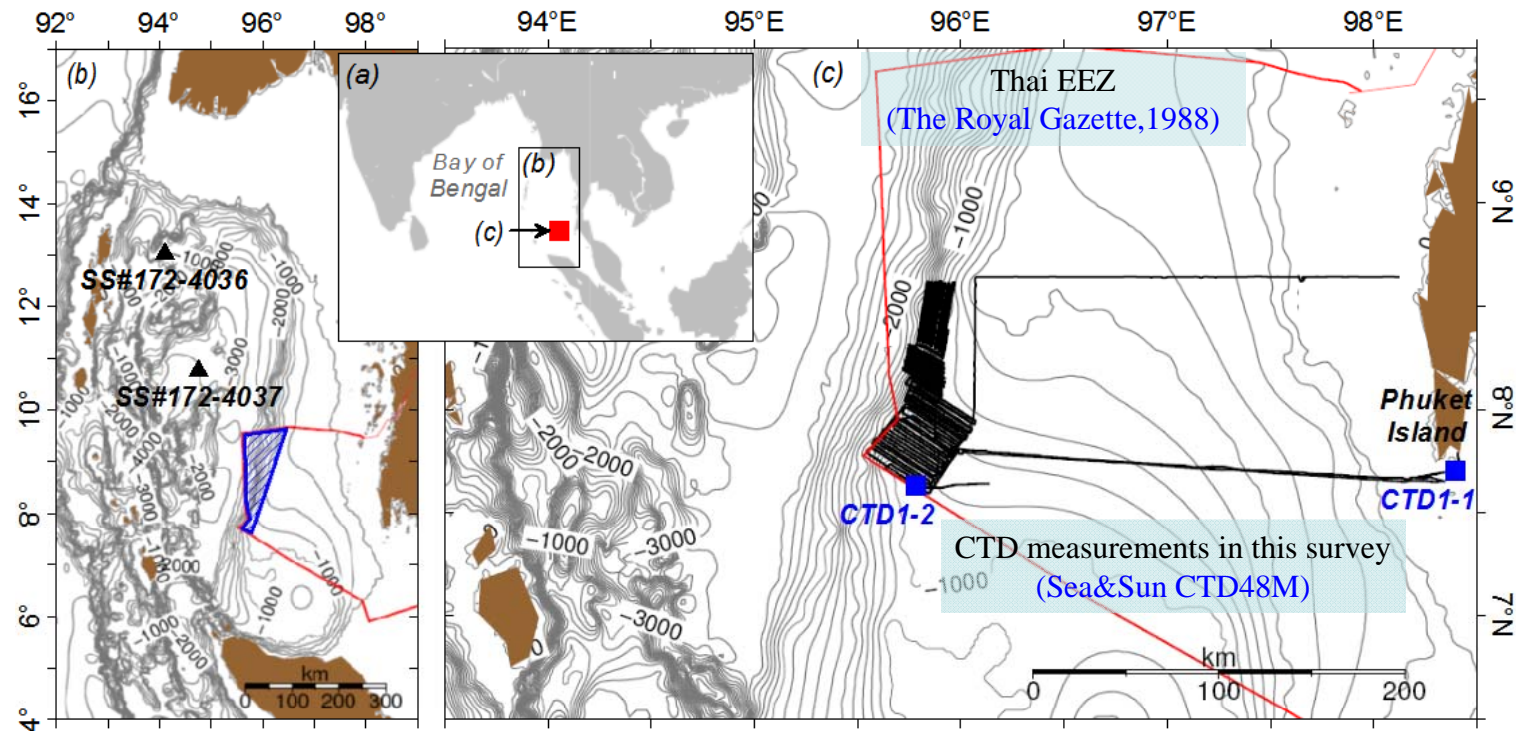
TUNWAT - Tsunami deposits in near-shore and coastal waters of Thailand

TRIAS-COAST - Tracing tsunami impacts in coastal geo- and bio-archives along the west coast of Thailand

TAPFOR - Tsunami attenuation performance of coastal forests

TRAIT - Tsunami risks and vulnerability in the Phang-Nga Province, Thailand





Objectives of MASS project

- **Assessing the potential risk for tsunamis generated by submarine mass-wasting in the Andaman Sea**
- Acquisition of bathymetric multibeam data and sediment echo sounder data
- Morphometric characterization of the survey area

Field surveys 32 days

- MASS-I, 1st-cruise : 20 November-6 December 2006
- MASS-II, 2nd-cruise : 6-15 November 2007

Equipment: SEABEAM1050 and INNOMAR “medium,, 2000 SBP

An area ~3000 km² has been mapped from ~500-1.600 m water depth



Thai research vessel
RV Chakratong Tongyai

MASS III, 11 January - 24 January 2011





future ocean
KIEL MARINE SCIENCES

Acoustic Imaging

Introduction



IFM-GEOMAR
Leibniz-Institut für Meereswissenschaften
an der Universität Kiel

MASS III Team



Aim of the short course: Introduction to the principles of acoustic imaging including data processing and interpretation

3 main topics

- Introduction to marine Mapping Techniques (bathymetry, sidescan sonar, high resolution seismics)
- Processing of the data using state of the art software (GMT, Fledermaus, Vista seismic processing, Kingdom Suite)
- Analysis of data (especially data collected in the Andaman Sea in the past years)

Day 1, 22 August 2011

8.30-9.00 Registration

9.00-9.15 Opening of the workshop MASS-Team

Morning: *(include coffee break)*

9.15-12.00 Introduction to hydroacoustic imaging: Principles and concepts,
Prof. Dr. Sebastian Krastel, IFM–GEOMAR

Afternoon: *(include coffee break)*

13.00-16.00 GMT Exercise I

18.00 Welcome Reception

Day 2, 23 August 2011

Morning: *(include coffee break)*

9.00-12.00 Bathymetric and sidescan sonar imaging,
Prof. Dr. Sebastian Krastel, IFM–GEOMAR
Mr. Pachoenchoke Jintasaeranee, *Burapha University*

Afternoon: *(include coffee break)*

13.00-16.00 GMT Exercise II and real multibeam data (MASS I&II)

Day 3, 24 August 2011

Morning: *(include coffee break)*

9.00-12.00 Seismic Imaging, some basic theory,
 Prof. Dr. Sebastian Krastel, IFM–GEOMAR
 Dr. Passakorn Pananont, Kasetsart University

Afternoon: *(include coffee break)*

13.00-16.00 Seismic exercise I
18.00 Reception Dinner

Day 4, 25 August 2011

Morning: *(include coffee break)*

9.00-12.00 Seismic Processing

Afternoon: *(include coffee break)*

13.00-16.00 Seismic exercise II

Day 5, 26 August 2011

Morning: *(include coffee break)*

9.00-12.00 Integrated data interpretation including exercise with KINGDOM

Afternoon: *(include coffee break)*

13.00-15.00 *cont.* Integrated data interpretation including exercise with KINGDOM

15.00-16.00 Conclusion and Discussion

16.00 Closing

Selected literature:

Marine Geophysics, E. J. W. Jones, Wiley

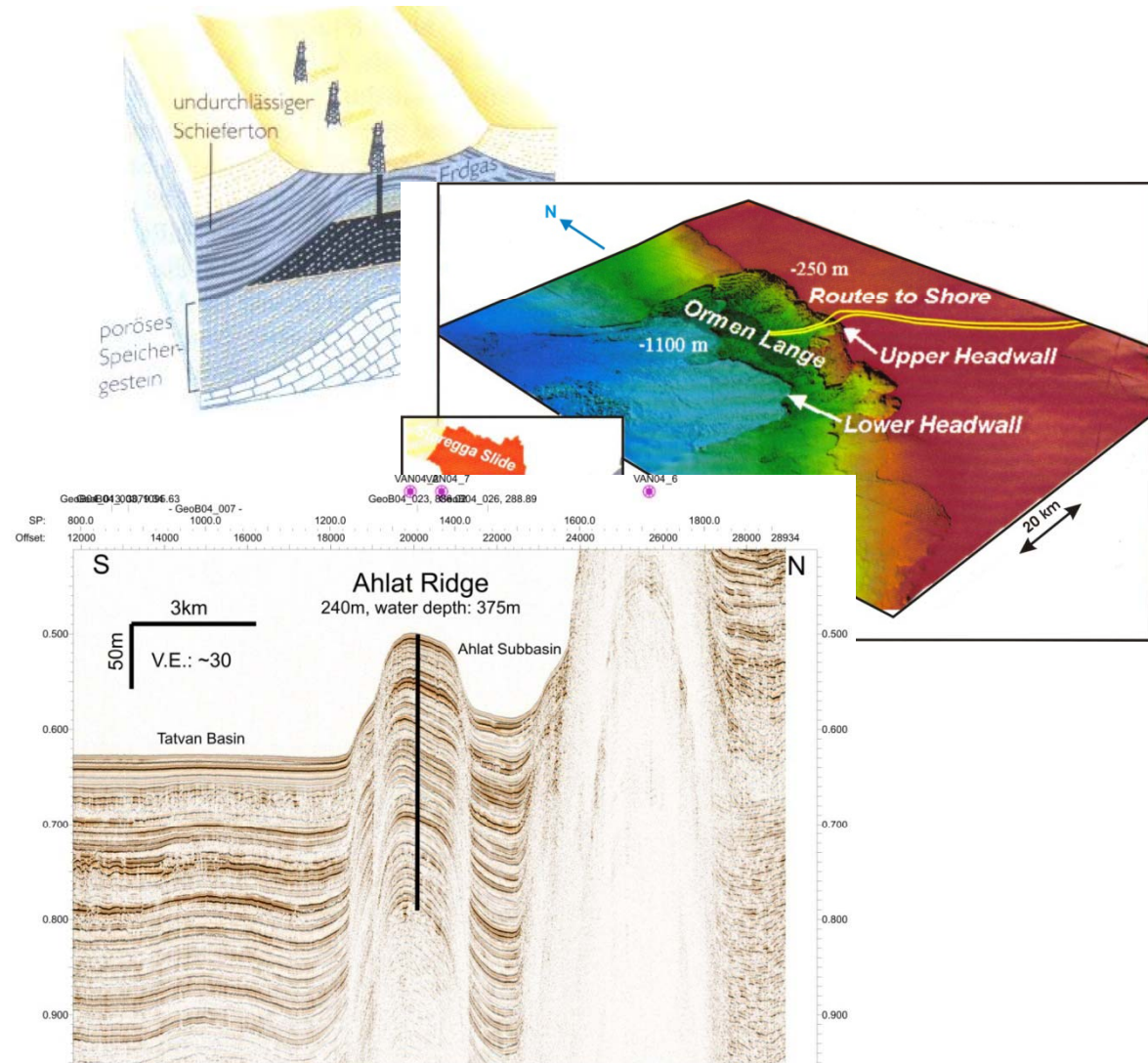
Sound Images of the Ocean, P. Wille, Springer

Several specialized books discussing individual methods and topics

Why?
Resources

Risks

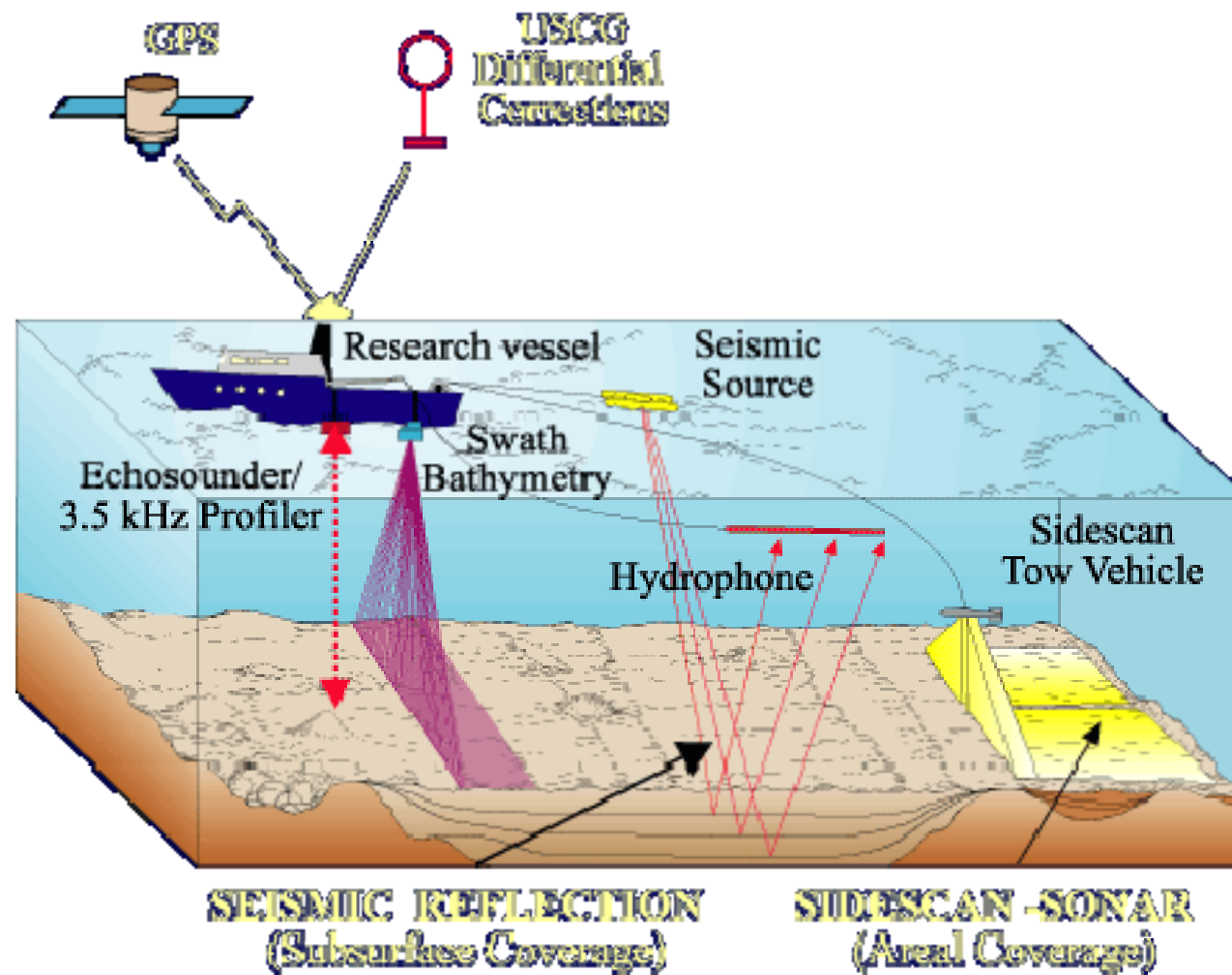
Climate

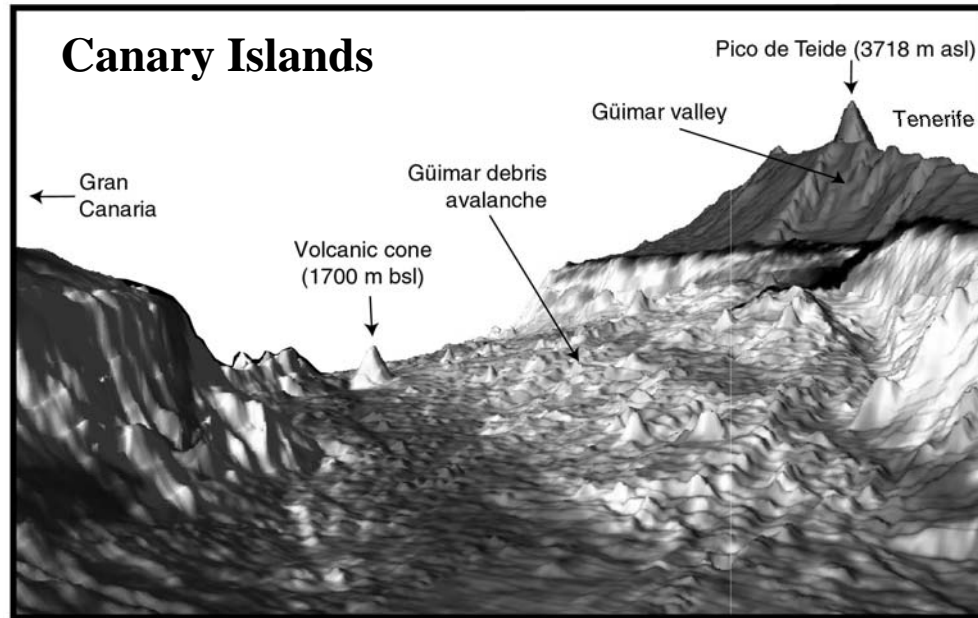


What mapping techniques are available?

- 2D/3D reflection-seismics (with different resolutions)
- Refraction-seismics (Ocean Bottom Seismometer, Bottom Cable)
- Sediment Echo Sounding
- High frequency sounders (Bubble Detection)
- Bathymetry
- Sidescan Sonar
- Deep-towed acoustics (AUVs, ROVs)

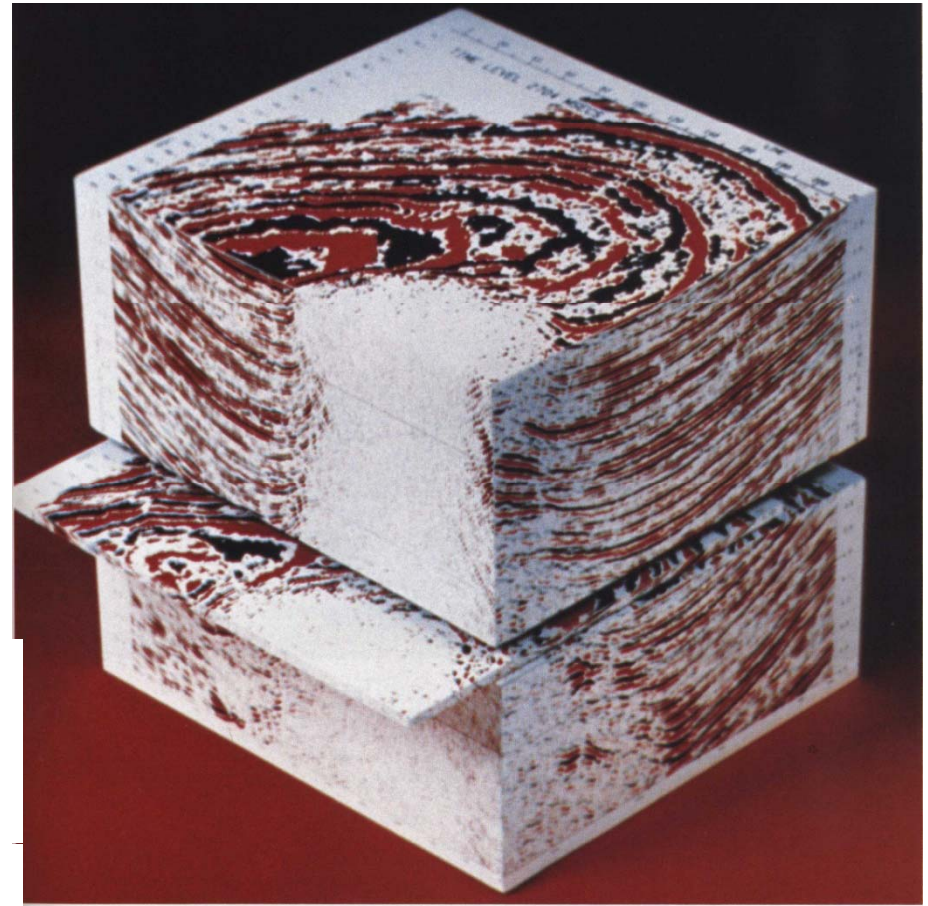
Configuration at Sea





↑ **Acoustic Surficial Mapping:** Swath Bathymetry and Sidescan Sonar Imaging

→ **Seismoacoustic Structural Imaging:** Sediment Echo Sounder, 2D- and 3D Seismics



3D Seismic Image of a Salt Dome (Brown, AAPG Memoir 42)



future ocean
KIEL MARINE SCIENCES

Acoustic Imaging

Introduction



IFM-GEOMAR
Leibniz-Institut für Meereswissenschaften
an der Universität Kiel

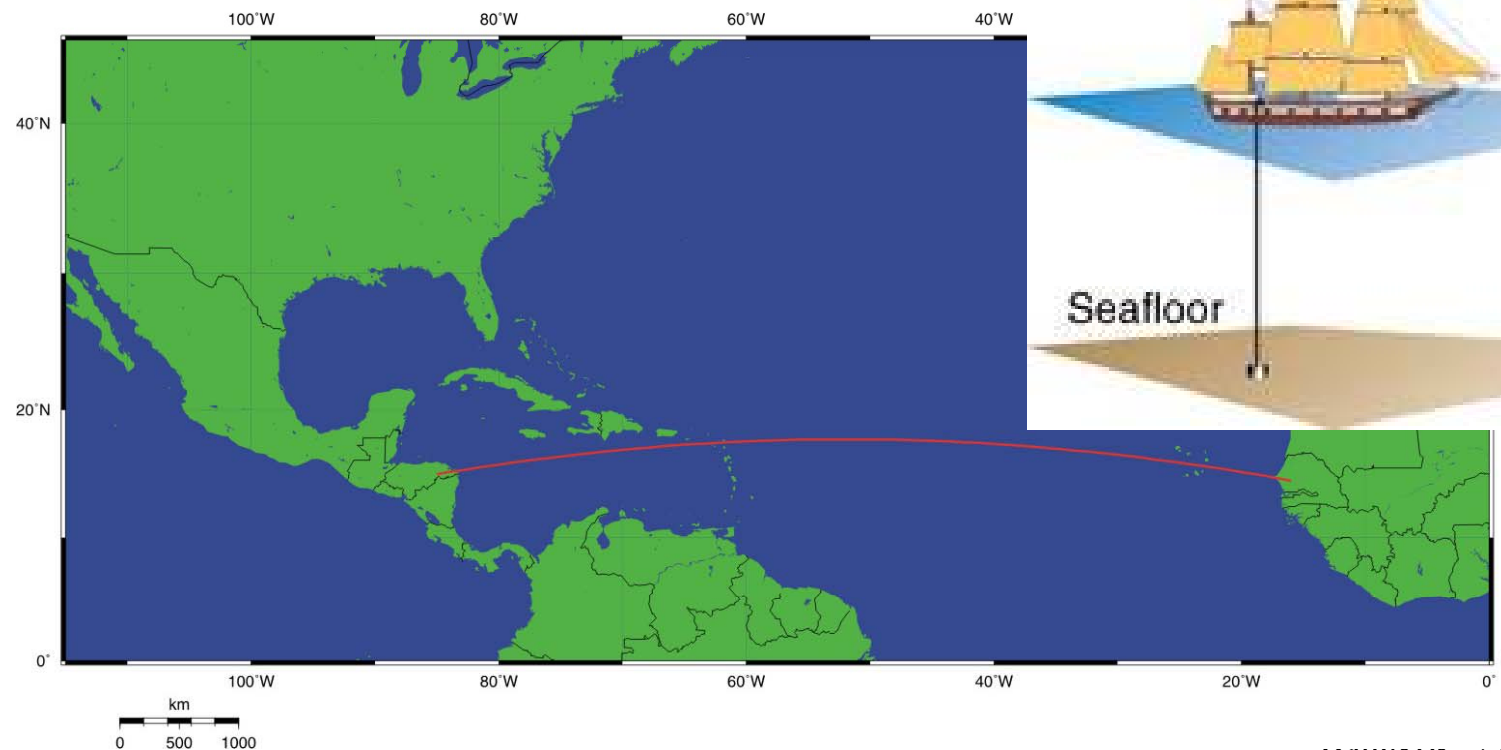
A historical, sepia-toned photograph of a large sailing ship, likely a research vessel, on the ocean. The ship has two prominent masts with complex rigging. The word "History" is overlaid in large white letters at the bottom of the image.

History

1702 Sir Edmond Halley publishes a world map showing magnetic declination at sea.

18th century First bathymetric measurements with plumbs

1855 Murray publishes a bathymetric profile between Mexico and NW- Africa





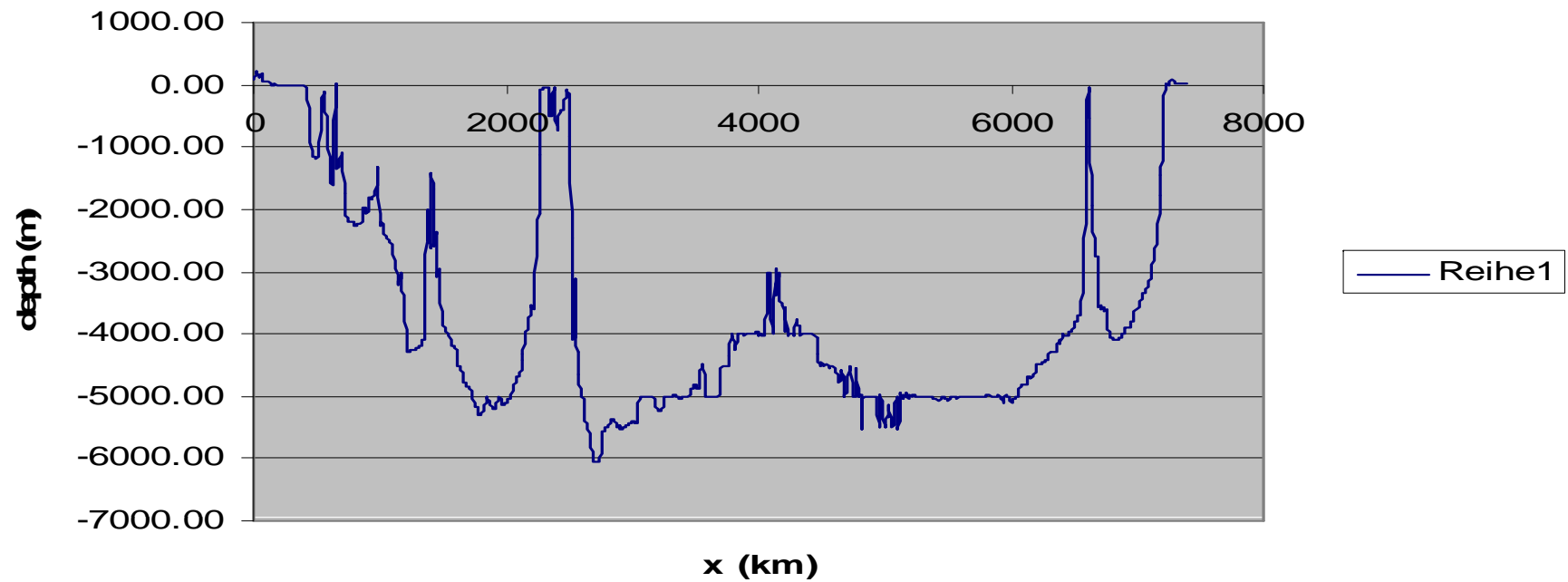
future ocean
KIEL MARINE SCIENCES

Acoustic Imaging

Introduction



IFM-GEOMAR
Leibniz-Institut für Meereswissenschaften
an der Universität Kiel



Bangkok, 22. – 26.08.11

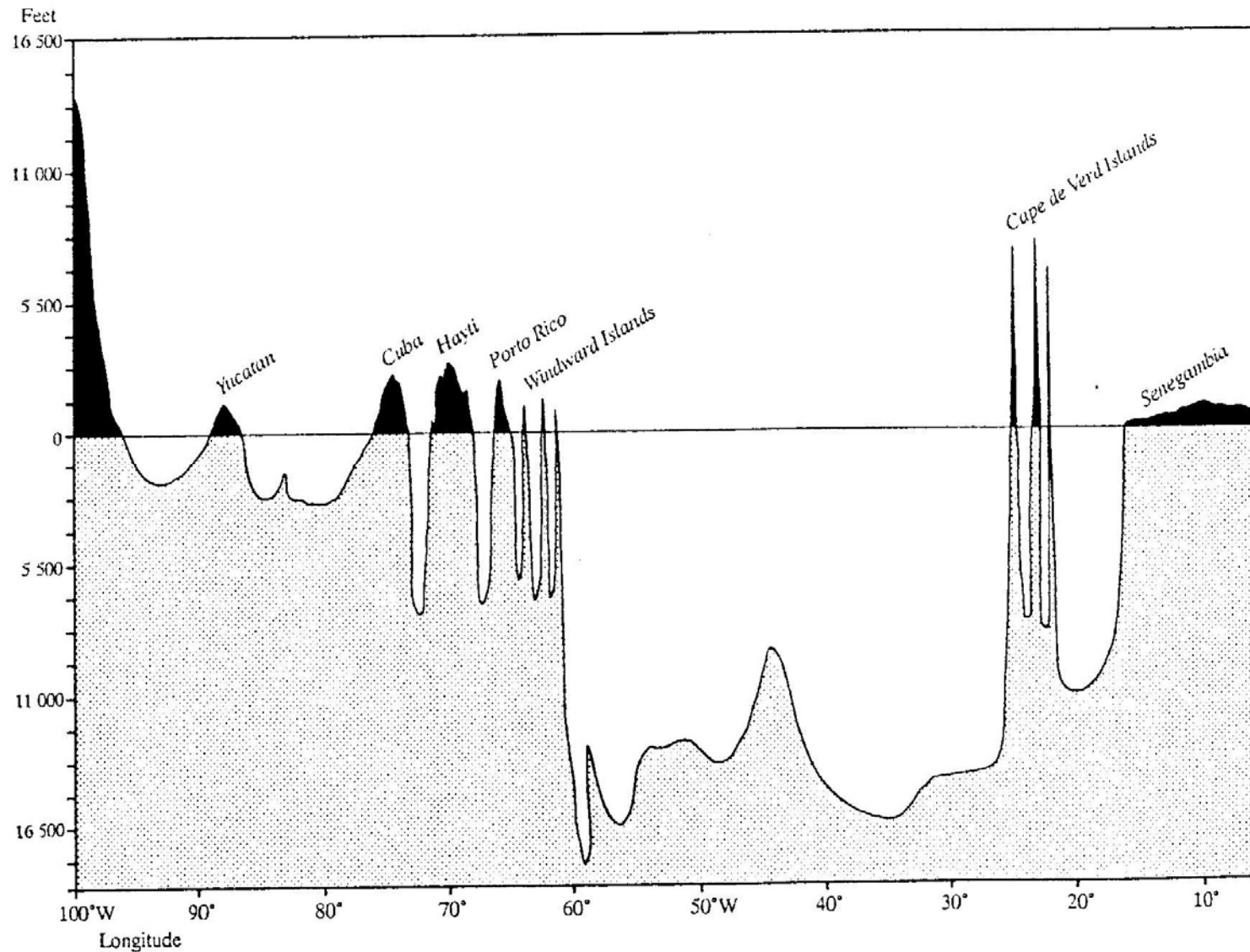


Figure 1.2 Bathymetric profile between Mexico and West Africa published by M.F. Maury (1855). Water depths and land elevations are in feet (5500 ft = 1676 m; 11 000 ft = 3353 m; 16 500 ft = 5029 m). The profile position is shown in Figure 1.1. The place names are those used by Maury.

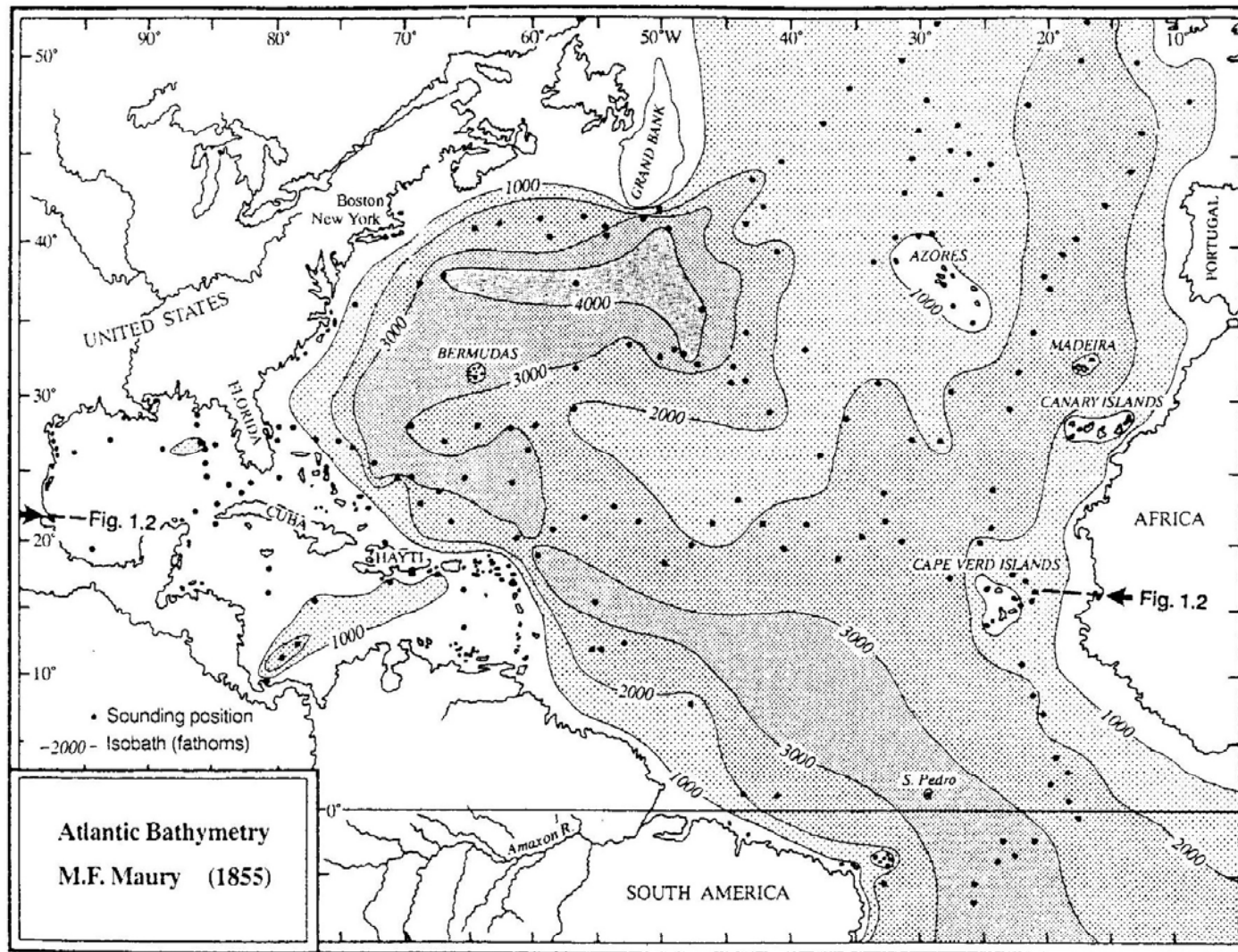


Figure 1.1 A bathymetric map of the North Atlantic, redrawn from a plate published by M.F. Maury (1855). Contours of water depth are given in fathoms (1000 fathoms = 1829 m). The continental margins, deep ocean basins and Mid-Atlantic Ridge are clearly outlined, despite the wide spacing of spot soundings. The place names used by Maury are retained.

1702 Sir Edmond Halley publishes a world map showing magnetic declination at sea.

18th century First bathymetric measurements with plumbs

1855 Murray publishes a bathymetric profile between Mexico and NW- Africa

1872-1876 The Challenger Expedition circumnavigates the globe in the first great oceanographic expedition.

Research is conducted on salinity, density and temperature of sea water as well as ocean currents, sediment and metrology. Hundreds of new species are discovered and underwater mountain chains documented. Modern oceanography is based on this research.

Sir Wyville Thomson leads the British *Challenger* expedition, the first worldwide oceanographic cruise. Thomson dies before all of the results are compiled. Sir John Murray finishes the great work, publishing 50 volumes of the *Challenger's* results and discoveries.

1876 C.W Siemens builds a bathometer for measuring the water depth (based on gravity)

1913 Alexander Behm builds the first echo sounder

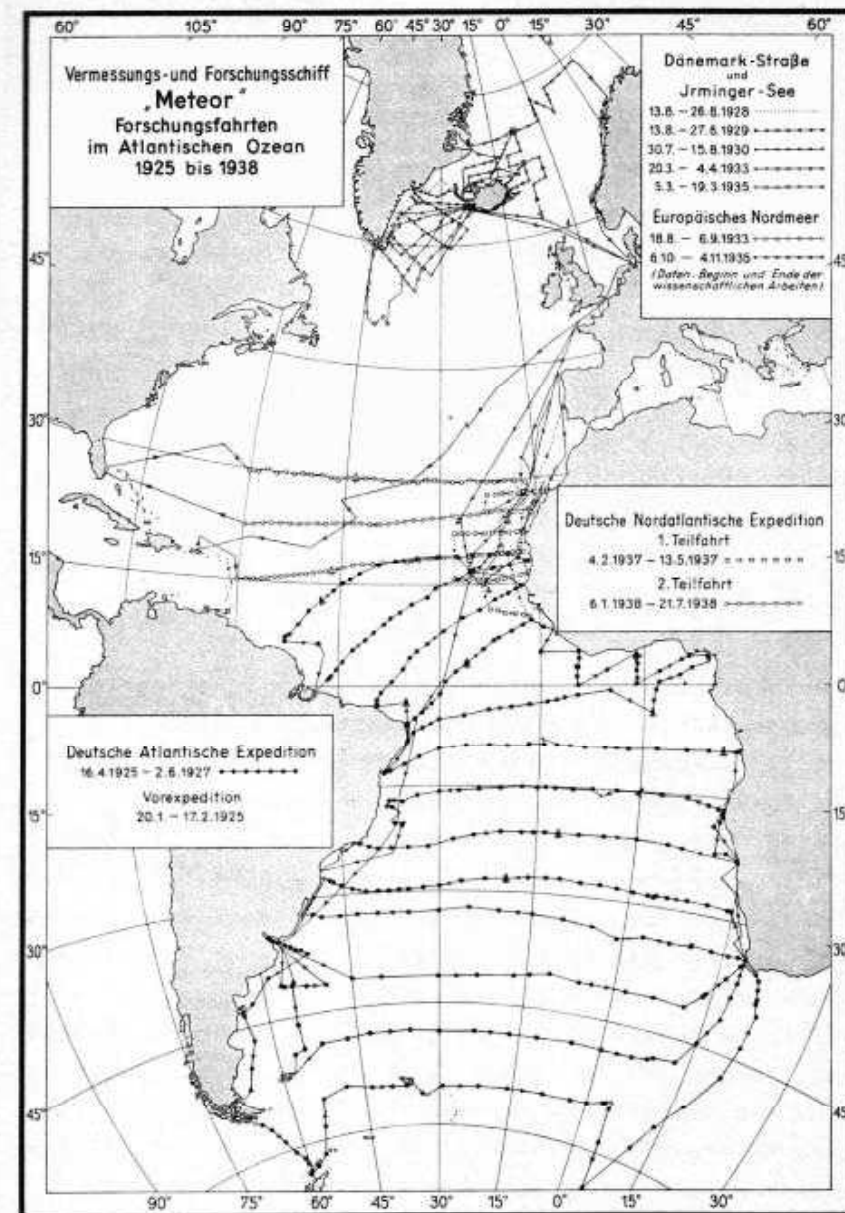
1922 The USS Stewart runs a line of soundings across the Atlantic Ocean using an acoustic echo sounder devised by Dr. Harvey Hayes, a U.S. Navy scientist. The French also run an acoustic sounding line from Marseilles to Phillipeville, Algeria, for a submarine cable survey.

1925-1927 The German *Meteor* expedition systematically surveys the South Atlantic with echo-sounding equipment and other oceanographic instruments, proving beyond a doubt the continuity of the Mid-Atlantic Ridge.

First systematic survey of an entire ocean basin.



FS Meteor



(Nach G. Böhmcke und A. Schumacher, Deutsche Hydrographische Zeitschrift 3 (1950) 1/2; Meteor (Schmidt-Ott-Hett)

1937 First seismic measurements at sea

2nd world war Development of magnetometers, hydrophones, sonars, and navigations systems, detailed investigations of the water column

1955 The Coast and Geodetic Survey Ship Pioneer in a joint project with the U.S. Navy and the Scripps Institution of Oceanography tows the first marine magnetometer and discovers magnetic striping on the seafloor off the west coast of the United States. Called the PIONEER Survey, this survey was called one of the most significant geophysical surveys ever conducted as it provided a key element to the Theory of Plate Tectonics.

Since 1955 Major advances in computer technology

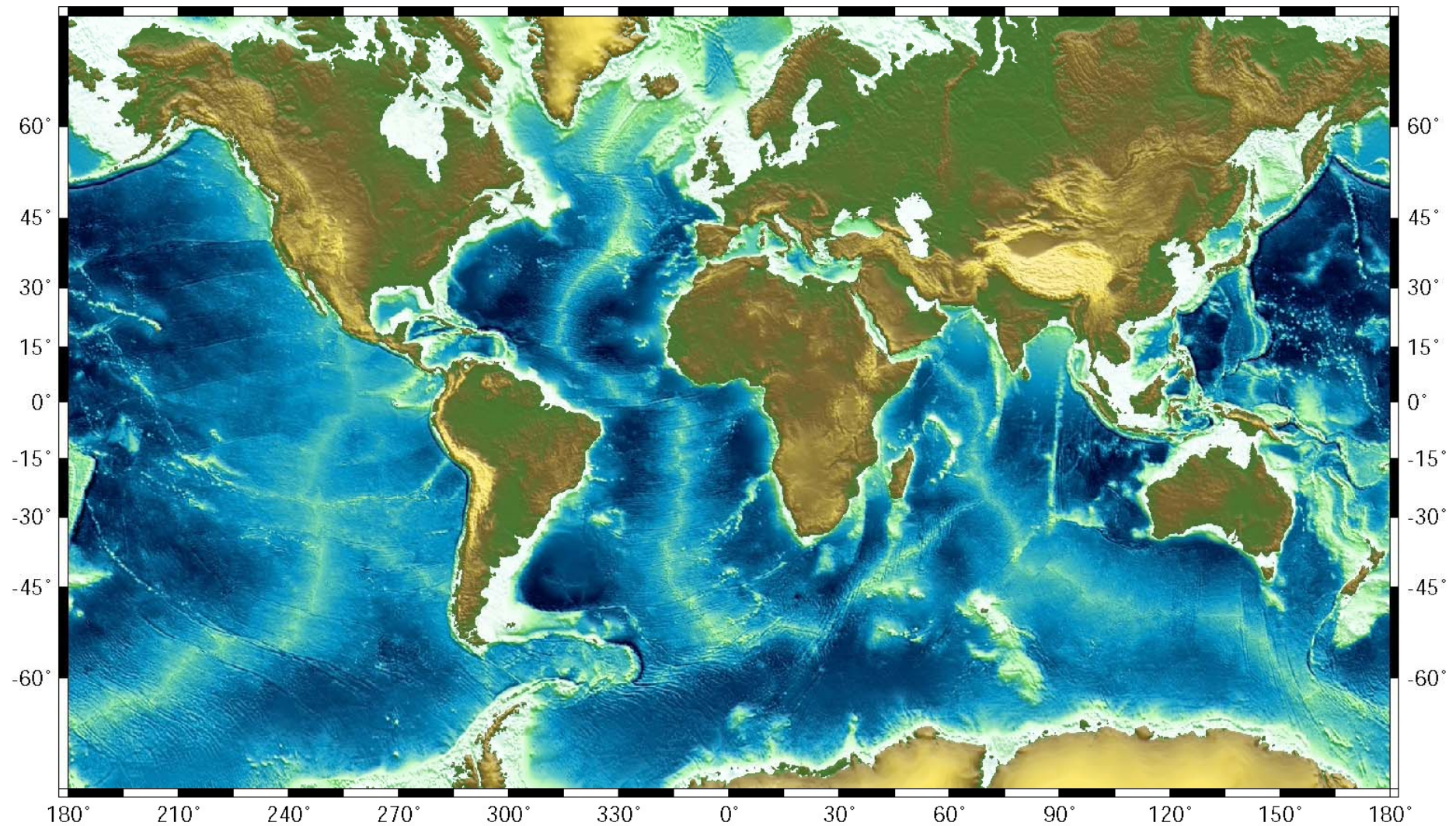
1963 The first operational multibeam sounding system was installed on the USNS Compass Island.

1968 Deep-Sea Drilling Project



1982 Gebco (GENERAL BATHYMETRIC CHART OF THE OCEANS) 5th Edition

1997 Smith and Sandwell: Global sea floor topography from satellite altimetry and ship depth soundings



nach Smith and Sandwell, 1997

Bangkok, 22. – 26.08.11



future ocean
KIEL MARINE SCIENCES

Acoustic Imaging

Introduction



IFM-GEOMAR
Leibniz-Institut für Meereswissenschaften
an der Universität Kiel

Some Principles of acoustic imaging

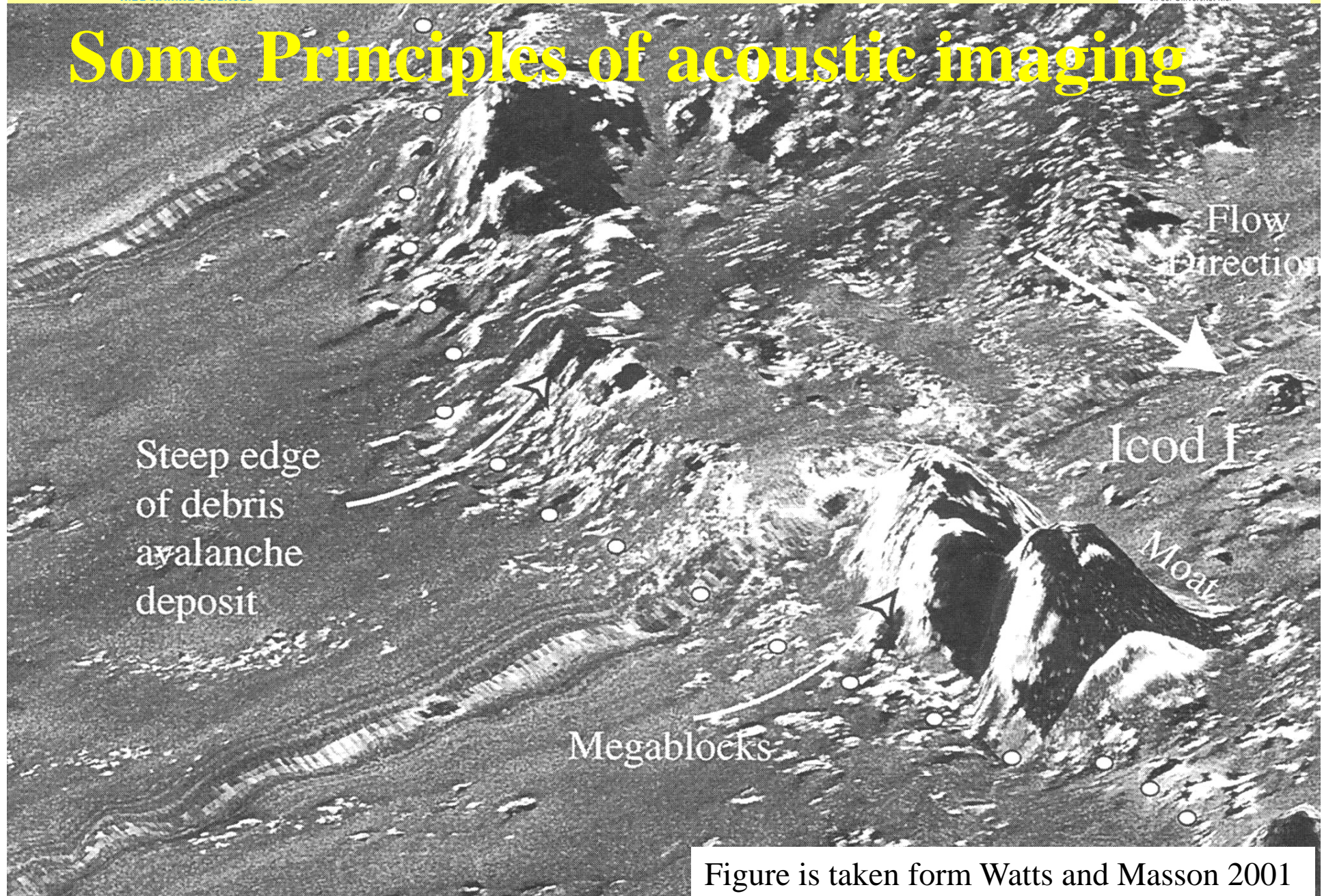
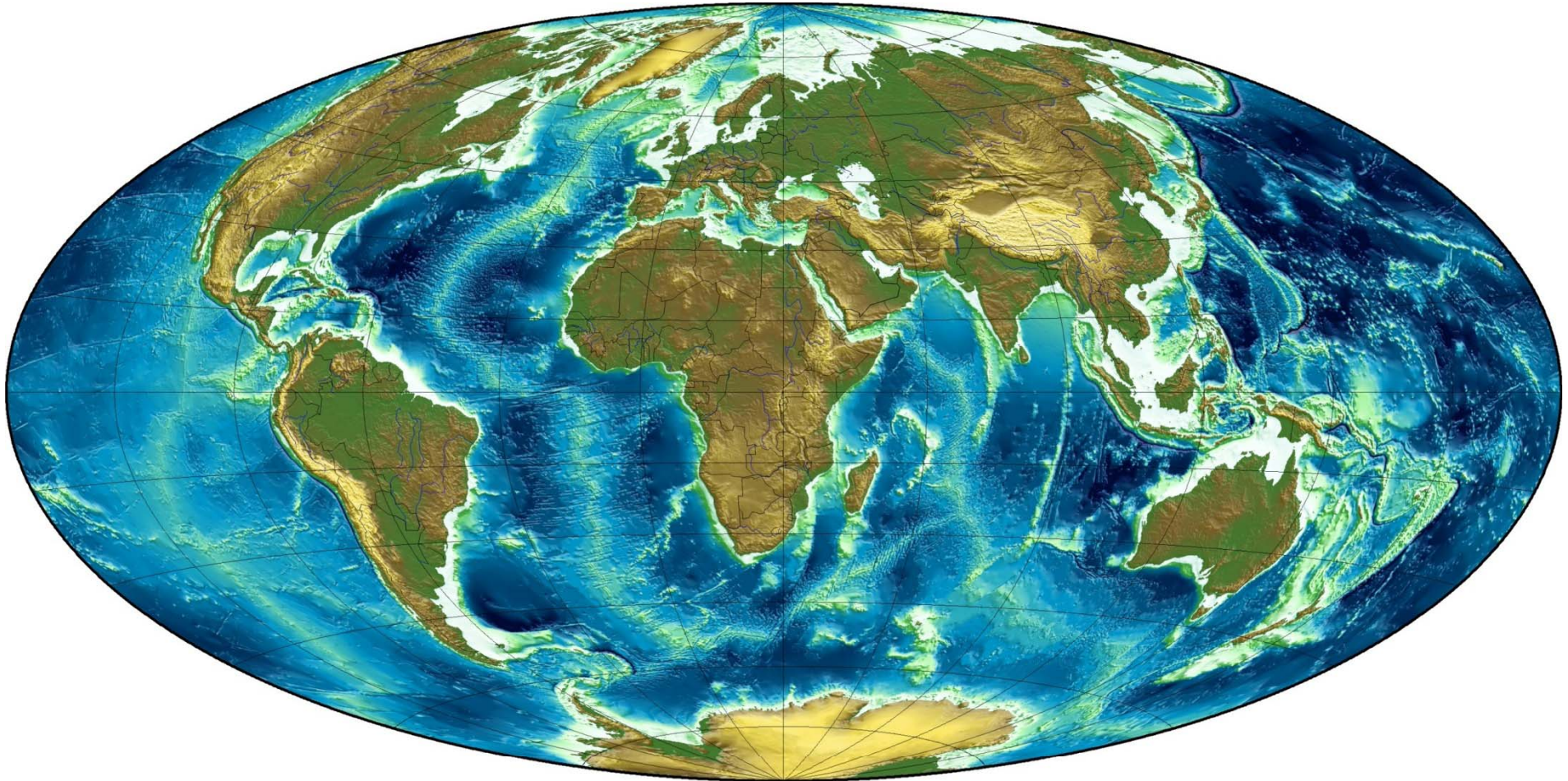


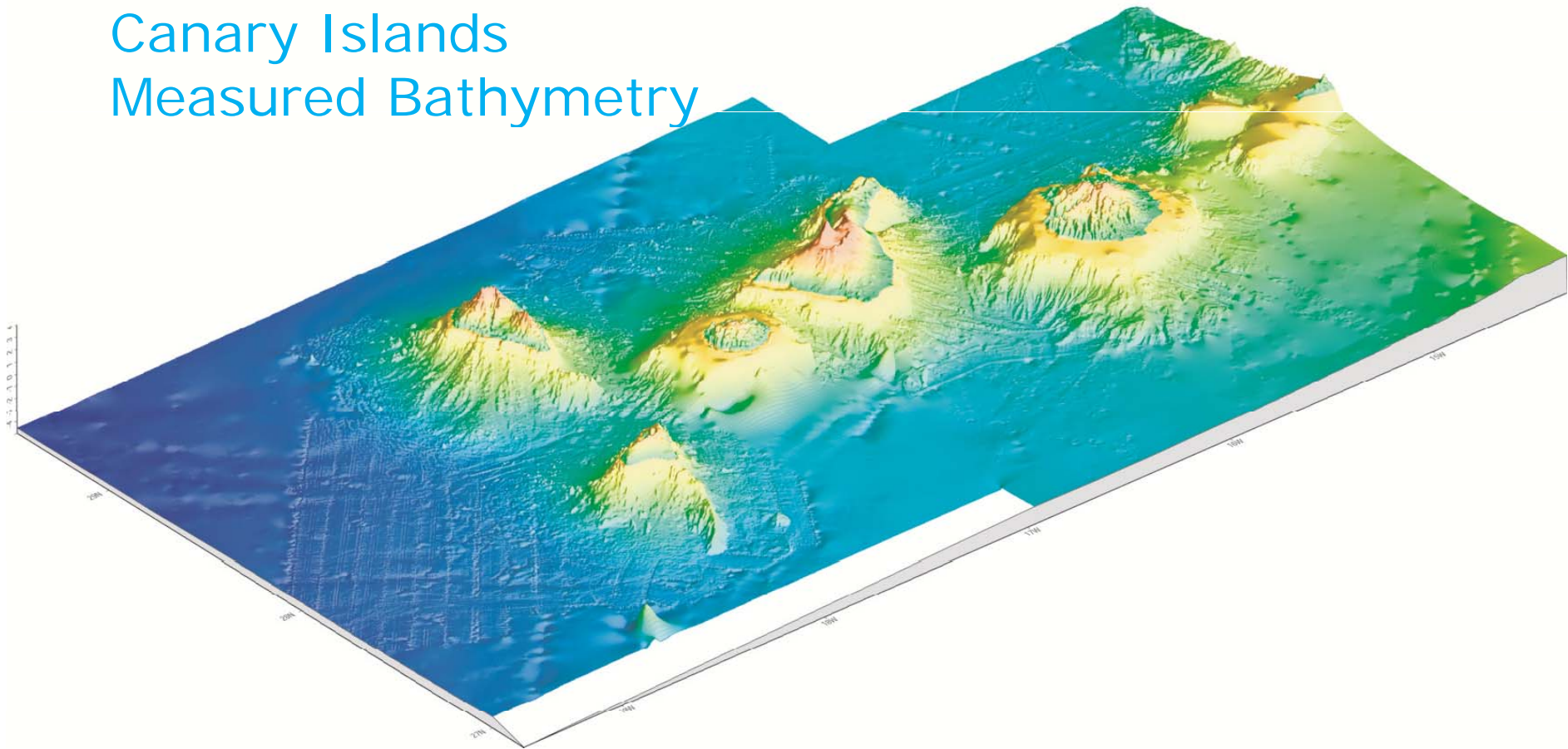
Figure is taken from Watts and Masson 2001

Ocean floor morphology on a global scale



Ocean floor morphology on a regional scale

Canary Islands
Measured Bathymetry



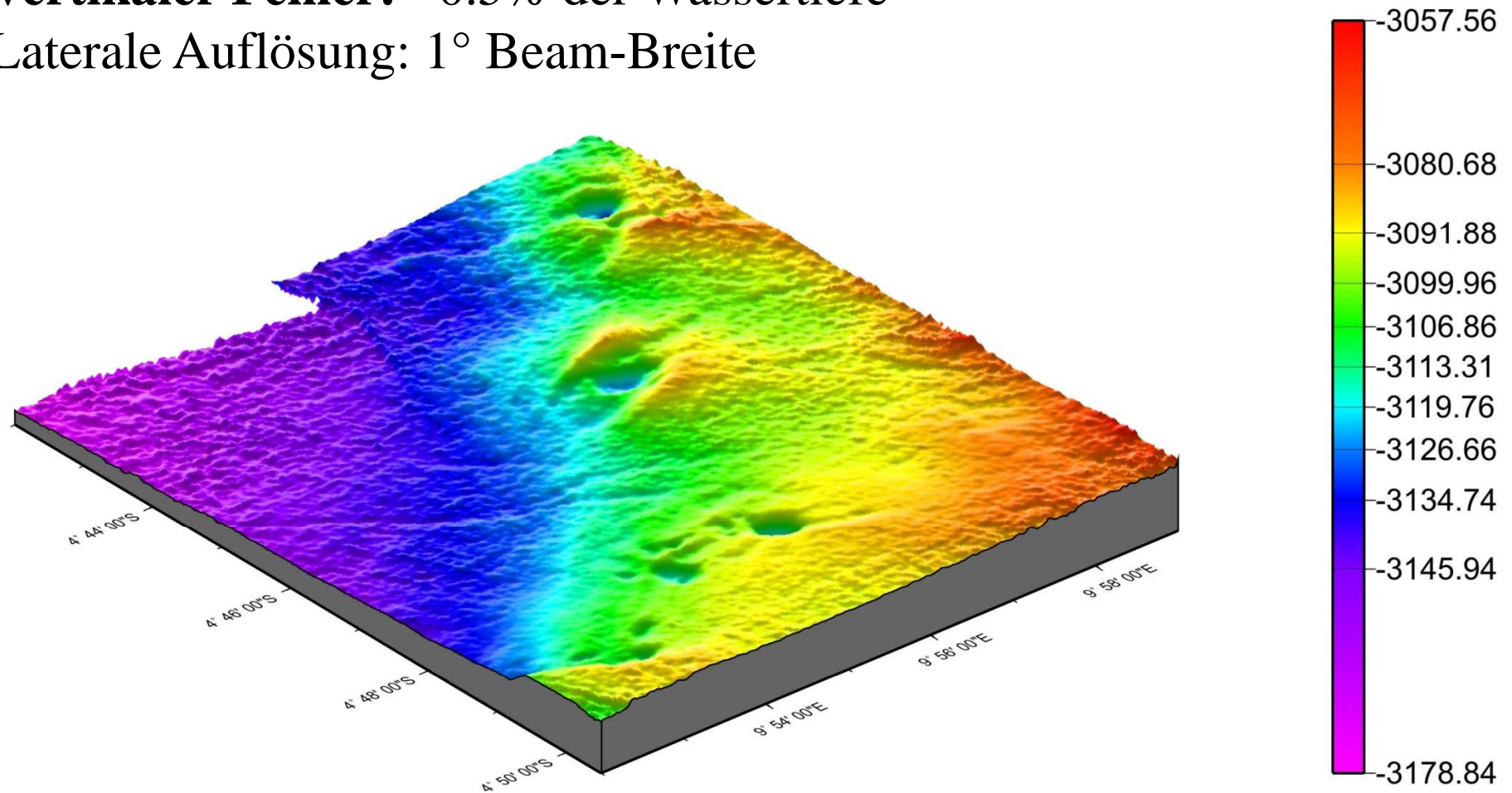
Ocean morphology on a local scale

Frequency Range: 15kHz

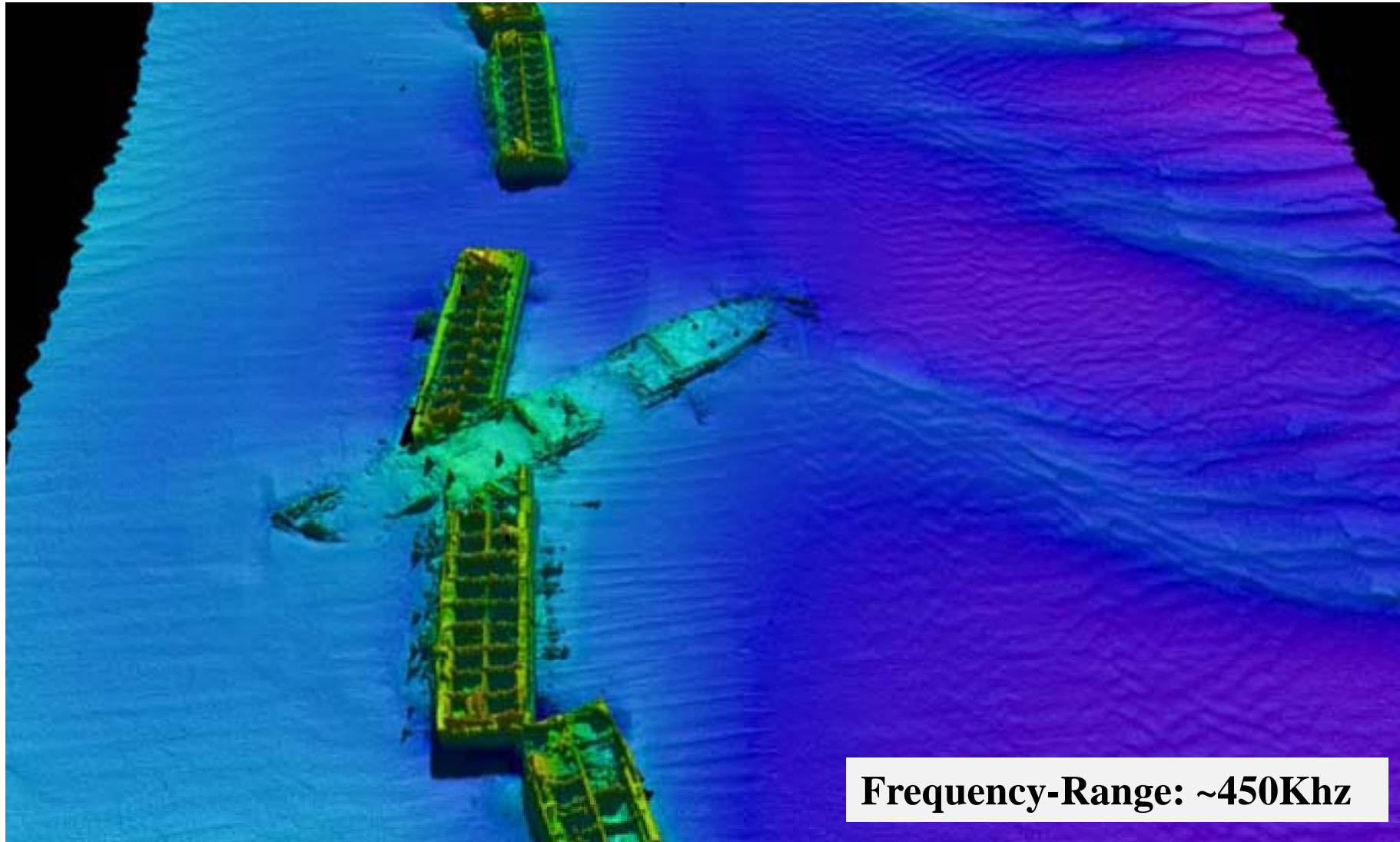
Wavelength: 10cm

Vertikaler Fehler: ~0.5% der Wassertiefe

Laterale Auflösung: 1° Beam-Breite



Micro-Bathymetrie



Mulberry Harbor: Data courtesy: Larry Mayer, University of New Hampshire
Bangkok, 22. – 26.08.11

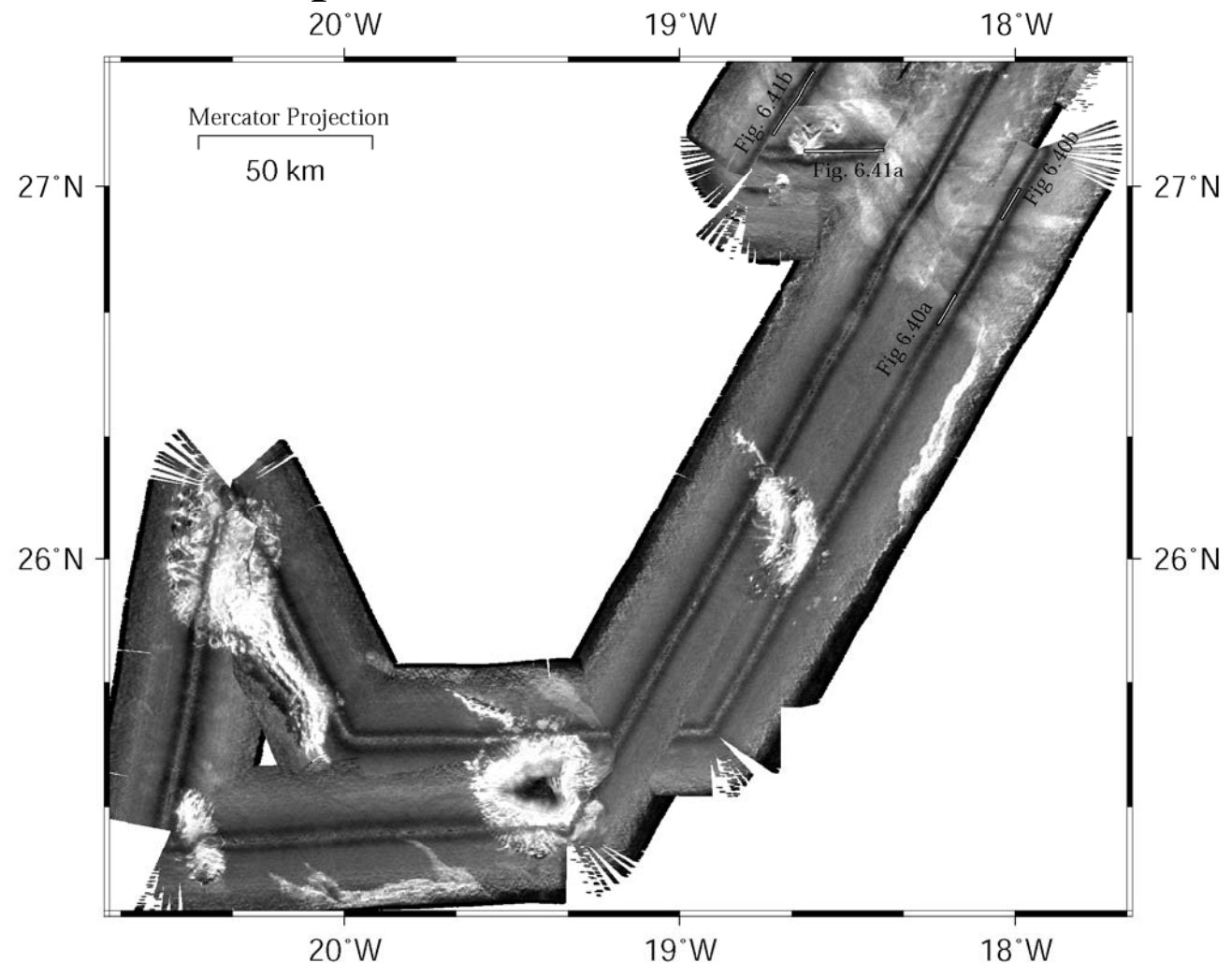
Sidescan Sonar

GLORIA (shallow towed deep water sonar)

Frequency: 7kHz

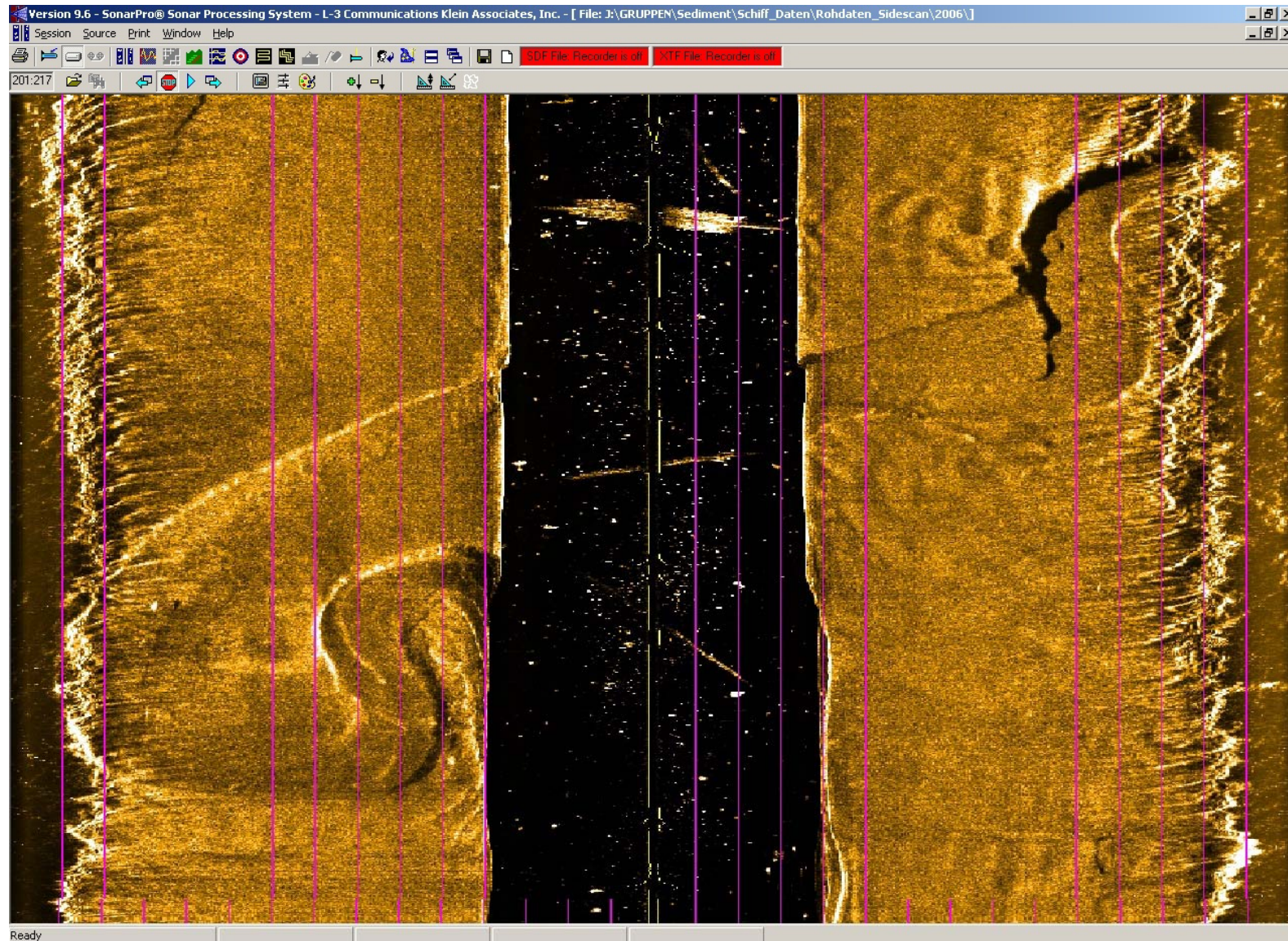
Coverage: 45km

Resolution: ~100m



Bangkok, 22. – 26.08.11

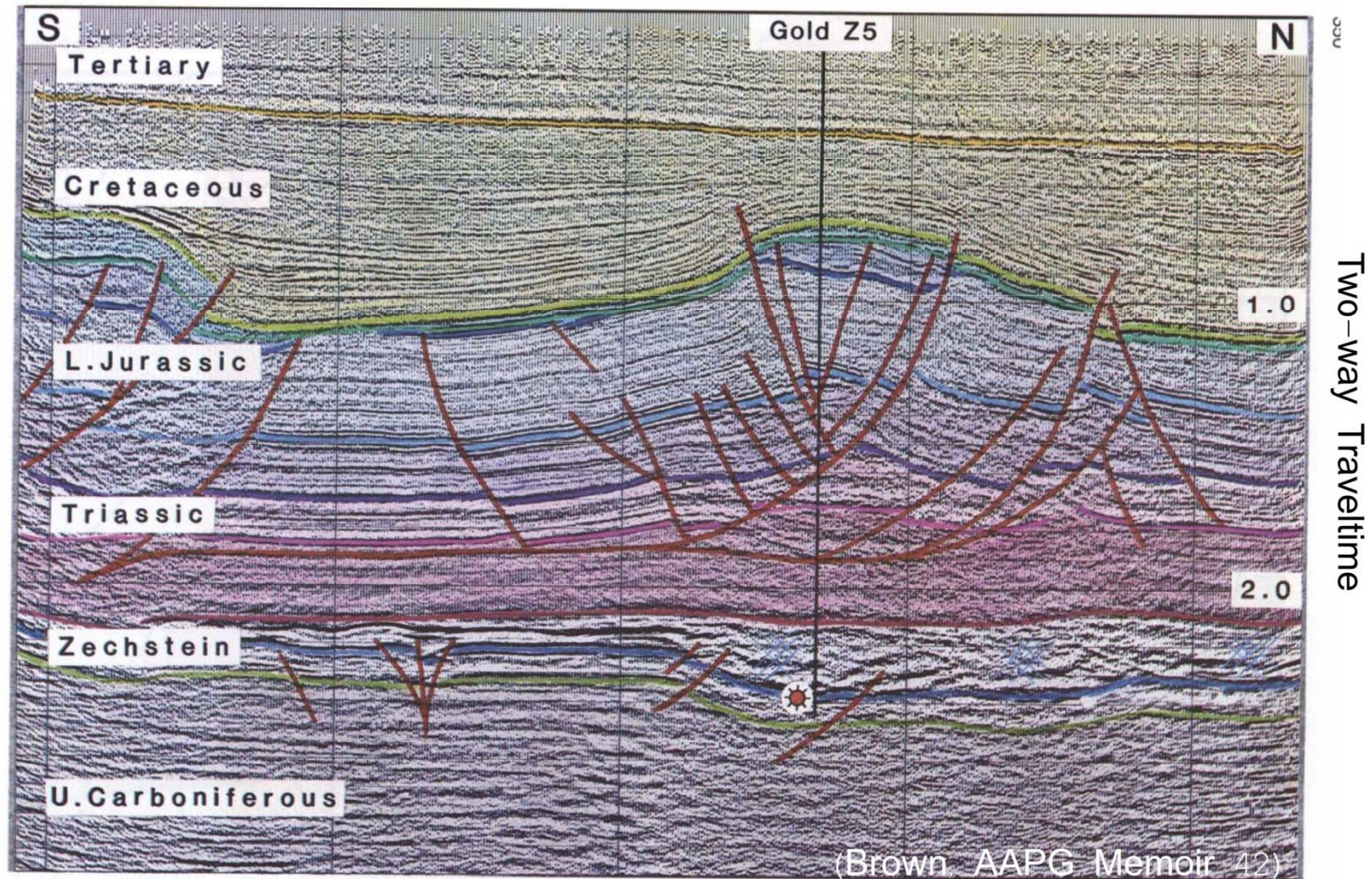
Sidescan Sonar: shallow water sonar, ~500kHz



Courtesy of Martin Wessels (ISF Langenargen)

Bangkok, 22. – 26.08.11

Conventional 2D-Seismics



Conventional 3D-Seismics

Frequency Range:

10 – 100 Hz

Wavelength:

15 – 150 meters

Vertical Resolution:

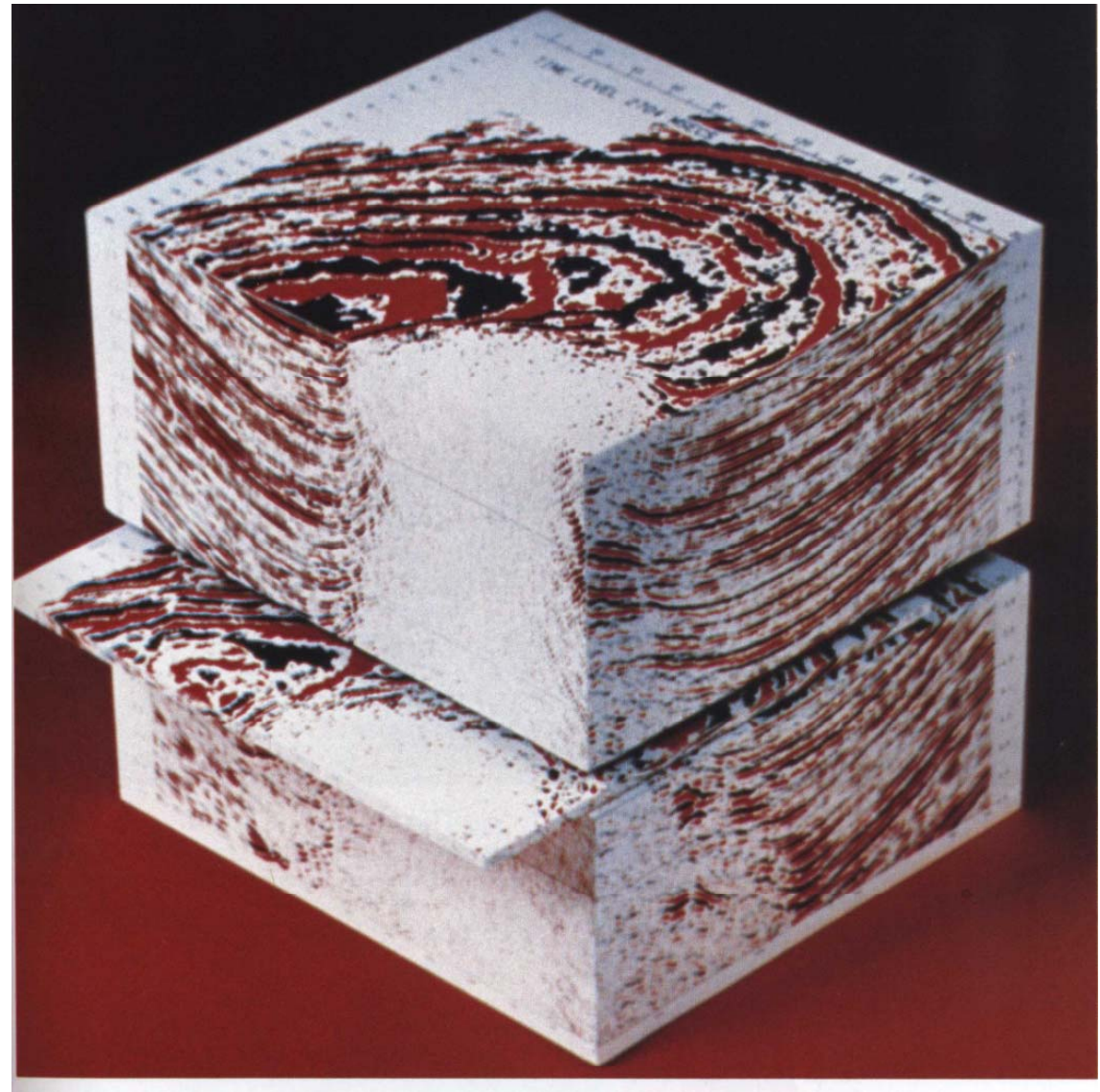
7 – 75 meters

Lateral Resolution:

10 – 20 meters

Penetration:

Up to 10000 meters



3D Seismic Image of a Salt Dome

(Brown, AAPG Memoir 42)

Bangkok, 22. – 26.08.11

High-resolution 2D-Seismic

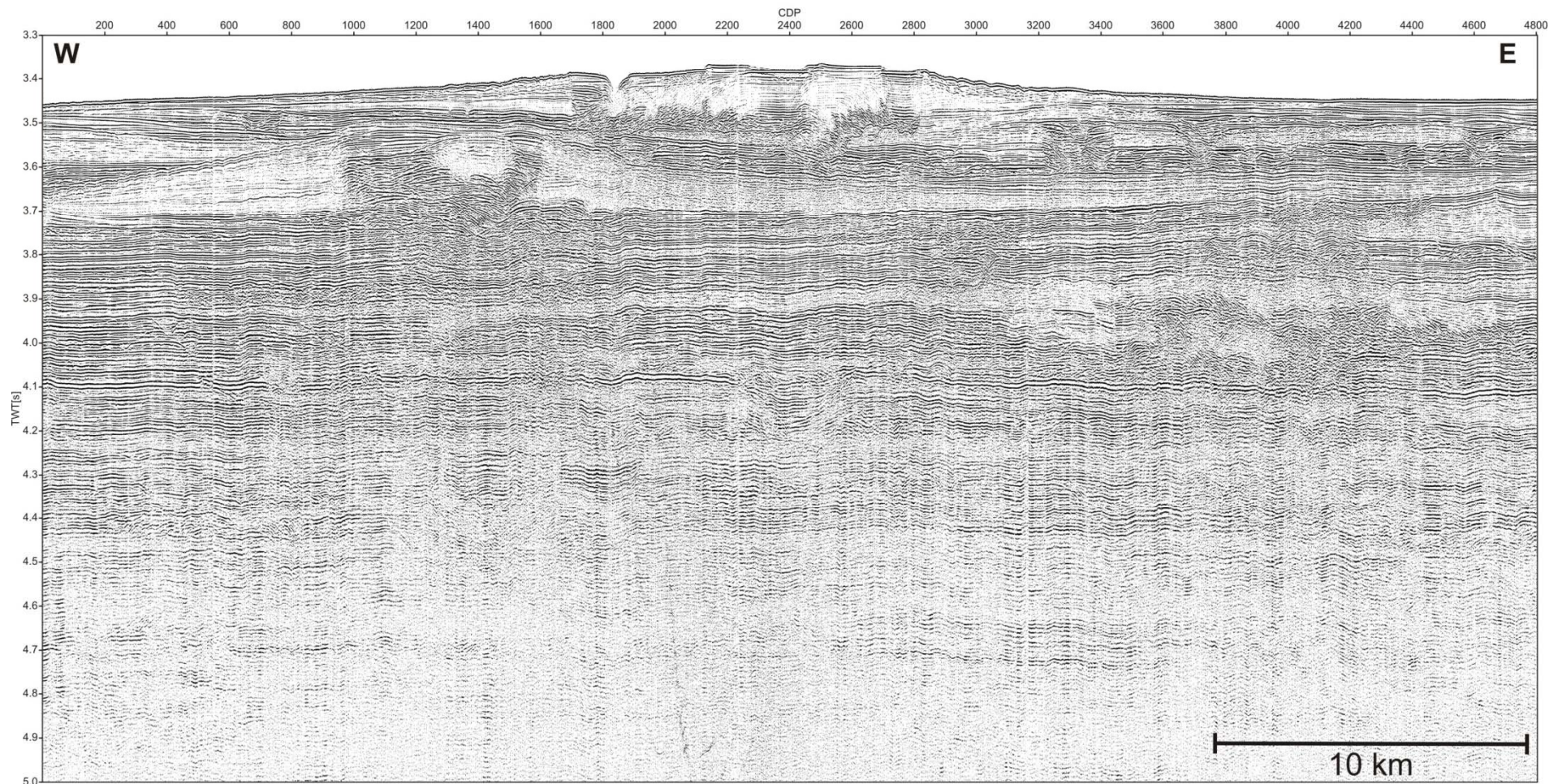
Frequency Range: 100 – 500 Hz

Lateral Resolution: 5 – 10 m.

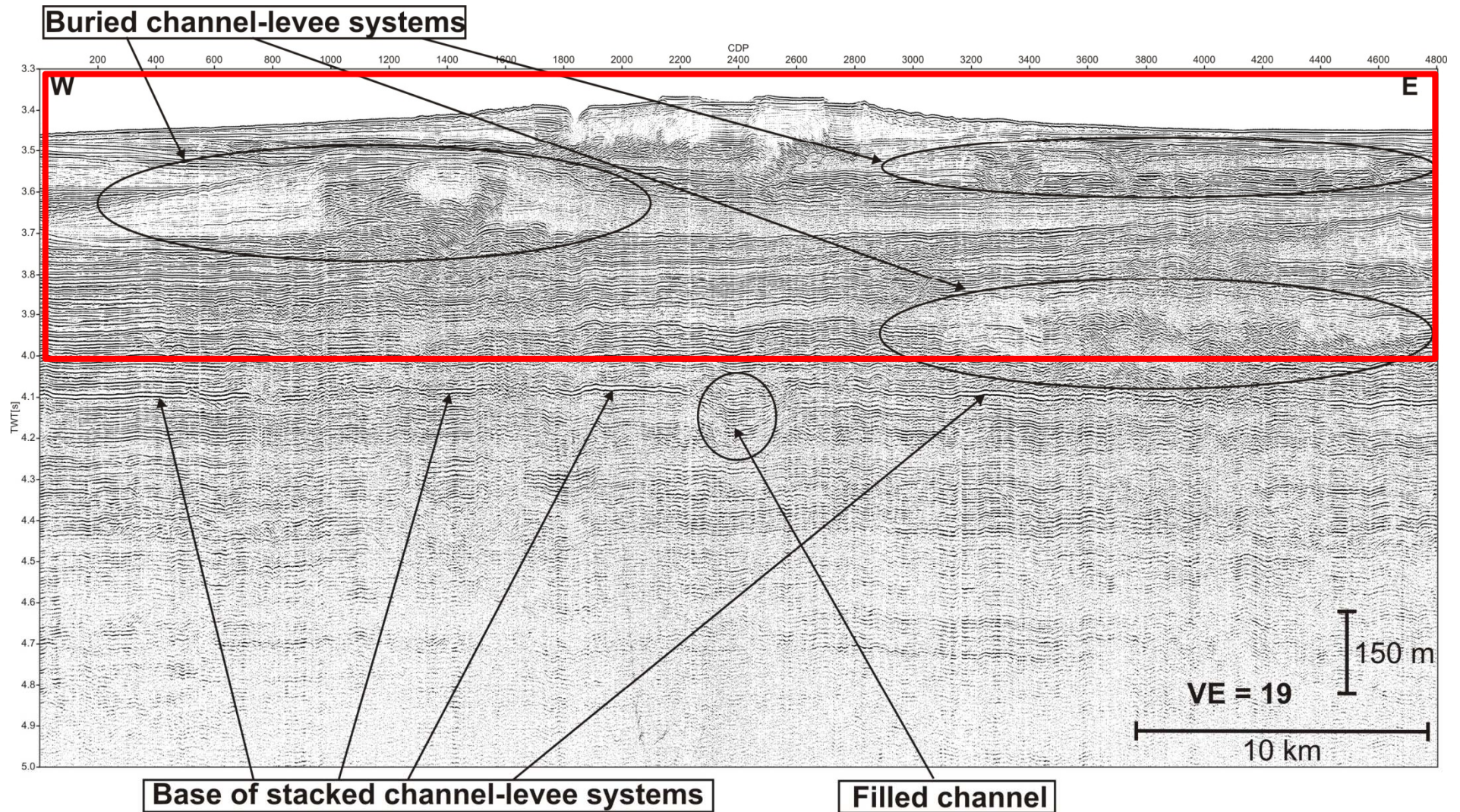
Wavelength: 3 – 15 m.

Penetration: Up to 2000 m.

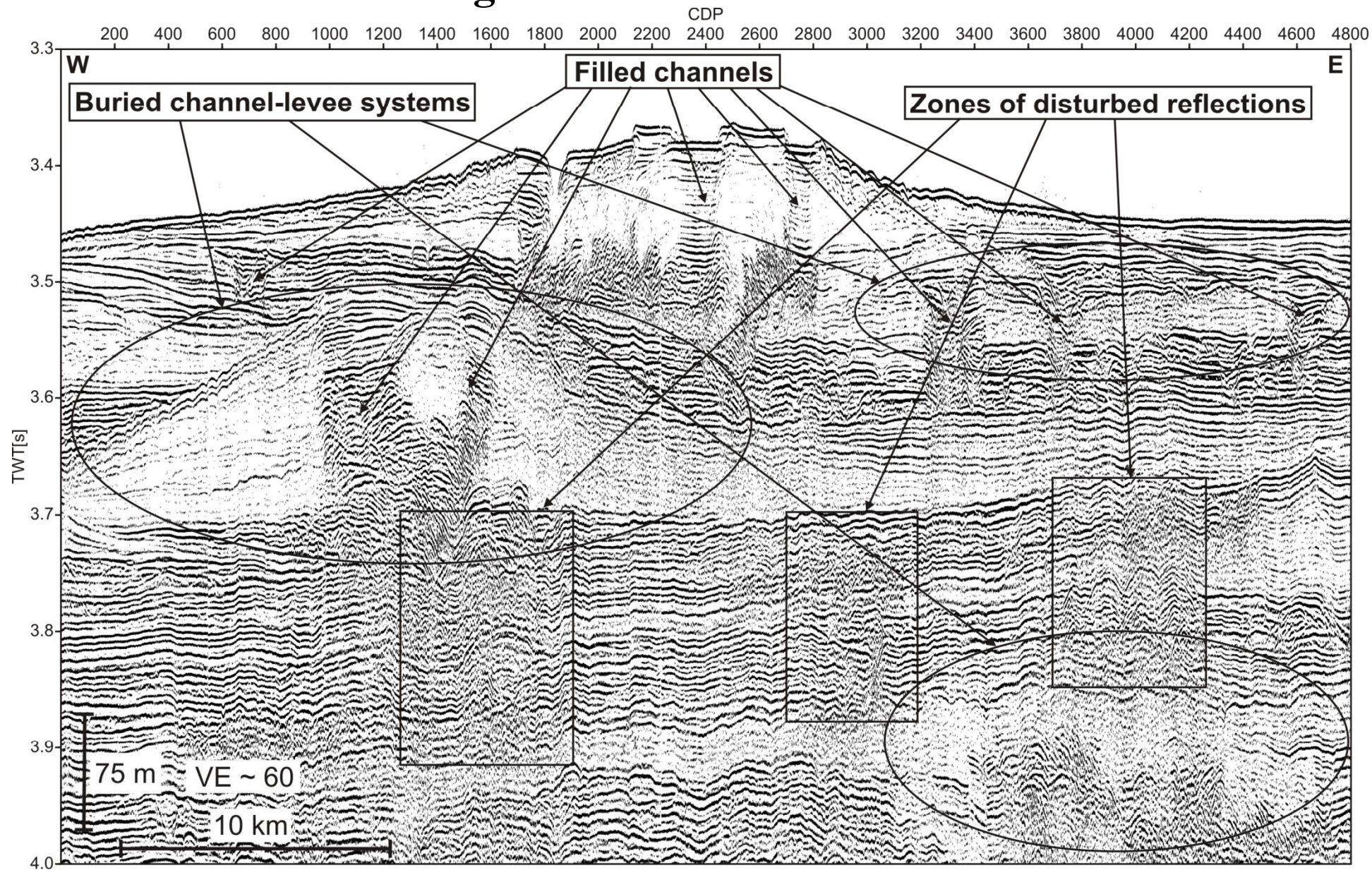
Vertical Resolution: 1 – 7 m.



High-resolution 2D-Seismic



High-resolution 2D-Seismic





future ocean
KIEL MARINE SCIENCES

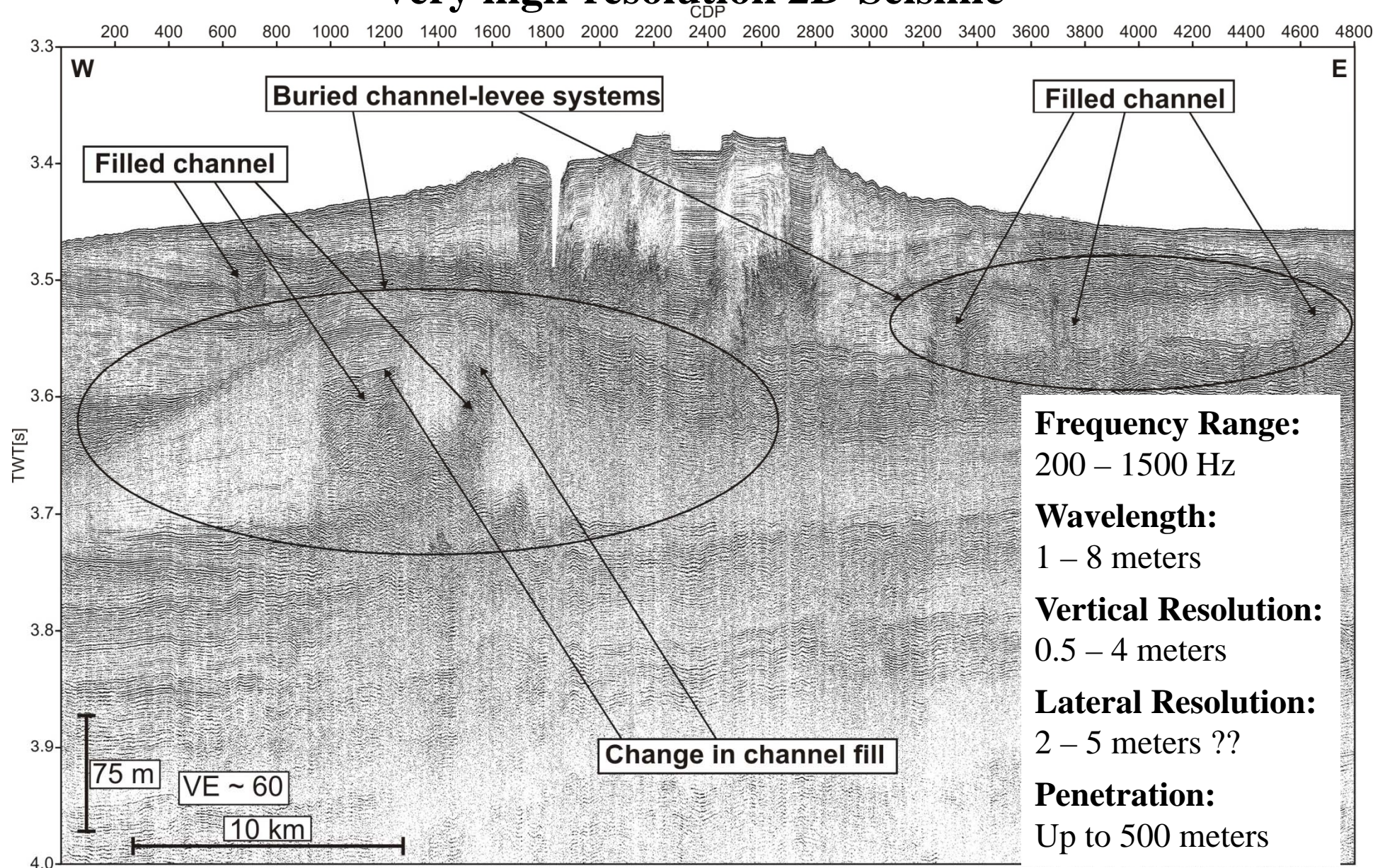
Acoustic Imaging

Introduction

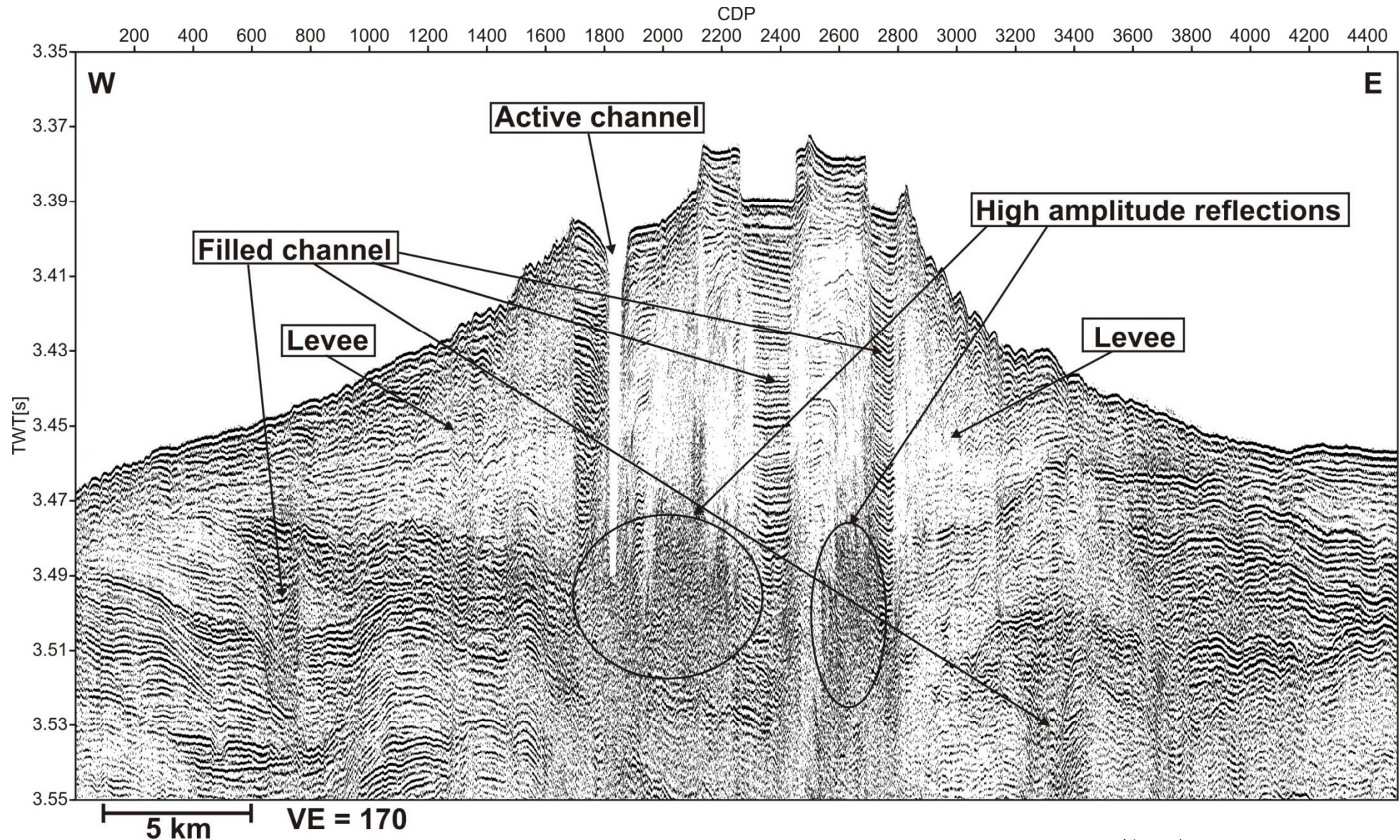


IFM-GEOMAR
Leibniz-Institut für Meereswissenschaften
an der Universität Kiel

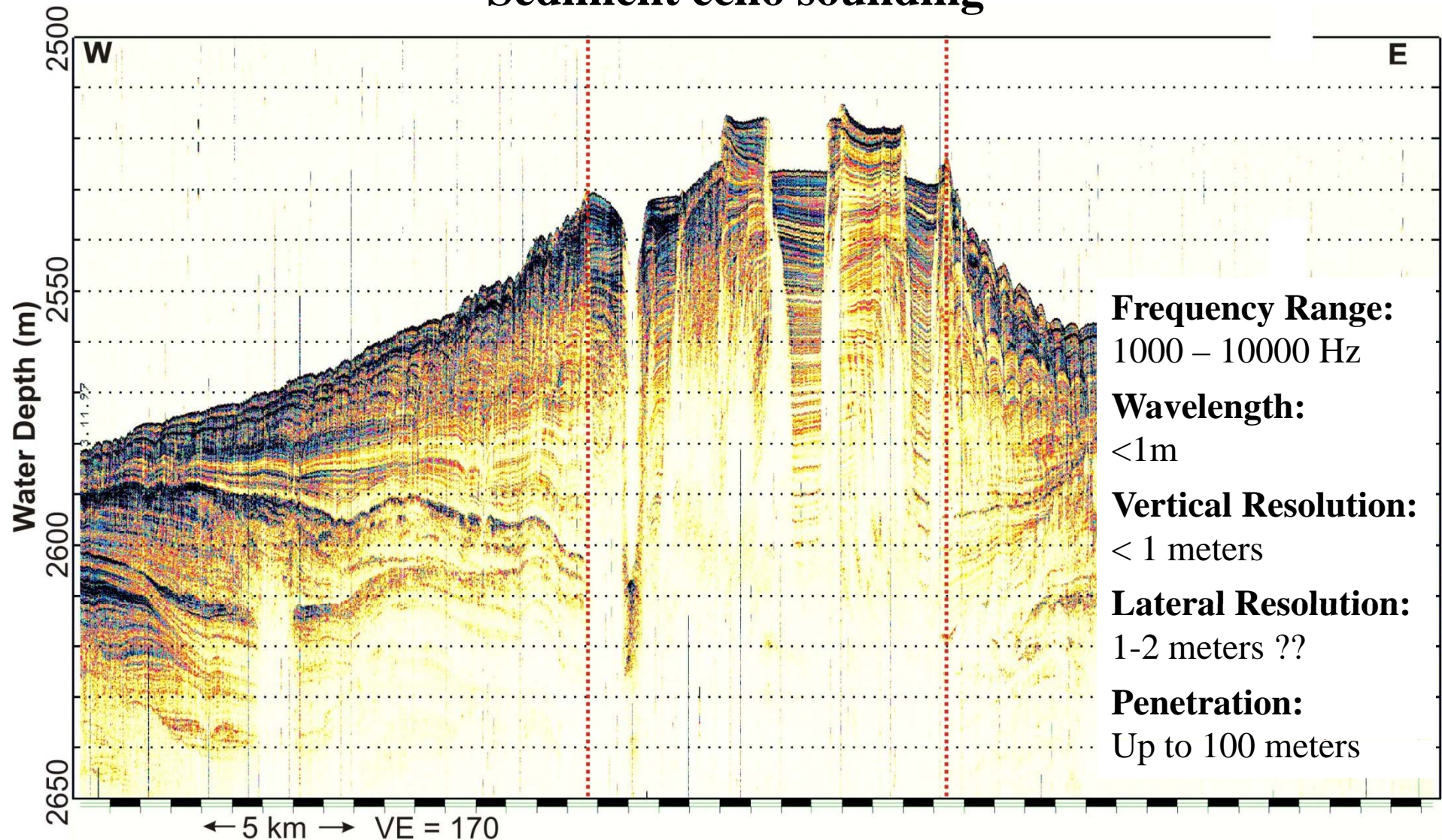
Very high-resolution 2D-Seismic



Very high-resolution 2D-Seismic



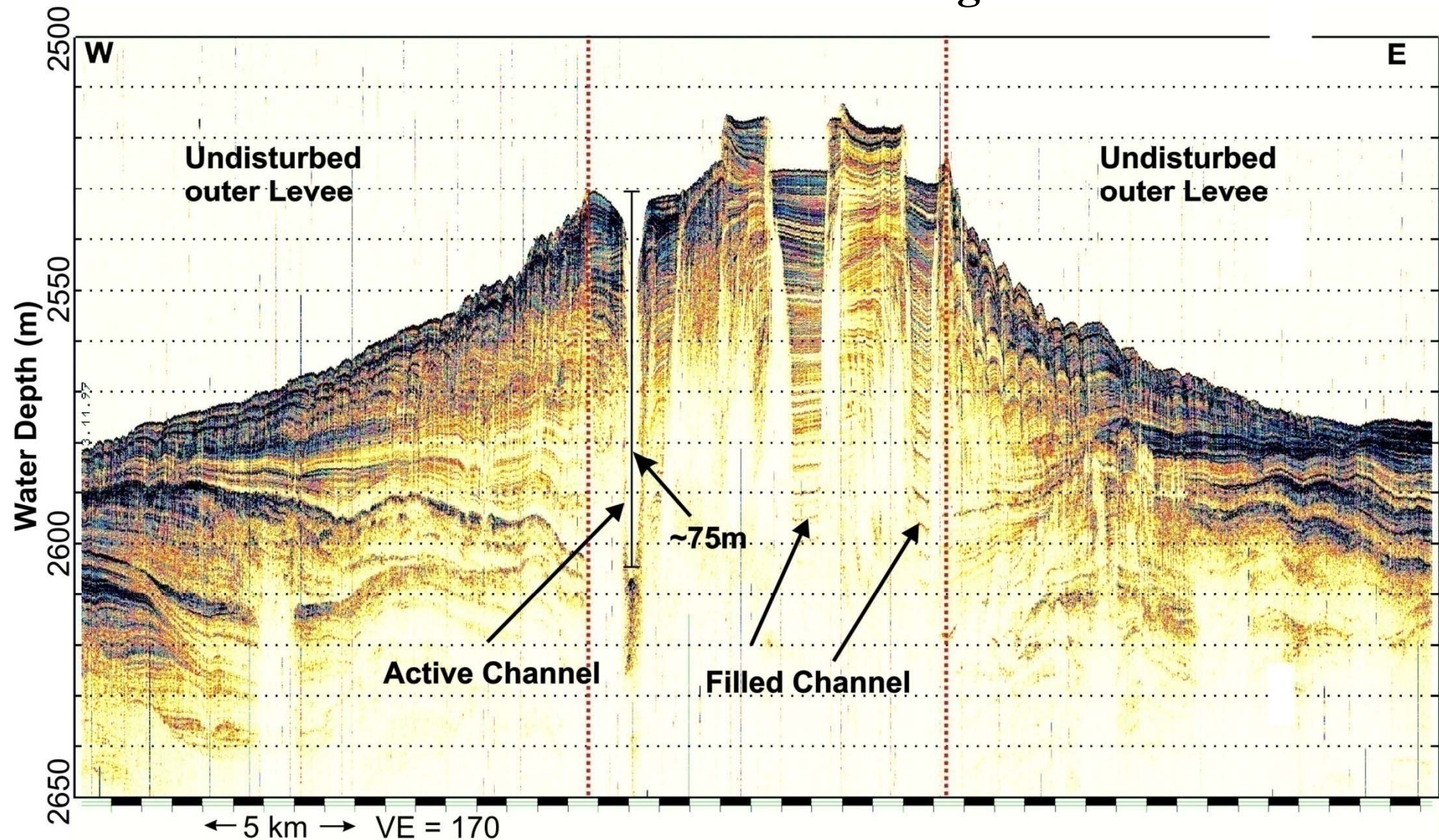
Ultra high-resolution 2D-Seismic Sediment echo sounding



Bangkok, 22. – 26.08.11



Ultra high-resolution 2D-Seismic Sediment echo sounding



Flare Imaging

Frequency Range:

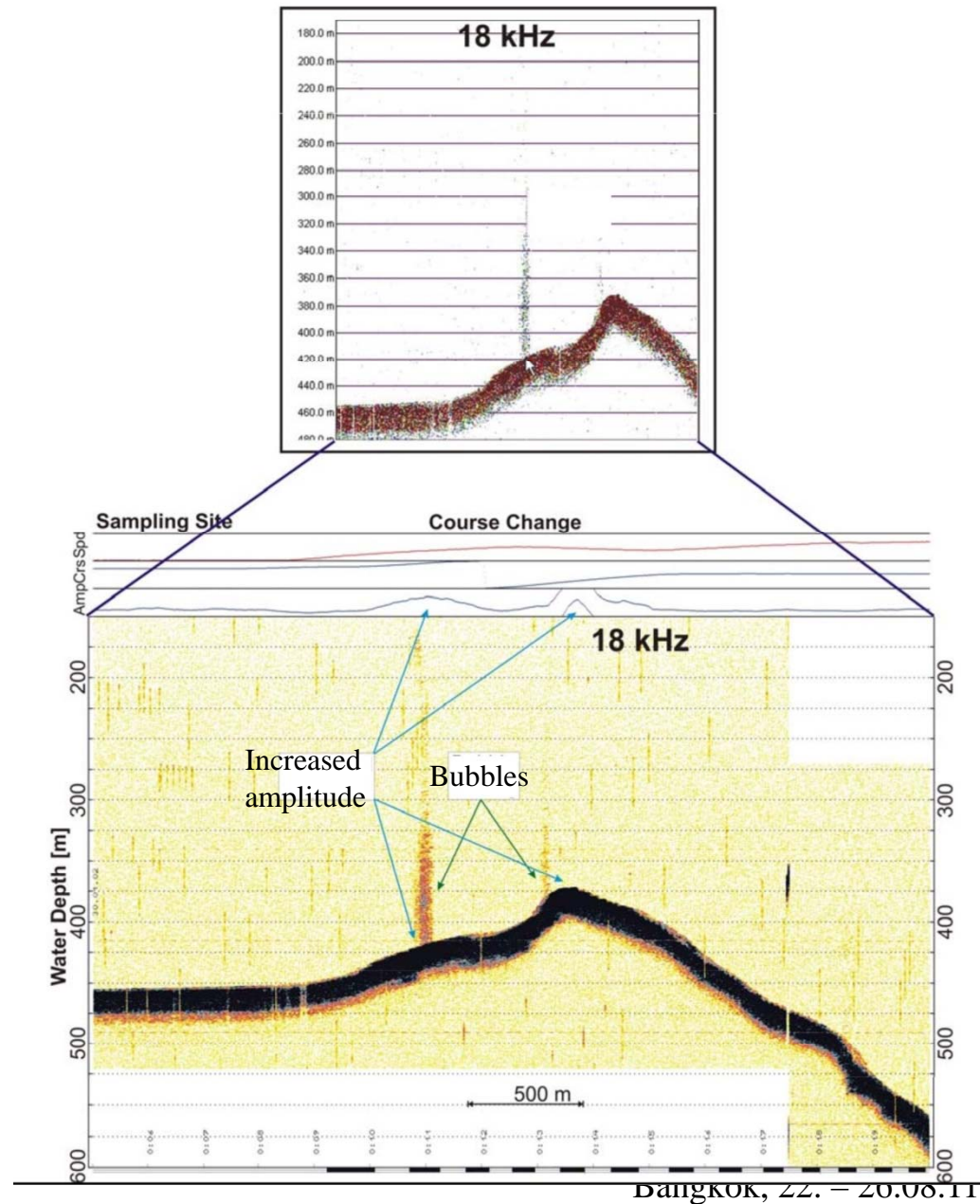
>15kHz

Wavelength:

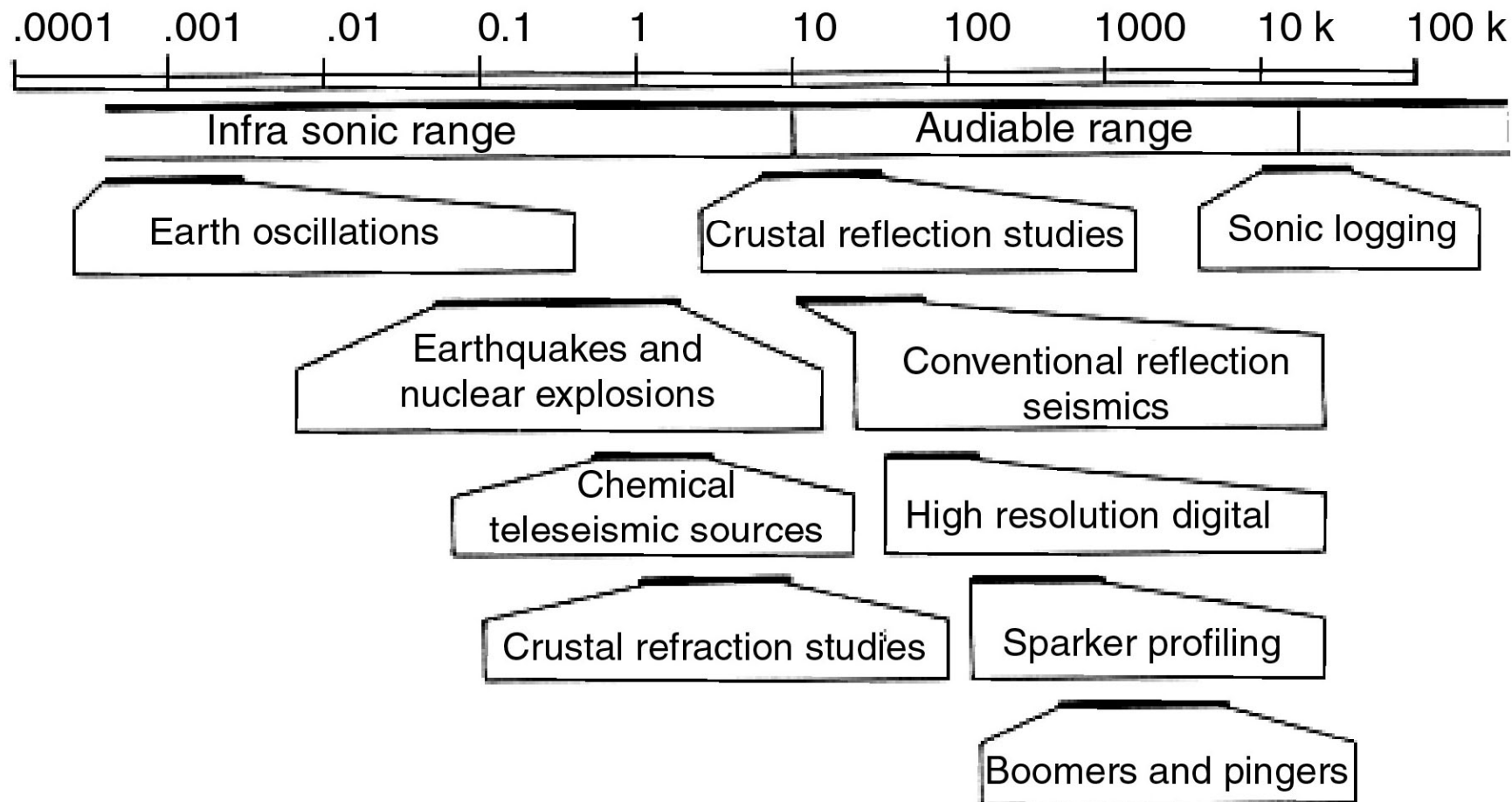
<10cm

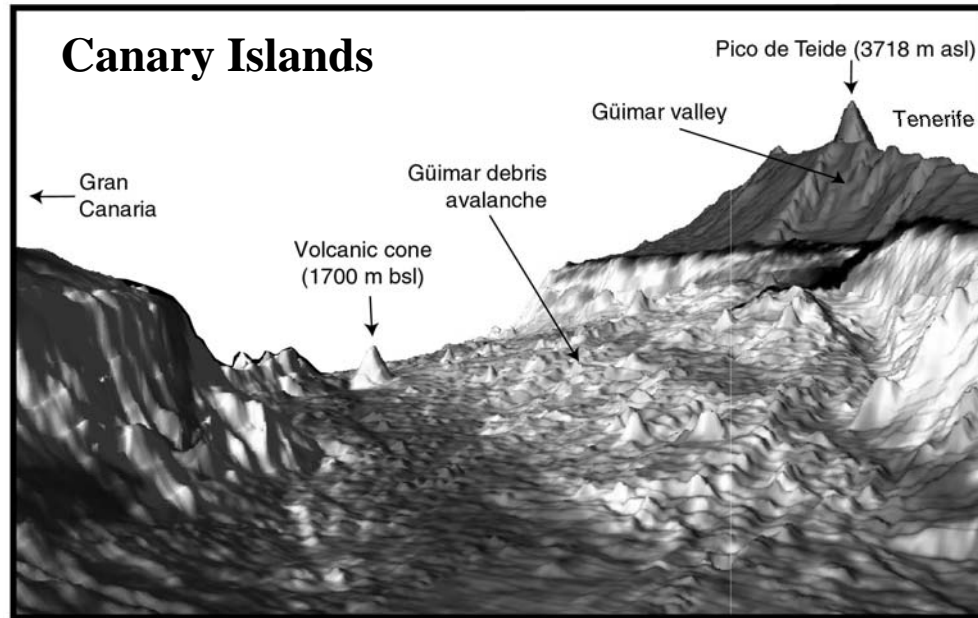
Penetration:

<10m



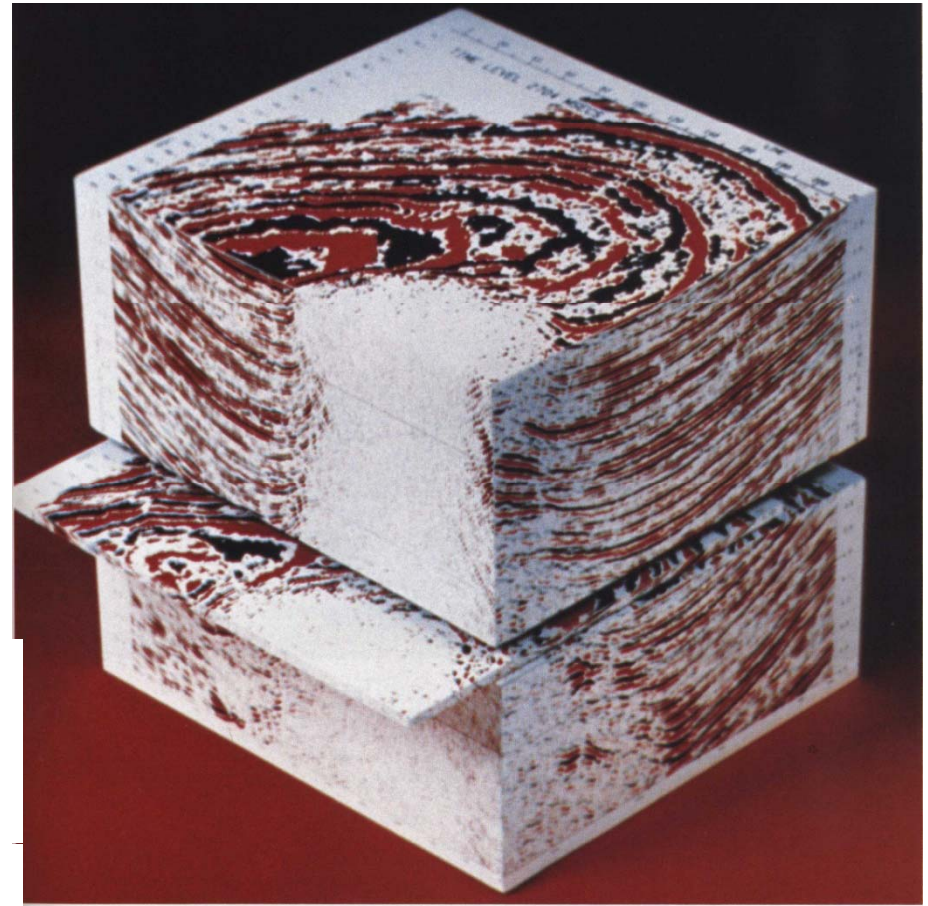
Frequency in Hertz





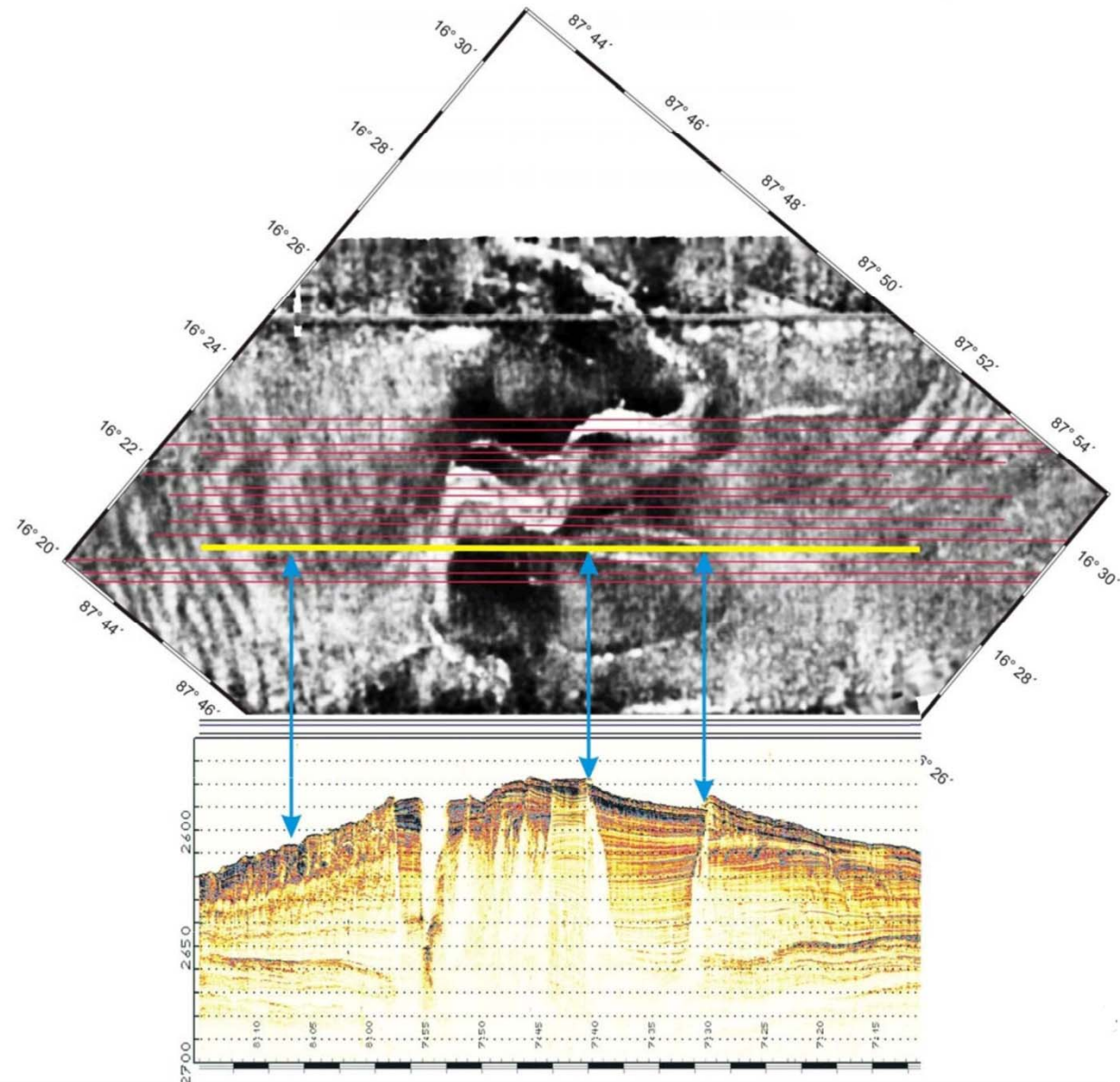
↑ **Acoustic Surficial Mapping:** Swath Bathymetry and Sidescan Sonar Imaging

→ **Seismoacoustic Structural Imaging:** Sediment Echo Sounder, 2D- and 3D Seismics

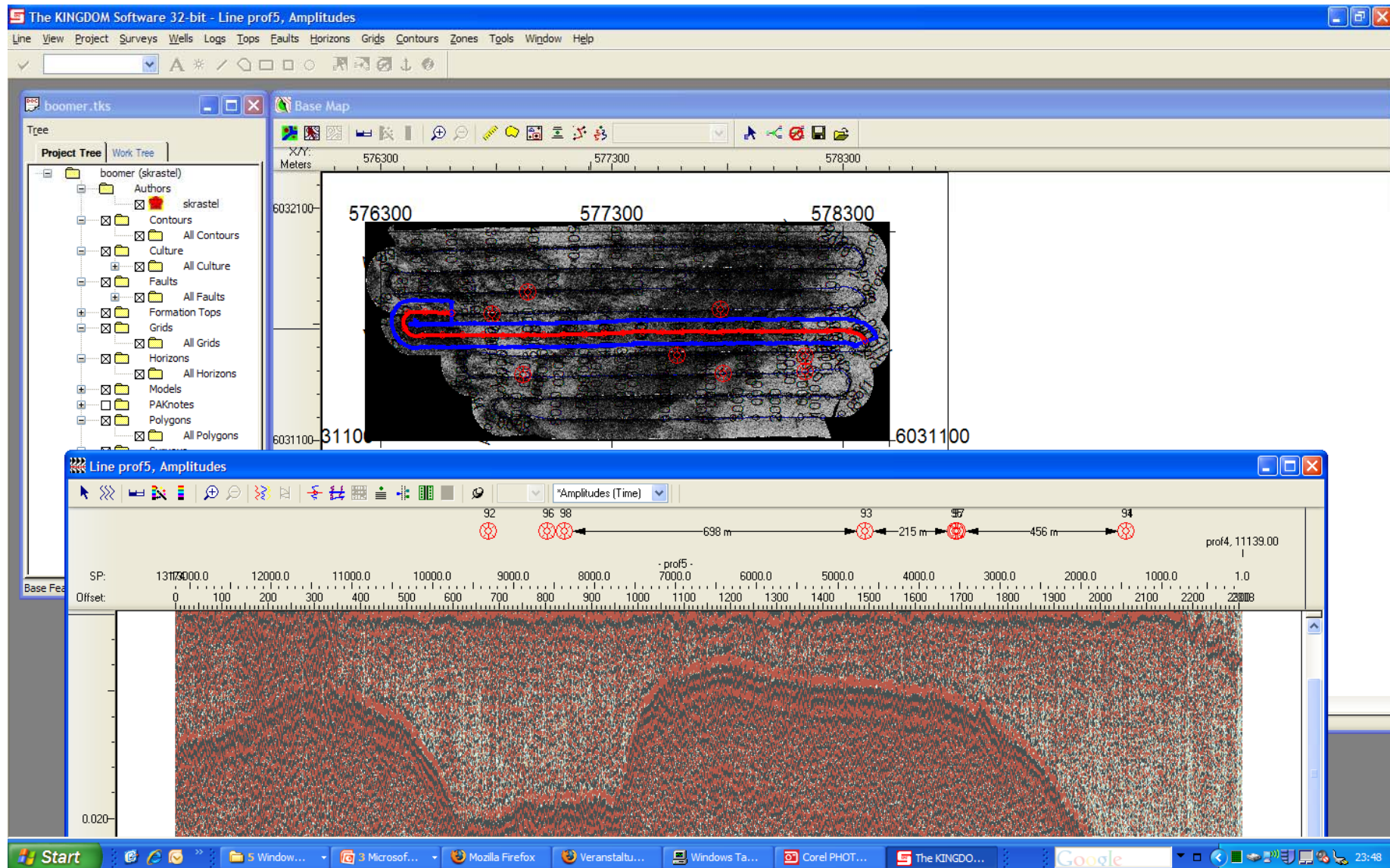


3D Seismic Image of a Salt Dome (Brown, AAPG Memoir 42)

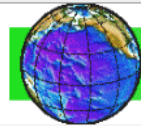
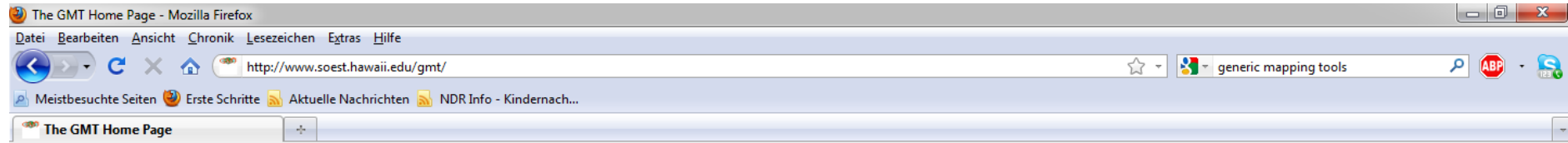
Data Integration



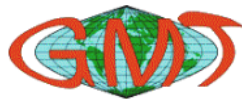
Practical work with data



Map Production using GMT



THE GENERIC MAPPING TOOLS



HOME
EXAMPLES
FAQ
DOWNLOAD
DOCS
MAILINGLISTS
REGISTRATION
MIRRORS
RESOURCES
BUGS
ARRRGHH!
RELEASES

GMT Pages maintained by:
Paul Wessel

Last updated:
March 10, 2011

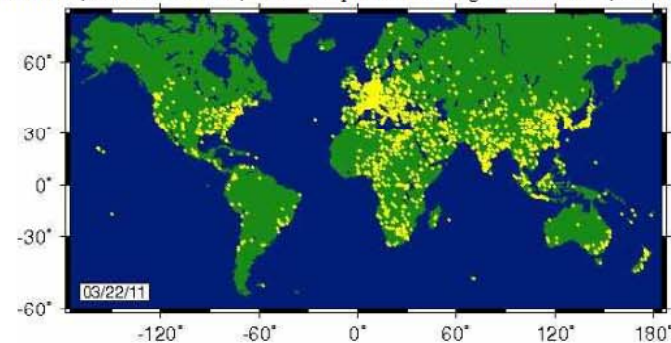


Visit SOEST home page

What is GMT?

GMT is an open source collection of ~60 tools for manipulating geographic and Cartesian data sets (including filtering, trend fitting, gridding, projecting, etc.) and producing Encapsulated PostScript File (EPS) illustrations ranging from simple x-y plots via contour maps to artificially illuminated surfaces and 3-D perspective views. GMT supports ~30 map projections and transformations and comes with support data such as GSHHS coastlines, rivers, and political boundaries. GMT is developed and maintained by [Paul Wessel](#) and [Walter H. F. Smith](#) with help from [a global set of volunteers](#), and is supported by the [National Science Foundation](#). It is released under the [GNU General Public License](#).

Current version is 4.5.6, Released March 10, 2011. For a peek at the next generation GMT 5, see our [GMT 5 pages](#).



GMT is used all over the world. Each yellow dot represent a 15x15 arc minute block with one or more registered user or institution. So far, almost 2000 such blocks have been registered, representing more than 15,000 individual GMT users. To add your dot, fill out the [registration form](#).



SCHOOL OF OCEAN AND EARTH SCIENCE AND TECHNOLOGY
UNIVERSITY OF HAWAII AT MĀNOA


Fertig



IVS 3D Fledermaus Professional but expensive software but free viewer

COMPANY
PRODUCTS
NEWS
SUPPORT
DOWNLOAD

Products > Fledermaus Standard



"3D Visualization - more than just a pretty picture"

Fledermaus Standard is a powerful interactive 3D data visualization system that is used for a variety of applications including environmental impact assessment, mining, geology, and research.

Innovative data exploration features including the ShiftScape™ rendering engine and the Bat (3D input device), allow for intuitive 3D exploration of geo-spatial data.

A wide variety of industry standard formats are supported for direct import of data to the 3D scene. Object types such as digital terrain maps, point clouds, lines, polygons, satellite imagery, etc. can all be loaded and analyzed in a single scene. Due to its flexible object oriented software design, Fledermaus can be easily tailored to support many additional visualization modules.

If you would like more information on Fledermaus, the [full documentation](#) is available online. A free viewer for Fledermaus files named [iView3D](#) is also available.

Product Links:

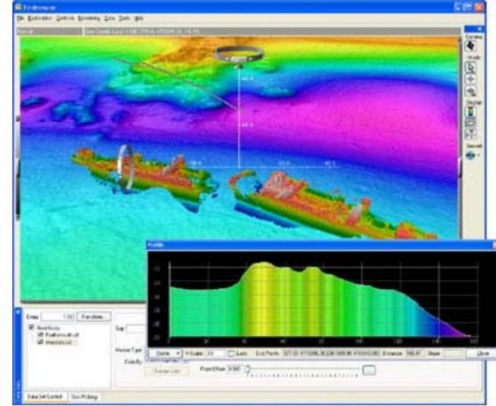
- Fledermaus Standard
- Fledermaus Professional
- iView3D

Application Links:

- Geological Surveys
- Hydrographic Survey QC
- Offshore Industry
- Academic Research
- Environmental Applications
- Military Applications
- Large Immersive Visualization Centers
- Marine Construction
- Coastal Zone Mapping
- Google Earth

Related Links:

- Evaluate Fledermaus Applications Technologies
- Purchase Information
- Academic Discounts
- Platforms Overview
- Standard vs. Pro
- Hardware Requirements
- Scientific Data Formats Supported

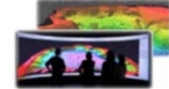


Screenshot of Fledermaus Standard

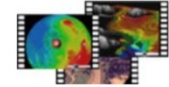
Features

- Display scales automatically from high-end to low-end systems using the powerful ShiftScape™ rendering engine.
- Multiple data sets and types of different resolution can be visualized and interactively explored at the same time.
- Integrated support for very large data sets.
- All data sets can be geo-referenced in the 3D scene.
- Users can interactively query data sets to select coordinates for profiles and measurements.
- Advanced object oriented architecture allows easy integration of new data types into the system.
- Explorations can be recorded and used to create movies of data exploration sessions.
- Visualizations can be displayed in 3D stereo with suitable graphics hardware.
- Software and data files can be used across wide variety of computer platforms from laptops to large immersive visualization systems.

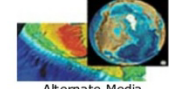
Images



Movies



Alternate Media





future ocean
KIEL MARINE SCIENCES

Acoustic Imaging

Introduction

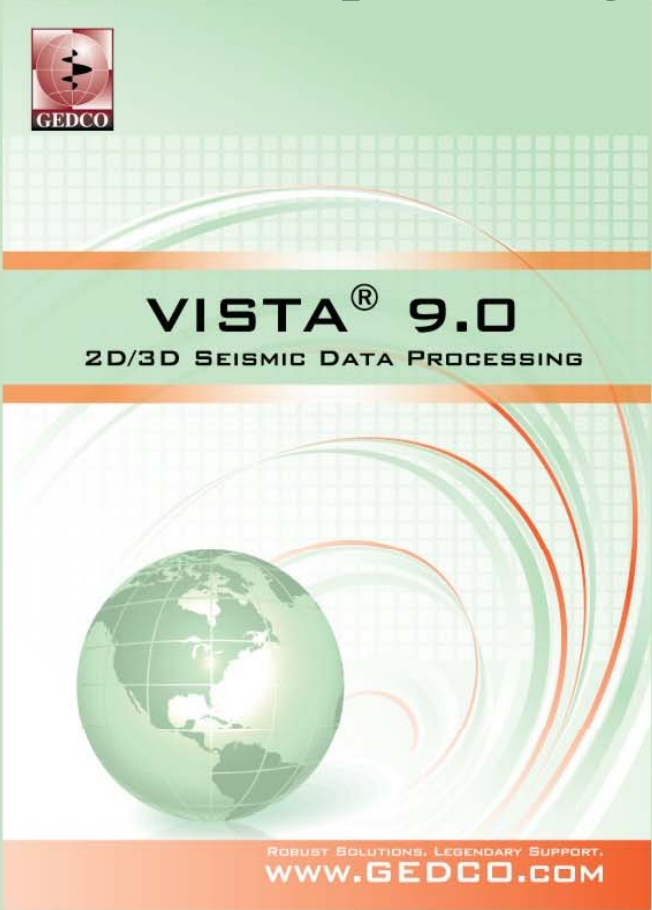



IFM-GEOMAR
Leibniz-Institut für Meereswissenschaften
an der Universität Kiel

VISTA 2D/3D Version: 9.000.377M(64-Bit) Project:

File Edit Project Dictionary Interactive Statics Velocity VSP Job Flow Utilities License Font Window Help

Seismic data processing



VISTA® 9.0
2D/3D SEISMIC DATA PROCESSING

ROBUST SOLUTIONS, LEGENDARY SUPPORT.
WWW.GEDCO.COM

Bangkok, 22. – 26.08.11



future ocean

Acoustic Imaging

Introduction

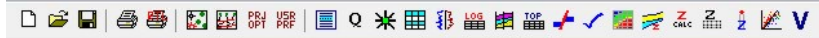


IFM-GEOMAR

Leibniz-Institut für Meereswissenschaften

The KINGDOM Software 32-bit - Base Map

Map View Project Surveys Culture Wells Logs Tops Faults Horizons Grids Contours Zones Tools Window Help



Maps



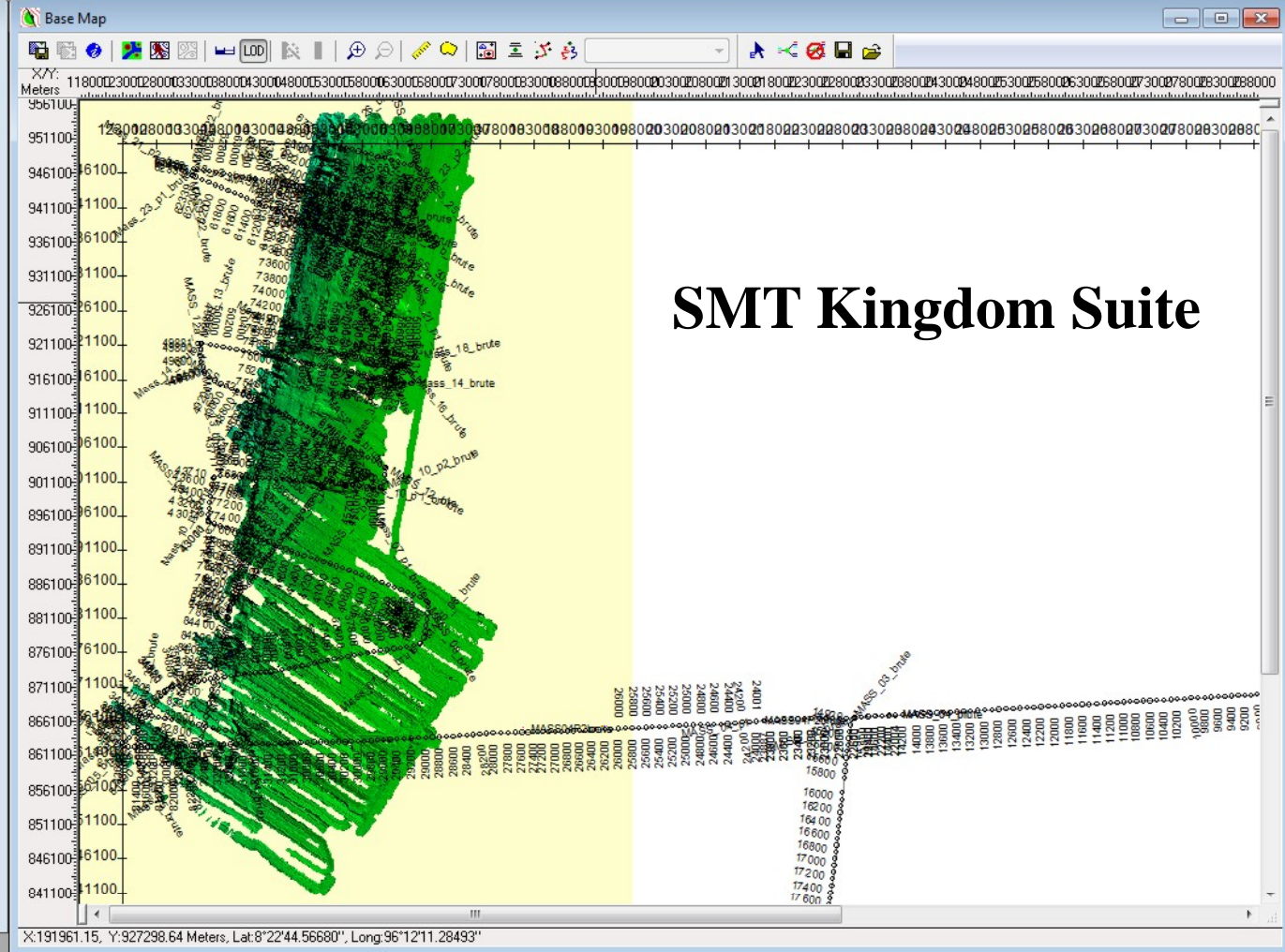
brute_kingdom.tks

Tree

Project Tree Work Tree

- brute_kingdom (Ship)
 - Authors
 - Ship
 - Contours
 - All Contours
 - Culture
 - All Culture
 - bathy
 - gebco
 - Rulers
 - Faults
 - All Faults
 - Unassigned (Ship)
 - Formation Tops
 - Grids
 - All Grids
 - Horizons
 - All Horizons
 - Models
 - All Models
 - PAKnotes
 - Polygons
 - All Polygons
 - Surveys
 - All Surveys
 - MASS04P2brute
 - MASS_01_brute
 - MASS_02_brute
 - MASS_02_p1_brute
 - MASS_02_p2_brute
 - MASS_02_p3_brute
 - MASS_02_p4_brute
 - MASS_02_p5_brute
 - MASS_02_p6_brute
 - MASS_03_brute
 - MASS_03_p1_brute
 - MASS_03_p2_brute

Base Feature: 2d/3dPAK-EarthPAK



Bangkok, 22. – 26.08.11



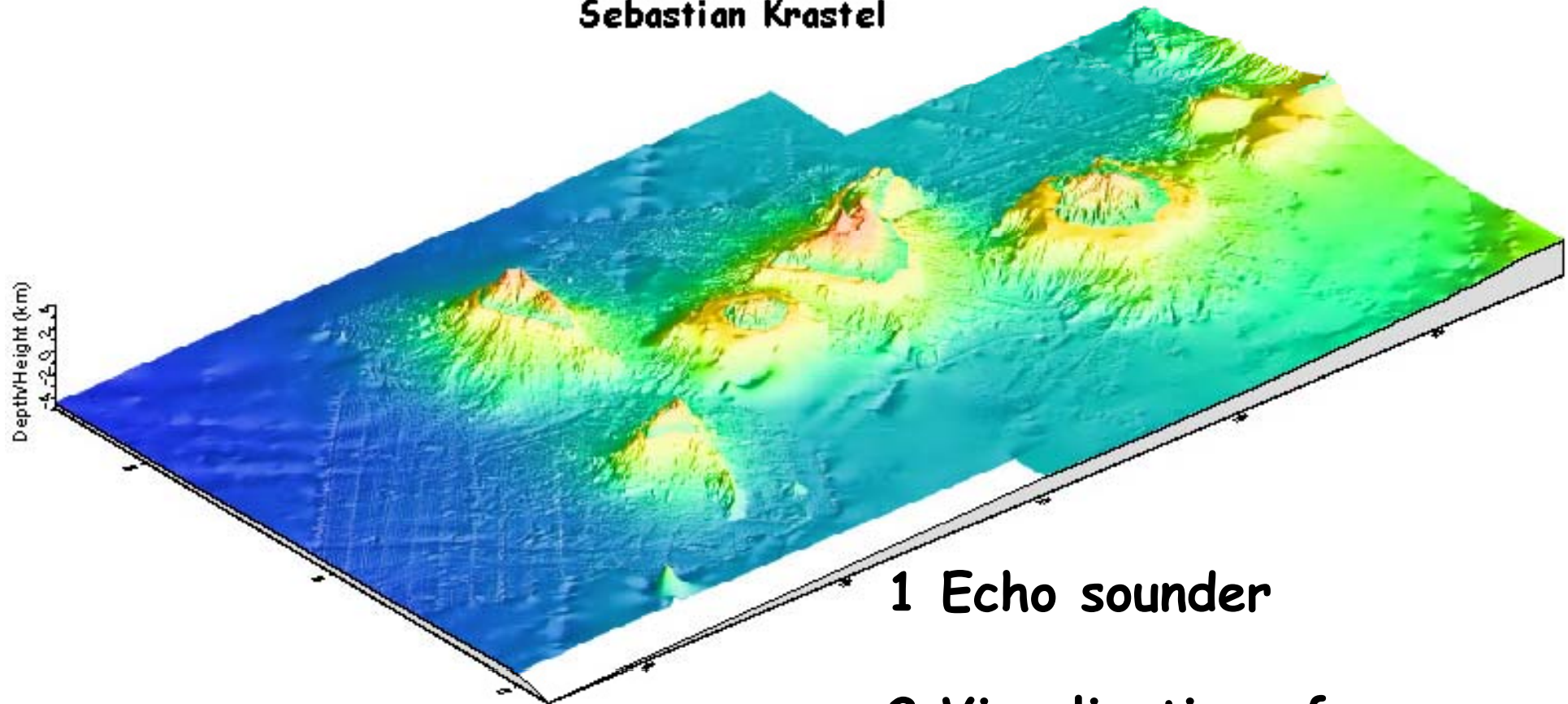
future ocean
KIEL MARINE SCIENCES

Acoustic Imaging

Bathymetry

Bathymetric Measurements at Sea

Sebastian Krastel

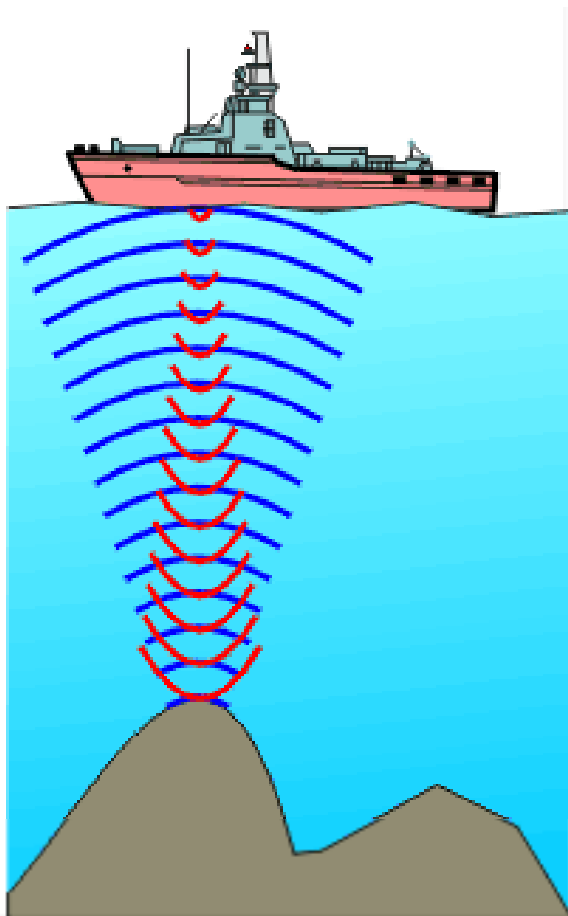


1 Echo sounder

2 Visualization of
bathymetric data

1 Echo sounders

Single-Beam echo sounder



$$2 * \text{water depth} = v_{\text{water}} * t$$

$$V_{\text{water}} \sim 1.5 \text{ km/s}$$

$$\text{depth (km)} = 1.5/2 * t = 3/4 * t \quad (t \text{ in seconds})$$

Typical frequencies:

10 – 300 kHz

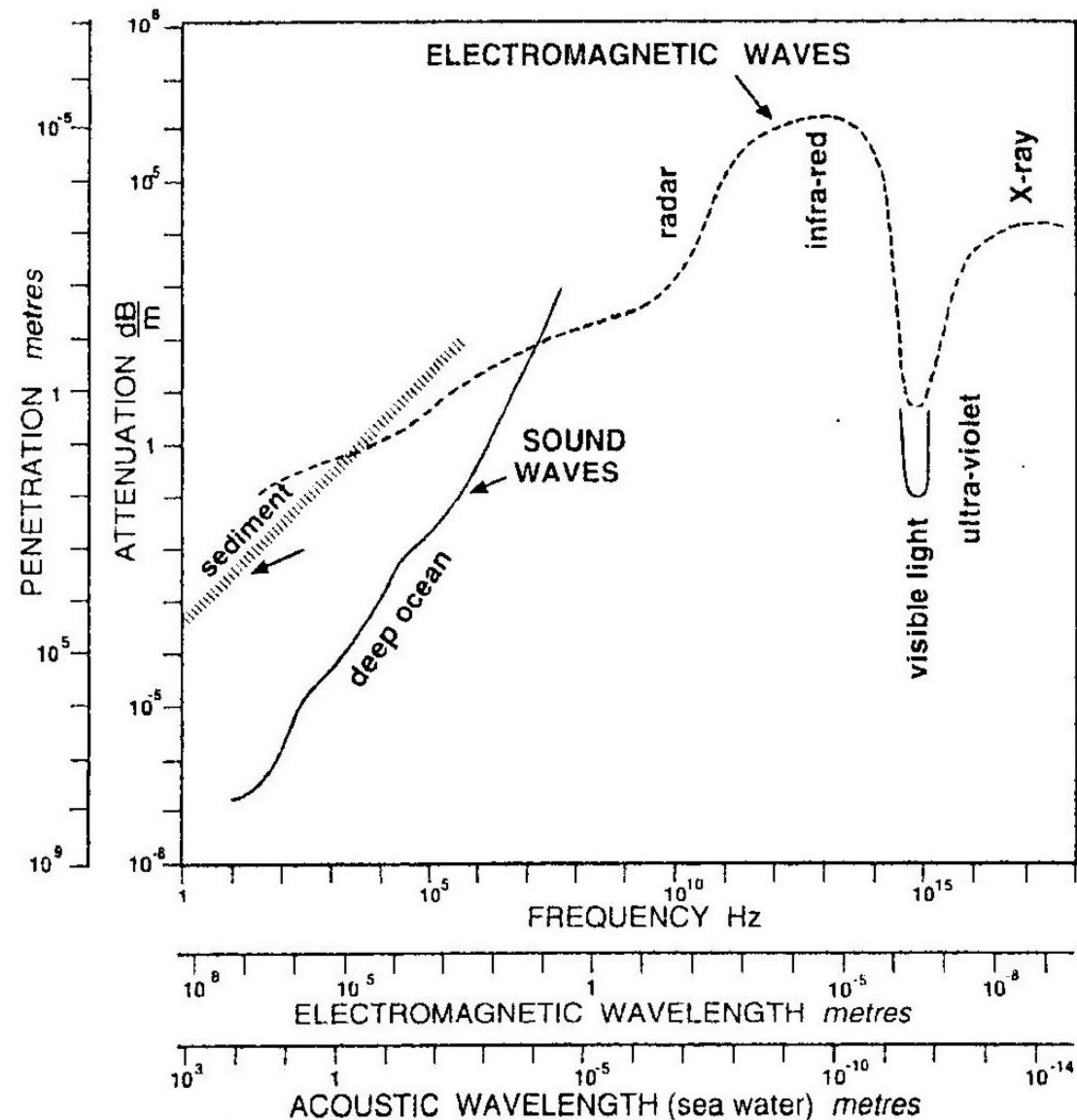
Velocity = wave length x frequency

⇒ Wave length: 3-15 cm

Attenuation in water Wasser:

300 kHz = 73 dB/km

12 kHz = 1 dB/km



Attenuation of electromagnetic and sound waves in seawater (after Wille, 1986).

What opening angle should we use?

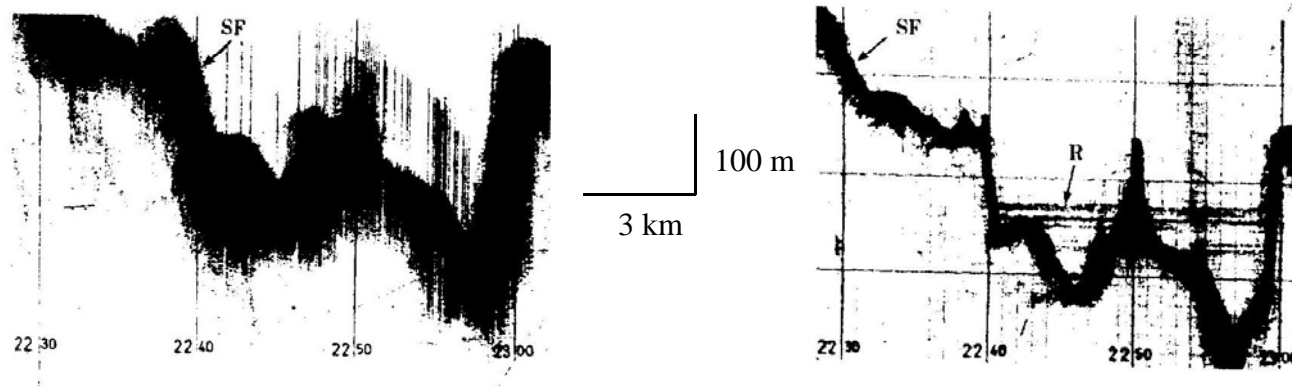
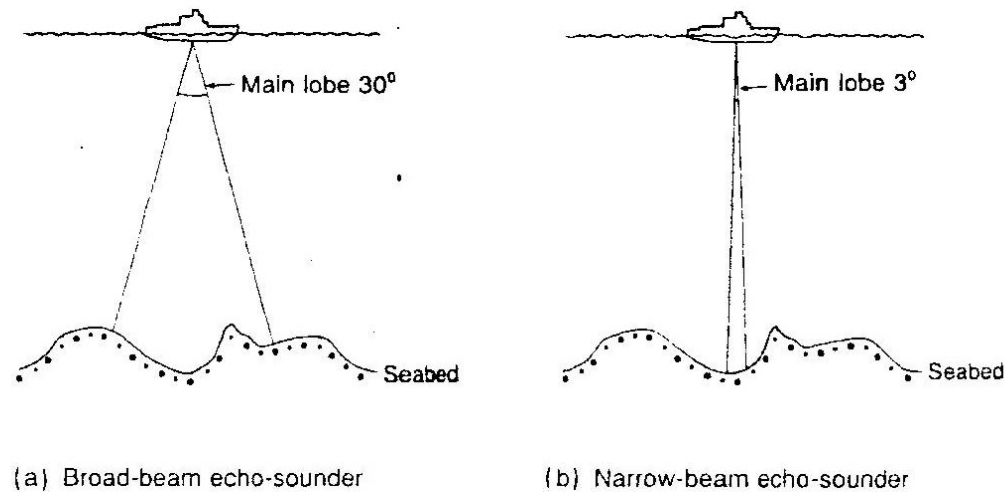


Figure 3.9 (a) and (b) Beam patterns of narrow- and wide-beam echo-sounder transducers. (c) and (d) Echo-sounder profiles recorded simultaneously across Atlantis II Deep in the central Red Sea: (c) wide beam (30° , 18 kHz); (d) stabilized narrow beam (1.3° , 30 kHz). The deepest sounding is 3800 m. The narrow-beam transducer provides far higher acoustic definition of the sea floor (SF) and reveals a reflecting zone (R) within the water column which marks the top of a hot brine layer associated with hydrothermal activity (reprinted from Ritcher *et al*, Copyright 1986, with permission from Elsevier Science).

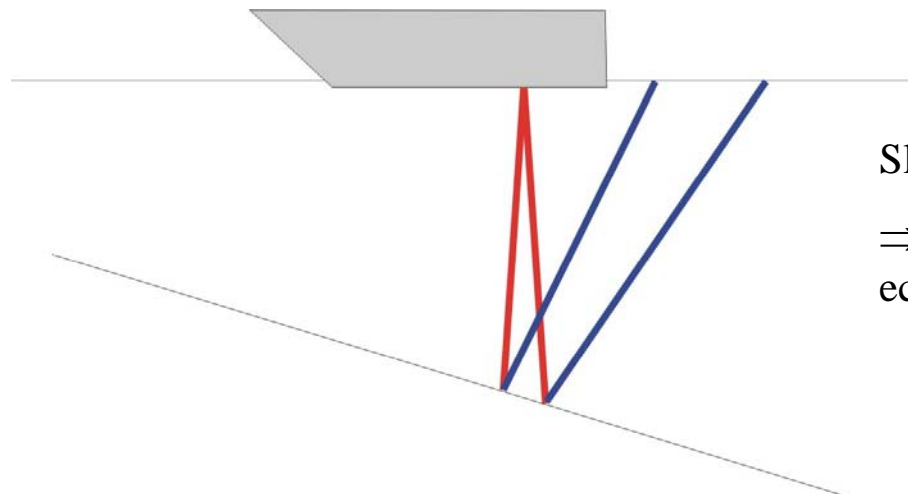
What opening angle should we use?

Footprint: The portion of the seafloor ensonified by the echosounder

Water depth	Opening Angle	Footprint diameter
5000m	40°	3600m
5000m	2°	~180m
200m	40°	~150m
200m	2°	~7m

The opening angle determines the lateral resolution

but ...

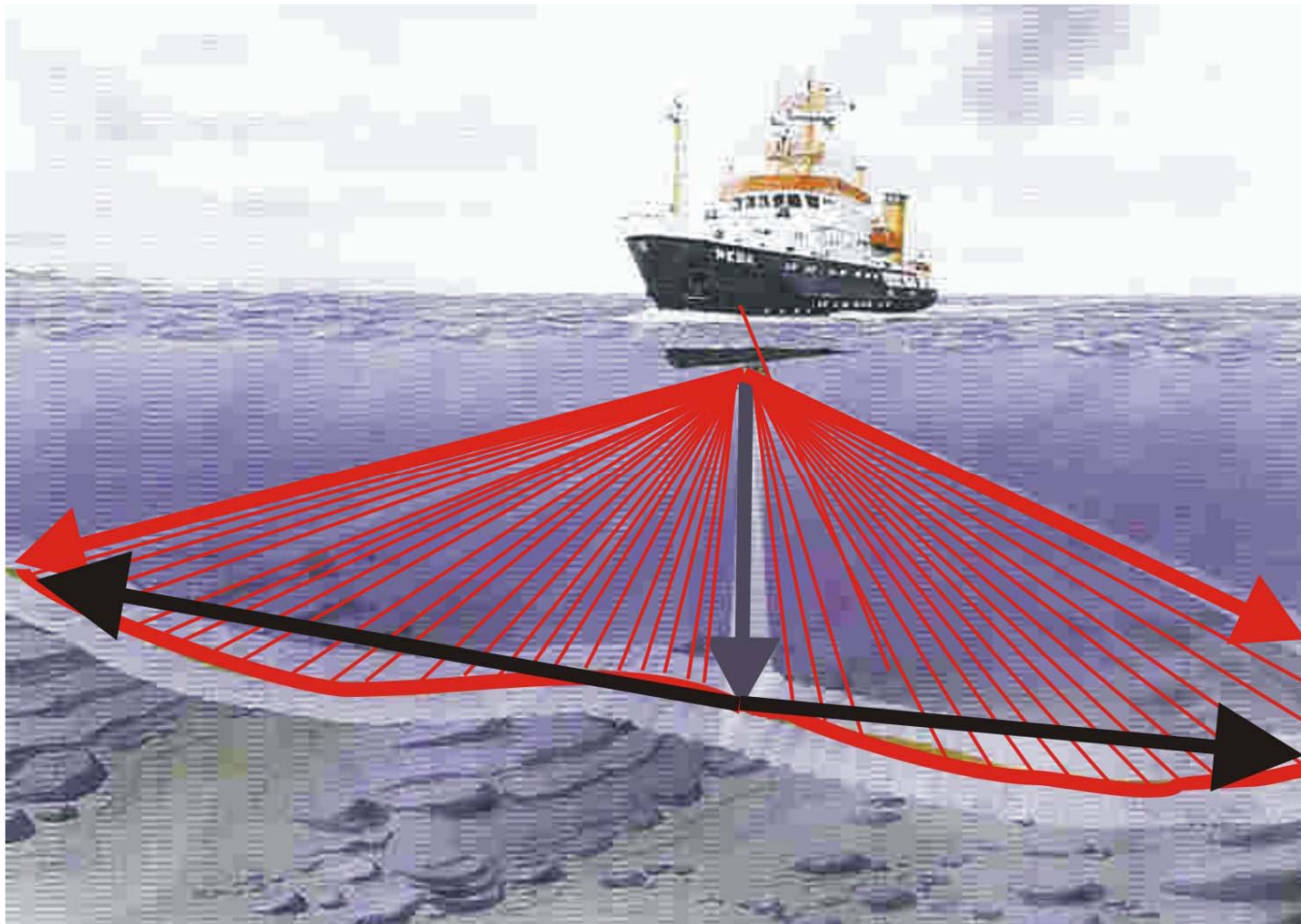


Slope angle $>$ opening angle/2

⇒ No energy return to the echosounder

Multibeam echosounder

Multi-beam echosounder are using a swath of beams giving off-track-depth



How do they work?

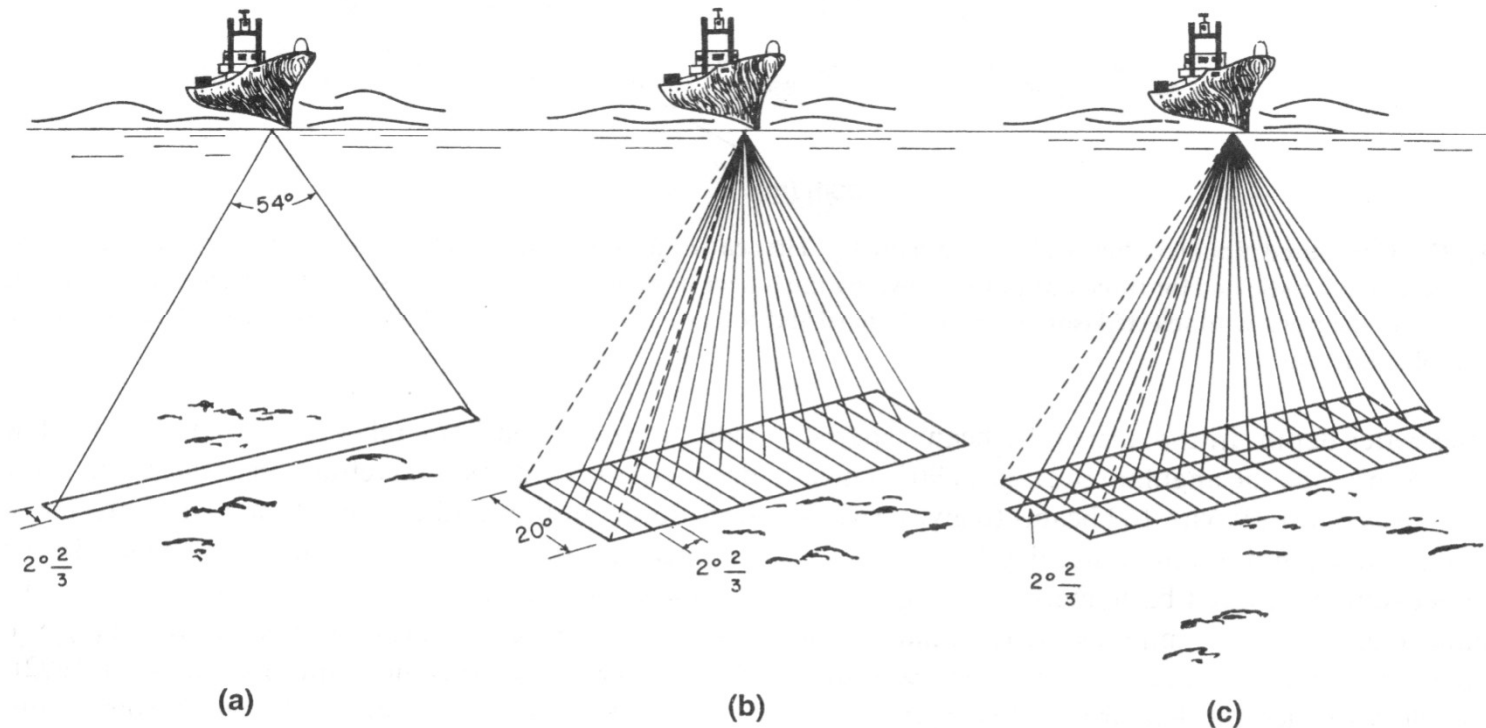
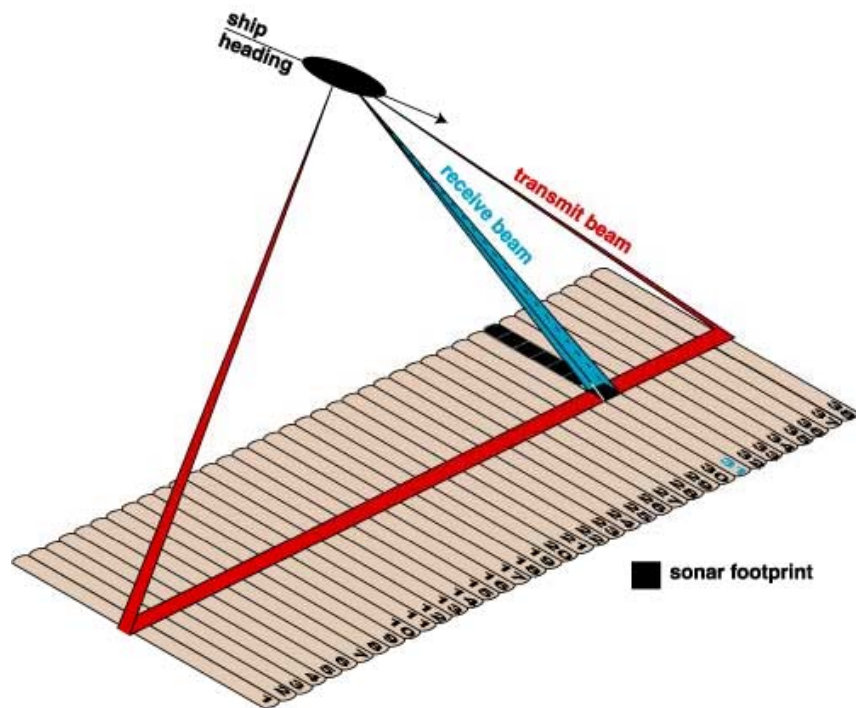


Figure 3.21 Principle of Seabeam swath-mapping system, manufactured by General Instruments Inc., USA. (a) Total area of sea floor insonified by transmission pulse. (b) Area of sea floor covered by receiving hydrophones. Signals are received from 16 rectangular zones. (c) Combination of (a) and (b), showing the received acoustic energy coming from 16 square zones on the sea floor (from Renard and Allenou, 1979). Reproduced by permission of the International Hydrographic Bureau.

Multibeam Echosounders



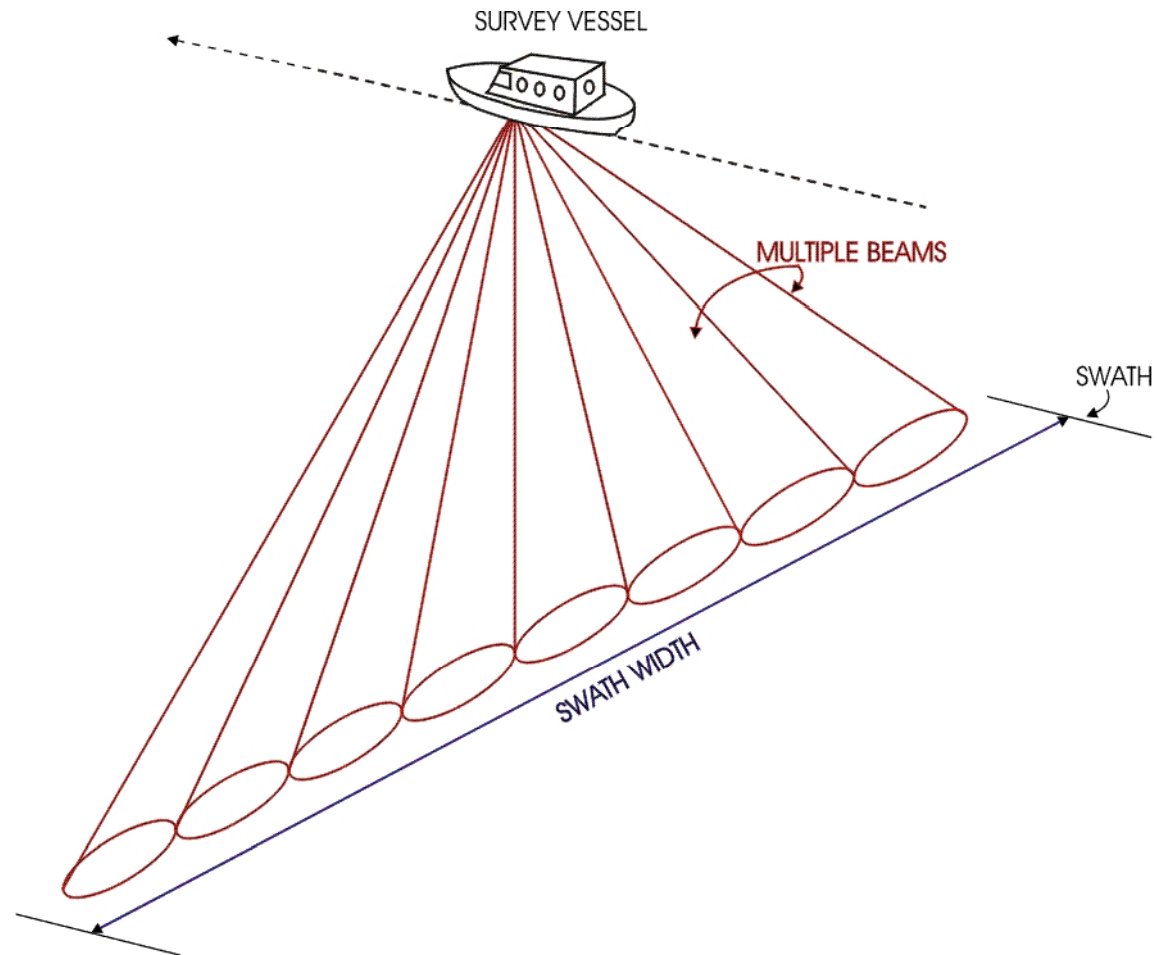


future ocean
KIEL MARINE SCIENCES

Acoustic Imaging

Bathymetry

The multibeam sonar

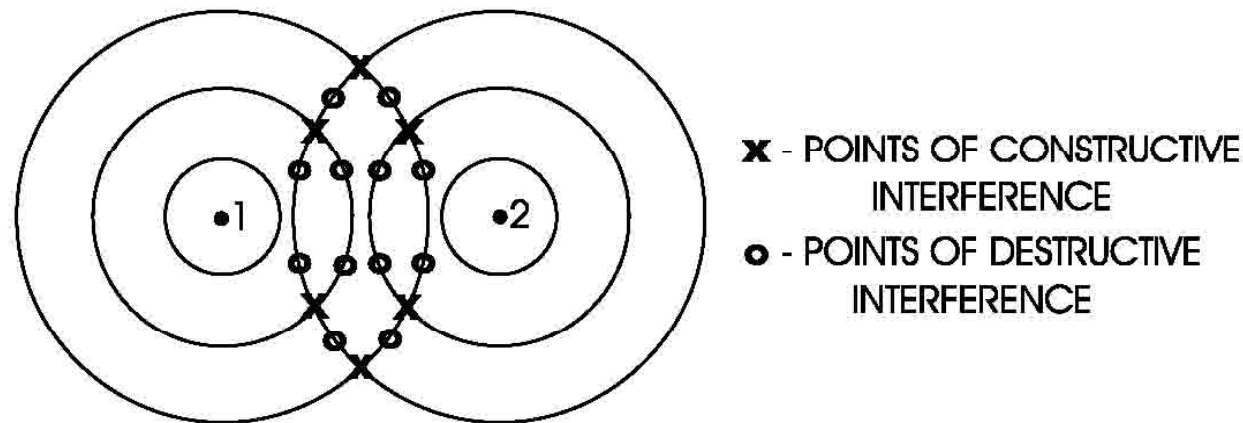


How can we realize such beams?

=> Beam forming (transmission) and beam steering (receiving)

Beam forming

Beam forming uses the principle of constructive and destructive interference:
Transmission of spherical waves results in points with constructive and destructive interference.

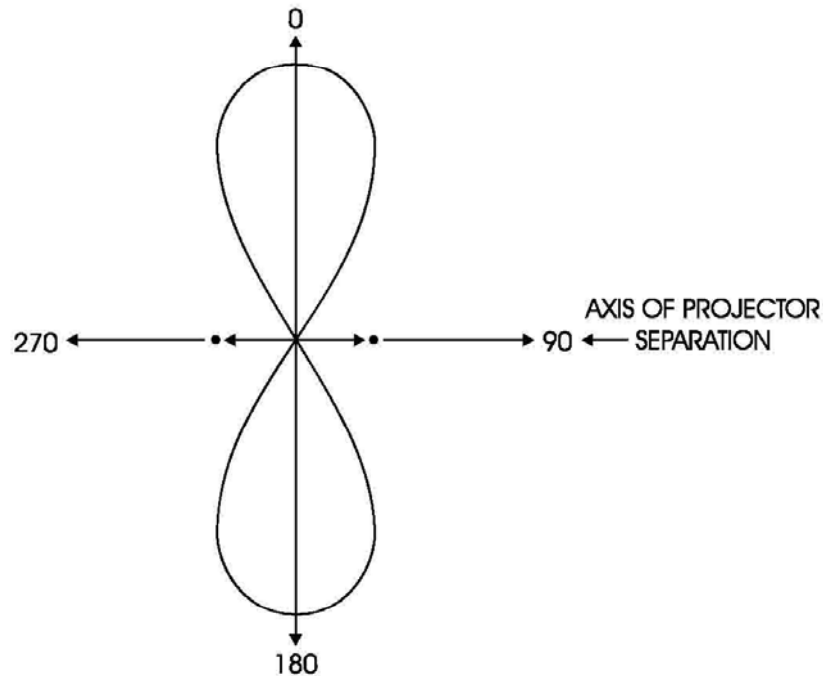


Constructive interference occurs at points with the same distance to the transducers or if the difference in distance corresponds to a multiple of the wave length.

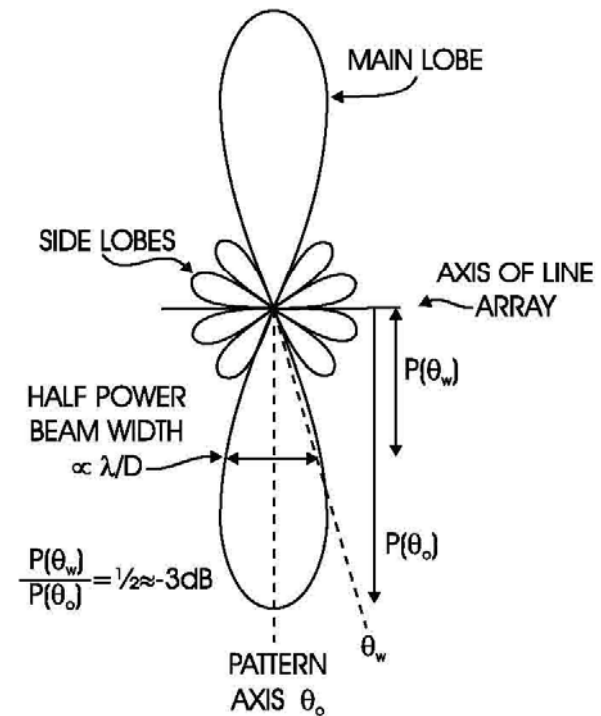


Beam forming

Beam Form for two transducers at a distance of $\lambda/2$:



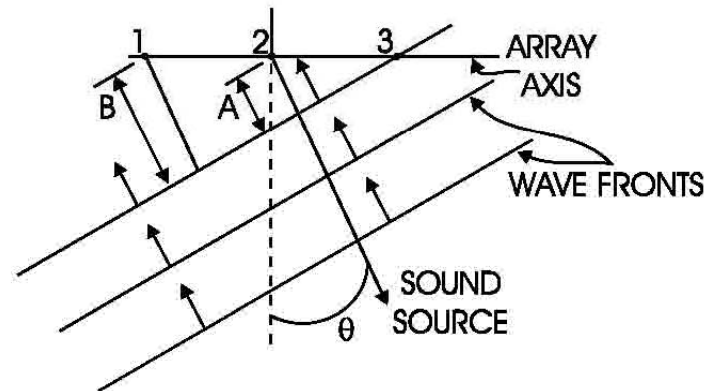
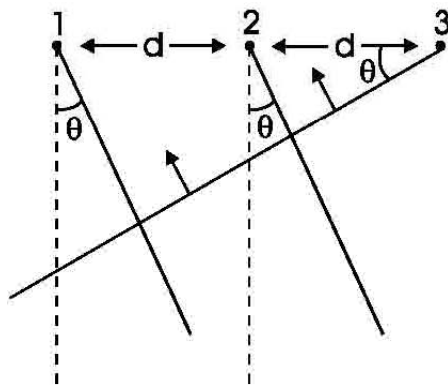
Beam Form for a Multiple-Element Line Array



***D = Length of sounding array
=> Narrow beams require a long array.***

„Beam steering“

„Beam steering“ = The hydrophone array is listening in specific directions through time-delayed scanning of individual hydrophones



Wave front arrives at array under the angle θ .

Sound waves arrive at hydrophone 3 first.

Afterwards they have to travel the distance A before they arriving at hydrophone 2, and B before arriving at hydrophone 1.

$$A = d \sin(\theta);$$

$$B = 2 d \sin (\theta)$$

$$\Rightarrow T2 \text{ (time to hydrophone 2)} = A / c = (d \sin \theta) / c$$

$$T1 \text{ (time to hydrophone 1)} = B / c = (2d \sin \theta) / c$$

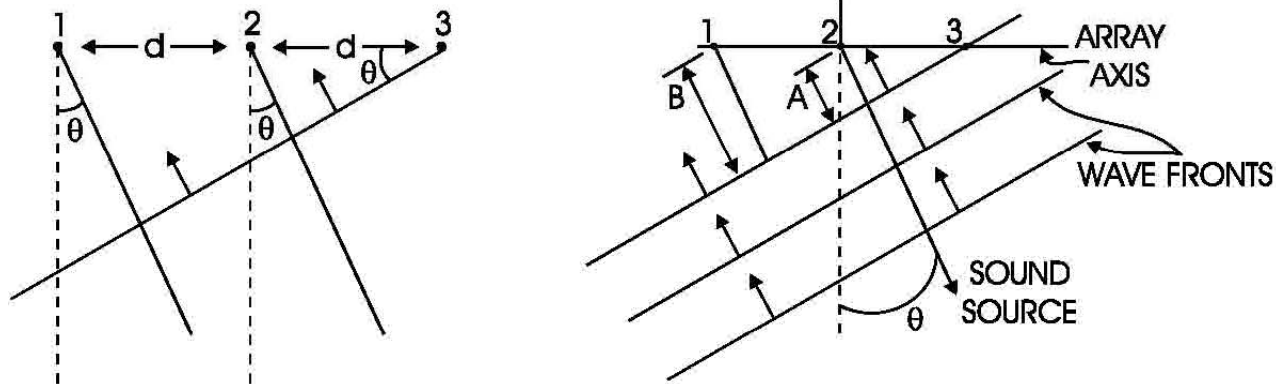


future ocean
KIEL MARINE SCIENCES

Acoustic Imaging

Bathymetry

Beam steering



$$T2 \text{ (time to hydrophone 2)} = (d \sin \theta) / c$$

$$T1 \text{ (time to hydrophone 1)} = (2d \sin \theta) / c$$

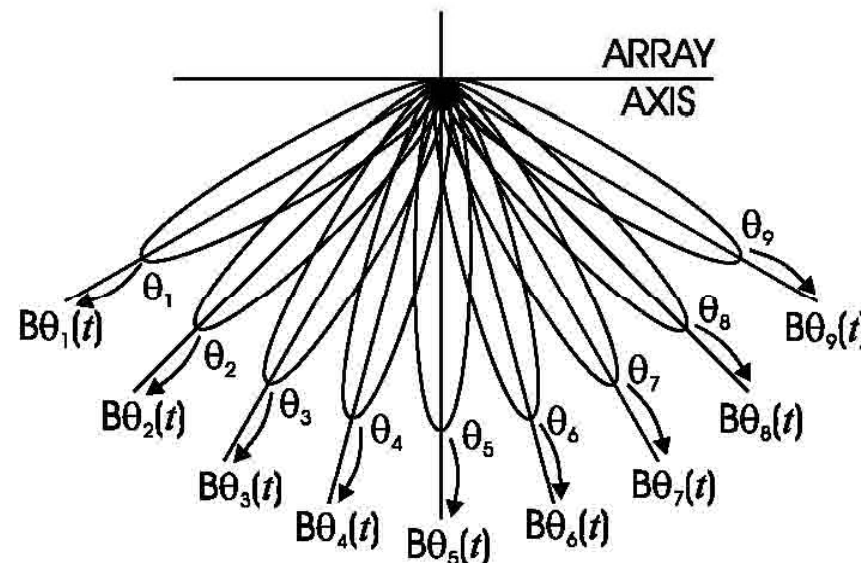
Variations in the time lag between individual hydrophones allows to listen in specific directions. This is done by summing up the signals of individual hydrophones. Constructive interference is only achieved, if the signal is coming from this direction. E.g. summing up hydrophones 3 and 2 with a time lag of $T2$ and hydrophone 1 with a time lag $T1 \Rightarrow$ Array “listens” in direction θ

In general: Using different time lags allows to listen in any direction but accurate knowledge of the sound velocity is needed (so-called keel)

Beam steering

Data processing allows to use the same array for a broad range of angles..

⇒ One data set can be processed simultaneously in that way, that sound waves arriving from different directions are recorded as individual beams.

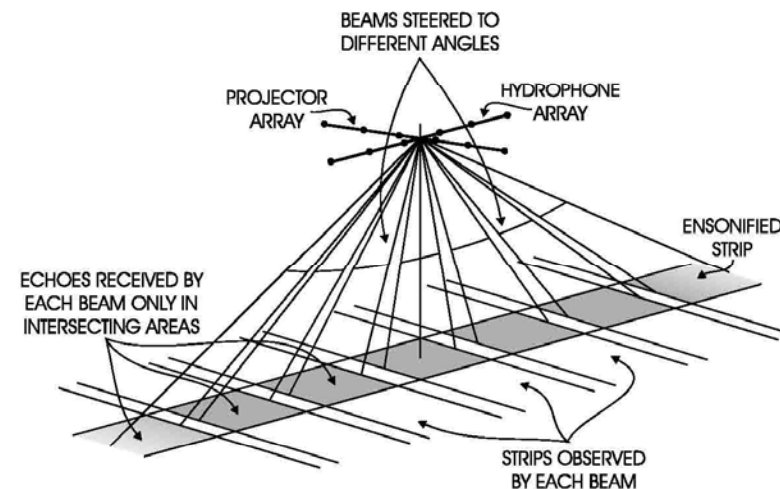
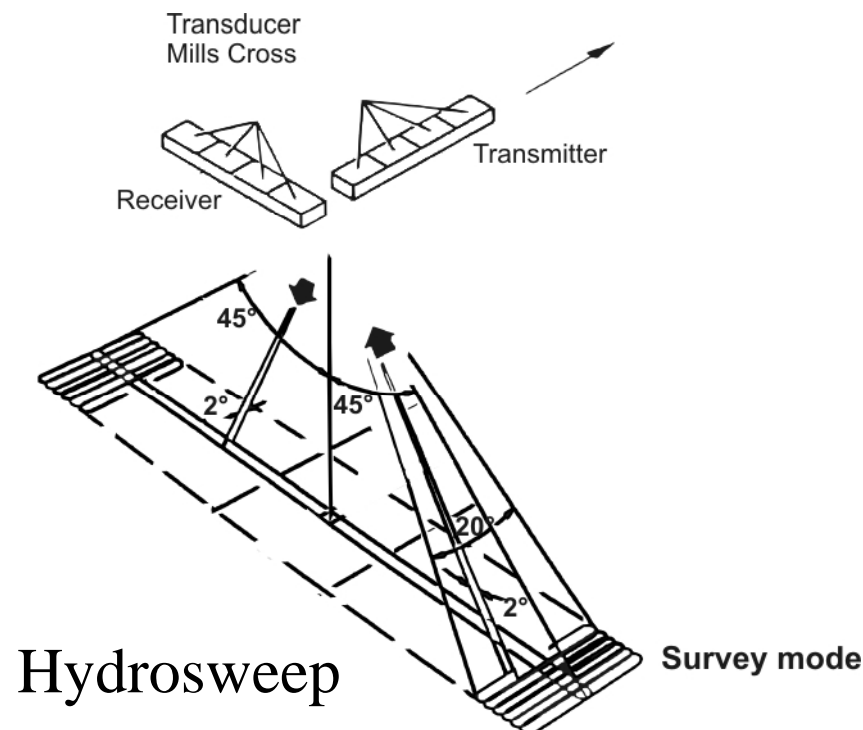


Mills Cross –

Bringing beam forming and beam steering together

The transmitted or received swath is narrow in the direction of the transducer array and broad perpendicular to the array.

=> In a **Mills Cross** configuration, transmitting and receiving arrays are orientated perpendicular to each other; hence the received energy is coming from portions of the seafloor characterized by small opening angles in along and across track direction.



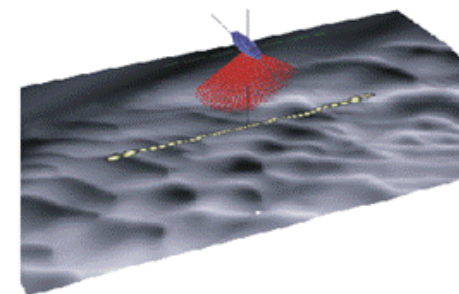
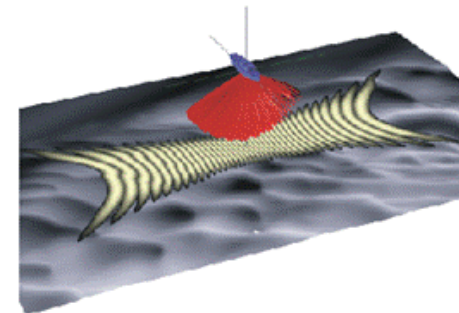
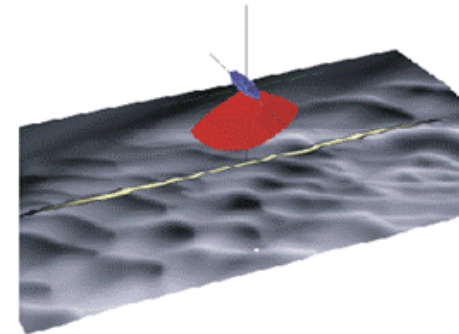
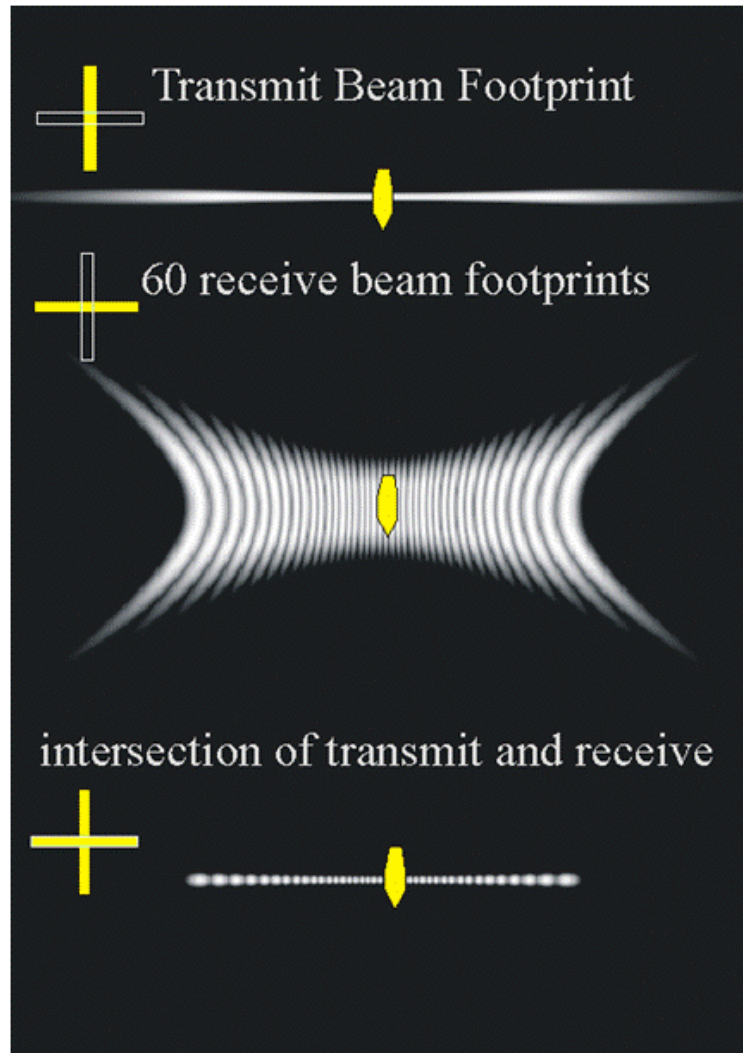
SeaBeam



future ocean
KIEL MARINE SCIENCES

Acoustic Imaging

Bathymetry

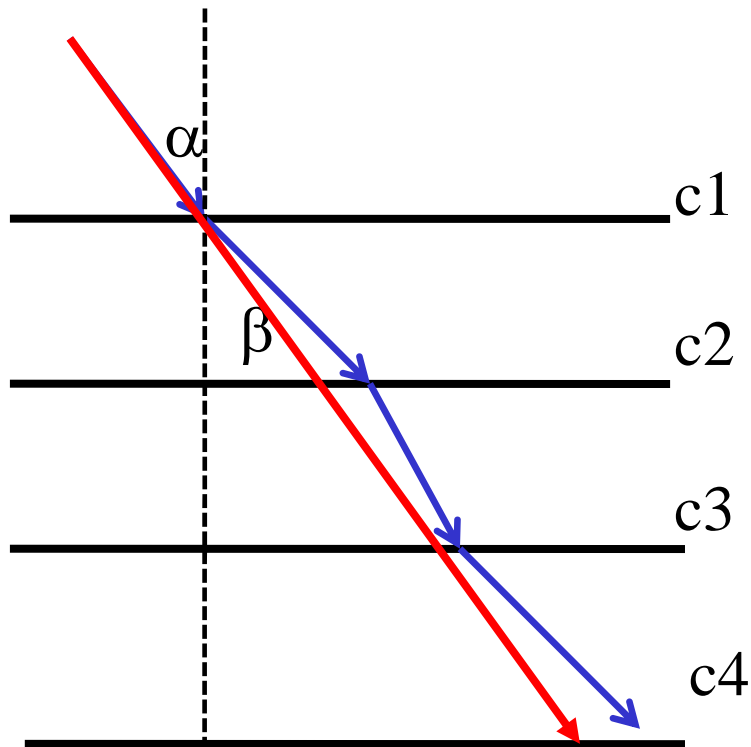


Ocean Mapping Group



SE 3353 Imaging and Mapping II :
Submarine Acoustic Imaging Methods
© J.E. Hughes Clarke, OMG/UNB

Can we use a constant sound velocity for multibeam sounders?



Snell's law:

$$\sin(\alpha)/c_1 = \sin(\beta)/c_2 = \text{const.}$$

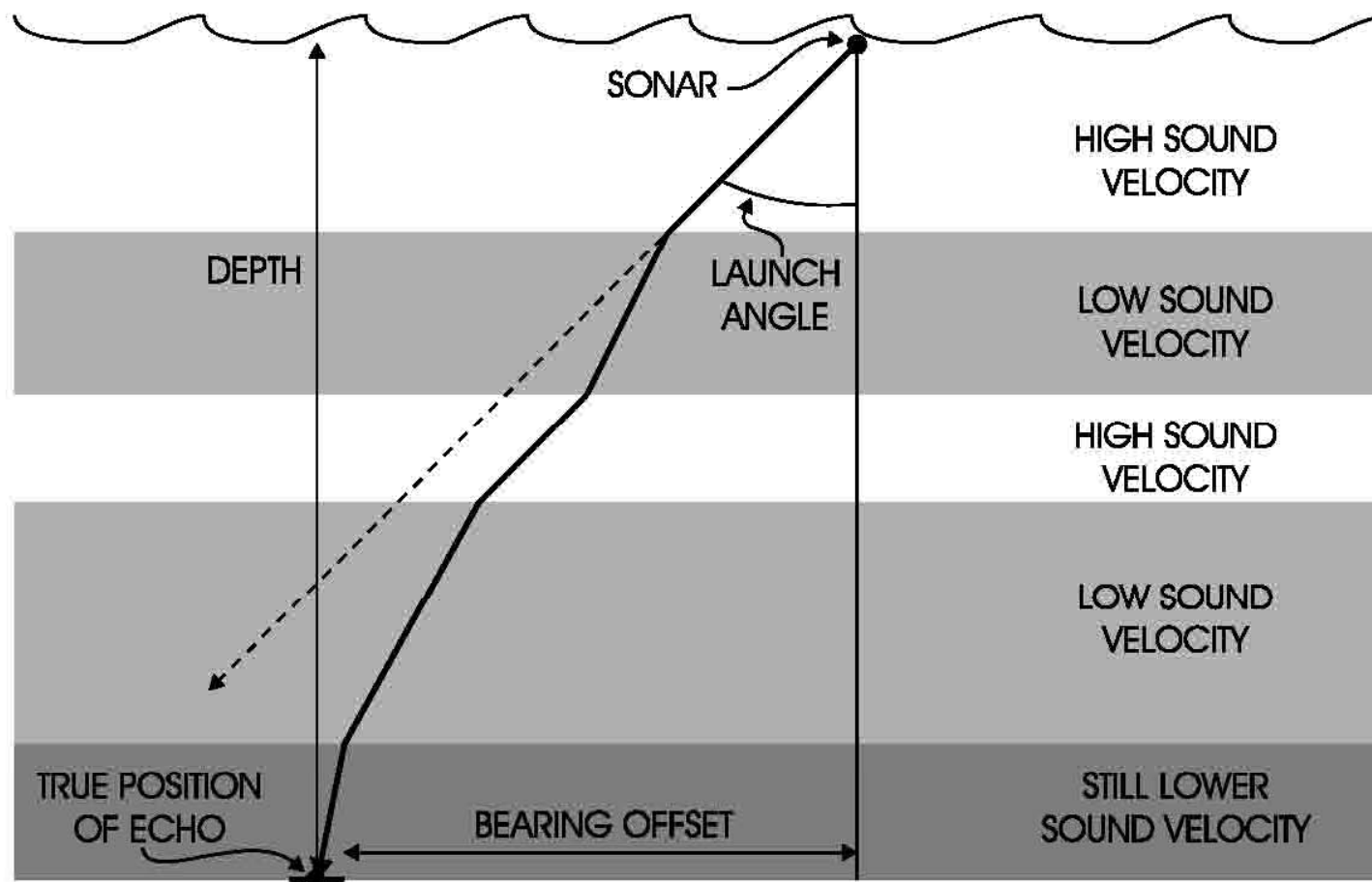
A detailed sound velocity profile is needed for multibeam sounders due to refraction of non vertical rays at water layer boundaries (change if sound velocity). Neglecting this effect results in wrong water depths and/or locations on the sea floor.



Velocity decrease: Refraction towards the normal line



Velocity increase: Refraction away from the normal line



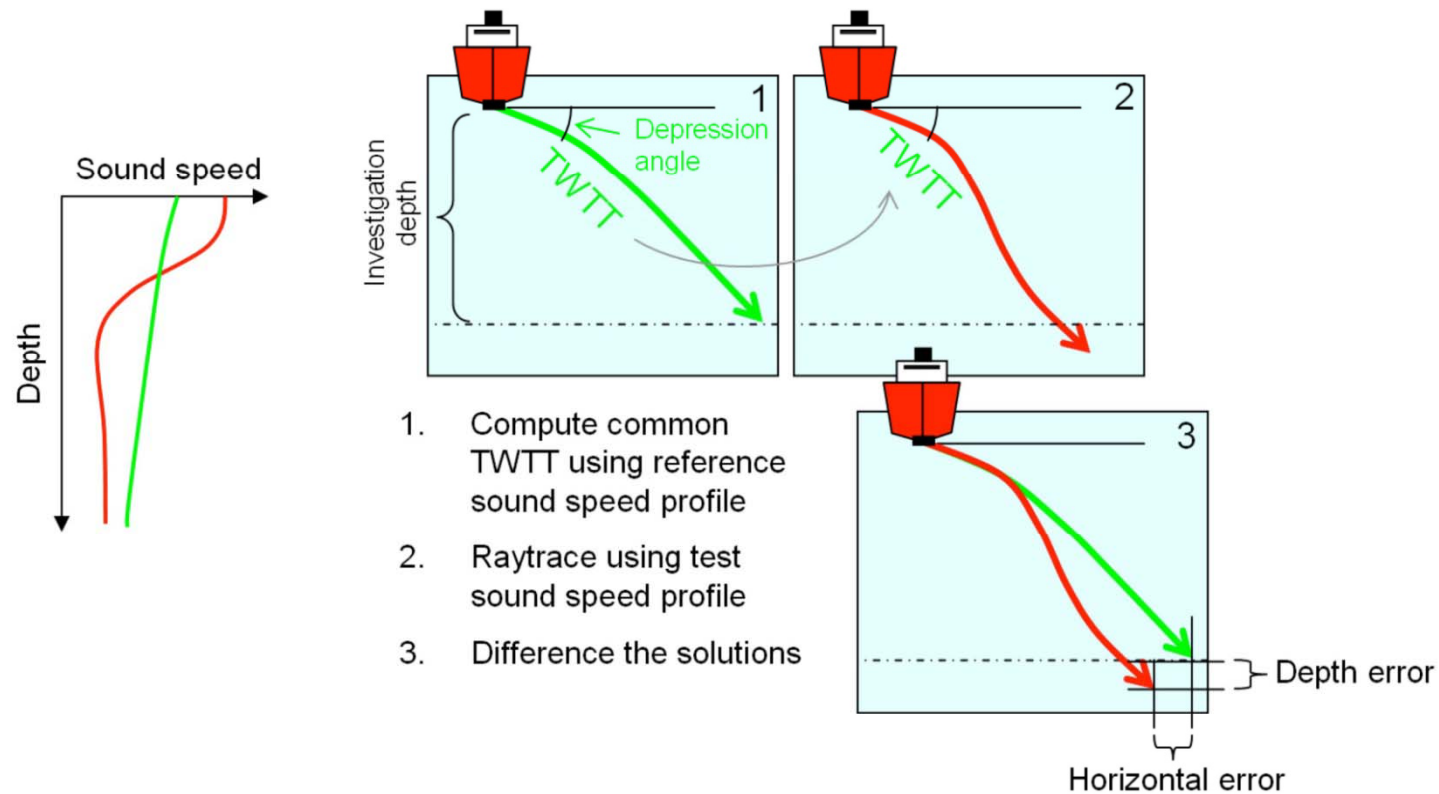
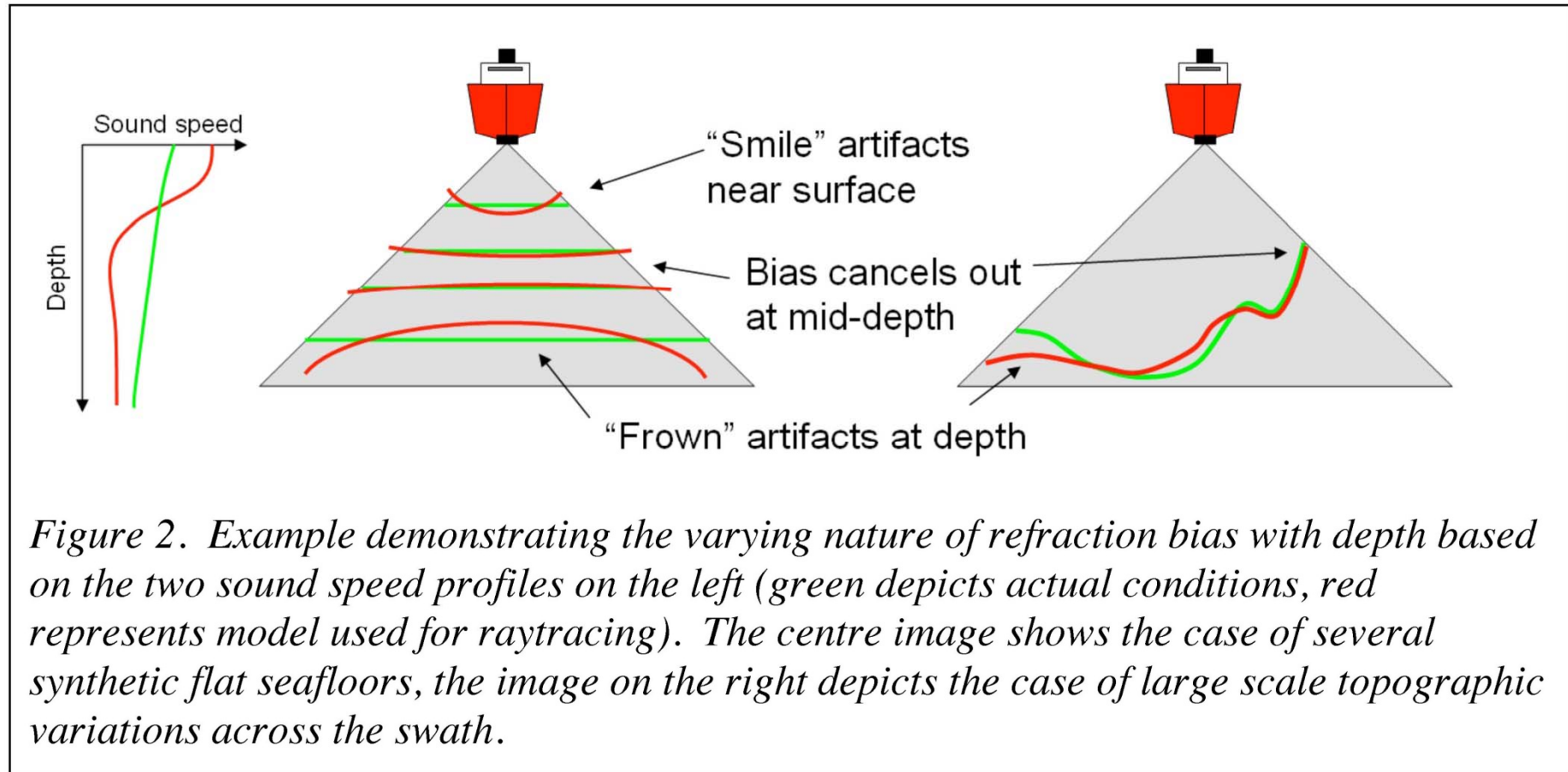


Figure 1. Depiction of raytracing simulator functionality in which errors for depth and horizontal positioning are computed for a particular investigation depth and depression angle. The two-way travel time (TWTT) to reach the particular depth of investigation is first computed using the reference sound speed profile. A second raytrace is done using the profile to be tested and the TWTT and depression angle. The discrepancy between the two solutions indicates the sensitivity of the raytraced solution to the differing depictions of the watercolumn conditions.



Typical sound-velocity profiles

V_{water} is dependent on

Temperature (T_w)

Salinity (S_w)

Pressure (P_w)

T_w increase $\Rightarrow V_w$ increase ($3\text{m s}^{-1} \text{ } ^\circ\text{C}^{-1}$)

S_w rise of 0.1% $\Rightarrow V_w$ increase of 1.3m s^{-1}

P_w rise of 10 bar (100m) $\Rightarrow V_w$ increase of 1.8m s^{-1}

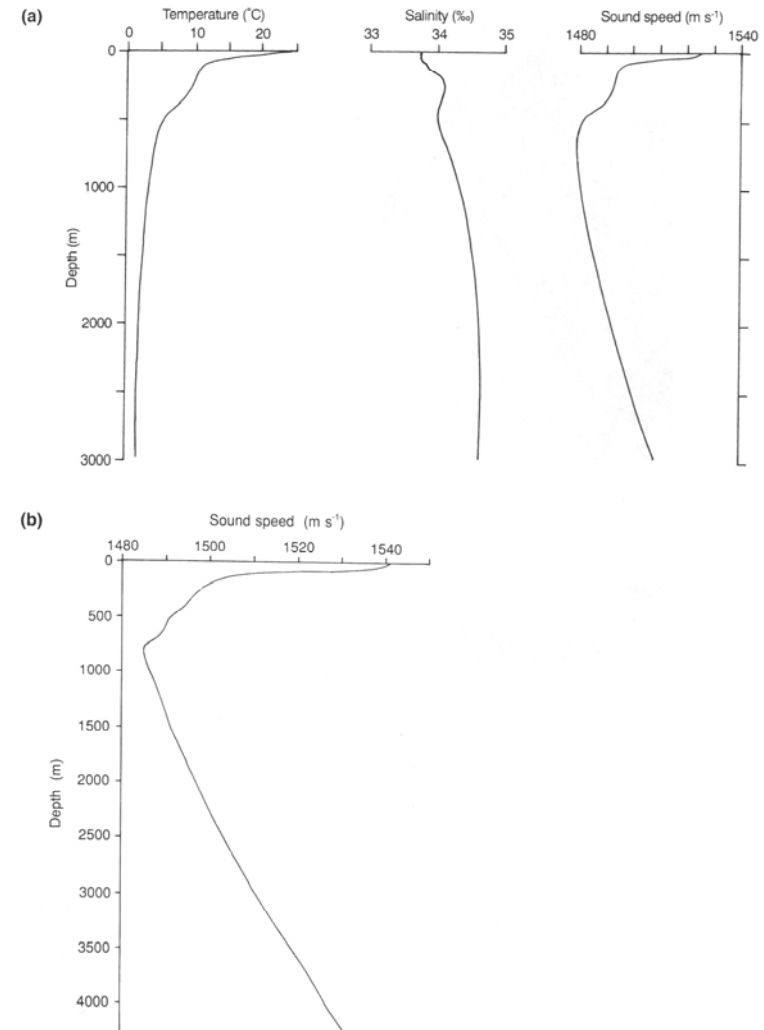


Figure 3.2 (a) Variation of temperature, salinity and sound speed in the central Pacific at 39°N, 146°W. A sound speed minimum occurs at 650 m (from Pickard and Emery, 1990). Reproduced by permission of Butterworth Heinemann. (b) Variation of sound speed with depth at 8° 15'N, 23° 32'W in the equatorial Atlantic measured with a velocimeter from RRS *Charles Darwin* in 1985.

What else do we need?

Motion sensor providing heading, roll and pitch. A good motion sensor is essential for high quality bathymetric data.



Transducer

Motion Sensor

Examples of multibeam echosounders

Deep Water

ATLAS HYDROSWEEP DS (STN-Atlas): up to 395 beams, angular coverage: 140° , swath width: 5.5-times the ocean-depth, frequency: 15.5 kHz

Simrad EM120: 191 beams, angular coverage: 150° , swath width: 6 times the ocean-depth, frequency: 12 kHz, depth range: 10 - 11000m

Middle water

Simrad EM710: 256 beams, angular coverage: 140° , swath width: 5.5-times the ocean-depth, frequency: 70-100 kHz, depth range: 3 - 2000m

Typical accuracy: 0.2%-0.5% of ocean depth (dependent on relief)



Acoustic Imaging

hyr



Example shallow water bathymetric swath sounder:

The **ATLAS FANSWEEP 20** is a wide swath multi-beam echosounder designed for survey of ports, waterways and coastal areas to depths of up to 600 m. The ATLAS FANSWEEP 20 has a dual head transducer that provides high quality bathymetric data with a swath angle of max. 161° and side-scan data with max. 180° aperture in parallel. It is available in two versions for 100 kHz and 200 kHz operation. erhältlich.



SeaBeam 1050 (used during the MASS-Cruises)

The dual-frequency multibeam system SeaBeam 1050 collects bathymetric and side scan data in shallow to medium water depths with a swath width of up to 150 degrees. The operating frequency can be changed with a single mouse click.

50/180 kHz dual frequency operation

126 individual beams

153° swath width

1500 m maximal depth

1500 m seafloor coverage

1.5° resolution

Integrated side scan sonar

Real time motion compensation

Control Unit



future ocean
KIEL MARINE SCIENCES

Acoustic Imaging

Bathymetry

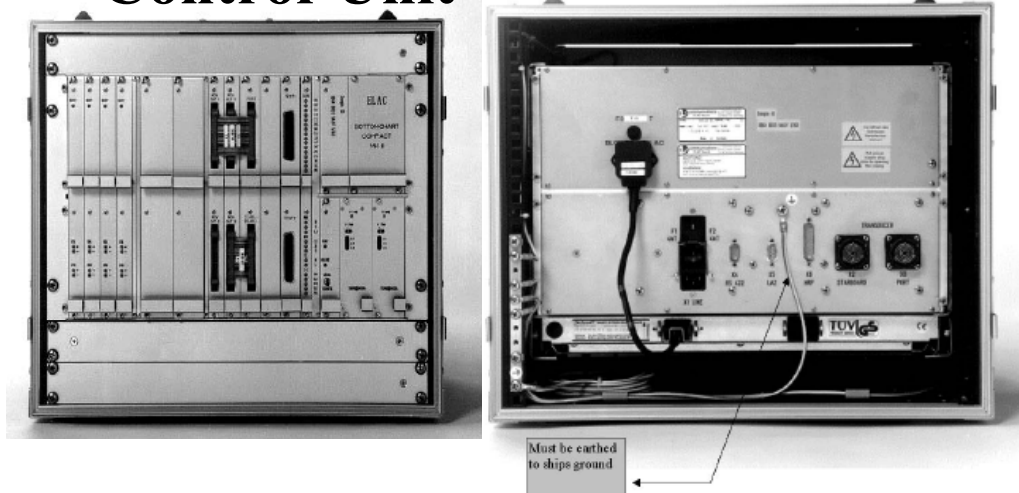
Components



SVP

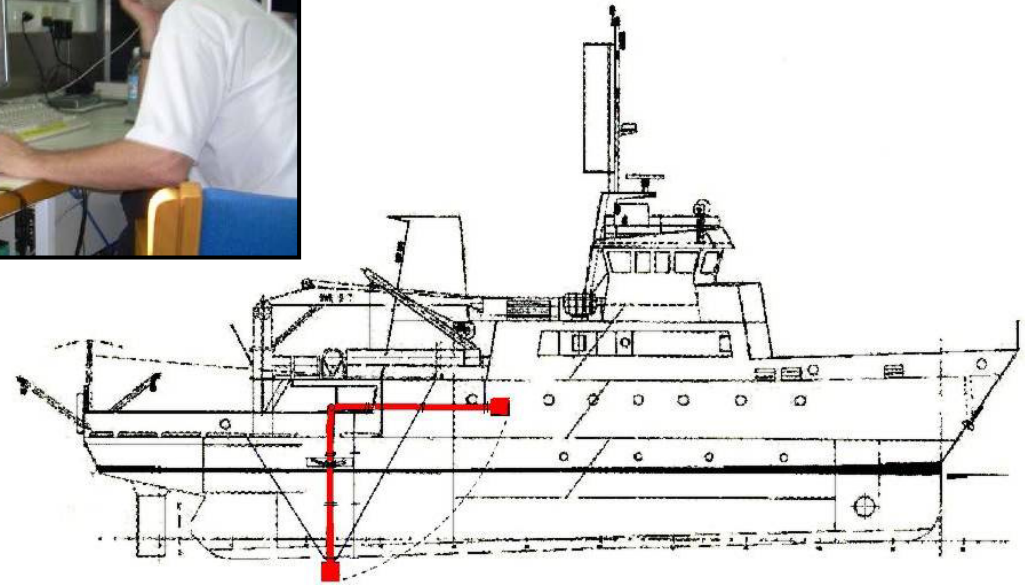


Control-Unit



Interface





A sketch of mounting Multibeam echosounder at port side.



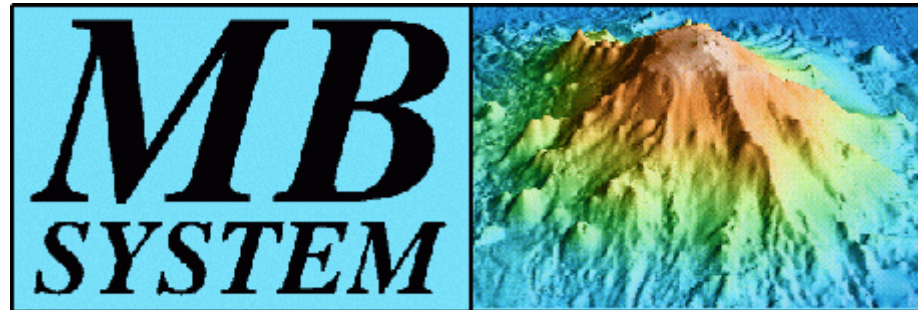
Multibeam Processing

1) Professional (expensive) Software:

- System independent software: i.e. Caris, Caribes,...
- Software delivered with system: i.e. Kongsberg, SeaBeam, Reson, Atlas Hydrographic, ...

2) Free software:

- MultiBeam System



The MB-System™ Cookbook

Val Schmidt, Columbia University

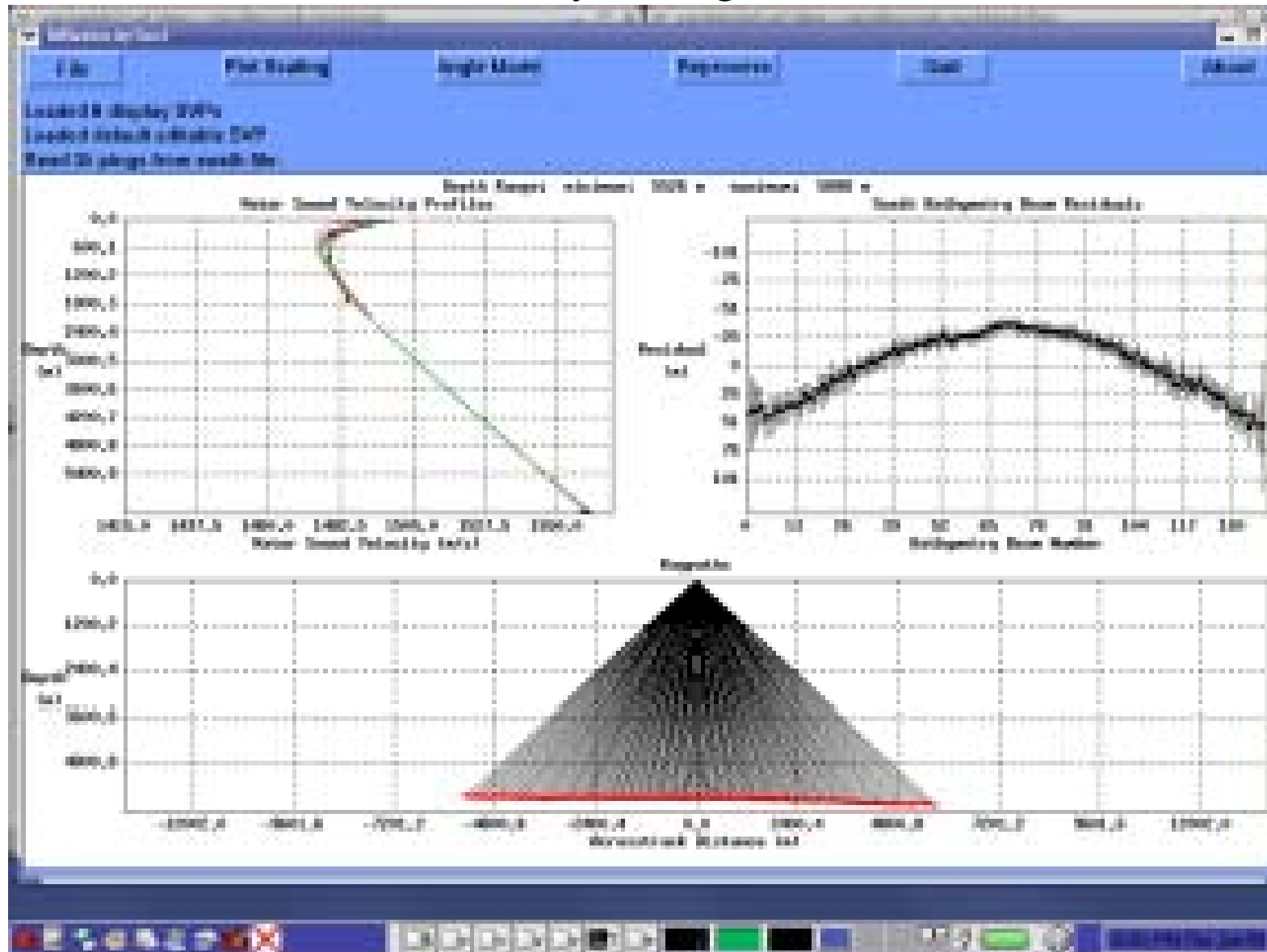
Dale Chayes, Columbia University

Dave Caress, Monterey Bay Aquarium Research Institute

<http://www.ldeo.columbia.edu/MB-System/MB-System.intro.html>

Processing strategy

- Organize your data in useful surveys (covered area, data size)
- Check the raw data to get an overview about area coverage and quality of depth data, navigation data, metadata (roll, pitch, heave)
⇒ plot data, look statistics
- Process Navigation data (smoothing)
- If necessary (and possible), recalculate depth data with better VSP
- Automatic data processing (filter)
- Interactive depth data processing
- Grid and display data



Automatic editing of multibeam data

1. Flag specified number of outer beams.
2. Flag soundings outside specified acceptable depth range (*difficult on profiles across slope*)
3. Flag soundings outside acceptable depth range using fractions of and/or deviation from local median depth.
4. Flag soundings associated with excessive slopes (*beware of real slopes in your data*)
5. Zap "rails".
6. Flag all soundings in pings with too few good soundings.

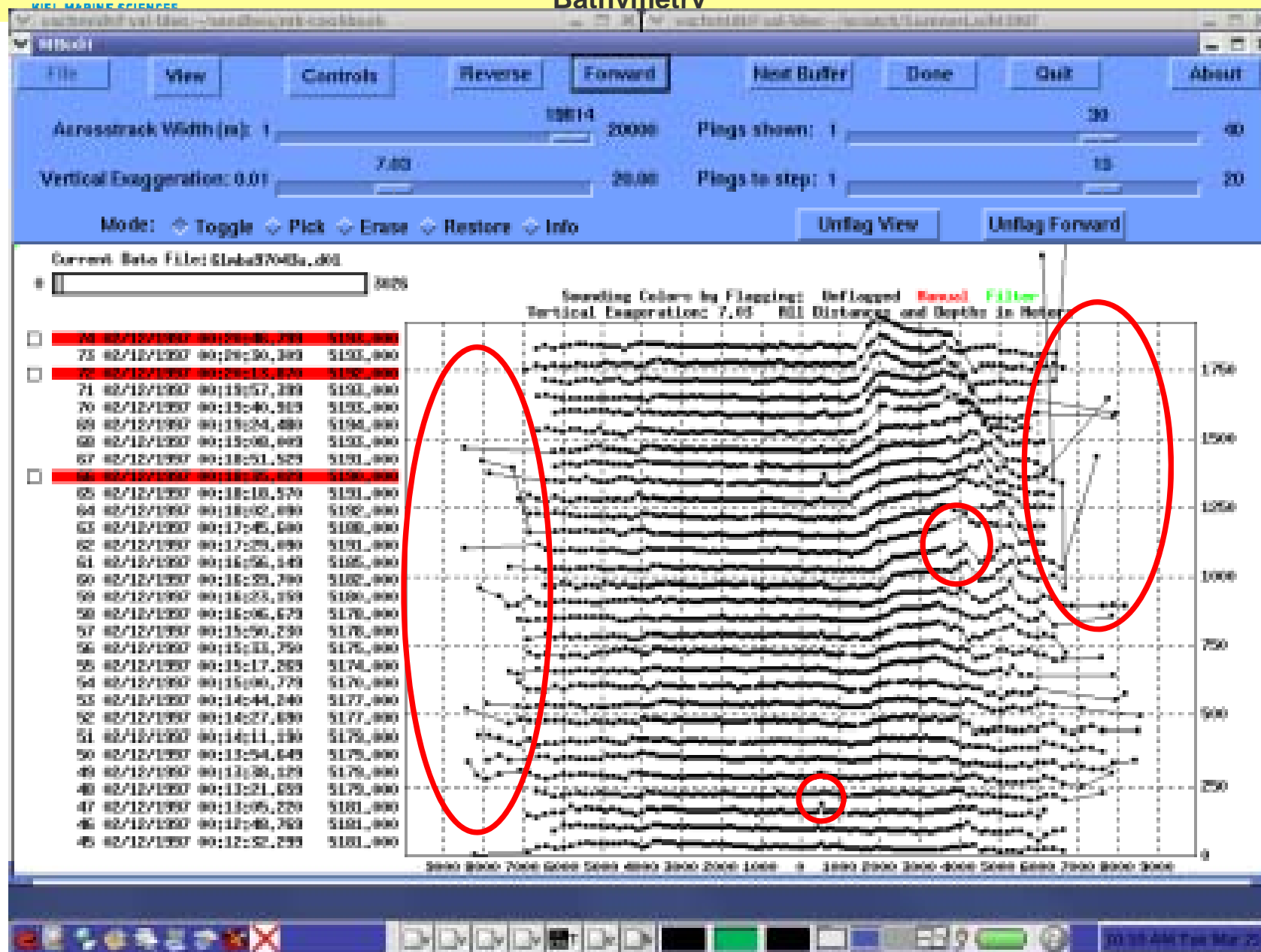


future ocean

WILL MARINE SCIENCE

Acoustic Imaging

Bathymetry



Typical applications

Characterization of morphological features on the sea floor

Tectonic Features

Deep sea trenches

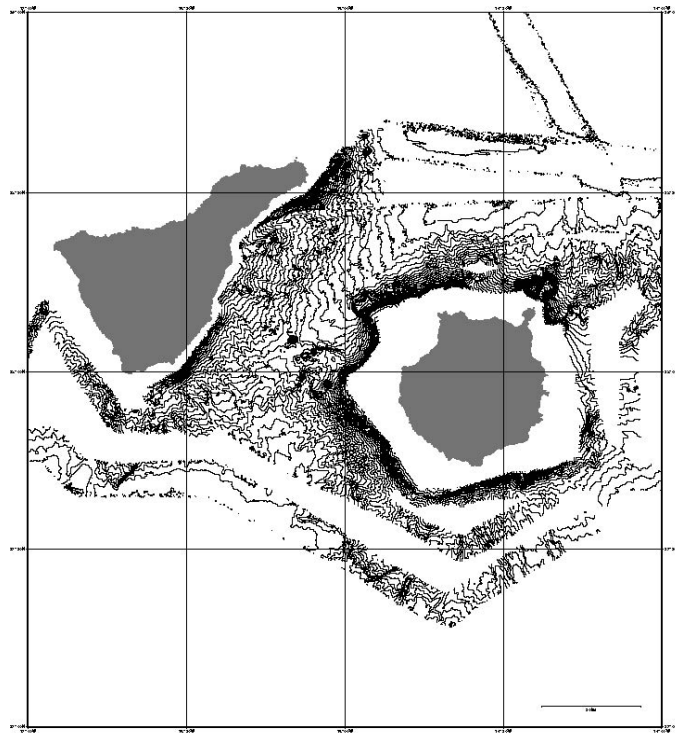
Sediment waves

Sediment transport

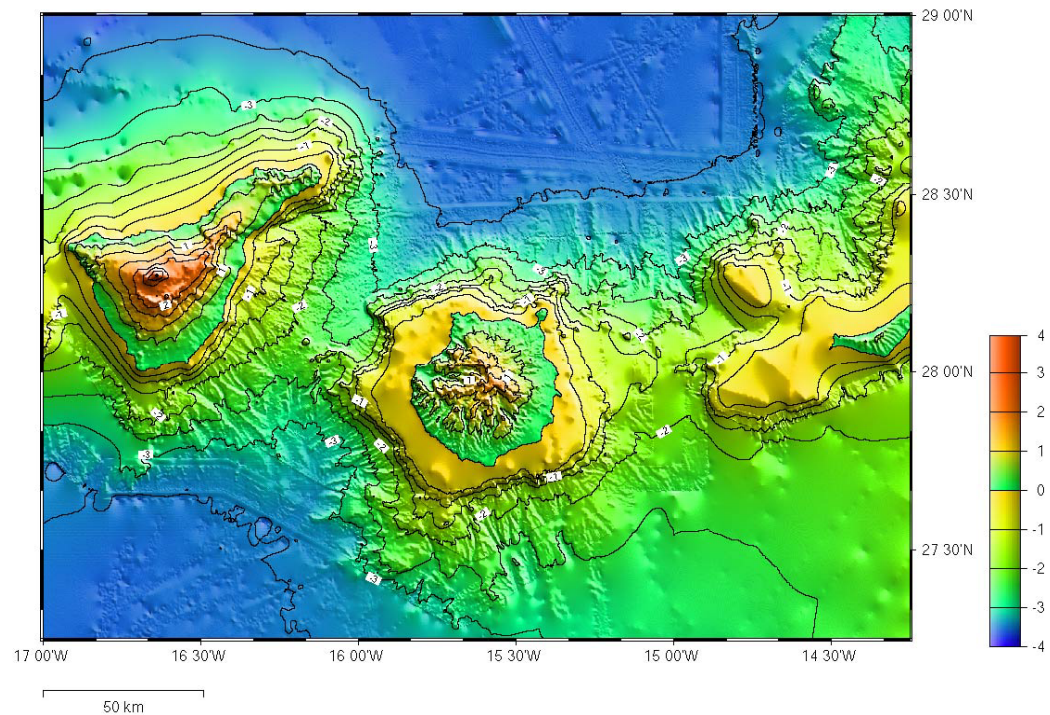
Cable route survey

Navigation channels

Examples (Canary Islands)

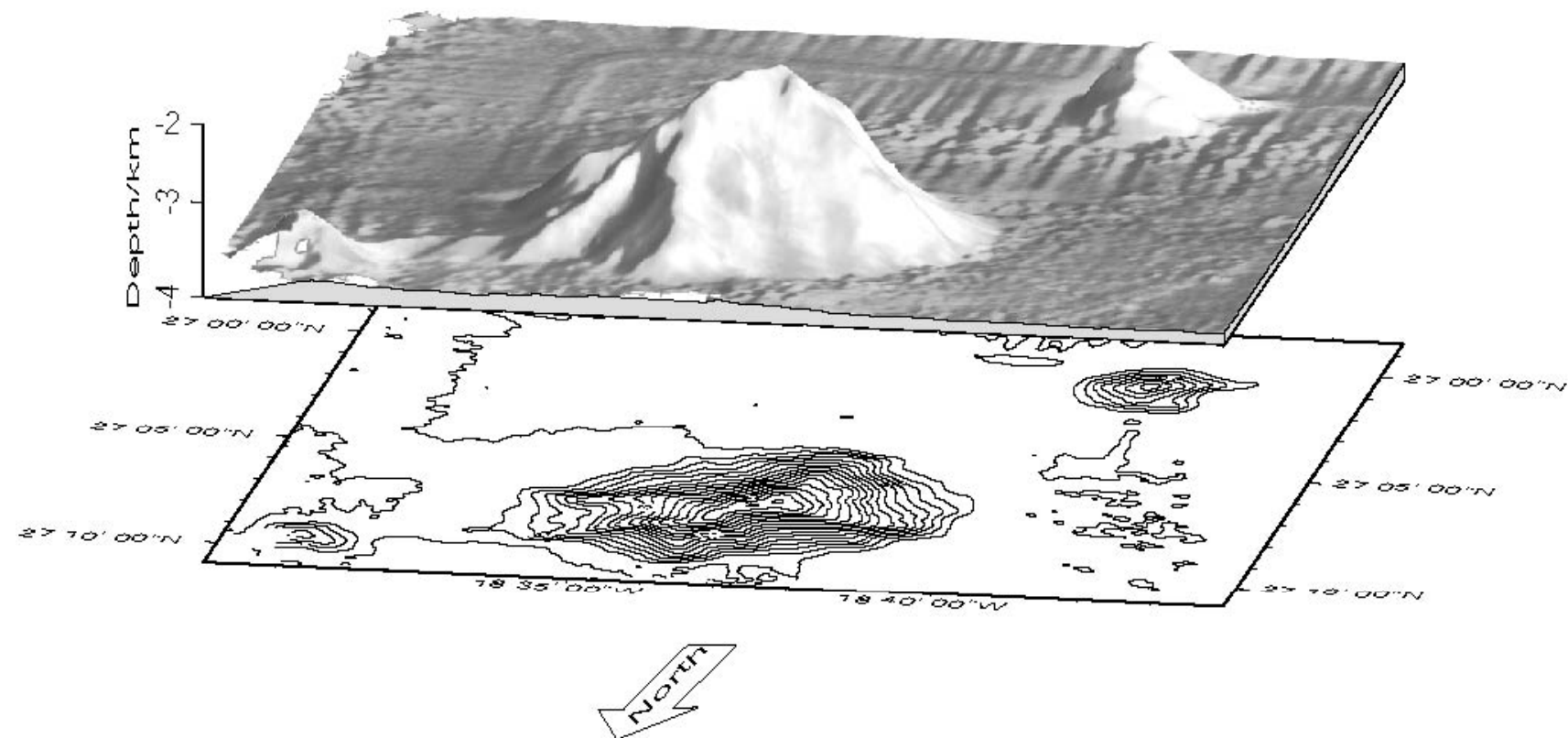


Contour-Plot

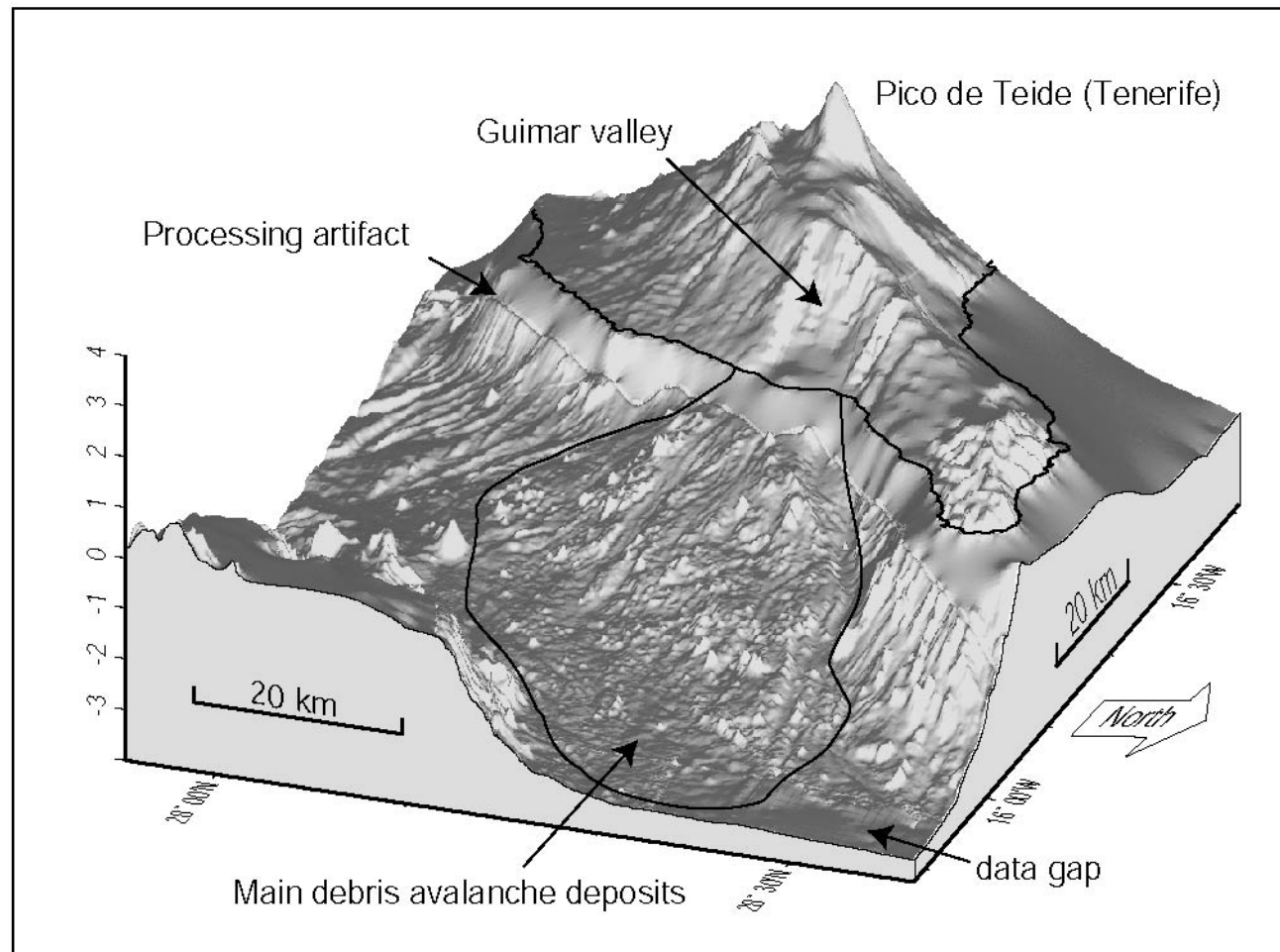


Color-coded image with artificial illumination

Las Hijas Seamounts



Tenerife (Guimar Debris Avalanche)

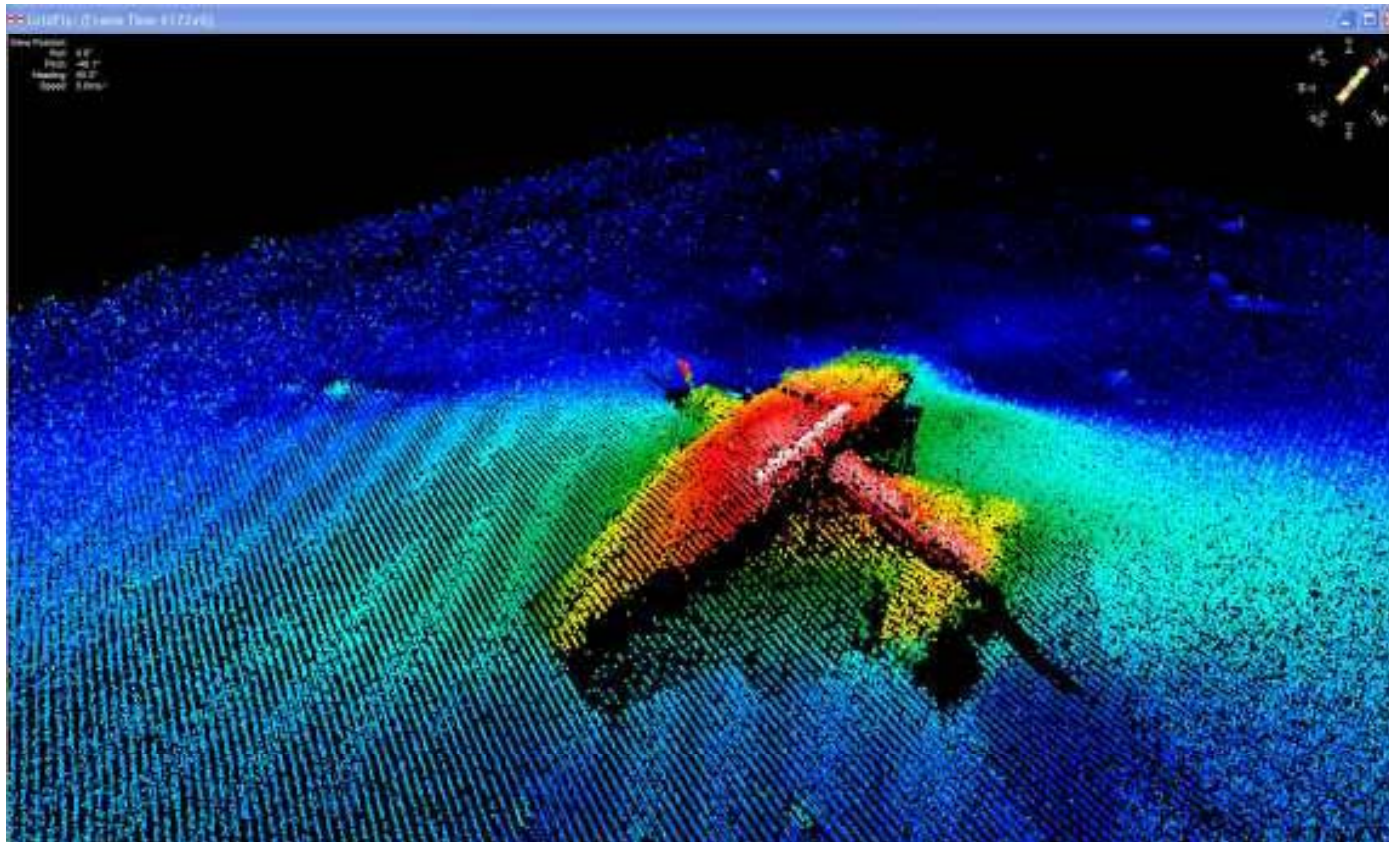


Micro Bathymetry

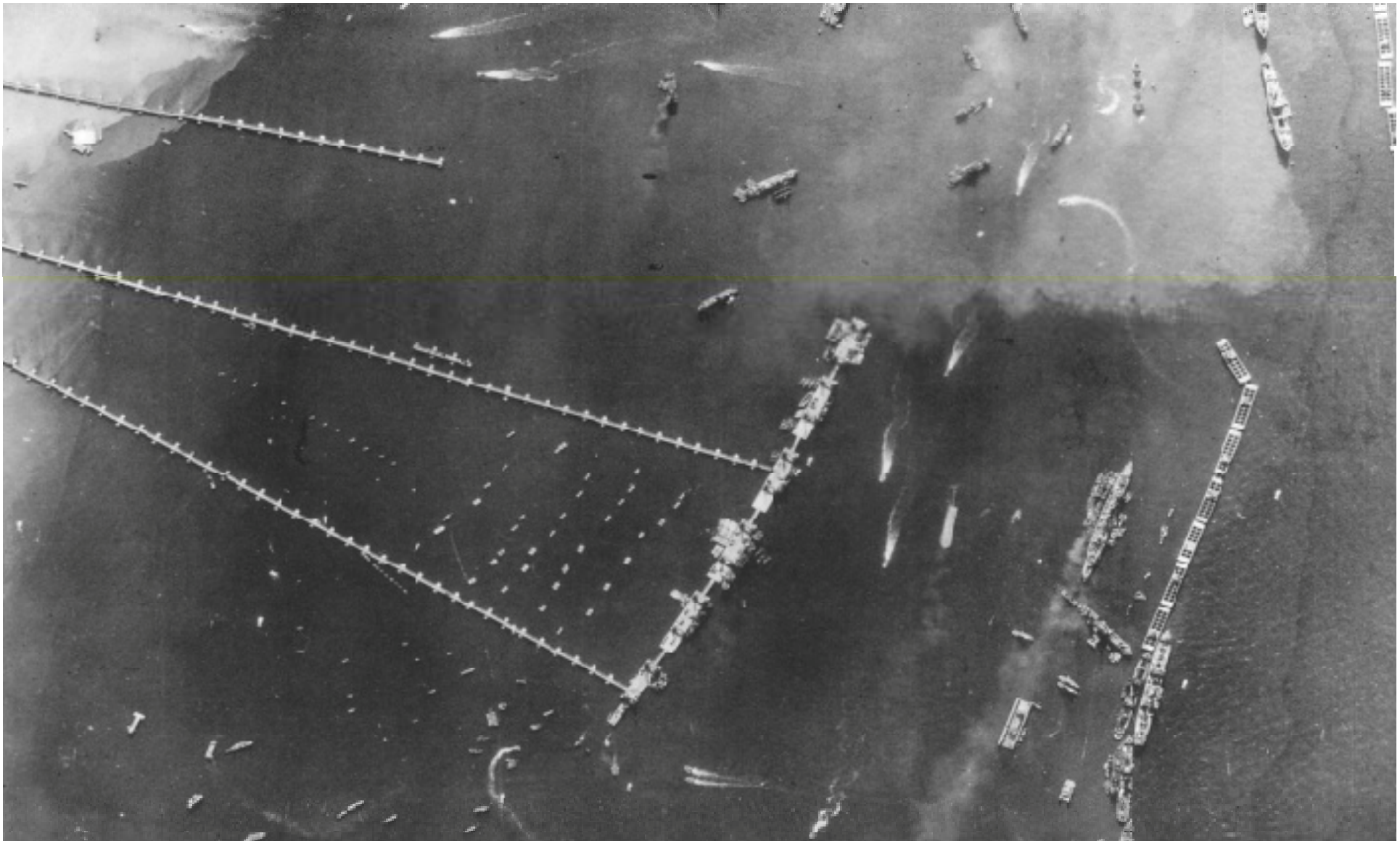
Very high resolution bathymetry (resolution $<1\text{m}$)

In shallow waters from research vessel

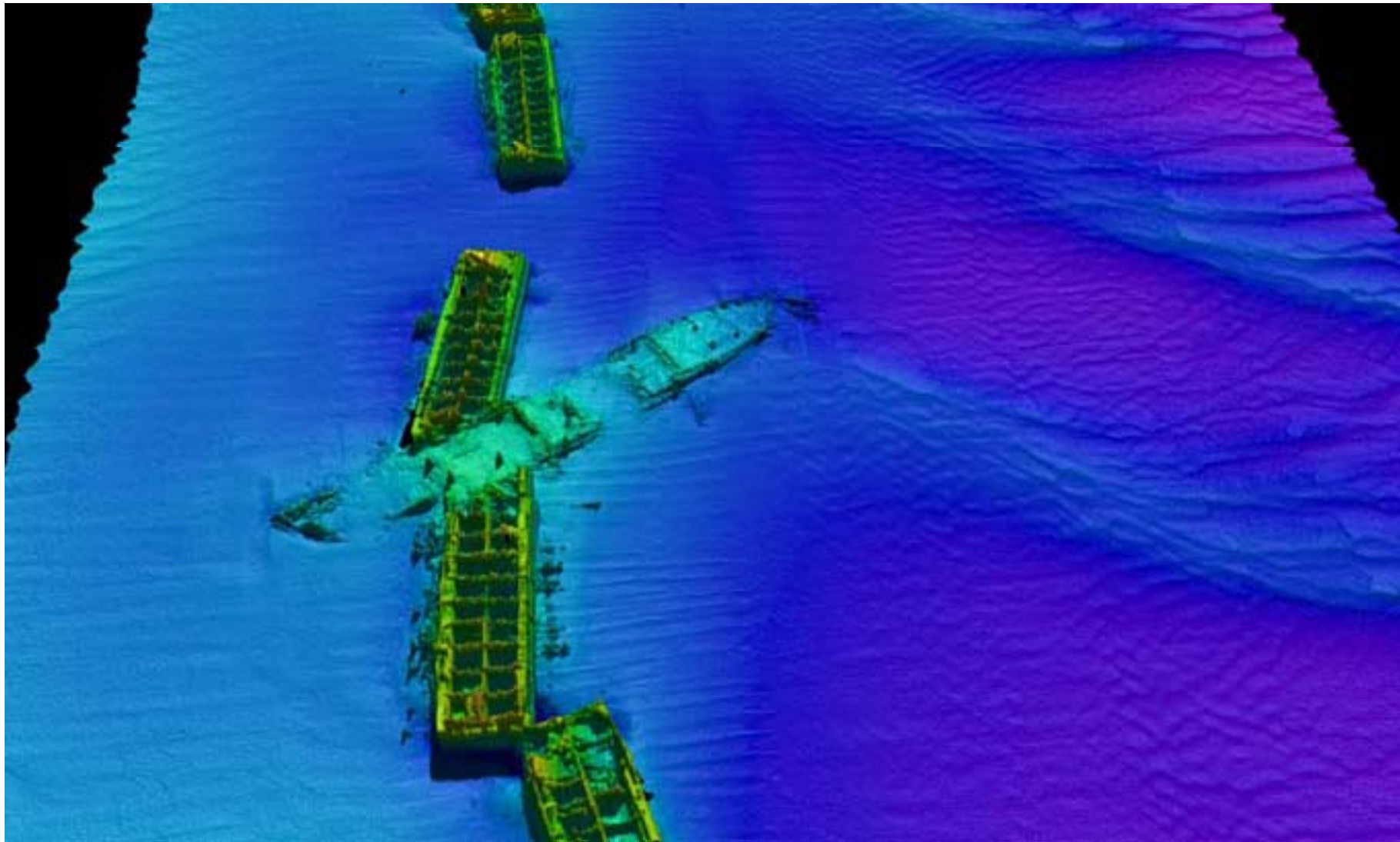
In deep water only by swath sounders on ROVs or AUVs



<http://www.geoacoustics.com/News%20Pictures/N-3PB%20Aircraft%20-%20Record%202.jpg>



Mulberry Harbor A. Start of Construction: 07.06.1944, Destroyed (storm): 20.06.1944



Mulberry Harbor: Data courtesy: Larry Mayer, University of New Hampshire



<http://www.reson.com/sw2165.asp> Shallow Water System

Micro Bathymetry in great water depth
Swath sounder on ROVs oder AUVs

AUV REMUS 6000 (IFM-GEOMAR)

Length: 3.89m

Diameter: 66cm

Weight: 880kg

Dive depth: 6000m

Operation time: 22h (120km)



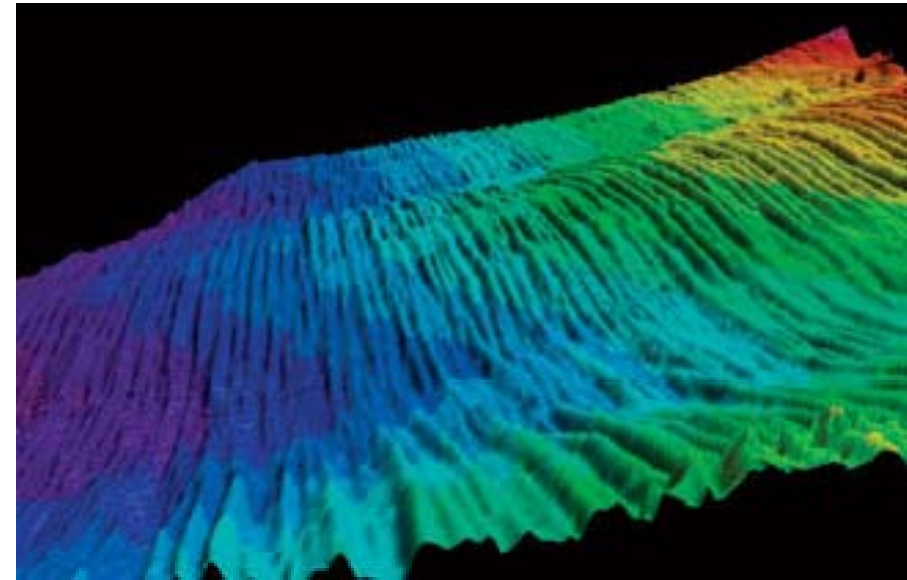


future ocean
KIEL MARINE SCIENCES

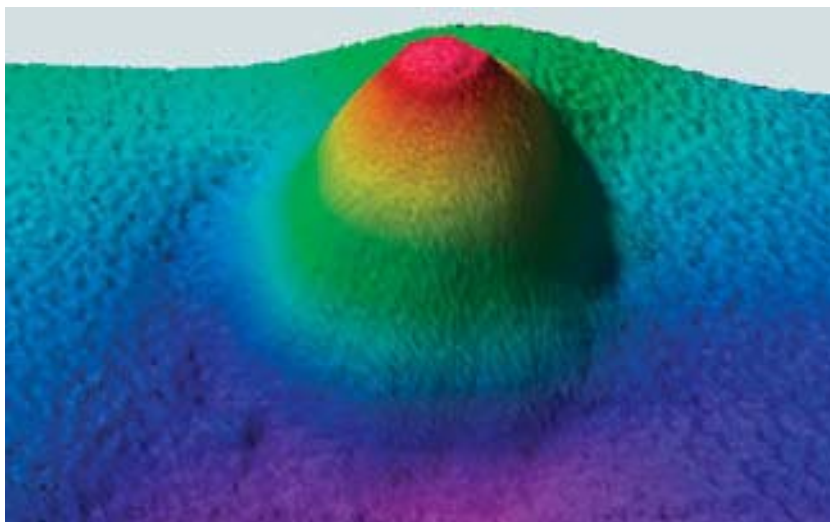
Acoustic Imaging

Bathymetry

Multibeam Echosounder



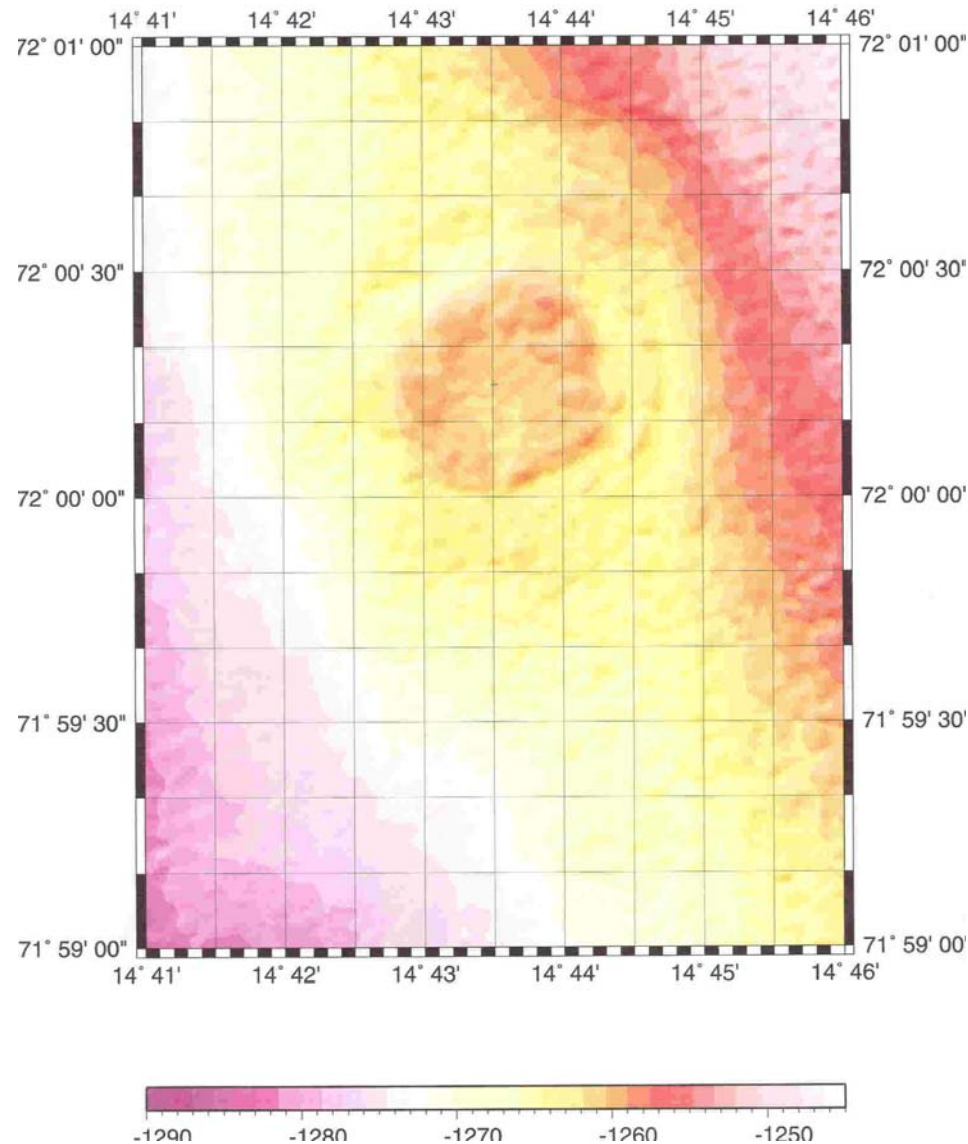
↑ Multibeam bathymetry rendering of longitudinal furrows found seaward of the toe of Sigsbee Escarpment (Gulf of Mexico). Ocean bottom currents formed furrows ranging in depth from 1 to 3 m and 5 to 10 m width.



← Multibeam bathymetry rendering of mud volcano in northern Green Canyon area of the US Gulf, 300 m wide at the base, protruding 12 m above the seabed.

Conventional Bathymetry of Haakon Mosby Mud Volcano with a Hydrosweep System

Date by A. Meyer,
AWI-Bremerhaven



Microbathymetry

 collected with a

 multibeam sounder

 mounted on a ROV

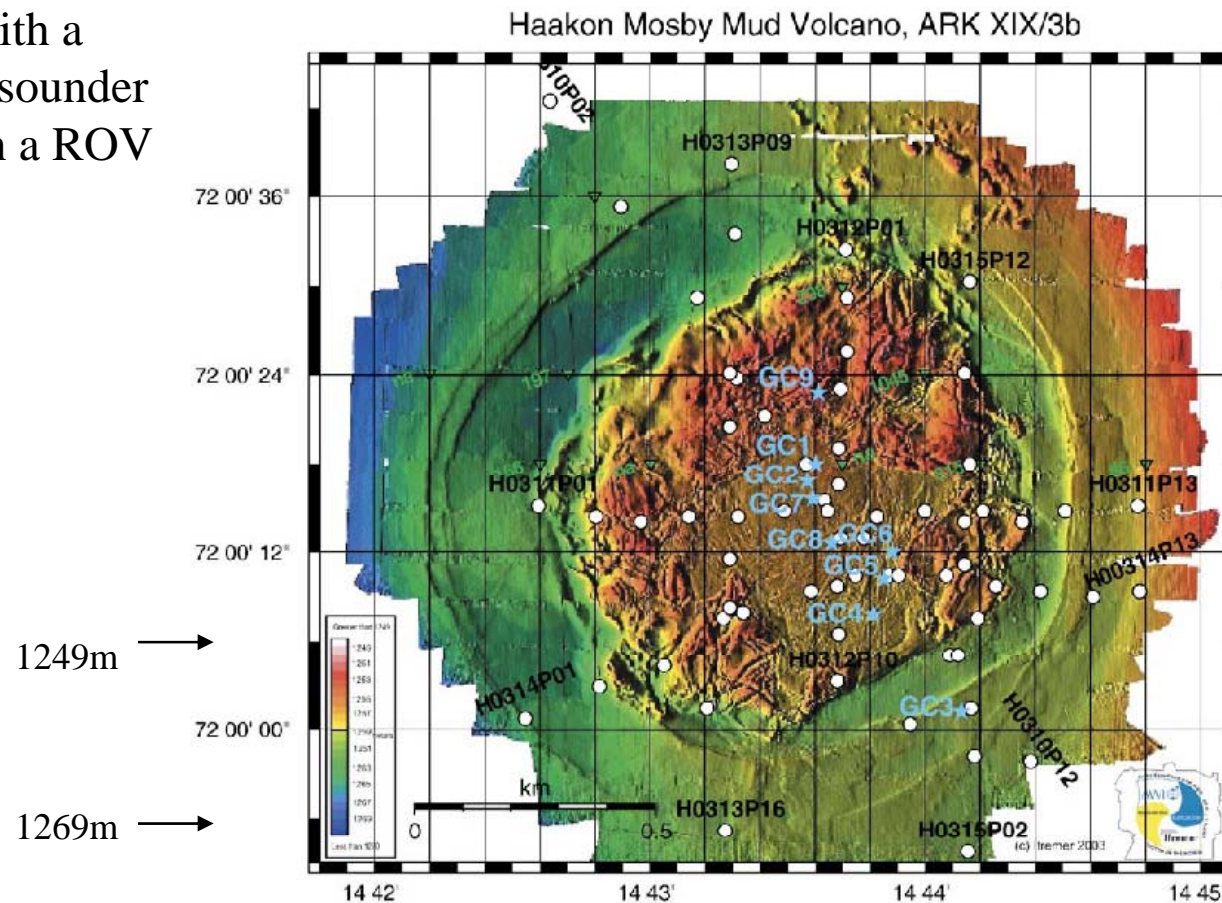
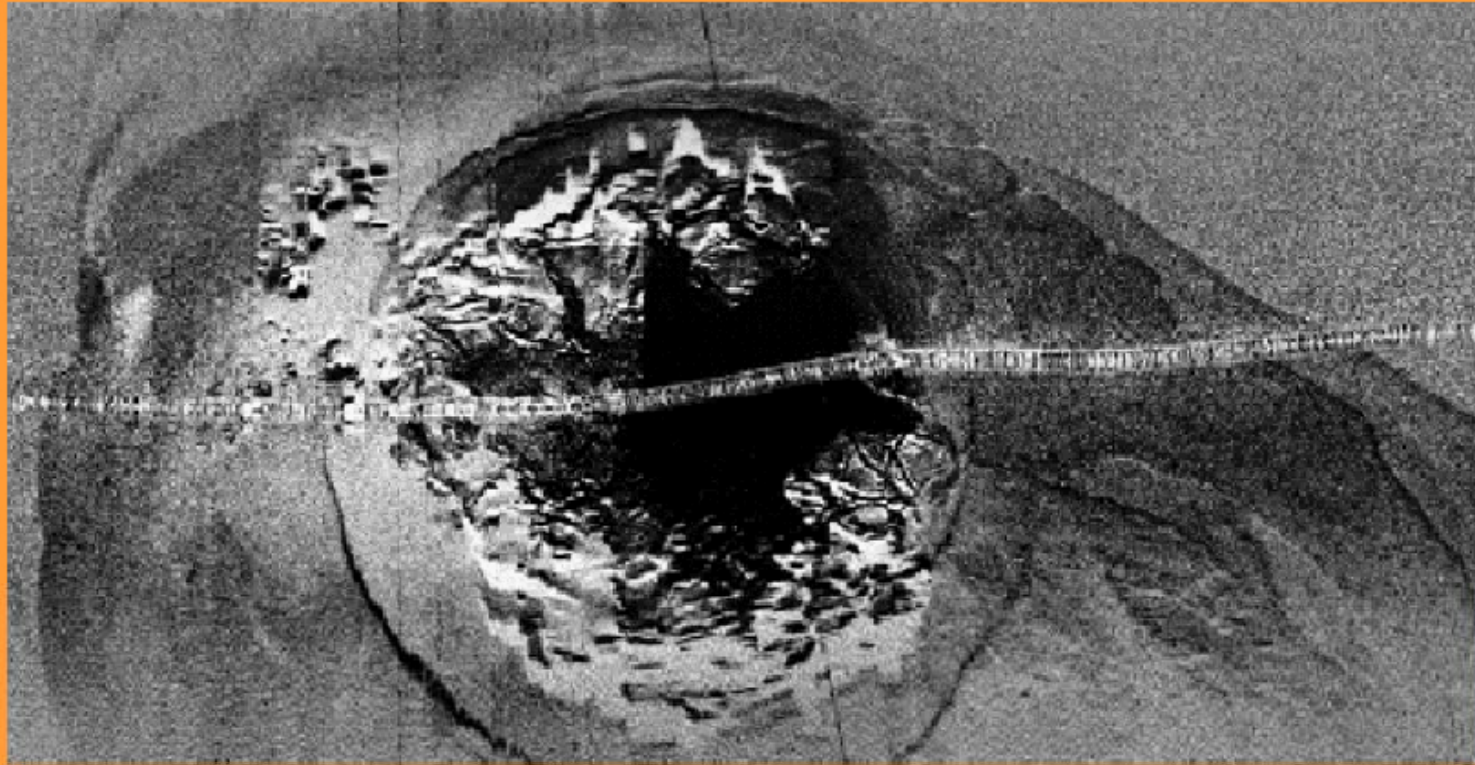


Fig. 3. High resolution bathymetry of Håkon Mosby Mud Volcano, produced by IFREMER, using deep towed multi-beam echo sounders, mounted beneath ROV Victor 6000. Overlain are positions of heat flow sites (white dots) and gravity corers (blue stars). A regional classification is (i) outside the moat, (ii) the moat ring, (iii) a rough area north and west of the centre and (iv) a smooth area expanding from the centre southwards. (For interpretation of the references to colour in this figure legend, the reader is referred to the web version of this article.)

HAAKON MOSBY MUD VOLCANO
30 kHz Side-scan Image



Side-scan image from U.S. Naval research Center, Stennis Space Center, MS)

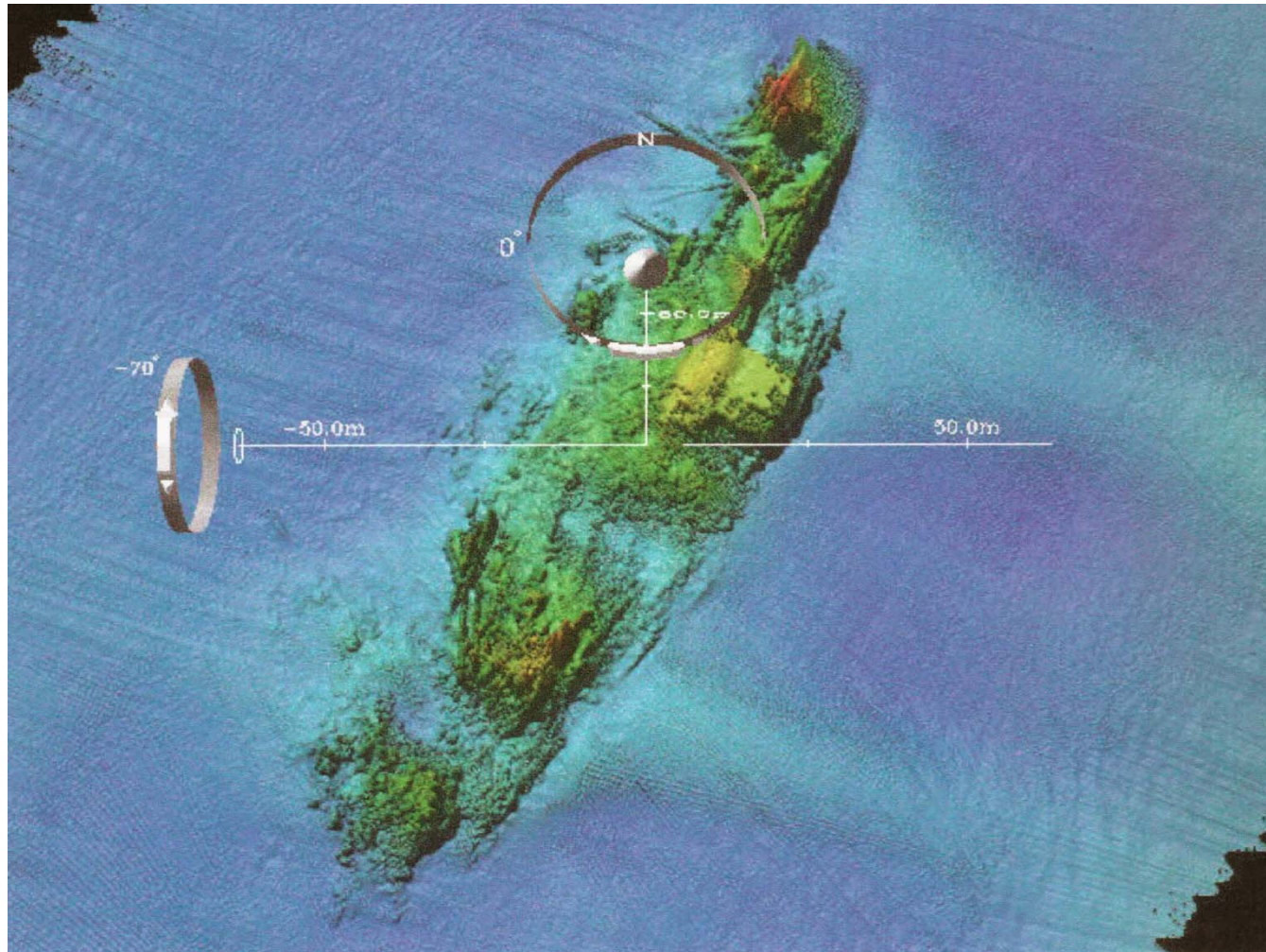


future ocean
KIEL MARINE SCIENCES

Acoustic Imaging

Bathymetry

Software for visualization (and processing) of bathymetric data



Generic Mapping Tools (GMT)

Used since 1988 (in house software at Lamont-Doherty Earth Observatory)

1991: First official release as public domain software

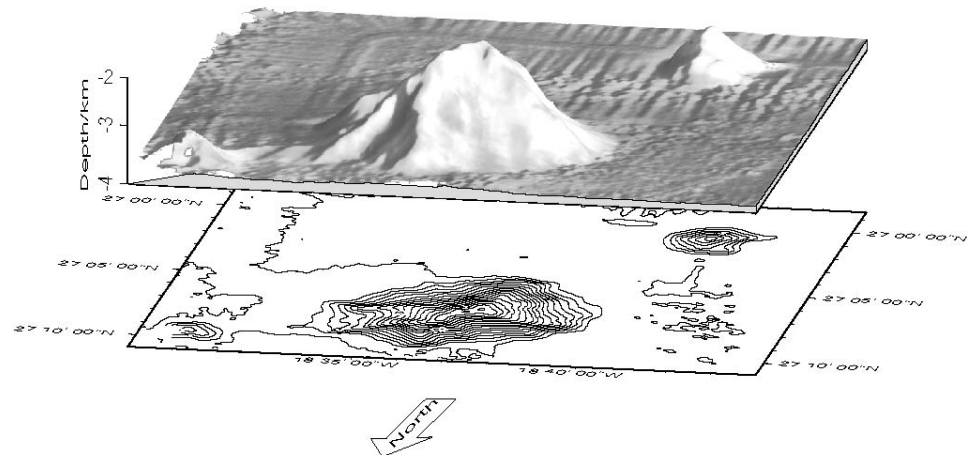
Used to manipulate columns of tabular data, time-series, and gridded data sets, and display these data in a variety of forms

Script language (same syntax as Unix)

GMT uses PostScript as output format

GMT includes more than 50 tools

Las Hijas Seamounts





future ocean
KIEL MARINE SCIENCES

Acoustic Imaging

Bathymetry

Global Mapper Interactive Low Cost program

Global Mapper Software, LLC

HOME

THE PRODUCT

DOWNLOAD TRIAL

PURCHASE

NEWS

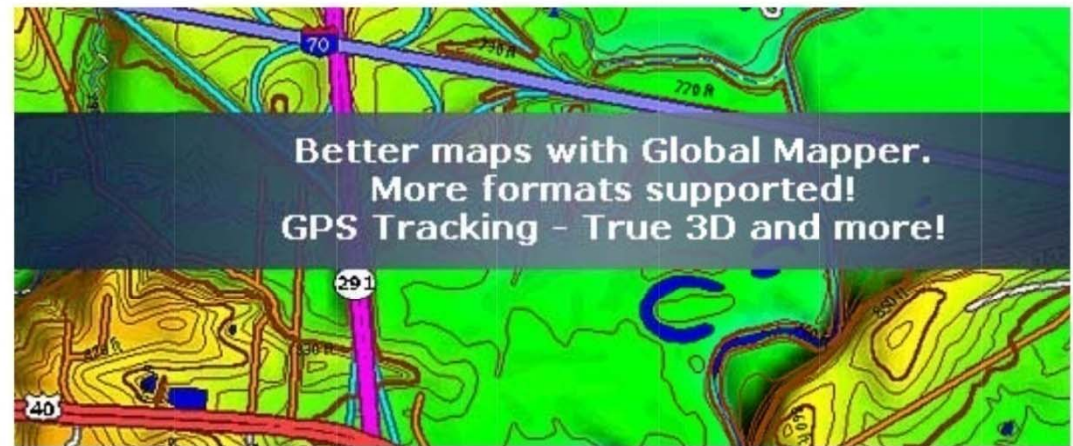
FIND DATA ONLINE

SUPPORT

DEVELOPERS

COMMUNITY

ABOUT US



Global Mapper is more than just a viewer capable of displaying the most popular raster and vector datasets. It converts, edits, prints, **tracks GPS** and allows you to utilize **GIS functionality** on your datasets in one low-cost and easy-to-use software package.

support@globalmapper.com

Global Mapper also includes the ability to directly access multiple online sources of imagery, including topographic maps, and gridded terrain data. This includes access to **worldwide high resolution color imagery from DigitalGlobe** (watermarked access for free) and access to the entire **TerraServer-USA database** of USGS satellite imagery and topographic maps free-of-charge. Global Mapper also has the ability to easily access WMS data sources, including **built-in elevation data and color imagery for the entire world**, and to view elevation data with any loaded raster imagery and vector data draped on top of it!

Global Mapper is a comprehensive software package which includes much more functionality listed here. Find out more by following this link. [Global Mapper overview](#).



future ocean
KIEL MARINE SCIENCES


Acoustic Imaging

Bathymetry

IVS 3D Fledermaus Expensive but free viewer

COMPANY
PRODUCTS
NEWS
SUPPORT
DOWNLOAD

Products > Fledermaus Standard



"3D Visualization - more than just a pretty picture"

Product Links:

- Fledermaus Standard
- Fledermaus Professional
- View3D

Application Links:

- Geological Surveys
- Hydrographic Survey QC
- Offshore Industry
- Academic Research
- Environmental Applications
- Military Applications
- Large Immersive Visualization Centers
- Marine Construction
- Coastal Zone Mapping
- Google Earth

Related Links:

- Evaluate Fledermaus Applications Technologies
- Purchase Information
- Academic Discounts
- Platforms Overview
- Standard vs. Pro
- Hardware Requirements
- Scientific Data Formats Supported

Fledermaus Standard is a powerful interactive 3D data visualization system that is used for a variety of applications including environmental impact assessment, mining, geology, and research.

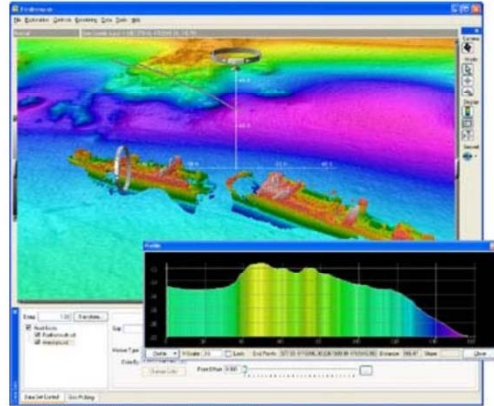
Innovative data exploration features including the ShiftScape™ rendering engine and the Bat (3D input device), allow for intuitive 3D exploration of geo-spatial data.

A wide variety of industry standard formats are supported for direct import of data to the 3D scene. Object types such as digital terrain maps, point clouds, lines, polygons, satellite imagery, etc. can all be loaded and analyzed in a single scene. Due to its flexible object oriented software design, Fledermaus can be easily tailored to support many additional visualization modules.

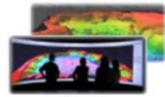
If you would like more information on Fledermaus, the [full documentation](#) is available online. A free viewer for Fledermaus files named [iView3D](#) is also available.

Features

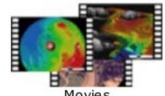
- Display scales automatically from high-end to low-end systems using the powerful ShiftScape™ rendering engine.
- Multiple data sets and types of different resolution can be visualized and interactively explored at the same time.
- Integrated support for very large data sets.
- All data sets can be geo-referenced in the 3D scene.
- Users can interactively query data sets to select coordinates for profiles and measurements.
- Advanced object oriented architecture allows easy integration of new data types into the system.
- Explorations can be recorded and used to create movies of data exploration sessions.
- Visualizations can be displayed in 3D stereo with suitable graphics hardware.
- Software and data files can be used across wide variety of computer platforms from laptops to large immersive visualization systems.



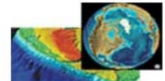
Screenshot of Fledermaus Standard



Images



Movies



Alternate Media



future ocean
KIEL MARINE SCIENCES

Submarine Mapping

Sidescan Sonar



Sidescan Sonar

5m

<http://www.marinesonic.com>

Knowledge of the Earth and its environment are proving increasingly crucial.

The morphology of the Earth is not well known because more than 2/3 of the Earth's surface is covered by oceans.

Sound waves are the only means of surveying large regions of the seafloor with reasonable accuracy.

Acoustic waves are the basis of sonars (Sound Navigation And Ranging).

Images and maps produced by sonars are not always easy to interpret, because of the complex processes at play during the reflection of the acoustic waves on the seafloor.

Topics:

Some basics

Specification of sidescan sonars

Processing of sidescan sonar data

Application and interpretation

Text Books

P. Blondel and B.J. Murton, Handbook of Seafloor Sonar Imagery, published by Wiley, 1997.

P. Blondel, The handbook of sidescan sonar, published by Springer, 2009

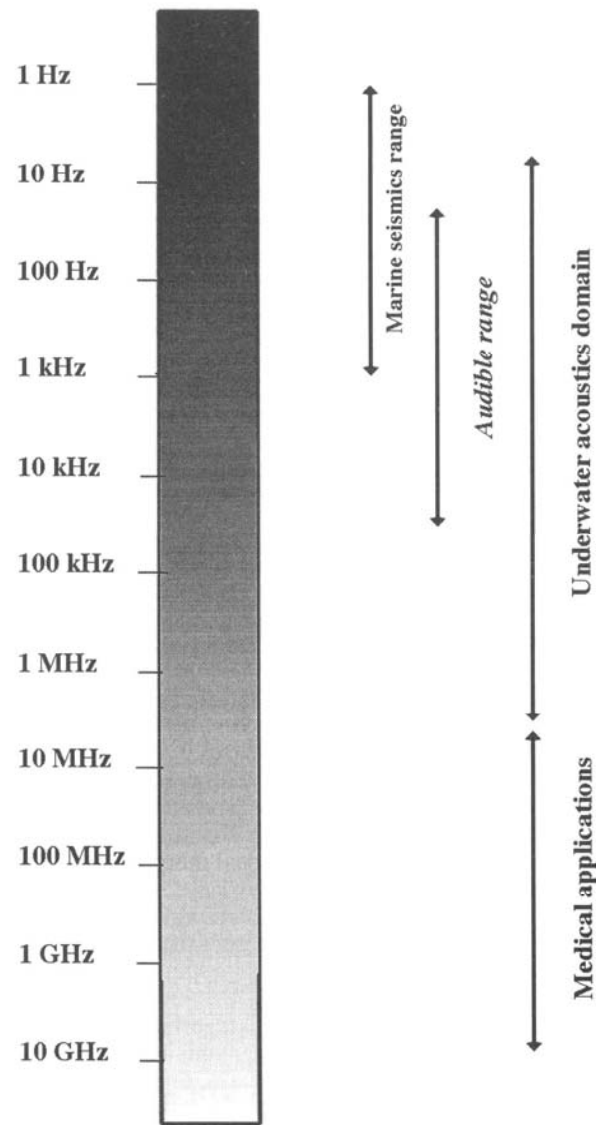


Figure 2.1. Frequencies in use by different acoustic systems

Acoustic remote sensing is the only means to map and study the surface morphology of the seafloor at all depths

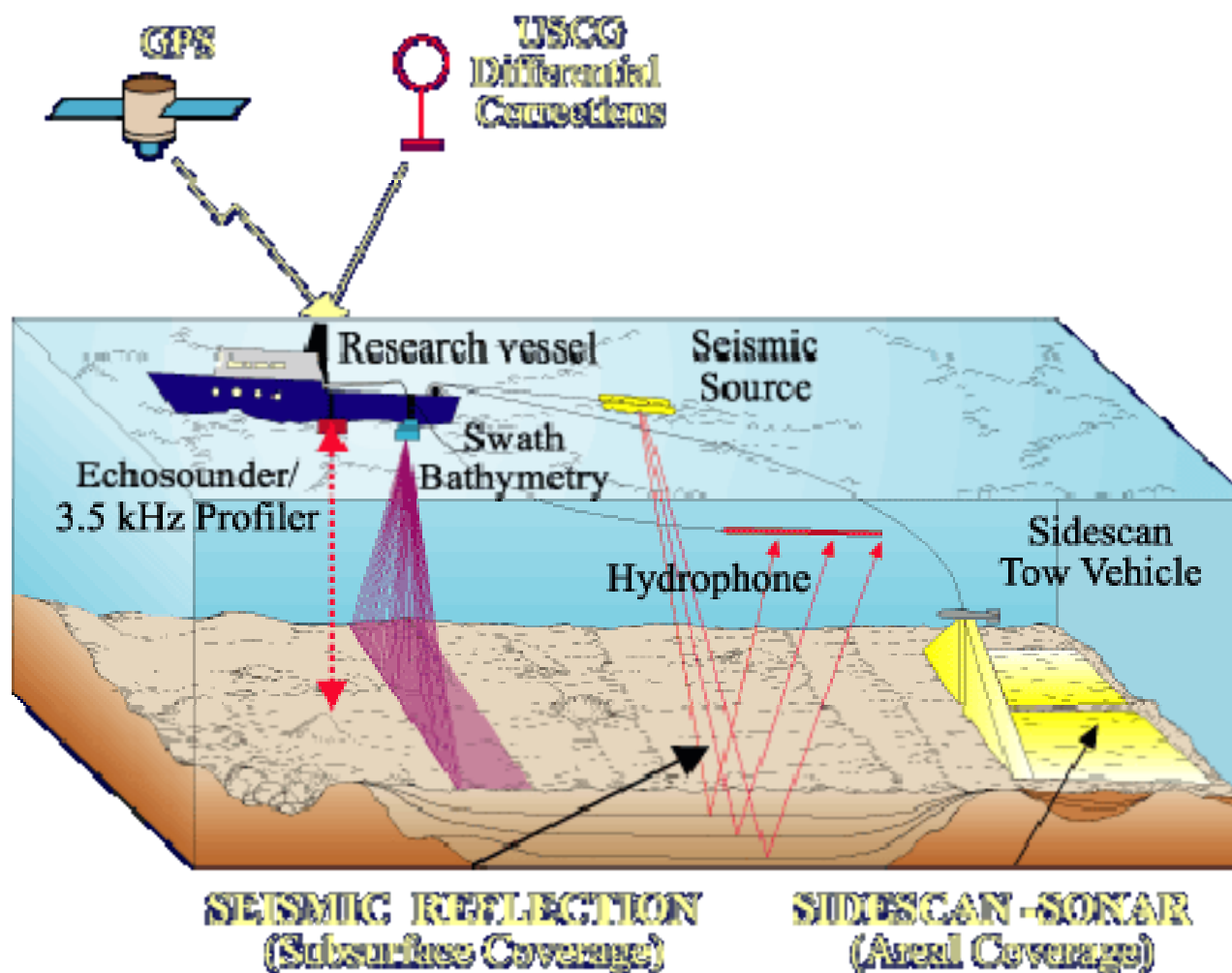
Three categories of sonars:

- Echo-sounders (one vertically orientated beam)
- Sidescan sonars (two beams, one on each side)
- Multibeam sonars (several tens of beams at each side)

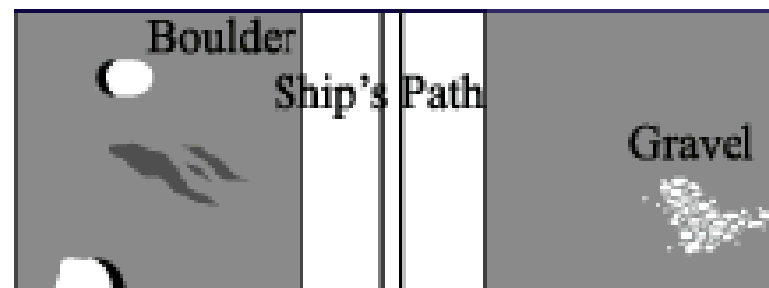
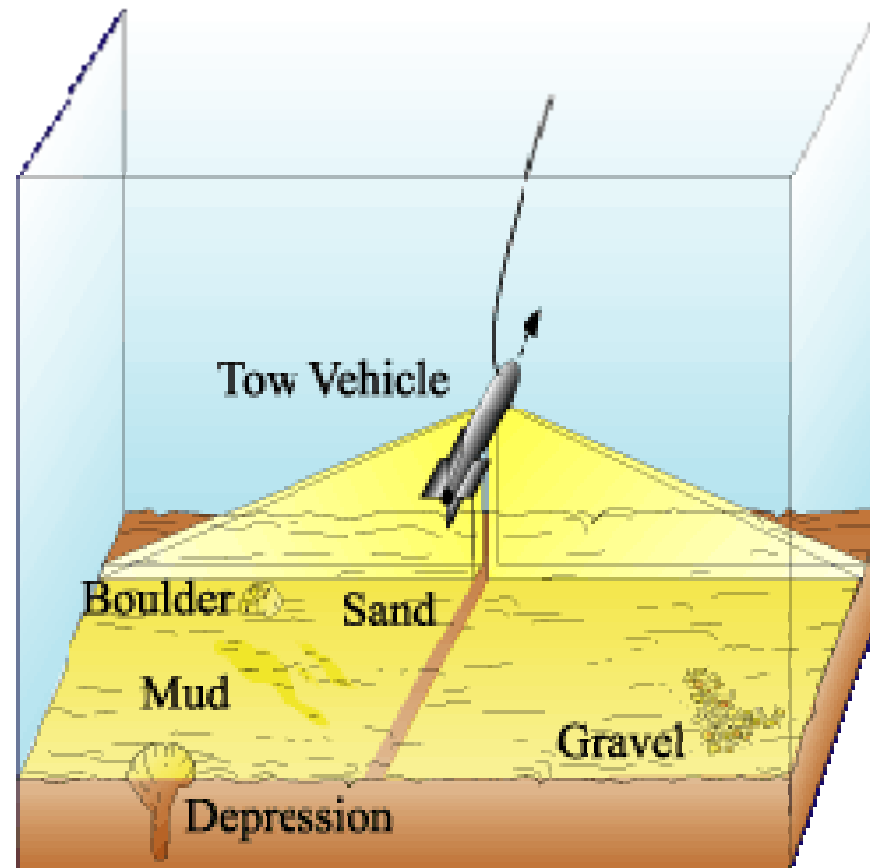
What can we measure?

- Time => Waterdepth
- Amplitude (Energy) => Acoustic imagery

Configuration at Sea



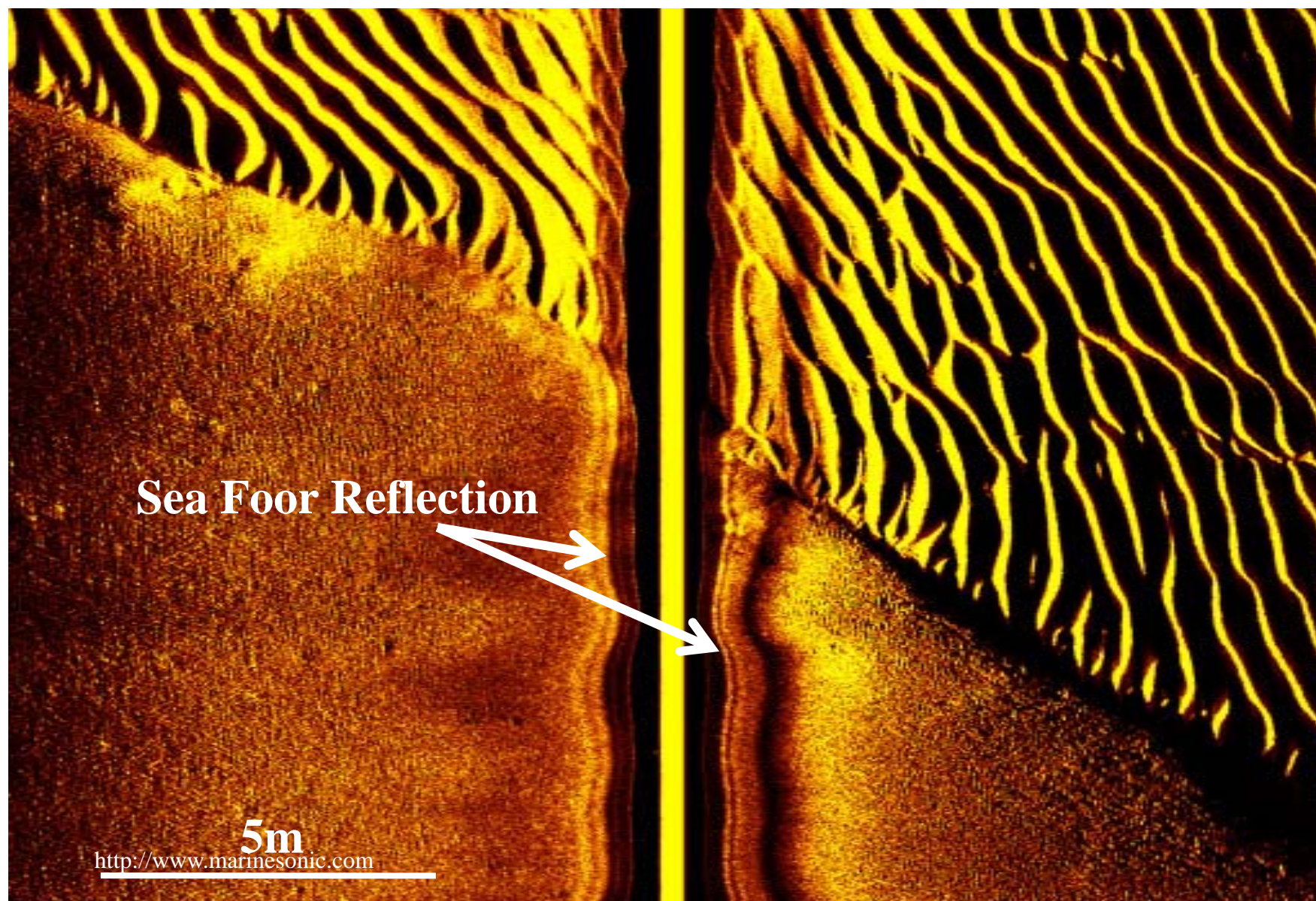
Sidescan Sonar Output: Imagery



Submarine Mapping

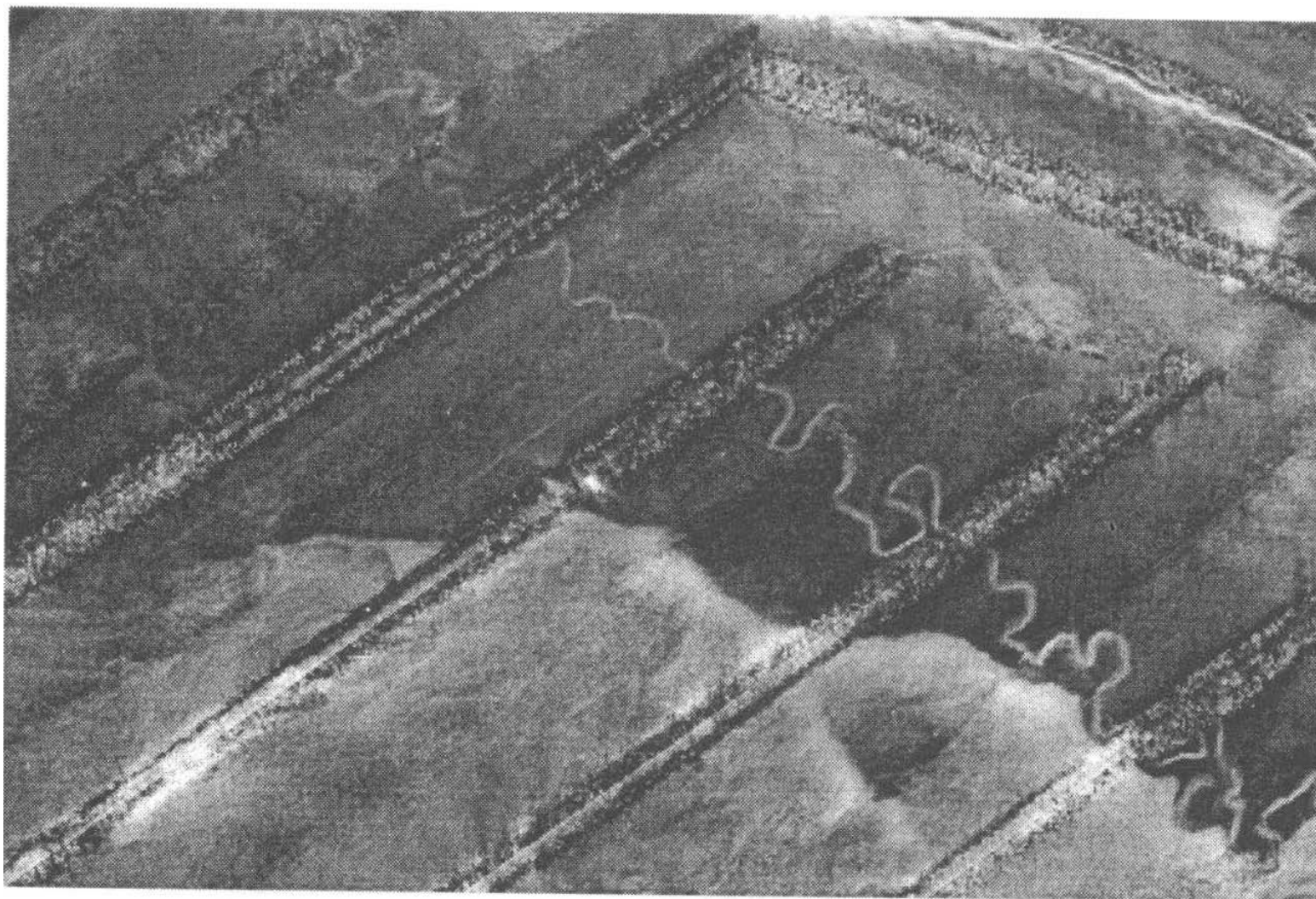
Sidescan Sonar

Unprocessed Image



Example





75 km

110 km

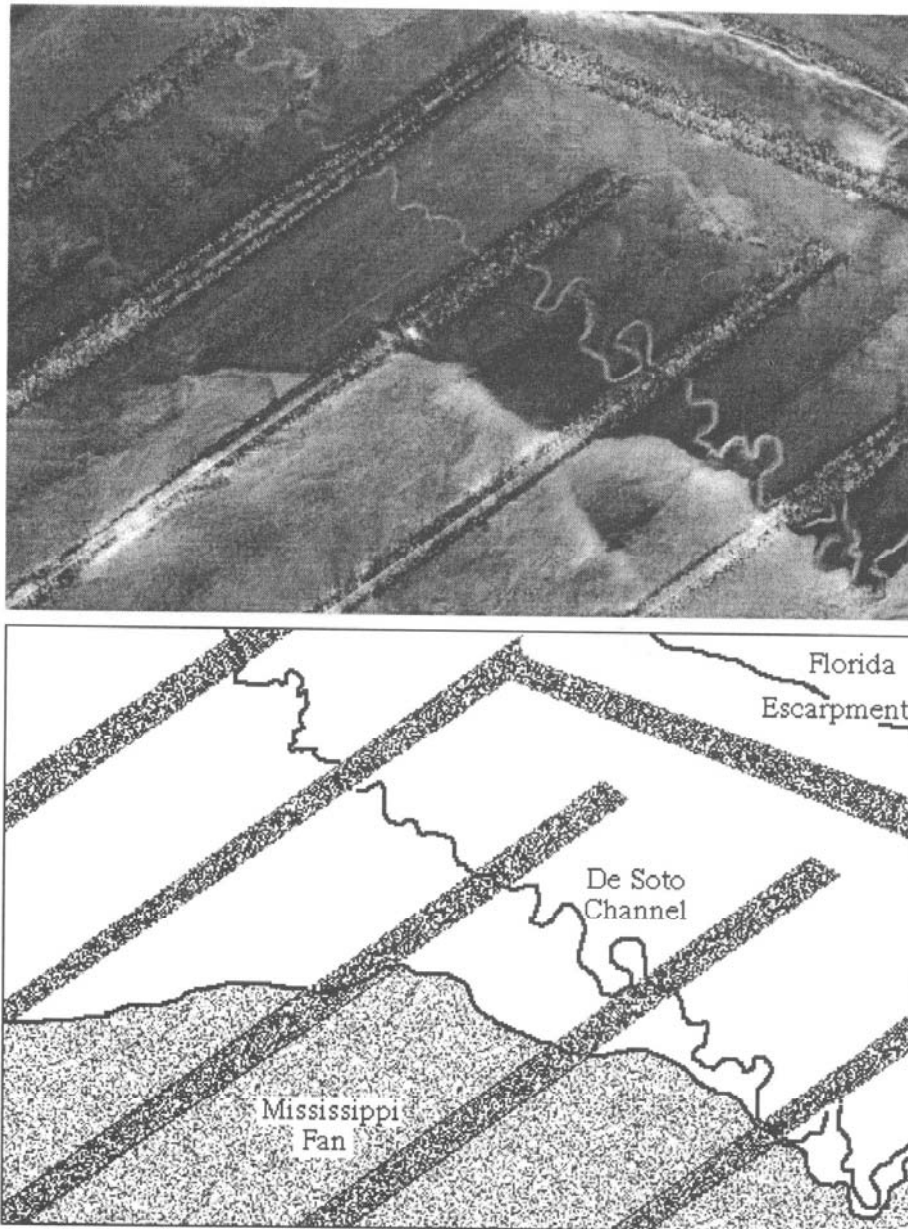


Figure 6.5. GLORIA imagery of the De Soto channel, Eastern Gulf of Mexico. The schematic interpretation shows the nadir tracks of the survey lines (dark grey pattern), the northern portion of the Mississippi Fan (light grey pattern) and the highly meandering canyon in black. The image covers a ground area of 110 x 75 km. Courtesy of the United States Geological Survey.

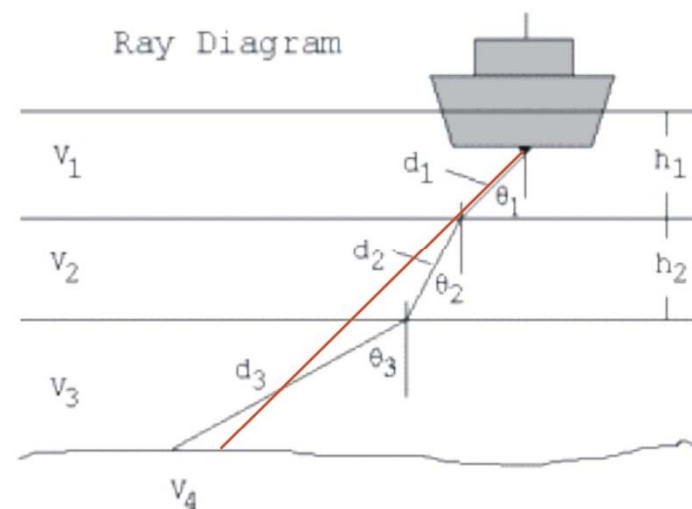
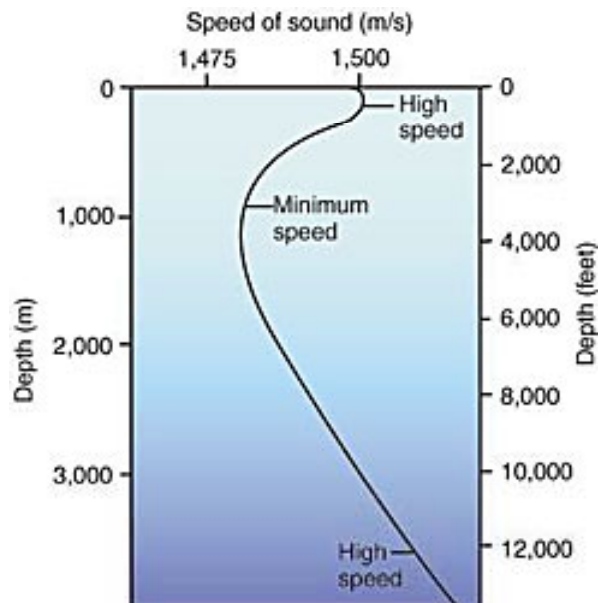
Sound waves travel through water and interact with the seafloor

1. Travel through water

Sound waves propagate in water with a velocity of ~ 1500 m/s

Local variations due to variations in water temperature, salinity, and hydrostatic pressure

Sound waves are refracted and bended due to velocity variations



2. Interaction with the seafloor (some definitions)

Slant Range: Distance between transducer and target on the seafloor

Ground Range: Horizontal distance between the sonar's nadir and the target

Incidence Angle: Angle between incoming wave and the local normal to the seafloor

Elevation Angle: Angle between the sonar's nadir and the incident beam

Line of Sight: Track of the sonar

Swath Width: Total distance ensonified across-track

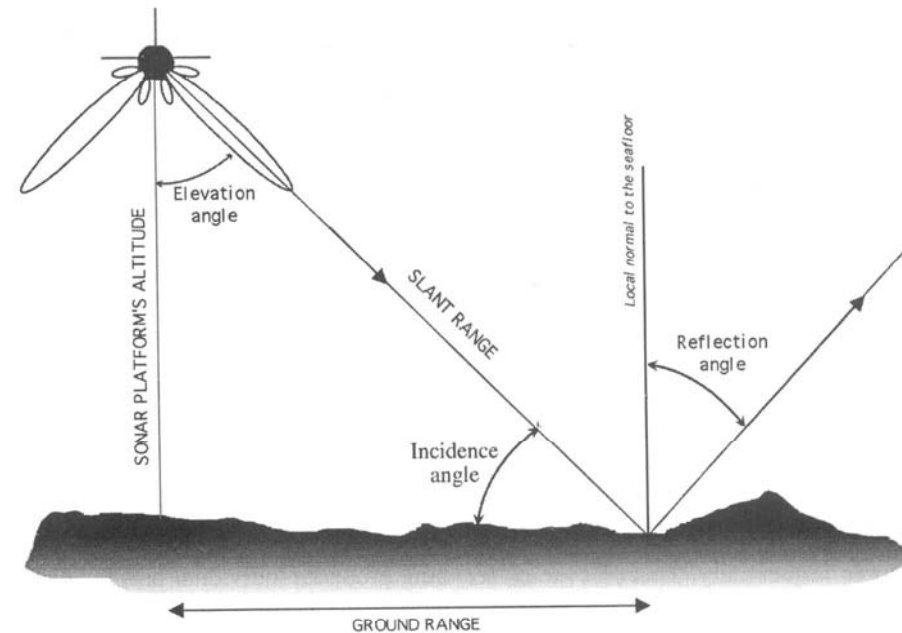


Figure 2.2. Definitions of some parameters.

Sidescan Sonar Imagery (What do we measure?)

Most of the energy is reflected away from the sonar

A small portion is lost in the ground

A small portion is scattered back to the sonar, amplified and recorded. This portion (the so called backscatter) is used to produce the Sidescan images.

The timeshift between the the transmission and the reception is directly proportional to the distance between the sensor and its target (slant range)

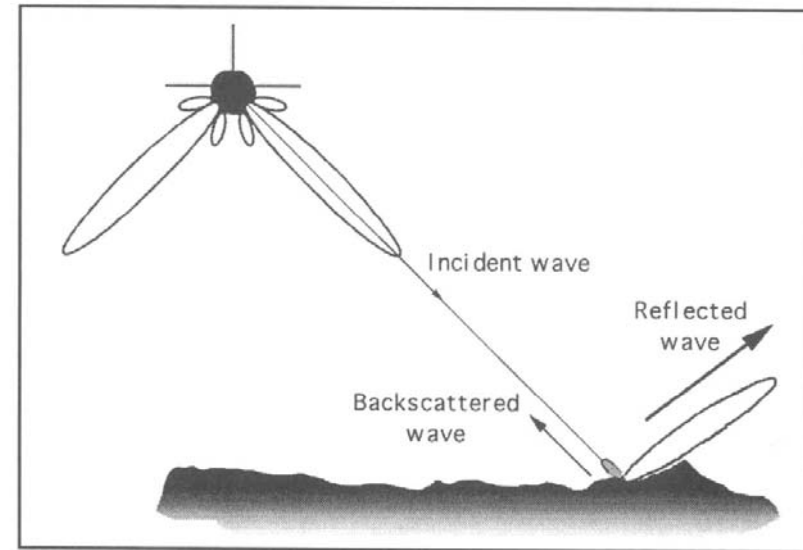


Figure 2.3. Interaction of the acoustic pulse with the seafloor.

Sidescan Sonar Imagery (What do we measure?)

For each ping, the received signal is recorded over a relatively long time-window, such that the energy returned from across a broad swath of seafloor is stored sequentially

This cross track scanning produces individual backscatter profiles

The successive along-track profiles are accumulated, and put together, form maps of the seafloor's backscatter

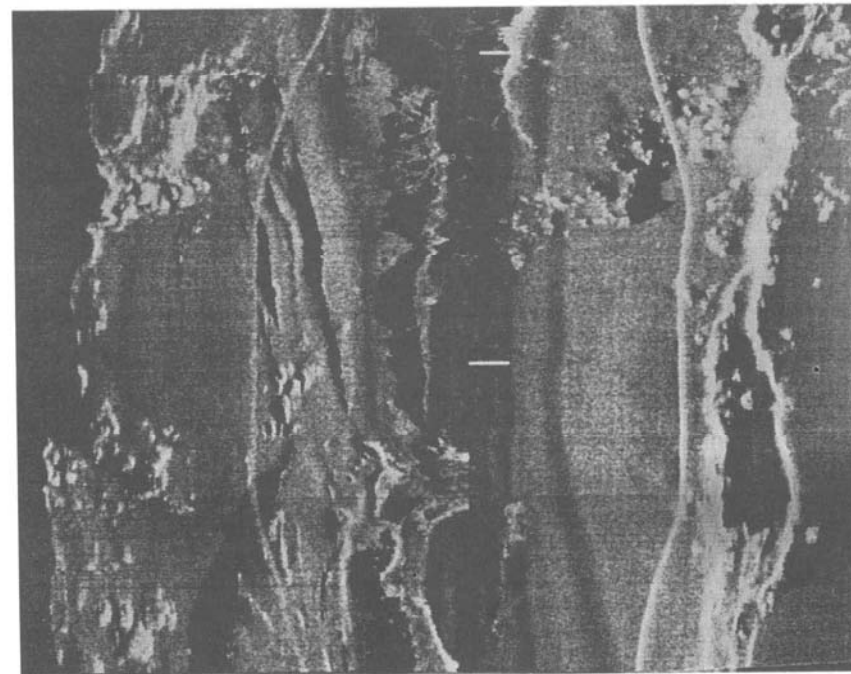
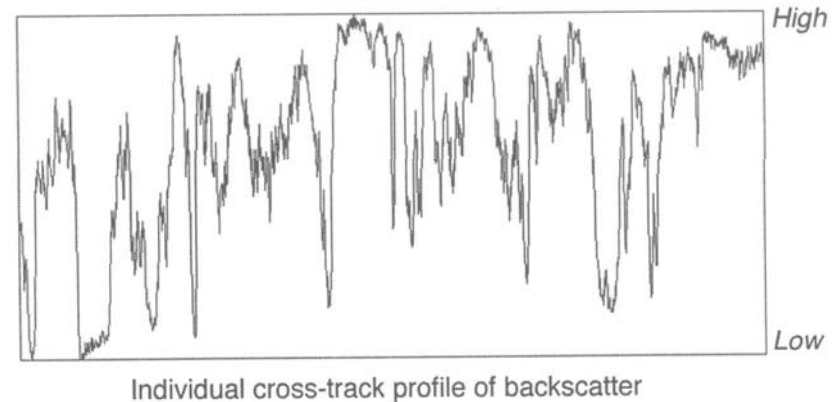


Figure 2.4. This TOBI image of the Reykjanes Ridge is formed by the acquisition of successive individual cross-track profiles of backscatter like the one above.

Sidescan Sonar Imagery (What do we measure?)

The backscattering is affected, in decreasing order of importance, by:

- The geometry of the sensor-target system (angle of incidence of each beam, local slope, etc.)
- The physical characteristics of the surface (micro-scale roughness, ...)
- The intrinsic nature of the surface (composition, density, ...)

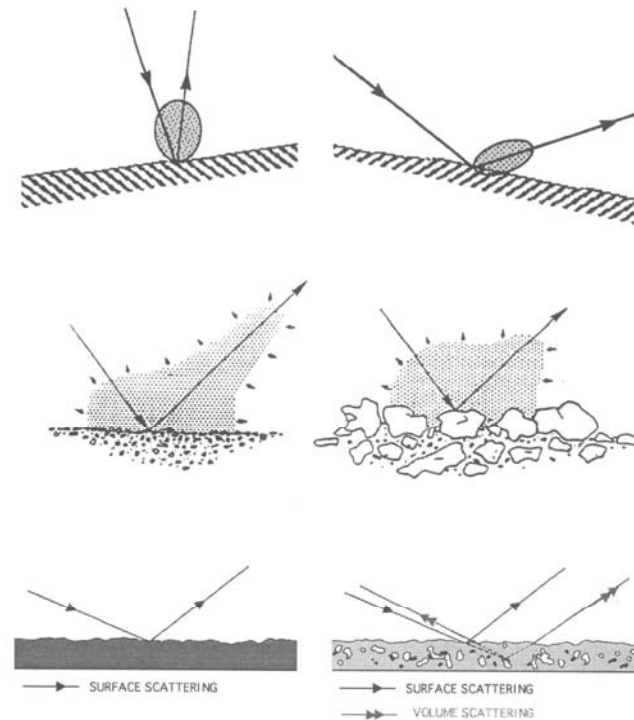


Figure 3.7. Backscattering from the seafloor is influenced by three factors (from top to bottom): local geometry of ensonification, roughness of the seafloor at scales comparable to the sonar's wavelength, intrinsic properties of the seafloor (e.g. rocks vs sediments).

Characteristics of Sonars

Towing Configuration: Deep-Tow, Shallow-Tow, Hull-mounted

Depth range: Deep-Sea Sonars, Shallow-Water Sonars

Frequency: 5kHz – 500 kHz

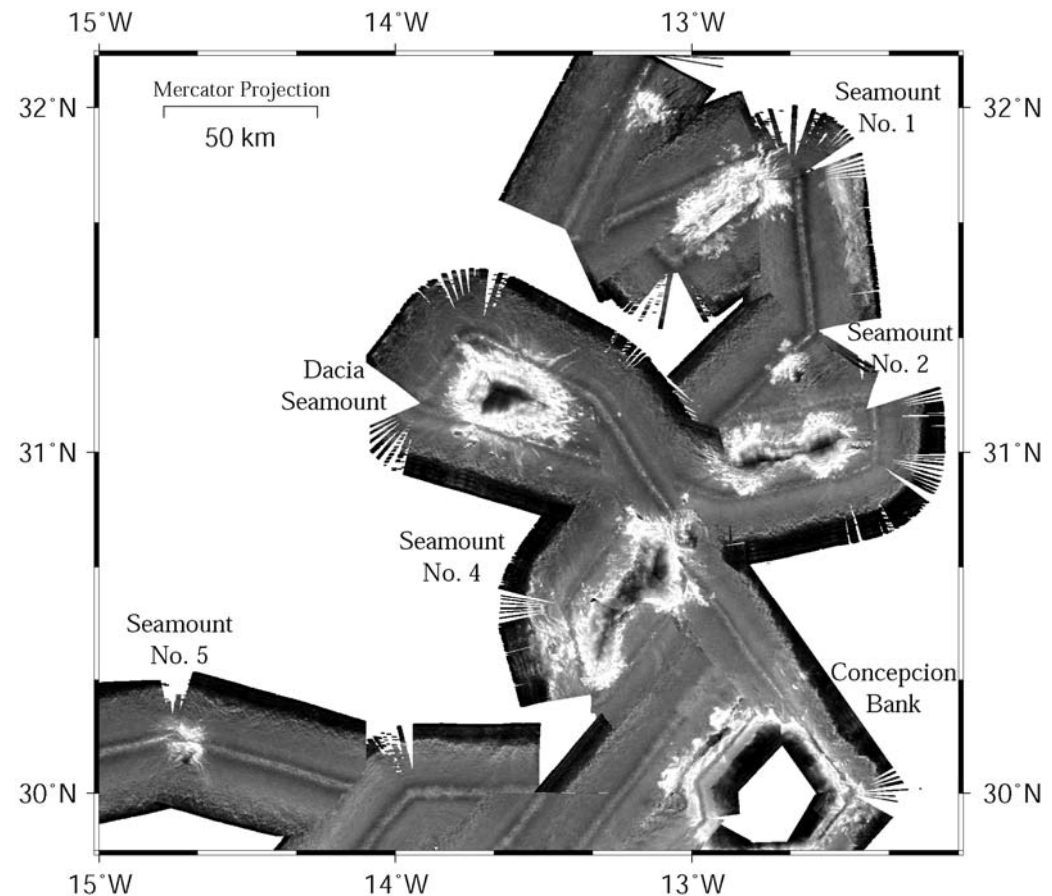
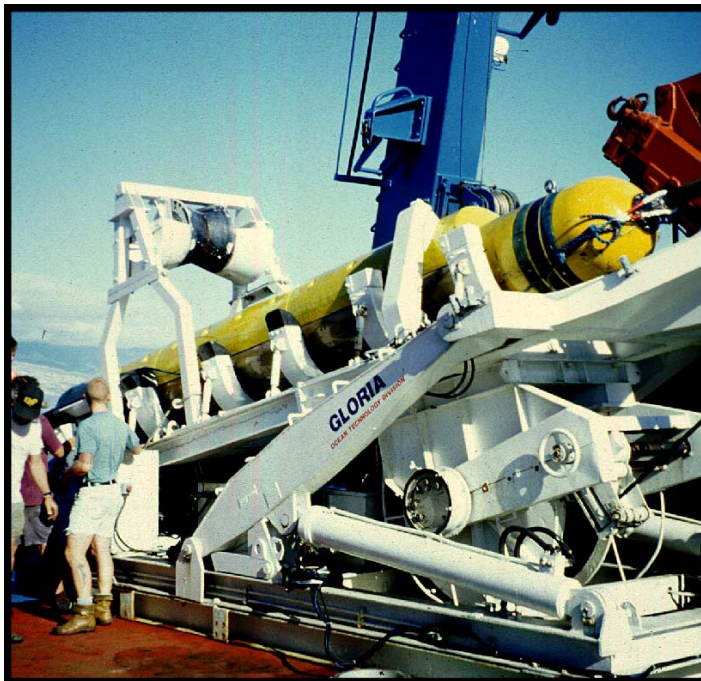
Resolution (area ensonified by each beam, the spacing between successive measurements, the pixel size in images, minimum scale at which one object can be detected or two distinct objects separated):
few cm to 100s of meters

Total Swath Width: 10 m – 60 km

Daily Coverage: $<10 \text{ km}^2$ – 20.000 km^2

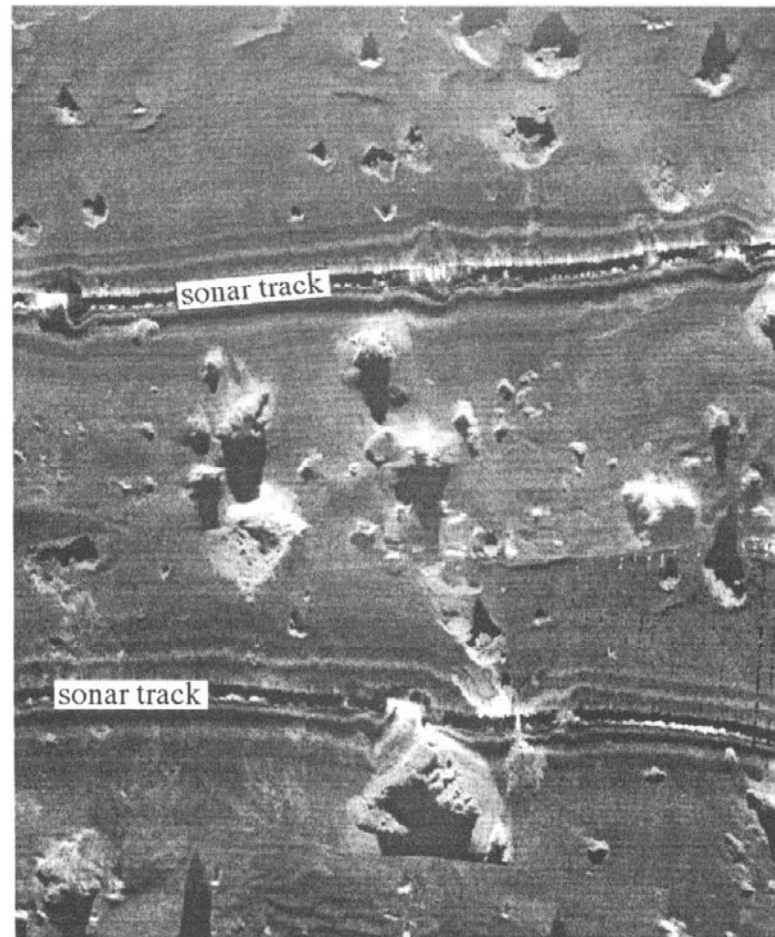
GLORIA: Geological Long-Range Inclined Asdic (ASDIC: Anti-Submarine Detection Committee)

Shallow-tow deep-water system for quick mapping of large areas (20.000 km² daily coverage)



TOBI: Towed Ocean Bottom Instrument

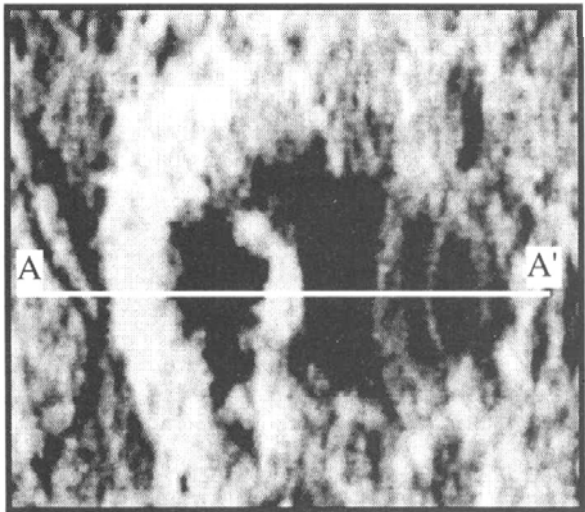
Deep-tow deep-water system for detailed surveys ($\sim 10\text{m}$ resolution, $\sim 500\text{ km}^2$ daily coverage)



9 km

Reykjanes Ridge

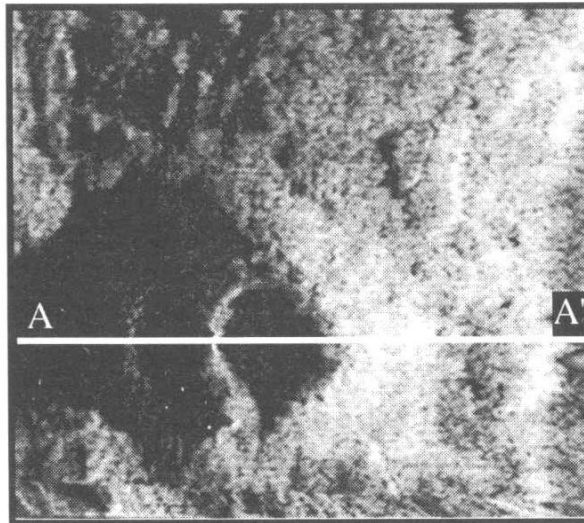
850m



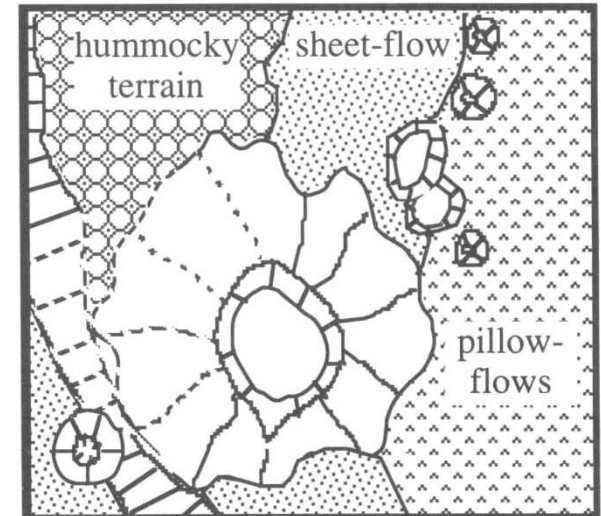
SeamarcII

Blondel and Murton, 1997

850m

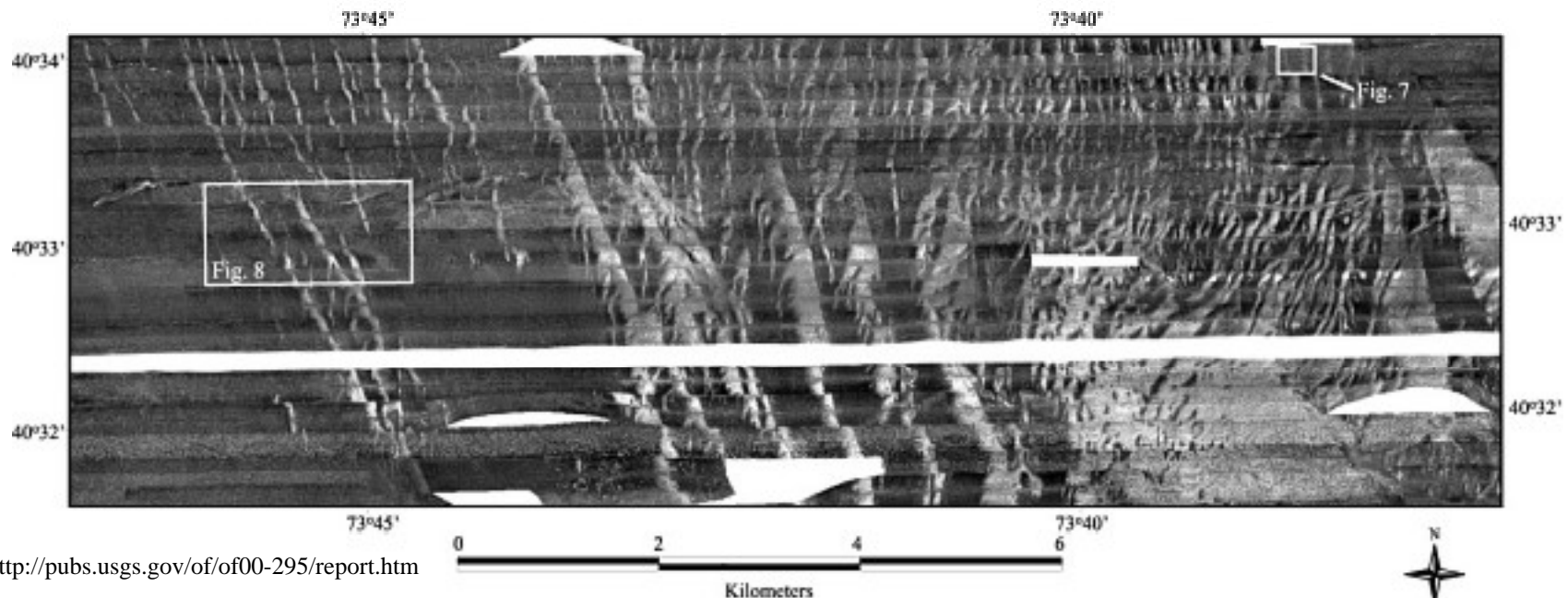


TOBI



Klein 520:

Shallow-tow shallow-water system



<http://pubs.usgs.gov/of/of00-295/report.htm>

Figure 6. Sidescan-sonar imagery showing linear, high-backscatter features interpreted to be rippled scour depressions (RSDs) offshore of Long Beach, New York. The RSDs are floored, in part, with rippled sandy gravel and gravelly sand. Areas between the RSDs are comprised of fine sand. High backscatter is represented by light tones, low backscatter by dark tones. See Figure 3 for location.

Characteristics of most commonly encountered deep-sea sonars

	GLORIA Mk II	GLORIA - B	TOBI	SeaMARC II / HMR-1	SAR 190 kHz	DSL-120	Jason 200 kHz
Operator(s)	SOC, USGS, ...	SOC	SOC	Univ. of Hawaii	IFREMER	WHOI	WHOI
Type	Shallow-tow	Shallow-tow	Deep-tow	Shallow-tow	Deep-tow	Deep-tow	Deep-tow
Depth range	200 - 11,000 m	200 - 11,000 m	< 10,500 m	100 - 11,000 m	< 6,200 m	< 6,100 m	< 6,000 m
Total swath width	up to 60 km (typically 45)	45 km (imagery) 4.5 x depth (bathymetry)	6 km	up to 10 km (typically 10 km)	up to 1.5 km	0.1 to 1 km (typically 1 km)	0.3 km
Typical navigation error	100 - 1000 m satellite	100 - 1000 m satellite	50-500 m long-baseline	100 - 1000 m satellite	5 - 10 m long-baseline	5 - 10 m long-baseline	0.1 - 10 m short- or long-baseline
Typical daily coverage	20,000 km ²	20,000 km ² (imagery) 11,500 km ² (bathymetry)	470 km ²	10,000 km ²	10 km ²	90 km ²	10 km ²
Frequency (wavelength)	6.3 - 6.7 kHz 23.8 - 22.4 cm	6.25 - 6.75 kHz 24 - 22.2 cm	30-32 kHz 5 - 4.7 cm	11-12 kHz 13.6 - 14.9 cm	170 - 190 kHz 0.9 - 0.8 cm	120 kHz 1.25 cm	200 kHz 0.75 cm
Footprint size (along- x across-track)	175 x 45 to 657 x 45 m	125 x 45 m to 1000 x 45 m	8 x 3.5 m to 43 x 2.1 m	120 x 10 m to 197 x 2 m	0.7 x 0.8 m to 3 x 0.4 m	3.3 x 0.33 m to 13.7 x 0.15 m	0.5 x 0.29 m to 2.4 x 0.15 m
Output data	Imagery	Imagery Bathymetry	Imagery	Imagery Bathymetry	Imagery	Imagery Bathymetry	Imagery Bathymetry
Typical size of daily data	< 1 Gbyte	~ 5.3 Mbyte	528 Mbyte	< 1 Gbyte	< 1 Gbyte	> 1 Gbyte	~ 100 Mbyte
Ancillary data	Heading	Heading + Roll, pitch, yaw	Heading, depth, speed + Roll, pitch, yaw	Heading + Roll, pitch, yaw	Heading, depth, speed	Heading, depth + Roll, pitch, yaw	Heading, depth + Roll, pitch, yaw

Characteristics of some commonly encountered shallow-water sonars (1)

	[TAMU] ²	EG&G Deep-Tow	EG&G model 272T	Klein 590/595	Klein 520	Simrad MS-992
Operator(s)	Texas A&M Univ.	Government and commercial surveys	Government and commercial surveys	Klein Assoc. Massachusetts, U. Kiel, ...	U. Kiel, Klein Assoc., etc.	Commercial, military ...
Type	Shallow-tow	Deep-tow	Shallow-tow	Shallow-tow	Shallow-tow	Deep-tow
Depth range	< 500 m	< 600 m		< 1,000 m	< 300 m	< 1,000 m
Total swath width	100 m - 30 km	< 1 km	N/A	< 600 m (100 kHz) < 400 m (500 kHz)	25 m - 600 m	10 - 800 m
Typical navigation error	< 100 m satellite + near-shore reckoning	< 100 m satellite + near-shore reckoning	< 100 m satellite + near-shore reckoning	< 100 m satellite + near-shore reckoning	< 100 m satellite + near-shore reckoning	< 100 m satellite + near-shore reckoning
Typical daily coverage	< 13,000 km ²	Dependent on survey speed	Dependent on survey speed	Dependent on survey speed	Dependent on survey speed	Dependent on survey speed
Frequency (wavelength)	11/12 kHz 72 kHz	59 kHz	105 kHz	100 kHz 500 kHz	500 kHz	120 kHz 330 kHz
Footprint size (along- x across-track)	Not available	1/400 of the range	N/A	N/A	N/A	N/A
Output data	Imagery Bathymetry	Imagery	Imagery	Imagery	Imagery	Imagery
Typical size of daily data	< 1 Gbyte					
Ancillary data	Depth + Roll, pitch, yaw	Speed, depth, temperature				N/A

Characteristics of some commonly encountered shallow-water sonars (2)

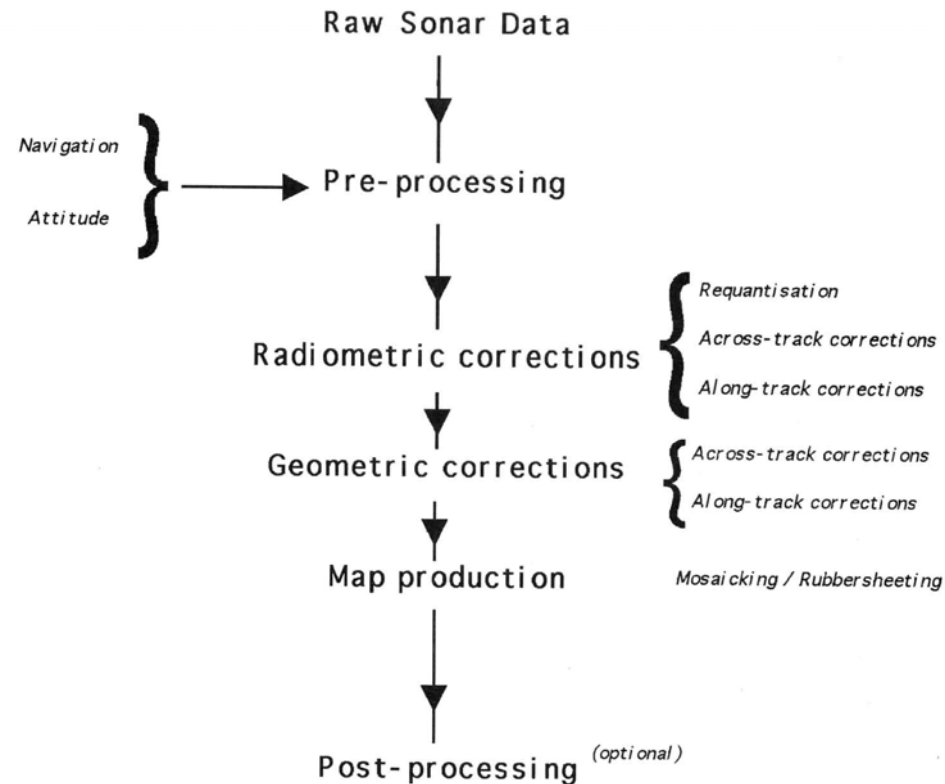
	OKEAN	MAK-1	EG&G990S	Widescan 60	AMS-36 /120S1	Sys09 (SSI Int'l.)
Operator(s)	CIS States	CIS States	Commercial applications, GPI Kiel	Commercial applications, SOC	Acoustic Marine Systems, Inc.	Commercial applications
Type	Shallow-tow	Deep-tow	Deep-tow	Shallow-tow	Deep-tow	Shallow-tow
Depth range				< 300 m	< 6,000 m	60 - 10,000 m
Total swath width	2 x 8,000 m	2 x 1,000 m or 2 x 250 m	2 x 400 m	37.5 m to 400 m	≤ 1,000 m	< 20 km
Typical navigation error	100 - 1000 m satellite	SBL net	< 100 m satellite + near-shore reckoning	< 100 m satellite + near-shore reckoning	100 - 1000 m satellite	100 - 1000 m satellite
Typical daily coverage	600 km ²	Dependent on survey speed	Dependent on survey speed	Dependent on survey speed	Dependent on survey speed	Dependent on survey speed
Frequency (wavelength)	9.5 kHz	30 kHz or 100 kHz		100 kHz/ 325 kHz	33.3 / 36 kHz	9/10 kHz
Footprint size (along- x across-track)	100 x 5 m	35 x 0.5 m	N/A	~ 0.2 m	< 1 m	0.2 x 0.2 m to 10 x 10 m
Output data	Imagery	Imagery	Imagery	Imagery	Imagery	Imagery Bathymetry
Typical size of daily data	≤ 350 Mbyte	≤ 1 Gbyte	Paper record	« 1 Gbyte	≤ 1 Gbyte	> 1 Gbyte
Ancillary data	N/A	N/A	Pressure, heading, speed, temperature	Altitude	Altitude, roll, pitch, yaw	N/A

Some multibeam systems also provide sidescan imagery of pseudo-sidescan imagery (backscatter values associated with each beam)

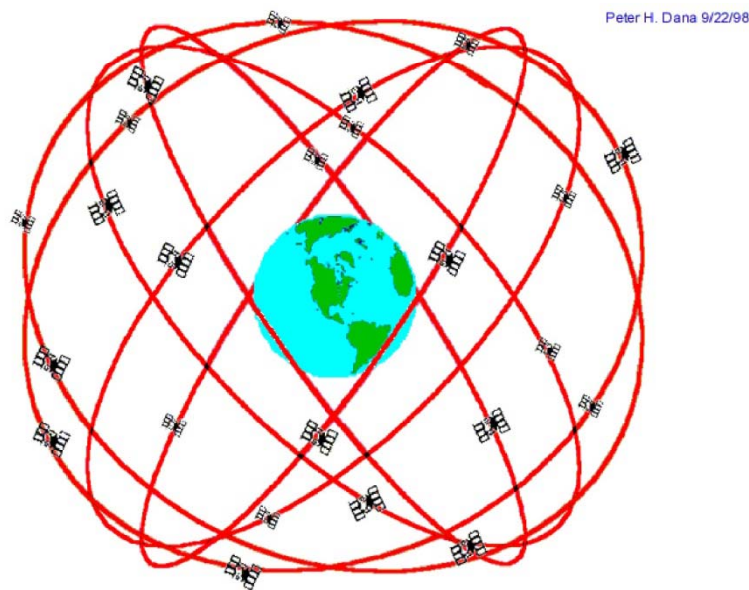
	SeaBeam 2000	Hydrosweep	Simrad EM-12	Simrad EM-100	Simrad EM-1000
Operator(s)	SIO, JMSA, KORDI	UW ¹ , LDEO ² , Germany, India, others ...	SIMRAD A/S, RVS, IFREMER ...	SIMRAD A/S, Canadian Hydrographic Service ...	SIMRAD A/S, Canadian Hydrographic Service ...
Type	Hull-mounted	Hull-mounted	Hull-mounted	Hull-mounted	Hull-mounted
Depth range	200 - 11,000 m	10 - 10,000 m	10-11,000 m	10-700 m	3-1,000 m
Total swath width	90° - 120 °	2 x water depth (less if depth > 7 km)	150° (7.3 x water depth) 90°-120° for EM-12S	150° (7.3 x water depth)	150° (7.3 x water depth)
Typical navigation error	100 - 1,000 m (satellite positioning)	100 -1,000 m (satellite positioning)	100 - 1,000 m (satellite positioning)	100 - 1,000 m (satellite positioning)	100 - 1,000 m (satellite positioning)
Typical daily coverage	2,500 km ²	3,700 km ²	4,000 km ²	Dependent on survey speed	Dependent on survey speed
Frequency (wavelength)	12 kHz (12.5 cm)	15.5 kHz 9.7 cm)	13 kHz (11.5 cm)	95 kHz (1.6 cm)	95 kHz (1.6 cm)
Footprint size (along- x across-track)	3.5% x 3.5% water depth	134 x 134 m	170 x 170 m	170 x 170 m	170 x 170 m
Output data	Bathymetry + backscattering amplitude	Bathymetry + backscattering amplitude	Bathymetry + backscattering amplitude	Bathymetry + backscattering amplitude	Bathymetry + backscattering amplitude
Typical size of daily data	< 1 Gbyte	~ 1 Gbyte	Not available	Not available	Not available
Ancillary data	Heading + Roll, pitch, yaw	Heading + Roll, pitch	Heading + Roll, pitch, yaw	Heading + Roll, pitch, yaw	Heading + Roll, pitch, yaw

Processing of Sidescan Sonar Data

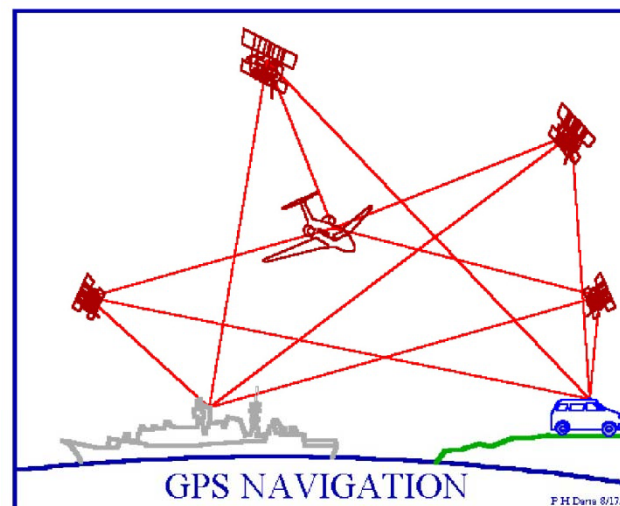
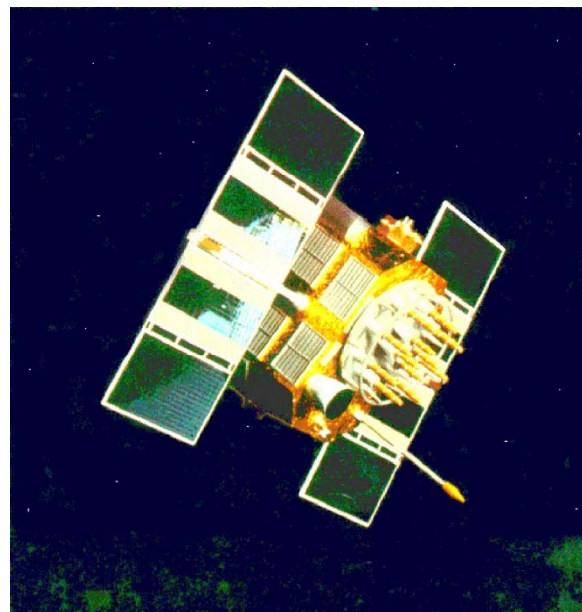
- Pre-Processing:** Preparation of the raw sonar data for processing
- Processing:** Processing per se is the transformation of the raw sonar data to usable images or grids
- Post-Processing:** All operations which are not necessary for a correct interpretation but constitute a definite plus



Navigation (Ship)



GPS Nominal Constellation
24 Satellites in 6 Orbital Planes
4 Satellites in each Plane
20,200 km Altitudes, 55 Degree Inclination



Navigation (Sonar)

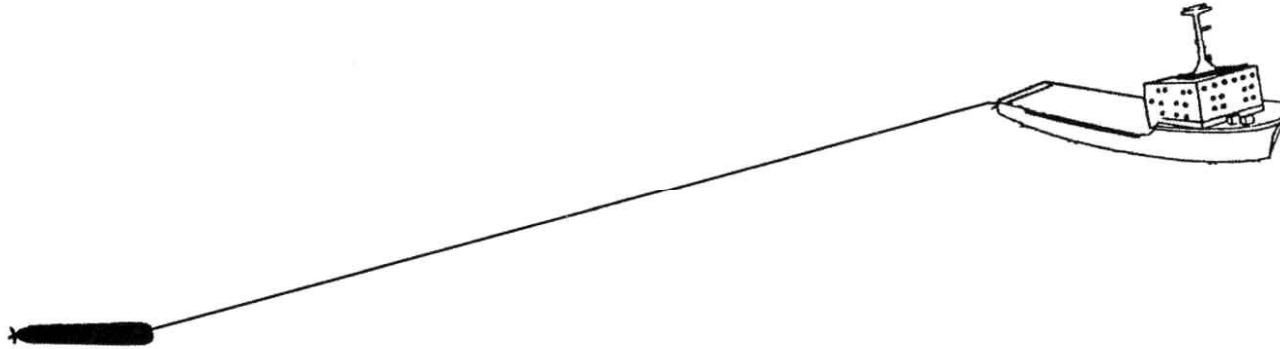


Figure 2.7. Layback of the towfish. The cable is assumed straight.

The layback of the towfish is computed from the length of cable out and simple trigonometric relations assuming the cable is straight. It is obviously inaccurate for long cable lengths, but it is the easiest and cheapest of the positioning methods.

Navigation (Sonar)

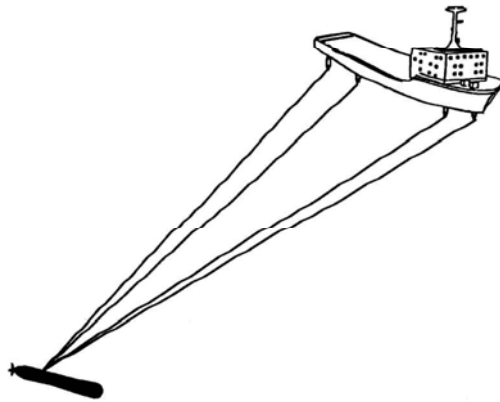


Figure 2.8. Short baseline system (SBL).

A short baseline (SBL) consists in acoustic transponders placed on the hull of the ship as a net, and receiving signals from a transponder on the towfish.

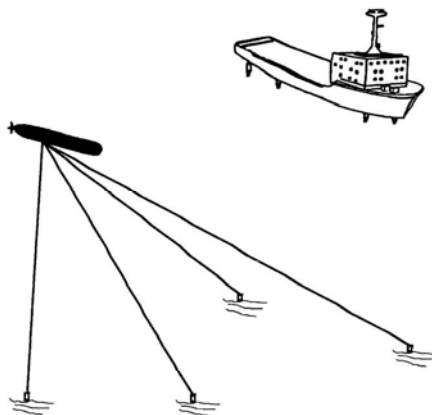
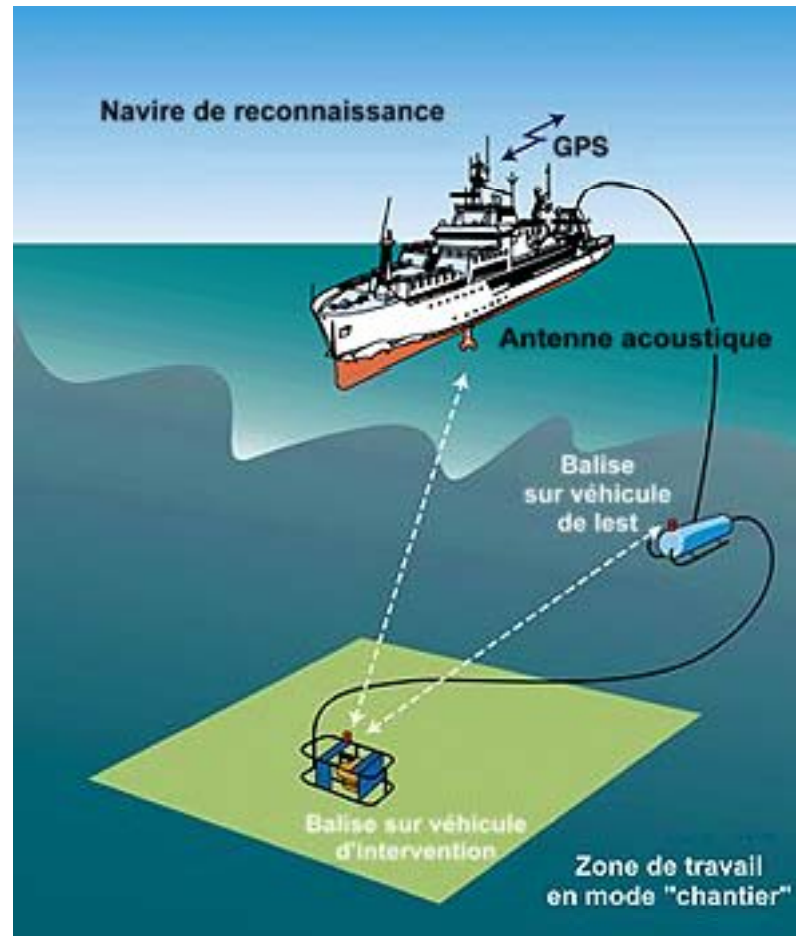


Figure 2.9. Long baseline system (LBL).

A long baseline (LBL) consists in acoustic transponders emplaced on the seafloor and accurately positioned. A transponder on the towfish interrogates acoustically the different elements of the net and computes the towfish position by triangulation.

USBL-Systems (Ultra short baseline)



Processing

Radiometric Corrections:

Recalibration of the individual sonar backscatter measurements

Geometric Corrections: Relocation of the individual sonar backscatter measurements

Map production: Merging of images and the production of maps

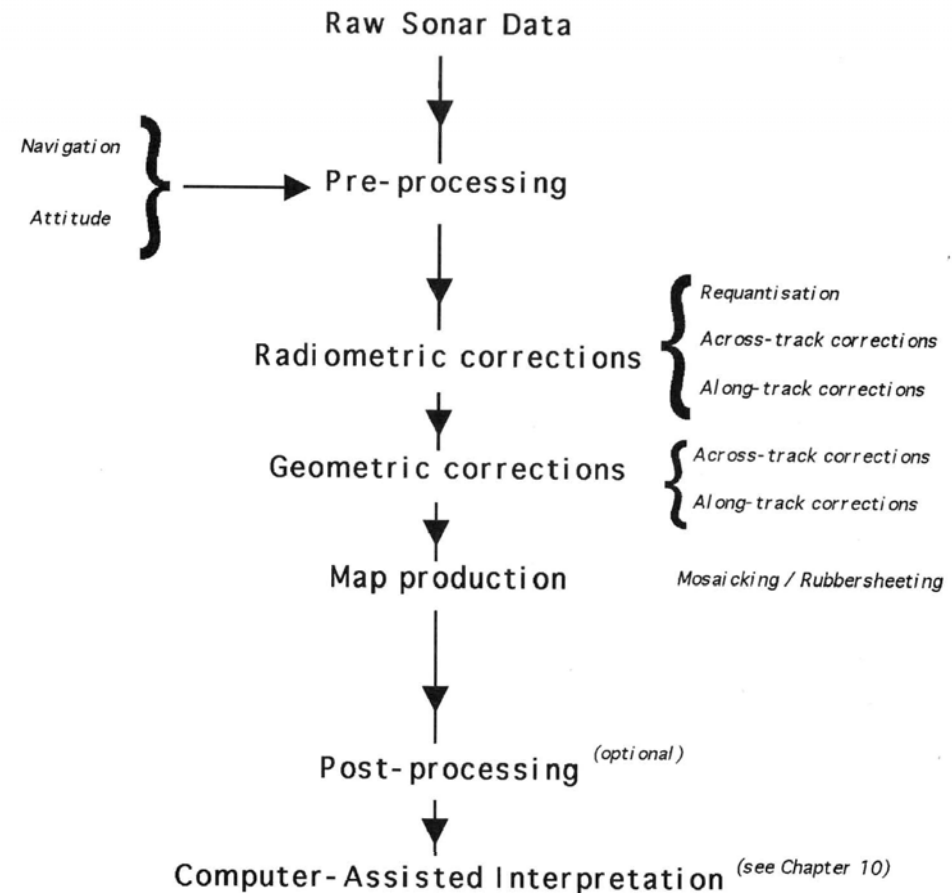
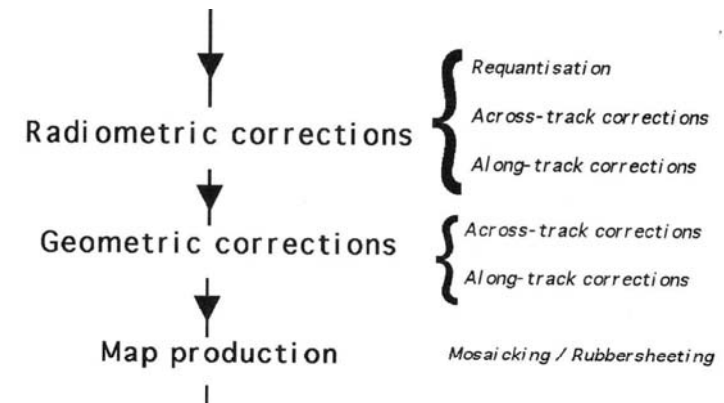


Figure 3.15. Data processing chain.

Radiometric Corrections

Requantisation: Most sonar processing packages work with measurements rescaled between 0 and 255 (8-bit quantisation). The output of the sonar data does not always follow the same quantisation schemes, and it is necessary to resample the data



Across-Track Corrections:

Backscatter signals are attenuated differently. Attenuation is a complex function of the beam width and is determined empirically for each sensor. This is usually performed by surveying a flat featureless portion of seafloor. The resulting tables are used to apply a time-varying gain (TVG) to amplify each backscattered return according to its arrival time

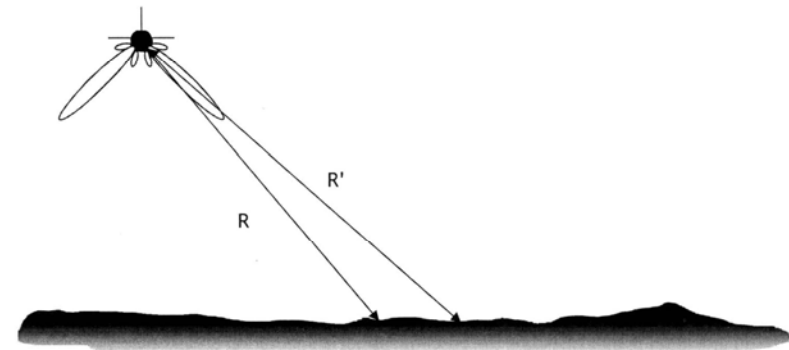


Figure 3.3. Backscatter signals are attenuated differently, depending on the distance they travel.

Radiometric Corrections

Along-Track Corrections: Systematic radiometric variations are often visible on the sonar images. These variations can be removed to special filtering processes

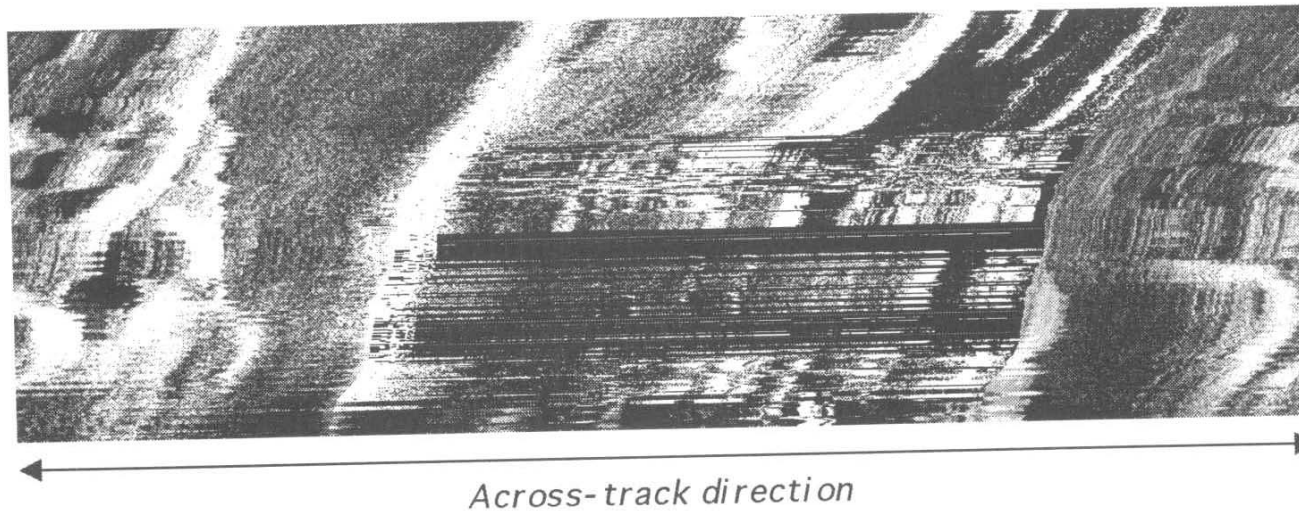
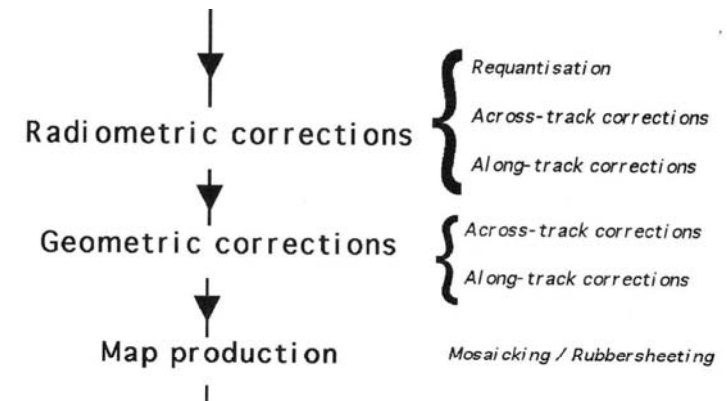


Figure 3.4. Examples of along- and across-track striping.

Geometric Corrections

Slant-Range Correction (Across-Track correction): Transformation of Slant-Range into Ground-Range.

Raw sidescan sonar imagery presents important across-track geometric distortions known as slant-range distortions, because the sonar measures times. Two targets close to the nadir (D1 and D2) will be associated with nearly identical slant-ranges R_1 and R_2 . Two targets at far range (D3 and D4), at the same distance from one another, will be associated with very different slant-ranges R_3 and R_4 and therefore placed further apart. Without slant-range correction, near range areas are more compressed than far-range areas.

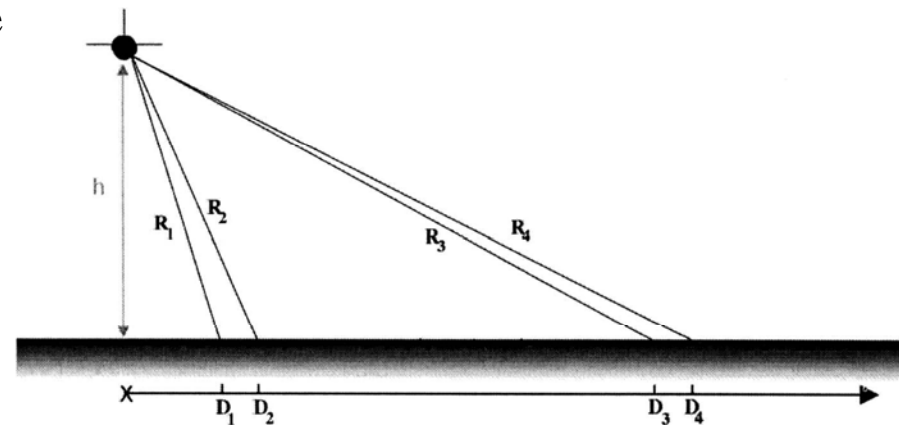
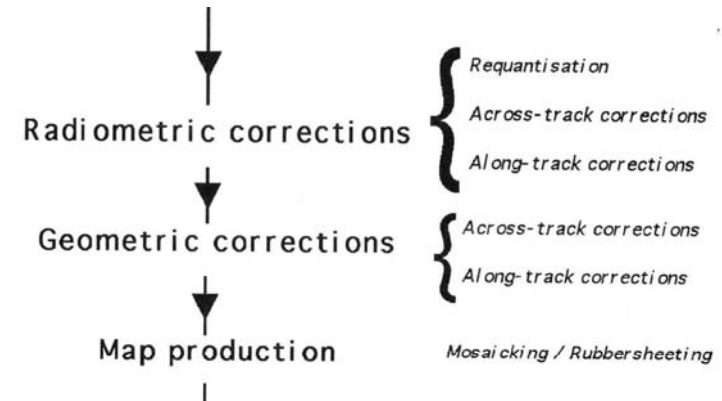


Figure 3.5. Slant-range distortion

Geometric Corrections

Anamorphic Correction (Along-Track correction): The anamorphic correction aims in producing an image with a 1:1 aspect ratio.

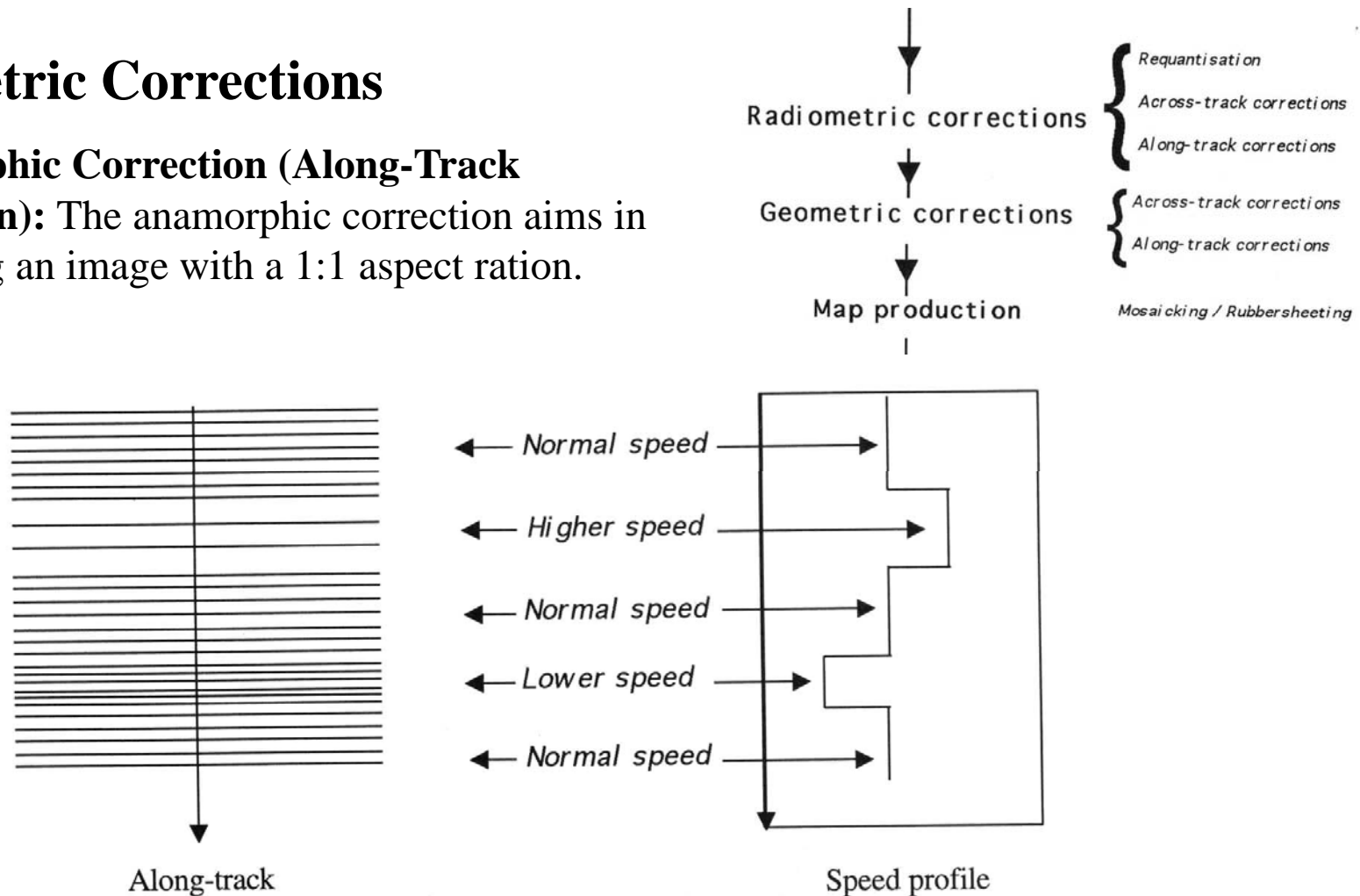


Figure 3.6. Variations in the survey speed create distortions in the along-track footprint. These distortions are corrected through anamorphosis.

Map Production

Mosaicking – Stencilling: The processed sidescan sonar imagery is composed of picture elements organized into one or several images. Geocoding allows to place these images on a map. Merging can be done by stencilling or mosaicking

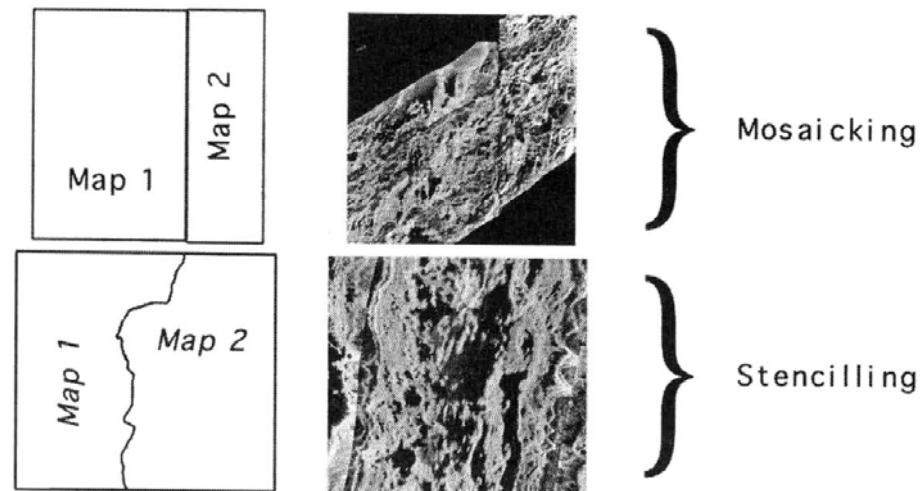
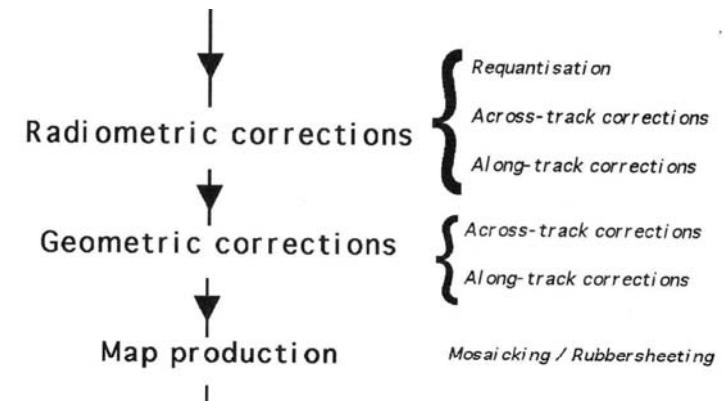


Figure 3.9. Overlapping images can be merged by mosaicking or stencilling.

Map Production

Rubbersheeting (Interpolation):

Interpolation schemes for small data gaps and overlapping pixels

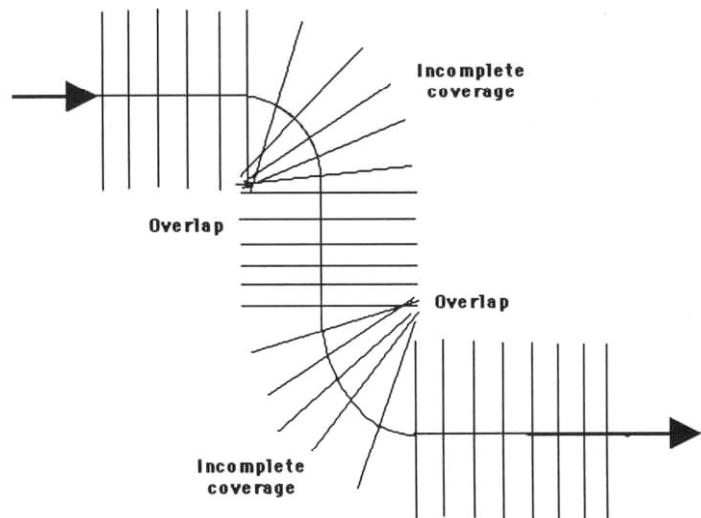
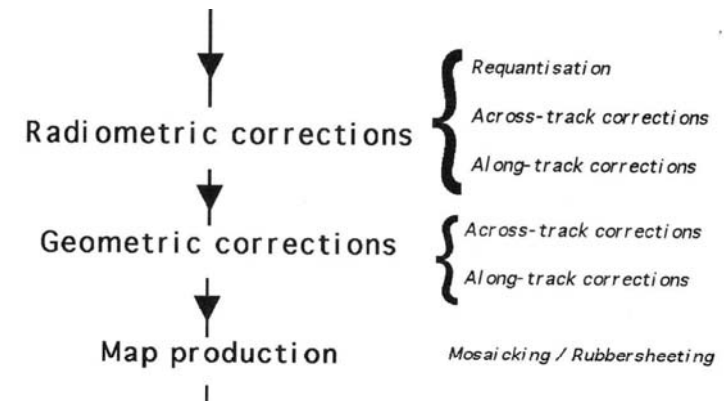


Figure 3.10. When the ship turns, the portions of the swaths in the inside corners are overlapping. The portions of the swaths in the outside corners are more widely spaced and the coverage is incomplete.

Post-Processing

- E.g. Histogram Manipulations

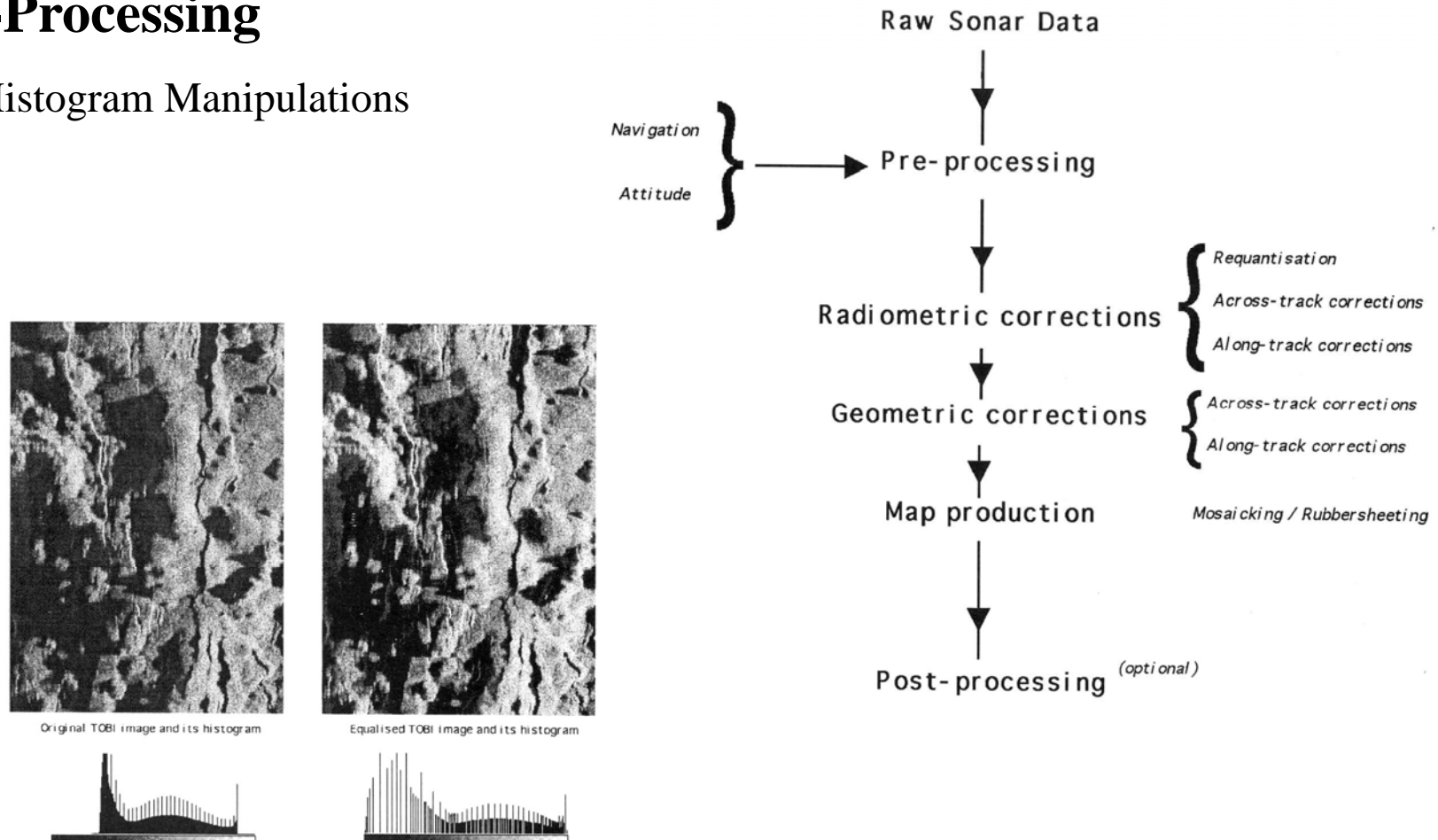


Figure 3.12. Example of histogram equalisation. The original TOBI image (left) shows a histogram with a high number of dark pixels. The histogram of the equalised image (right) shows increasing contrasts for grey levels which occur frequently, and decreasing contrasts for the other grey levels.

Application and Interpretation of Sidescan Sonars

Mapping of the Seafloor

- Analysis of sedimentary and tectonic structures
- Hazard assessment (Landslides, Pockmarks, ..)
- Study of anthropogenic structures (Wrecks, Dump Sites)
- Searching for Cable Routes

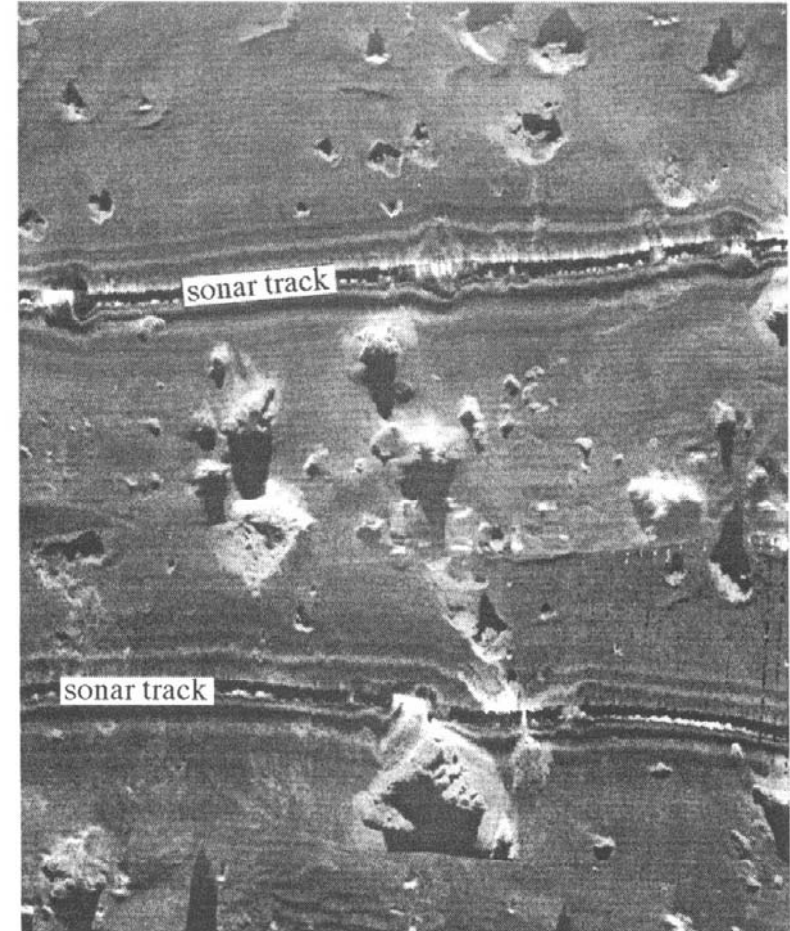
INTERPRETATION CHECKLIST

For the whole image:

- How was it acquired ?
- Type of sonar
- Frequency
- Configuration (hull-mounted, deep-towed, altitude above the seafloor ...)
- Beam width, swath width, resolution
- Vehicle information: heading, speed, attitude (roll, pitch, yaw)
- How was it processed ?
- Analogue or digital processing ?
- Time-varying gain ? Angle-varying gain ?
- Slant-range correction ?
- Anamorphosis ?
- Additional processing ?

For each identifiable region:

- What was the illumination geometry for this particular region ?
- Range (far, close, intermediate ?)
- Angle (sub-perpendicular, grazing, varying ... ?)
- Is the region viewed obliquely, i.e. at several angles and ranges ?
- What is the backscatter ?
- Relative values (high or low)
- Variations inside the region (homogeneous or not, contrasted or not ...)
- What are the characteristic textures ?
- Appearance (smooth, grainy, mixed ...)
- Organisation (random, regular patterns, directionality ...)
- What are the dimensions of the region ?
- What is the relation of the region to its surroundings ?
- What can it be ? (extraction of the 3-D object from the 2-D sonar image)

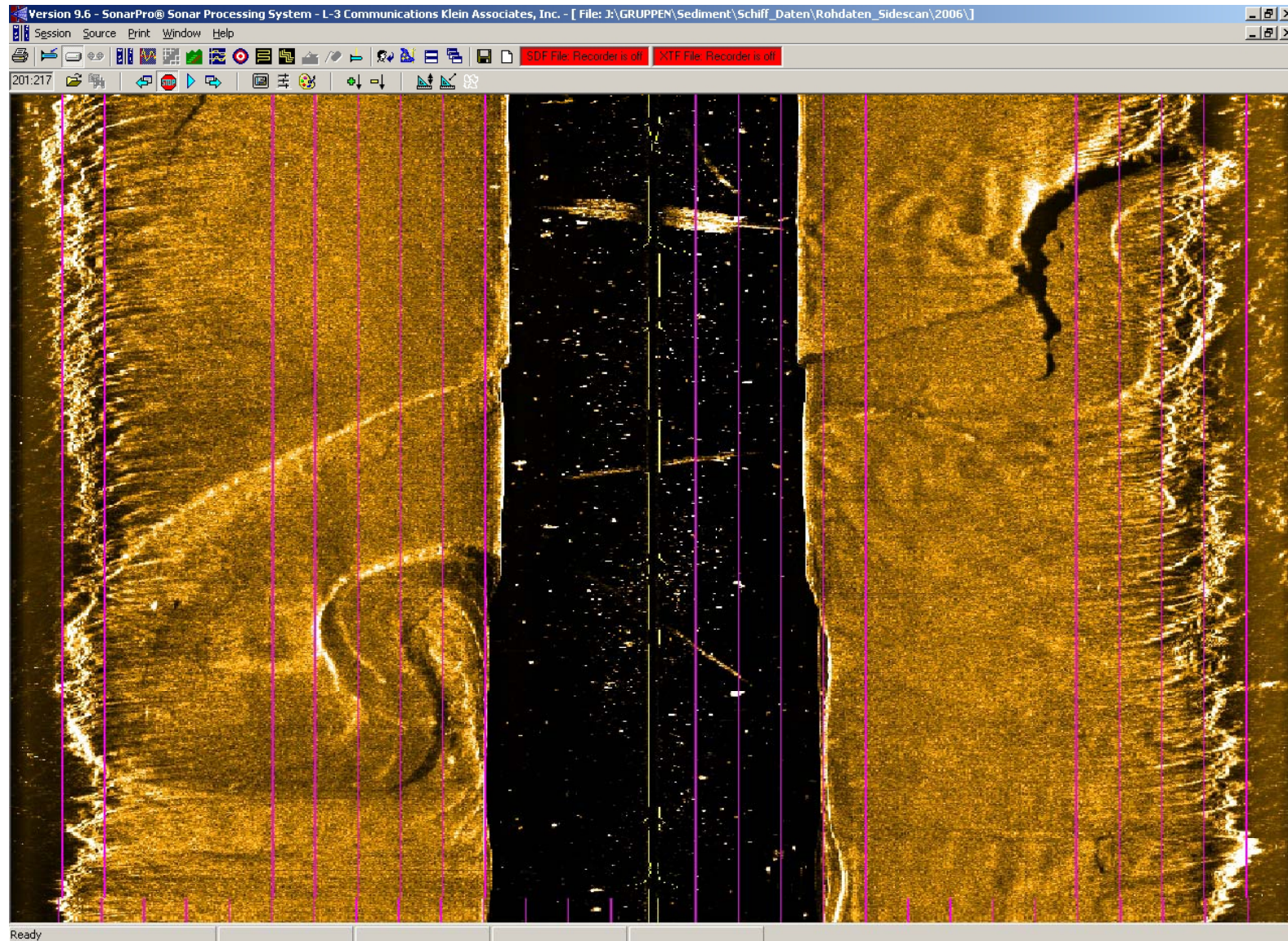


9 km

Figure 6.6. Blocks in the El Golfo debris avalanche, close to Hierro Island, Canaries. This TOBI image is made up of two overlapping swaths and is approximately 9 km high. Courtesy D. Masson, SOC (UK.)

Table 4.1. Sidescan sonar interpretation checklist.

Sidescan Sonar: Shallow water, ~500kHz



Courtesy of Martin Wessels (ISF Langenargen)



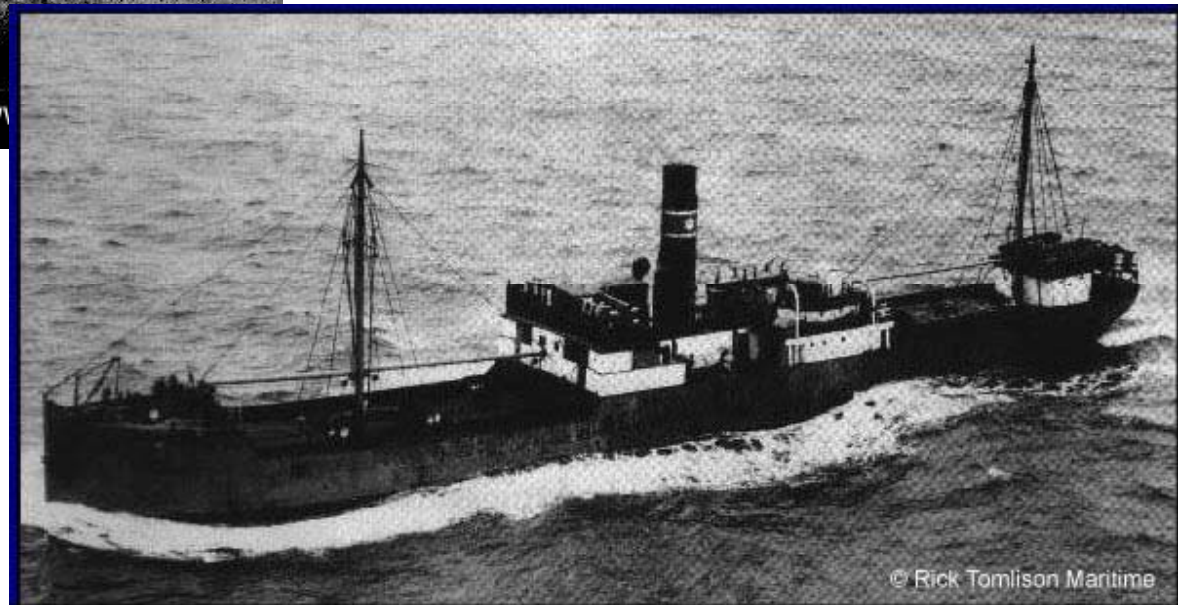
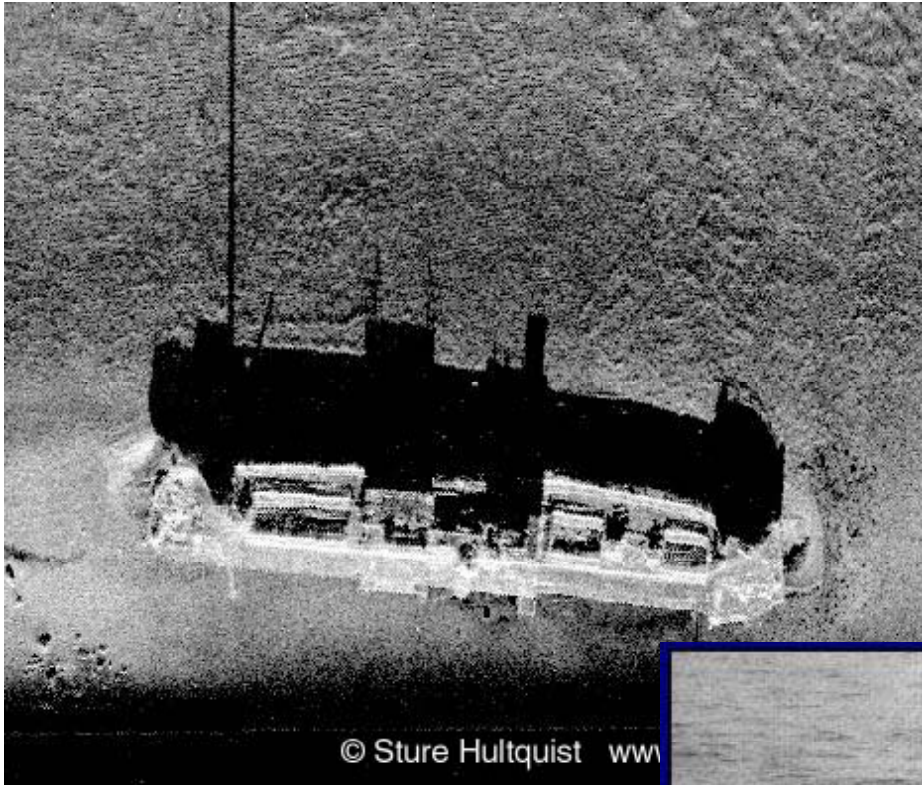
future ocean
KIEL MARINE SCIENCES

Submarine Mapping

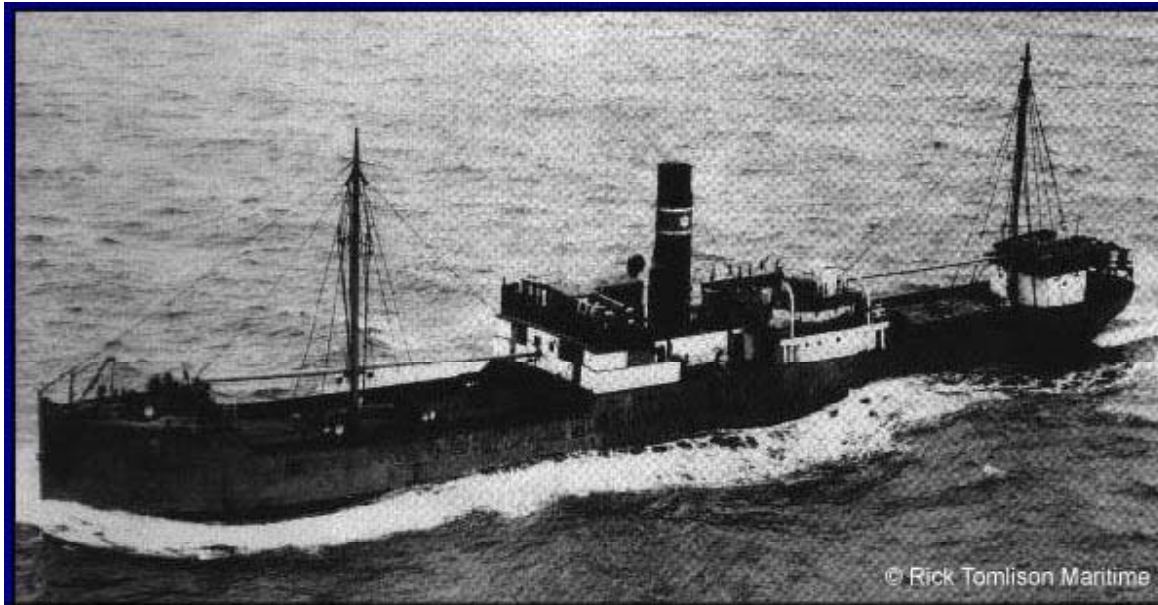
Sidescan Sonar

Example 2

Steamer Nedjan



Source:
www.abc.se/~pa/mar/sidescan.htm

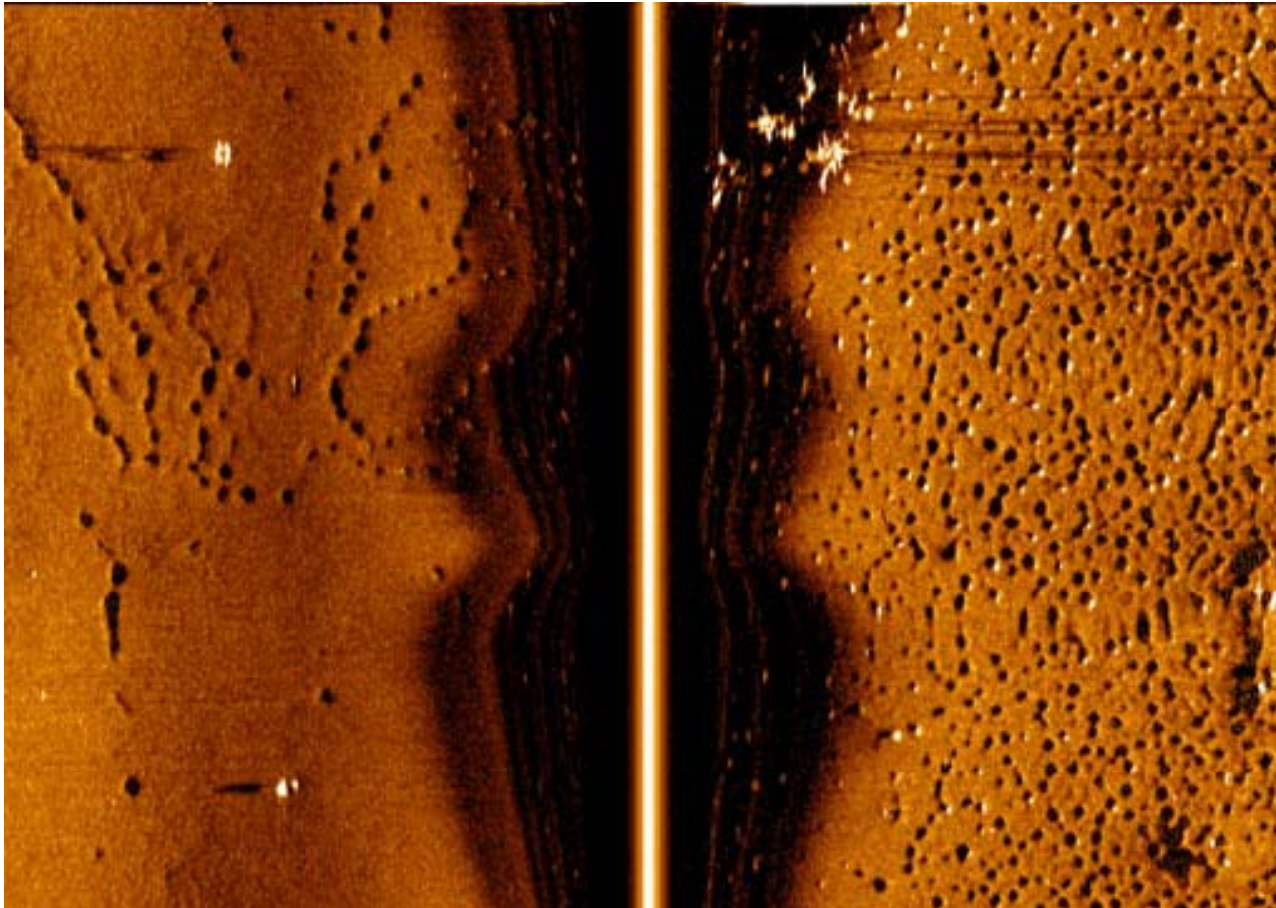


Steamer Nedjan

This Swedish steamer was 64 m long and built in Greenock, Scotland, in 1893. In January 1954 she left Gävle harbour, Sweden, in storm and freezing temperature. She was then already an old steamer in poor condition. During the night, her steam powered steering ceased to work and she started to drift. She had a long radio conversation with a coast guard station. This conversation was tape recorded, and is still preserved. Eventually the contact was lost.

She was presumed lost somewhere off the coast. There were no survivors and the wreck position remained unknown. First in 1996 she was found on 32 m depth by Stiftelsen Marinhistorik, using side scan sonar. She is standing upright and very well preserved. No remains of the 17 dead have been found onboard.

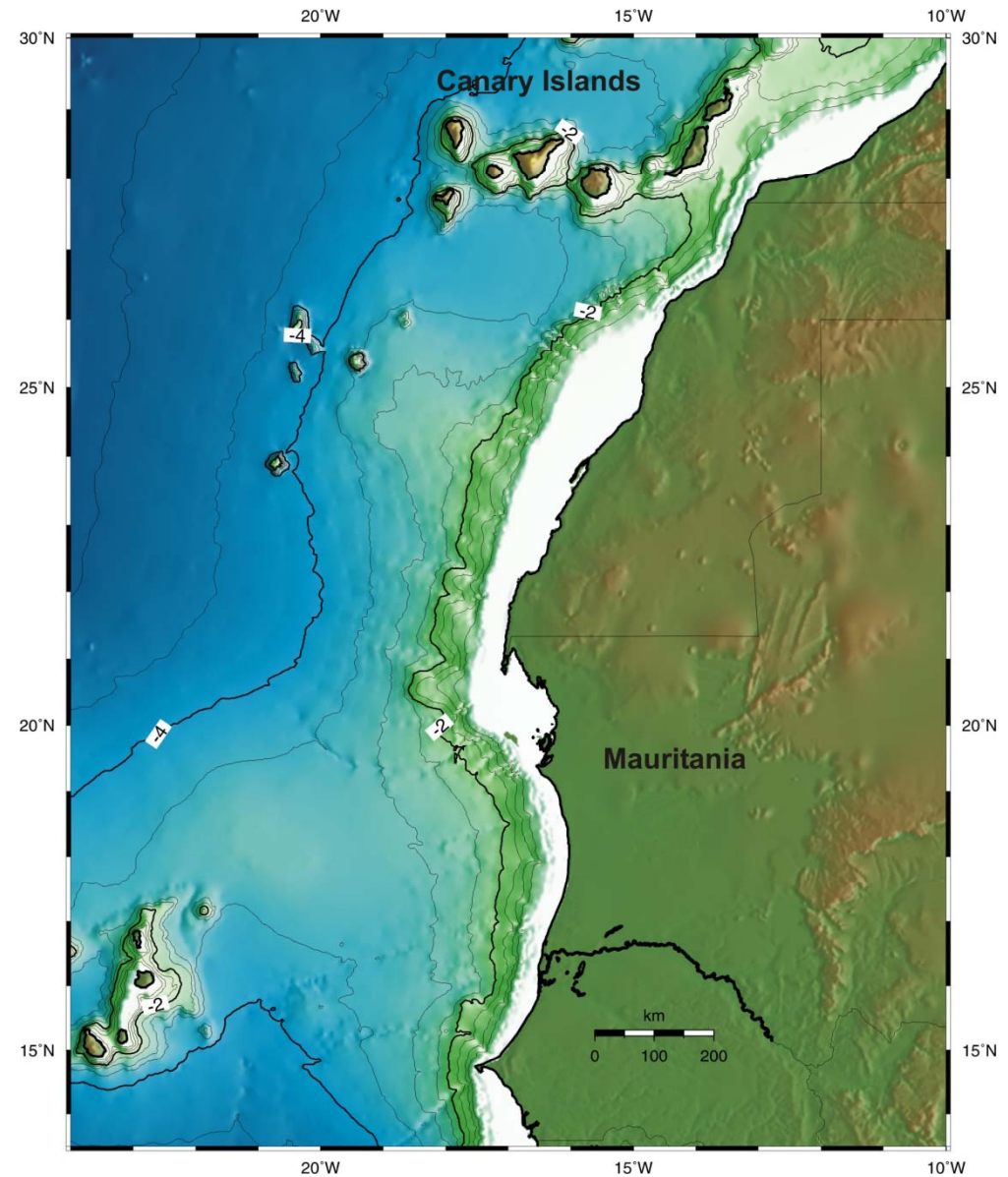
10m, 600kHz sonar



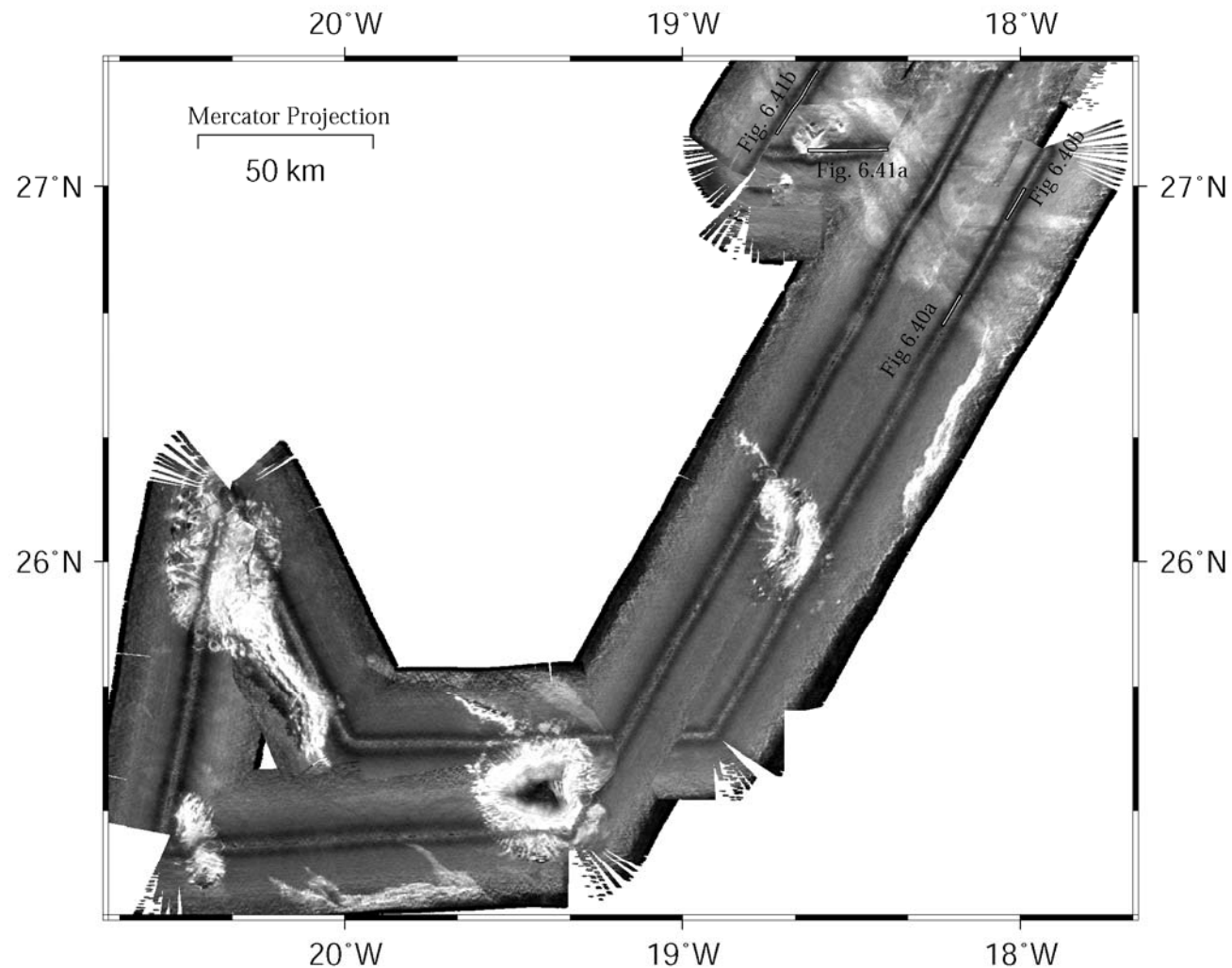
<http://www.marinesonic.com>

The holes are fish breeding beds located in a lake at a water depth of 146 feet.

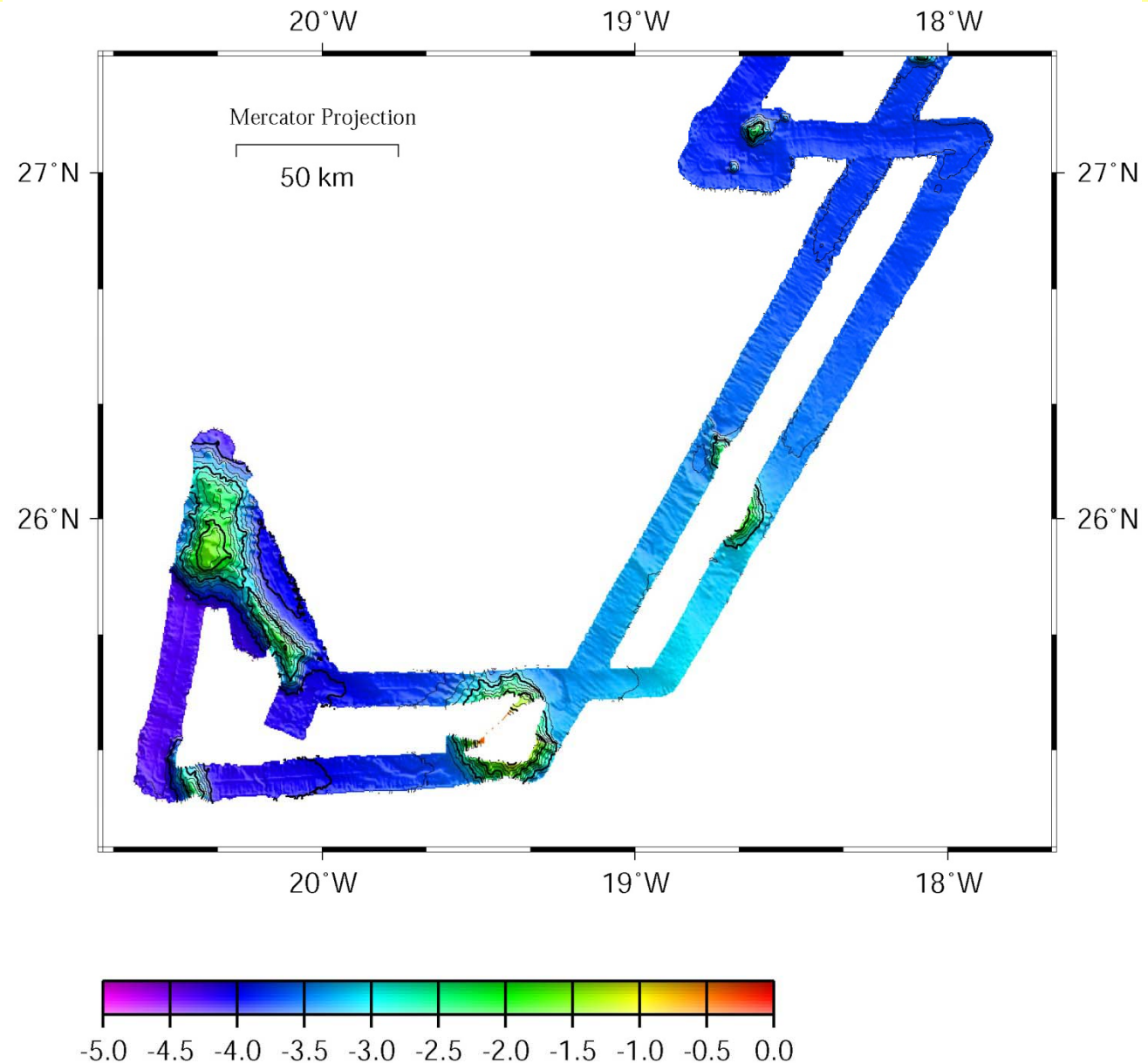
GEBCO Map off NW-Africa



GLORIA Mosaick, south of the Canary Islands



Measured Multibeam Bathymetry



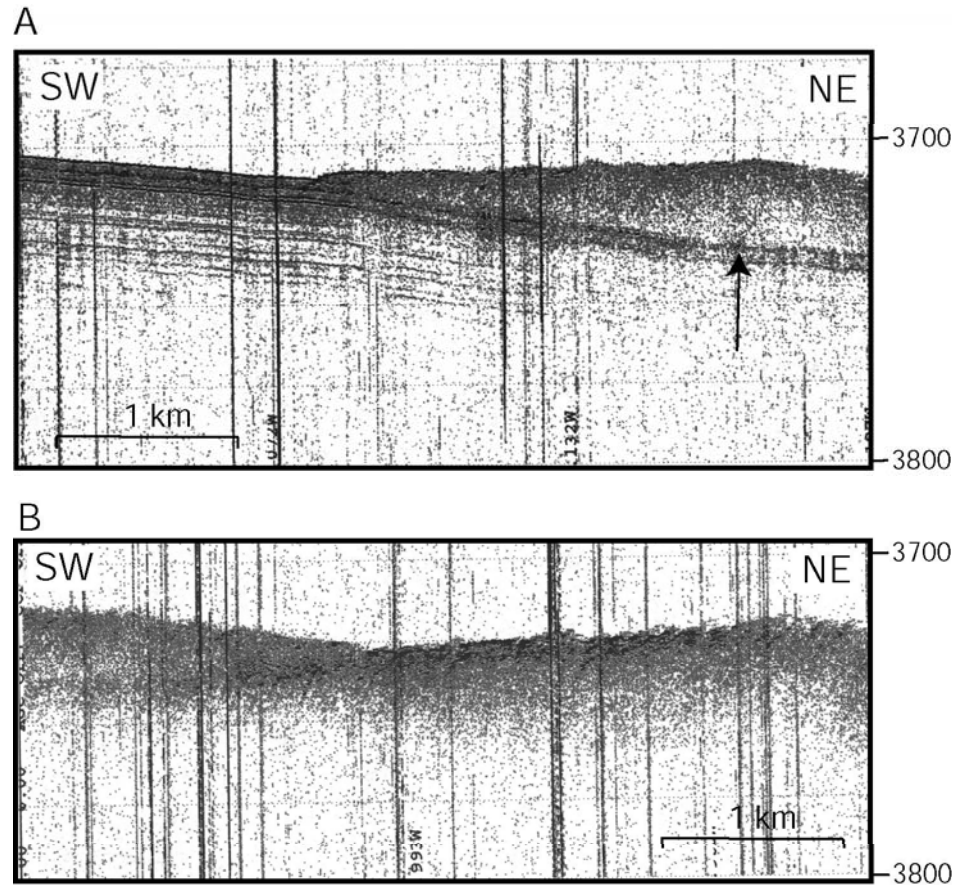


Fig 6.40 (Parasound Profile)

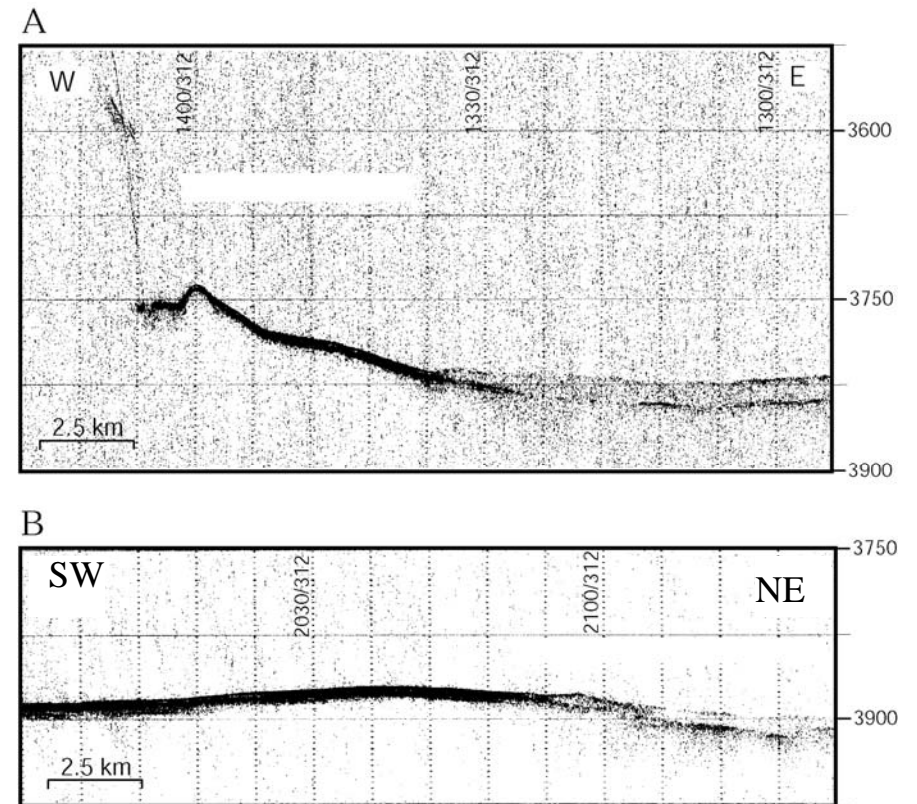
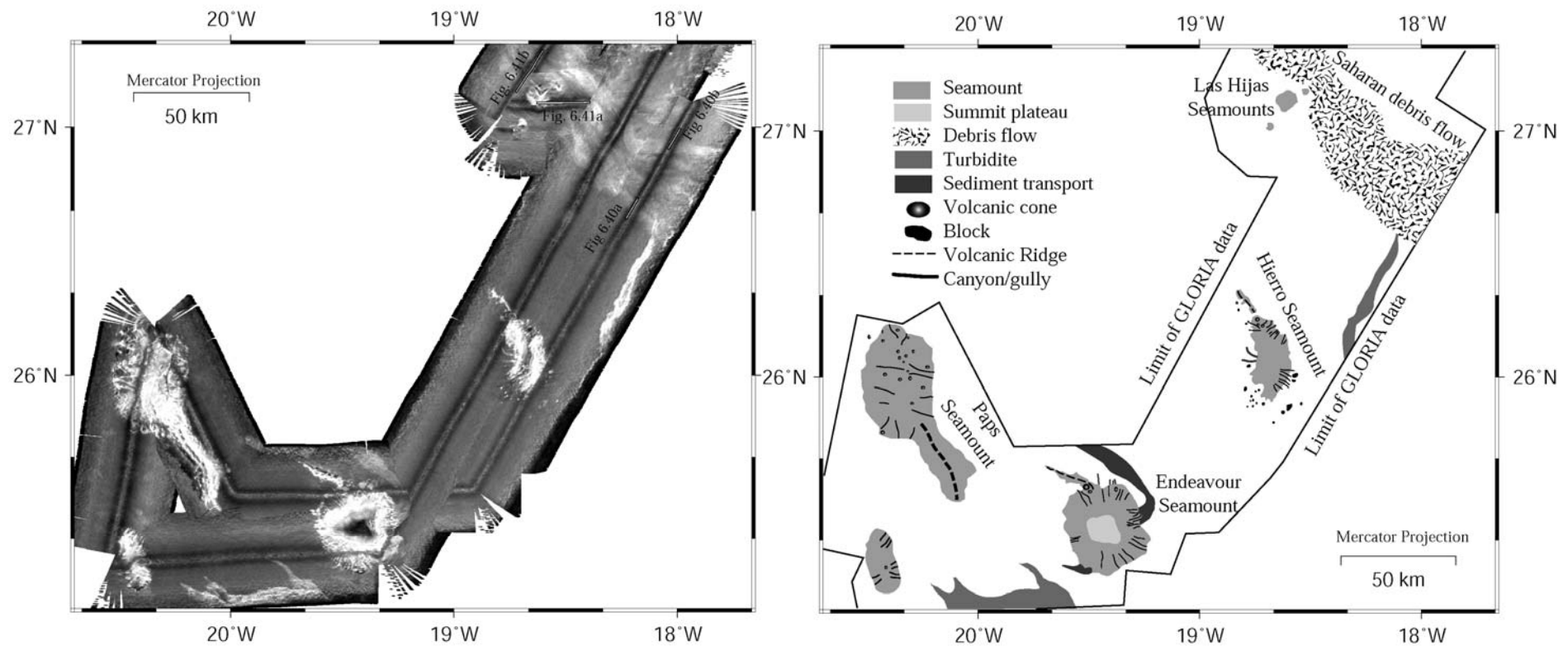
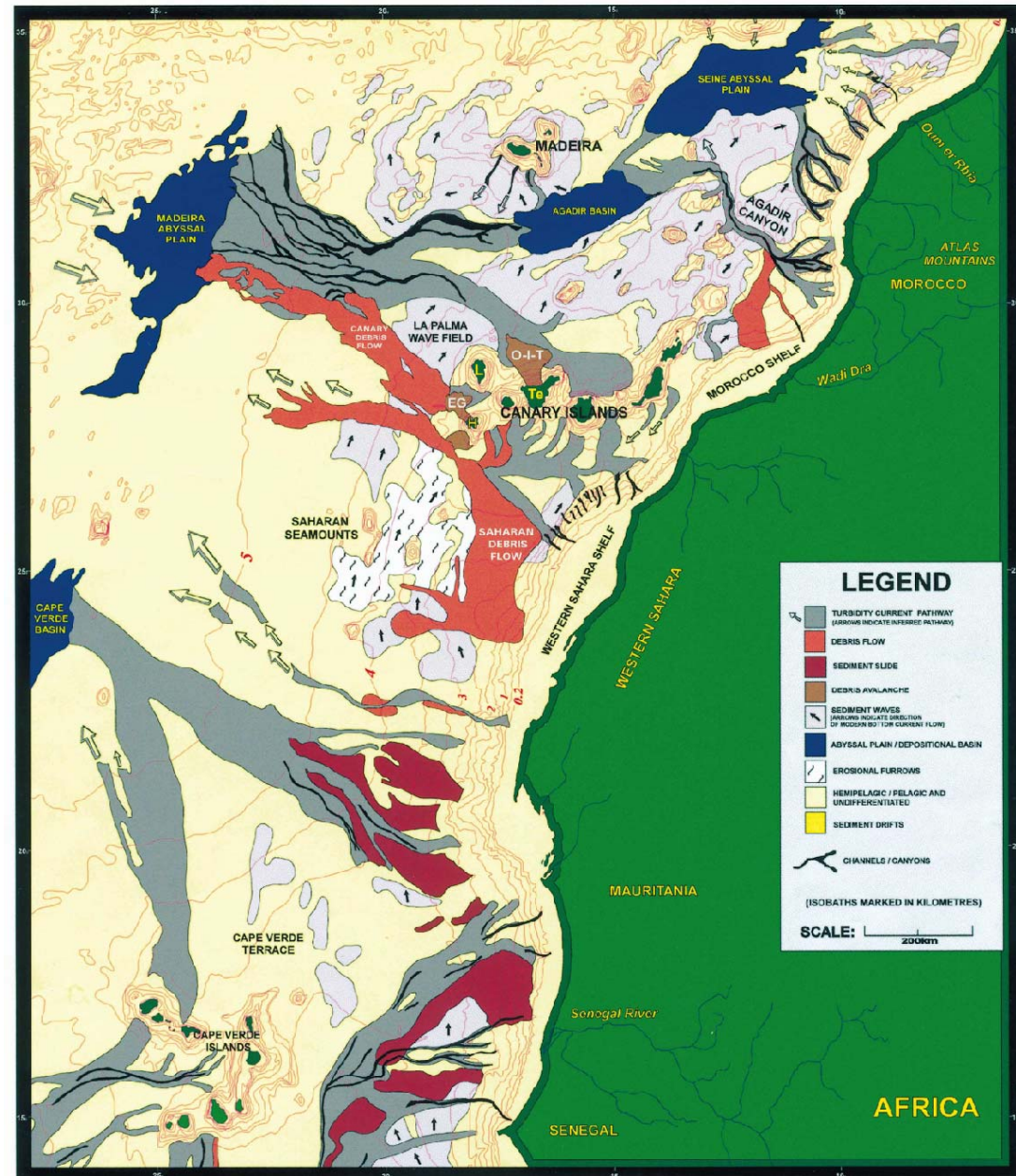


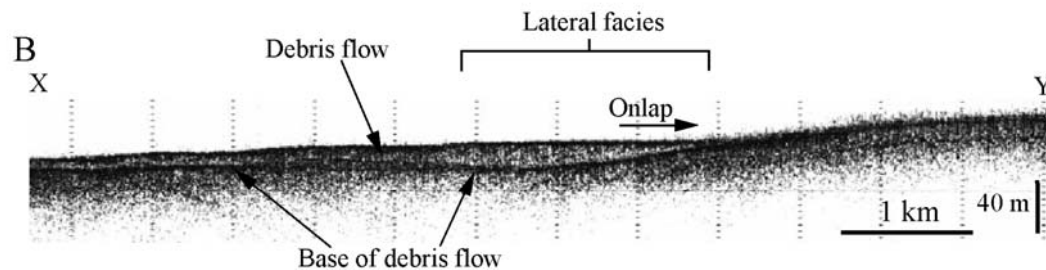
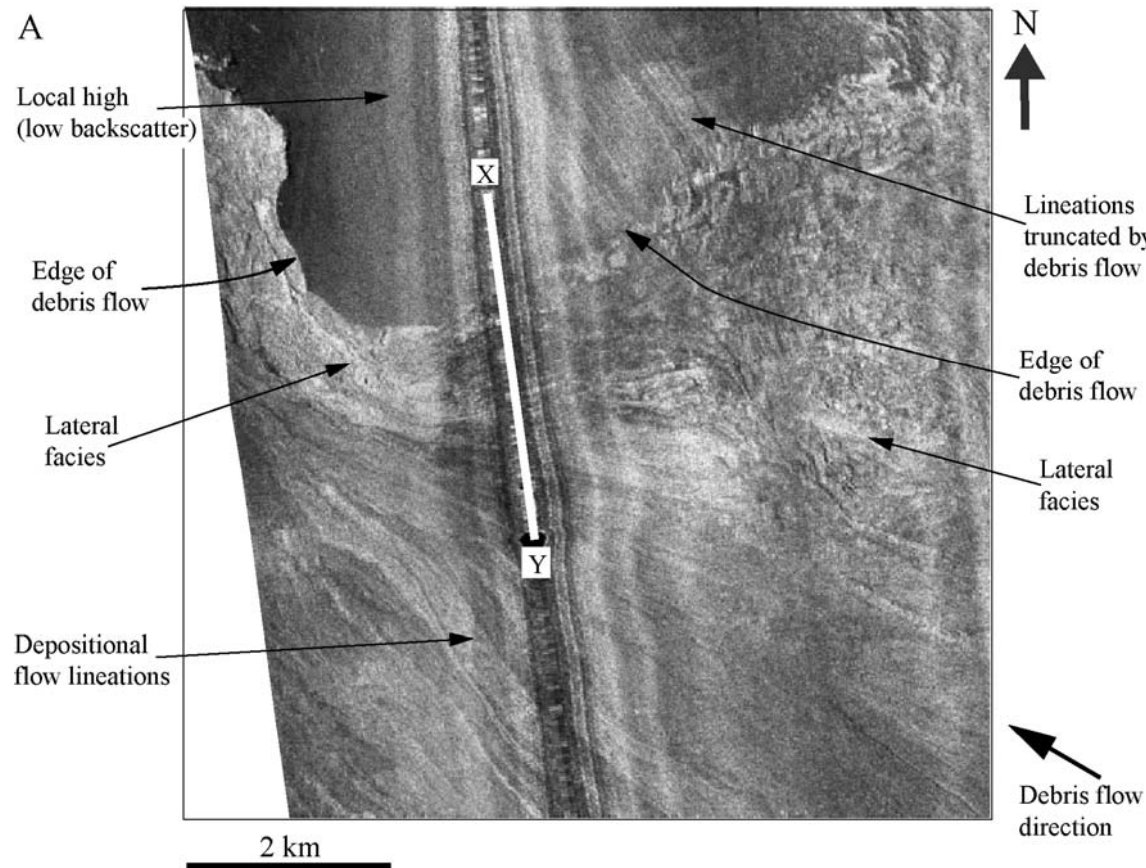
Fig 6.41 (3.5 kHz Profile)

GLORIA Mosaick and Interpretation Map (south of the Canary Islands)



Sediment process map of the Northwest African Margin (Wynn et al., 2000)

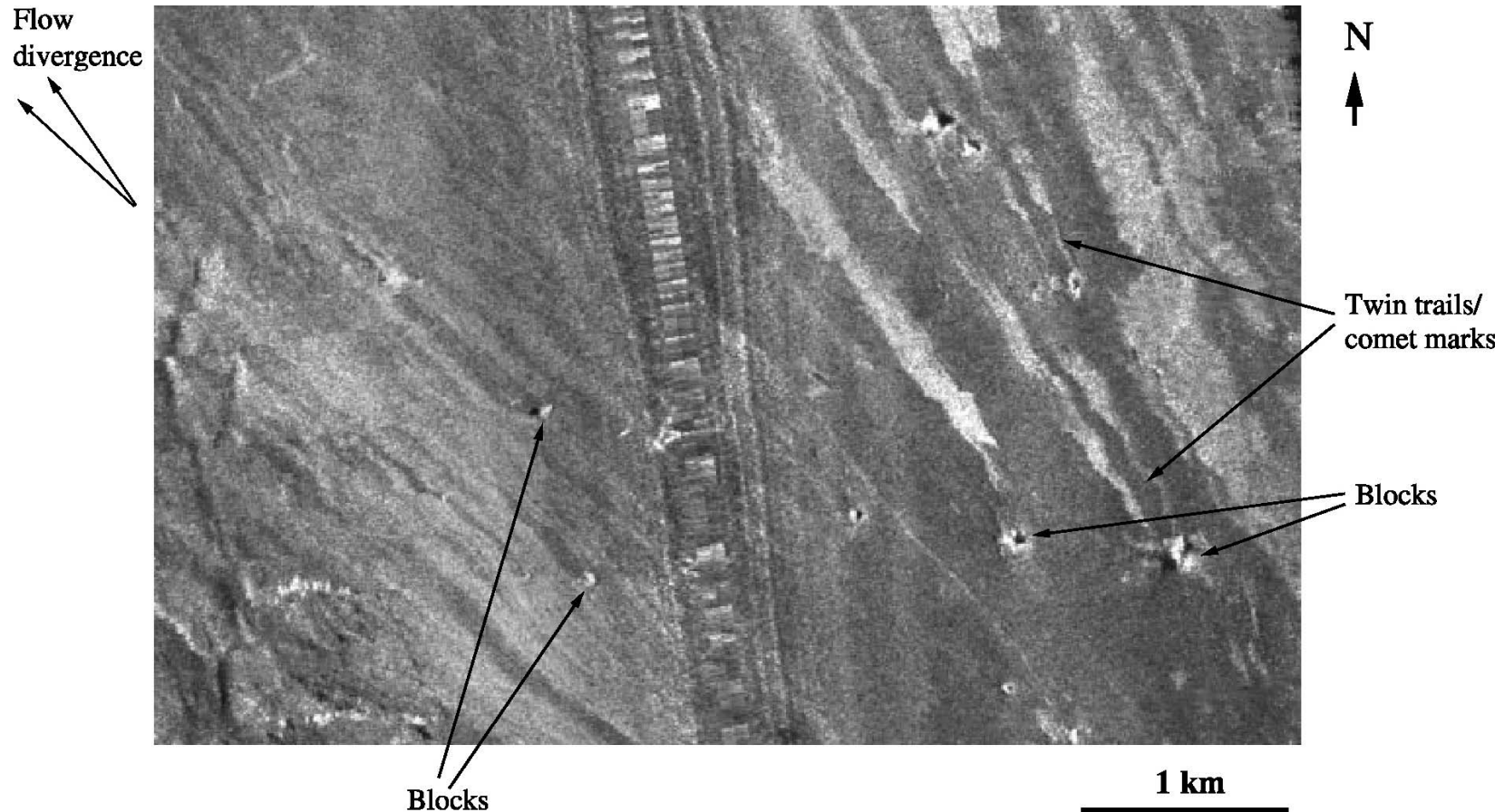




TOBI 30-kHz sidescan sonar data. (A) Northern boundary of the Saharan debris flow showing onlapping of the debris flow on a local topographic high. Note flow direction, convergent depositional flow lineations and lineations truncated by the debris flow. (B) A 3.5-kHz profile; X-Y shows the debris flow deposit onlapping the topographic high. Light tones represent high backscatter.

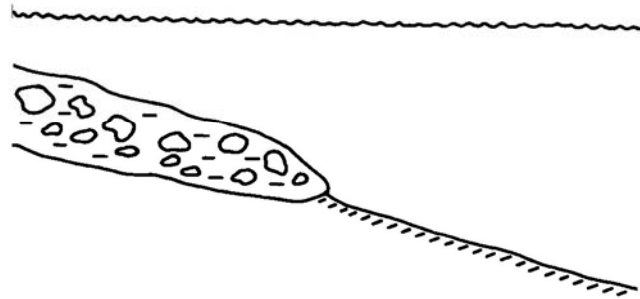
Gee et al, 2001

Saharan Debris Flow (Gee et al, 2001)



TOBI 30-kHz sidescan sonar data of strongly lineated fabric showing detail of blocks and comet marks. Note slight divergence in the lineations towards the NW. Light tones represent high backscatter.

Debris Flows



Turbidite



future ocean
KIEL MARINE SCIENCES

Submarine Mapping

Sidescan Sonar

Example 5

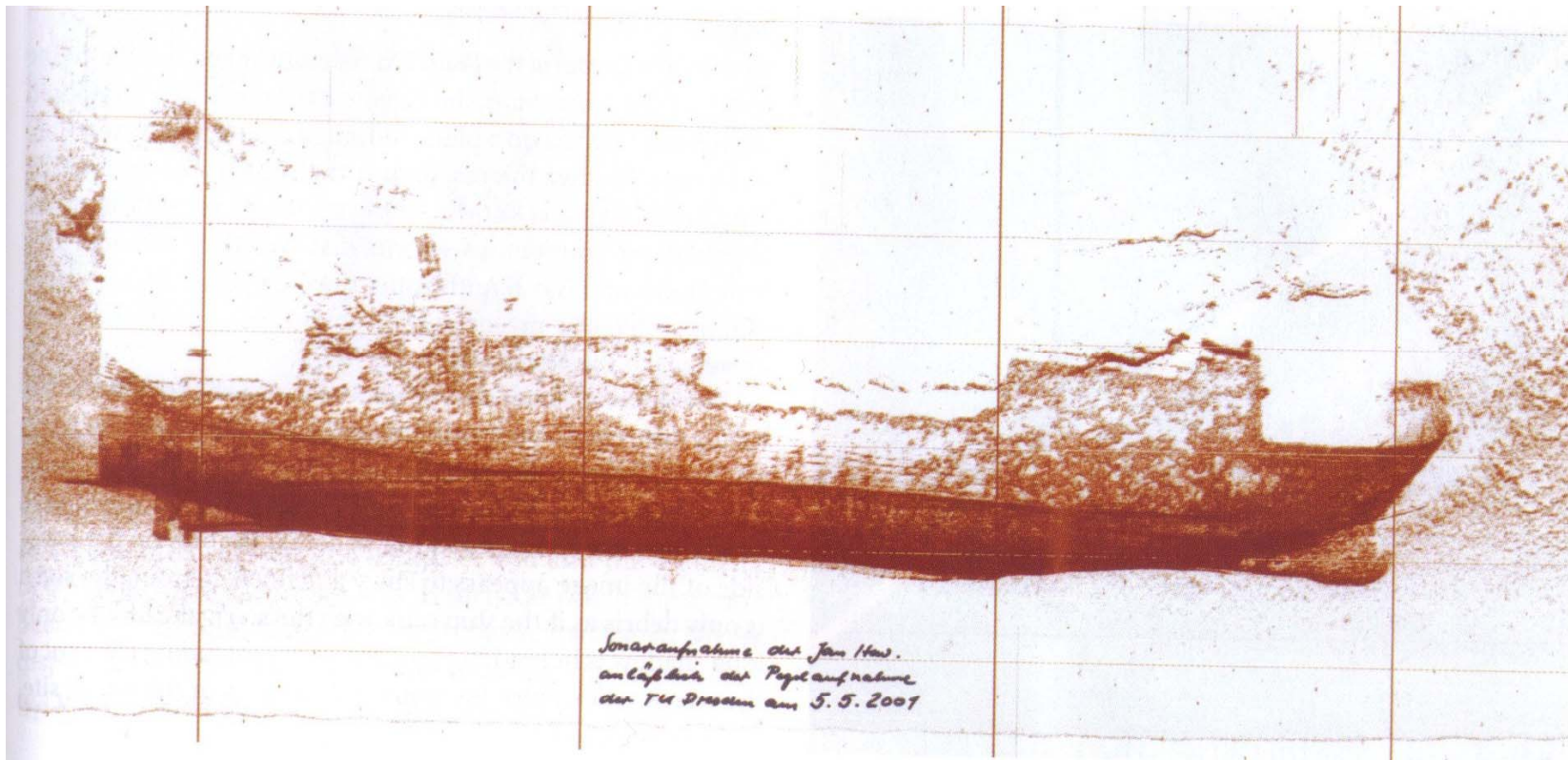


Image 7.1.1-1a. The wreck of the ferry Jan Hevelius. Sidescan sonar image. The ferry, 125 m long, built in 1977 sank in 1993 in the southern Baltic off the Island of Rügen. The sidescan image taken in 2001, viewing the wreck from the keel side, shows an essentially intact hull and superstructure lying on the portside at about 20 m depth. The bow – as well as the stern construction – can be identified in detail. The pair of funnels near the stern are still in place (the port side one lies under the starboard funnel here). Conspicuous is the acoustic difference between the strongly reflecting hull coded dark and the less reflecting superstructure of considerable height. The broken upper contour in the middle is an open deck; the railings are only weakly recognizable. The mast constructions are not resolved. The white shadow contours are most evident on the stern side; near the bow the sea floor surface appears rough; part of the bow near the keel is buried by sediment.

Image documentation: ...
Aus Wille, Sound Images of the Ocean

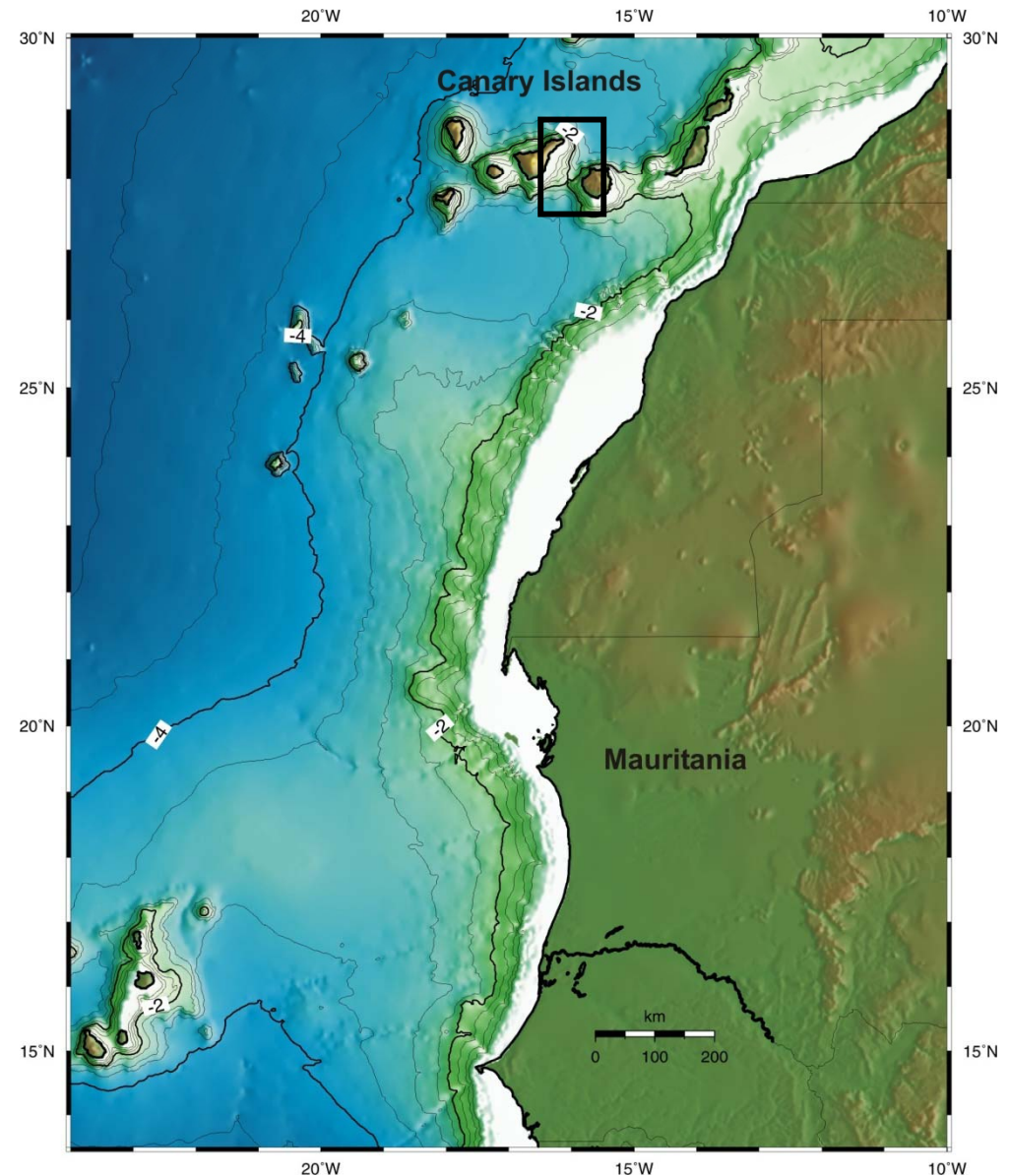
GEBCO Map off NW-Africa

Channel between Gran Canaria and Tenerife

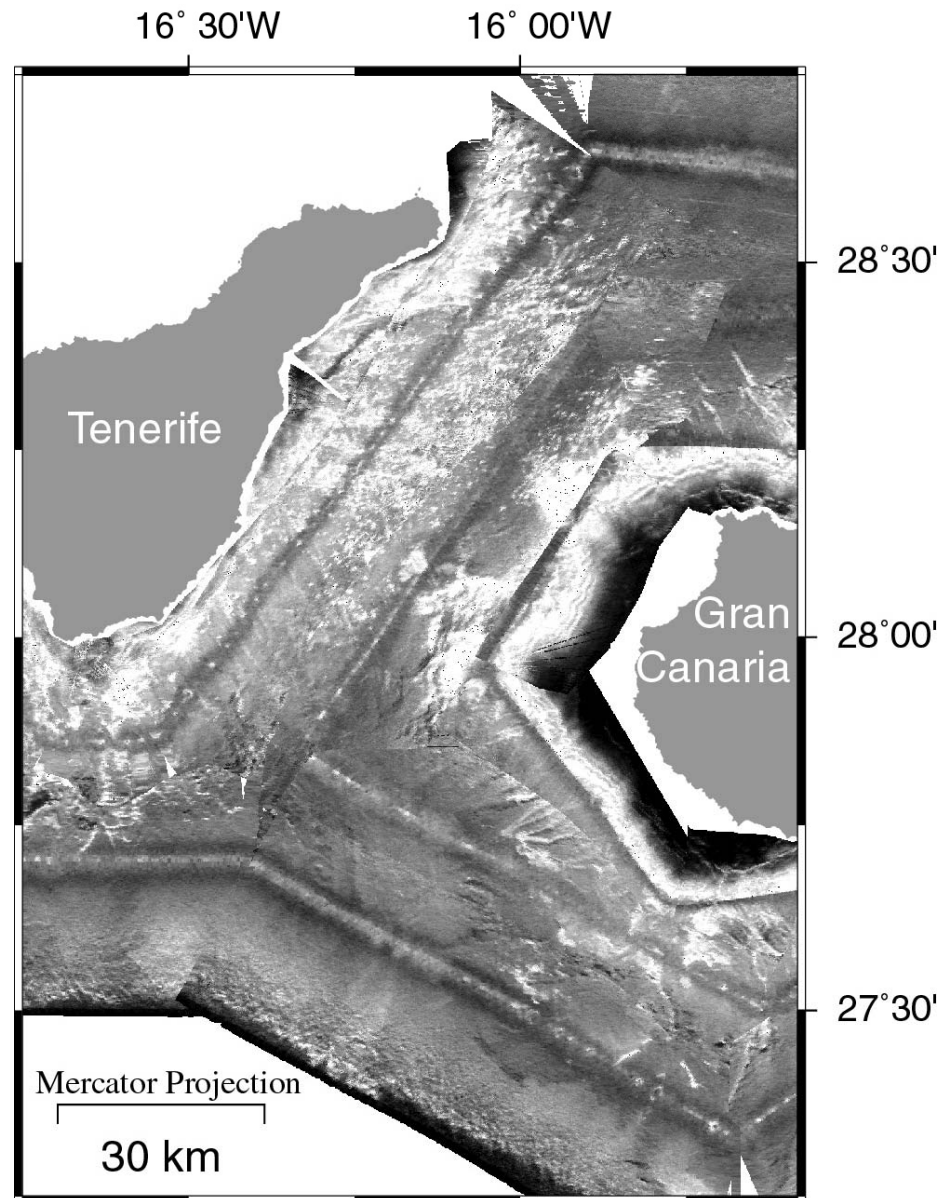
Canary Islands are volcanic islands (Hot Spot volcanism)

2 main types of sediment-transport

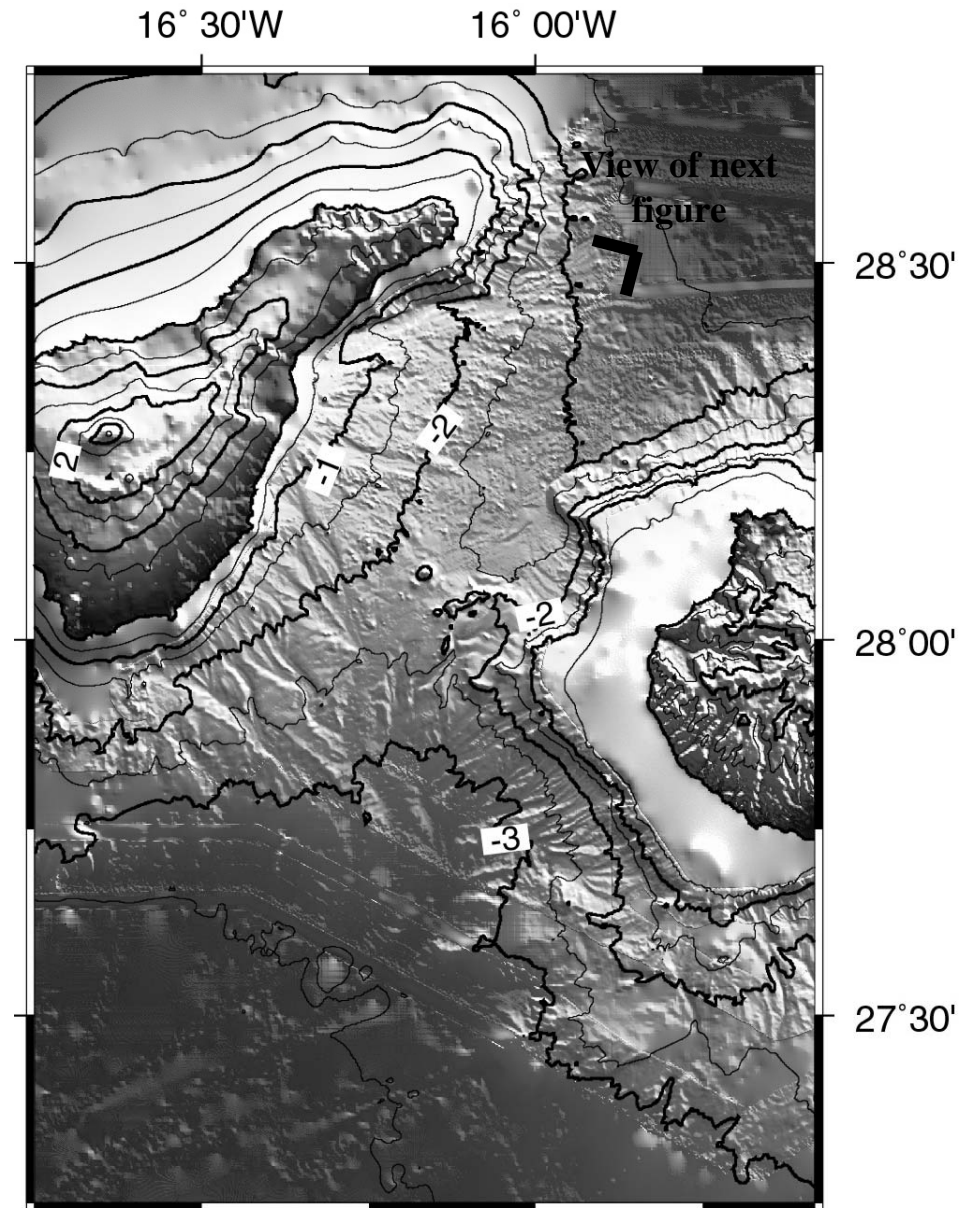
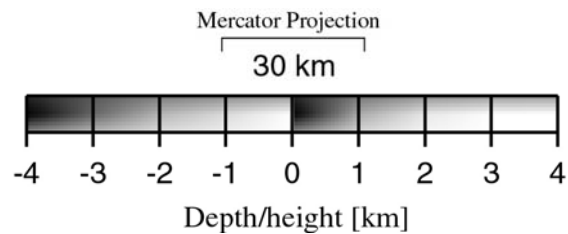
- Large-scale rapid catastrophic sediment-transport as a result of flank-collapses (debris avalanche)
- Channelized sediment-transport through submarine canyons



GLORIA Image of the channel between Gran Canaria and Tenerife. Light tones present high backscatter (Krastel et al., 2001).



Bathymetric map of the channel between Gran Canaria and Tenerife. Contour-interval is 500 m. (Krastel et al., 2001).

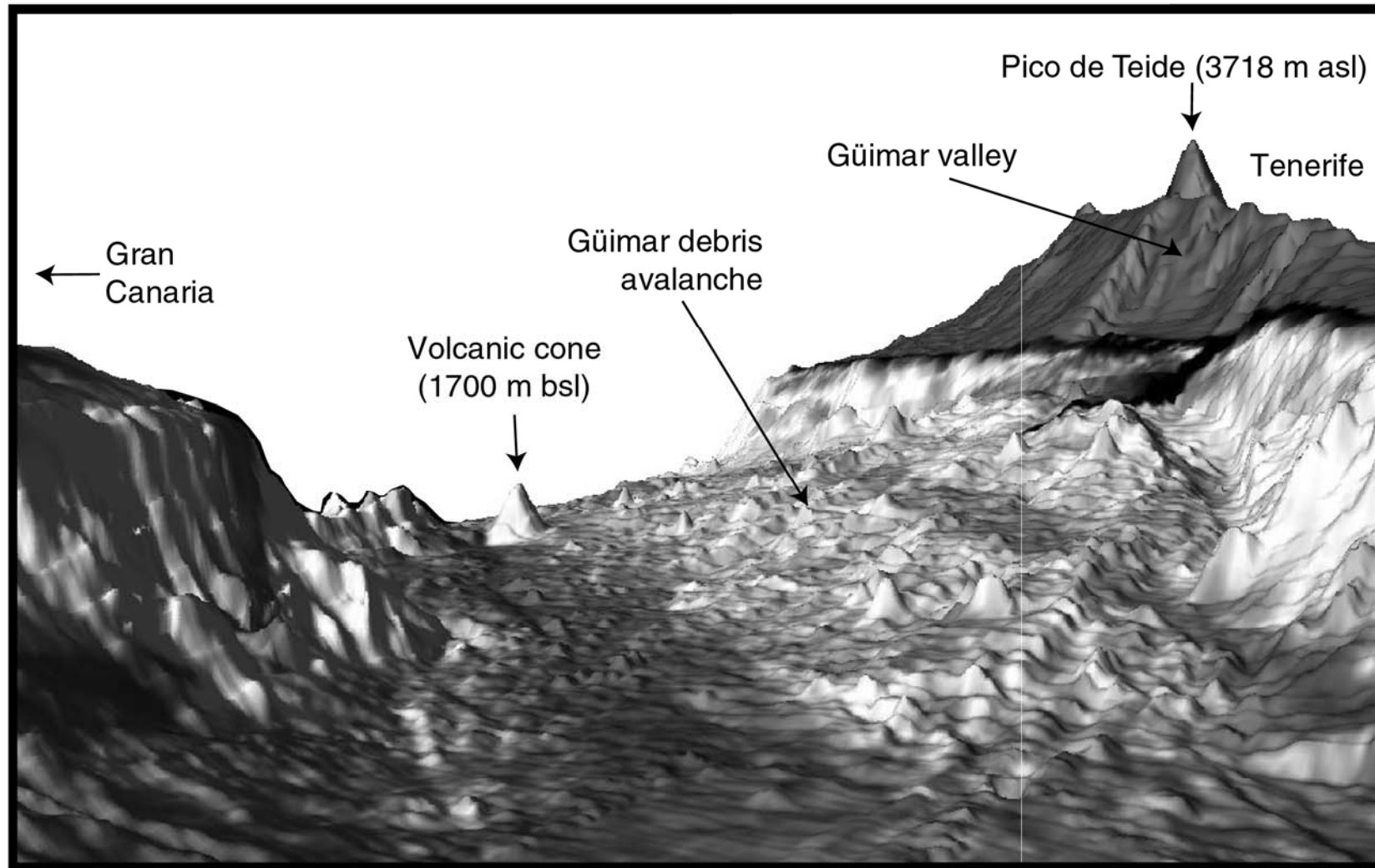




future ocean
KIEL MARINE SCIENCES

Submarine Mapping

Sidescan Sonar



Krastel et al., 2001



Perspective view of Güimar debris avalanche. Vertical exaggeration is 5. Shading is taken from the GLORIA data. The lighter color of the debris avalanche is due to stronger backscatter of the hummocky terrain.

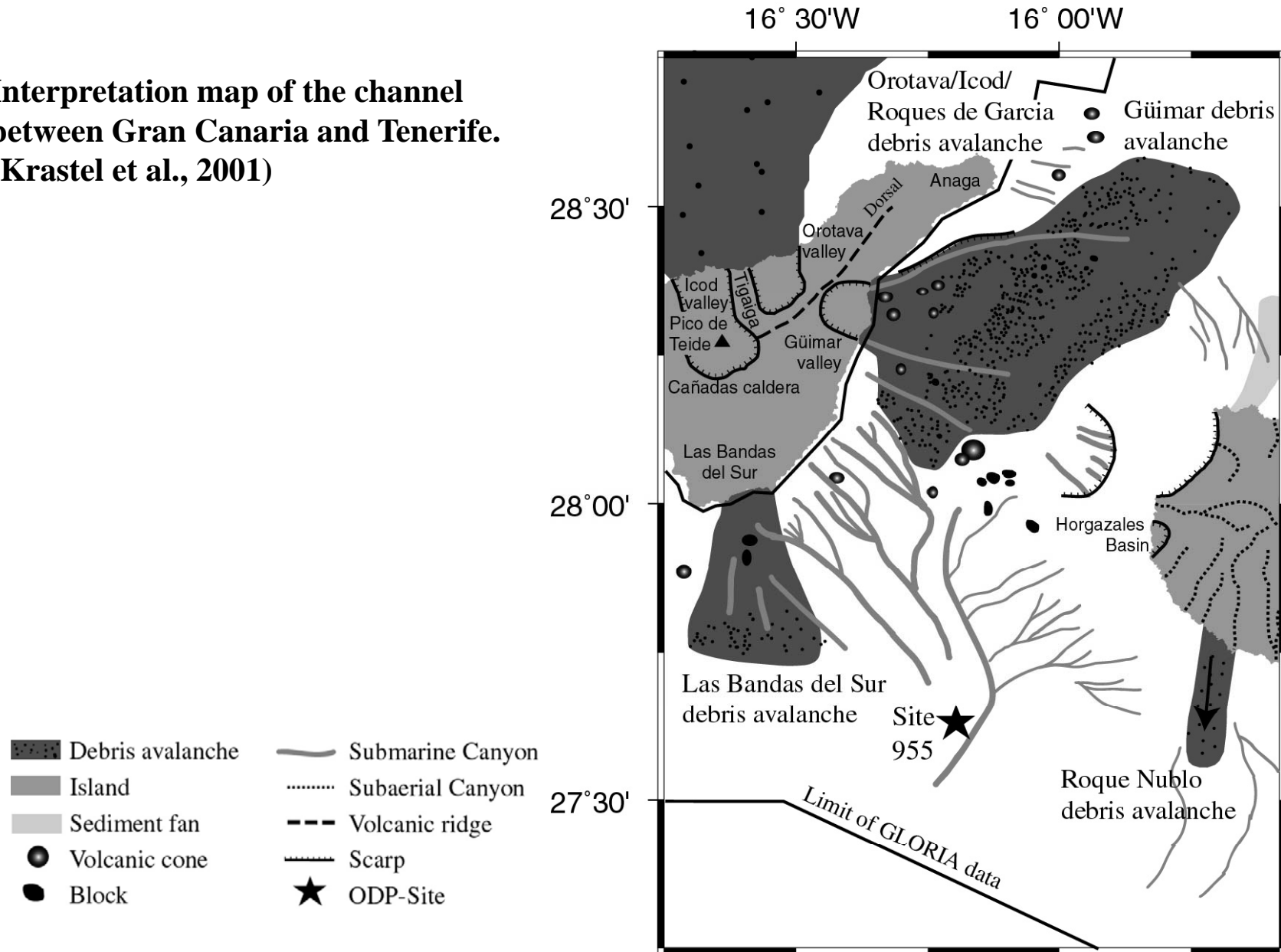


future ocean
KIEL MARINE SCIENCES

Submarine Mapping

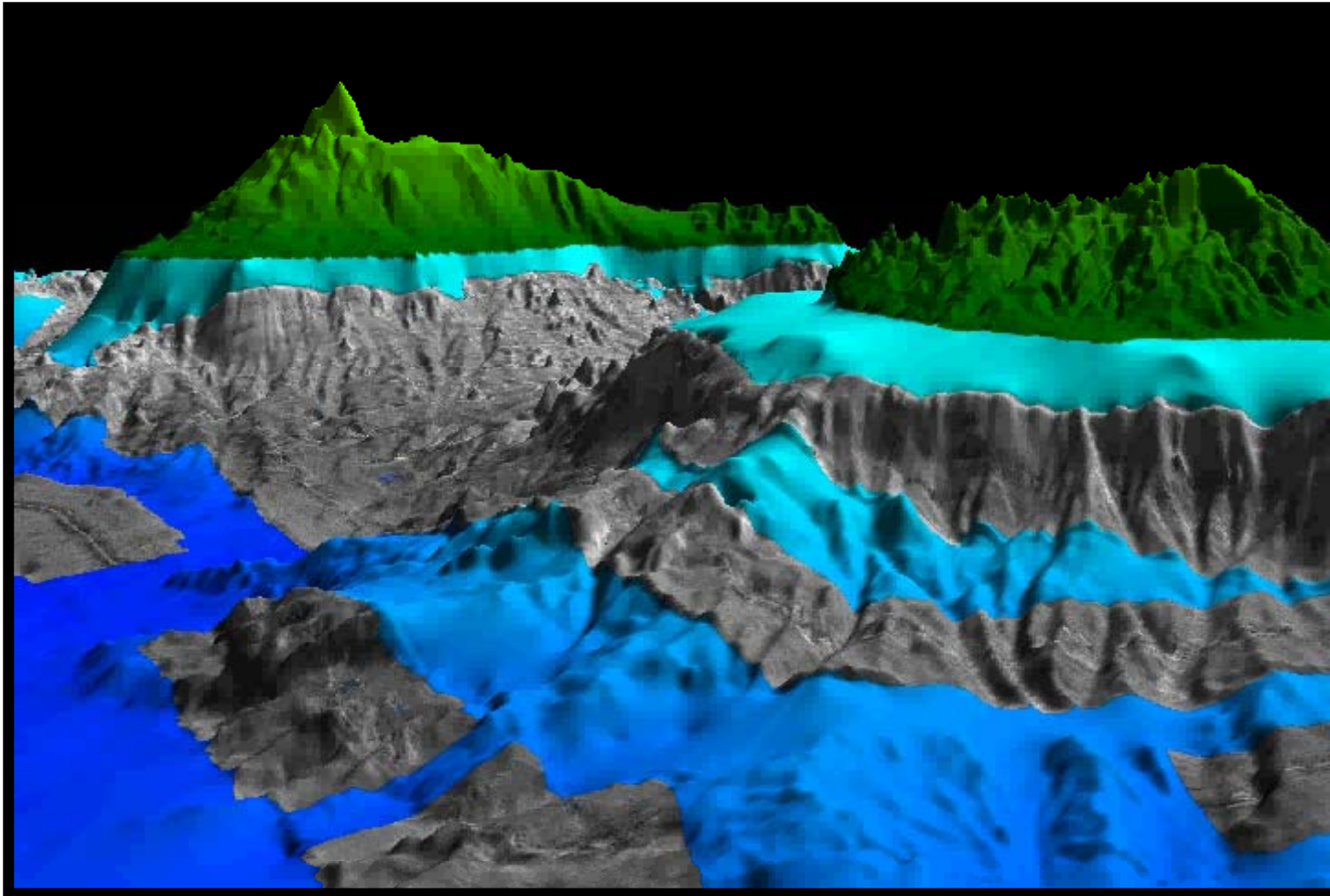
Sidescan Sonar

**Interpretation map of the channel
between Gran Canaria and Tenerife.
(Krastel et al., 2001)**



EM12 Backscatter data draped on top of the bathymetric map

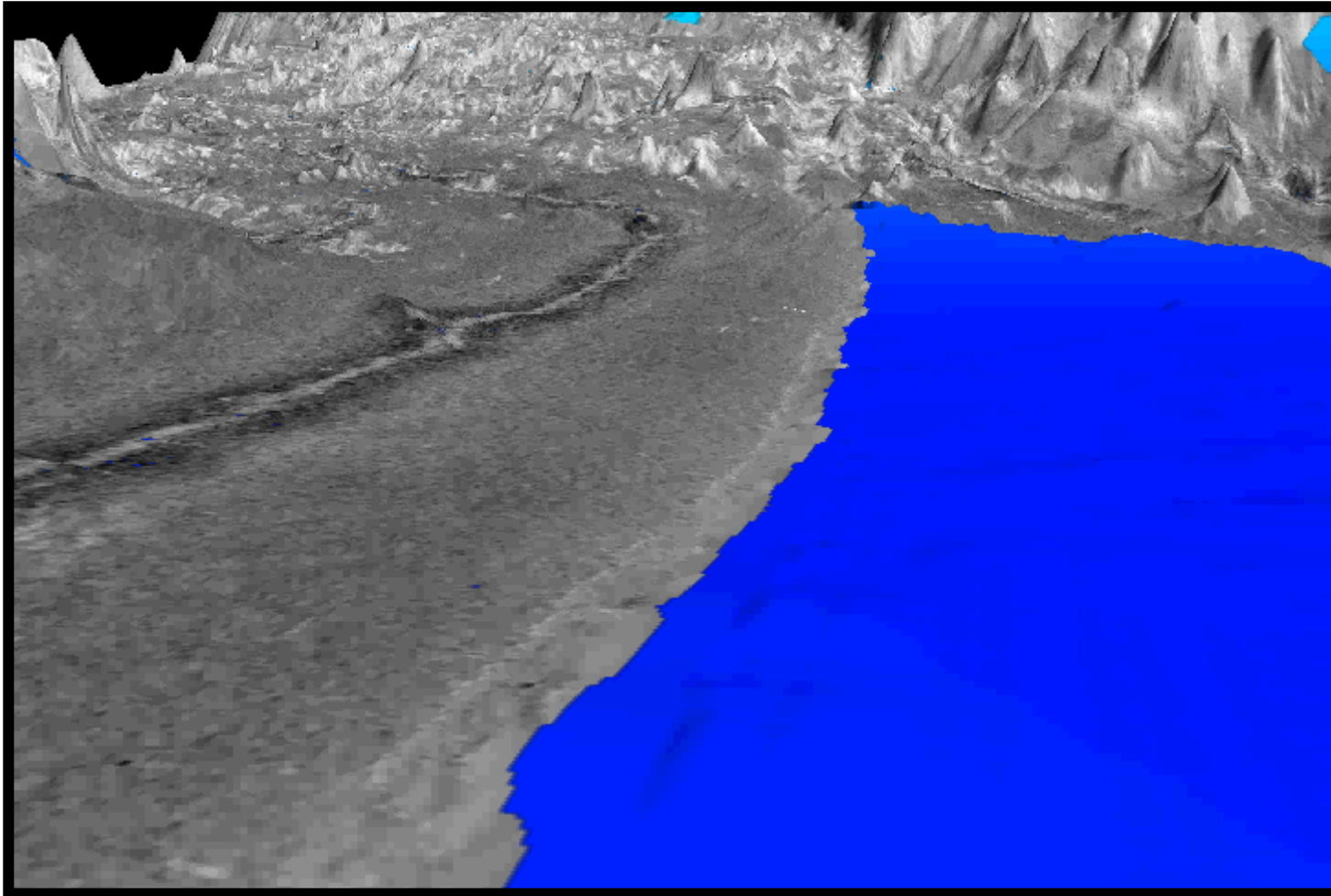
(area between Gran Canaria and Tenerife)



Krastel, unpublished data

EM12 Backscatter data draped on top of the bathymetric map

(area between Gran Canaria and Tenerife)



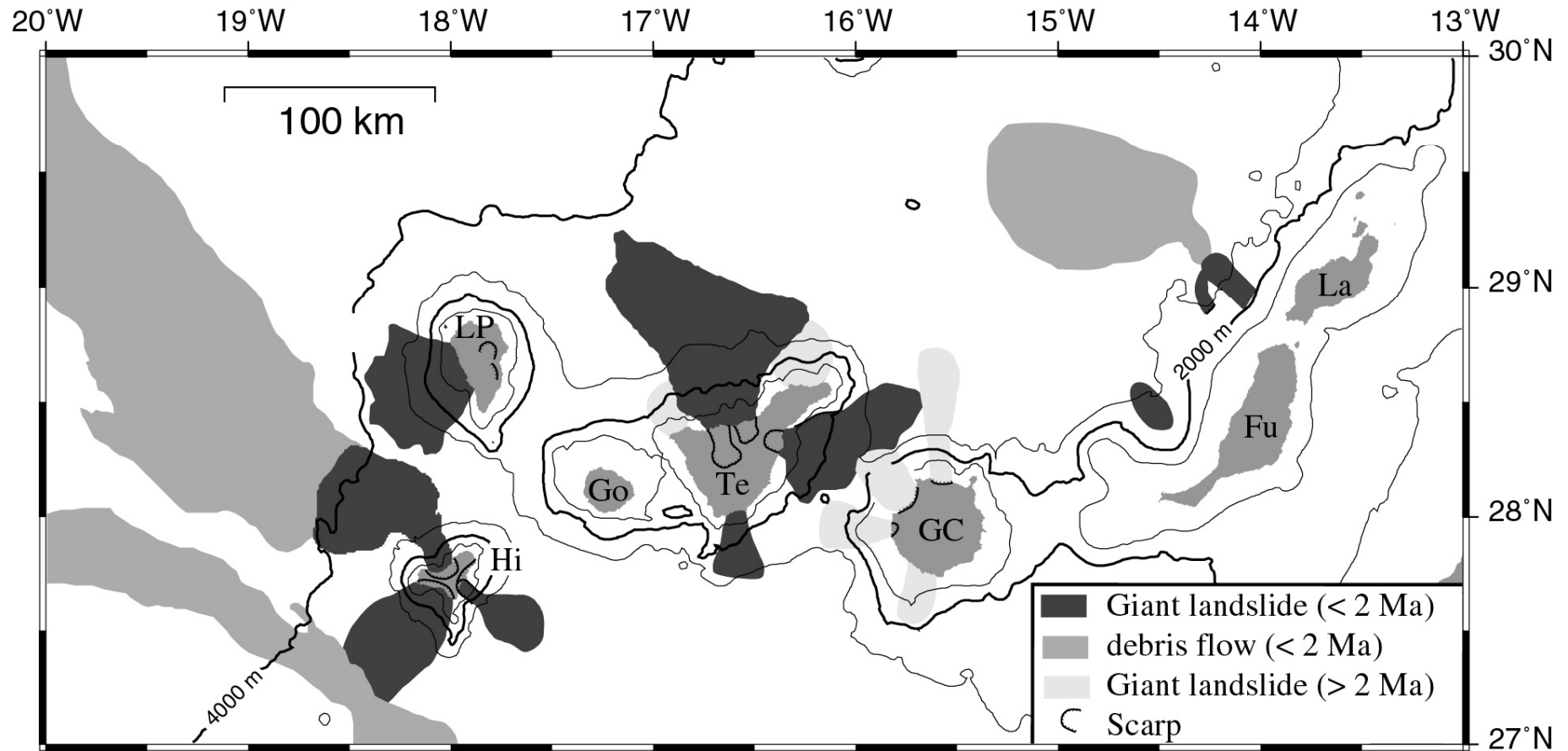
Krastel, unpublished data



future ocean
KIEL MARINE SCIENCES

Submarine Mapping

Sidescan Sonar



Giant landslides on the flanks of the Canary Islands. All periods of major magmatic activity are accompanied by large scale mass wasting. The long-lasting volcanic activity of the islands of the Canary Archipelago is balanced by a corresponding long history of destruction. (Krastel et al., 2001).

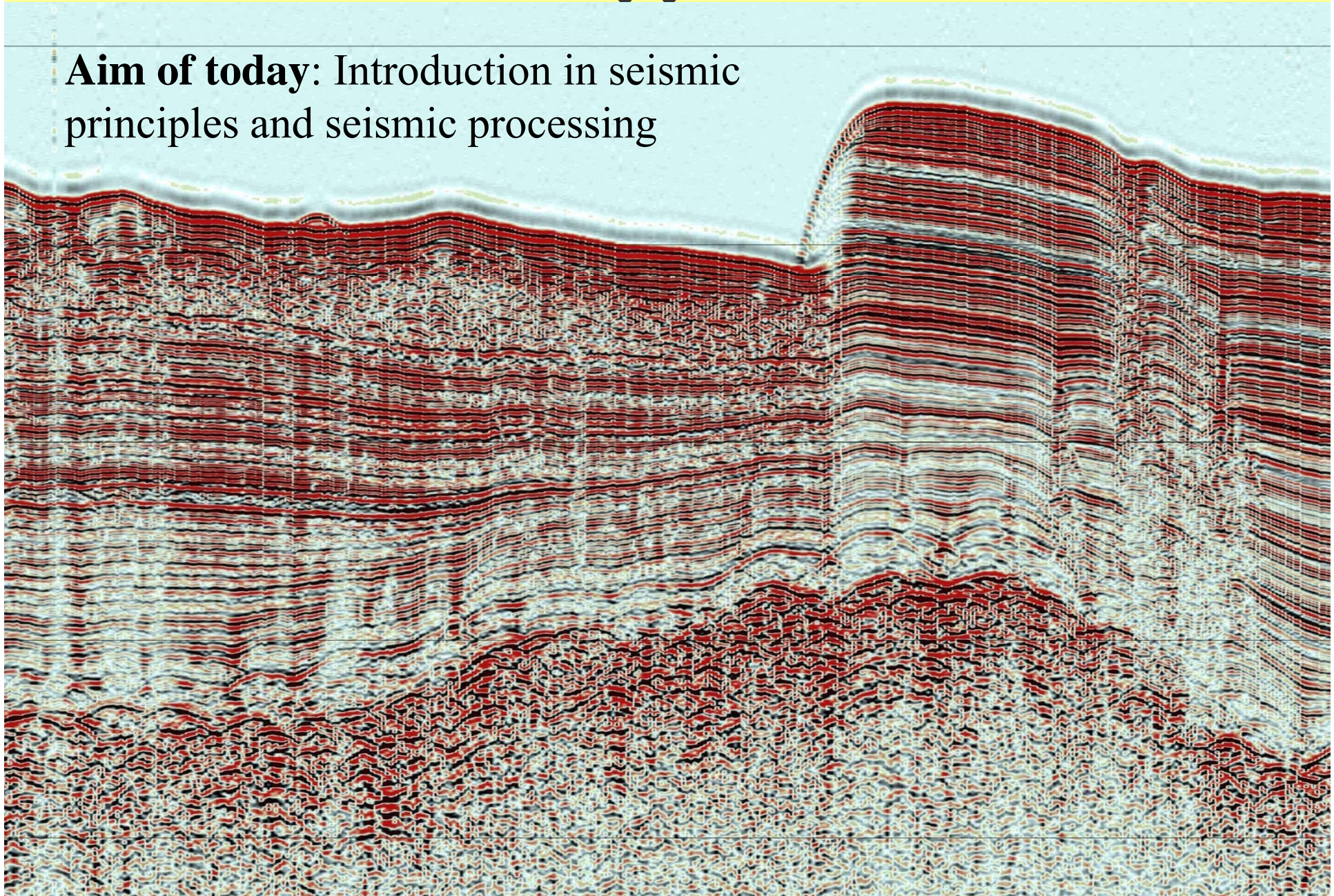


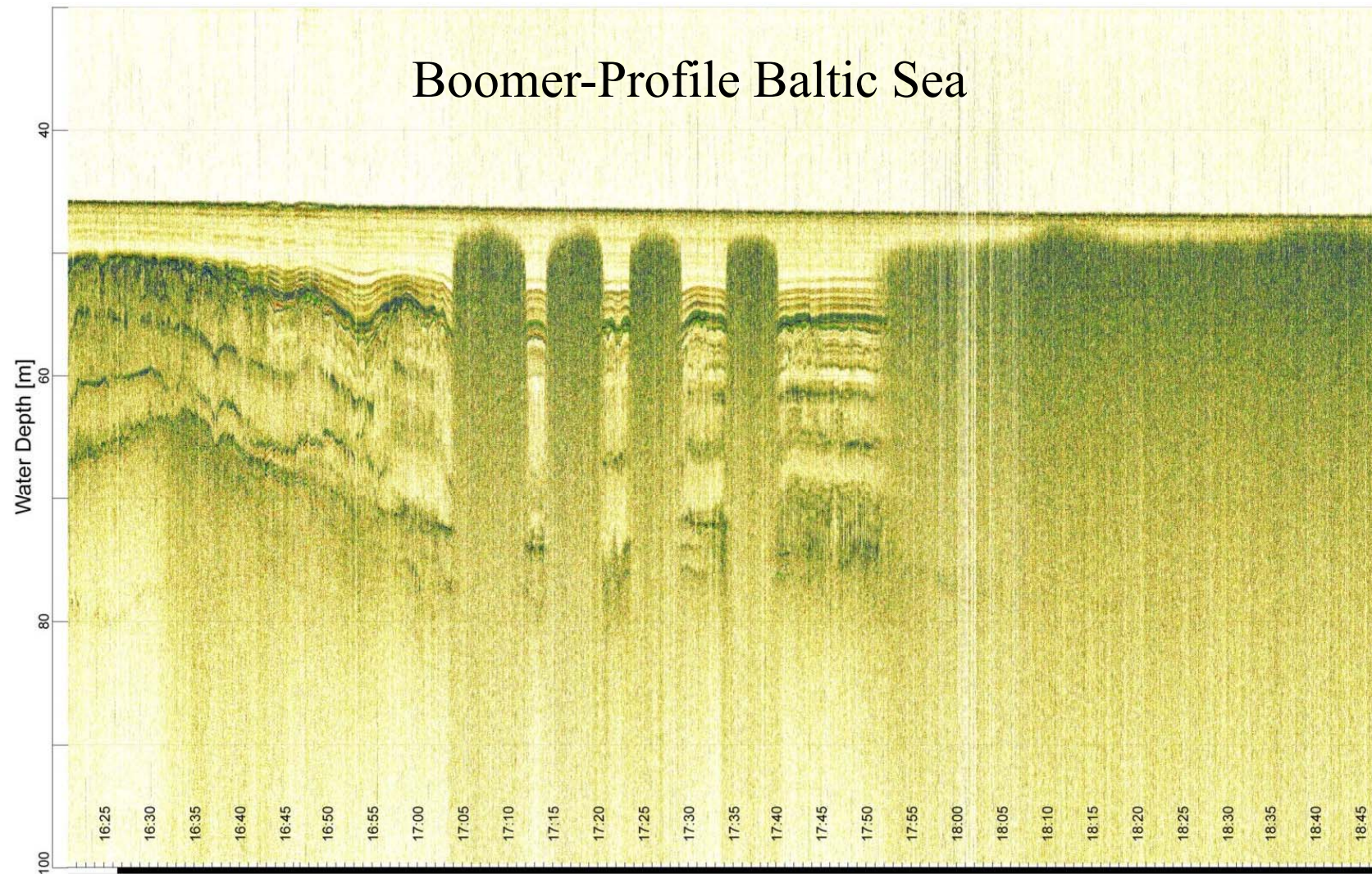
future ocean
KIEL MARINE SCIENCES

Submarine Mapping

Seismic imaging – some basics

Aim of today: Introduction in seismic principles and seismic processing



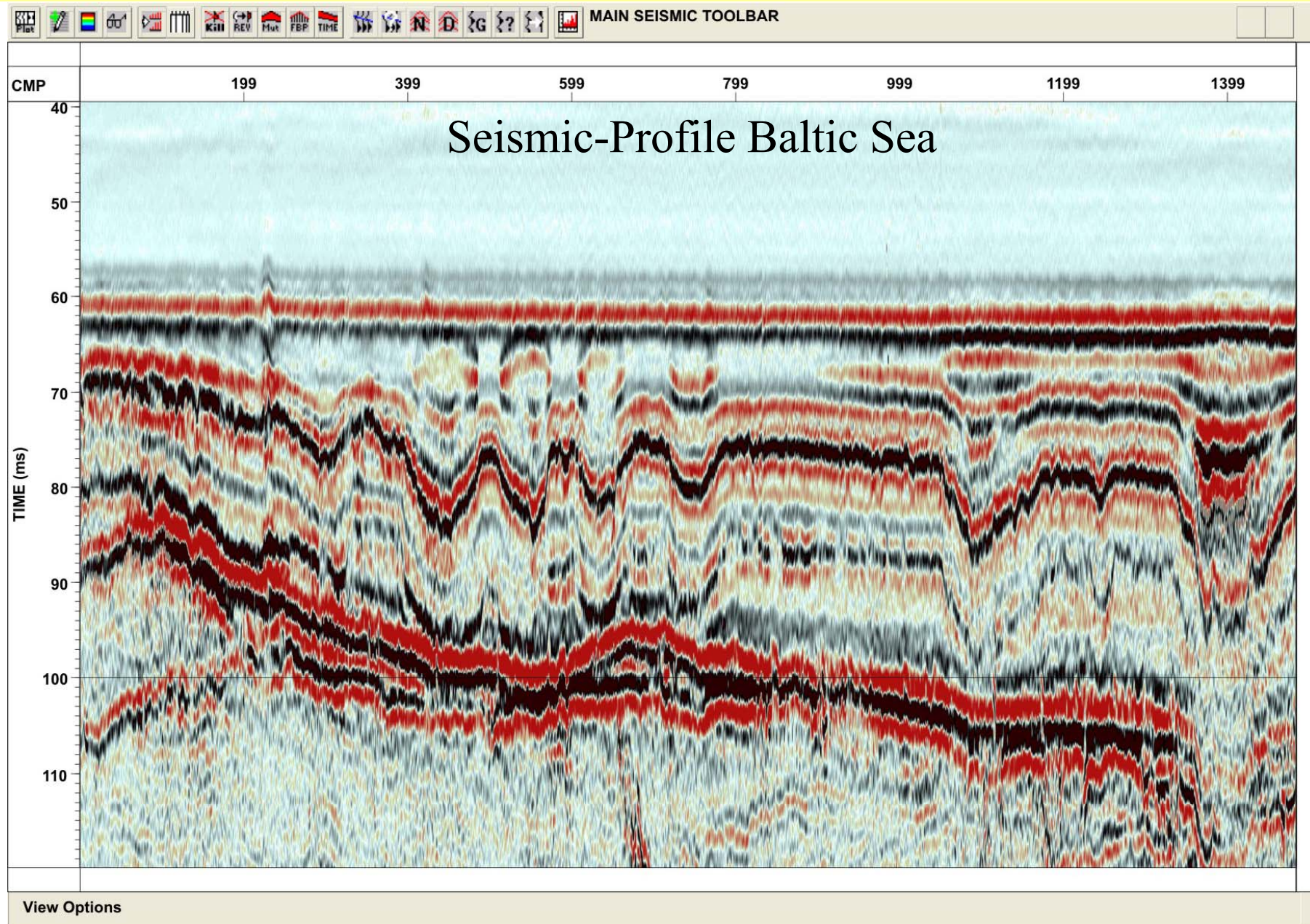




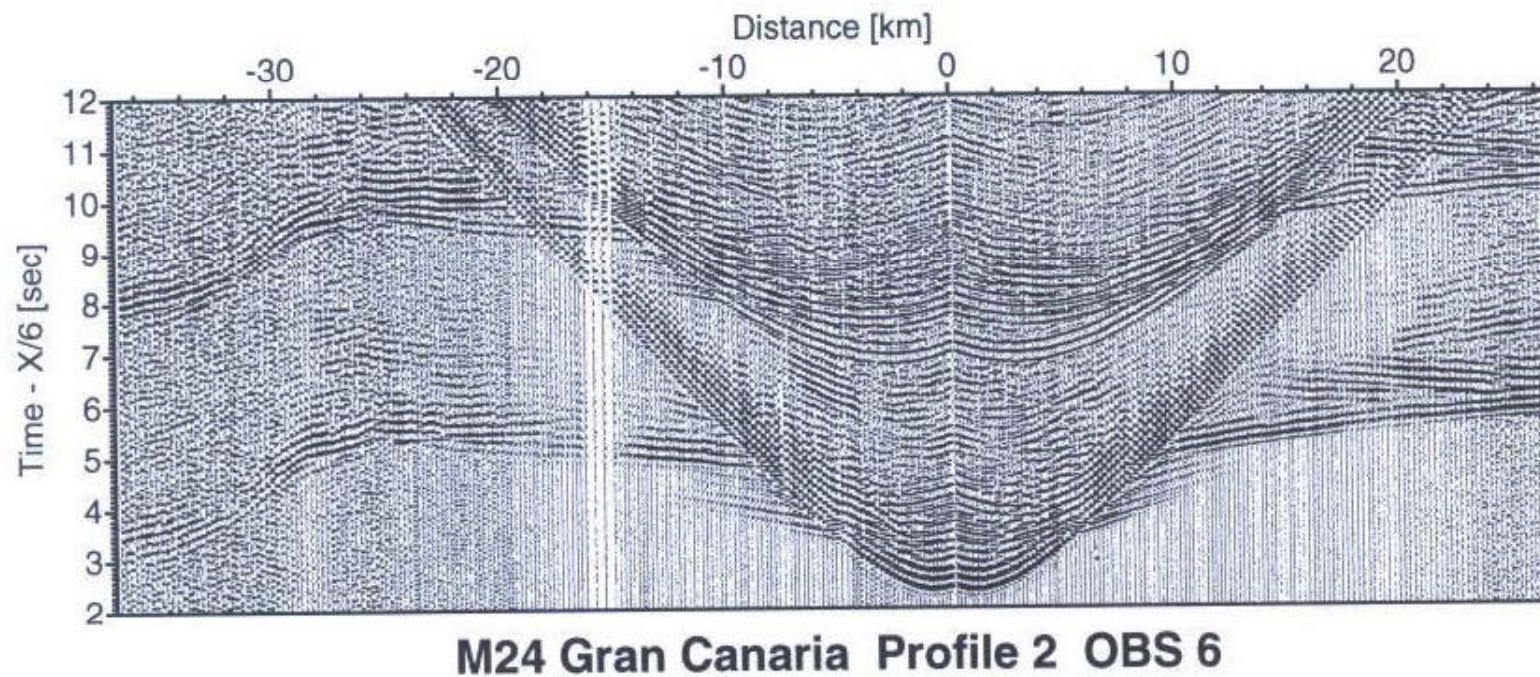
future ocean
KIEL MARINE SCIENCES

Submarine Mapping

Seismic imaging – some basics



OBS-Sektion



Aim of seismic measurements

Structural imaging by means of acoustic waves

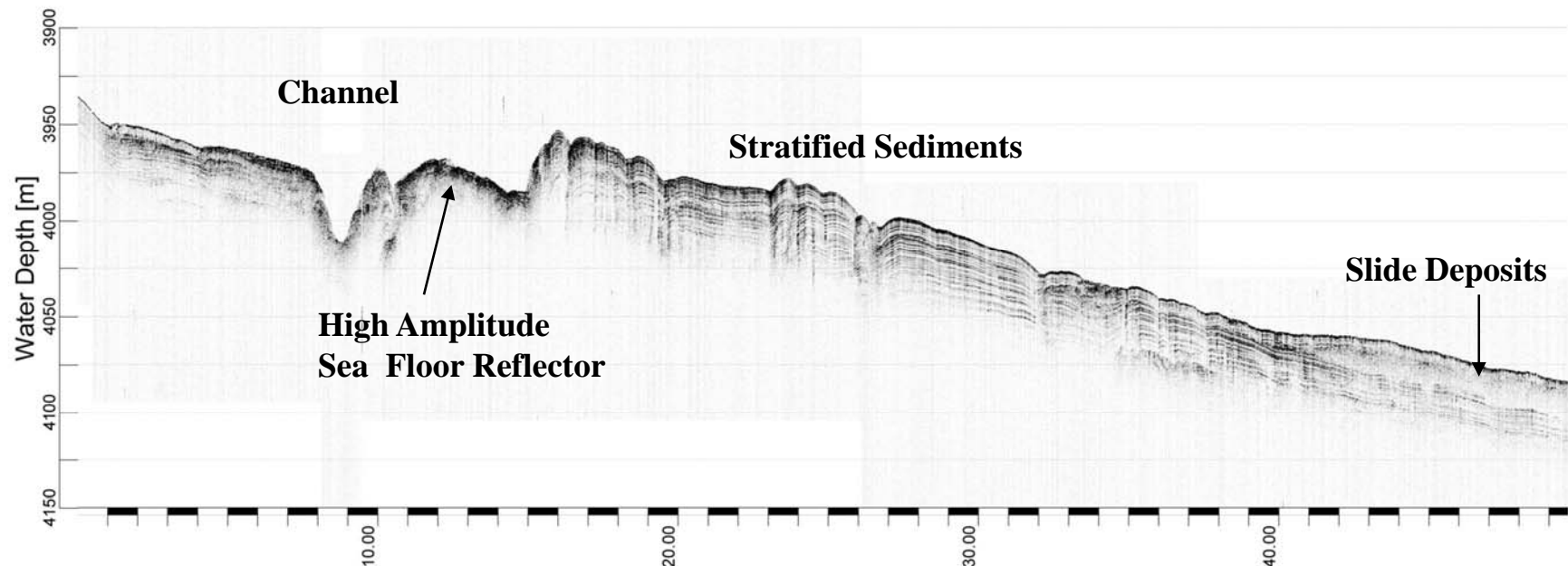
Output

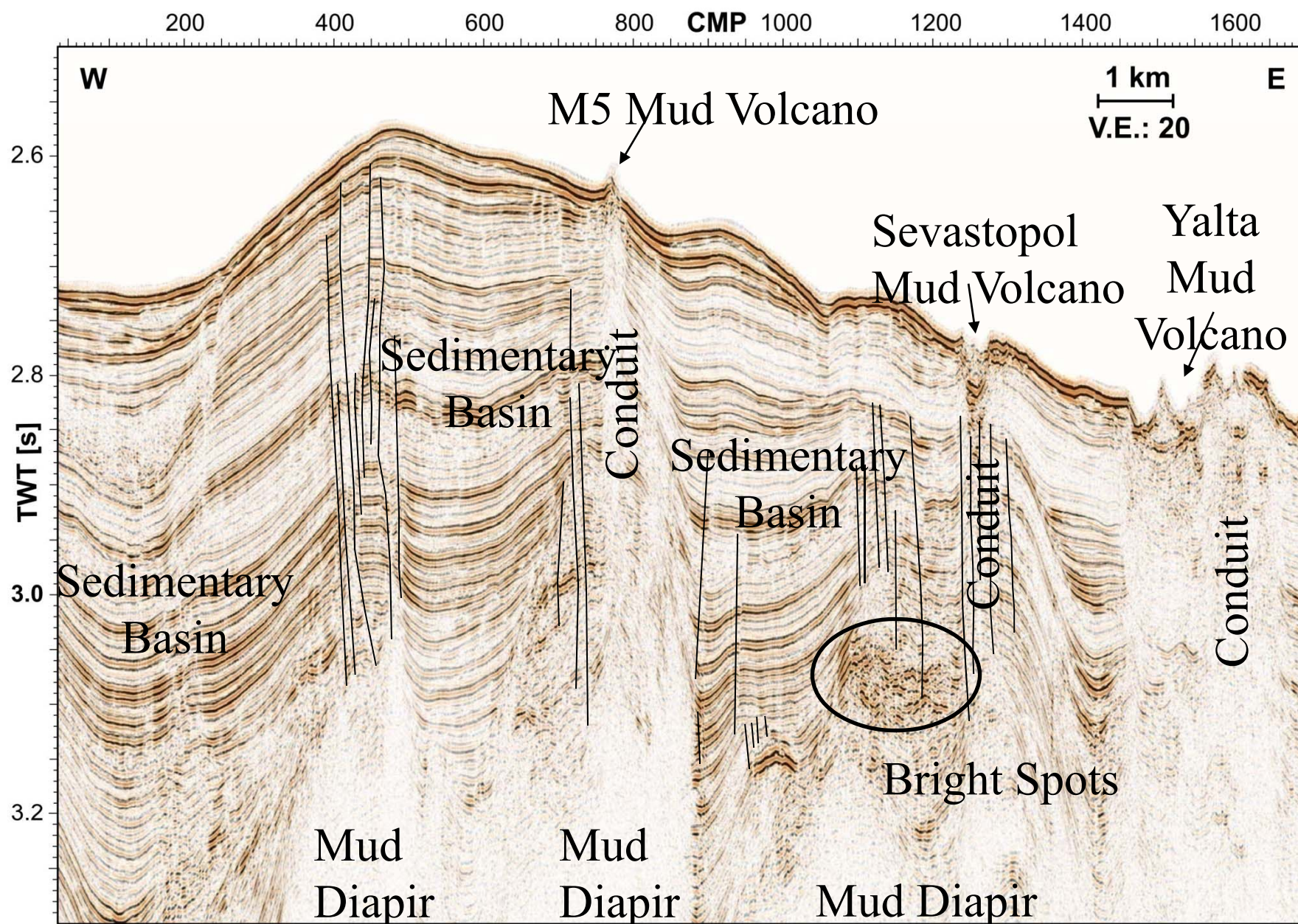
Seismogram with travel times and amplitudes

Resulting information

Imaging of structures

Physical properties (e.g. sound velocity)





Main applications:

Hydrocarbon exploration

Structural imaging at different scales

Crustal structures

Sediments (e.g., slides, contourites, channels, clinoforms)

Archeology

Fluid migration

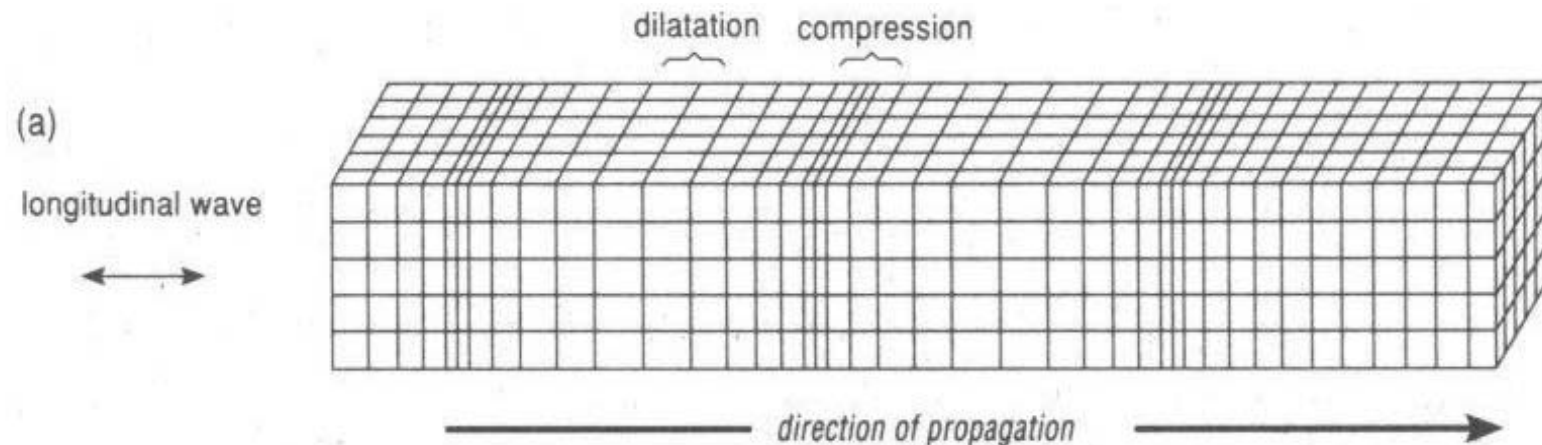
Gas Hydrates

Faults, Tectonics

Seismic wave propagation

Body waves

P-waves: (Compressional or primary waves)



Particles move in direction of propagation

$$v_p = \left(\frac{\kappa + \frac{4}{3}\mu}{\rho} \right)^{\frac{1}{2}}$$

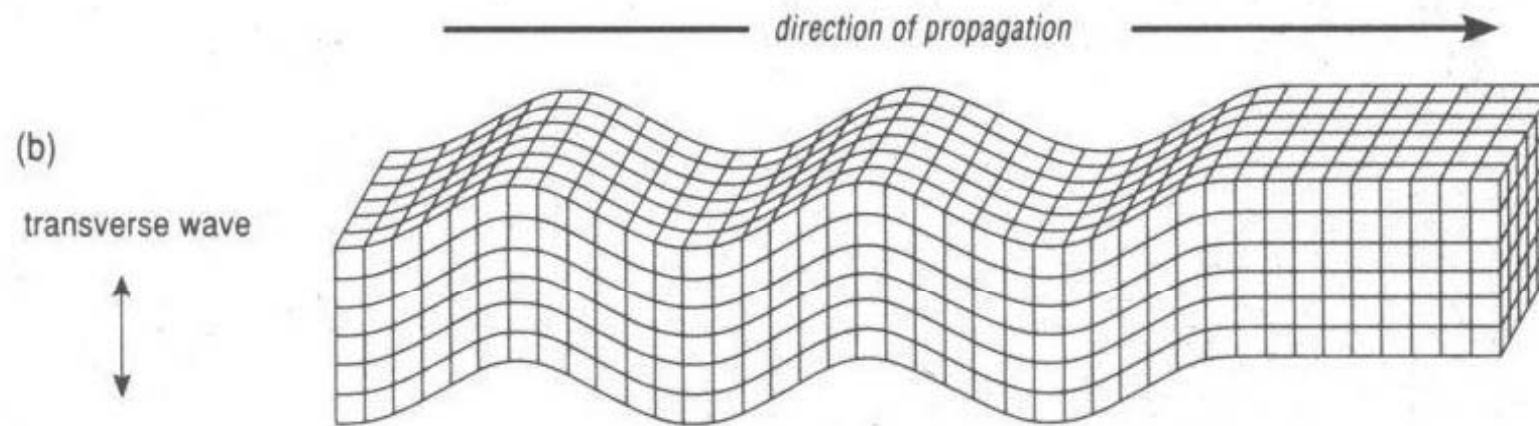
mit Kappa κ =Kompressionsmodul (Bulk modul)

Mu μ =Schermodul

Rho ρ = Dichte

Body waves

S-waves: (Shear- or secondary waves)



Particles move perpendicular to direction of propagation

$$v_s = \left(\frac{\mu}{\rho} \right)^{\frac{1}{2}}$$

Shear modulus in fluids=0 =>

No shear waves in water =>

Cannot be recorded with a streamer

Table 4.1 Approximate ranges of compressional wave velocities in common offshore materials.

Lithology	V_p (km s ⁻¹)
Seawater	1.45–1.53
Unconsolidated sand	1.5–2.0
Deep-sea pelagic ooze	1.5–1.9
Clay	1.0–2.5
Shales	2.0–4.1
Permafrost	3.5–4.0
Sandstones (Tertiary)	2.0–2.5
Sandstones (Carboniferous)	4.0–4.5
Chalk (Cretaceous)	2.0–2.5
Limestones (Jurassic)	3.0–4.0
Limestones (Carboniferous)	5.0–5.5
Dolomite	2.5–6.5
Halite	4.0–5.5
Basalt	3.5–6.0
Gabbro	6.0–7.0
Granite	4.0–6.1
Ultrabasic rock	7.5–8.5
Serpentinite	5.5–6.5
Gneiss	3.5–7.6

Data sources: Christensen (1982), Kearey and Brooks (1991), Sheriff and Geldart (1995), Reynolds (1996).

What happens at an interface?

$$\frac{\sin i}{\alpha_1} = \frac{\sin e_1}{\alpha_1} = \frac{\sin f_1}{\beta_1} = \frac{\sin e_2}{\alpha_2} = \frac{\sin f_2}{\beta_2} = p \quad (4.80)$$

Reflection

Refraction

Conversion

We neglect conversion

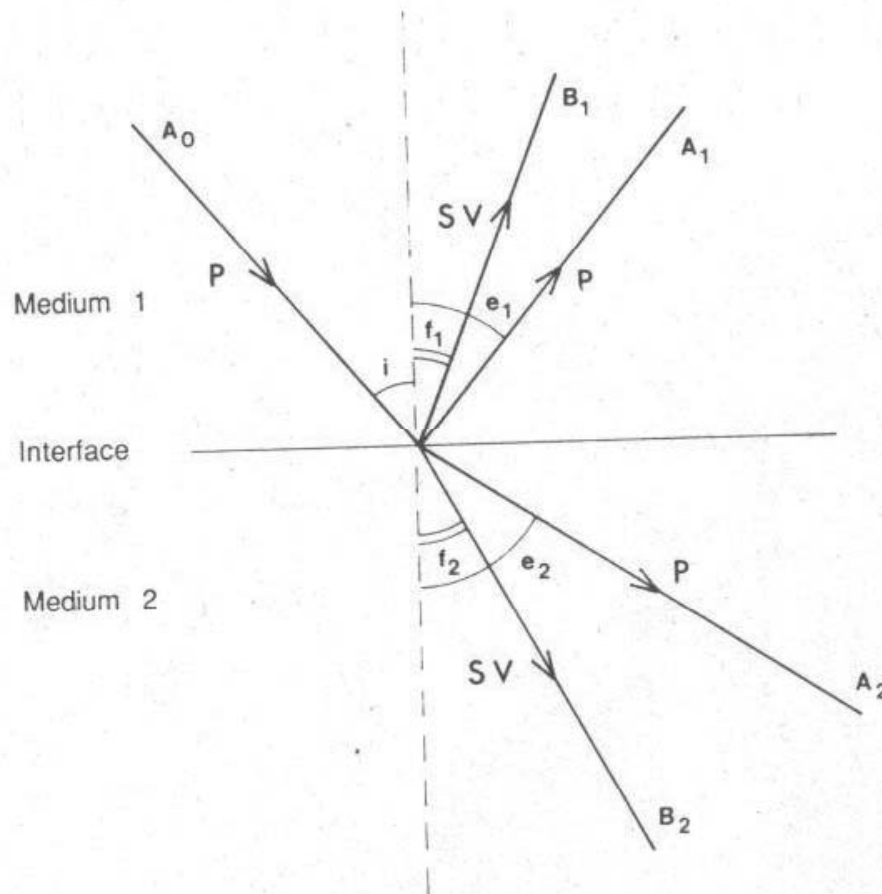


Figure 4.43. Waves generated at an interface between two elastic media by an incident P-wave. The incident P-wave has amplitude A_0 and angle of incidence i . The reflected P- and SV-waves have angles of reflection e_1 and f_1 and amplitude A_1 and B_1 , respectively. The transmitted P- and SV-waves have angles of refraction e_2 and f_2 and amplitude A_2 and B_2 , respectively.

Acoustic energy is reflected if the seismic impedance is changing

$$Z = v * \rho$$

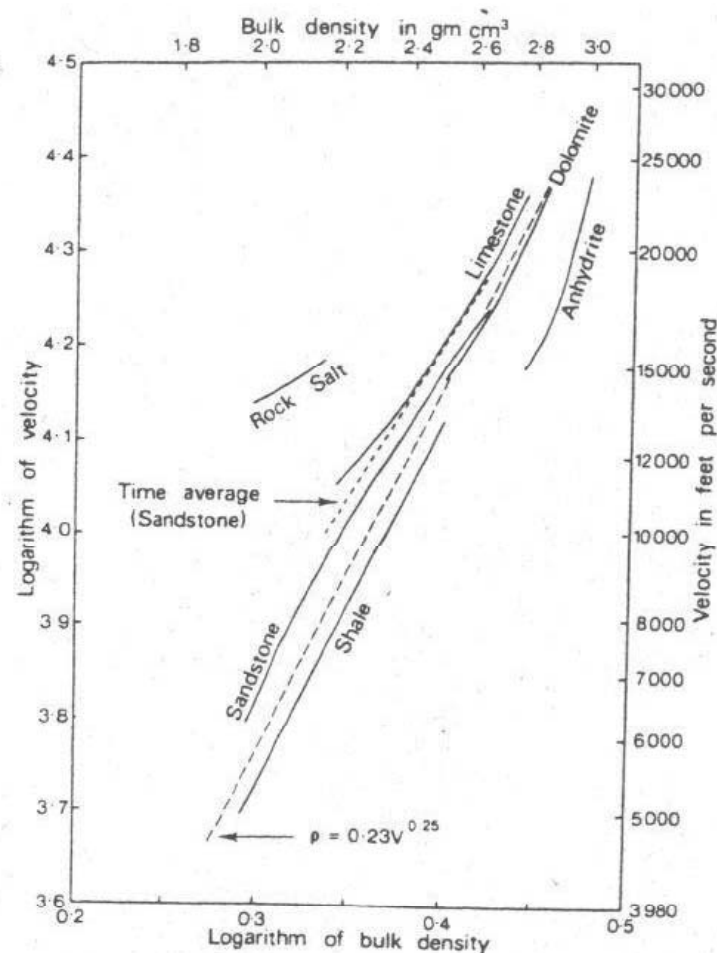


Figure 2/7 Velocity–density relationships in rocks of different lithology (after Gardner *et al.*, 1974).

Table 7.3 Typical seismic reflection coefficients (*R*)

Interface	Approximate <i>R</i>
Air over sea	1.0
Sea over limestone	0.65
Sea over boulder clay	0.45
Sea over recent sand/clay	0.3
Clays over gas sand, 500 m	–0.30
Sea-bed multiples	0.25
Sand/shale over limestone, 1500 m	0.20
10% change in acoustic impedance	±0.05

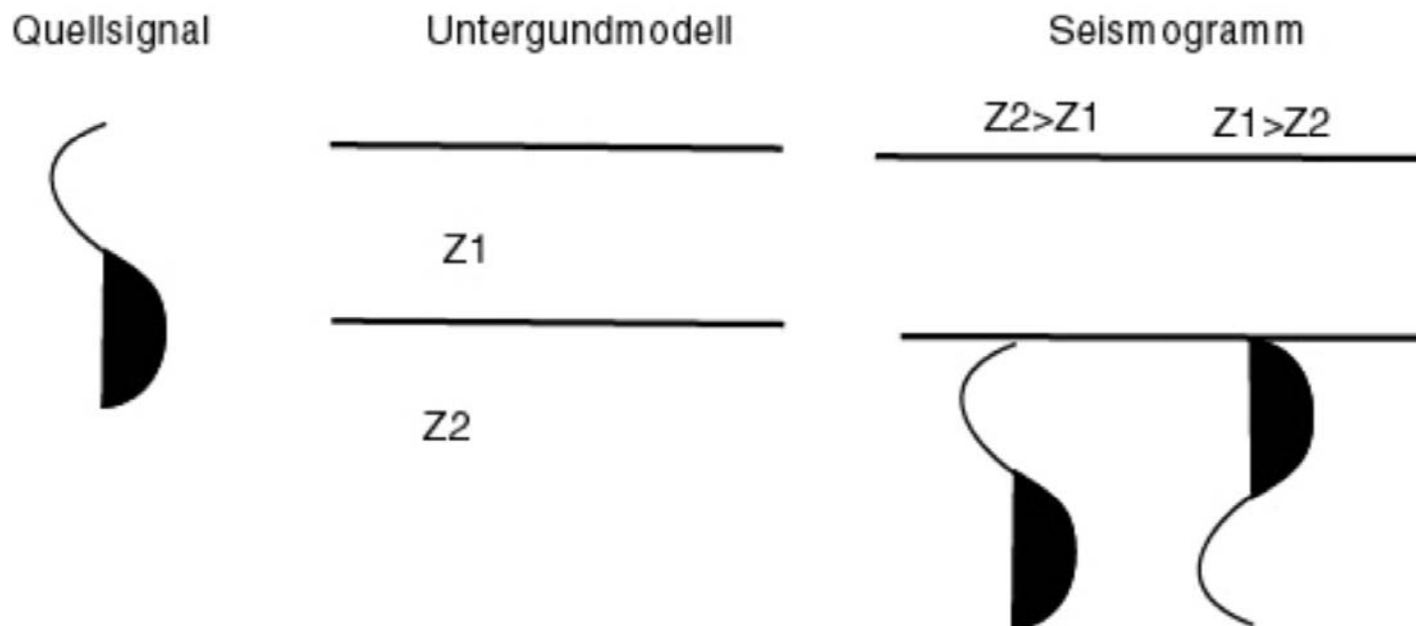
Strong impedance contrasts result in strong reflections

Reflections coefficient: $R = (Z_2 - Z_1) / (Z_2 + Z_1)$.

Transmission coefficient: $T = 1 - R = 2Z_1 / (Z_2 + Z_1)$

(Only for normal incidence)

Reflections can be positive or negative:



Seismograms are the result of reflections at layer boundaries. Interference at closely-spaced layers are common.

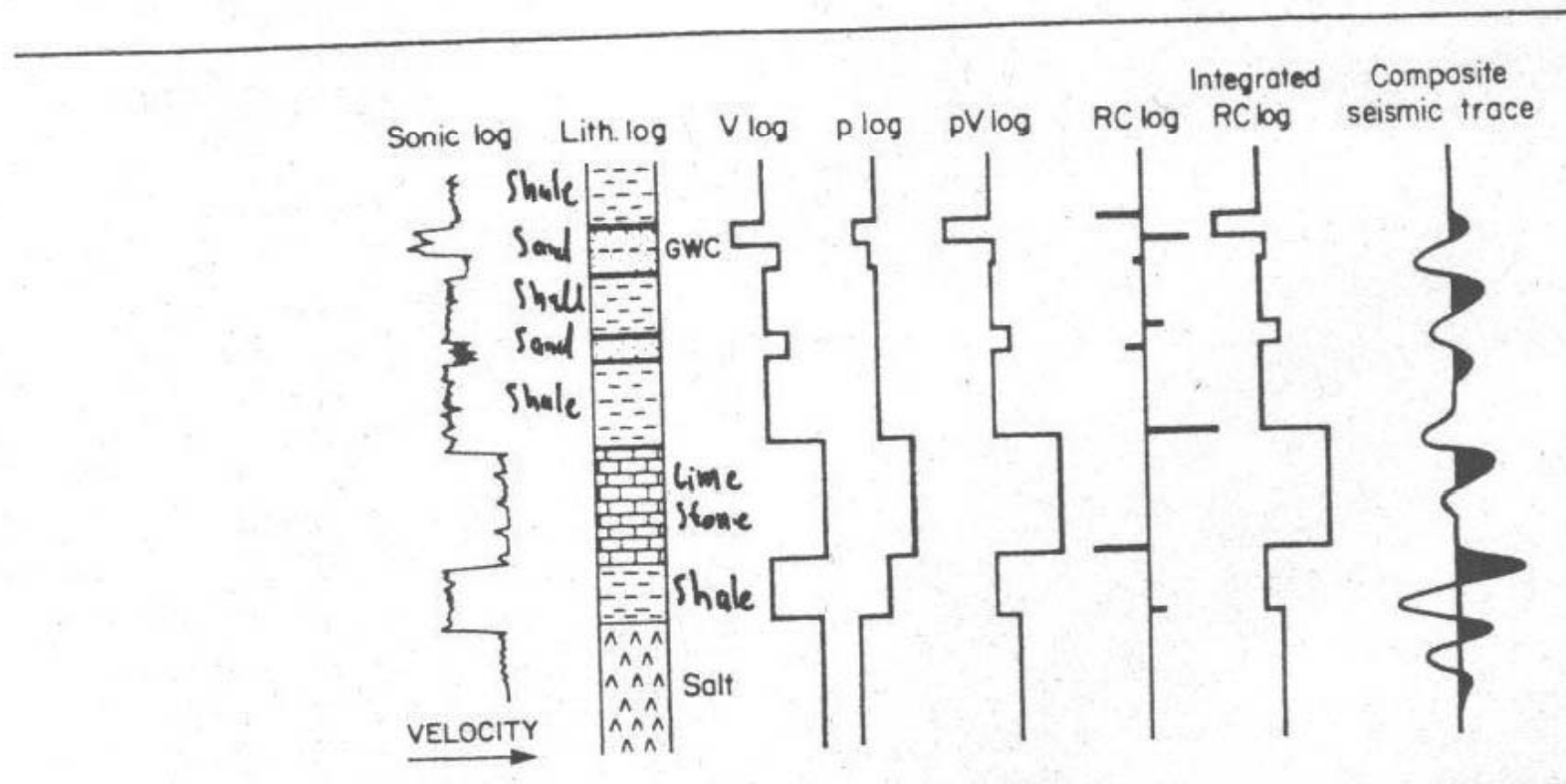


FIGURE 2.9 Diagram showing the difference in resolution between a wireline sonic log and a seismic trace. After Anstey, 1980a, by permission of IHRDC Press.

The exact behavior at interfaces for non vertical incidence is described by the Zoeppritz-equation:

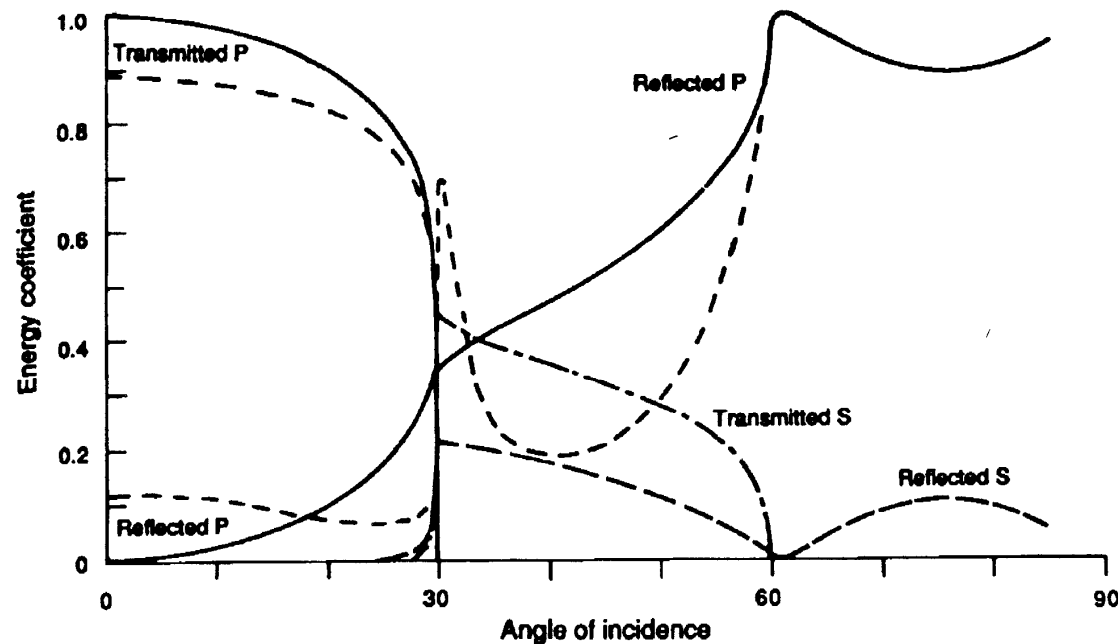


Figure 4.44. Reflected and transmitted energy (energy/incident energy) for the situation illustrated in Figure 4.43: a P-wave incident on an interface between two solid media. For this example, $\alpha_1/\alpha_2 = 0.5$, $\rho_1/\rho_2 = 2.0$, $\alpha_1/\beta_1 = 1.87$ and $\alpha_2/\beta_2 = 1.73$. Solid lines, reflected and transmitted P-wave; long dashed line, reflected S-wave; the dashed and dotted line, transmitted S-wave; the short dashed lines, reflected and transmitted P-wave when $\rho_1/\rho_2 = 1.0$. (After Tooley et al. 1965.)

Calculation of travel time curves (for two layers)

Direct wave

Straight Line with gradient $1/v_1$

$$t = x/v_1$$

Reflected wave

Hyperbola

$$t = \frac{2}{v_1} \sqrt{h_1^2 + \frac{x^2}{4}}$$

Refracted wave

Straight line with gradient $1/v_2$

$$t = \frac{2h_1}{v_1} \sqrt{1 - \frac{v_1^2}{v_2^2}} + \frac{x}{v_2}$$

Occurs from the critical distance on

$$i_c = \arcsin\left(\frac{v_1}{v_2}\right)$$

$$x_c = 2 * h_1 * v_1 * \frac{1}{\sqrt{v_2^2 - v_1^2}}$$

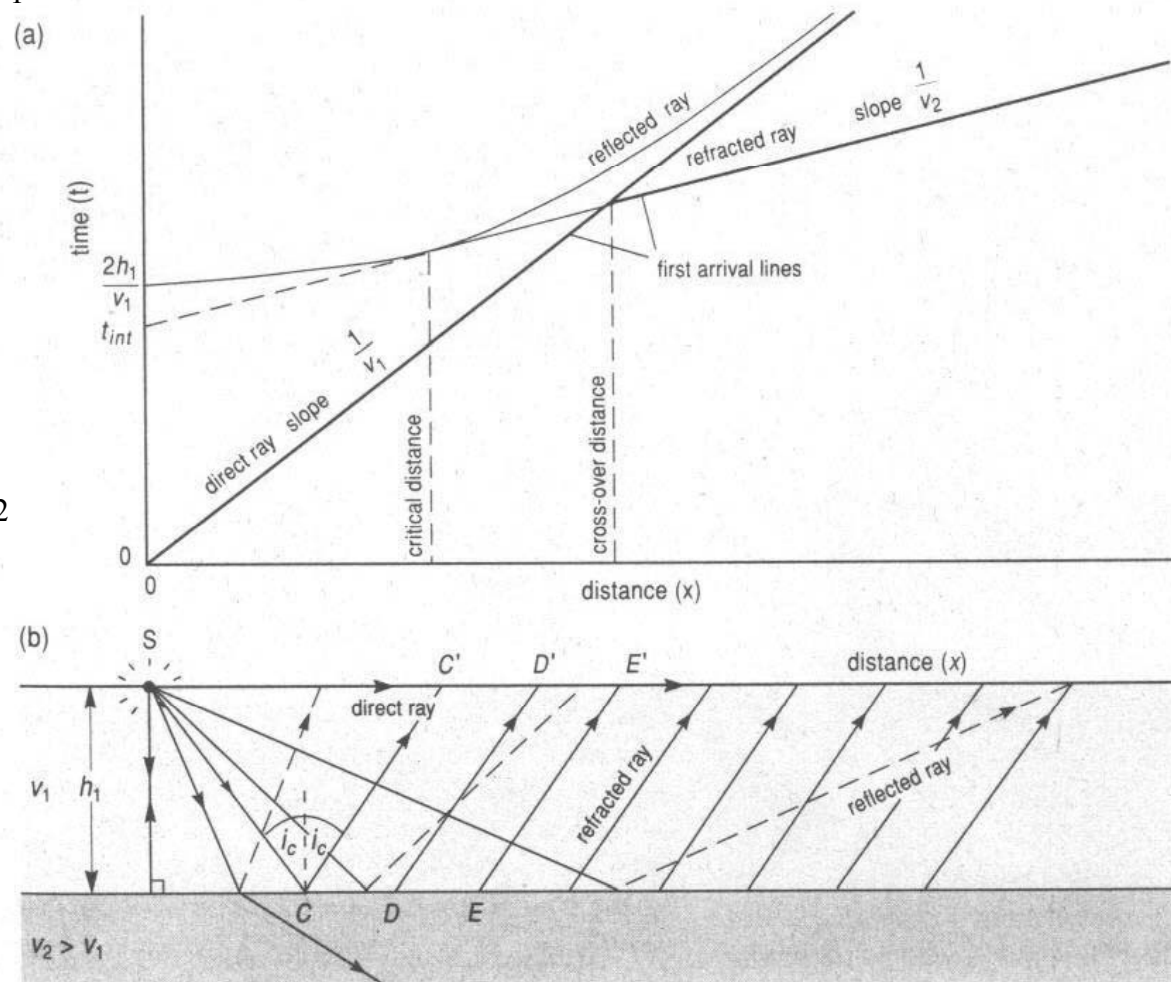


Figure 6.5 Travel-times of refracted and other rays.

Calculation of travel-time curves: Three and more layers

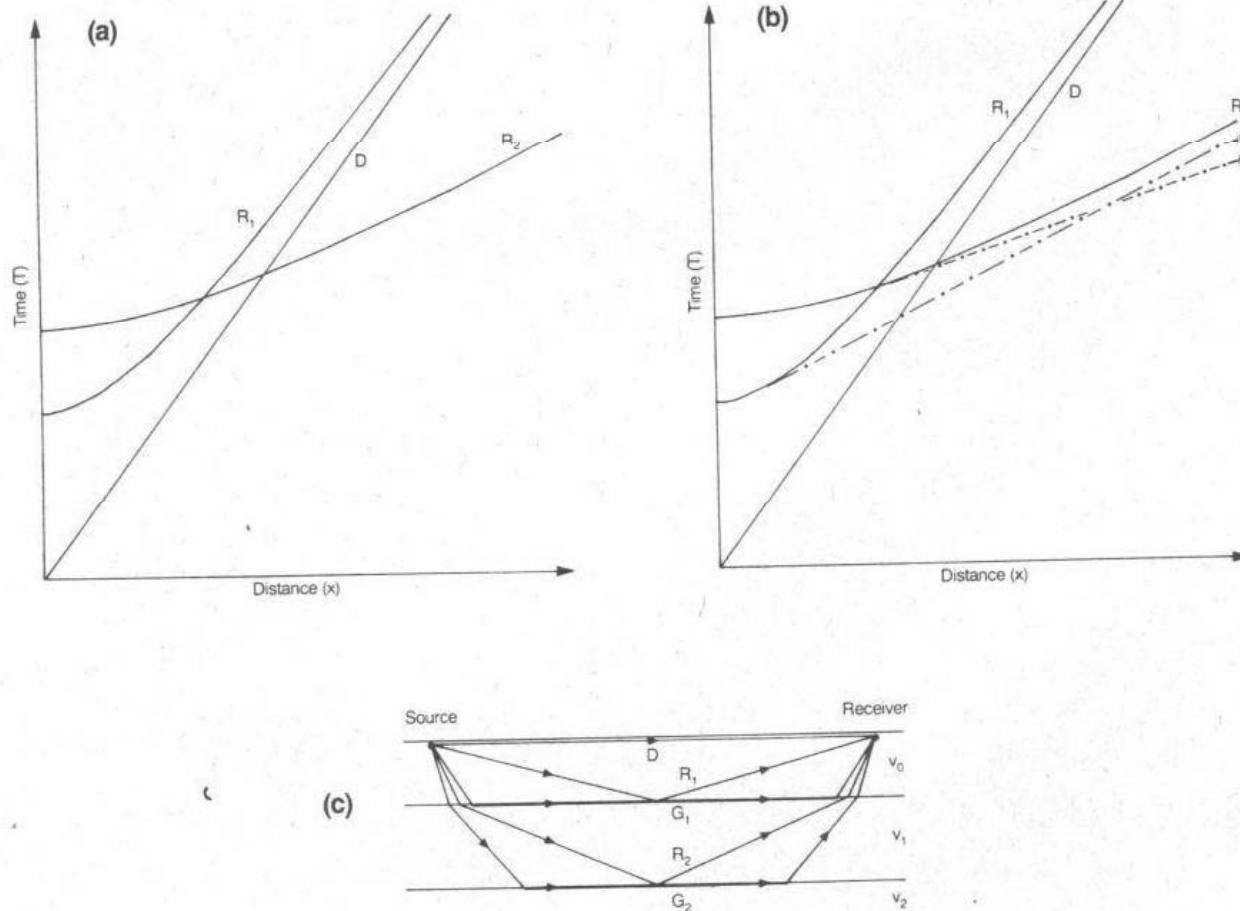


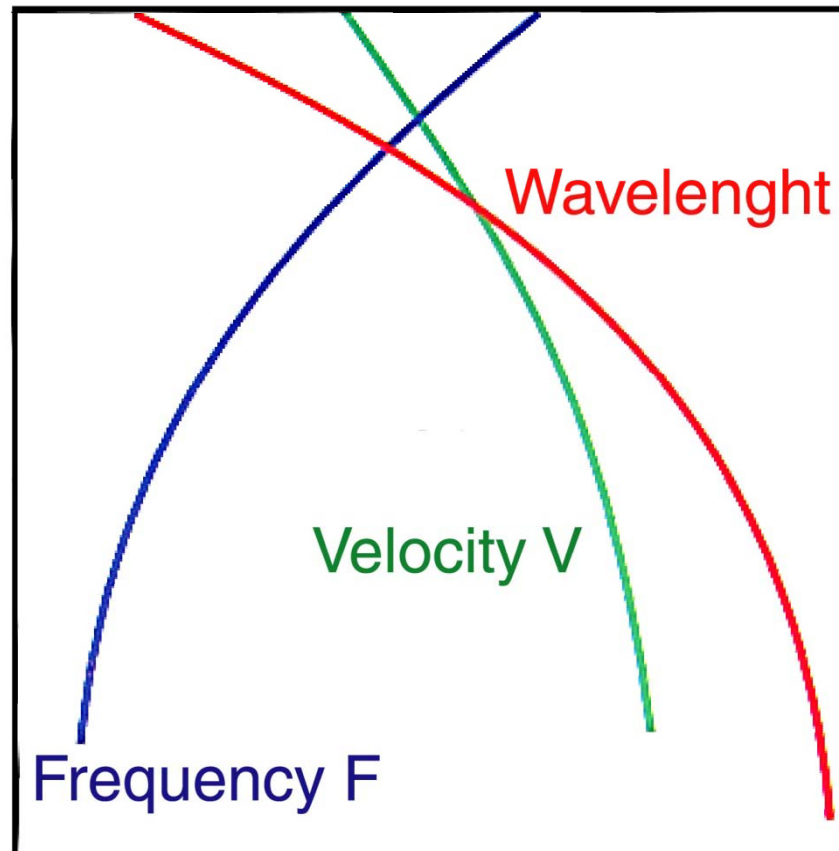
Figure 4.10 Seismic ray paths for three horizontal layers and the corresponding time-distance diagram (after Ewing, 1963).
 Copyright © 1963 John Wiley & Sons Inc.

Vertical resolution

Vertical resolution is controlled by the wavelength

$$\lambda = \frac{v}{f}$$

λ : Wavelength, f : Frequency, v : Velocity



The wavelength is increasing with depth due decreasing frequencies and increasing velocities .

$f = 10$ Hz (Large Airgun)

$v = 5000$ m/s (e.g. limestone)

$\lambda = 500$ m

$f = 1000$ Hz (Watergun)

$v = 1500$ m/s (e.g. water-saturated mud)

$\lambda = 1.5$ m

What is the minimum thickness of a unit for receiving separate impulses from its lower and upper boundary?

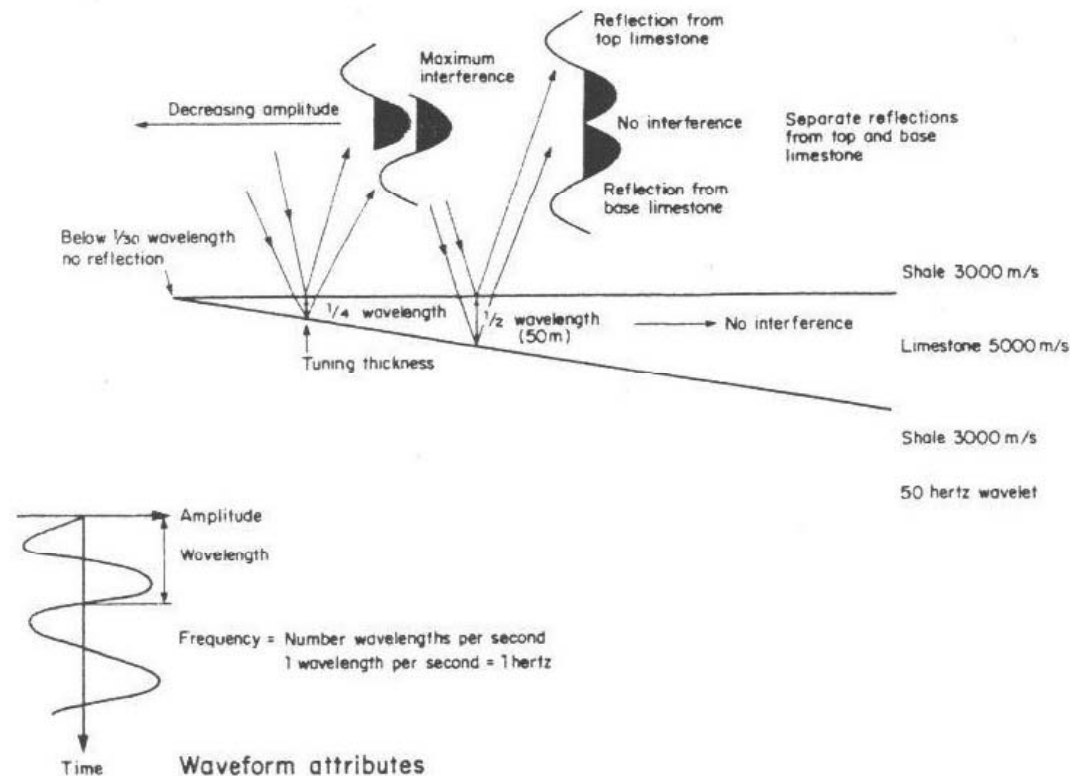


FIGURE 2.14 Interference effects associated with a high acoustic-impedance wedge encased in lower acoustic-impedance shale. The limestone must be thicker than half the seismic wavelength for no interference between reflections from its top and base. Maximum interference and amplitude of the resulting reflection occurs at a limestone thickness equivalent to one quarter of the seismic wavelength—the tuning thickness. For limestone thicknesses below one-quarter wavelength, the reflection remains the same shape but decreases in amplitude. Once the limestone is about one-thirtieth wavelength or less, reflections from the top and base effectively cancel and there is no detectable seismic response.

What is the minimum thickness of a unit for receiving separate impulses from its lower and upper boundary?

Answer: $h > \lambda/2$

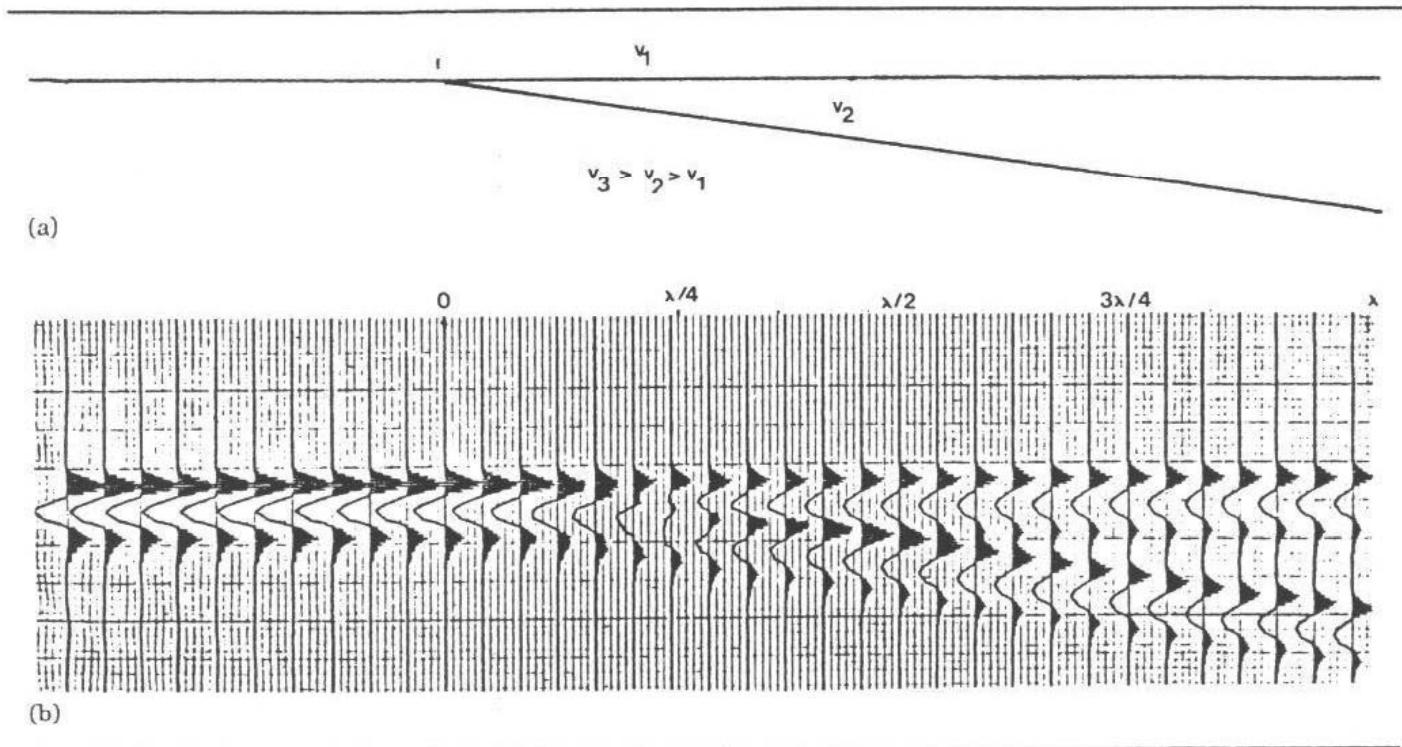


FIGURE 2.16 Reflection from a wedge of acoustic impedance intermediate in magnitude between that of the over- and underlying units. The thickness of the wedge is indicated as a fraction of the dominant wavelength. Note that there is still a reflection beyond the limit of the wedge due to the contrast in acoustic impedance between the over- and underlying layers. (a) Model. (b) Seismic section. Reprinted by permission of the EAEG from Sheriff, 1975, fig. 6.9, p. 128.

What is the minimum thickness of a layer for being imaged in a seismogram? Answer: ca. 1/30 of the wave length.

Horizontal resolution:

The horizontal resolution is controlled by the width of the Fresnel Zone

$$r_f = \frac{v}{2} \sqrt{\frac{t}{f}}$$

Some examples for radius of Fresnel Zones:

$$f = 10 \text{ Hz}$$

$$v = 1500 \text{ m/s}$$

$$t = 4 \text{ s (3000 m Wassertiefe)}$$

$$r_f = 750 * \text{SQR}(4/10) = 474 \text{ m}$$

$$f = 200 \text{ Hz}$$

$$v = 1500 \text{ m/s}$$

$$t = 20 \text{ ms (15 m Wassertiefe)}$$

$$r_f = 750 * \text{SQR}(0.02/200) = 7.5 \text{ m}$$

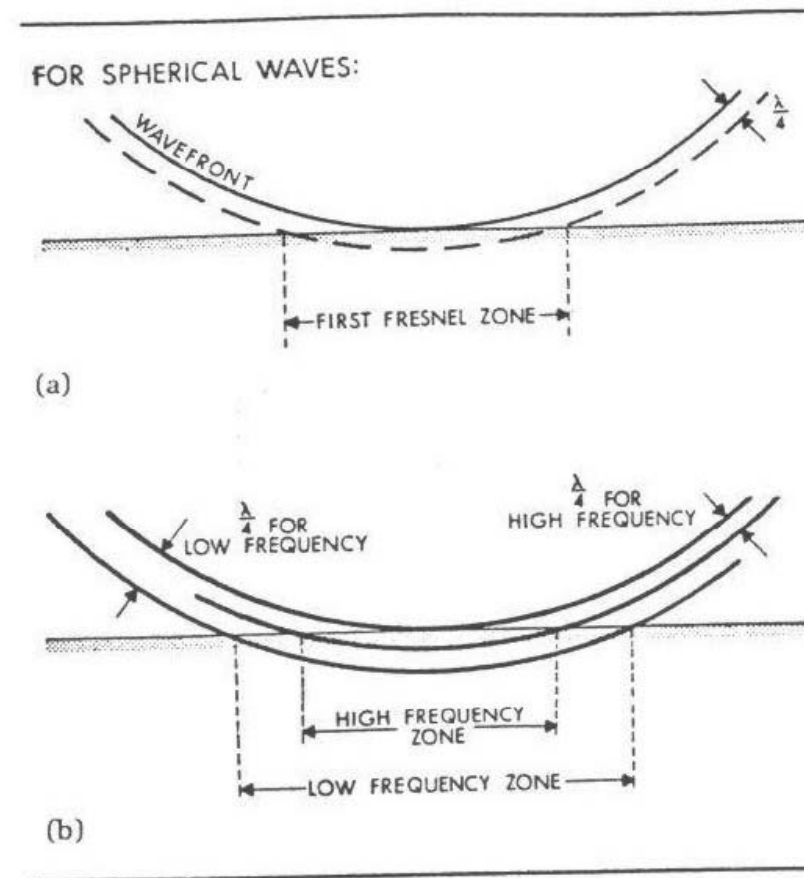


FIGURE 2.18 *Fresnel zone.* (a) The first energy to reach a geophone from a plane reflector is from the point where the reflector is first tangent to the wavefront. The area of the reflector that produces the reflection is limited by the area that the wavefront one-quarter wavelength later makes with the reflector. The energy arriving within this interval sums constructively to produce the reflection. (b) The Fresnel zone is larger for low-frequency components than for high-frequency ones. Reprinted by permission of the AAPG from Sheriff, 1977, fig. 7, p. 11.

Improving resolution through deconvolution and migration

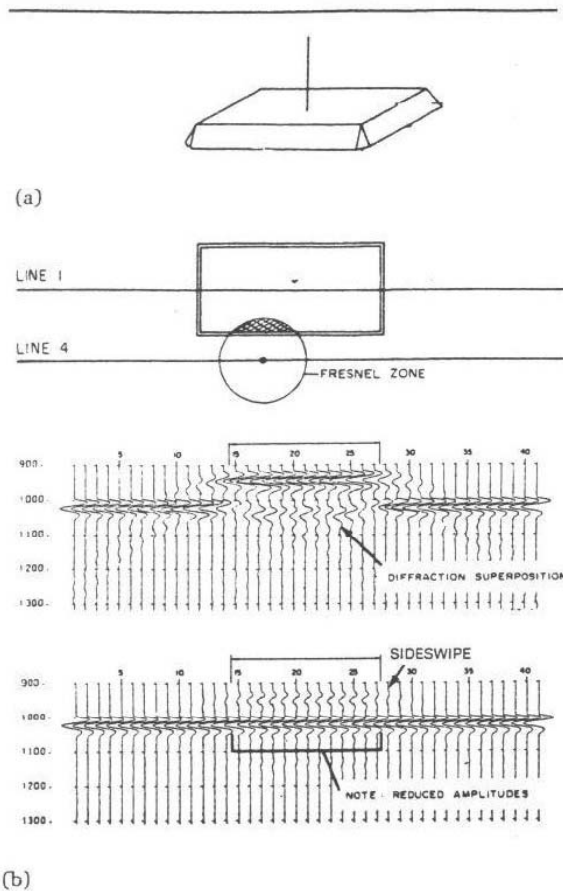
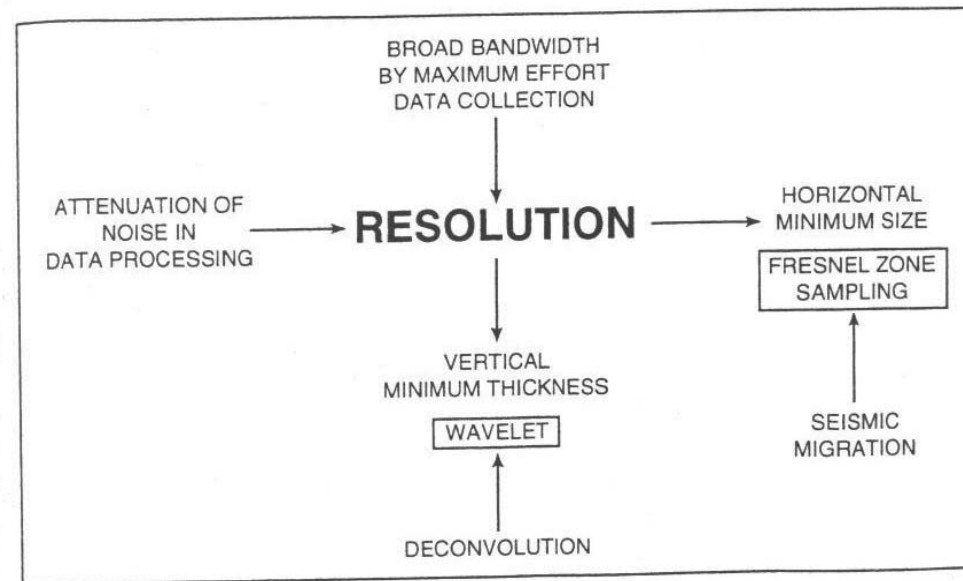


FIGURE 2.20 Reflections from a box model. (a) Isometric diagram of the model; the length:width:height:depth ratios are 10:5:1:10. (b) Plan showing Fresnel-zone dimensions relative to box dimensions. Line 1 passes over the box. Line 4 passes to the side of the box, but close enough for part of the Fresnel zone to impinge on the box. Reprinted by permission of IHRDC Press from Sheriff, 1980a; after Neidell and Poggiolmi, 1977.

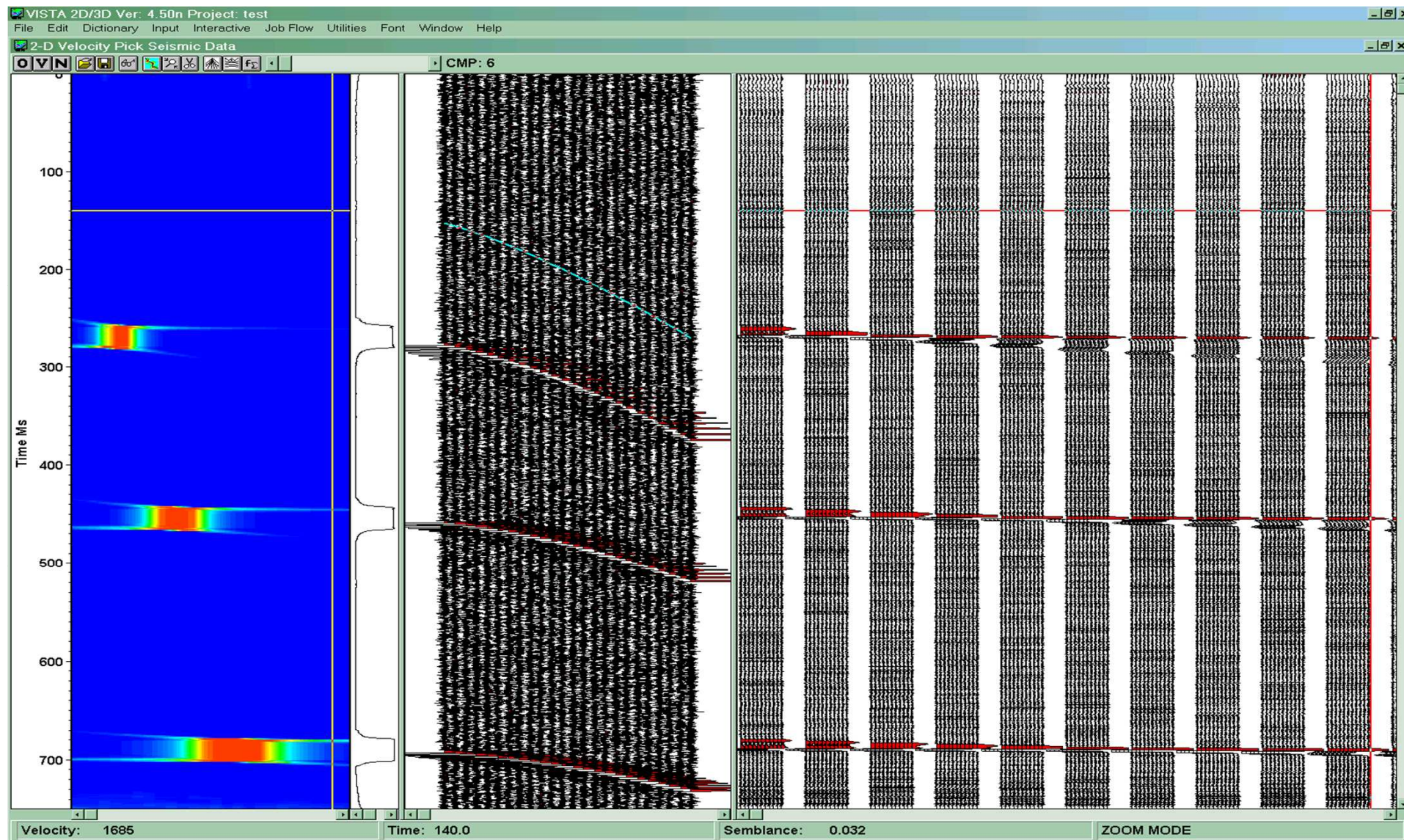




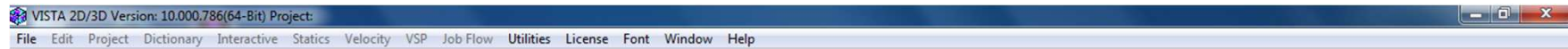
future ocean
KIEL MARINE SCIENCES

Acoustic Imaging

Seismic Data Processing

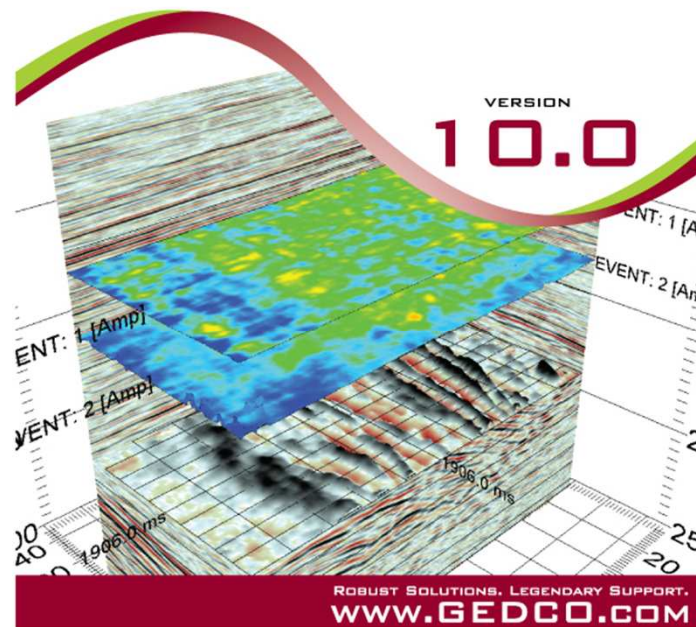


We will use Vista 2D/3D (GEDCO) , a low cost commercial software.
GEDCO provided free training licenses for this course

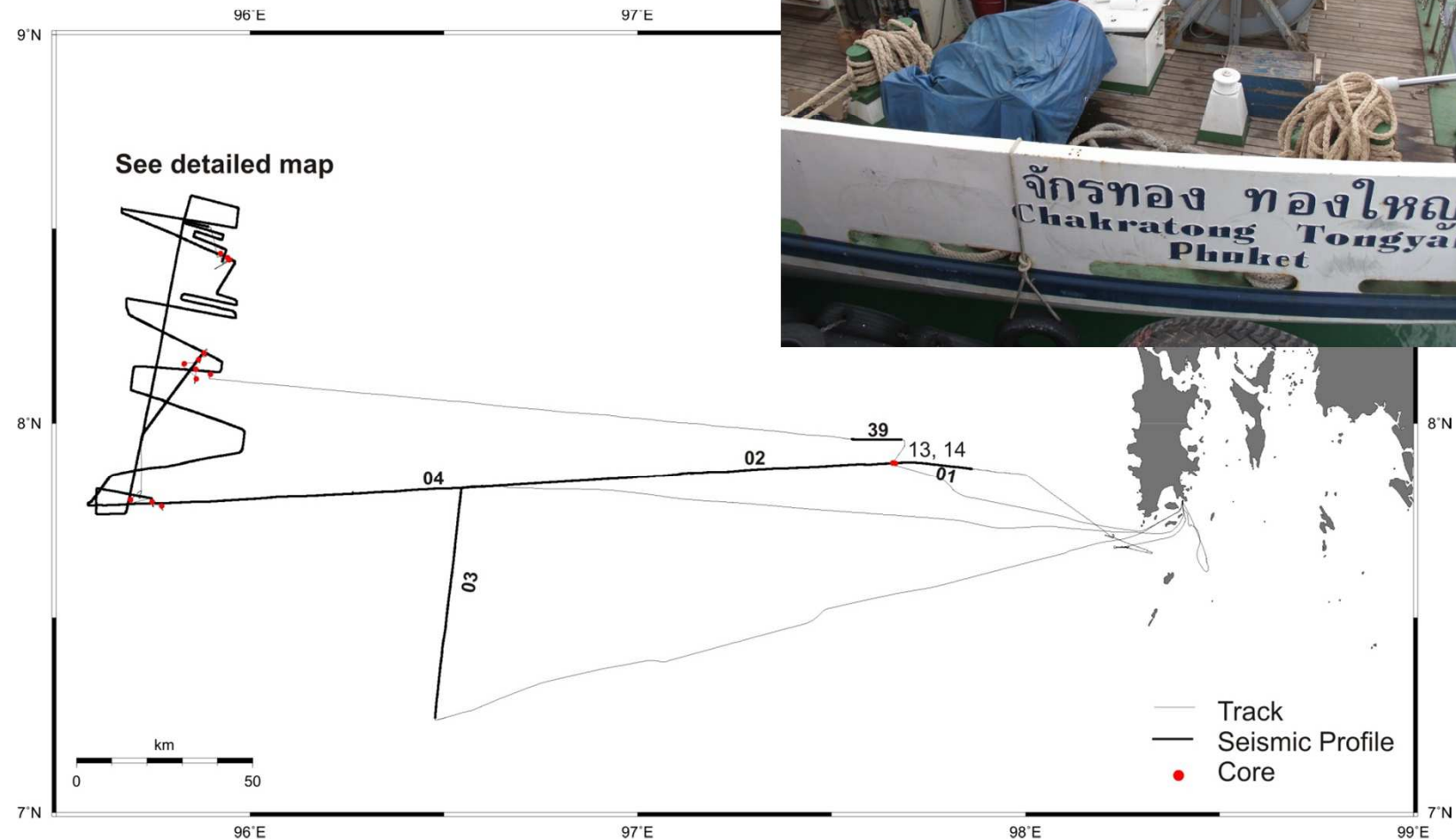


VISTA[®]

2D/3D SEISMIC DATA PROCESSING



We will process data collected during Mass III-cruise early this year





future ocean
KIEL MARINE SCIENCES

Acoustic Imaging

Seismic Data Processing



Digital Streamer, 96 channels
Distance between groups: 1.56 m
2 Birds for depth control

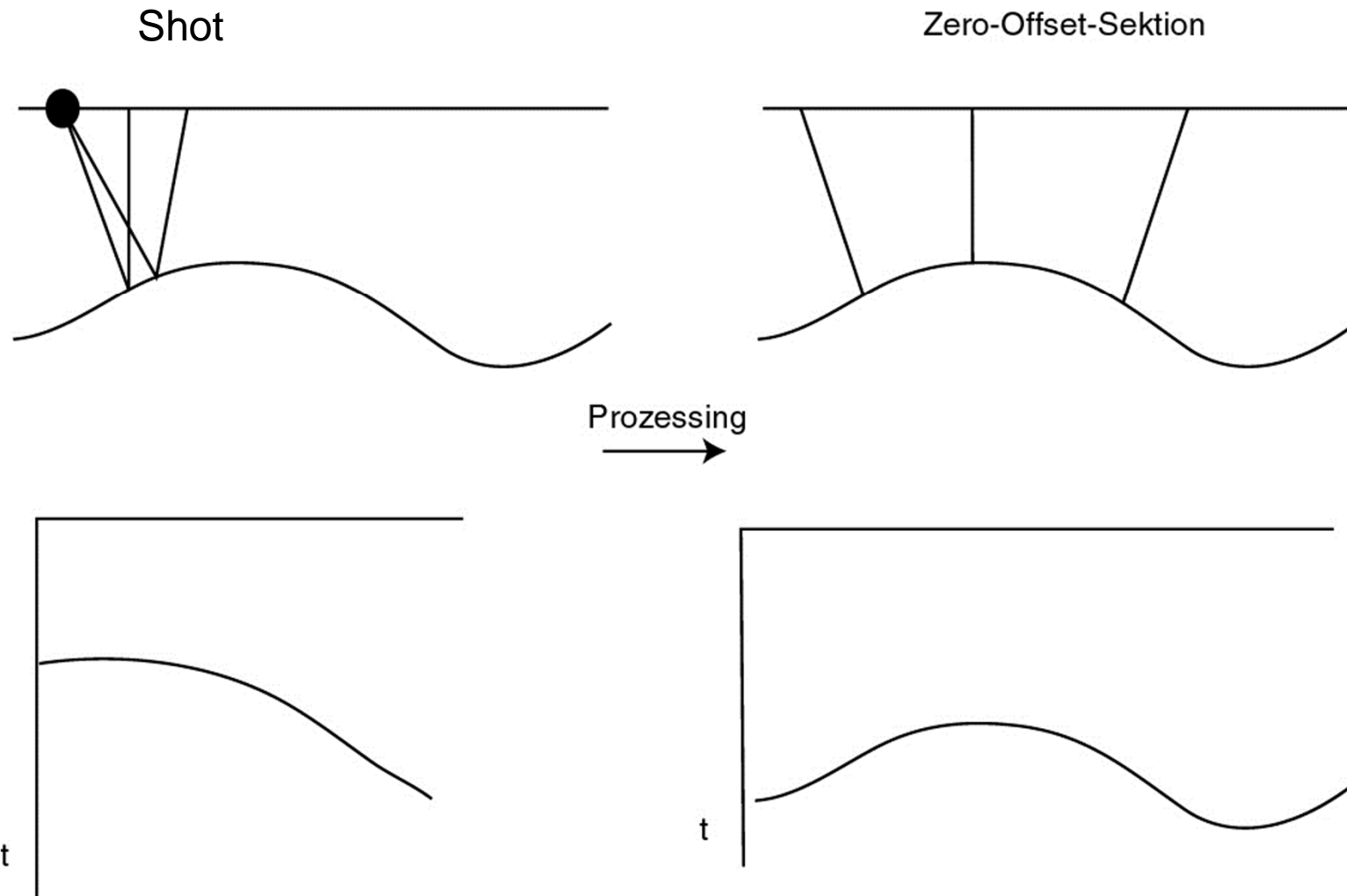


Mini GI-Gun with a
avolume of 0.1l

We will work with this data this afternoon

Aim of seismic data processing:

Production of a zero-offset section with good signal-to-noise ratios





future ocean
KIEL MARINE SCIENCES

Acoustic Imaging

Seismic Data Processing

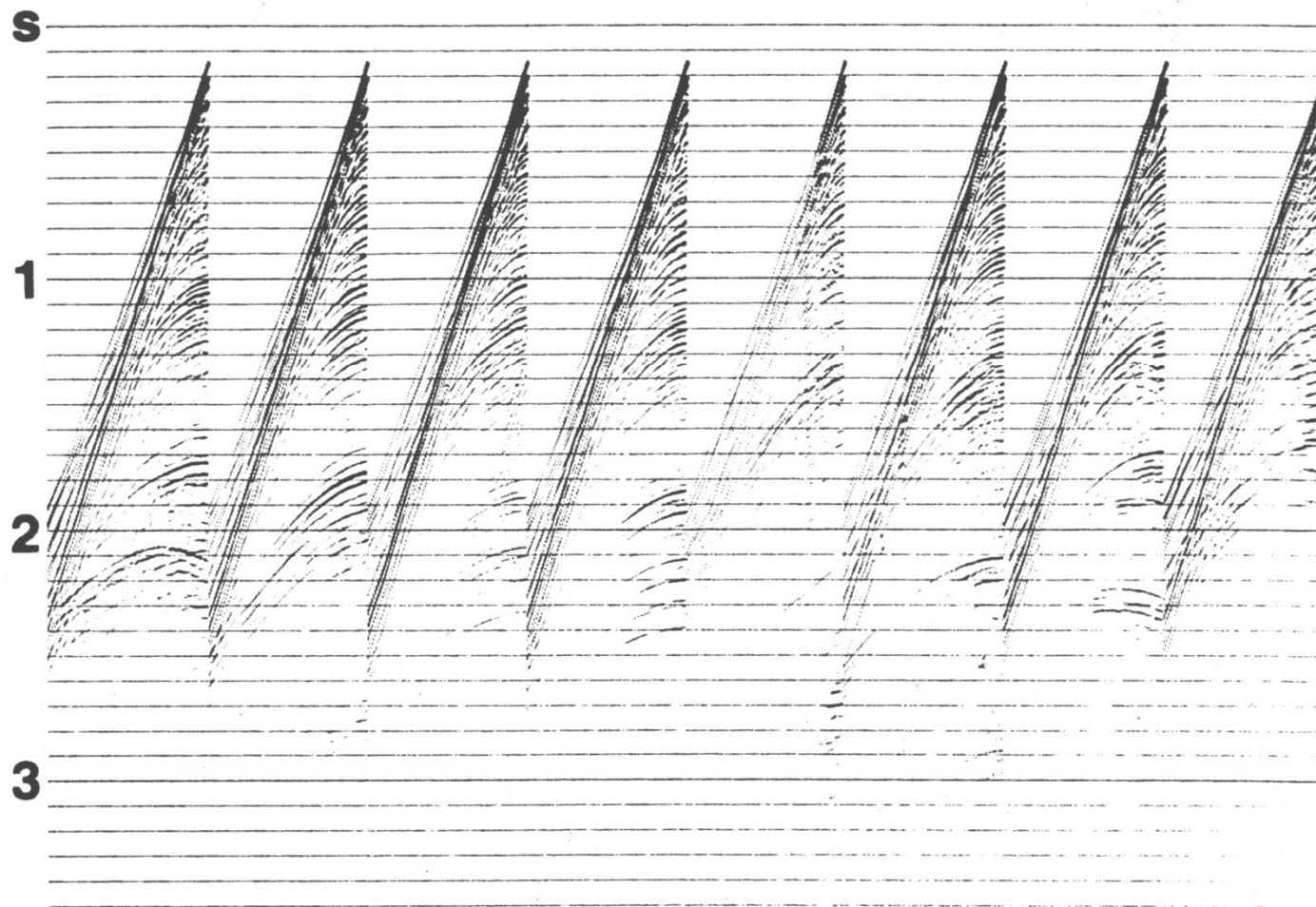


FIG. 1-36. Common-shot gathers just after demultiplexing. These are from an offshore survey. Note the strong amplitudes at the early part and the relatively weaker energy at the deeper part of the records. Such decay in amplitude primarily is due to wavefront divergence.

Long way from shots to

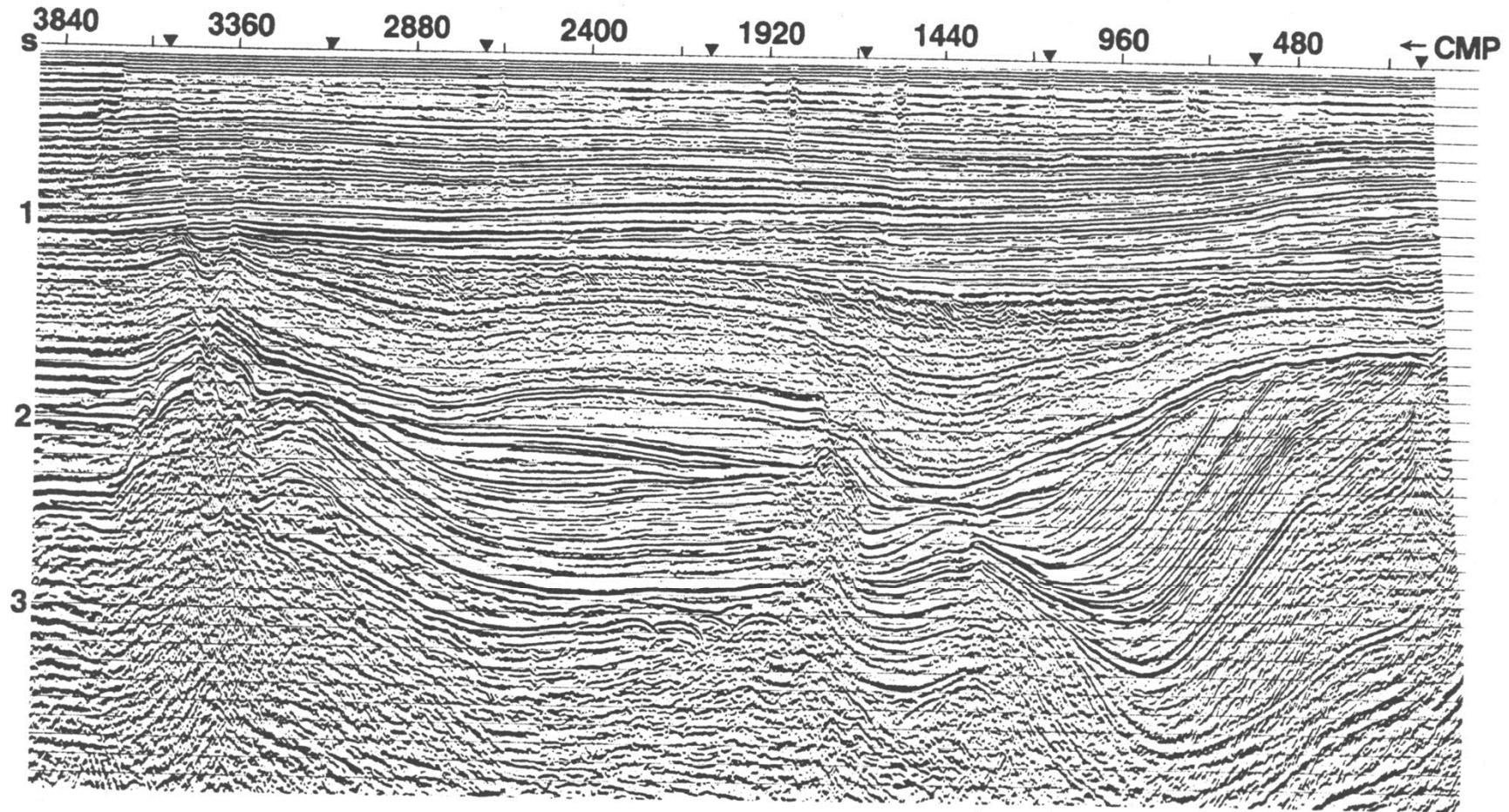


FIG. 1-54. Migrated CMP stack. The input to migration is the filtered stacked section. The migration output was gained as in Figure 1-53.

Zero-Offset-Section

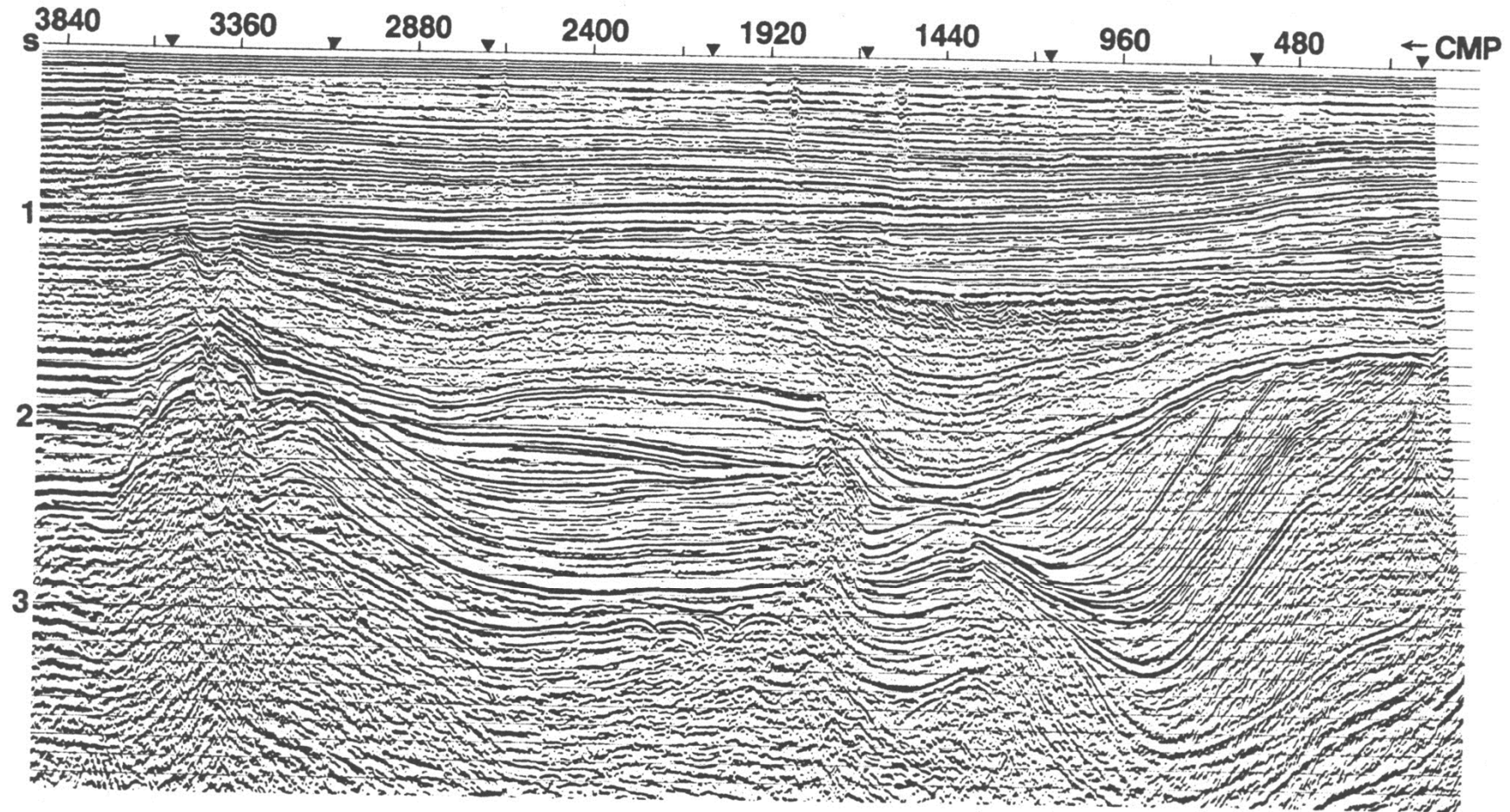


FIG. 1-54. Migrated CMP stack. The input to migration is the filtered stacked section. The migration output was gained as in Figure 1-53.

Zero-Offset-Section

The CMP (Common Midpoint) Concept

Rearrangement of data from shots to CMPs

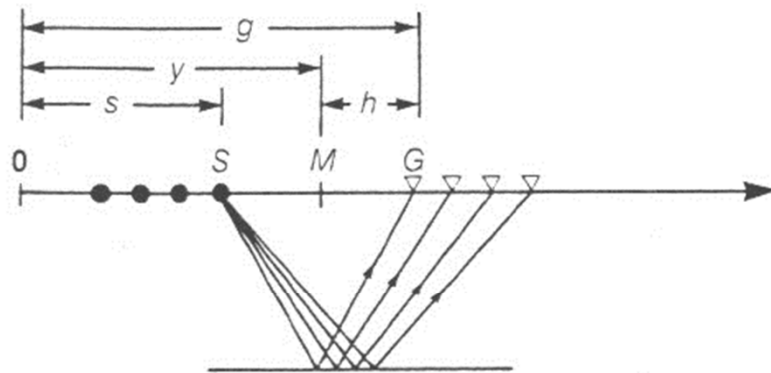


FIG. 1-40. Seismic data acquisition is done in shot-receiver (s, g) coordinates. The raypaths shown are associated with a planar horizontal reflector from a shotpoint S to several receiver locations G . The processing coordinates, midpoint-(half) offset, (y, h) are defined in terms of (s, g): $y = (g + s)/2$, $h = (g - s)/2$. The shot axis here points opposite the profiling direction, which is to the left.

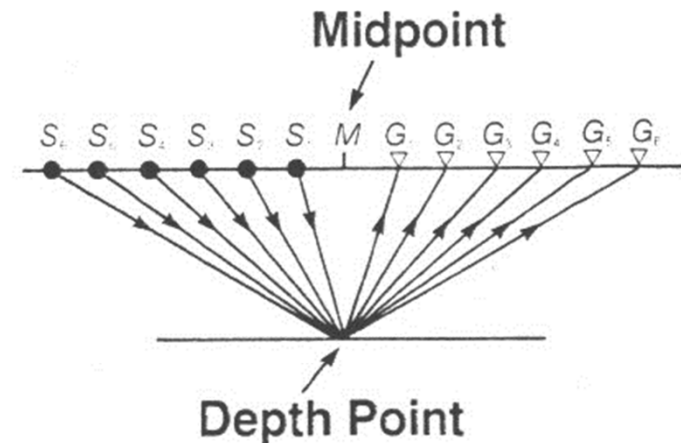


FIG. 1-41. Seismic data processing is done in midpoint-offset (y, h) coordinates. The raypaths shown are associated with a single CMP gather. A CMP gather is identical to a CDP gather if the depth point were on a horizontally flat reflector and if the medium above were horizontally layered.

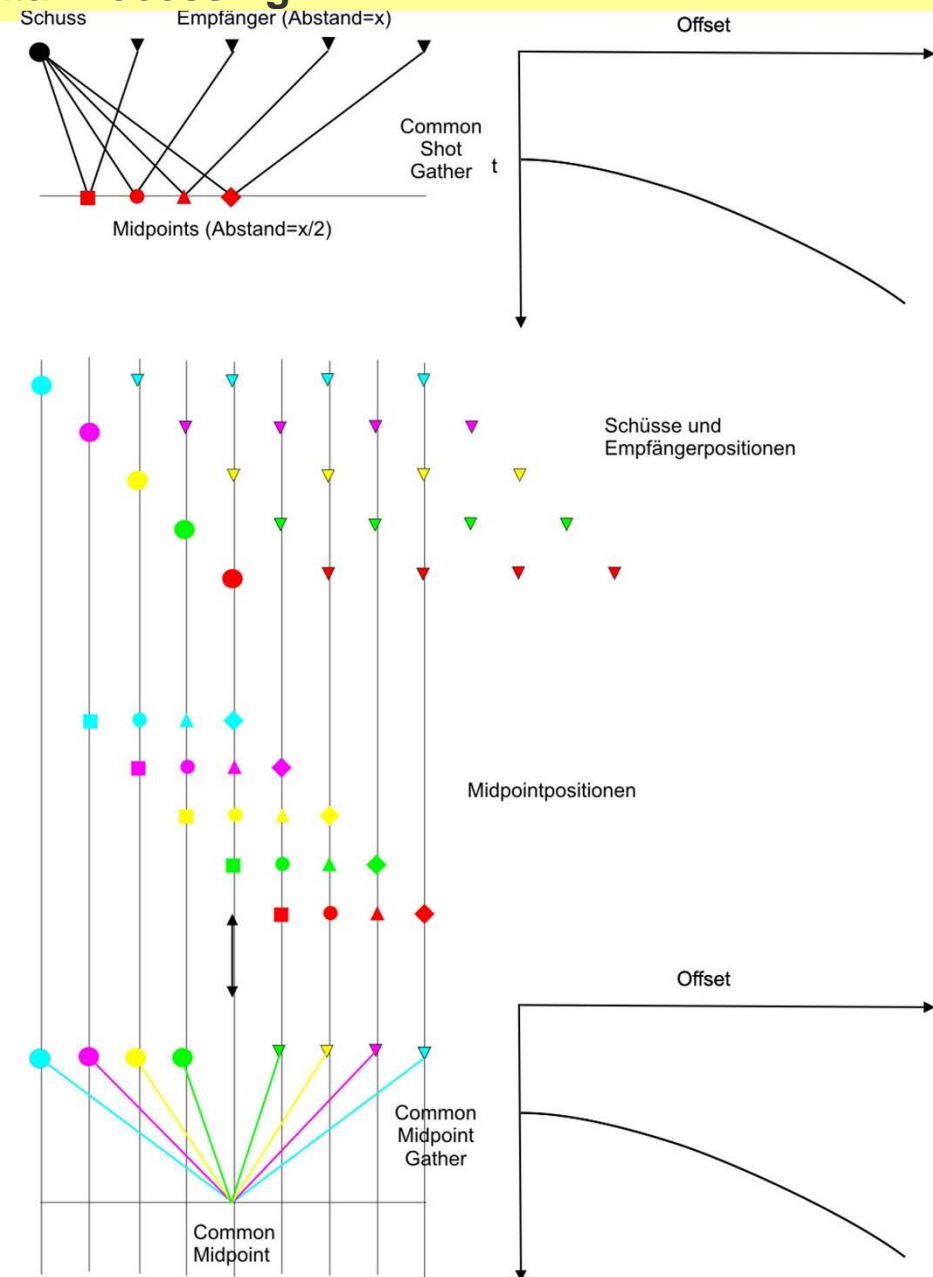
Offset is the distance between shot and receiver

A Midpoint is the ,midpoint' between shot and receiver

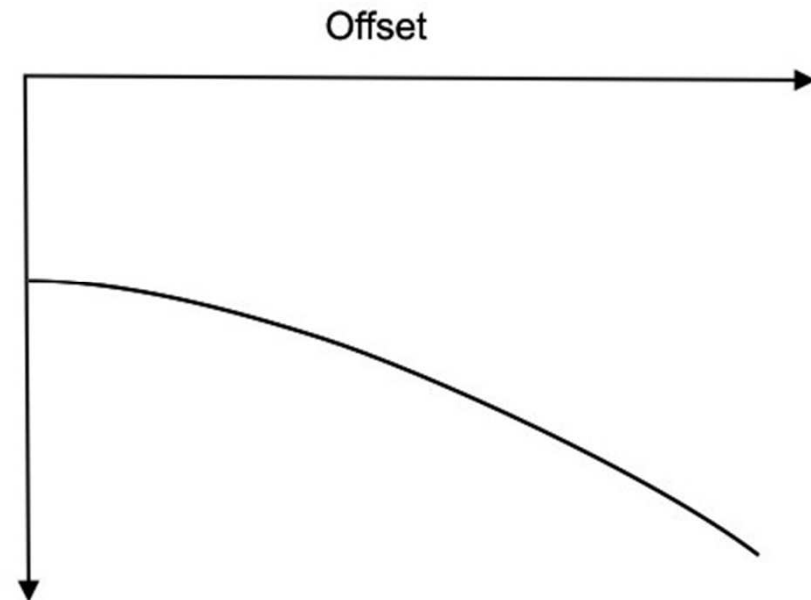
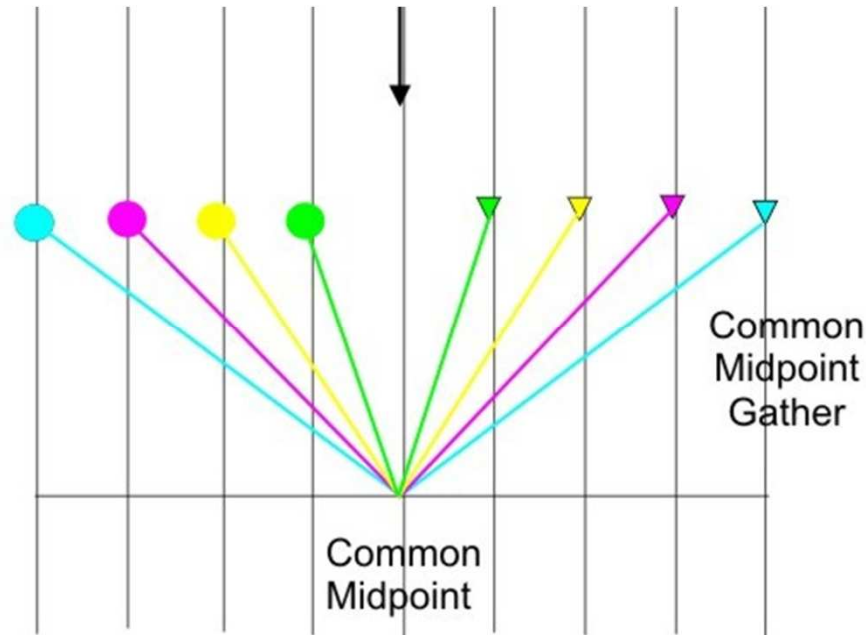
A CMP-Gather (Common Midpoint) consists of all traces of shot-receiver pairs with the same midpoint.

Fold: Number of traces in a CMP-Gather

A distance x between individual receivers results in a midpoint-distance of $x/2$



What travel-time curves do we get in a CMP-Gather?



$$t^2 = (t_{0,n})^2 + \frac{x^2}{v_n^2} \quad \text{mit} \quad t_{0,n} = \sum_{m=1}^n \frac{2z_m}{v_m} = \sum_{m=1}^n t_m$$

Vertical two-way-traveltime

Hyperbola

$$v_n^2 = \frac{\sum_{m=1}^n t_m v_m^2}{\sum_{m=1}^n t_m}$$

rms (root mean square) **velocity**

Implementation of CMP-Sorting

Regular Geometries: Construction of a stacking-chart

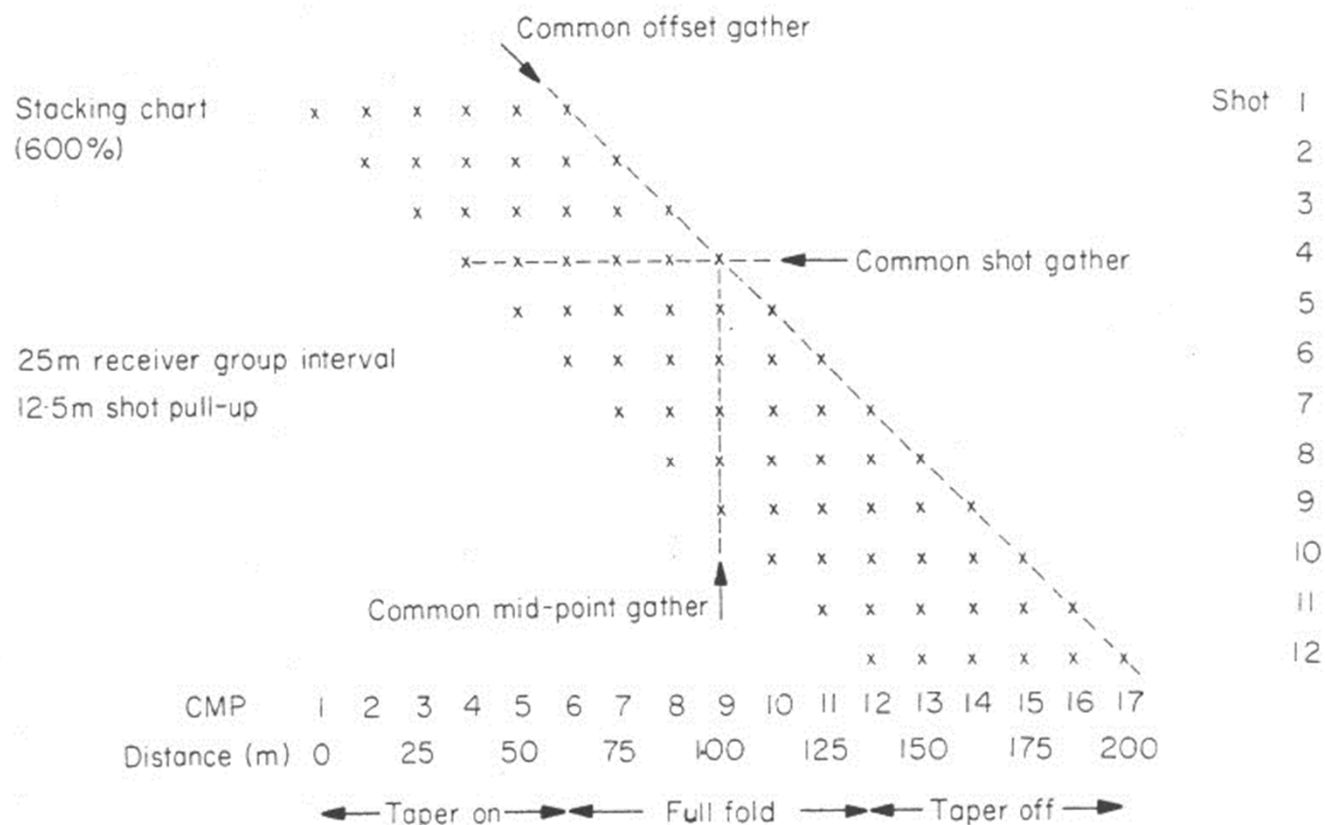


Fig. 3.12. A subsurface stacking chart for a 6 trace cable with a 25 m receiver group interval and a 12.5 m shot spacing.

Required information for a stacking chart

Shot distance, Receiver distance, Number of channels, Minimum offset

⇒ Calculation of CMP-Numbers, which are written in the trace-header

⇒ sort for CMPs

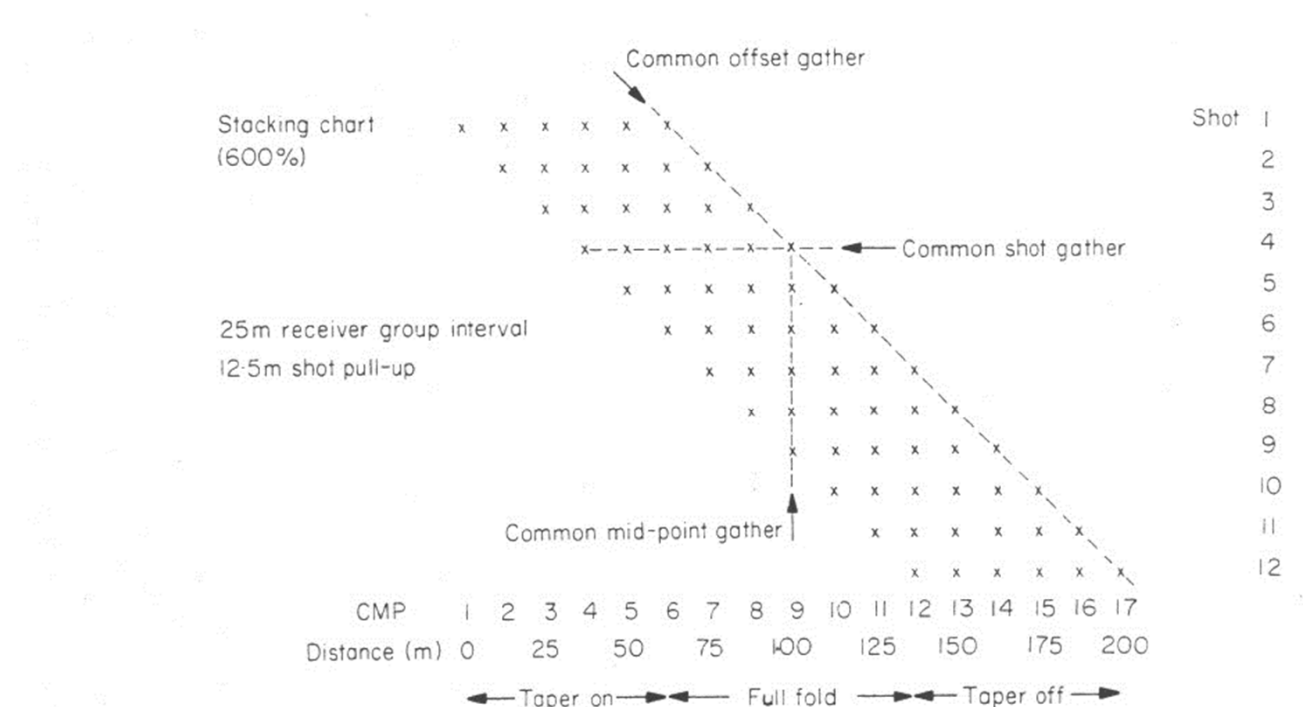


Fig. 3.12. A subsurface stacking chart for a 6 trace cable with a 25 m receiver group interval and a 12.5 m shot spacing.

Irregual Geometries (e.g. velocity variations during acquisition, no straight lines):

Binning

- Small areas (bins) are defined instead of a CMP
- Binning: Allocation of midpoints to bins
- Sort for bins

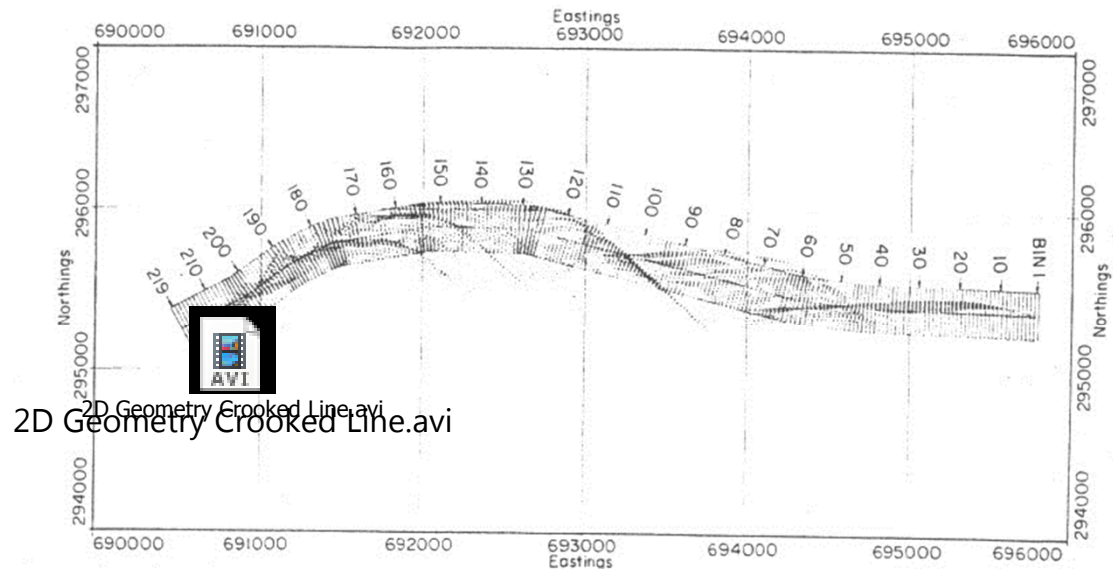


Fig. 3.92. A 'binning strategy' for the mid-point distribution of Fig. 3.91.

Required Information: Distance of Bins, Shape of Bins, Location of Bins

⇒ Allocation of midpoints to bins, Bin-Number is written to header

⇒ Sort for bins

In Vista two movies are available for binning at Vista\Vista Movies (Tutorial A 2D Geometry.avi, 2D Geometry Crooked Line.avi)

CMP versus CDP

CDP: Common Depth Point (Common point in the subsurface)

CMP: Common Mid Point

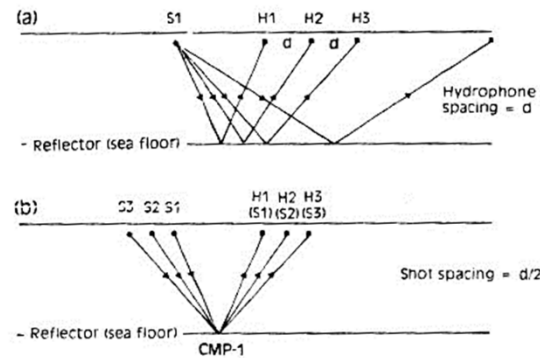
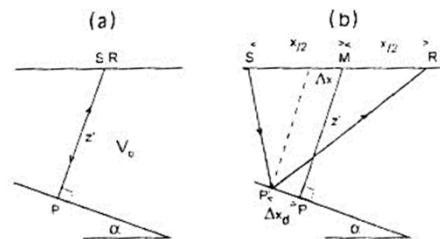


Figure 4.19 (a) Field recording of common mid-point (CMP) reflection data. (b) Organization of shot and receiving points to form CMP gather.

Horizontal Layering:
CMP is also a CDP

Inclined layers:
CMP is not a CDP



S = Source R = Receiver M = Source / receiver mid-point

Figure 4.20 Relation between source-receiver mid-point and reflection point for a single interface. (a) Ray path for dipping reflector, with coincident source and receiver. (b) Ray path for dipping reflector with source-receiver offset.

NMO-correction and velocity-analysis

Seismic data offer the possibility to extract velocities using the so-called Normal Moveout (NMO)

Normal Moveout (NMO)

Travel-time curve of a horizontal layer in a CMP-Gather

$$t(x)^2 = t(0)^2 + \frac{x^2}{v^2} \text{ mit}$$

x: Offset

v: Velocity of sediments above the reflector

t_0 : Vertical two-way-traveltime

Difference between $t(x)$ and $t(0)$ is called NMO



future ocean
KIEL MARINE SCIENCES

Acoustic Imaging

Seismic Data Processing

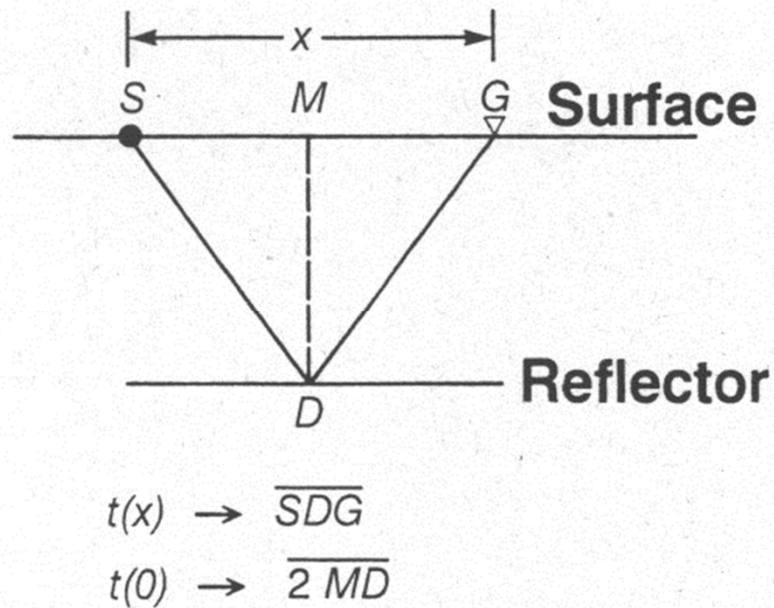


FIG. 3-4. The NMO geometry for a single horizontal reflector [refer to equation (3.1)].

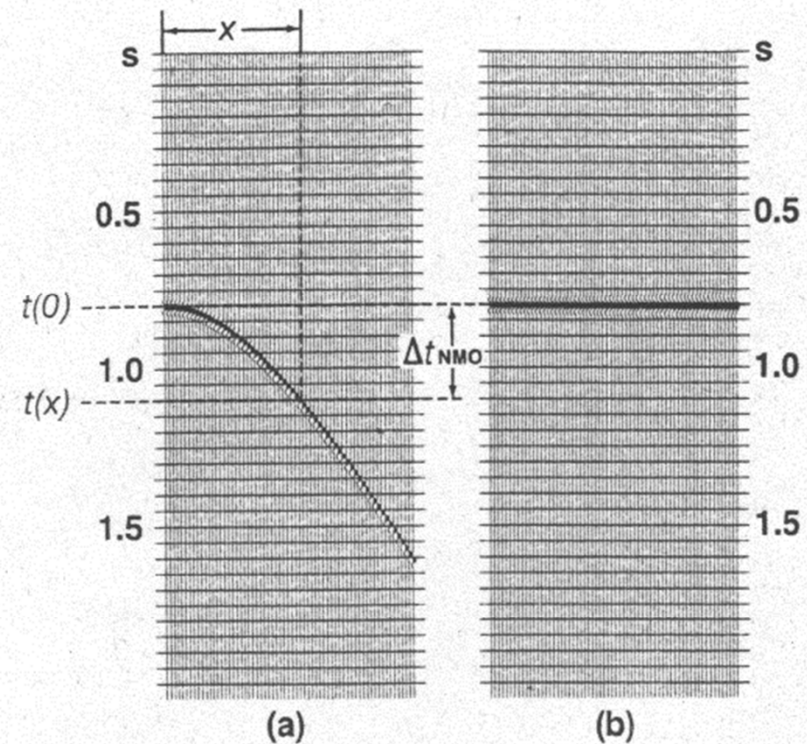


FIG. 3-6. NMO correction [equation (3.2)] involves mapping nonzero-offset traveltime $t(x)$ onto zero-offset traveltime $t(0)$. (a) Before and (b) after NMO correction.

Difference between $t(x)$ and $t(0)$ is called NMO



Acoustic Imaging

Seismic Data Processing

$$\Delta t_{NMO} = t(x) - t(0) = \sqrt{t(0)^2 + \frac{x^2}{v_{nmo}^2}} - t(0) = t(0) \left(\sqrt{1 + \left(\frac{x}{v_{NMO} t(0)} \right)^2} - 1 \right)$$

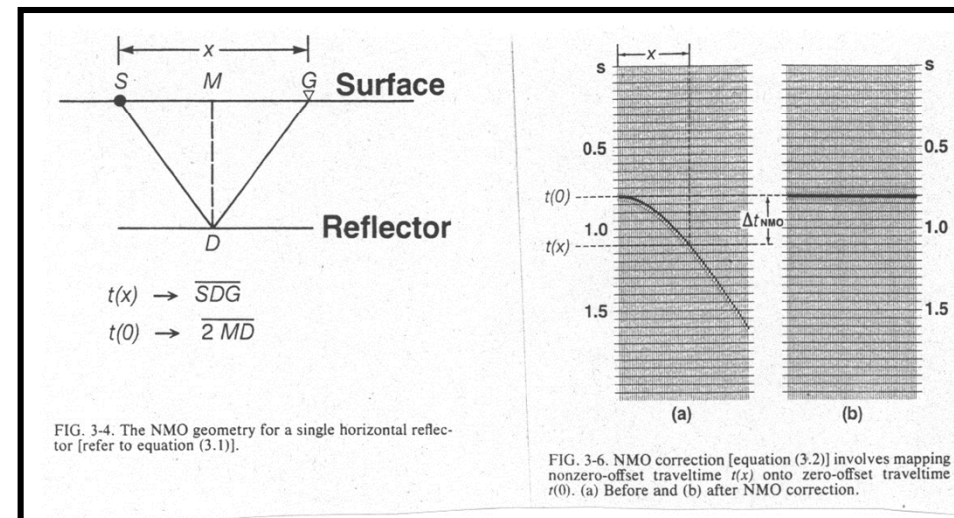
Series expansion of the root

$$\Delta t_{NMO} = t(0) \left[\left(1 + \frac{1}{2} \left(\frac{x}{v_{NMO} t(0)} \right)^2 - \frac{1}{8} \left(\frac{x}{v_{NMO} t(0)} \right)^4 + \dots \right) - 1 \right]$$

Delete higher terms

$$\Delta t_{NMO} \approx \frac{x^2}{2v_{NMO}^2 t(0)}$$

ie





$$\Delta t_{NMO} \approx \frac{x^2}{2v_{NMO}^2 t(0)}$$

Offset: 2 km

Water depth: 3 km

=>t(0)=4s

$$\Delta t_{NMO} = \frac{4km^2}{2 * 2.25 \frac{km^2}{s^s} * 4s} = 222ms$$

Offset: 0.6 km =>

$$\Delta t_{NMO} = 20ms$$

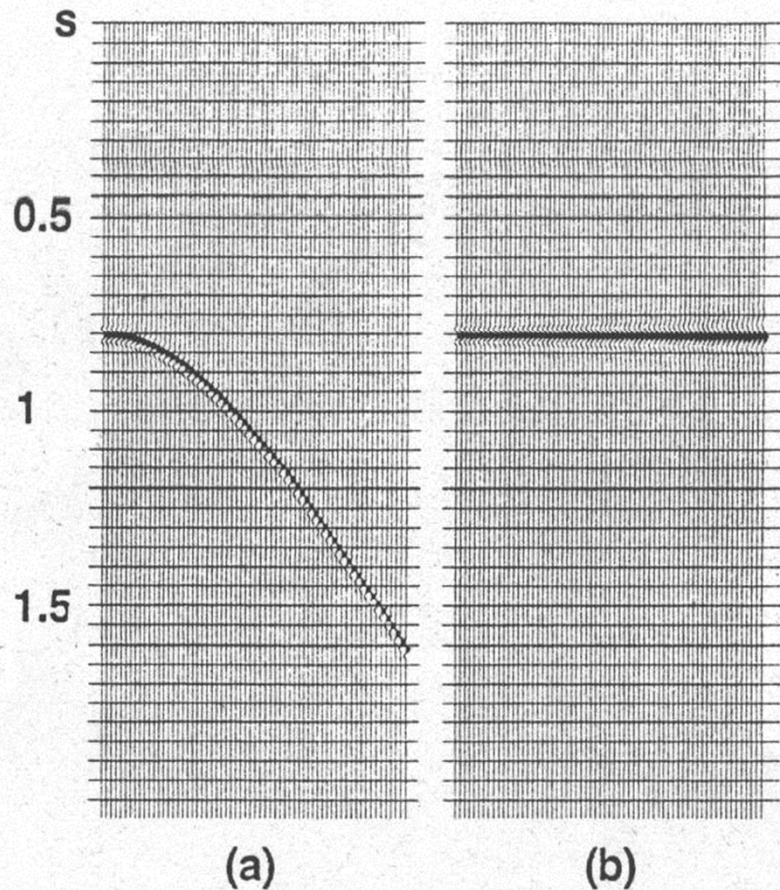


future ocean
KIEL MARINE SCIENCES

Acoustic Imaging

Seismic Data Processing

NMO-correction: Correction of offset depending NMOs NMOs => Hyperbolas become a horizontal arrivals.



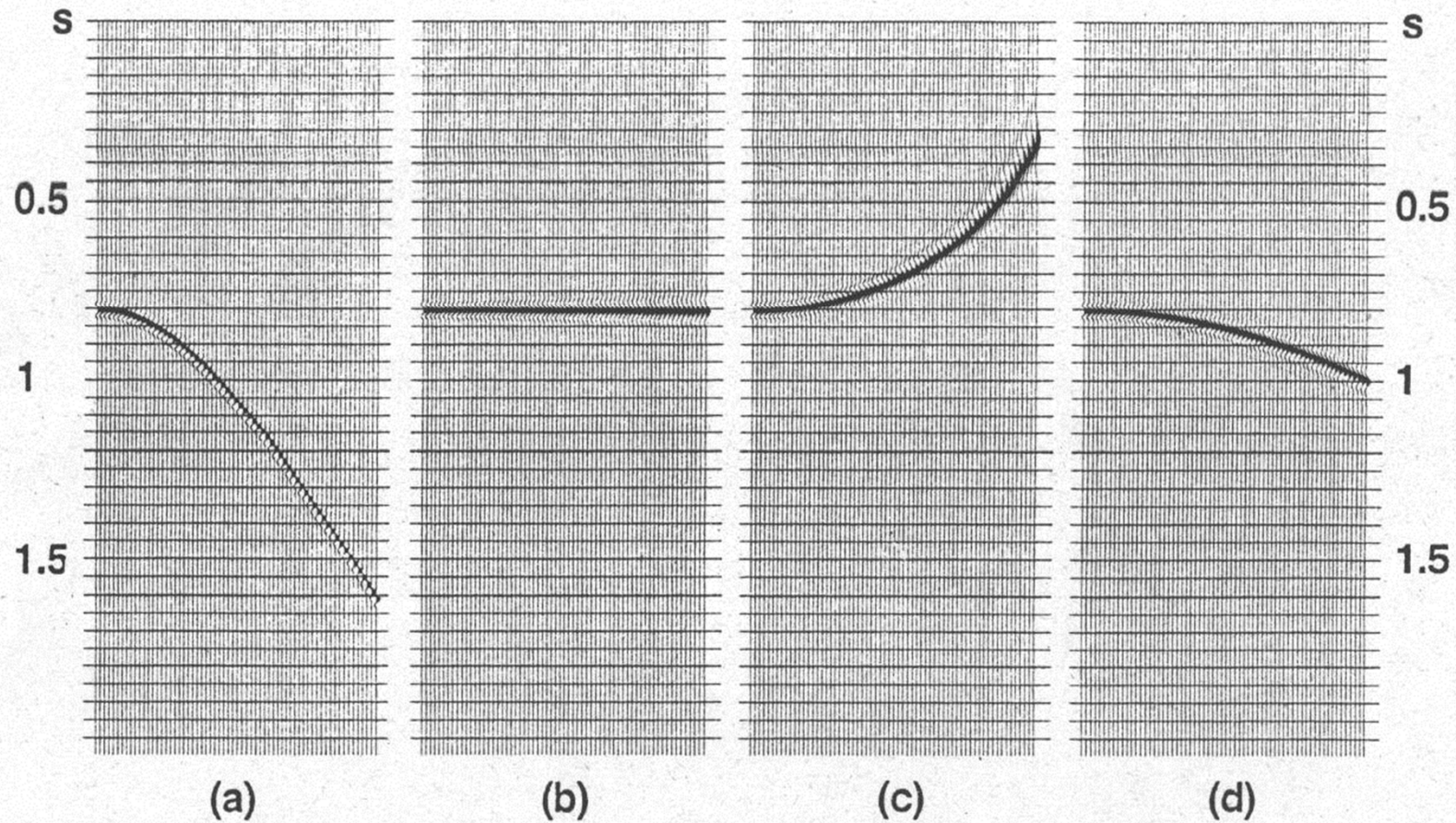
What happens, if velocities for NMO-correction are too high or low?



future ocean
KIEL MARINE SCIENCES

Acoustic Imaging

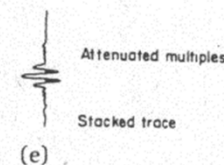
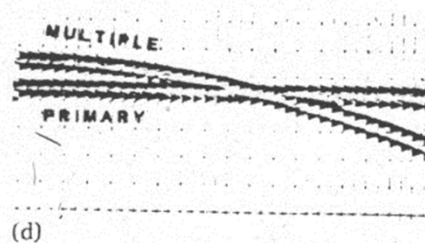
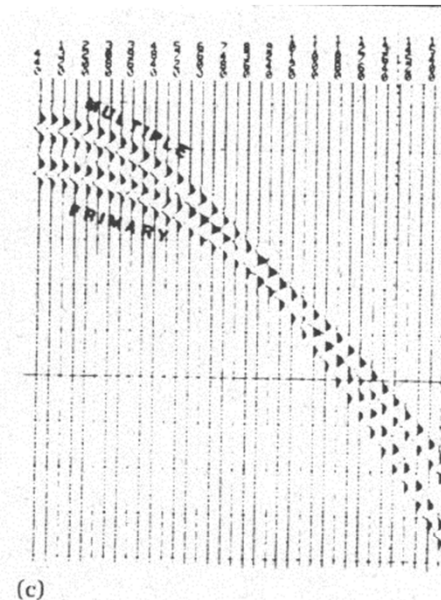
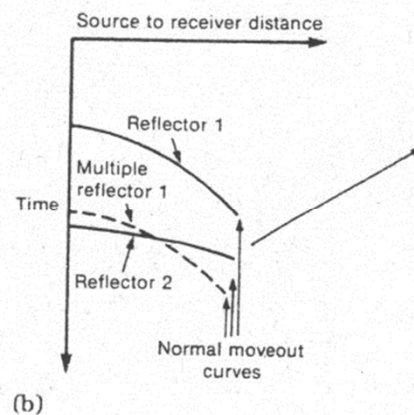
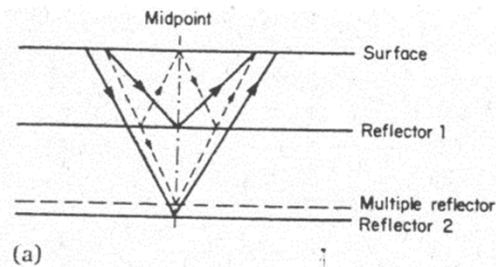
Seismic Data Processing



v_{NMO} too high \Rightarrow correction too small

v_{NMO} too low \Rightarrow correction too large

What happens with multiples during NMO-Corrections?



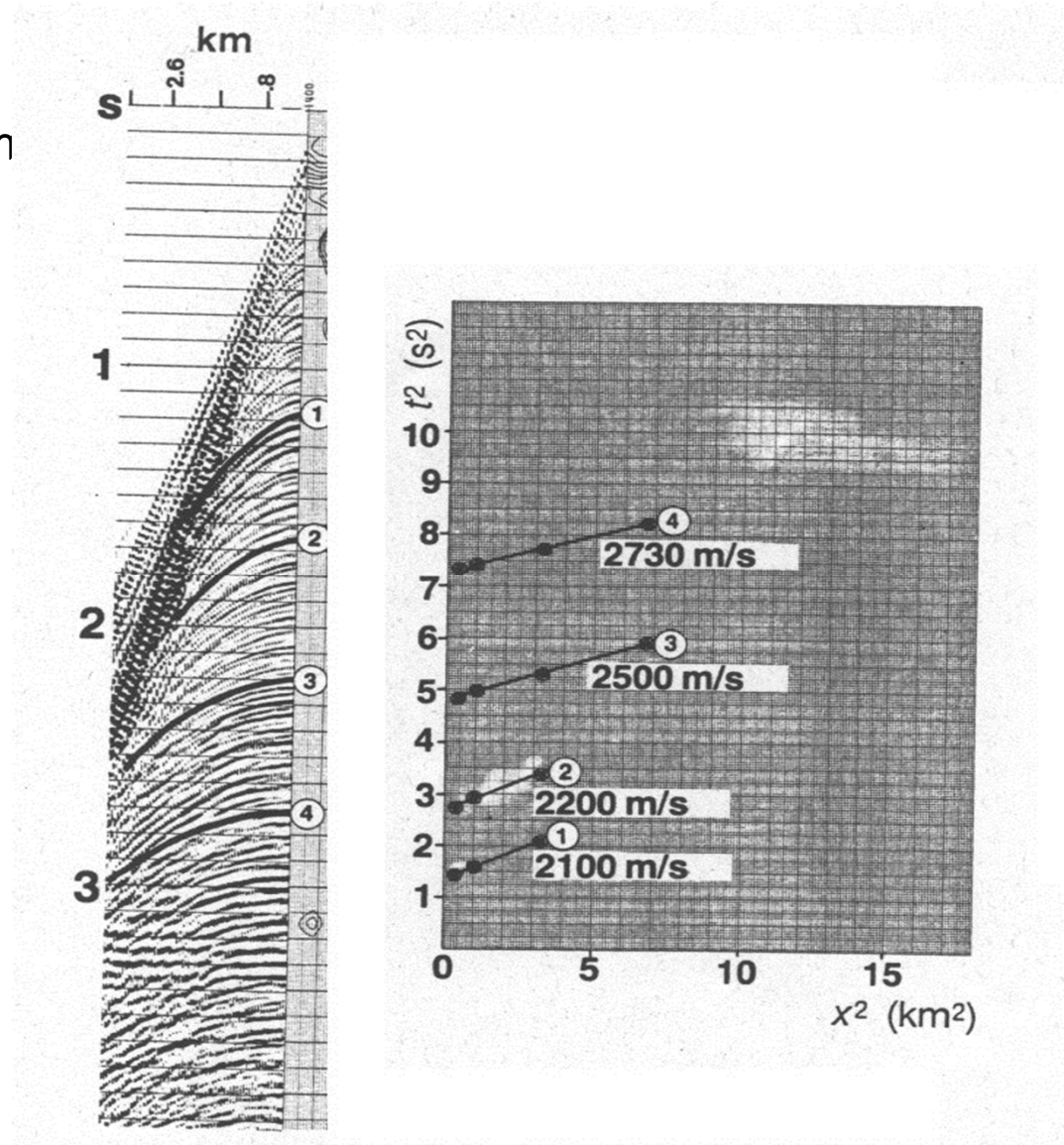
Multiples do have lower velocities than primary structures; hence the correction for the multiple is too small. Stacking results in partly destruction of the multiple, while primary structures are enhanced.

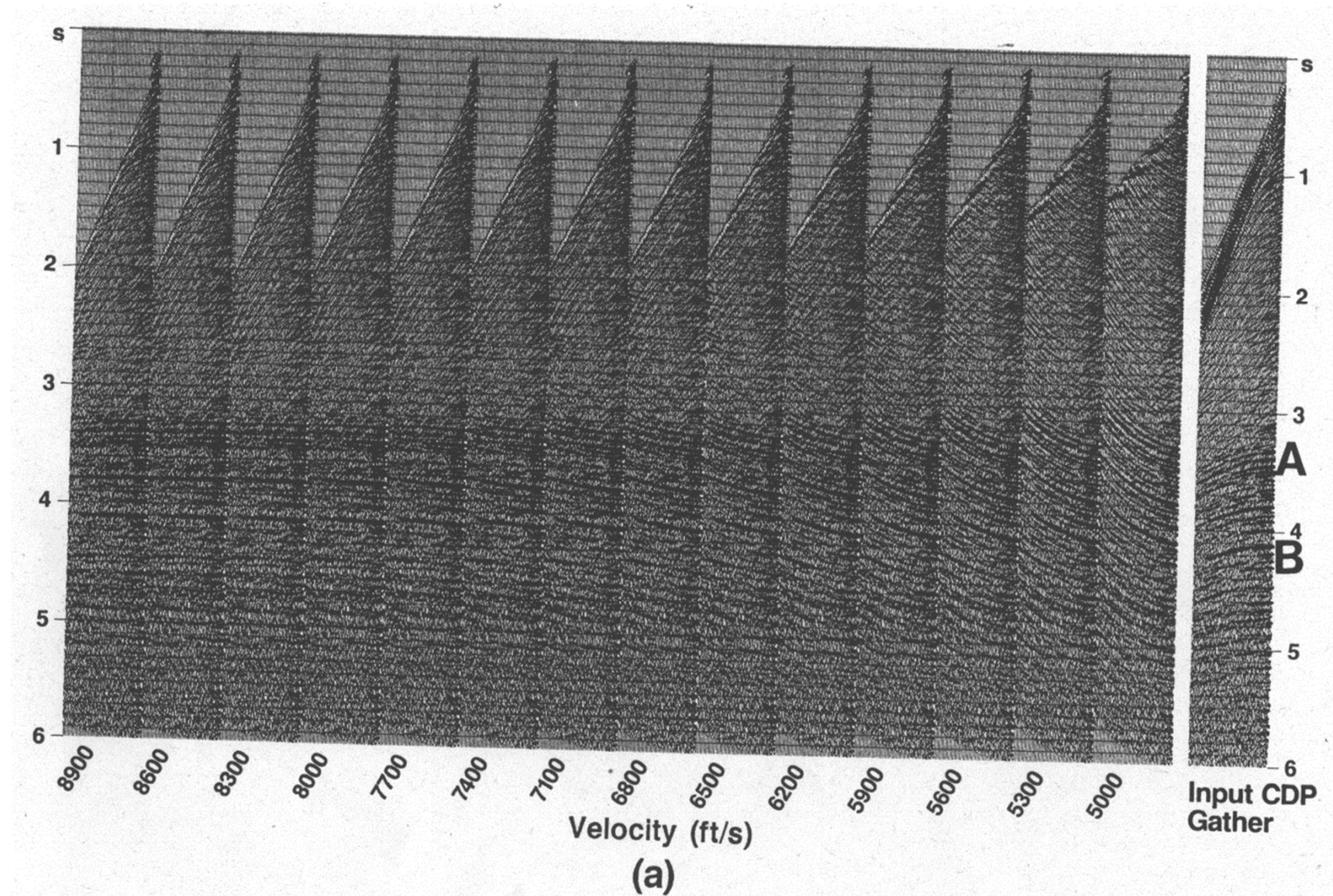
Velocity-Analysis

1. t^2 - x^2 -Method

Determination of velocity from inclination of the straight line.

$$t(x)^2 = t(0)^2 + x^2/v_{\text{NMO}}^2$$



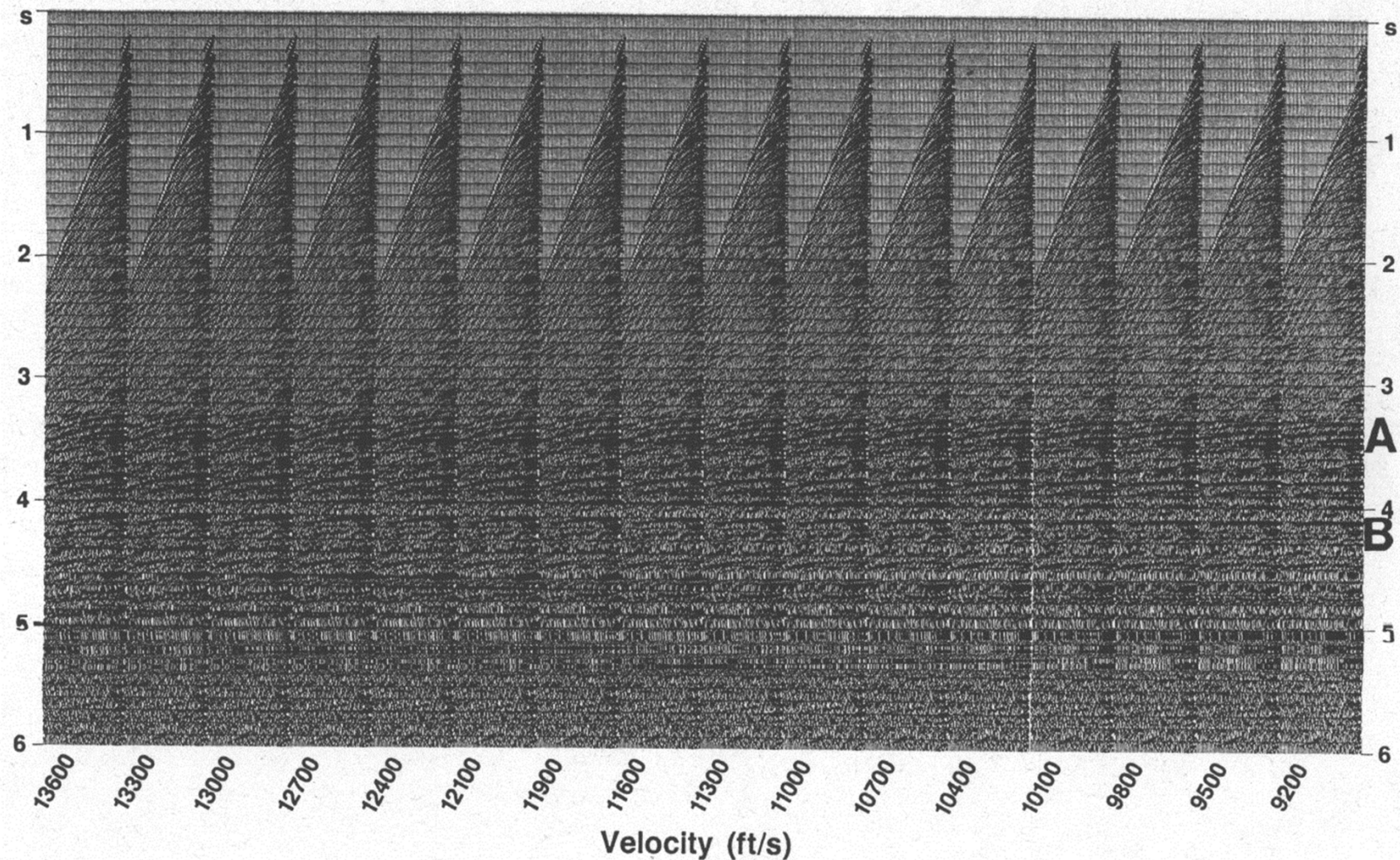




future ocean
KIEL MARINE SCIENCES

Acoustic Imaging

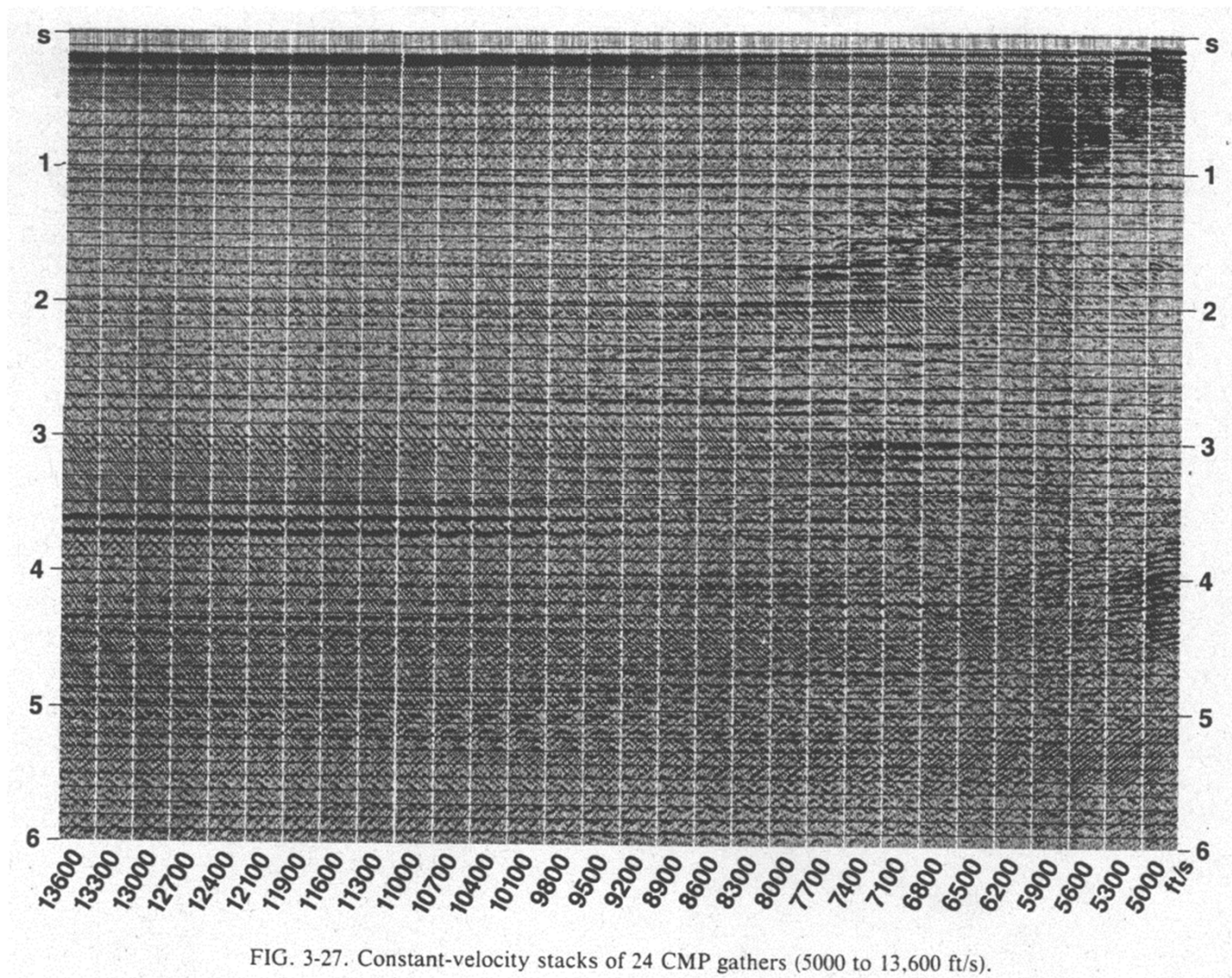
Seismic Data Processing



For the determination of a velocity-depth profile those velocities are selected which result in horizontal reflectors in a NMO-corrected gather.

3. Costant Velocity Stacks (CVS)

A velocity-depth model is constructed out of optimal stacking results.



4. Calculation of Semblance

Mathematical characterization of amplitudes of constant velocity stacks

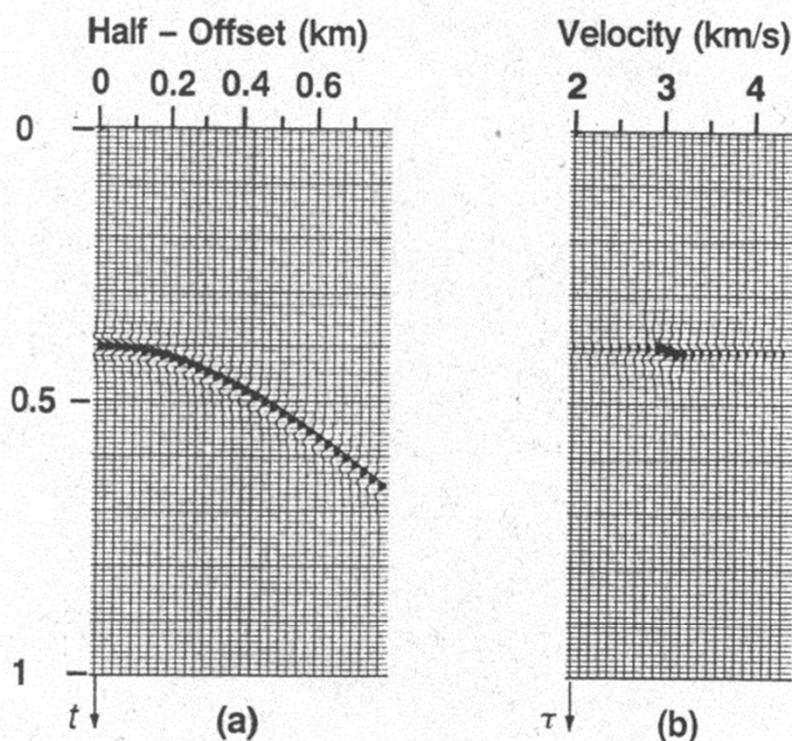


FIG. 3-28. Mapping the offset axis to the velocity axis. Each trace in the $[v, \tau = t(0)]$ gather (b) is a stack of the traces in the CMP gather (a) using a constant velocity NMO correction.

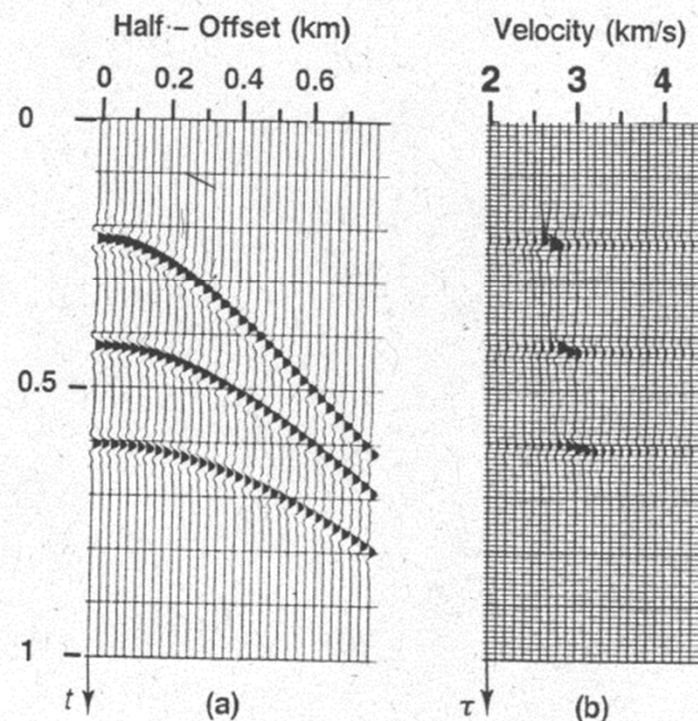


FIG. 3-29. Mapping the offset axis to the velocity axis. Each trace in the $[v, \tau = t(0)]$ gather (b) is a stack of the traces in the CMP gather (a) using a constant velocity NMO correction.



future ocean
KIEL MARINE SCIENCES

Acoustic Imaging

Seismic Data Processing

Cross-correlation in a cmp-gather allows to determine the velocity with highest semblance.

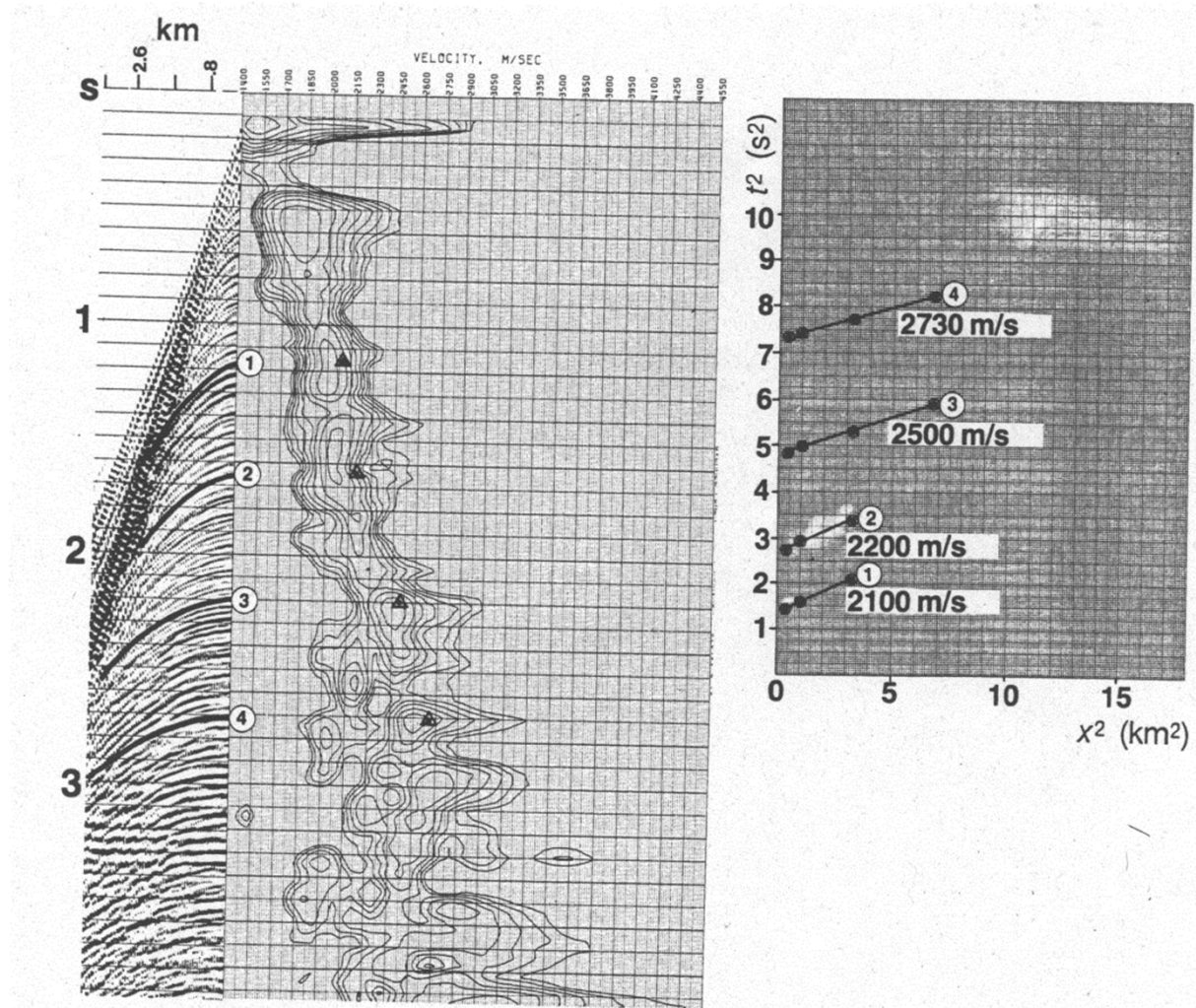


FIG. 3-24. The $(t^2 - x^2)$ velocity analysis applied to a CMP gather. The triangles on the velocity spectrum [center panel, based on equation (3.19)] represent velocity values derived from the slopes of the lines shown on the graph at the right.



future ocean
KIEL MARINE SCIENCES

Acoustic Imaging

Seismic Data Processing

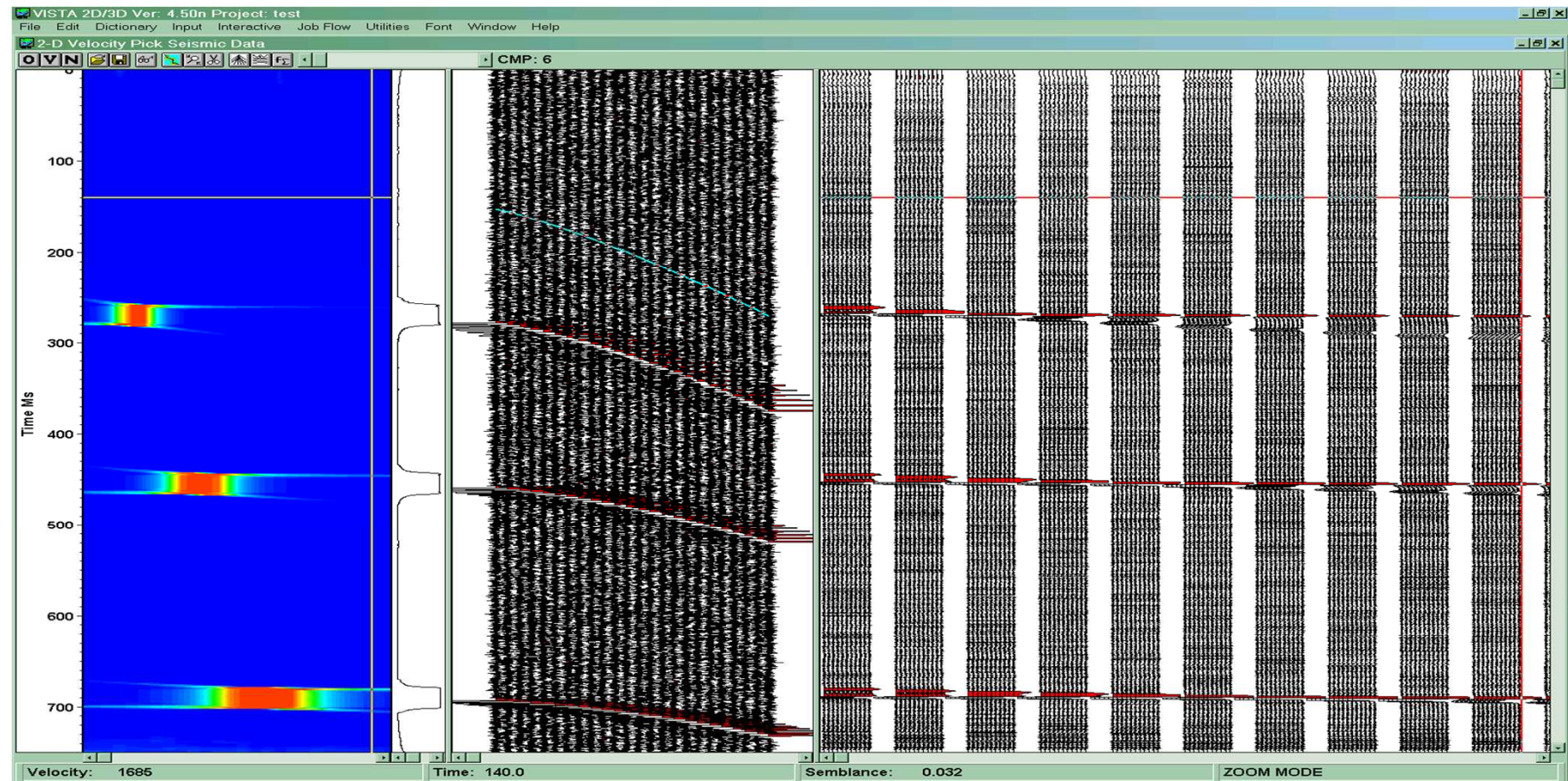
Velocity analysis

Quality of velocity analysis is depending on

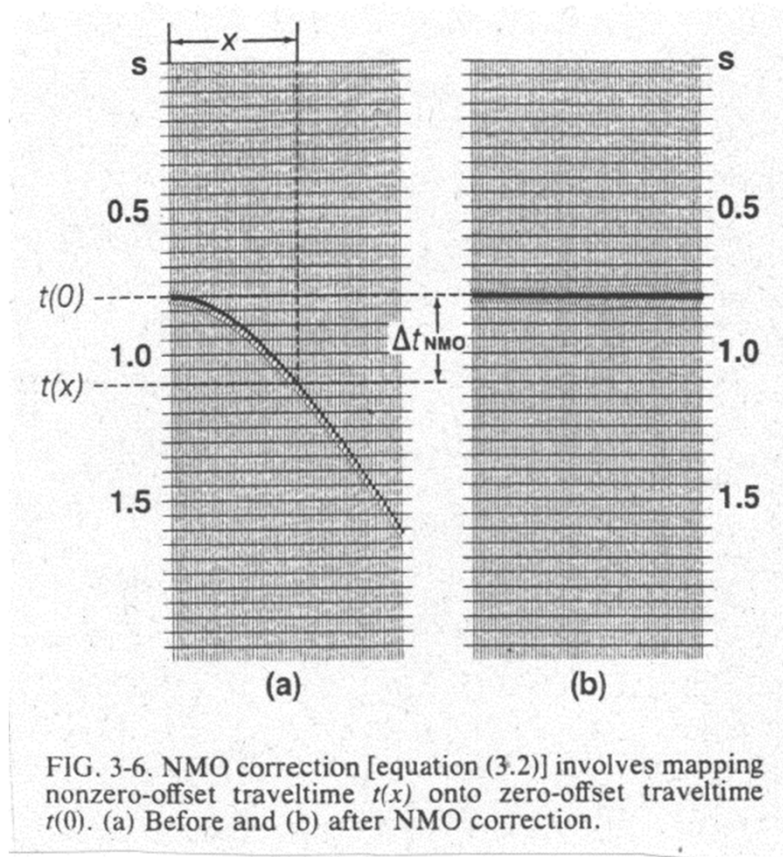
Maximum offset

Fold

Signal-to-Noise ratio



Stacking



Stacking: Summation of NMO-corrected traces in a CMP-Gather.

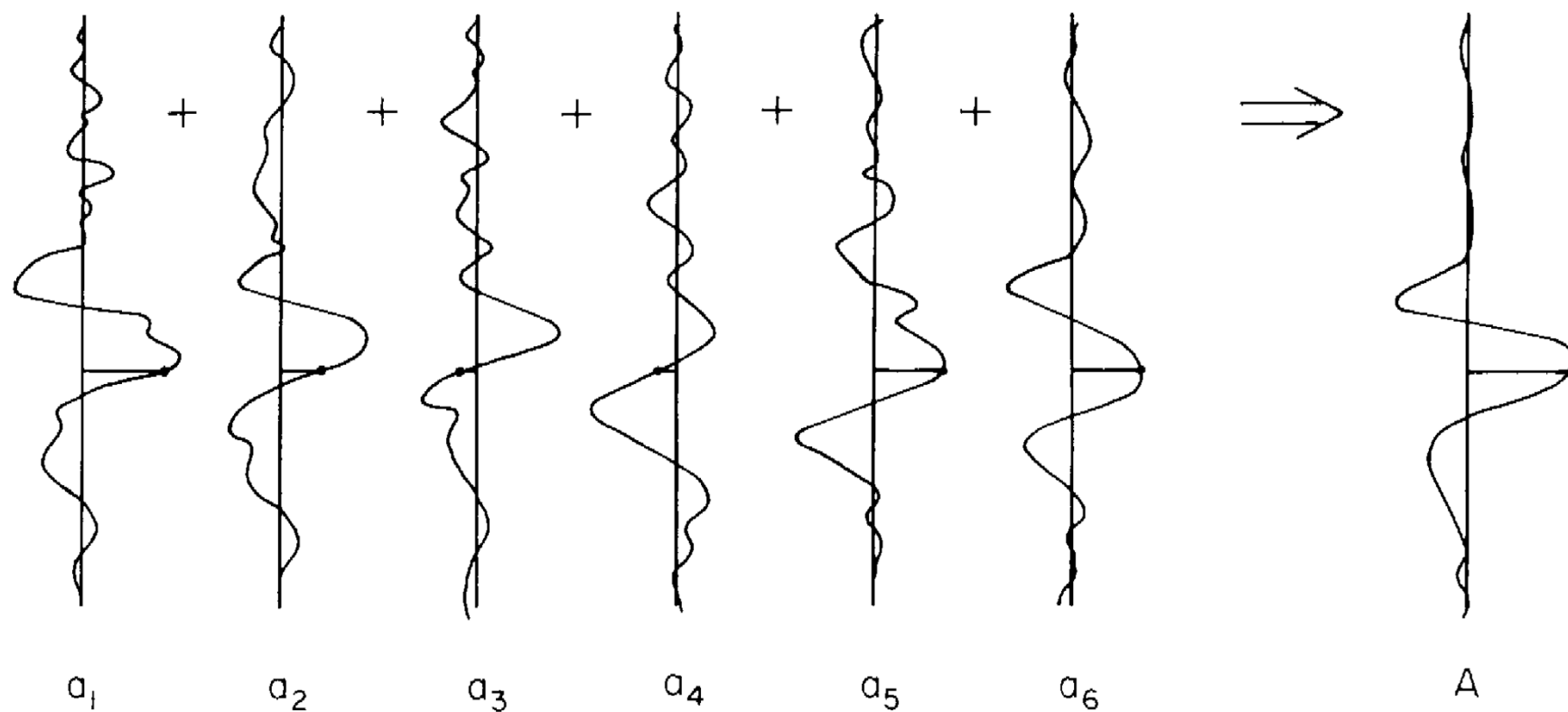
Aim: Improvement of the S/N-ratio (Signal/Noise).

Improvement of S/N-ratio: $\sim \text{SQR}(\text{Fold})$.



Stacking

Fig. 3.39. The action of stacking.





future ocean
KIEL MARINE SCIENCES

Acoustic Imaging

Seismic Data Processing

Processing Example

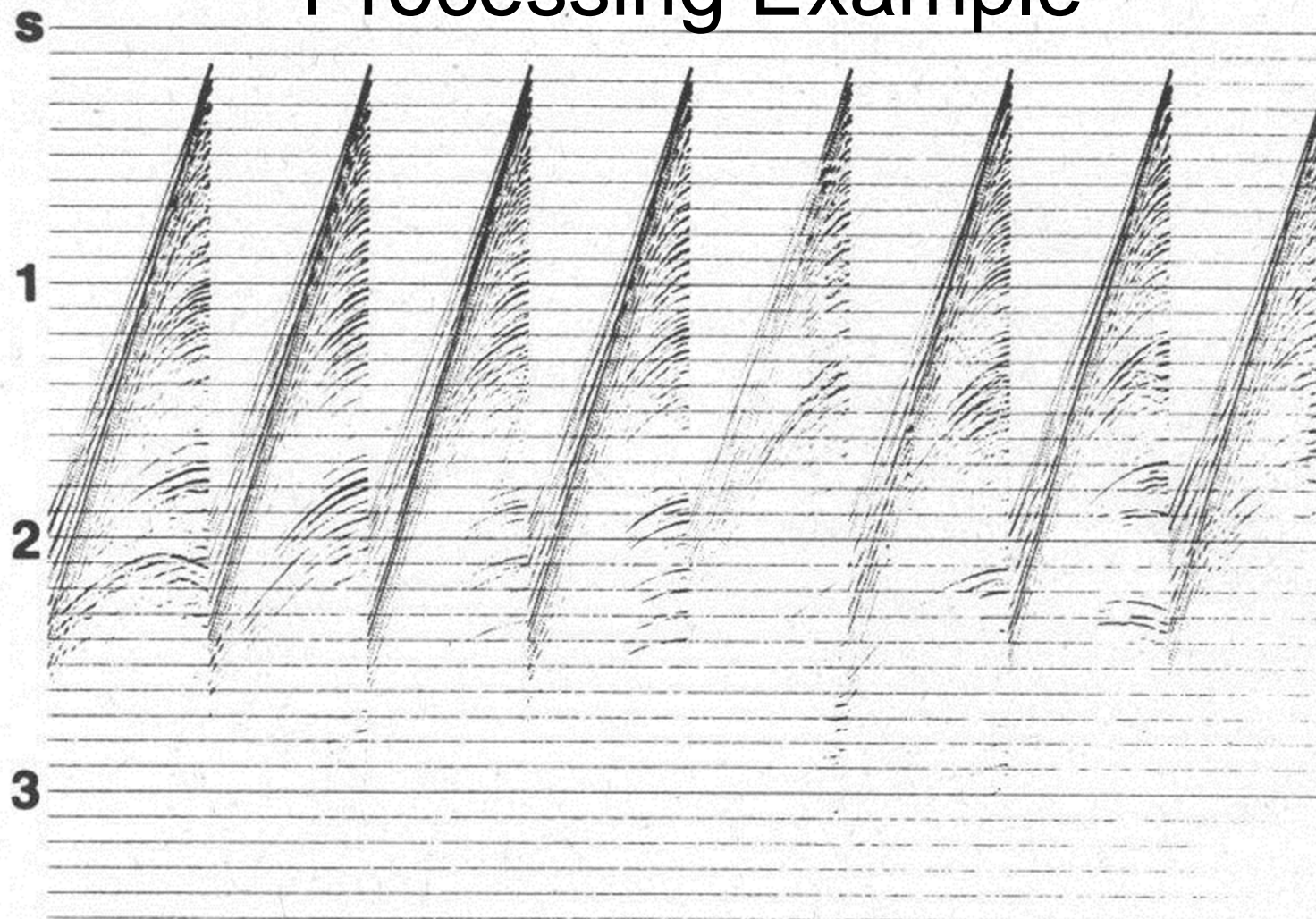


FIG. 1-36. Common-shot gathers just after demultiplexing. These are from an offshore survey. Note the strong amplitudes at the early part and the relatively weaker energy at the deeper part of the records. Such decay in amplitude primarily is due to wavefront divergence.



future ocean
KIEL MARINE SCIENCES

Acoustic Imaging

Seismic Data Processing

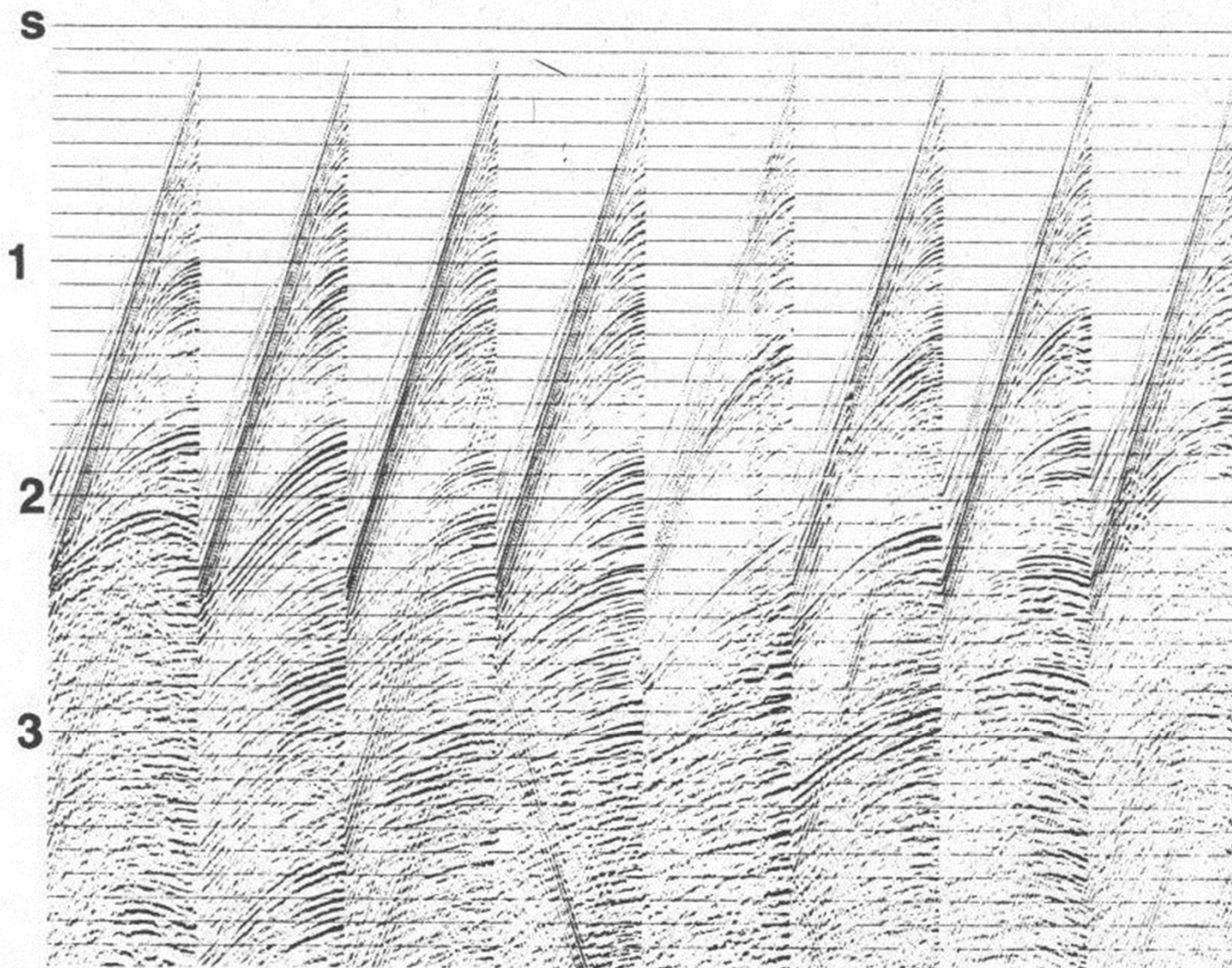


FIG. 1-37. Common-shot gathers of Figure 1-36 after correcting for the amplitude effects of wavefront divergence. Note the restored amplitudes at late times on the records.



future ocean
KIEL MARINE SCIENCES

Acoustic Imaging

Seismic Data Processing

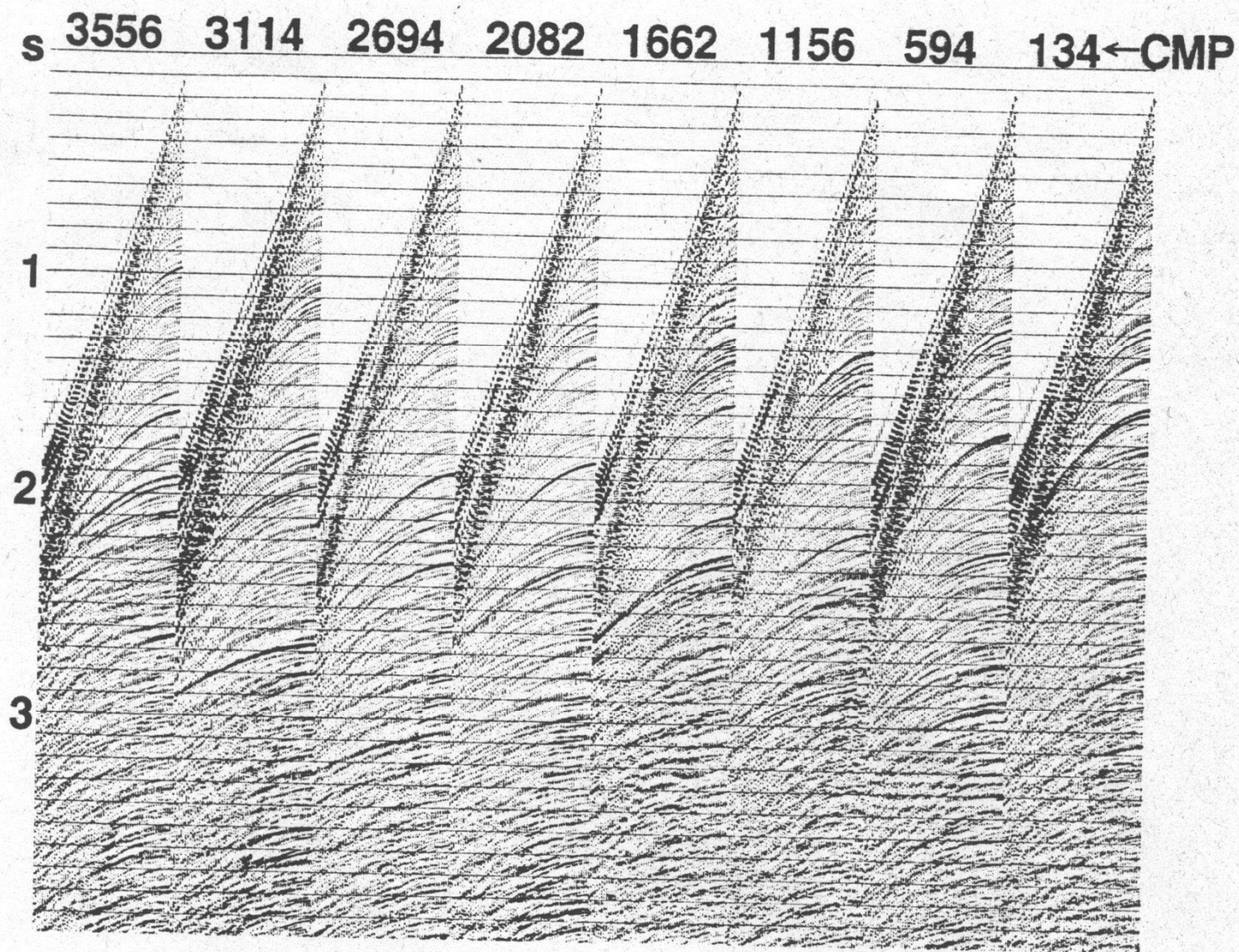


FIG. 1-42. Selected CMP gathers corresponding to the same data as in Figure 1-39.



future ocean
KIEL MARINE SCIENCES

Acoustic Imaging

Seismic Data Processing

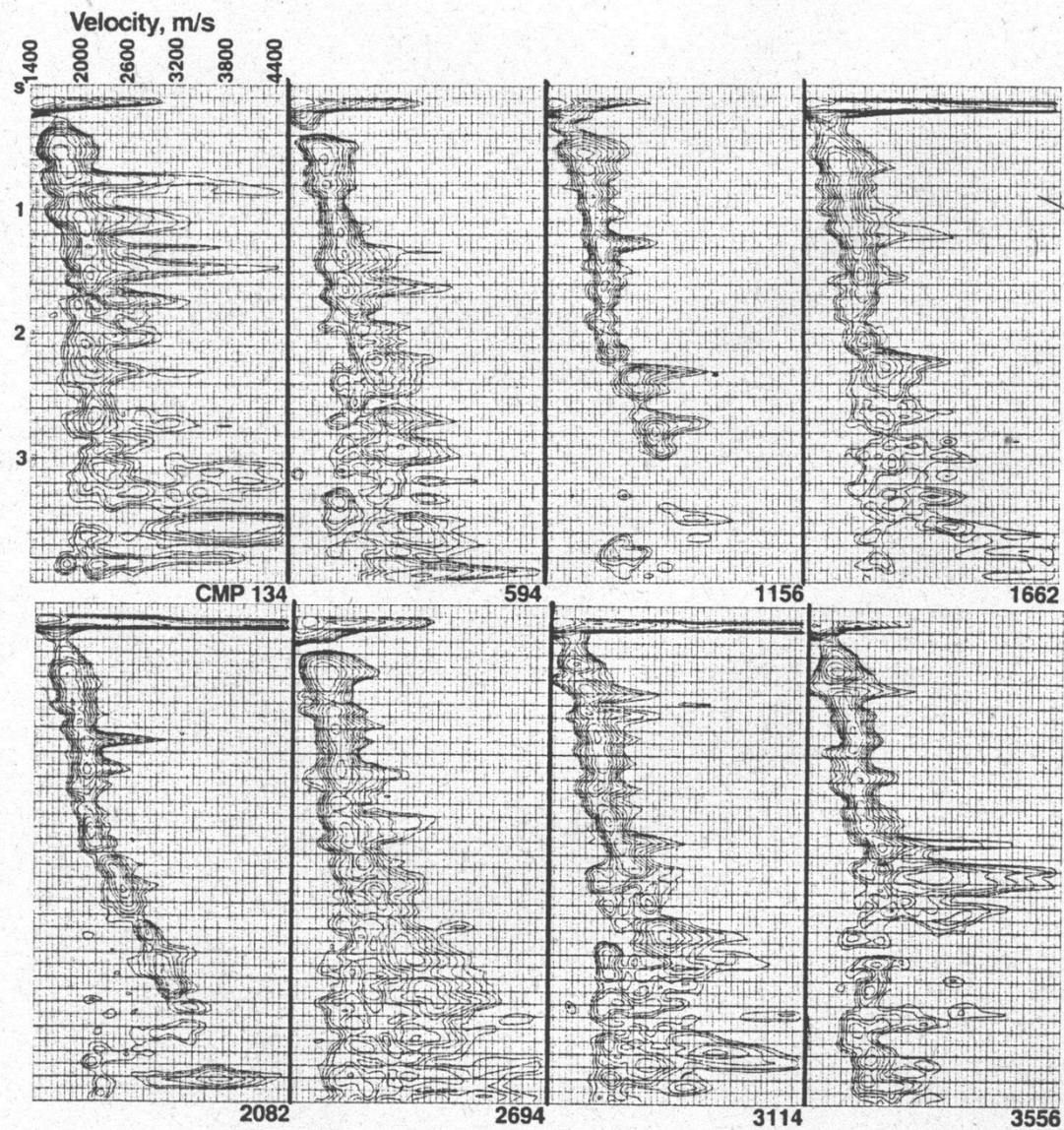


FIG. 1-44. Velocity spectra derived from the CMP gathers in Figure 1-42. Note the general trend common to all velocity functions and the progressive loss of velocity resolution in the trends at late times.



future ocean
KIEL MARINE SCIENCES

Acoustic Imaging

Seismic Data Processing

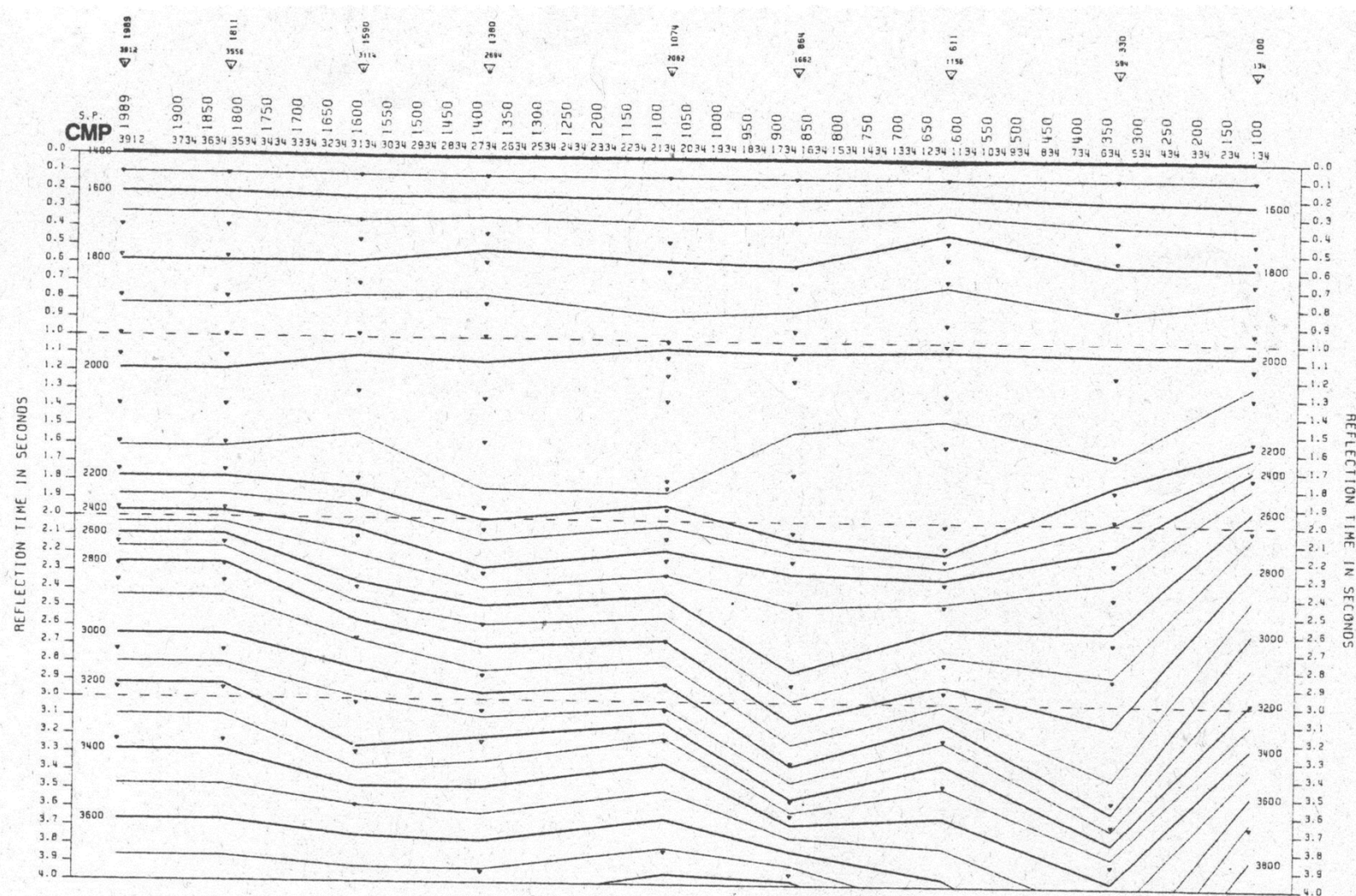


FIG. 1-45. Stacking velocity field over the length of the seismic line under consideration. This isovelocity contour map was derived using the velocity picks from the spectra in Figure 1-44. When compared with Figure 1-48, this figure reflects the structural trend in the subsurface. Triangular symbols on top indicate the locations of the velocity analyses in Figure 1-44.



future ocean
KIEL MARINE SCIENCES

Acoustic Imaging

Seismic Data Processing

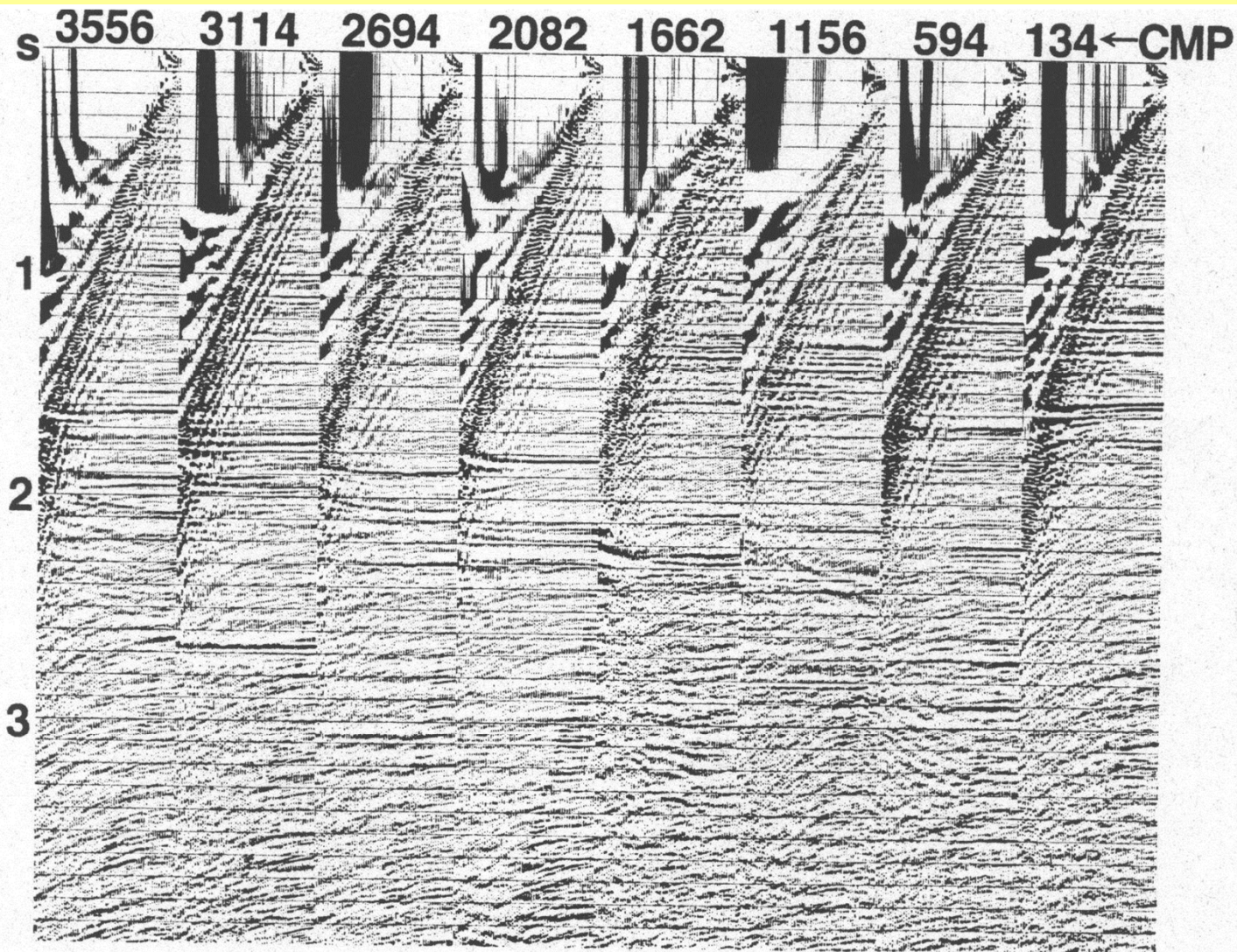


FIG. 1-46. The CMP gathers of Figure 1-42 after NMO correction using the velocity picks derived from the spectra in Figure 1-44. Note the stretching effect at the shallow part of the gathers, particularly at the far offsets. By properly selecting the velocities, the primaries are flattened. (Compare the individual events in this figure and in Figure 1-42.)



future ocean
KIEL MARINE SCIENCES

Acoustic Imaging

Seismic Data Processing

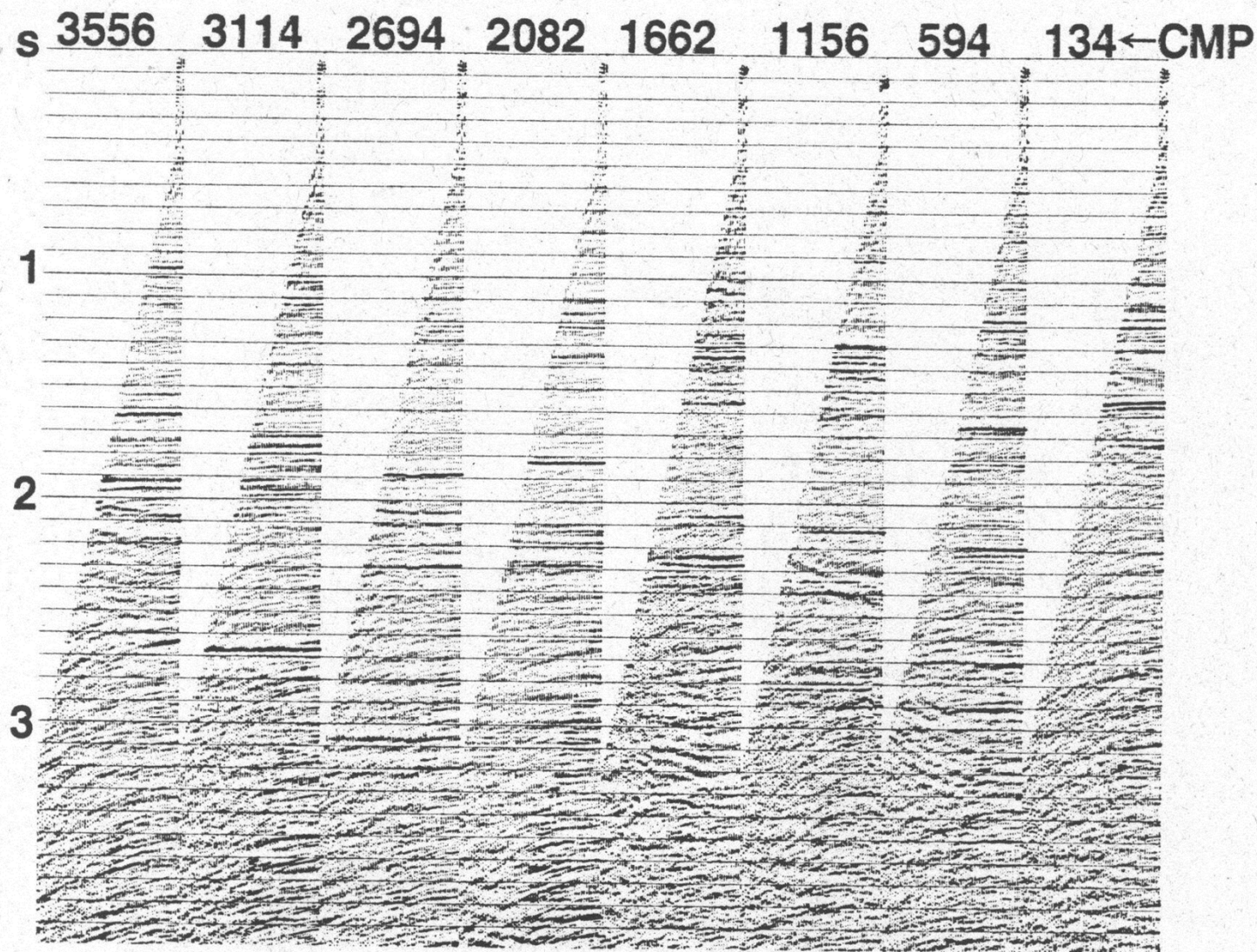


FIG. 1-47. The CMP gathers of Figure 1-46 after muting the stretched zones. By muting, the degrading effect of the stretched signal (very low frequency) on stacking quality is eliminated.



future ocean
KIEL MARINE SCIENCES

Acoustic Imaging

Seismic Data Processing

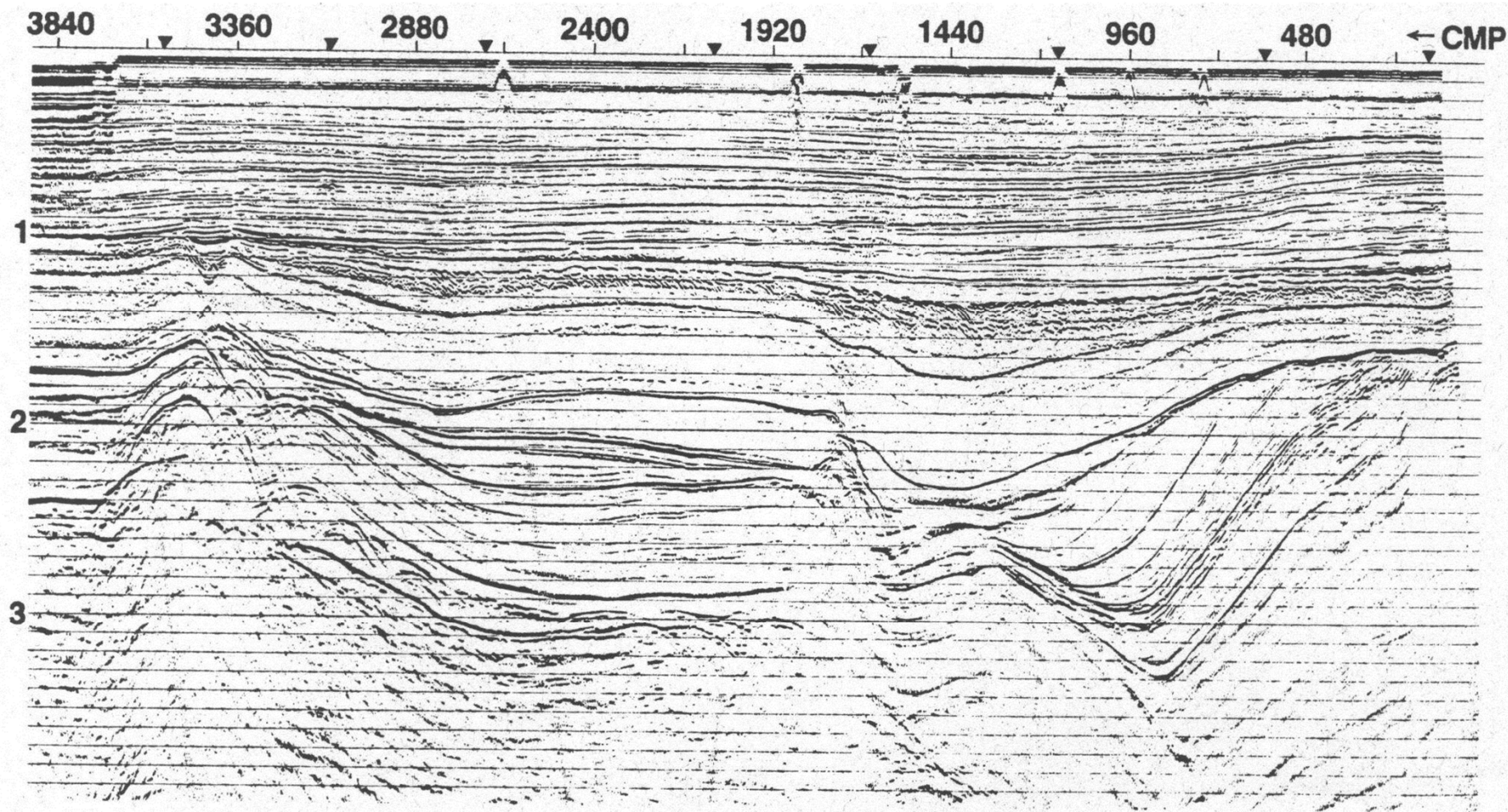


FIG. 1-48. The CMP stack associated with the gathers in Figure 1-47. The triangles refer to the locations of the velocity analyses in Figure 1-44.

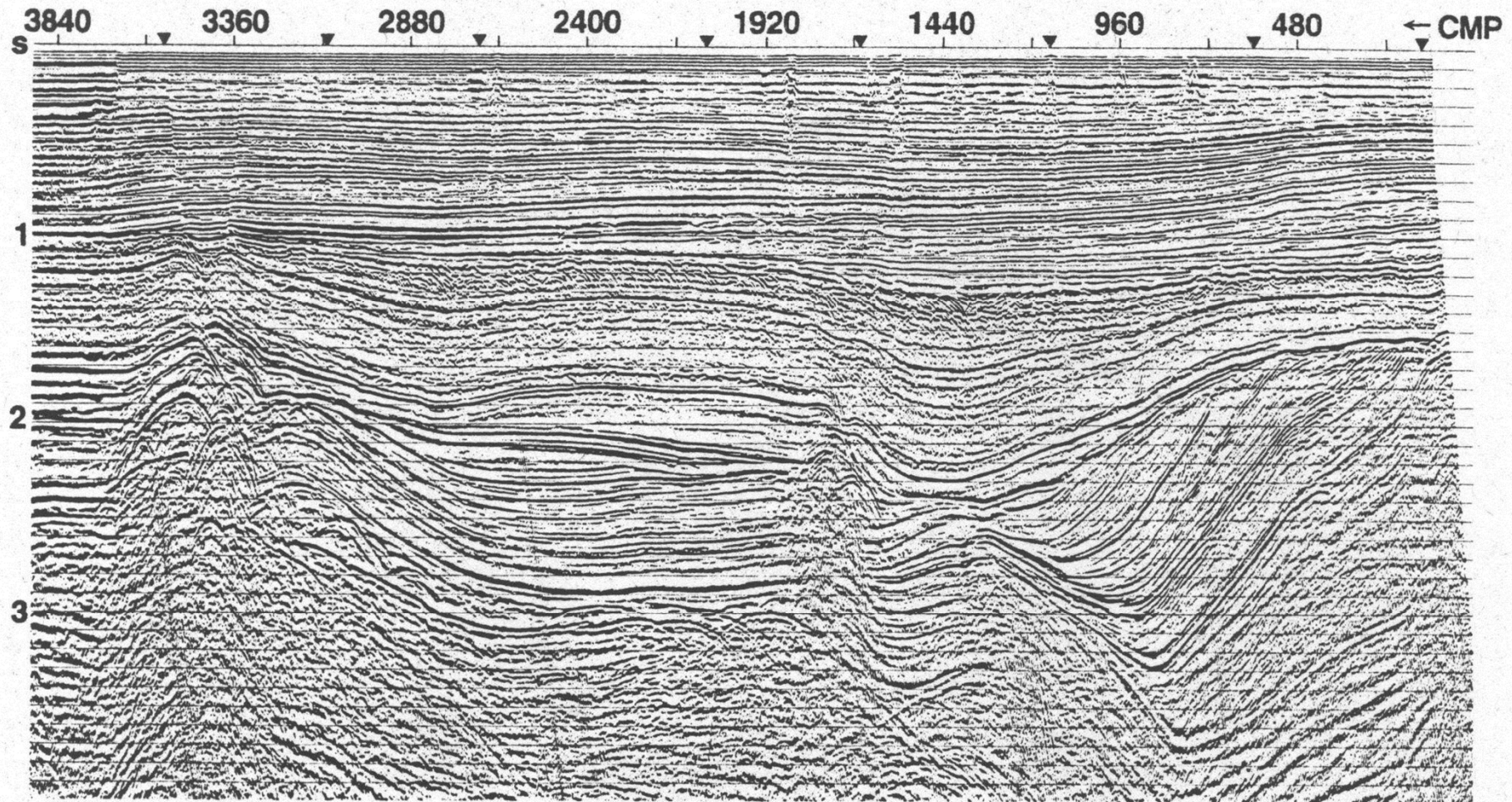


FIG. 1-53. The CMP stack associated with the gathers in Figure 1-47. This stack is the same as in Figure 1-48 with a time-variant filter (TVF) followed by an rms gain application.

Migration

Aim: Optimize the similarity of a seismic and geological section.

Migration moves reflectors to their correct location and collapses diffraction hyperbolas.

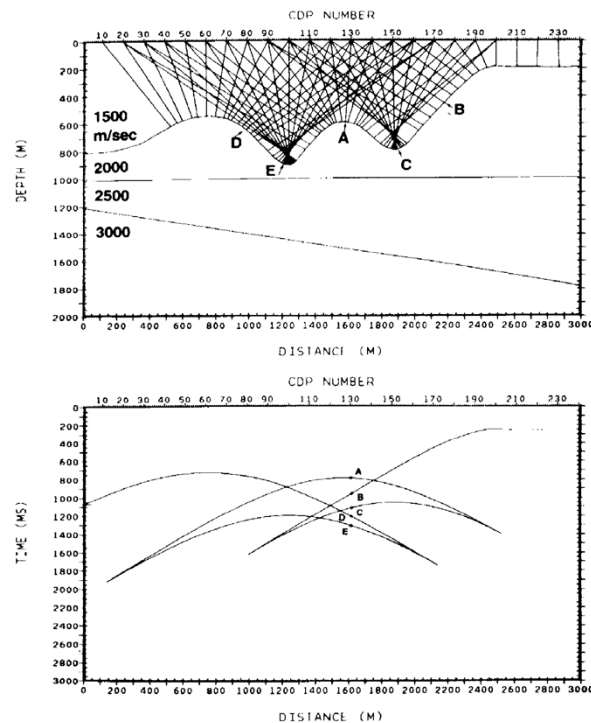


FIG. 4-7. A velocity-depth model (top) and the zero-offset response (bottom) obtained from normal-incidence rays. Note the five arrivals (A, B, C, D, and E) at CMP 130, all from the water bottom.

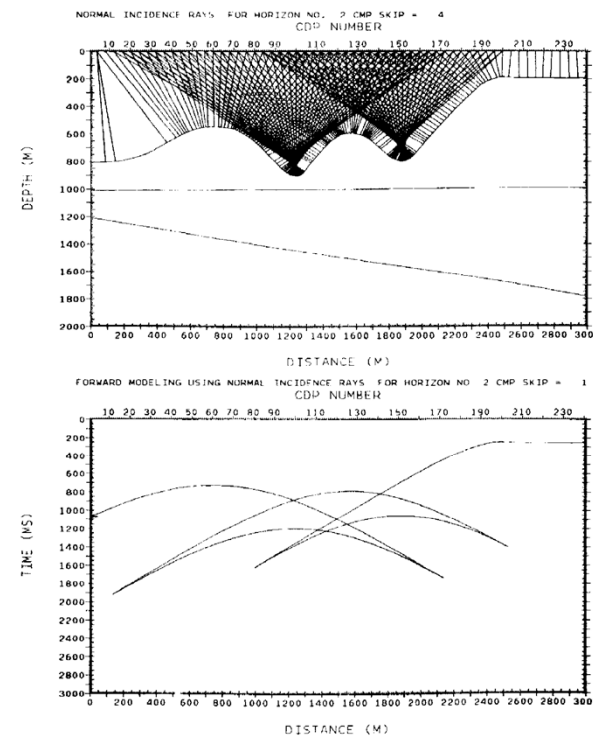


FIG. 4-8. Exploding-reflector modeling of the water bottom. The time section is equivalent to a zero-offset section; i.e., the vertical axis is in two-way time.

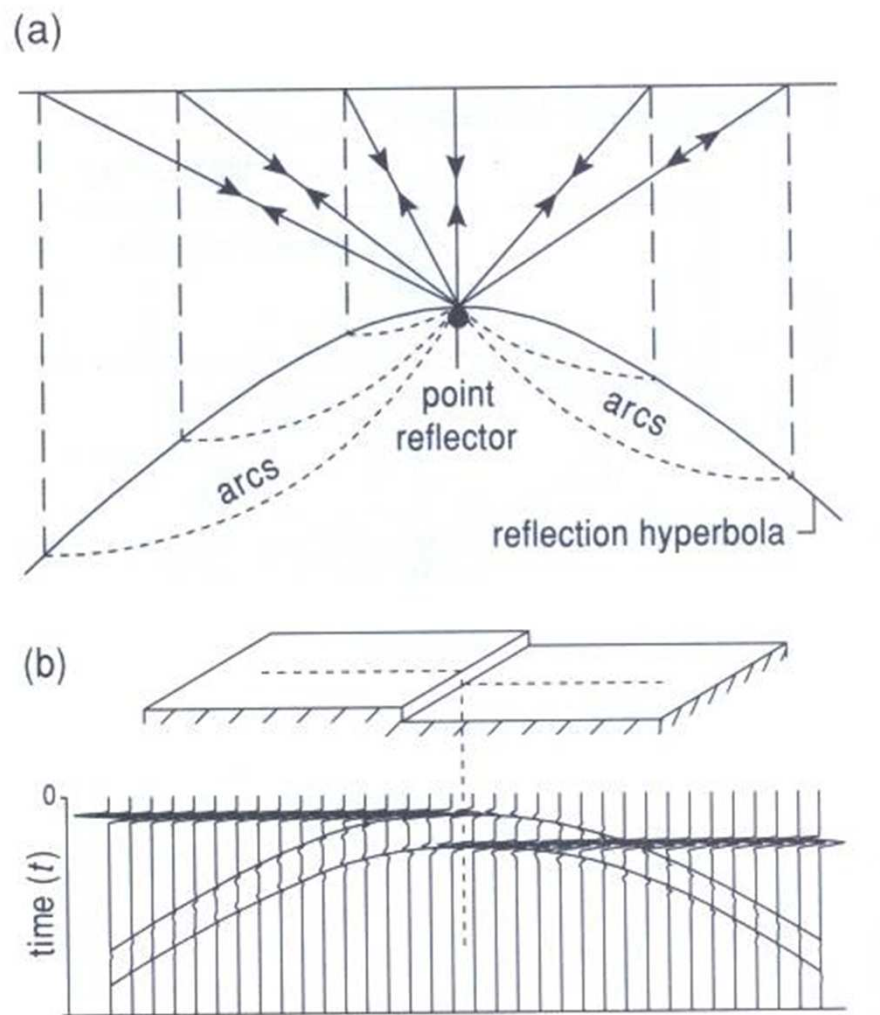


Figure 7.11 (a) Point and (b) stepped reflector.

Diffraction points create diffraction hyperbolas in a seismic section.

Migration causes the diffraction hyperbola to collapse at the diffraction point.

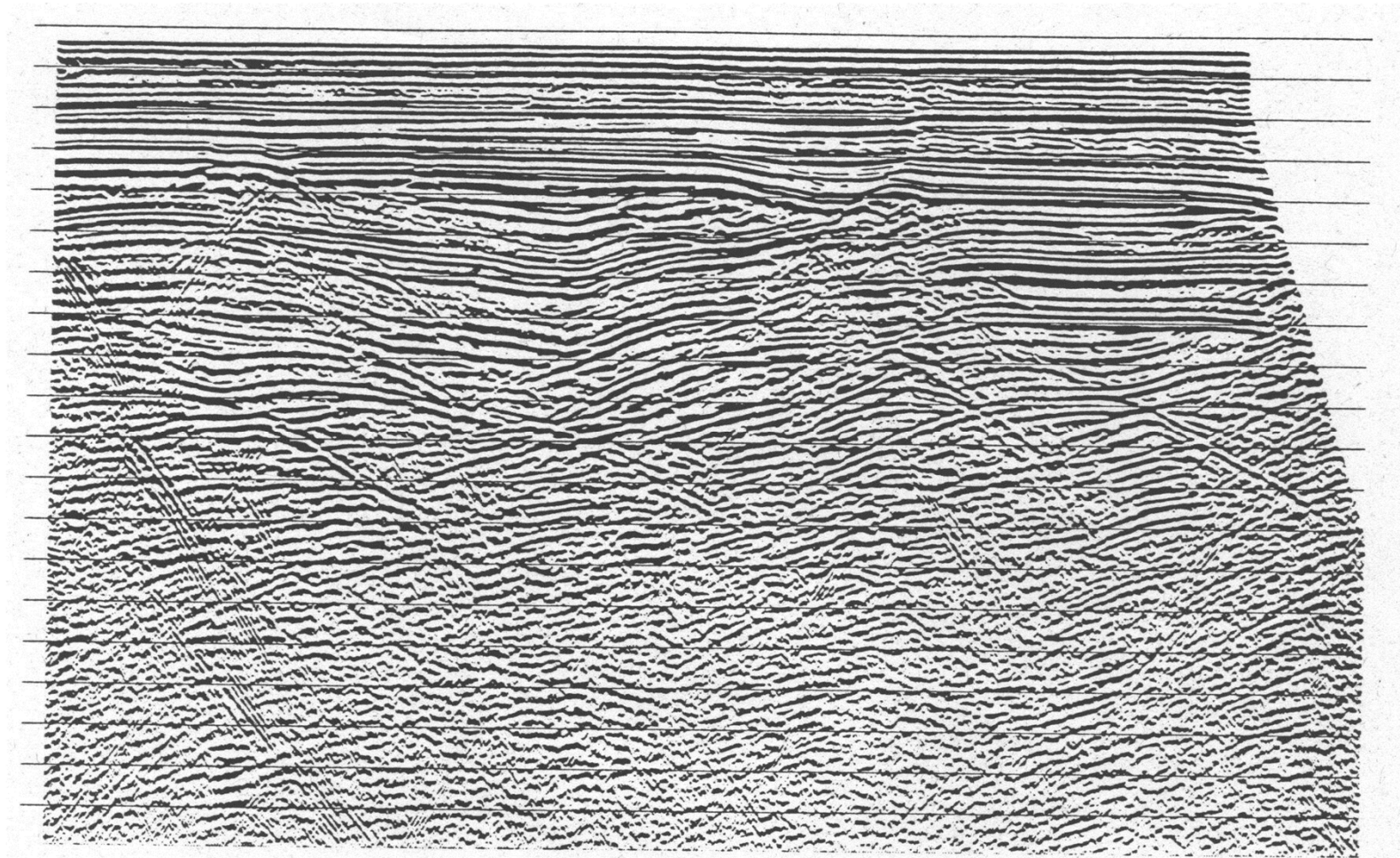


future ocean
KIEL MARINE SCIENCES

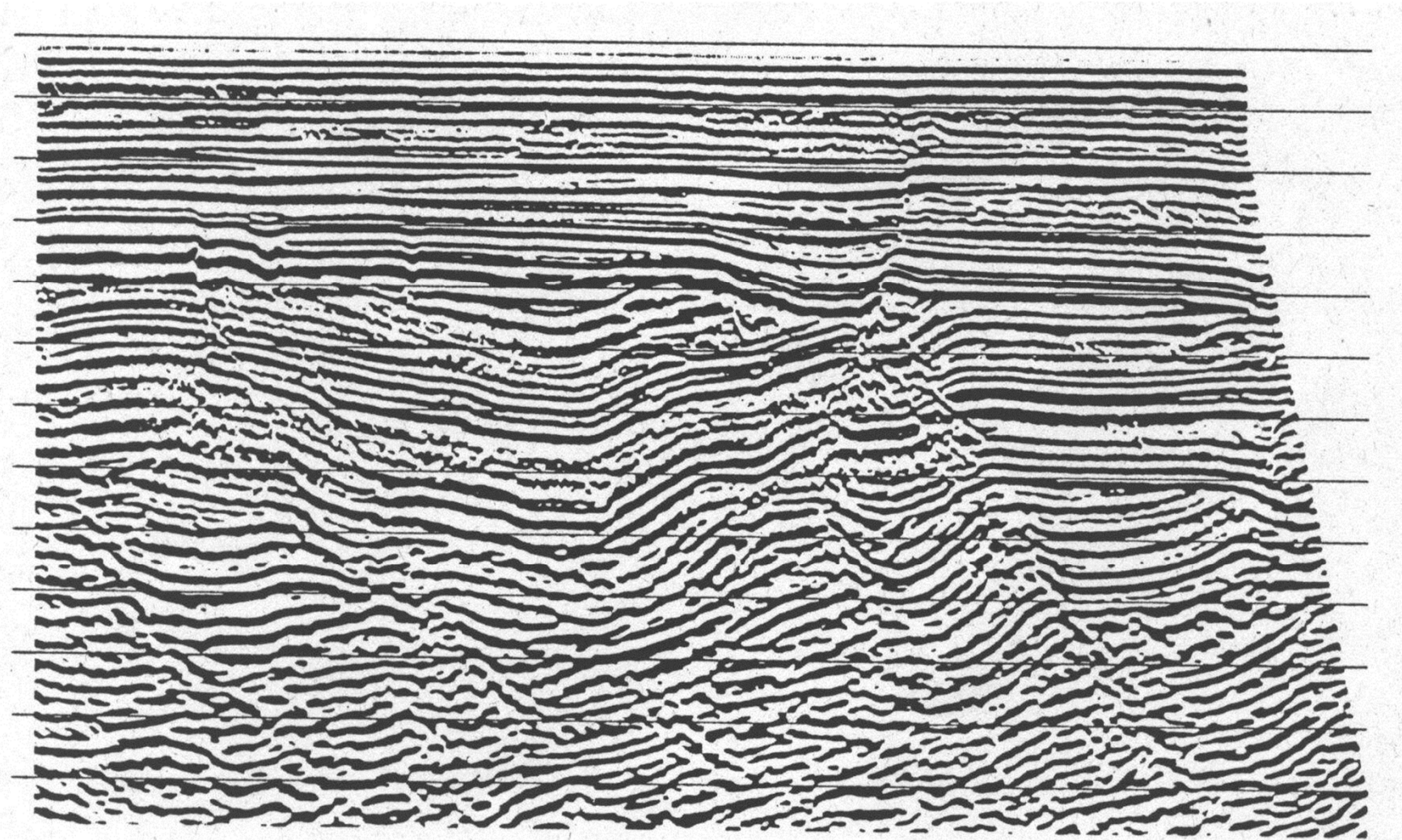
Acoustic Imaging

Seismic Data Processing

Stacked section with migration hyperbolas

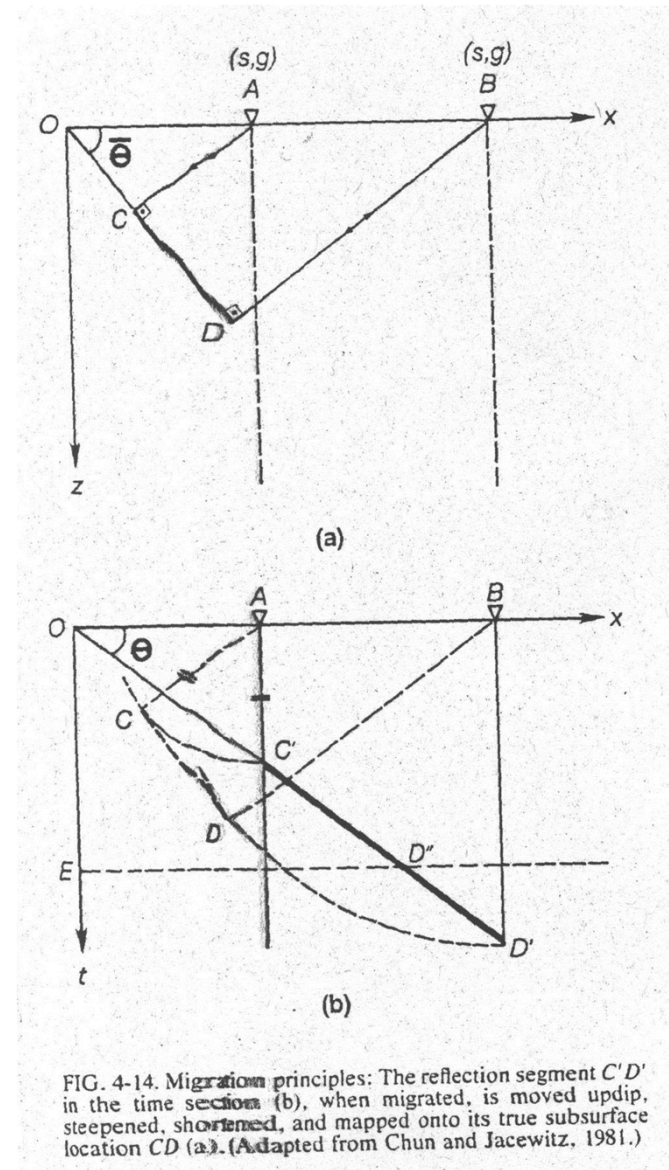


Migrated Section



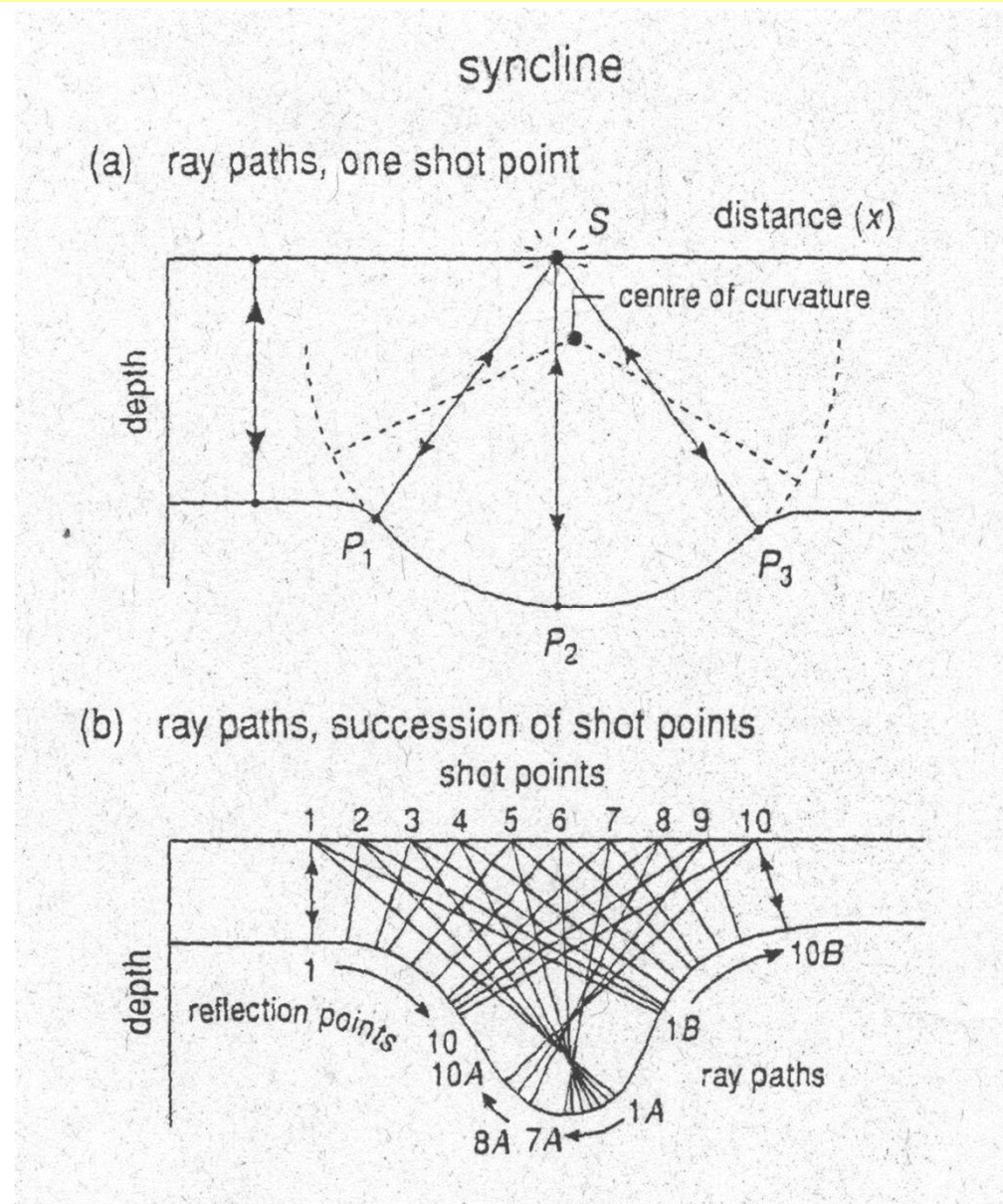
Inclined reflectors

- Migration enlarges the angle of the reflector
- Migration shortens inclined reflectors
- Migration moves the reflector in the updip direction



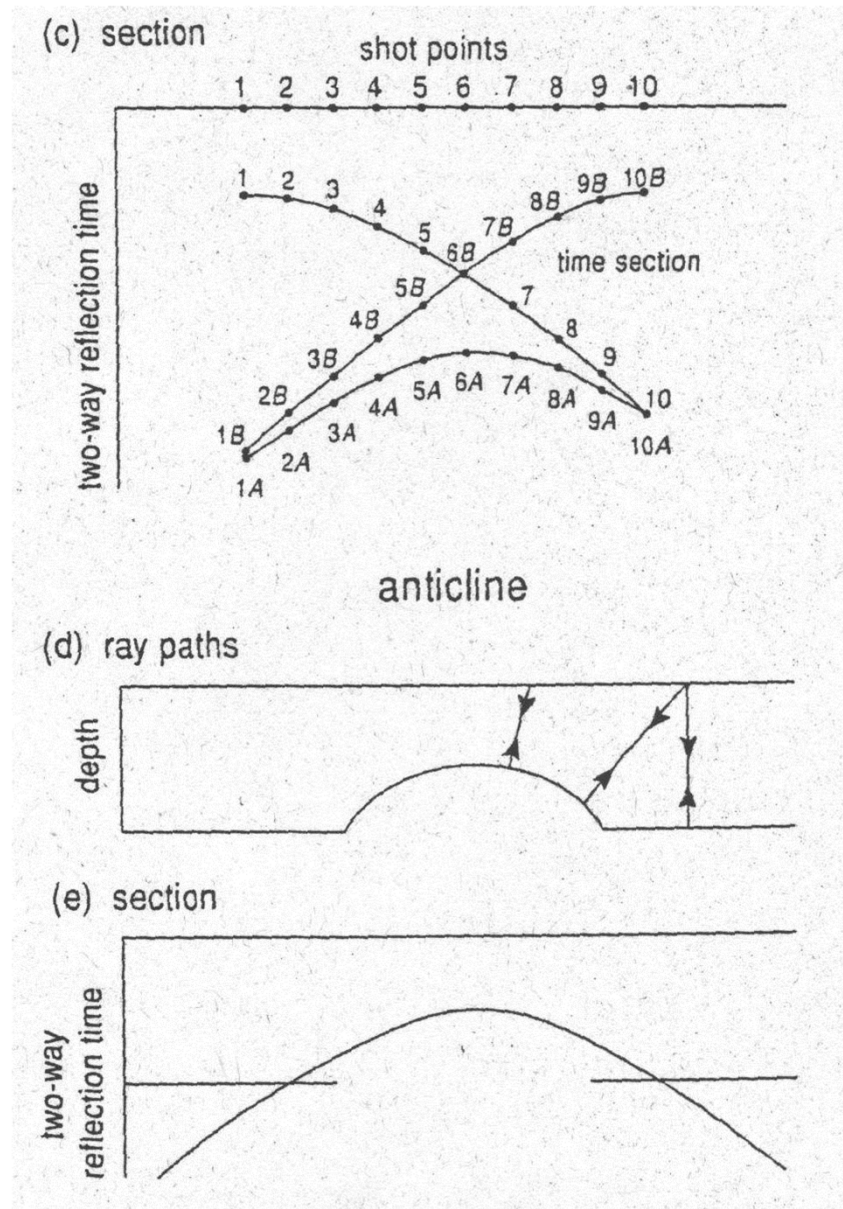
Synclines:

Migration broadens synclines and delete bowties.



Anticlines:

Migration narrows anticlines

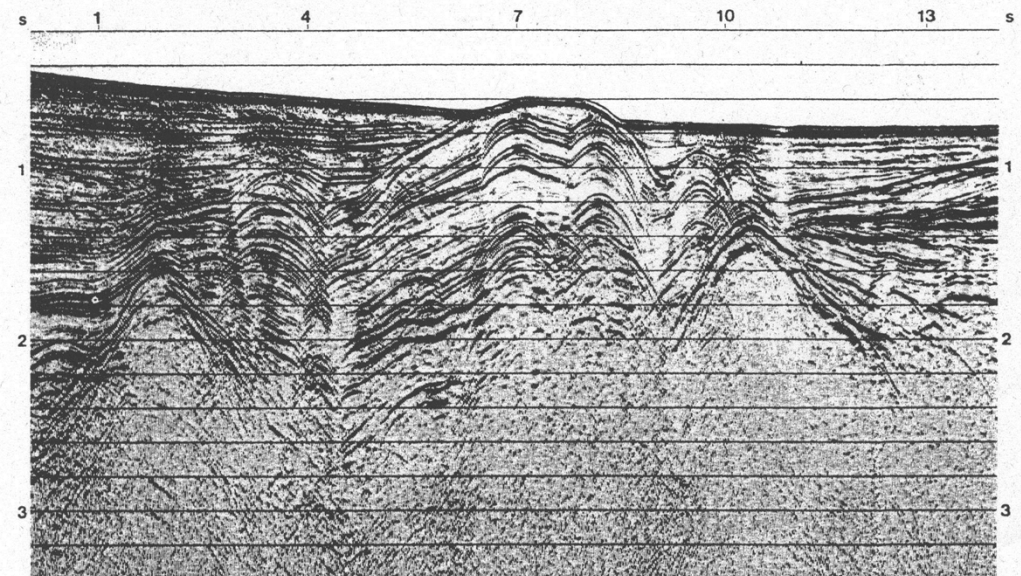




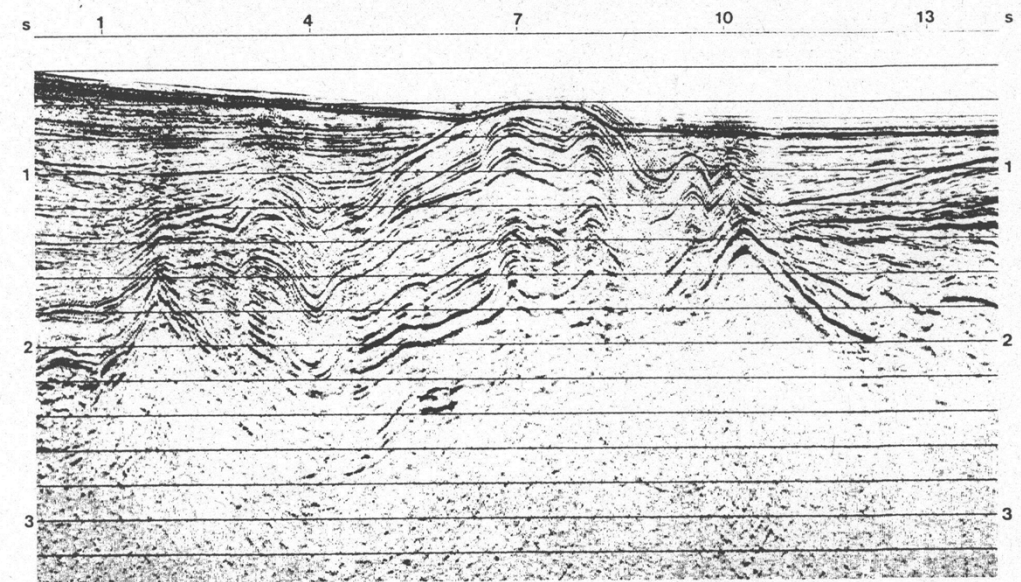
future ocean
KIEL MARINE SCIENCES

Acoustic Imaging

Seismic Data Processing



(a)



(b)



future ocean
KIEL MARINE SCIENCES

Acoustic Imaging

Seismic Data Processing

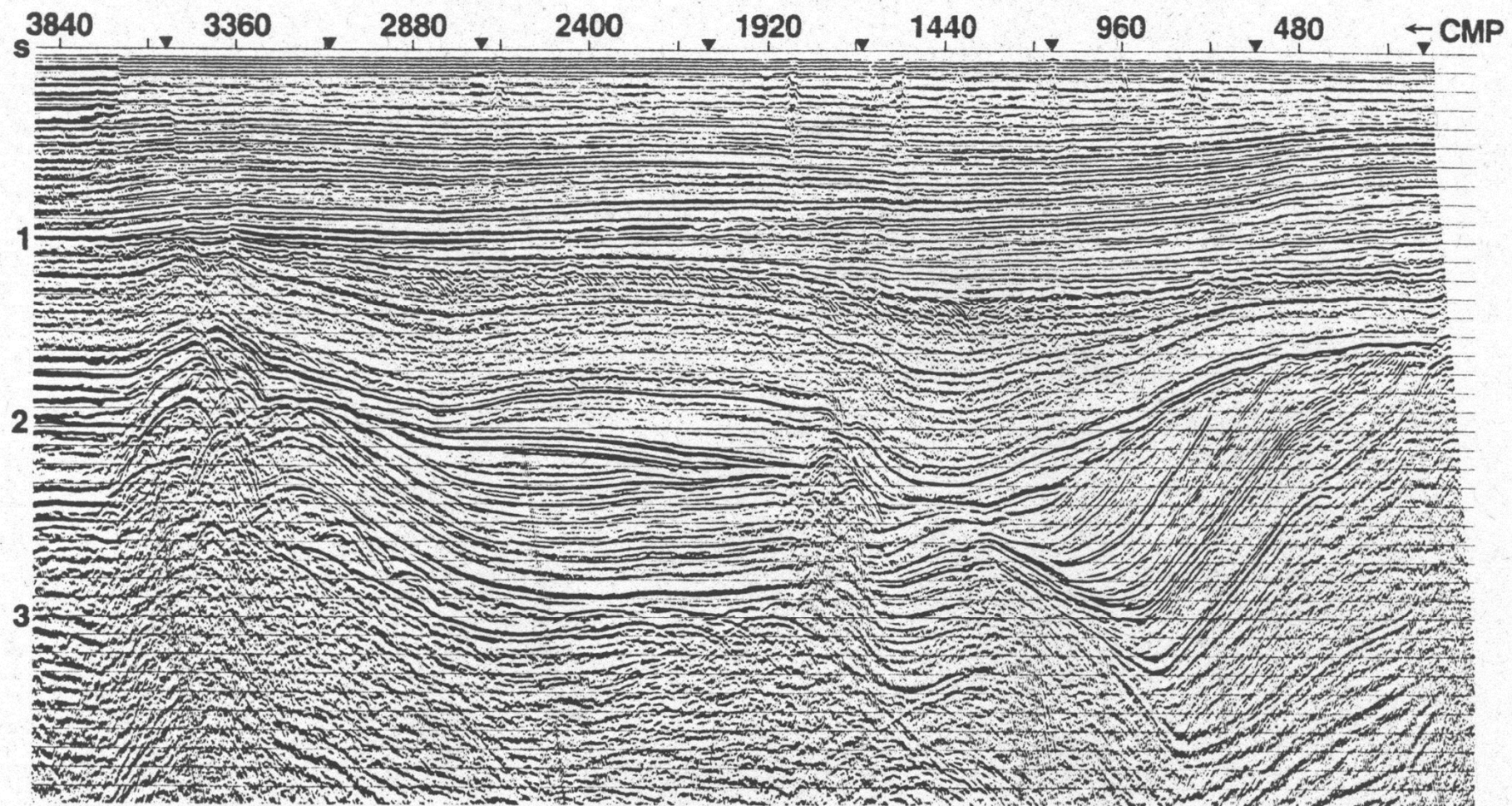


FIG. 1-53. The CMP stack associated with the gathers in Figure 1-47. This stack is the same as in Figure 1-48 with a time-variant filter (TVF) followed by an rms gain application.



future ocean
KIEL MARINE SCIENCES

Acoustic Imaging

Seismic Data Processing

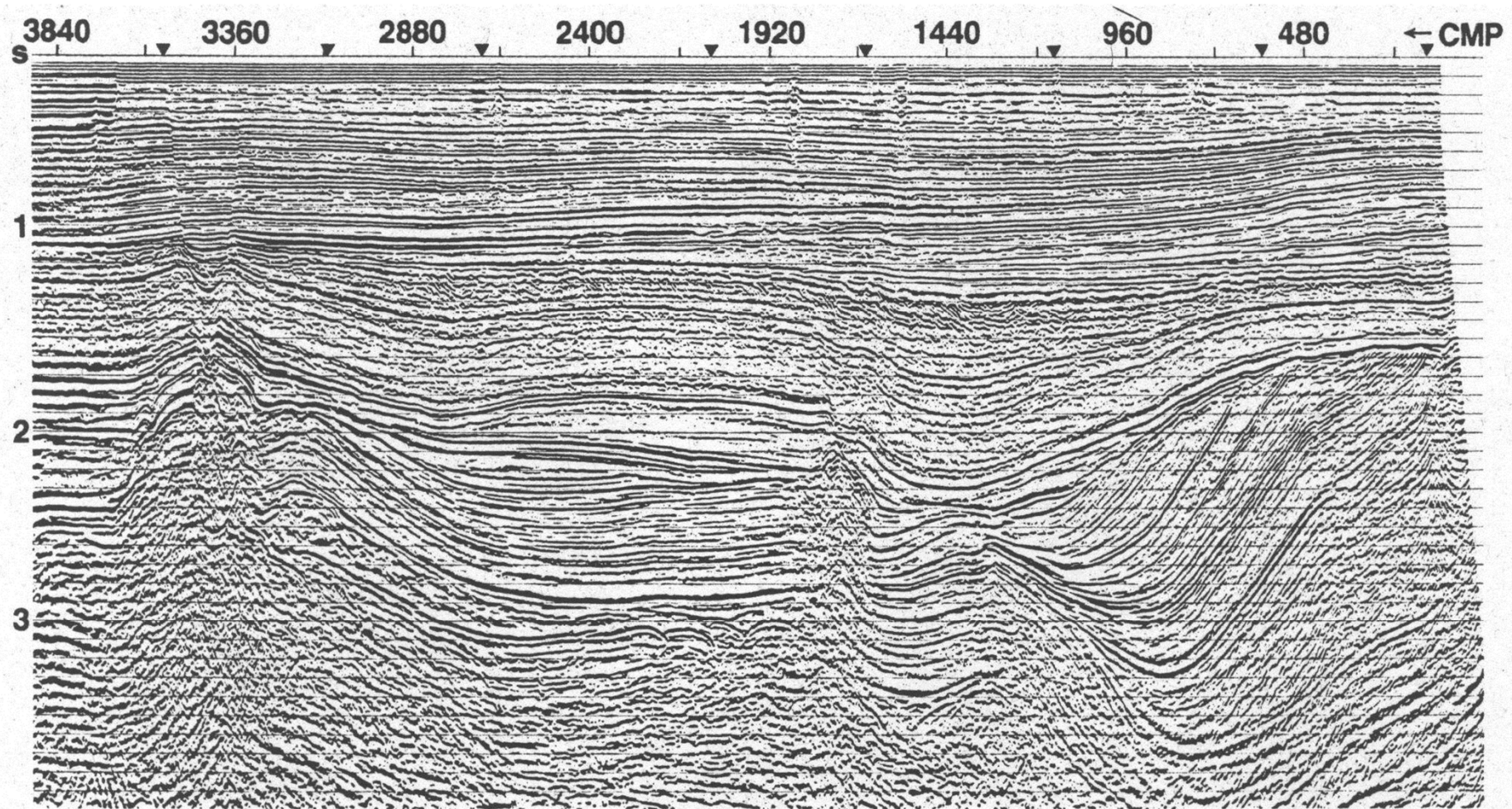


FIG. 1-54. Migrated CMP stack. The input to migration is the filtered stacked section. The migration output was gained as in Figure 1-53.



future ocean
KIEL MARINE SCIENCES

Acoustic Imaging

Seismic Data Processing

Migration with lower velocity:
Undermigration

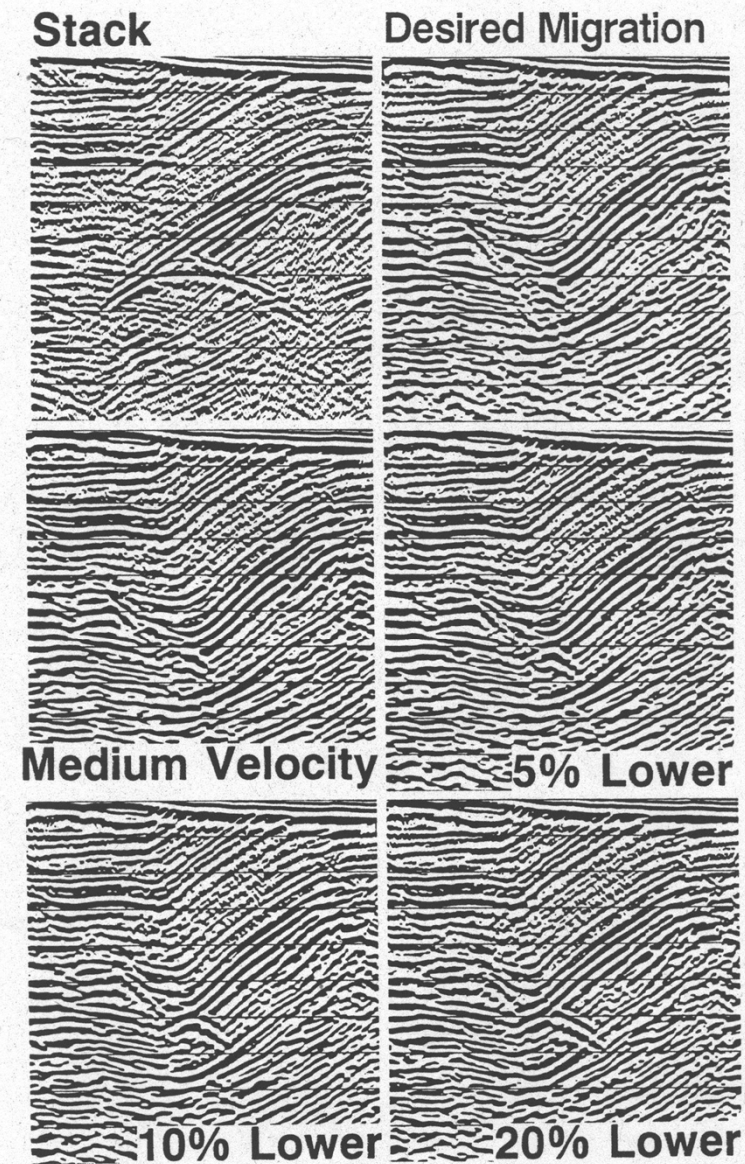


FIG. 4-53. Tests for velocity errors in Kirchhoff migration. Undermigration manifested as inadequate handling of the bowtie is caused by the use of velocities lower than velocities believed to be optimum (indicated as medium velocity).

Migration higher velocity:
Overmigration (Creation of
'Smilies')

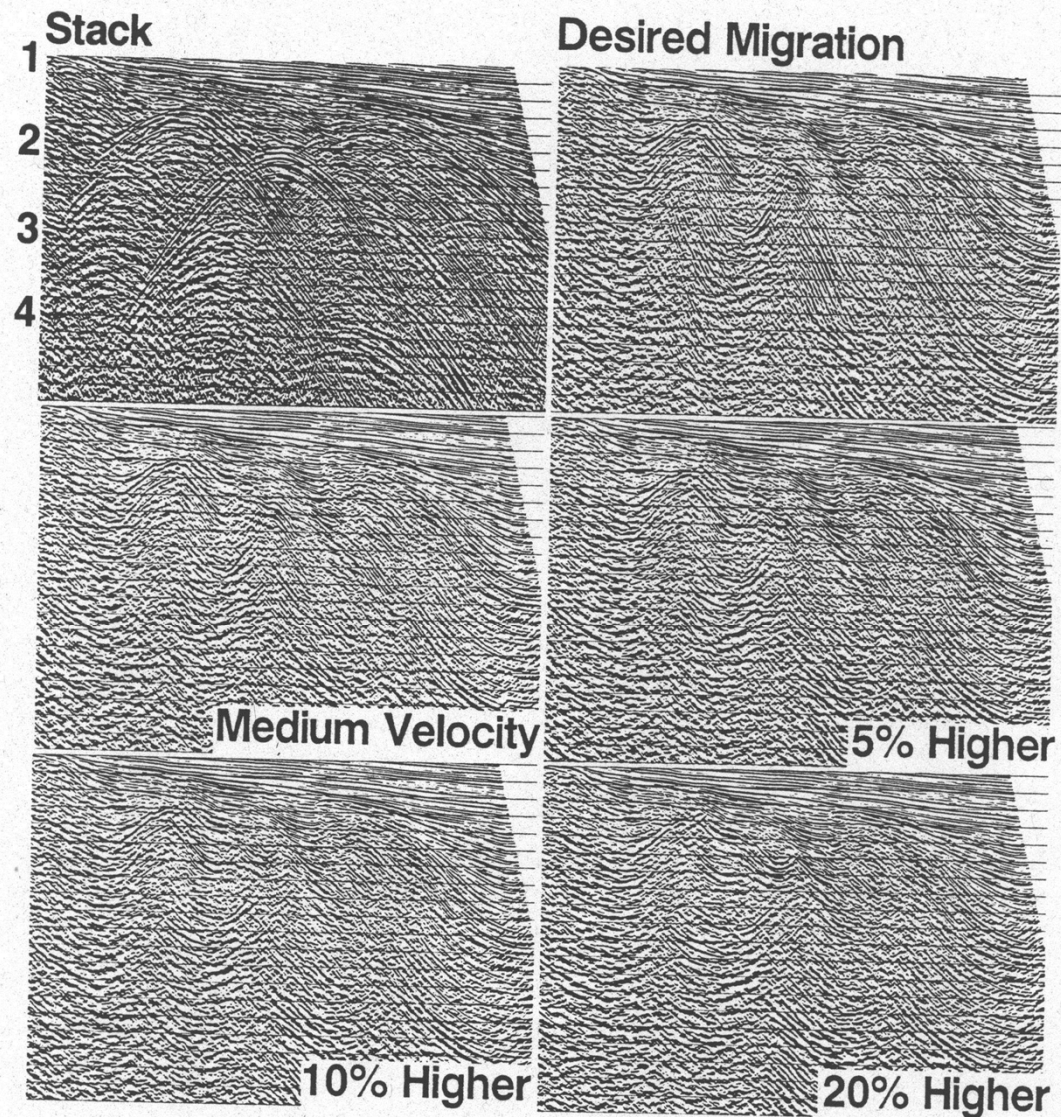


FIG. 4-54. Tests for velocity errors in Kirchhoff migration. Overmigration manifested as crossing events is caused by the use of velocities higher than velocities believed to be optimum (indicated as medium velocity). (Data courtesy Meridian Oil Inc.)

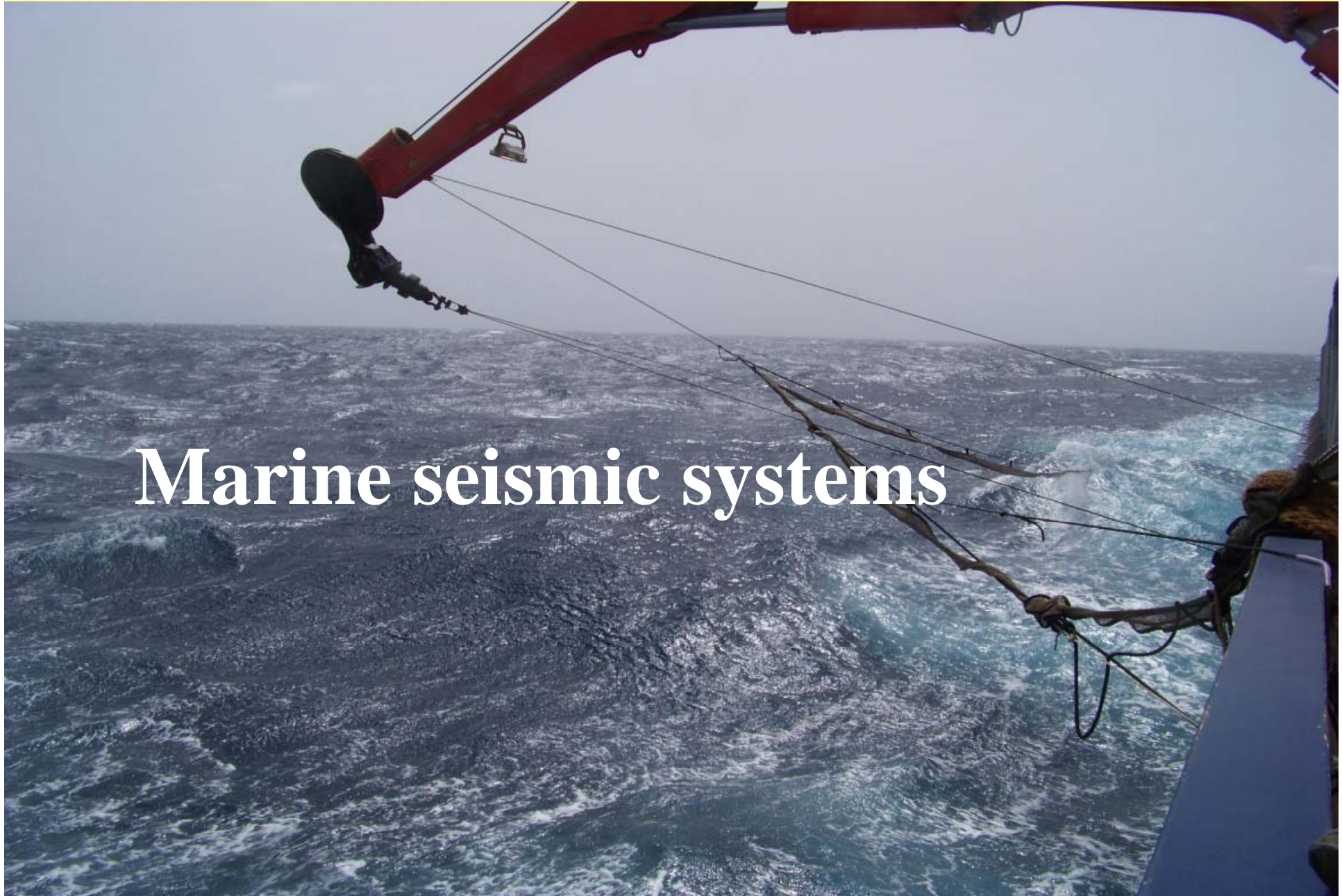


future ocean
KIEL MARINE SCIENCES

Acoustic Imaging

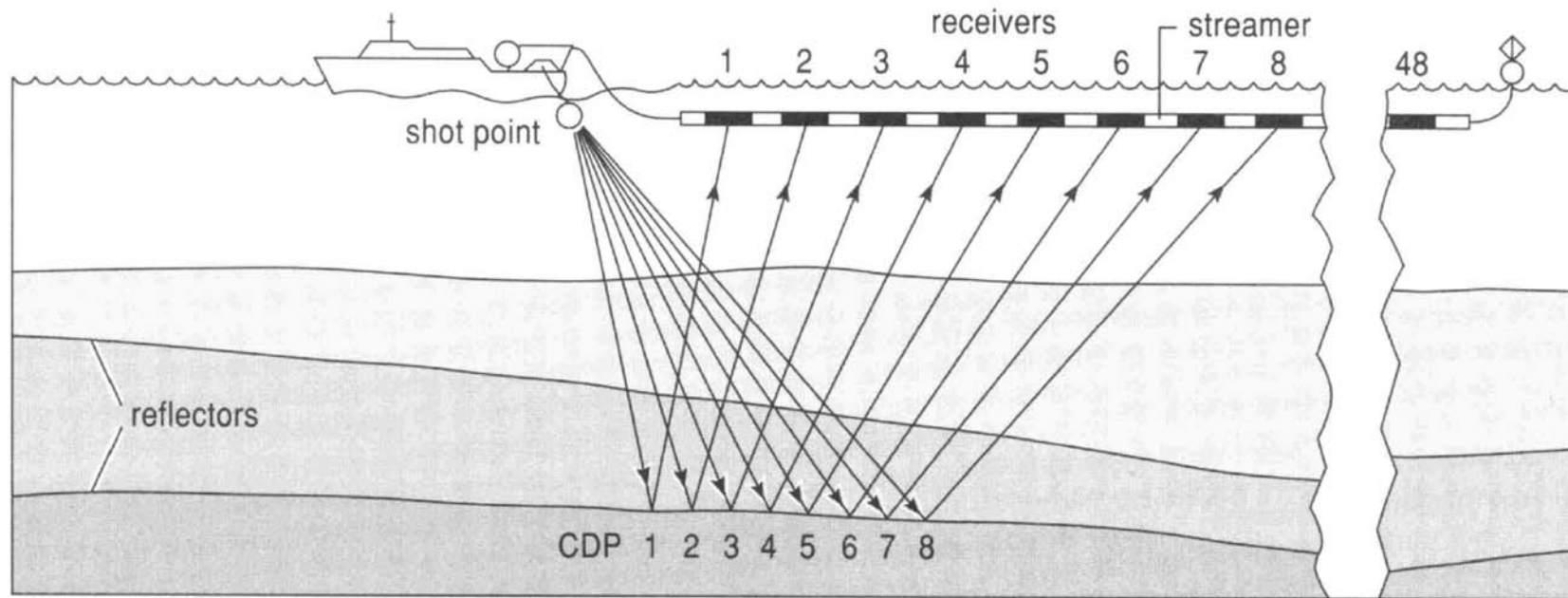
Seismic Systems

Marine seismic systems



Marine Seismics

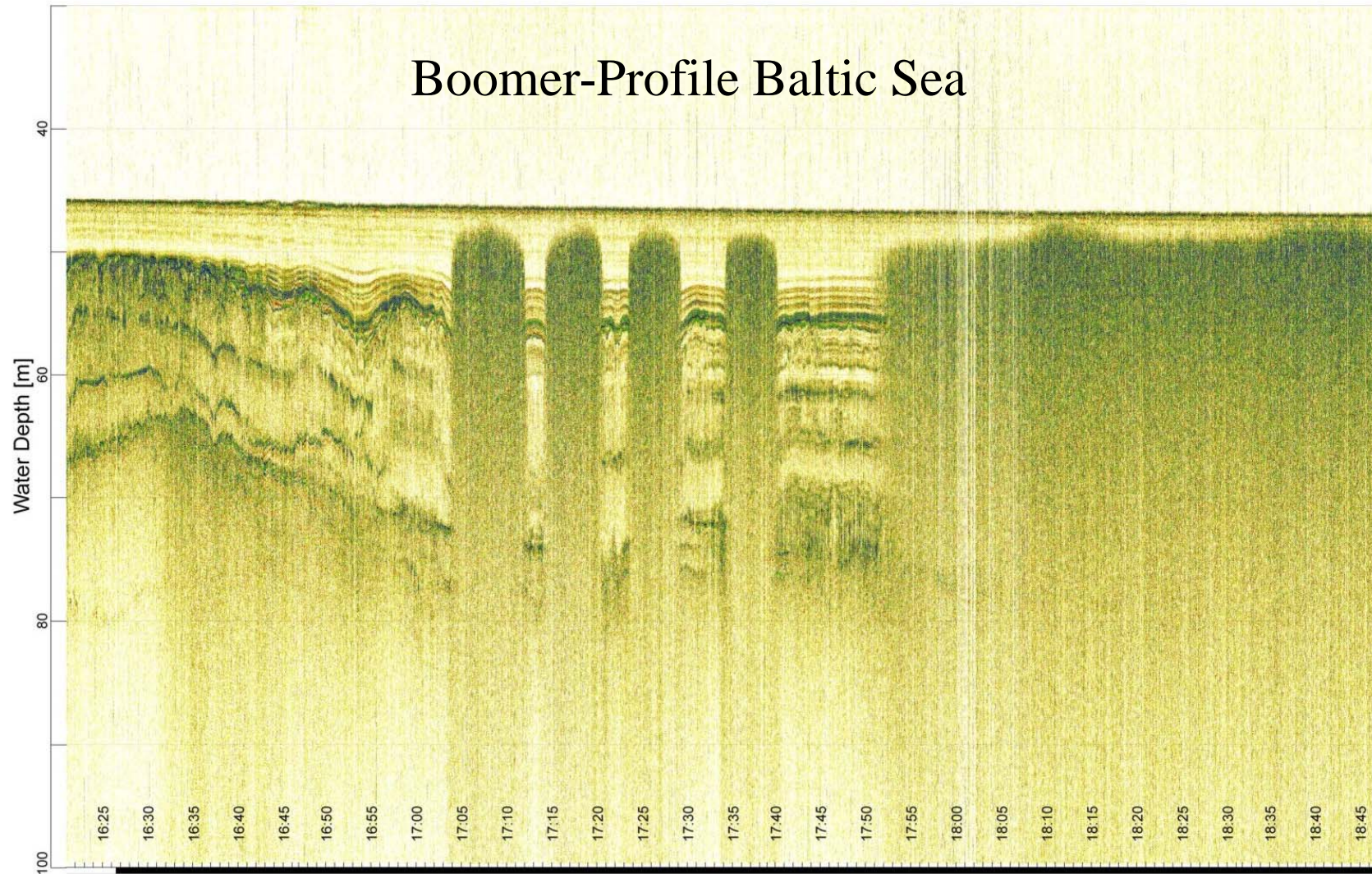
What do we need?



Source: Airgun, Watergun, Boomer, Sparker, Chirp

Receiver: Streamer, Ocean Bottom Seismometer, Ocean Bottom Cable

Recording Unit

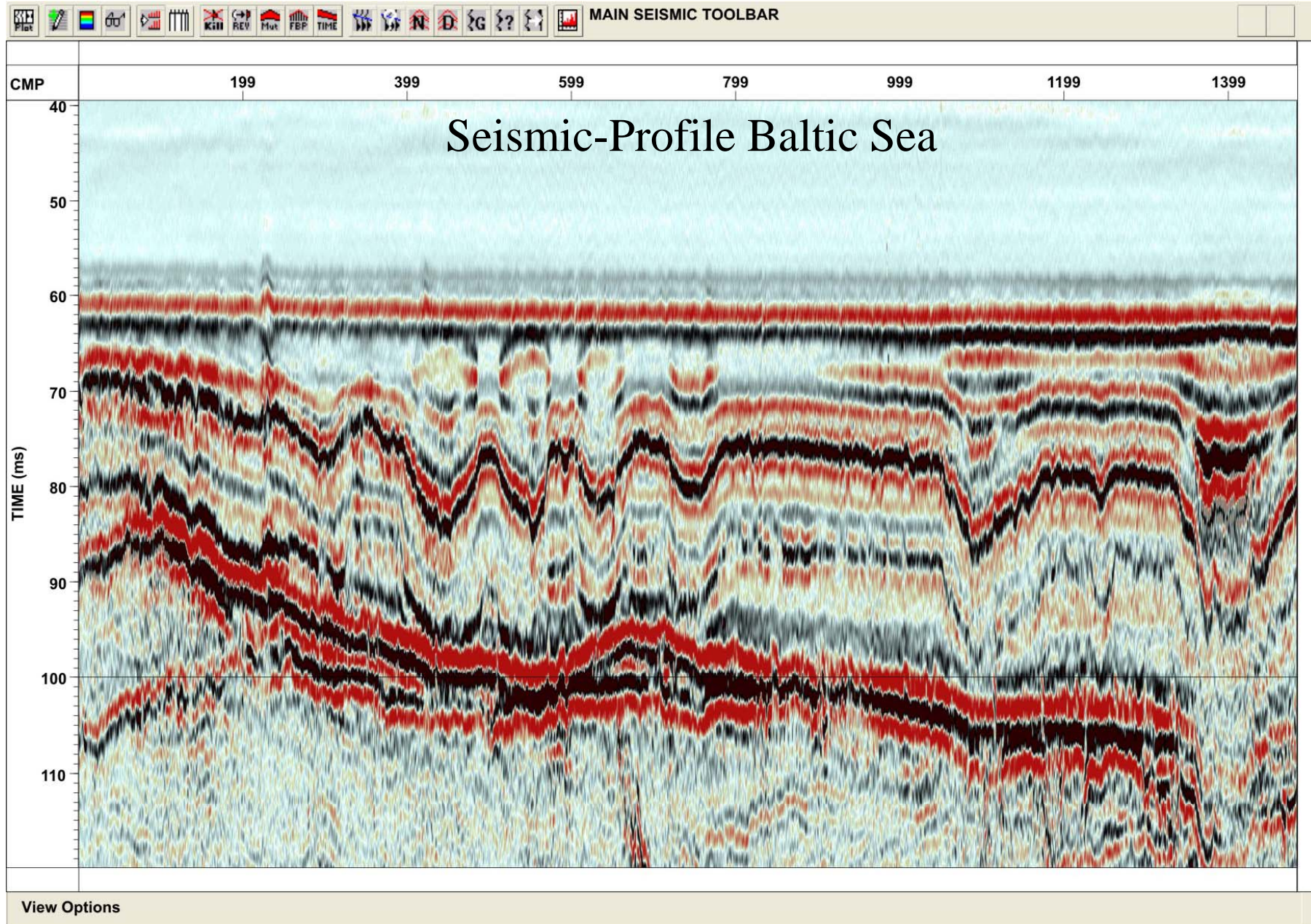




future ocean
KIEL MARINE SCIENCES

Acoustic Imaging

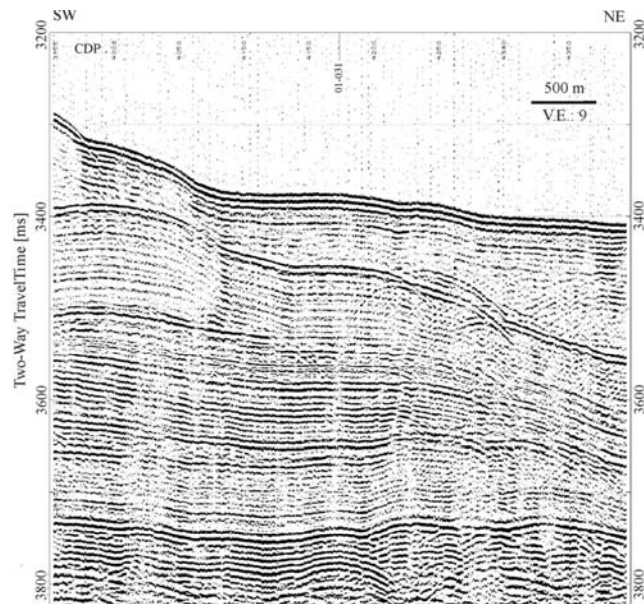
Seismic Systems



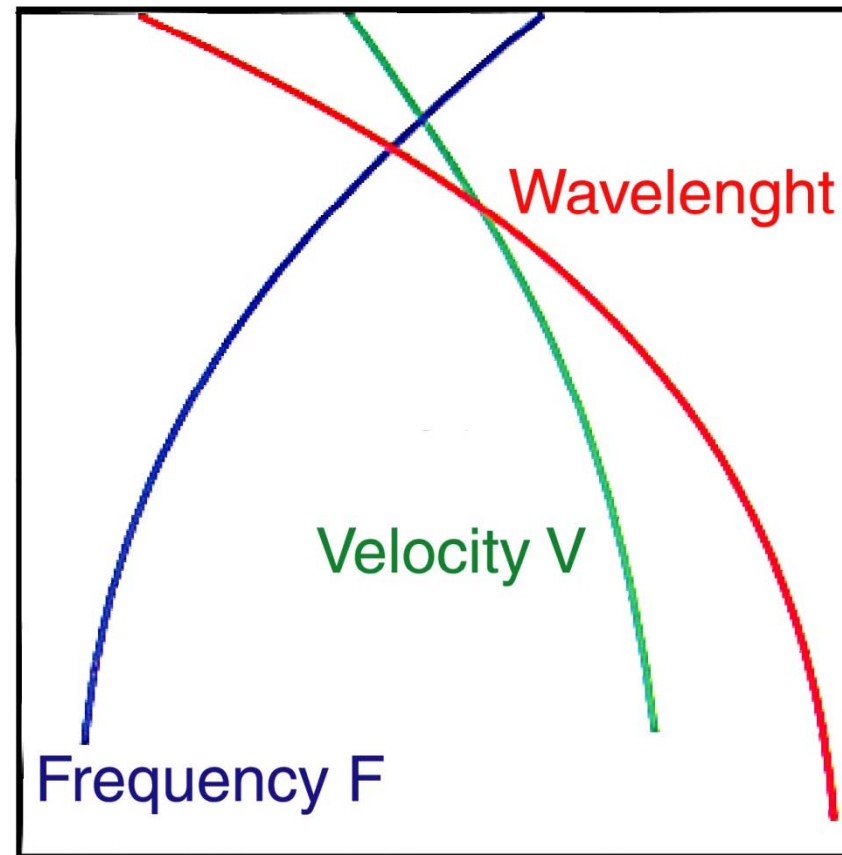
What would we like to achieve?

High resolution

3D- controll

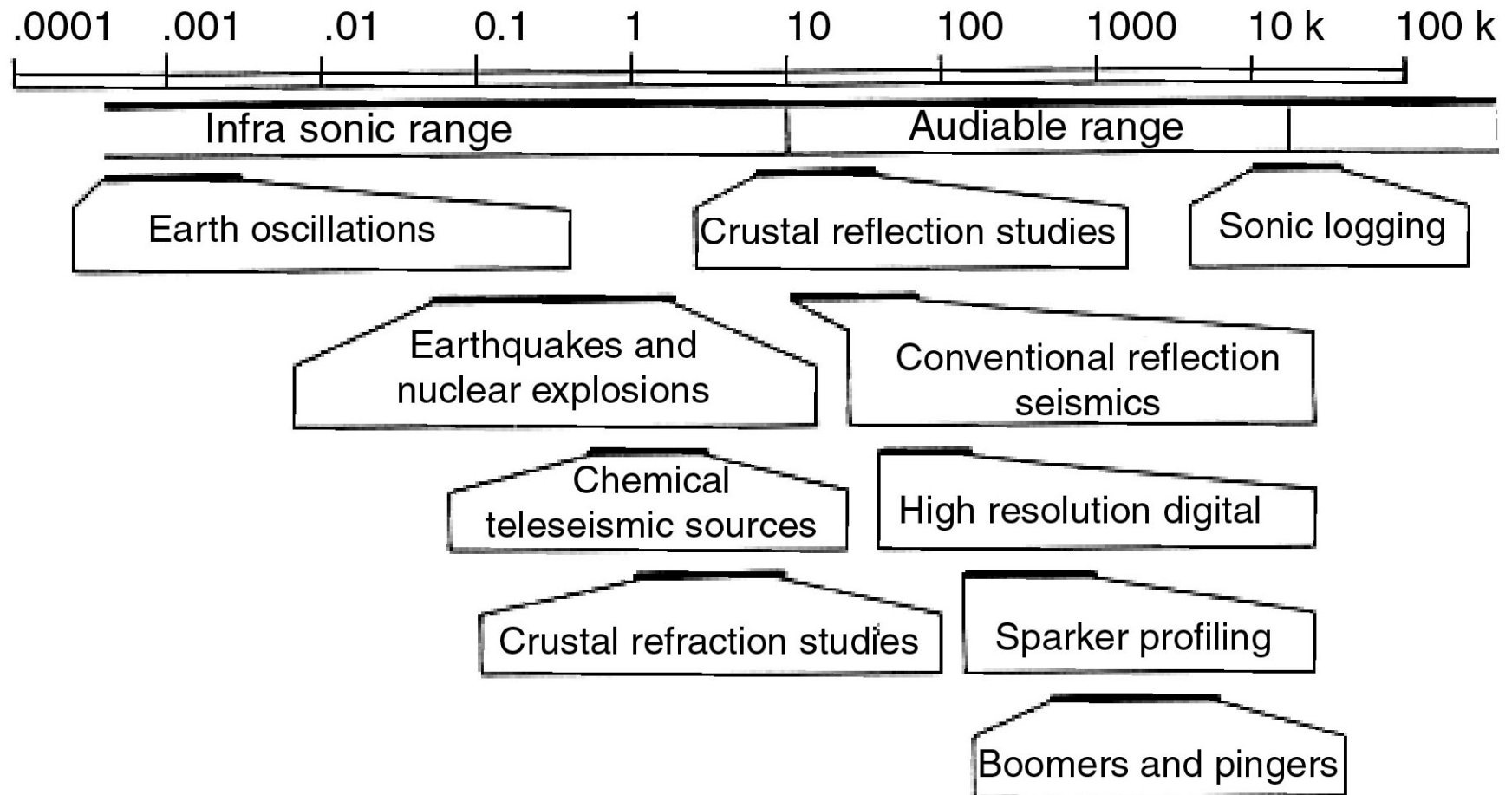


What is the problem?



$$\text{Wavelength} = \text{Velocity} / \text{Frequency}$$

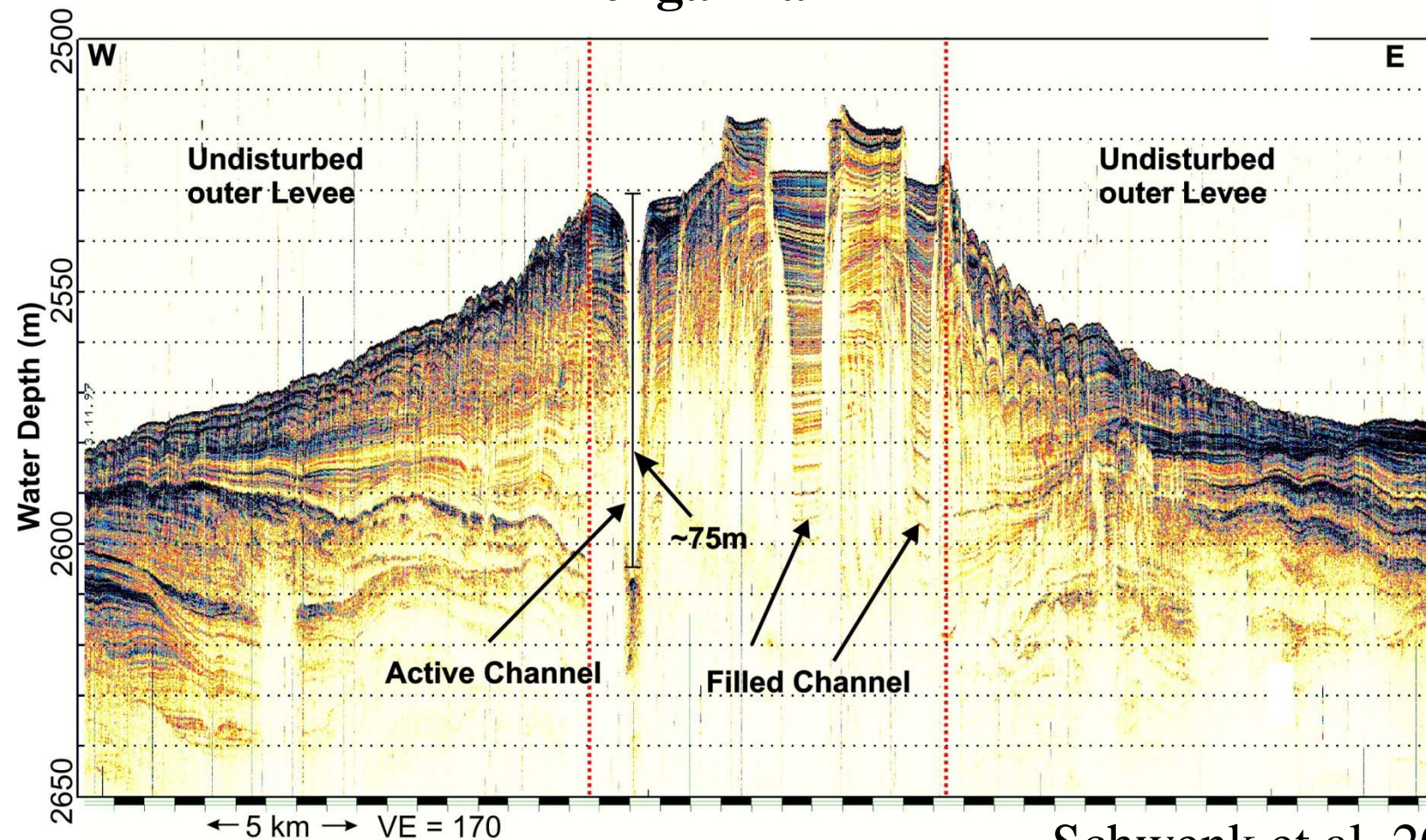
Frequency in Hertz



Sources

Echo Sounders: Typical frequencies: 2-200kHz, Penetration <100m

Bengal-Fan

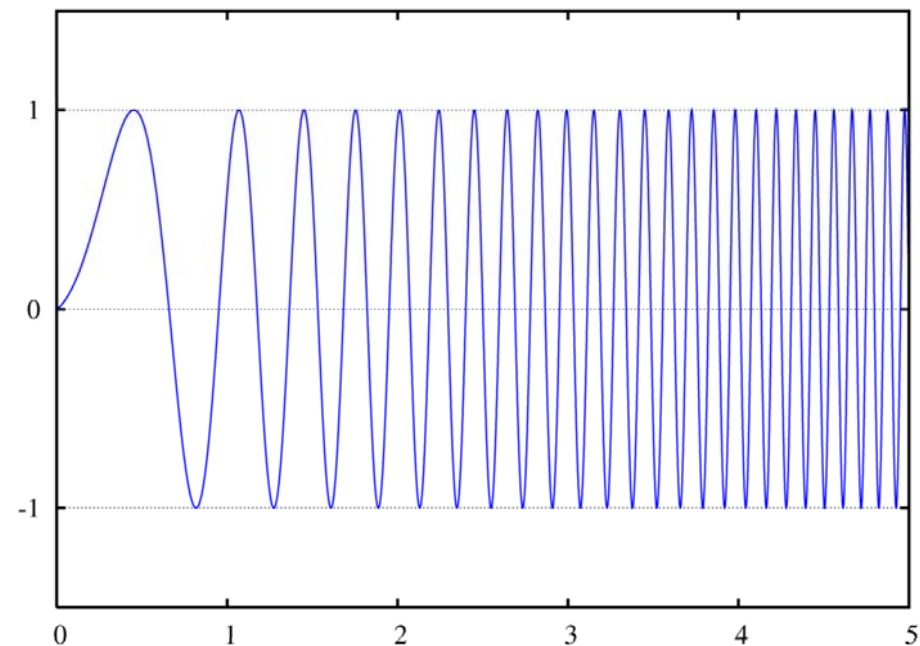


Schwenk et al, 2003

Boomer und Chirp-Systeme:

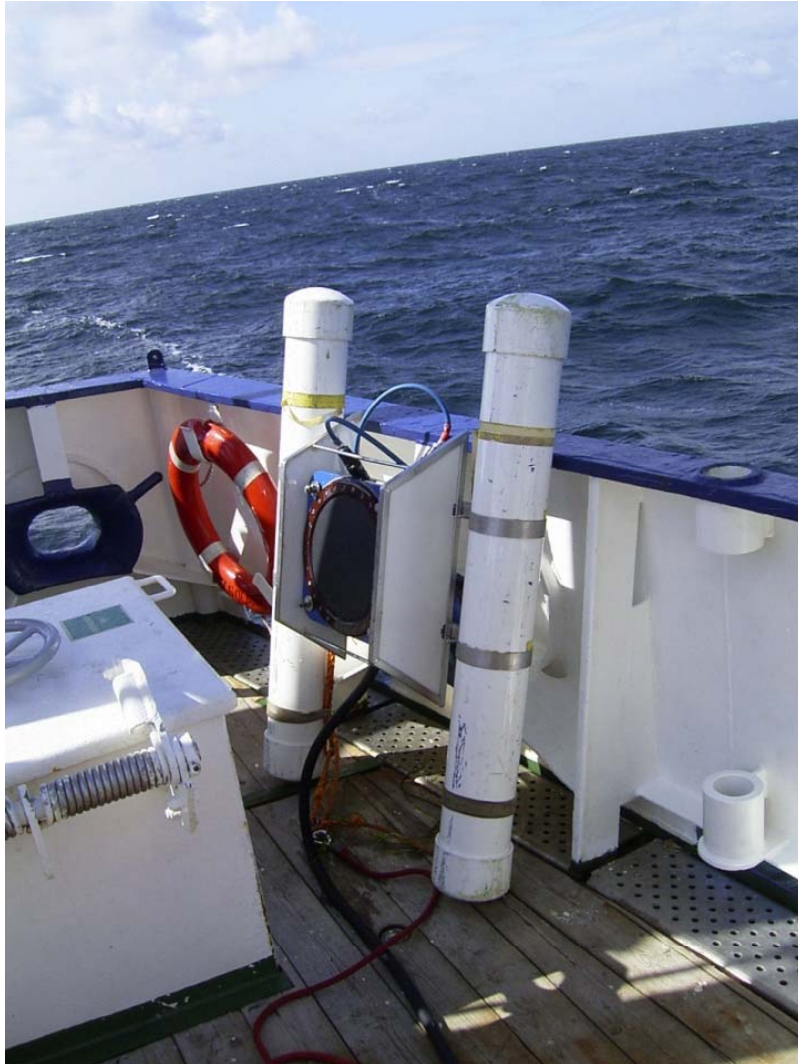
Typical frequencies: 0.5-10kHz, Penetration <200m

GeoChirp



Waveform can sweep between 500Hz and 13.5kHz at high amplitude, giving high bandwidth and thus high resolution. The waveforms contain significant amounts of energy at low frequencies, giving the system high penetration. Output power levels can also be controlled to minimise environmental impact.

Boomer



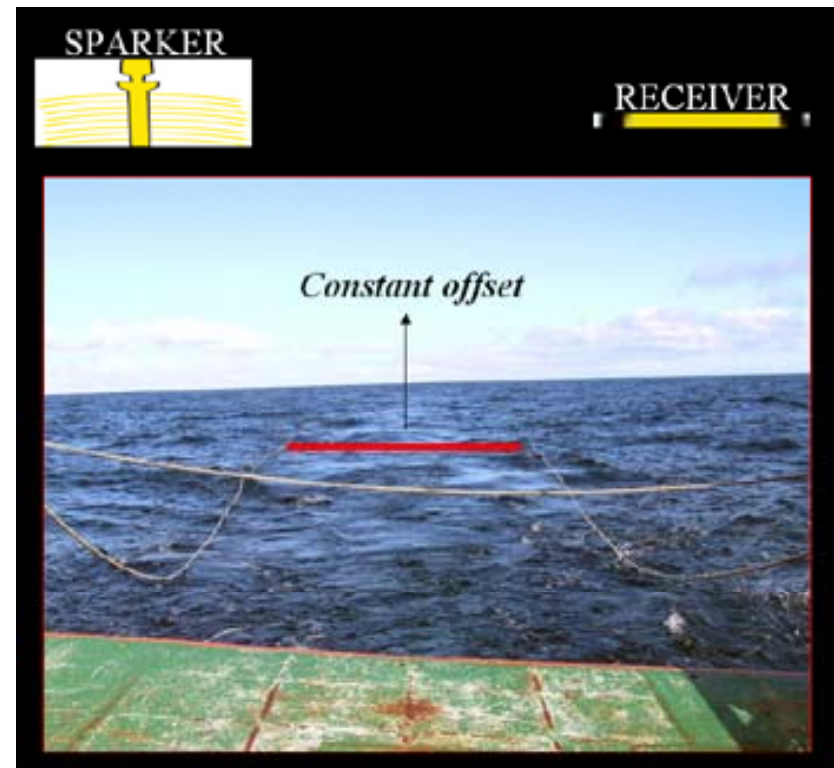
Electromagnetic Source

Sudden separation of a plate from a coil. The plate is initially held against the coil. On rapidly discharging an electrical capacitor bank through the coil, eddy currents are induced in the aluminum plate causing a rapid repulsion of the plate.

Sparker:

Typical frequencies: 0.5-2 kHz (some systems with significantly lower frequencies), Penetration ~100-500m

The seismic source is created by the sudden release of high voltage electrical energy to the sparker which forms a plasma pulse as it is discharged in sea water. The collapsing plasma forms a seismic pulse in the water.



Watergun

Typical frequencies : 200-1500 Hz, Penetration: several hundred meter

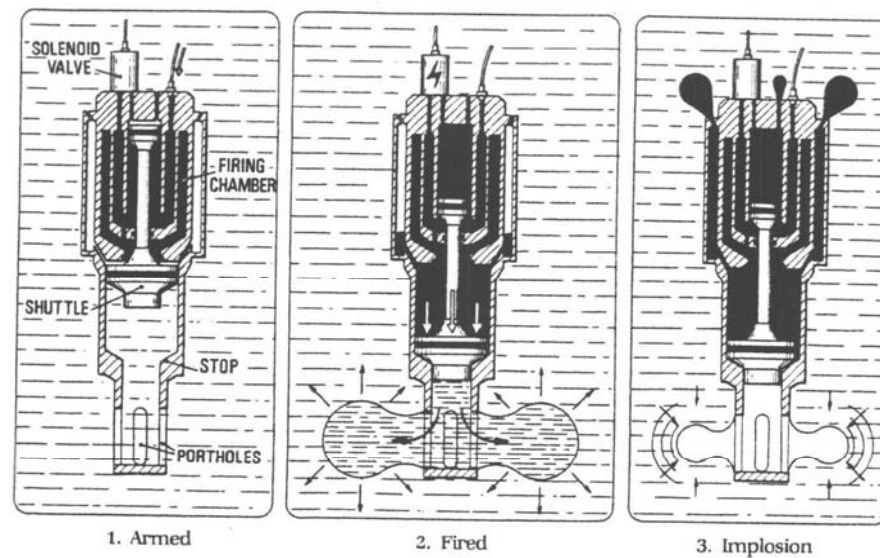


Figure 5.6 A water gun at three stages of the firing cycle. (courtesy of Société pour le Développement de la Recherche Appliquée and Seismic Systems Inc).

Airguns

Typical frequencies :5-500 Hz, Penetration: up to several km

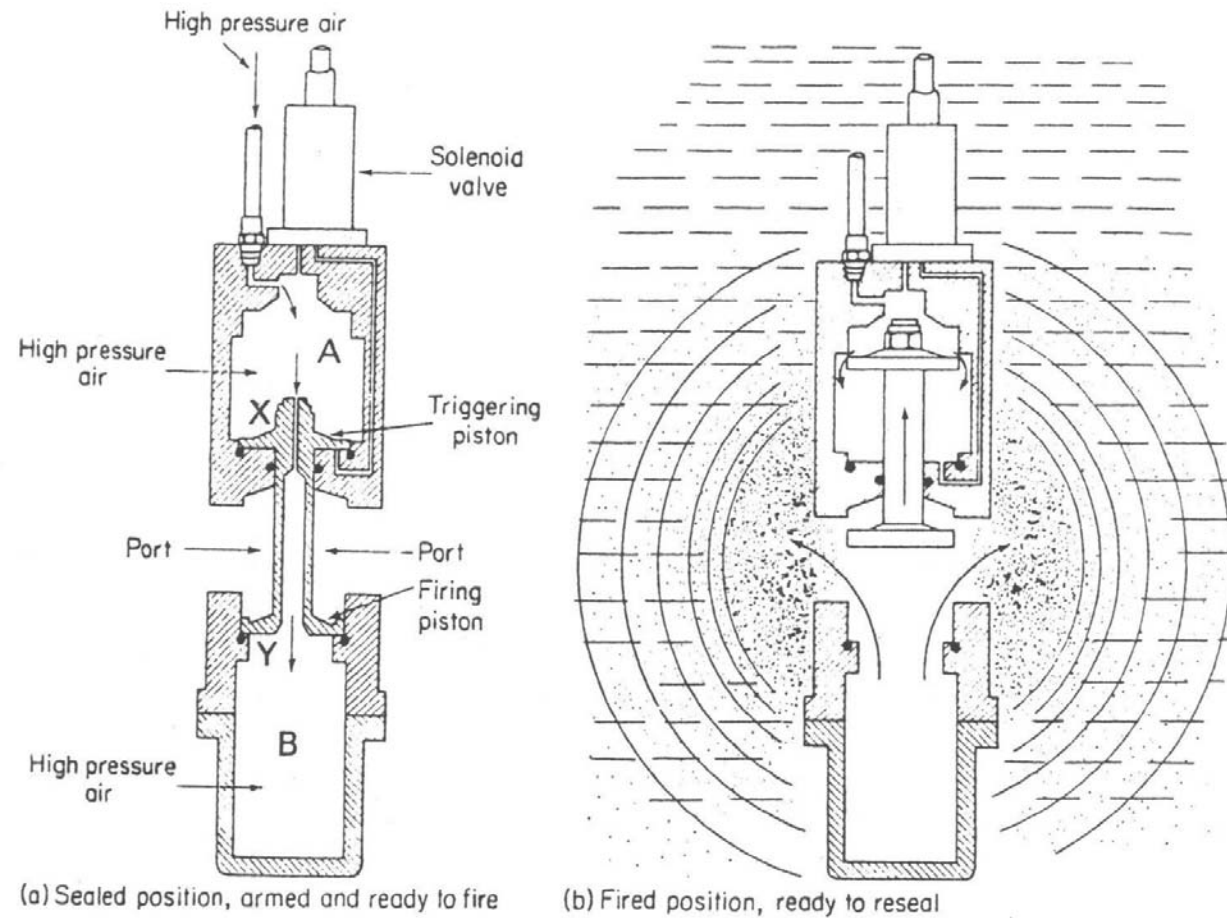


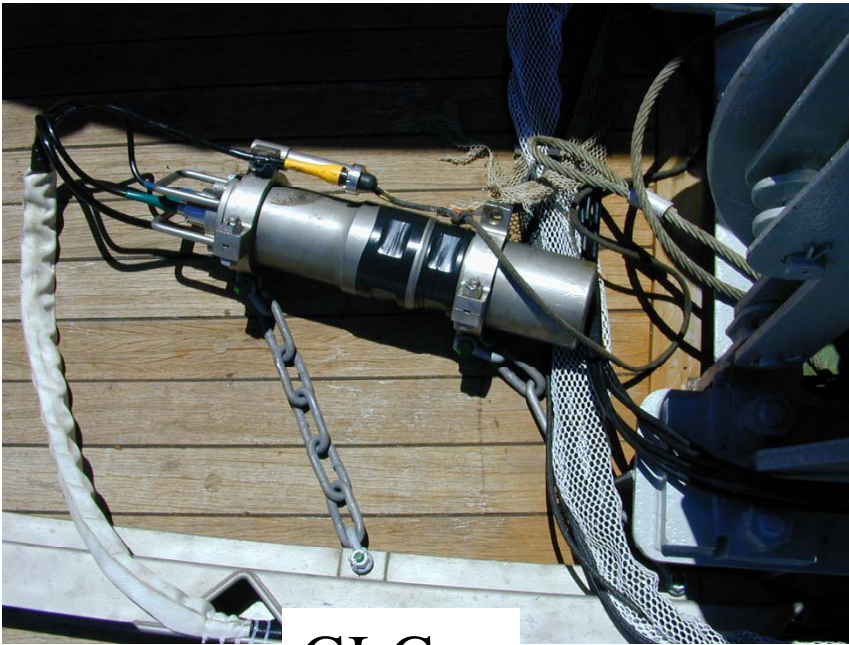
Figure 5.4 Airgun seismic source. Reproduced by permission of Bolt Technology Corporation.



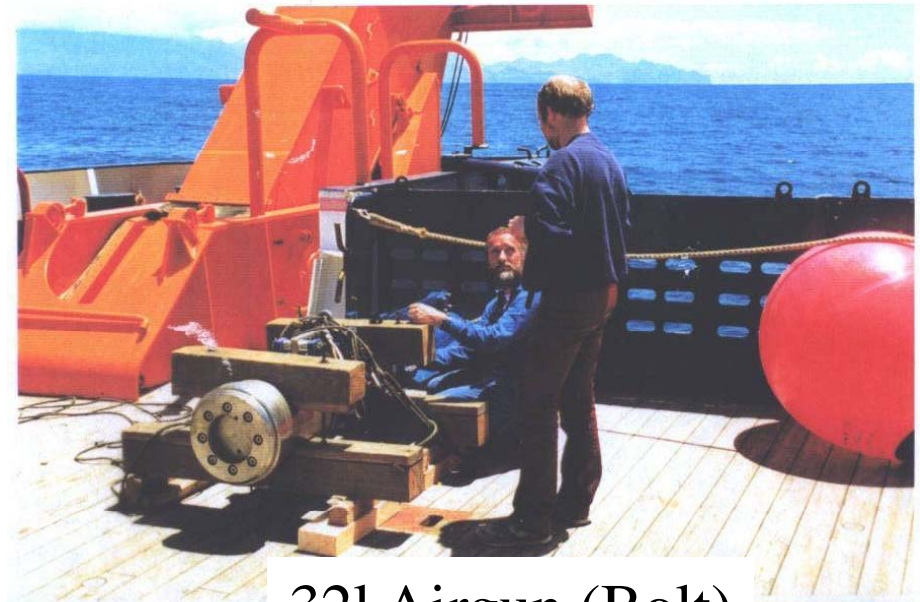
future ocean
KIEL MARINE SCIENCES

Acoustic Imaging Seismic Systems

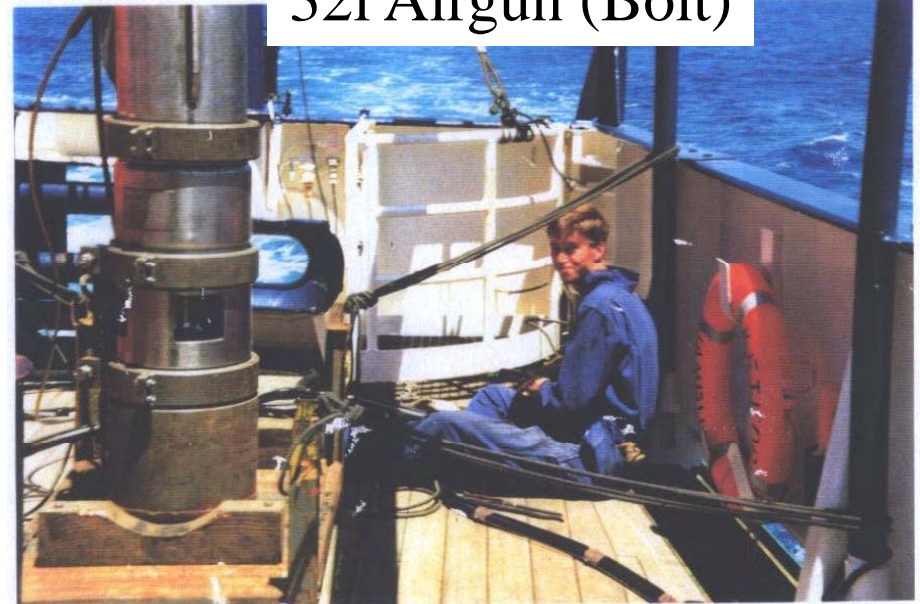
Quellen



GI-Gun



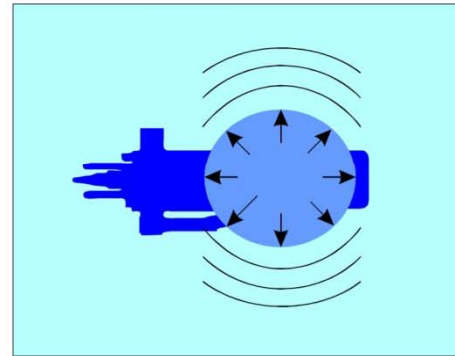
321 Airgun (Bolt)



Acoustic Imaging

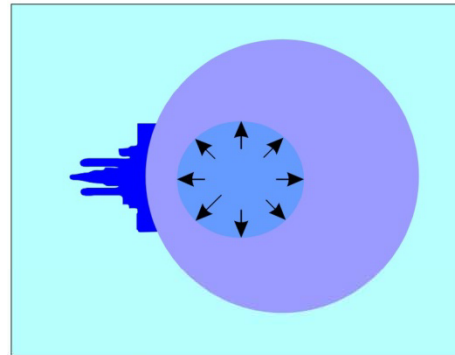
Seismic Systems

GI-Gun



Phase 1:

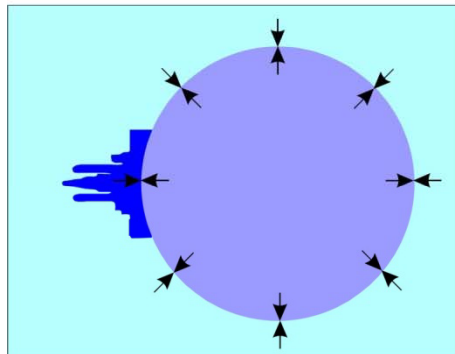
The GENERATOR is fired. The blast of compressed air produces the primary pulse and the bubble starts to expand.



Phase 2:

When the bubble approaches its maximum size, it encompasses the INJECTOR ports, and its internal pressure is far below the outside hydrostatic pressure.

At this time, the INJECTOR "I" is fired, injecting air directly inside the bubble. Due to the quasi-static state of the bubble, the timing of the INJECTOR is not critical.



Phase 3:

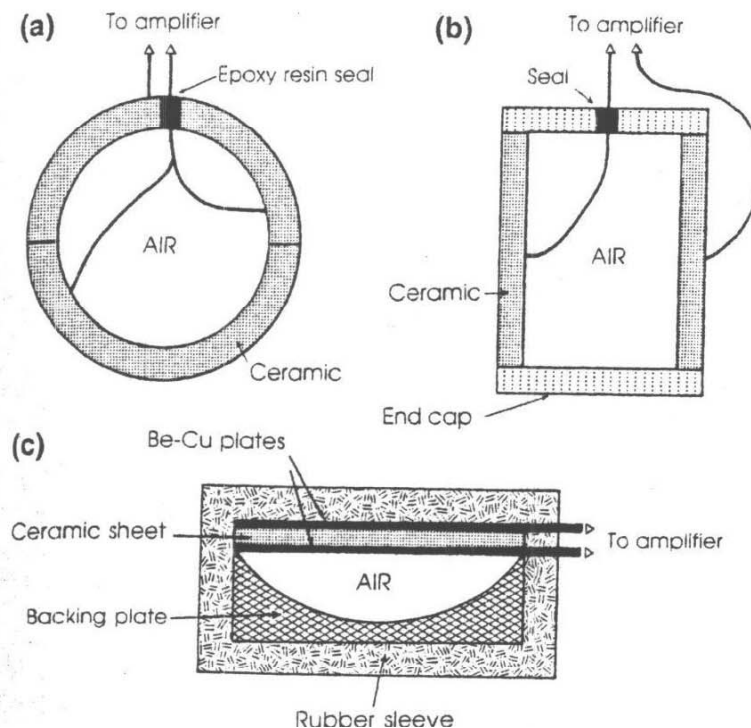
The volume of air released by the INJECTOR increases the internal pressure of the bubble, and prevents its violent collapse. The oscillations of the bubble and the resulting secondary pressure pulses are reduced and re-shaped.

Receiver

Types of receivers:

Hydrophones

(Pressure sensors in the water column)



Geophones

(Ground movement at the sea floor)

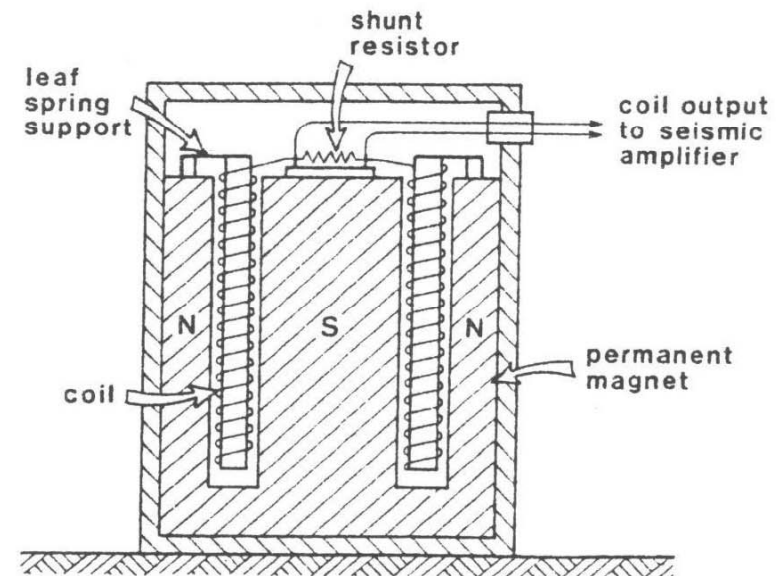


Figure 5.9 A moving-coil geophone (from Kearey and Brooks, 1991). Reproduced by permission of Blackwell Science.

Configuration of hydrophones:

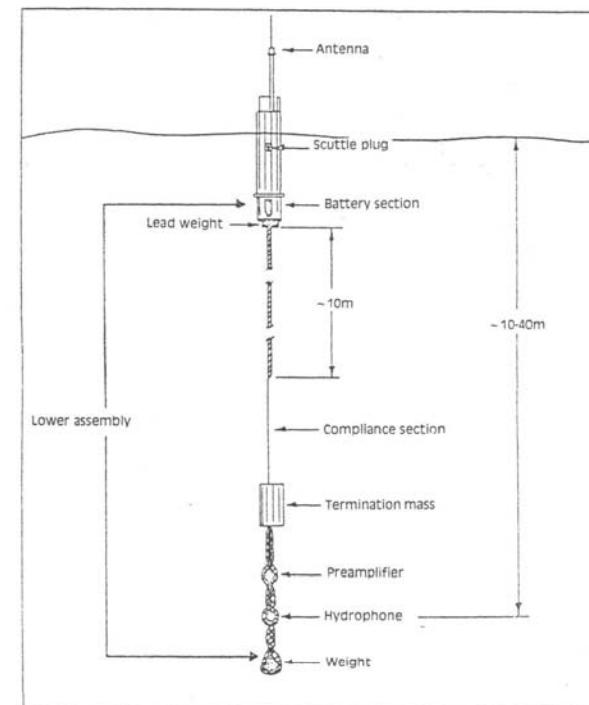
Streamer

Hydrophones in a long cable



Sonobuoy

Hydrophon at a free floating buoy



Streamer

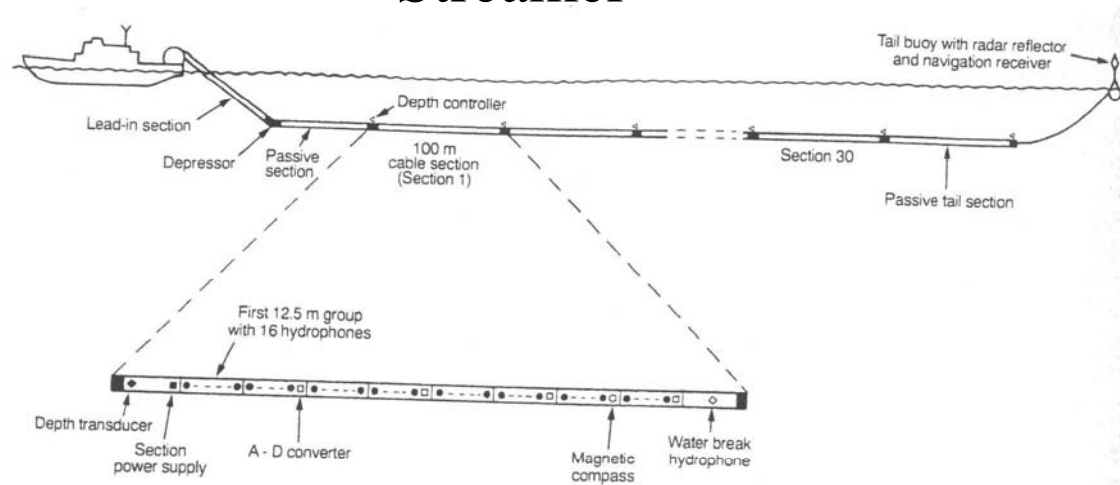


Figure 5.15 A multichannel hydrophone array (courtesy of Western Geophysical).

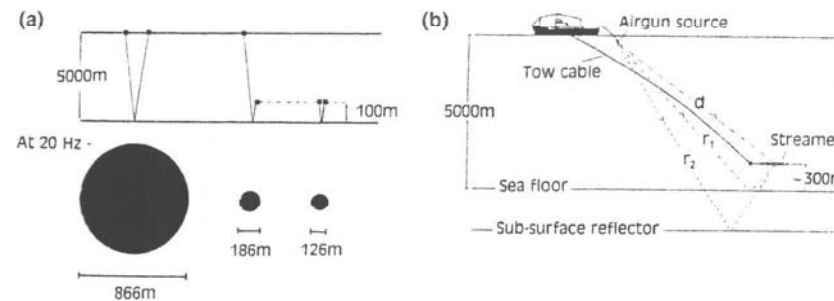
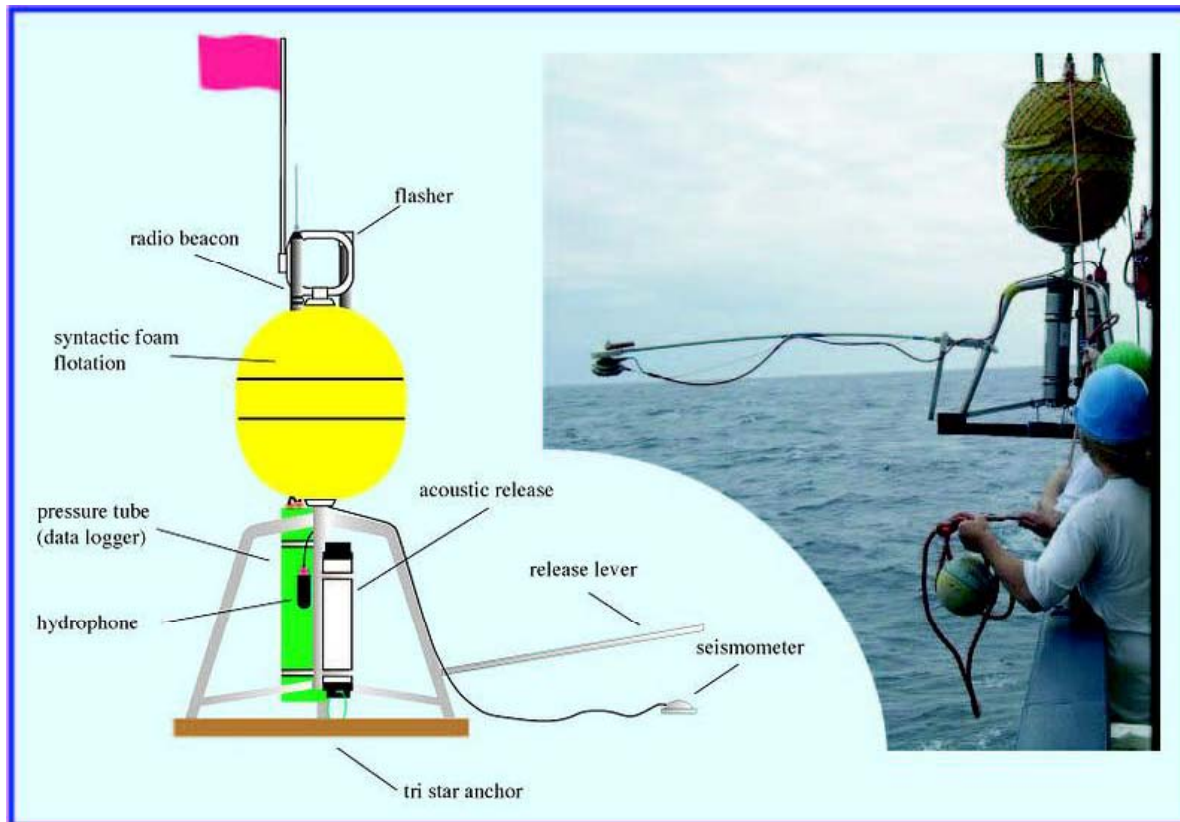


Figure 5.16 (a) Comparison of the areas of the first Fresnel zone at 20 Hz for surface source and receiver, surface source and deep-tow receiver and for deep-tow source and receiver above a plane horizontal reflector. The source and receiver are assumed to be vertically coincident. Sound speed in seawater is 1500 m s^{-1} . (b) Source-receiver geometry used for recording deep-tow profiles in the Vema Fracture Zone: d , direct wave; r_1 , sea-floor reflection; r_2 , sub-bottom reflection (after Bowen and White, 1986). Reproduced by permission of the Geological Society.

Configuration of seismometer:

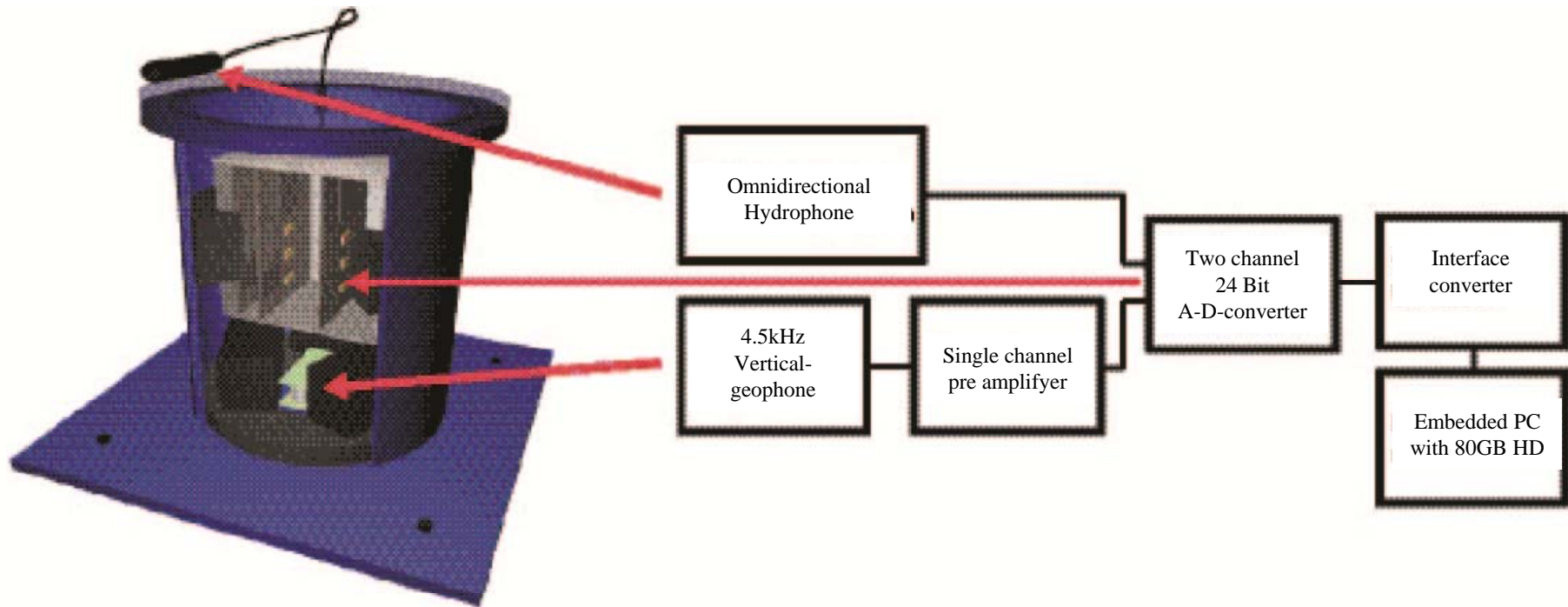
OBS: Ocean-Bottom-Seismometer (Geophone on the sea floor)



OBS Uni Kiel



OBS Uni Kiel



Streamer versus OBS/OBH

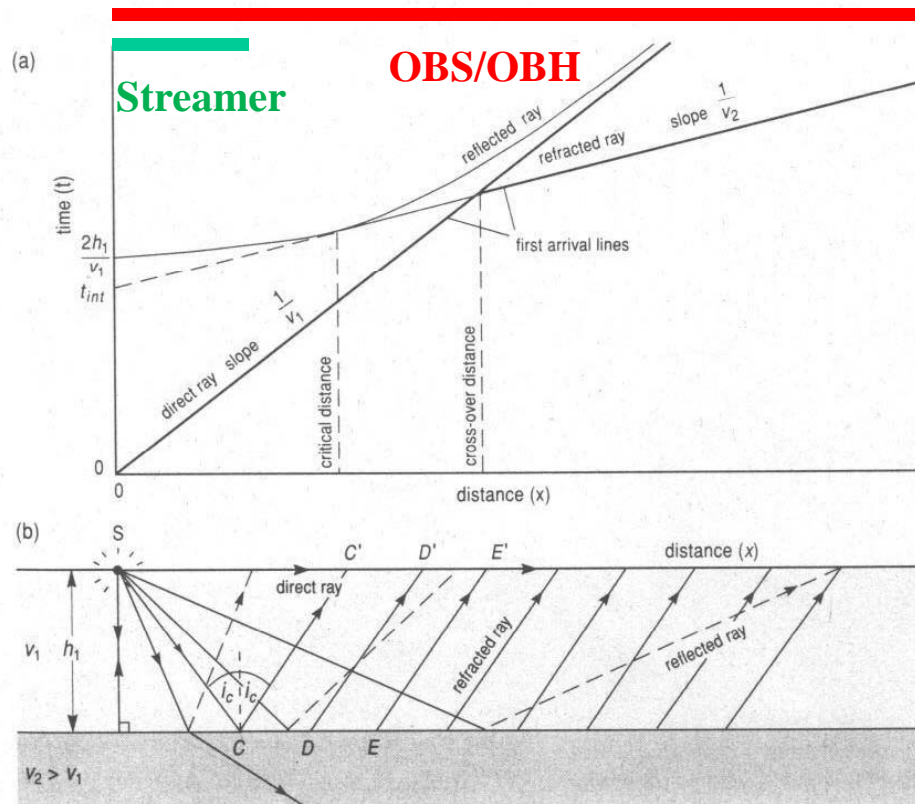


Figure 6.5 Travel-times of refracted and other rays.

Streamer

Near vertical incidence

Strength: good vertical resolution, goof for structural imaging

OBS/OBH

Wide-angle seismics (Refraction)

Strength: Detailed velocity imaging

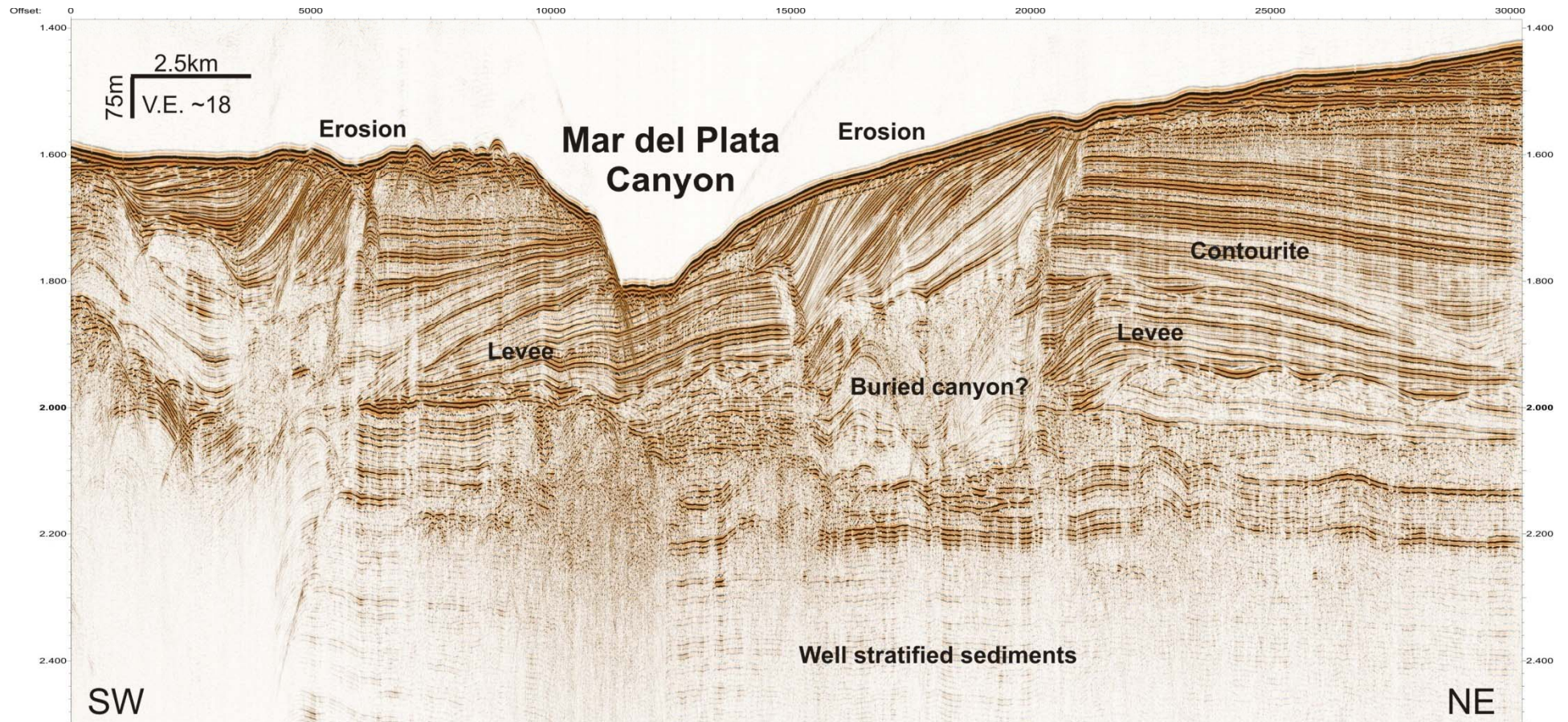


future ocean
KIEL MARINE SCIENCES

Acoustic Imaging

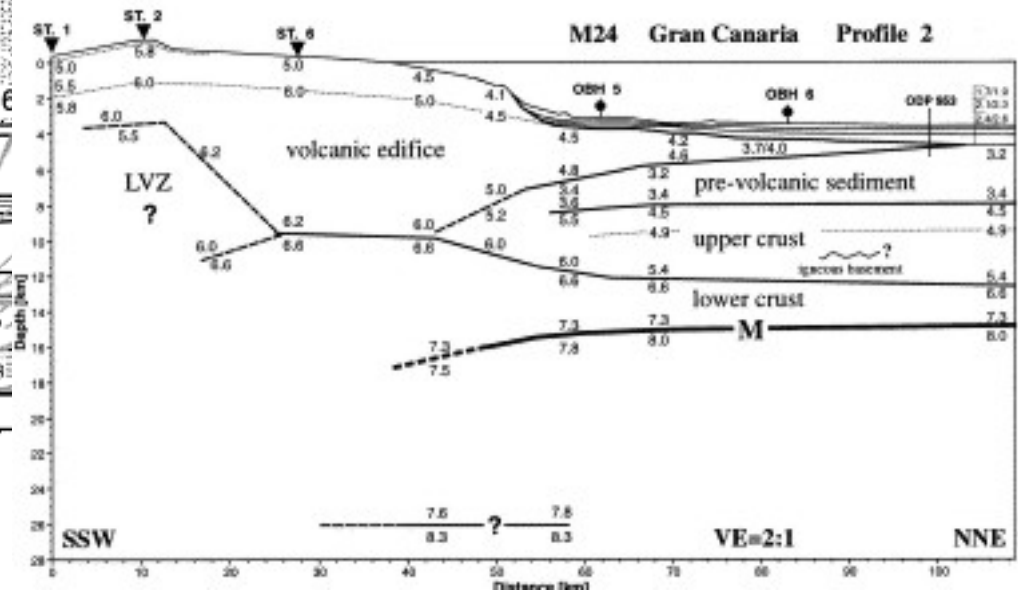
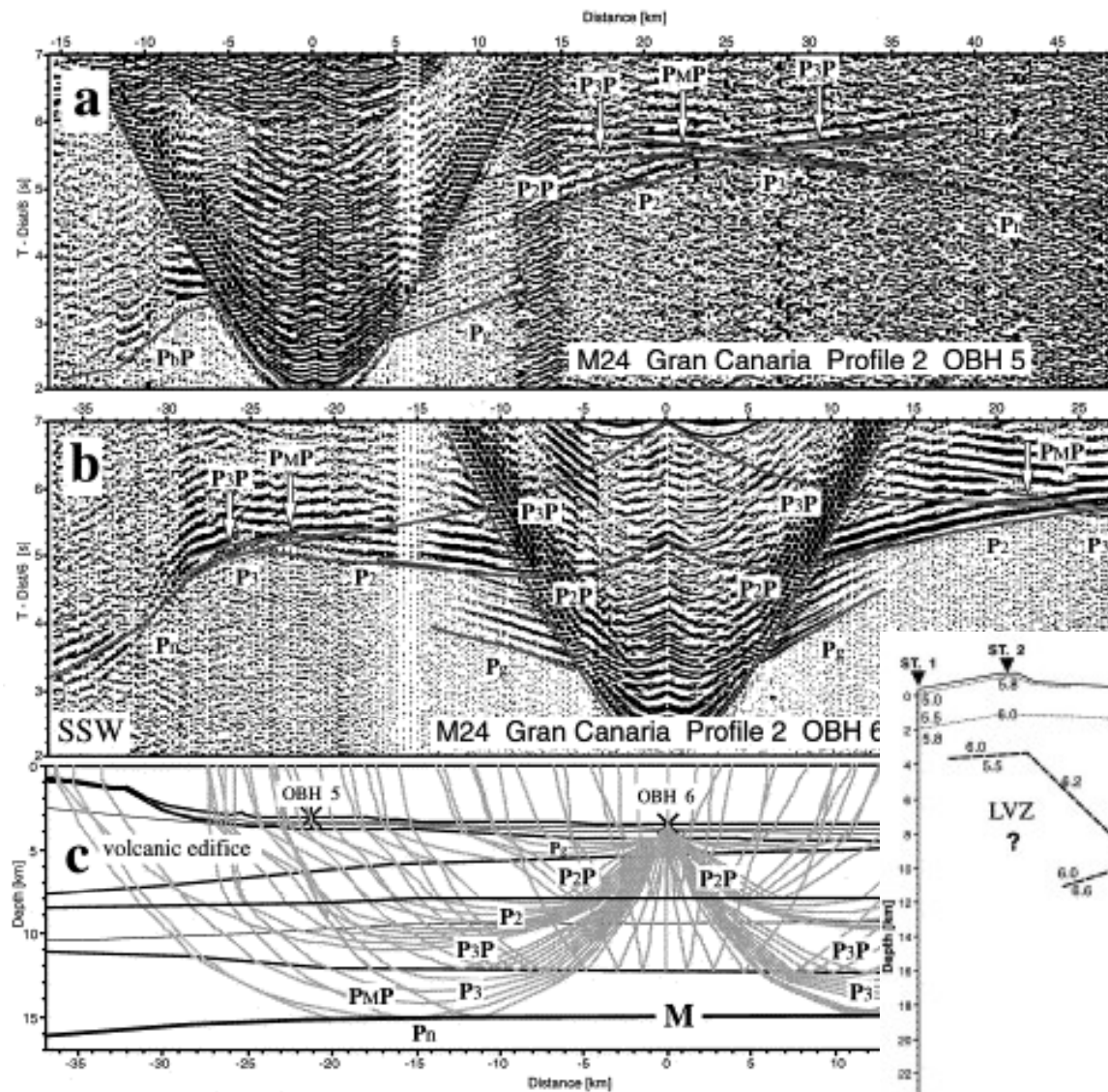
Seismic Systems

Reflection-Profile



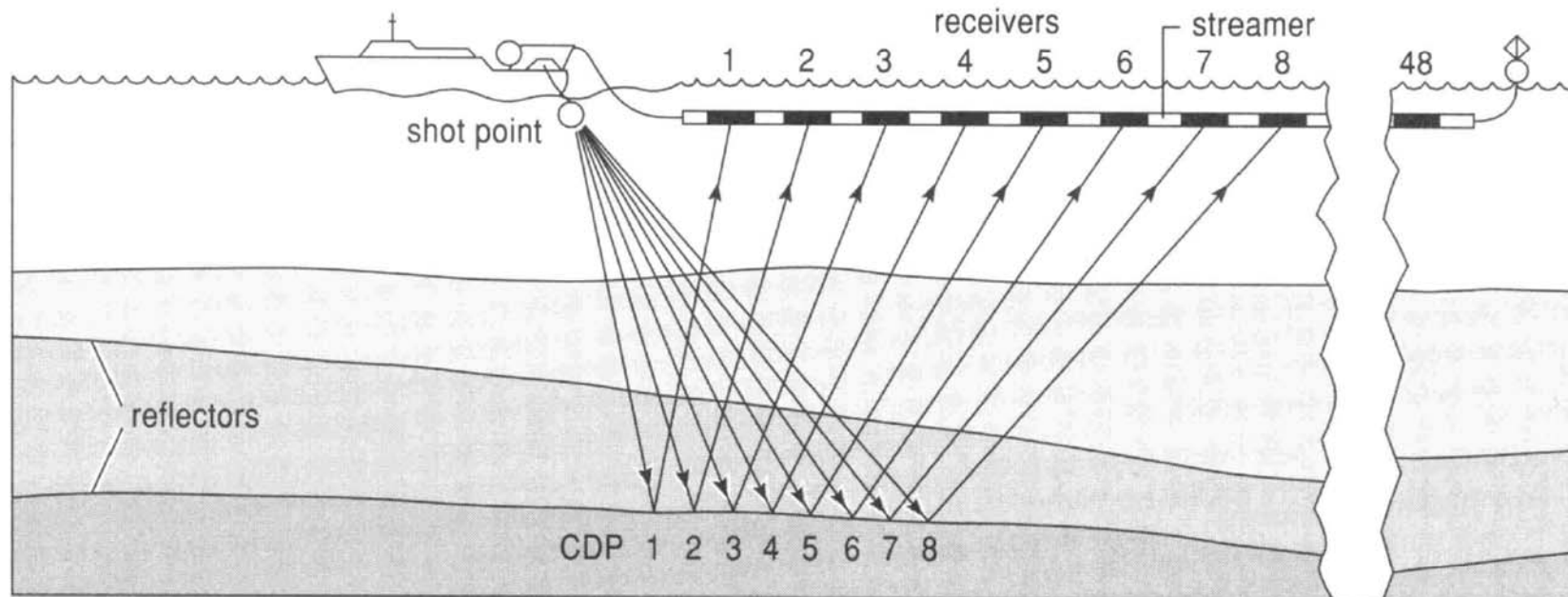
OBS/OBH-Section

The subsurface is reconstructed by modeling



Source-receiver Configuration

Near normal incidence reflection seismics (1 Ship+ 1 Streamer)





future ocean
KIEL MARINE SCIENCES

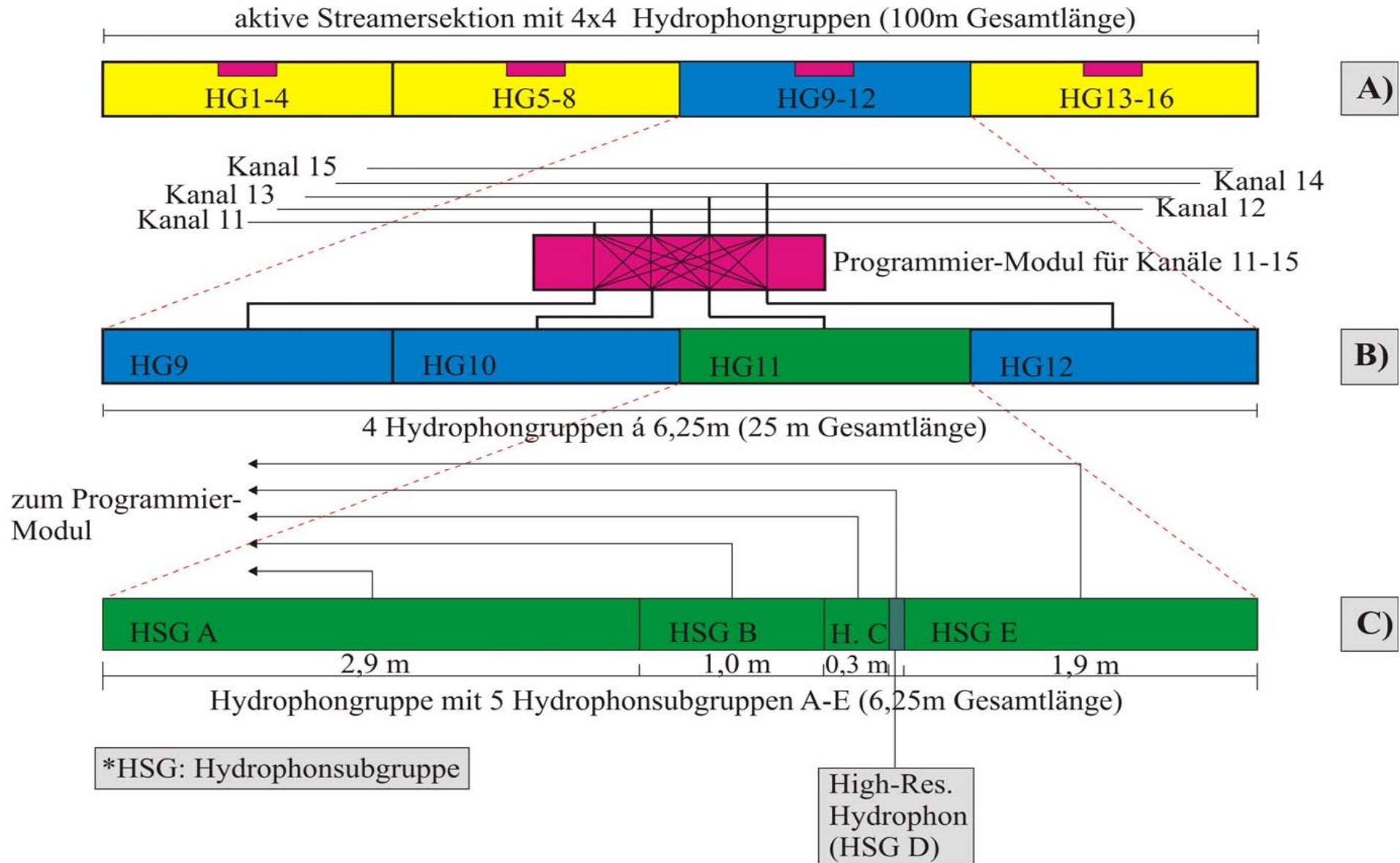
Acoustic Imaging

Seismic Systems

Configuration of Streamers:



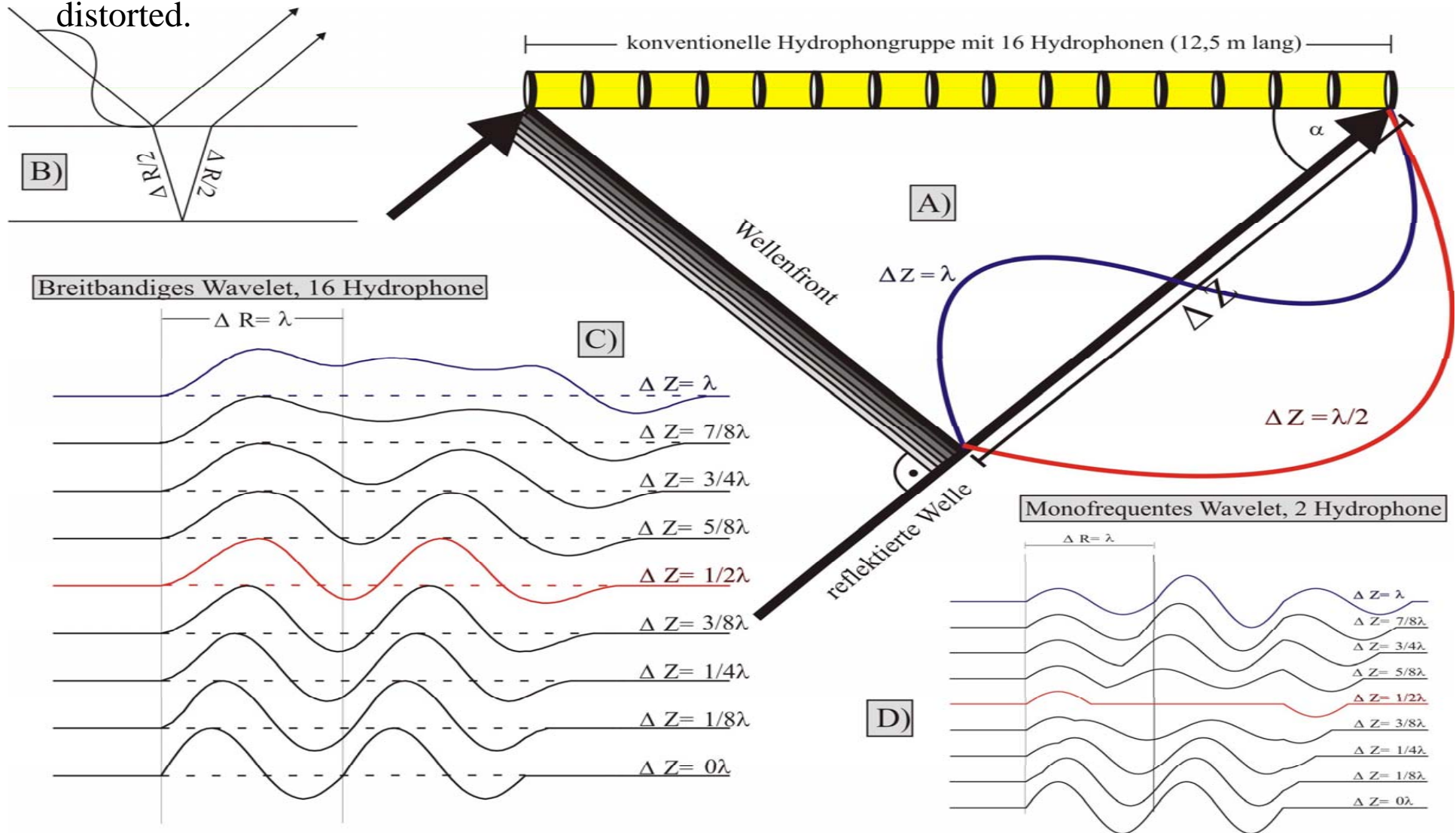
A streamer consists of several hydrophone groups representing one channel each



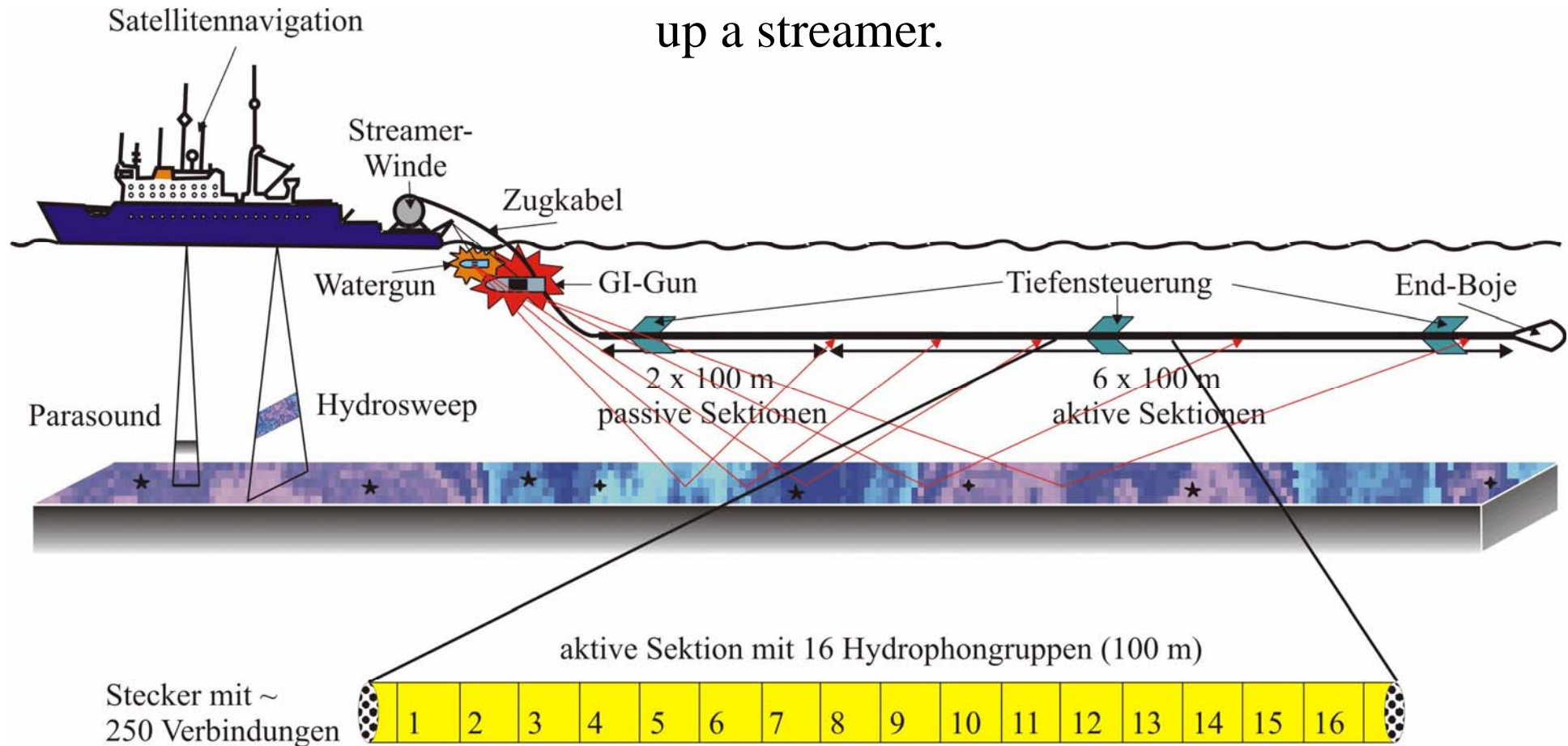
Acoustic Imaging

Seismic Systems

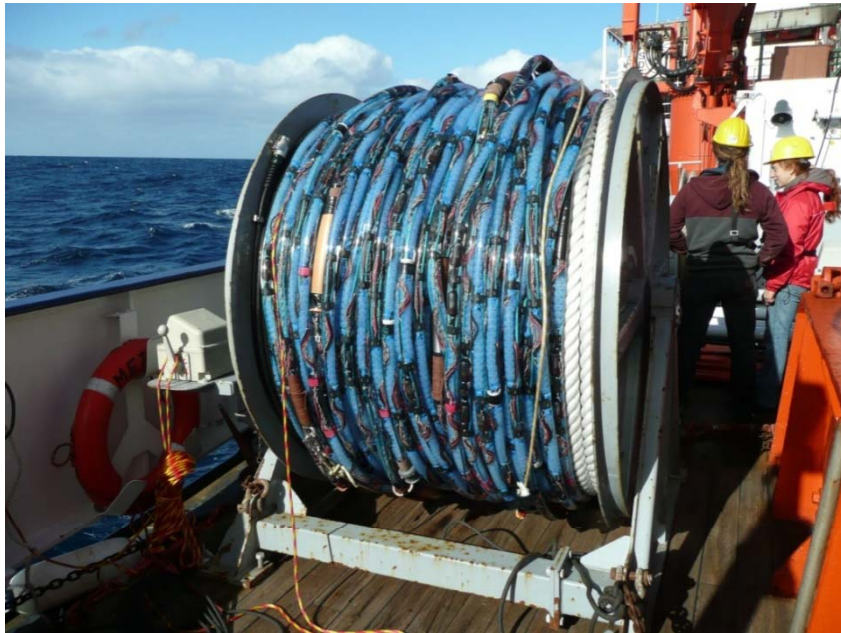
Individual hydrophone groups must not be too long, as incoming wave-fronts might get distorted.



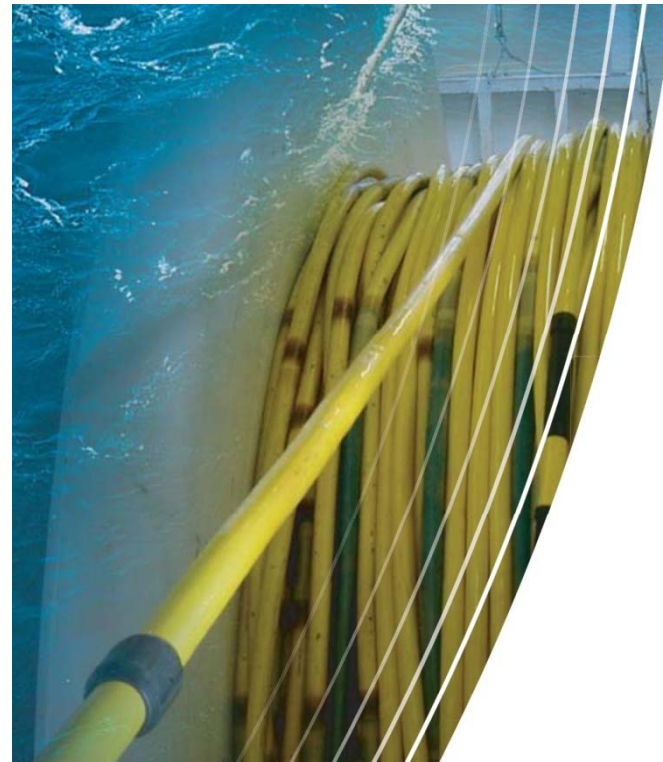
Several sections with a specific number of channels per section make up a streamer.



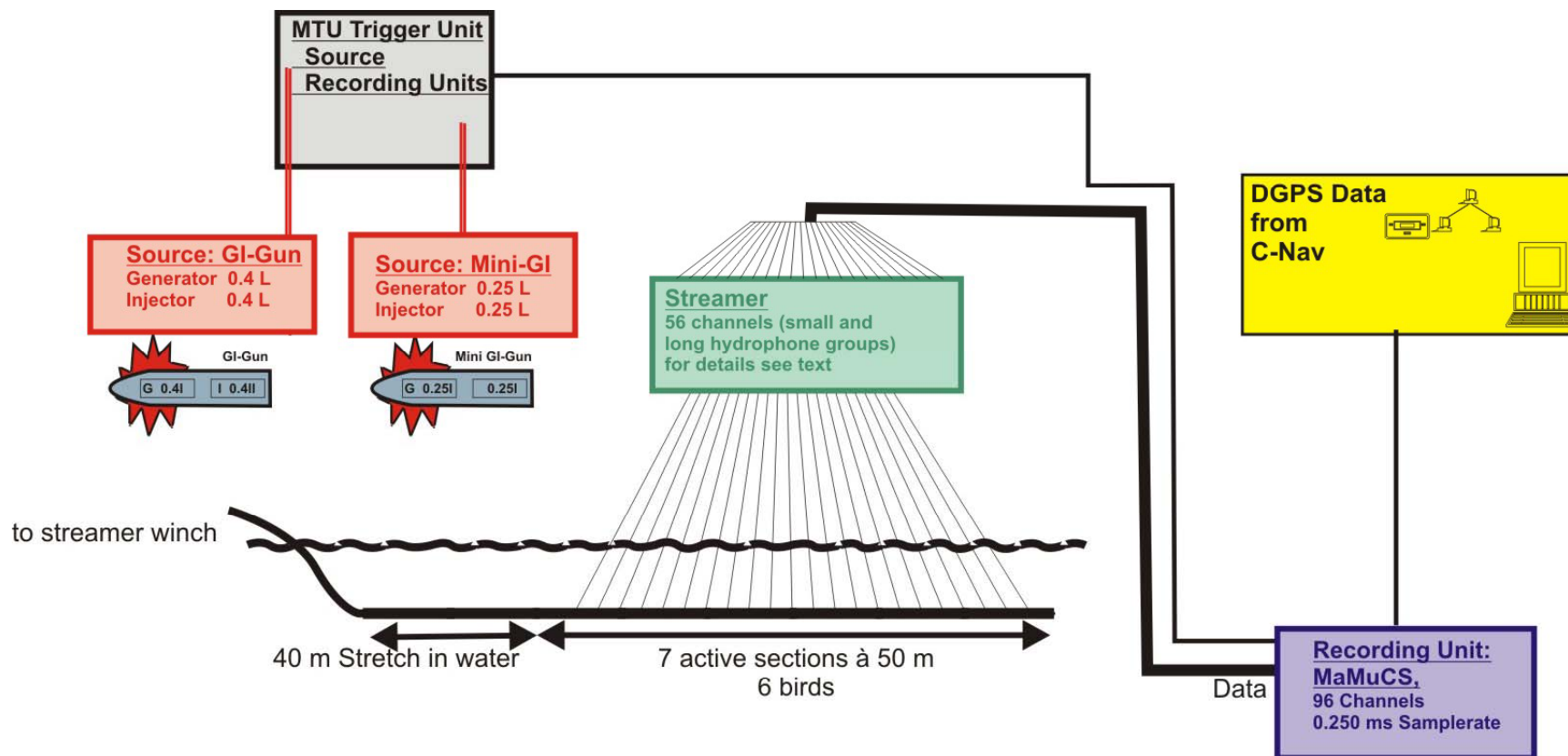
Characteristics of streamer Oil-filled



Solid State

















Analogue



Digital



Components:

-  Streamer Power Supply Unit (SPSU)
-  Deck Cable
-  Tow Cable
-  Repeater Module
-  Stretch Section
-  A/D Digitizer Module
-  Bird
-  8-channel Active Section
-  Digital Connector Pair
-  Analog/Digital Combo Connector Pair
-  Bird Coil
-  Tail Swivel
-  Tail Buoy
-  Optional

Configuration MSM11/2

60m deck cable

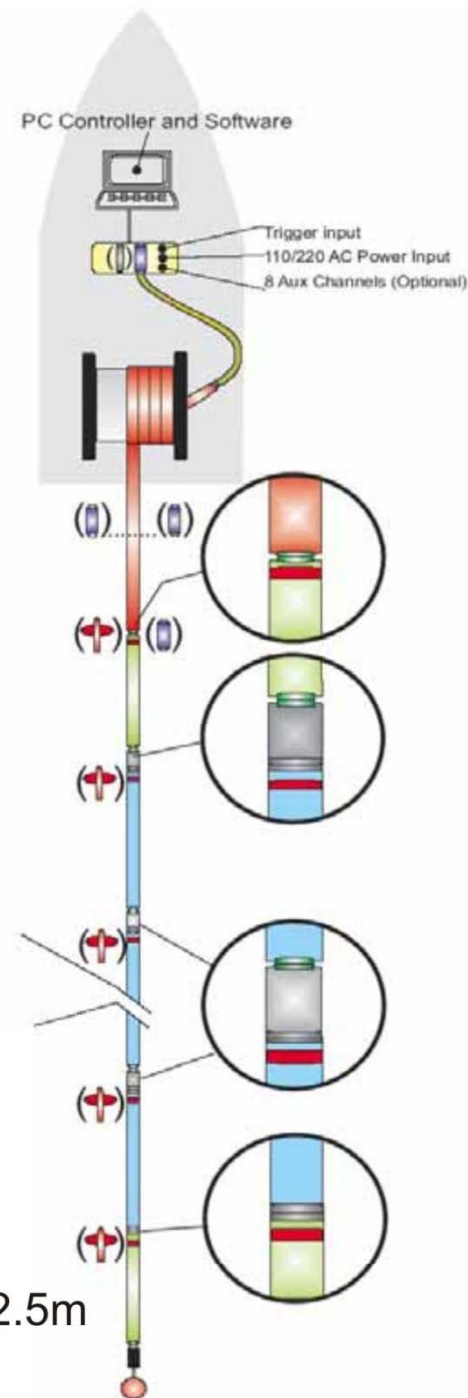
80m Tow Cable

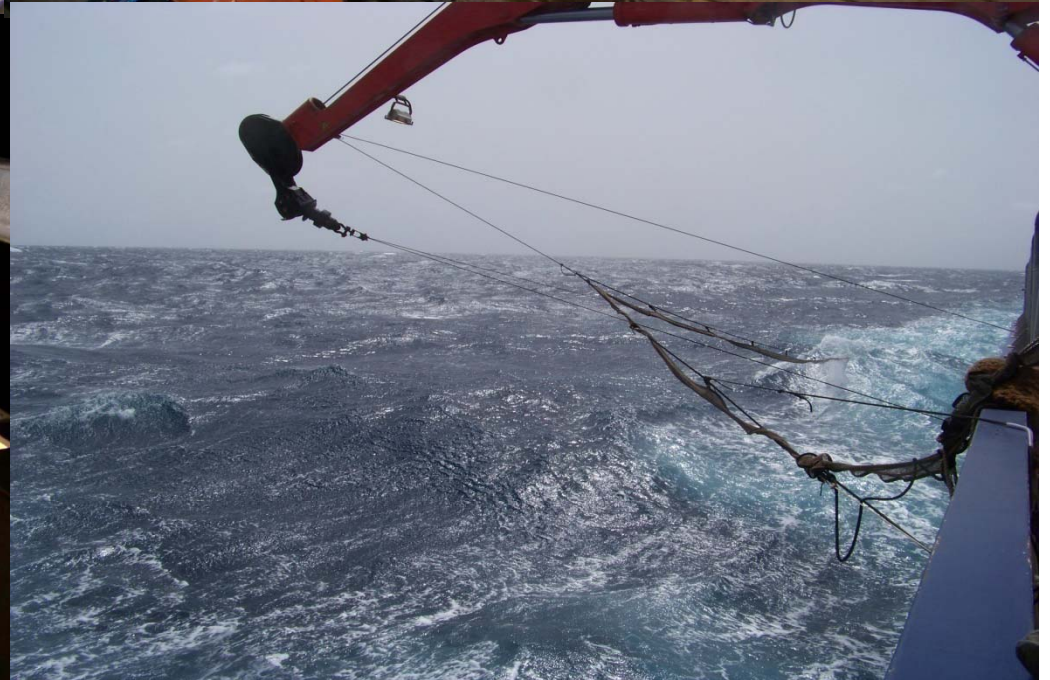
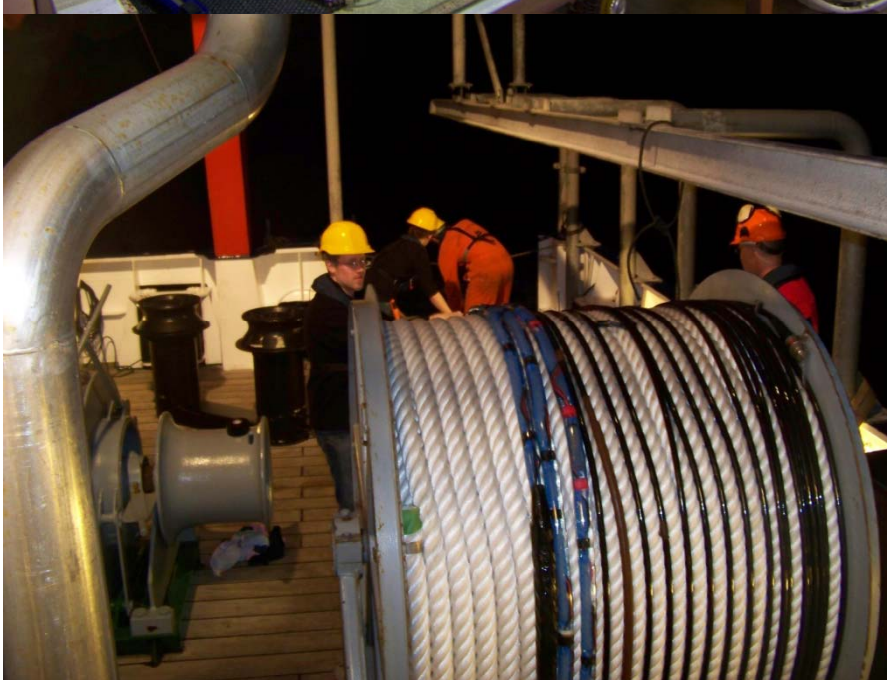
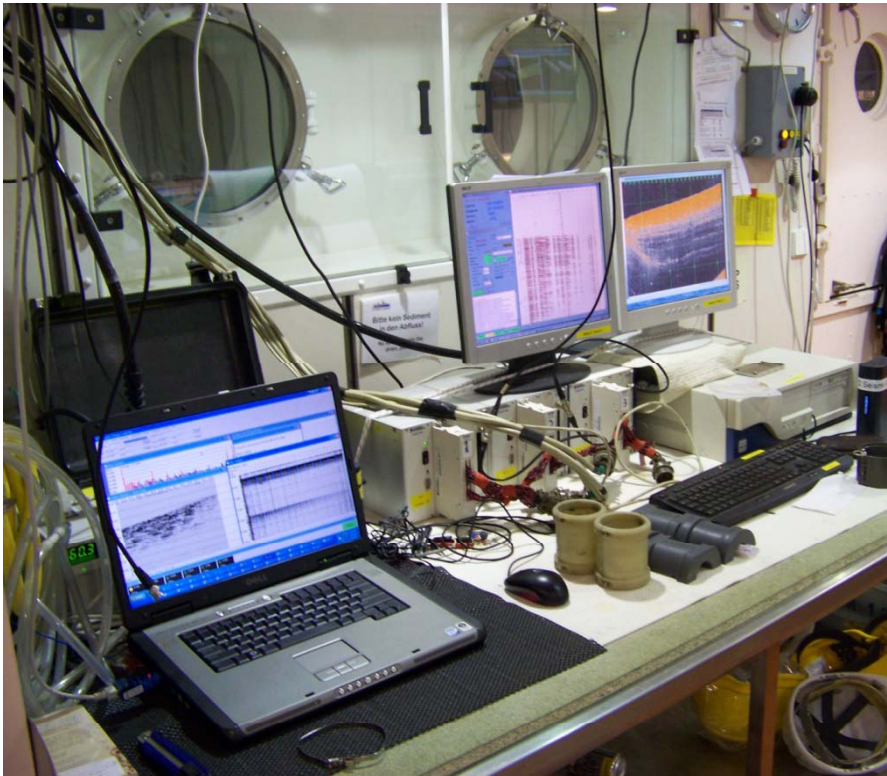
25m Stretch

16 active sections (8channels) a 12.5m

2 Birds

Tail buoy





Important characteristics of streamers:

Length: a few meters up to 15km

Channels: 1 – to several 1000s

Group distance: 1m – 25m

Group length: Single hydrophone to 12.5 m

Number of hydrophones per Group: 1-30

Digital ↔ Analogue

Solid State ↔ Oil-filled

Frequency range: 1Hz - 10er kHz

Shot-Receiver Configurations

Refraction Profile: ship for shooting, OBS/OBH for recording

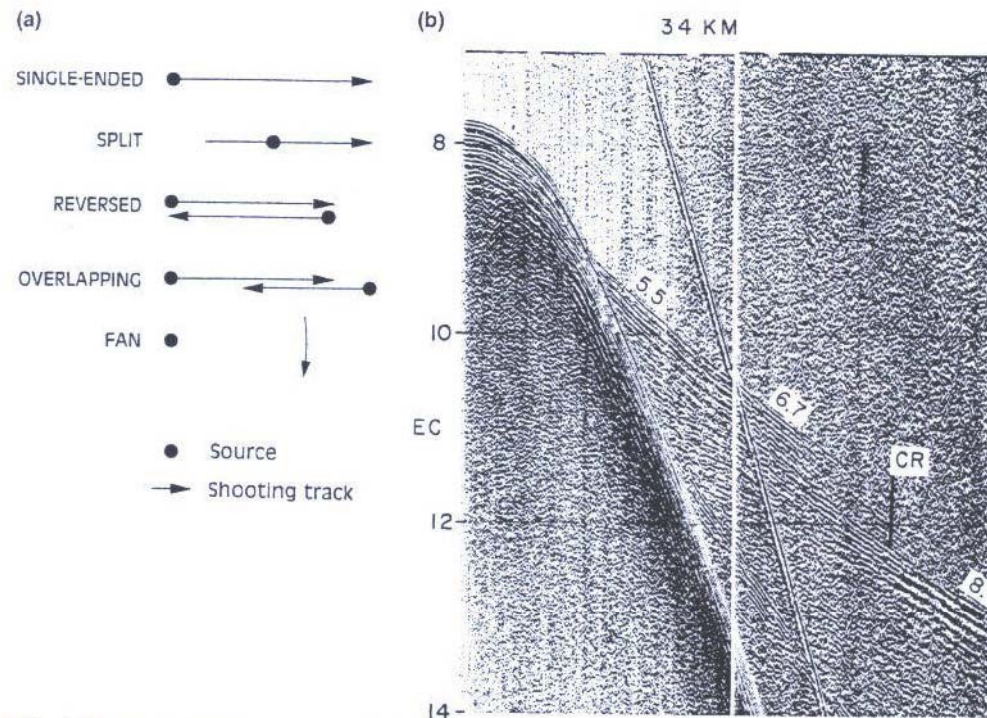
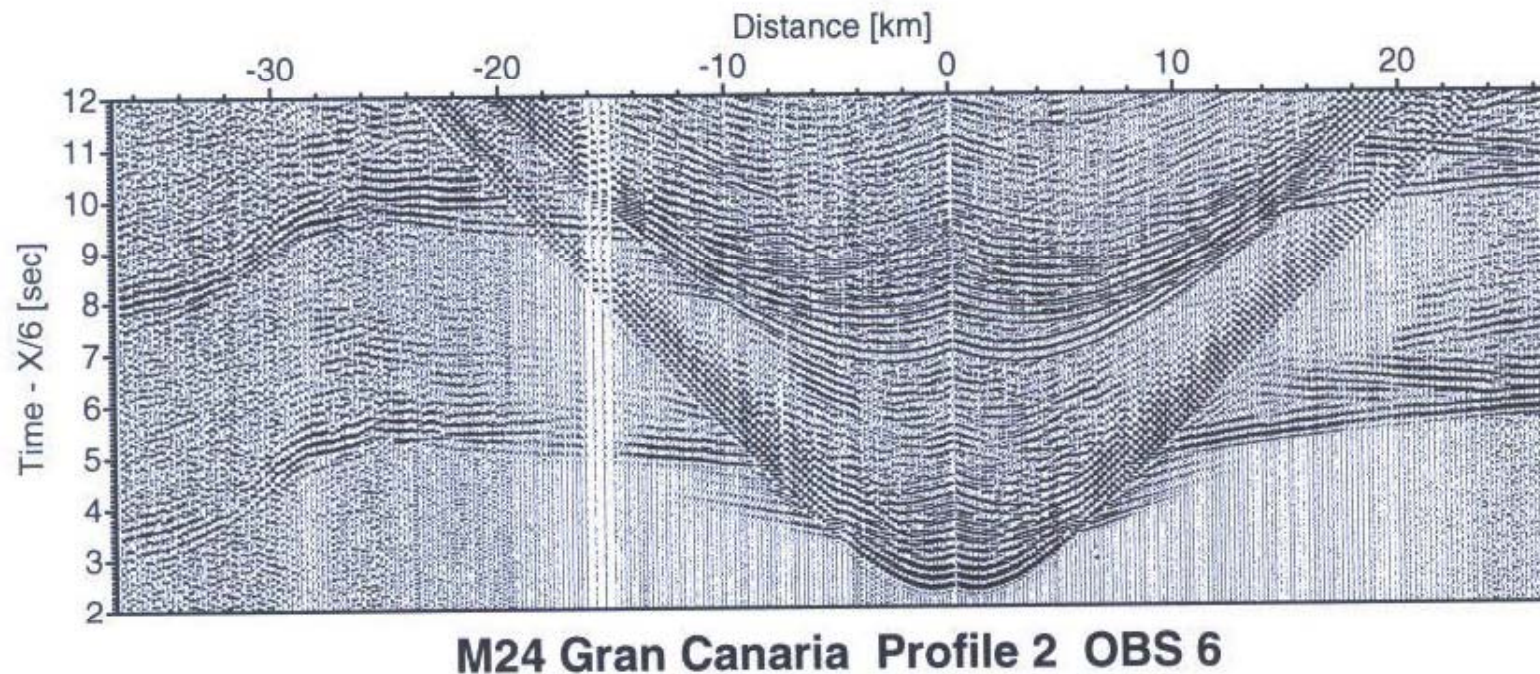


Figure 5.18 (a) Tracks for shooting seismic refraction profiles (after Shor, 1963). Copyright © 1963 John Wiley & Sons Inc. (b) Single-ended seismic profile recorded with a sonobuoy and an airgun source in a water depth of approximately 5800 m. Velocities of head waves are indicated in km s^{-1} . CR is the critical distance for reflections from the 8.1 km s^{-1} interface (from Houtz, 1977). Reproduced by permission of the American Geophysical Union.

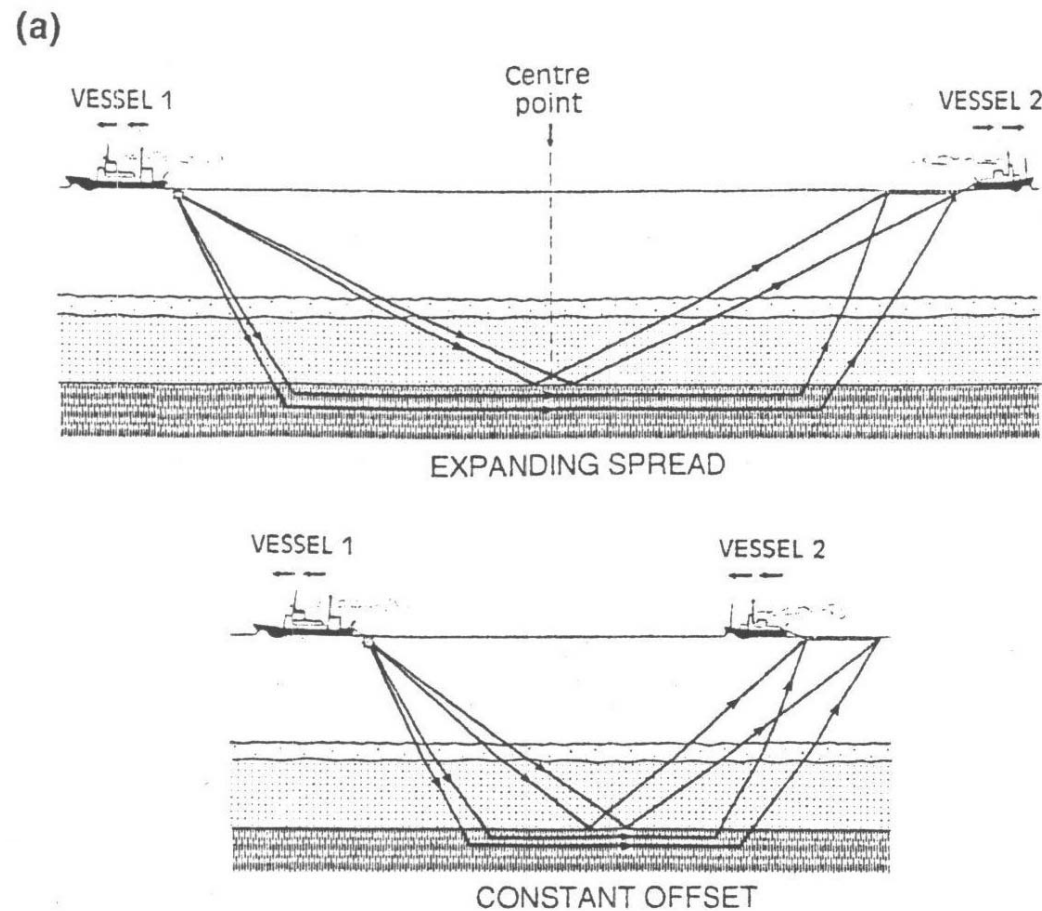
Shot-Receiver Configurations

Refraction Profile: ship for shooting, OBS/OBH for recording



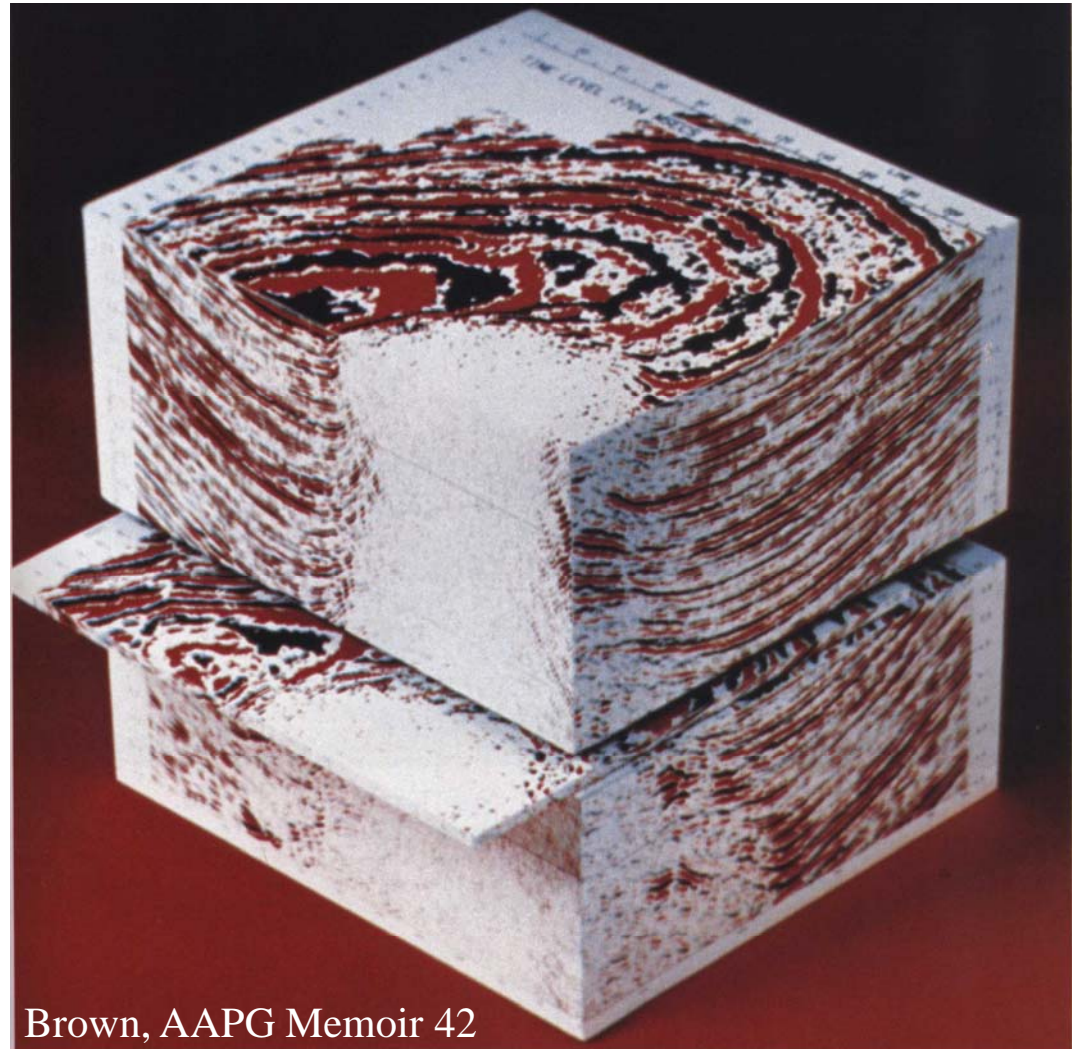
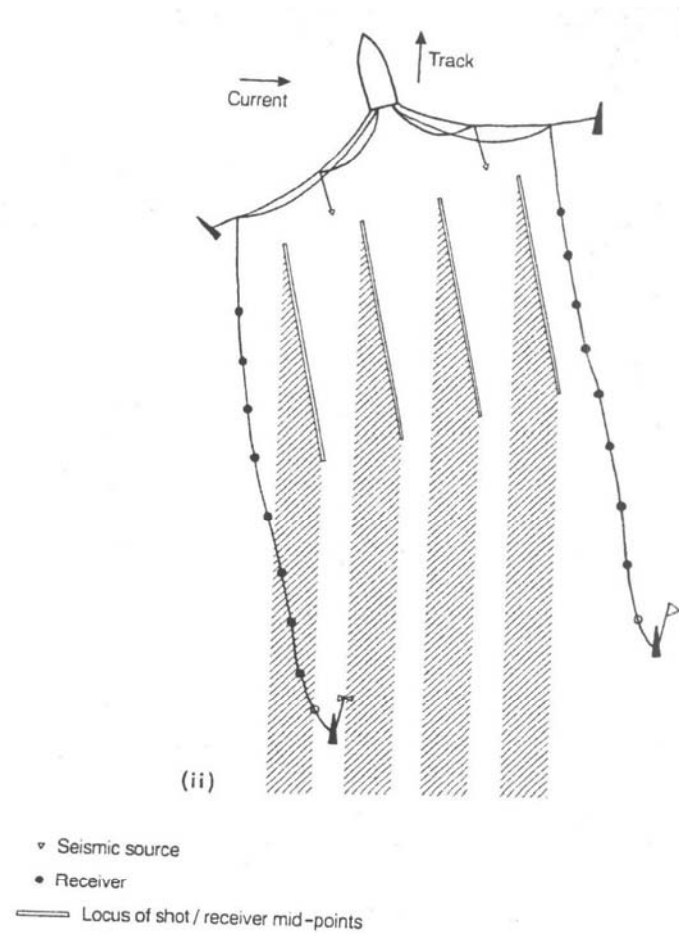
Shot-Receiver Configurations

Wide-angle profiles



Shot-Receiver Configurations

3D-Seismics



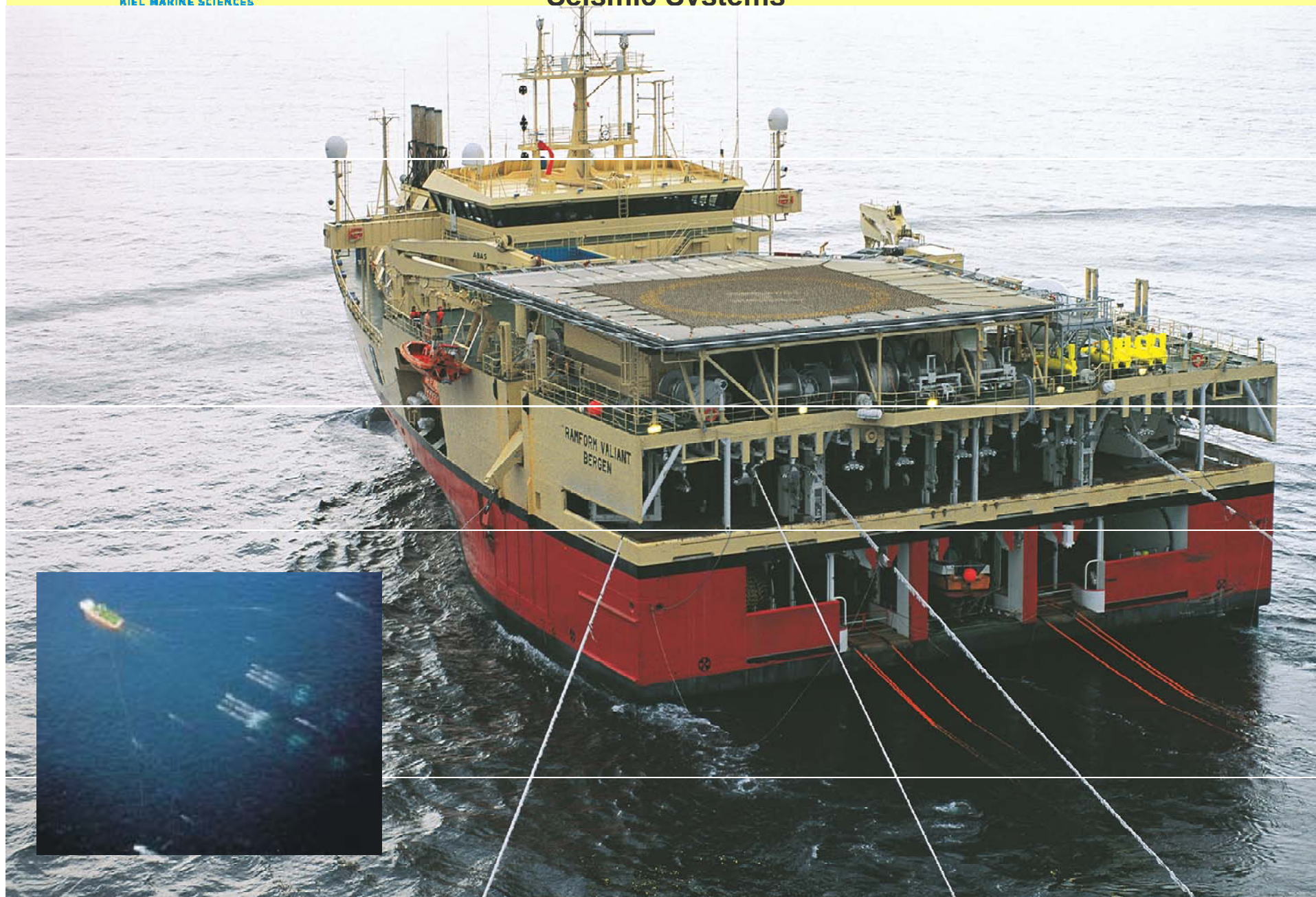
Brown, AAPG Memoir 42



future ocean
KIEL MARINE SCIENCES

Acoustic Imaging

Seismic Svstems



Acoustic Imaging Seismic Systems

Built at: Aker Yards, Langsten

Owner: PGS Geophysical AS

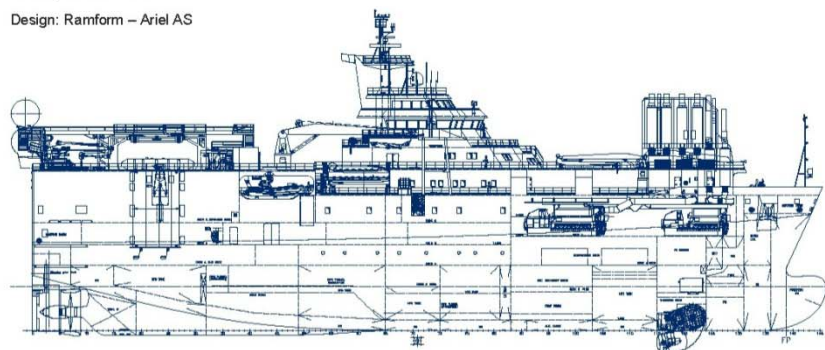
Yard No: 213

Delivery: March 2008

Design: Ramform – Ariel AS

The vessel is designed for collection and processing of seismic data by up to 22 towed streamers. High efficiency seismic vessel, with high streamer capacity and high bollard pull. Large fuel capacity and high transit speed. Clean class.

Total main propulsion effect: 13 000 kW on main propellers.



MAIN PARTICULARS

Length over all	102.20 m
Length between pp	95.00 m
Breadth moulded	40.00 m
Depth to gun deck	8.50 m
Draught max	7.38 m
Gross tonnage	15 086 t
Speed	approx. 16 knots at draft 7.00 m

ACCOMODATION

70 persons (34 single cabins and 17 double berth cabins)

CLASS

DNV +1A1, Ice C, E0, HELDK, RP, Clean, TMON, SPS

CARGO CAPACITIES

Heavy fuel oil	6 184 m ³
Diesel oil	450 m ³
Ballast water	4 766 m ³
Fresh water	377 m ³
Cable fluid	75 m ³
Deadweight	6 763 t

MAIN GENERATOR SETS

4 x Bergen Diesel B32.40L9, each 4 145 kW
2 x Bergen Diesel B32.40L6, each 2 765 kW

HIGH VOLTAGE POWER PLANT

ABB

MAIN PROPULSION

2 x Wärtsilä gear/shaft/propeller lines, twin-in-single-out, each driven by 2 x 3 250 kW frequency controlled ABB el-motors, CP propellers, diameter 5.00 m, HR nozzle

EMERGENCY GENERATOR

1 x Mitsubishi DPMG 437-S6B3A, 350 kW

THRUSTERS

Foreship 1 x RRM Ulstein Aquamaster swing-up combi-thruster, 1 800 kW, CP and frequency controlled

AUTOMATION PLANT

Høglund alarm and monitoring system

Joystick Redundant seismic cJoy, Kongsberg

Nav. com O. Øverland

Power management Høglund PMS

CARGO PUMPS

Engine room pumps Allweiler

DECK EQUIPMENT

Winches Streamer and gun winches Odime
Anchoring and mooring Aker Yards Electro

Deck cranes 2 off 12 t / 20 m knuckle boom cranes make ABAS
1 off 5 t / 10 m knuckle boom crane make ABAS
1 off 3 t / 16 m knuckle boom crane make ABAS

Helideck Hydra Marine Aluminium, roll compensation from TTS / Evomec

LIFESAVING EQUIPMENT

MOB boat 1 x MOB boat Magnum 750
2 x Scarf Harding 70 persons covered life boats

BOILERS

1 x exhaust boiler and 1 x combined boiler, total 5 320 kg / h

ACQUISITION CONFIGURATION

High capacity multi-streamer operations, up to 22 streamers (26 streamer reels)

Source Typical 2 x 3090 cu in
Air compressors 3 x LMF 48 / 138–207 – E60

HULL

Steel hull built at Aker Yards, Tulcea





future ocean
KIEL MARINE SERVICES

Acoustic Imaging

Seismic Systems

MAIN PARTICULARS

Length over all	102.20 m
Length between pp	95.00 m
Breadth moulded	40.00 m
Depth to gun deck	8.50 m
Draught max	7.39 m
Gross tonnage	15 086 t
Speed	approx. 16 knots at draft 7.00 m

ACCOMODATION

70 persons (34 single cabins and 17 double berth cabins)

CLASS

DNV +1A1, Ice C, E0, HELDK, RP, Clean, TMON, SPS

CARGO CAPACITIES

Heavy fuel oil	6 184 m³
Diesel oil	450 m³
Ballast water	4 766 m³
Fresh water	377 m³
Cable fluid	75 m³
Deadweight	6 763 t

MAIN GENERATOR SETS

4 x Bergen Diesel B32:40L9, each 4 145 kW
2 x Bergen Diesel B32:40L6, each 2 765 kW

HIGH VOLTAGE POWER PLANT

ABB

MAIN PROPULSION

2 x Wärtsilä gear/shaft/propeller lines, twin-in-single-out, each driven by 2 x 3 250 kW frequency controlled ABB el-motors, CP propellers, diameter 5.00 m, HR nozzle

EMERGENCY GENERATOR

1 x Mitsubishi DPMG 437-S6B3A, 360 kW

THRUSTERS

Foreship 1 x RRM Ulstein Aquamaster swing-up combi-thruster, 1 800 kW, CP and frequency controlled

AUTOMATION PLANT

Høglund alarm and monitoring system

Joystick Redundant seismic cJoy, Kongsberg

Nav. com O. Øverland

Power management Høglund PMS

CARGO PUMPS

Engine room pumps Allweiler

DECK EQUIPMENT

Winches
Streamer and gun winches Odim
Anchoring and mooring Aker Yards Electro

Deck cranes 2 off 12 t / 20 m knuckle boom cranes make ABAS
1 off 5 t / 10 m knuckle boom crane make ABAS
1 off 3 t / 16 m knuckle boom crane make ABAS
Helideck Hydra Marine Aluminium, roll compensation from TTS / Evomec

LIFESAVING EQUIPMENT

MOB boat 1 x MOB boat Magnum 750
2 x Scarf Harding 70 persons covered life boats

BOILERS

1 x exhaust boiler and 1 x combined boiler, total 5 320 kg / h

ACQUISITION CONFIGURATION

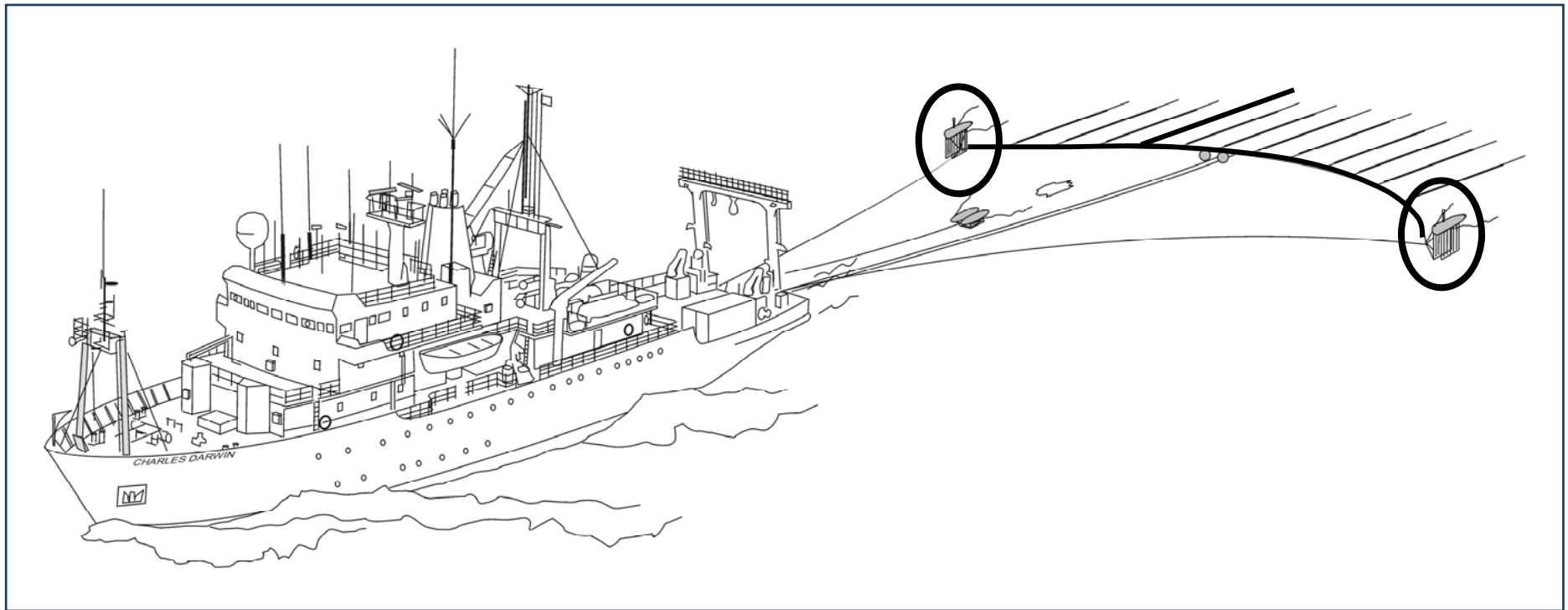
High capacity multi-streamer operations, up to 22 streamers (26 streamer reels)

Source Typical 2 x 3090 cu in
Air compressors 3 x LMF 48 / 138-207 – E60

HULL

Steel hull built at Aker Yards, Tulcea

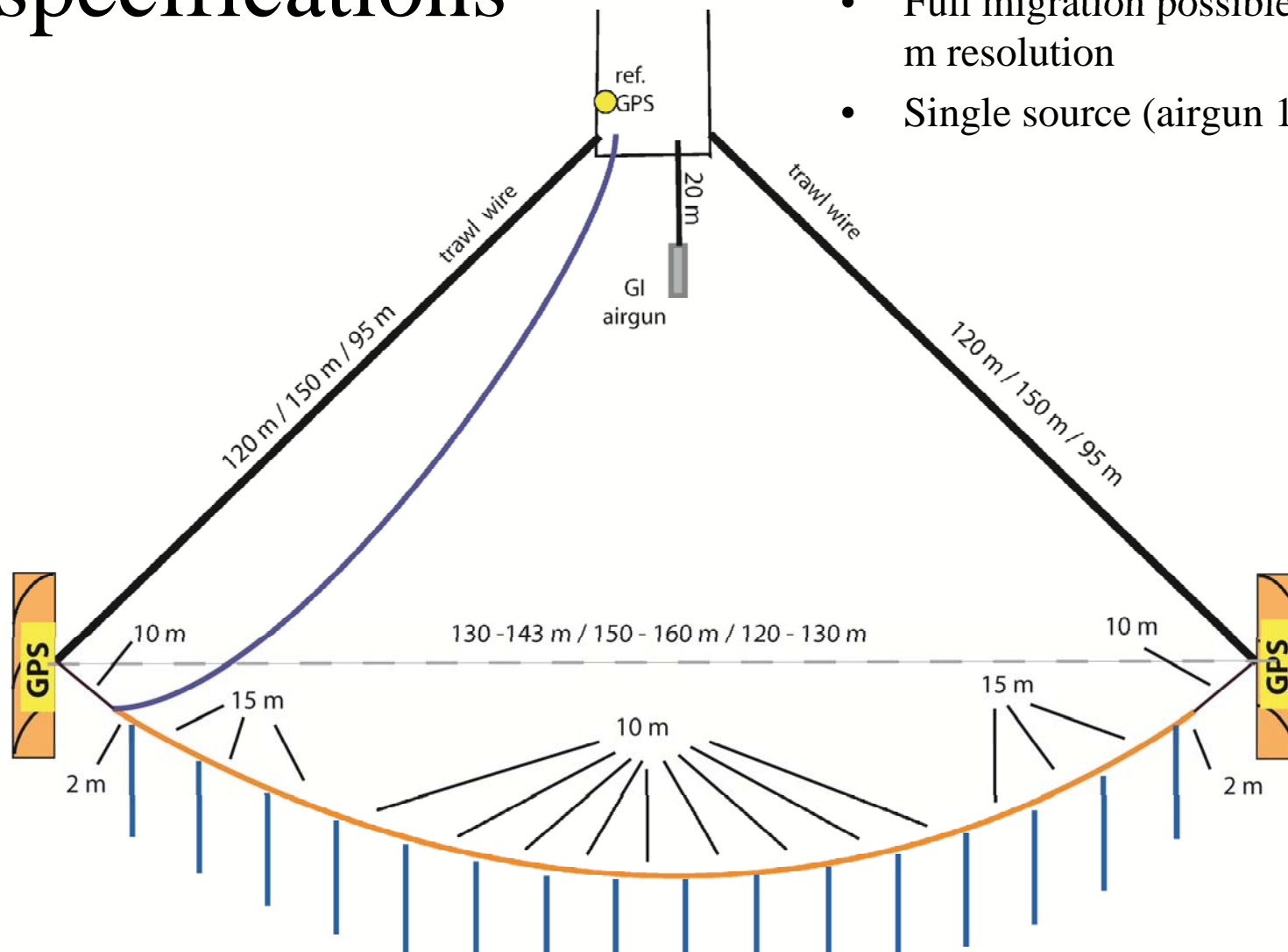
P-Cable concept



- A seismic cable towed perpendicular to the vessel's steaming direction

Technical specifications

- 16 short streamers
- 6.25 m inline separation
- Full migration possible up to 250 Hz \cong 1.5 m resolution
- Single source (airgun 1.7 - 4.1 litres)



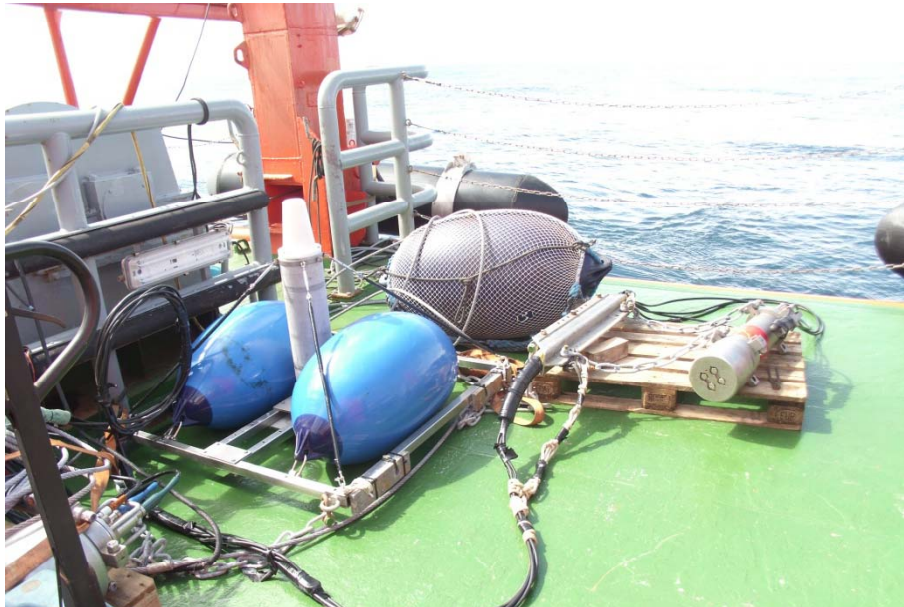
R/V Sonne Deployment





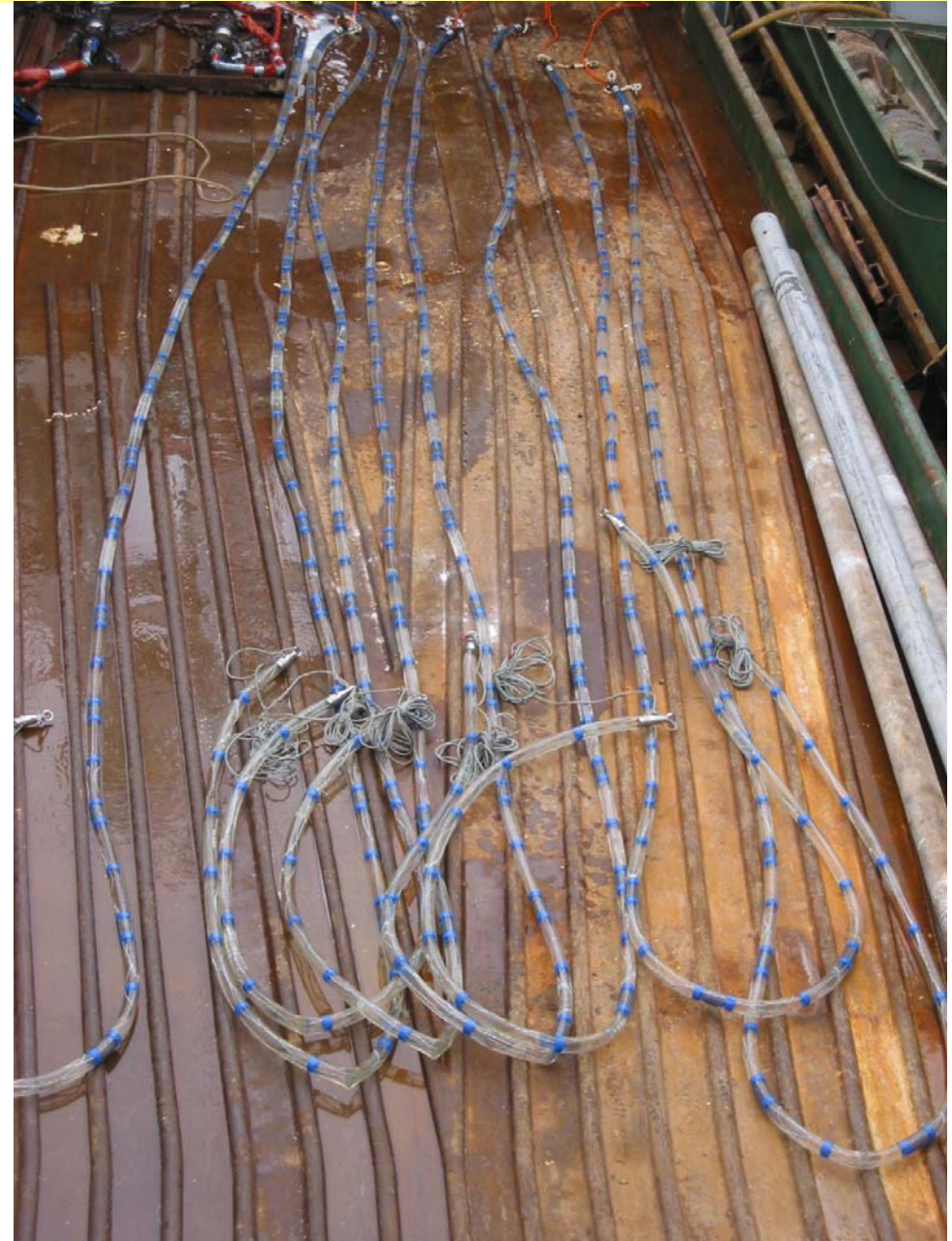
future ocean
KIEL MARINE SCIENCES

Acoustic Imaging Seismic Systems



Receiver system

- 8 channel-channel digital streamer
- Spacing: 10 - 15 m
- Frequency response: 8 – 10000 Hz
- Towing depth: ~1 m
- Swath width: 150 m





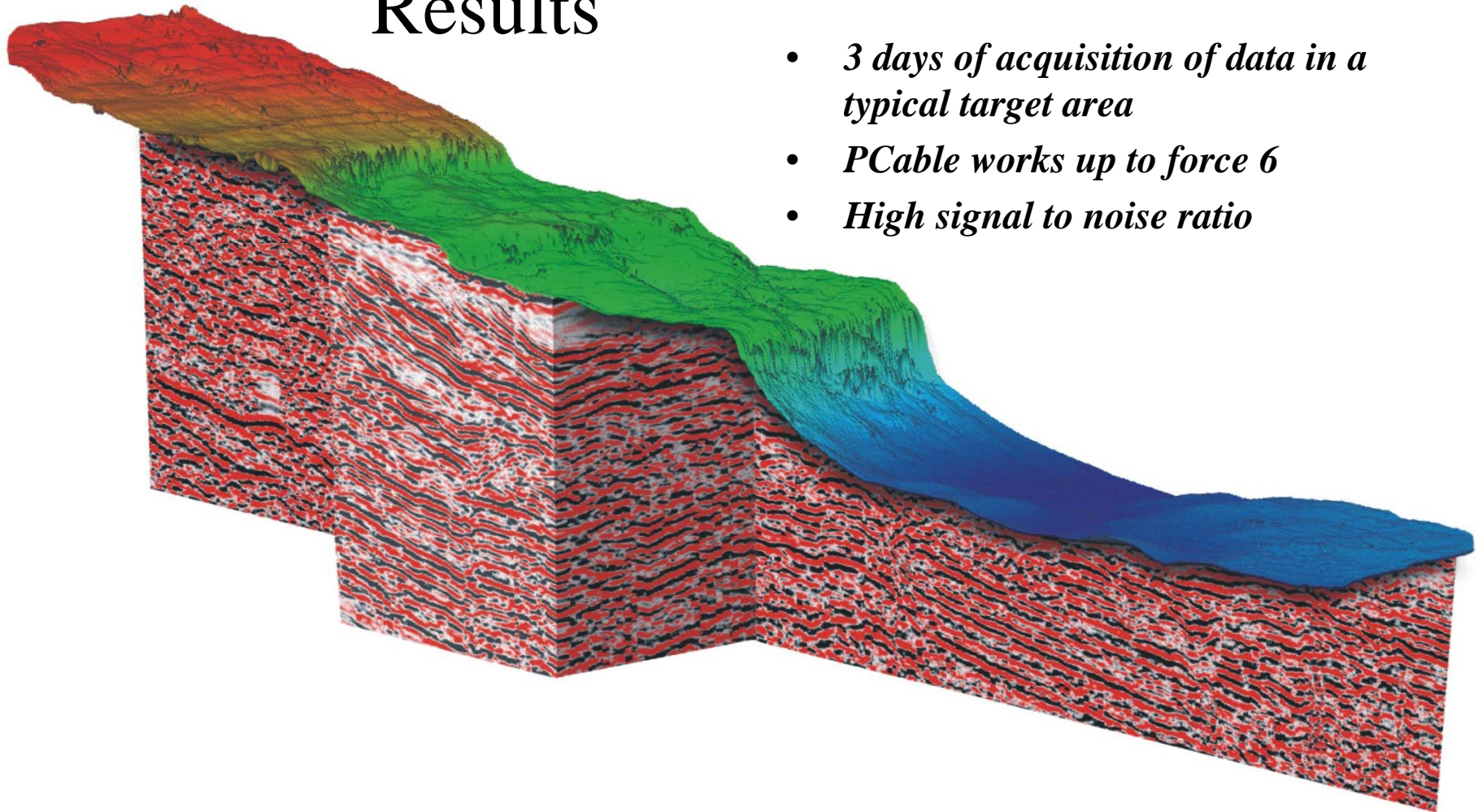
future ocean
KIEL MARINE SCIENCES

Acoustic Imaging

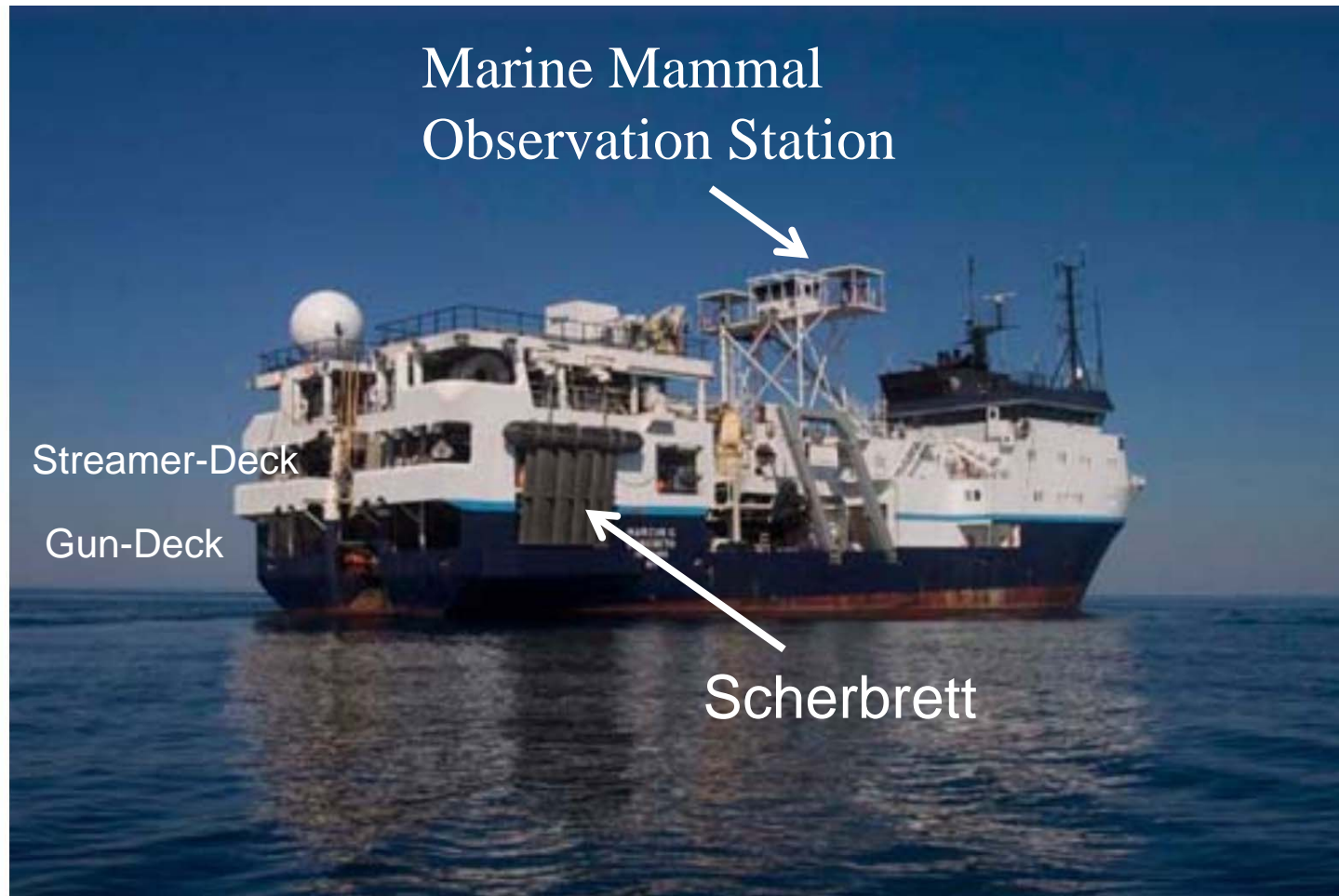
Seismic Systems

Results

- *3 days of acquisition of data in a typical target area*
- *PCable works up to force 6*
- *High signal to noise ratio*

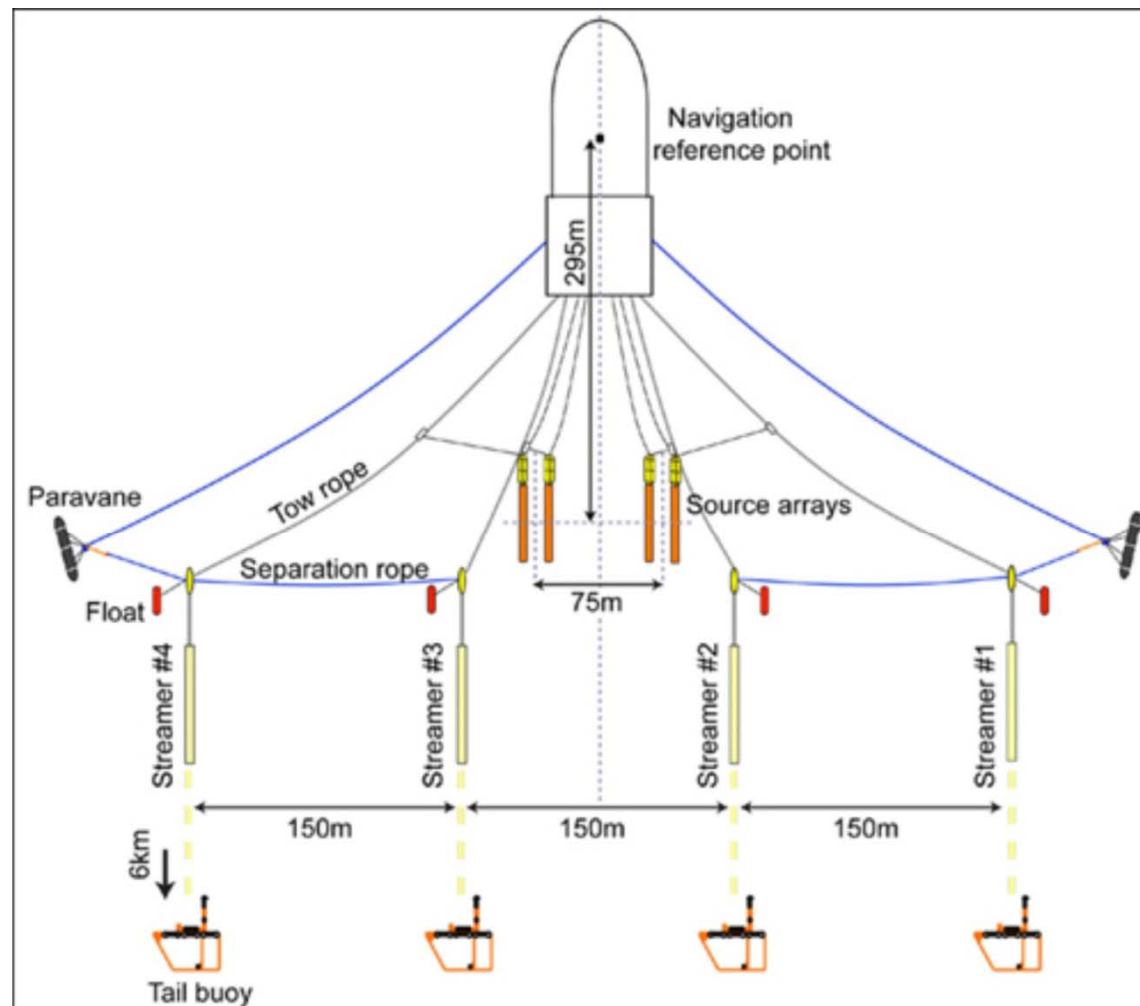


R/V Marcus G. Langseth

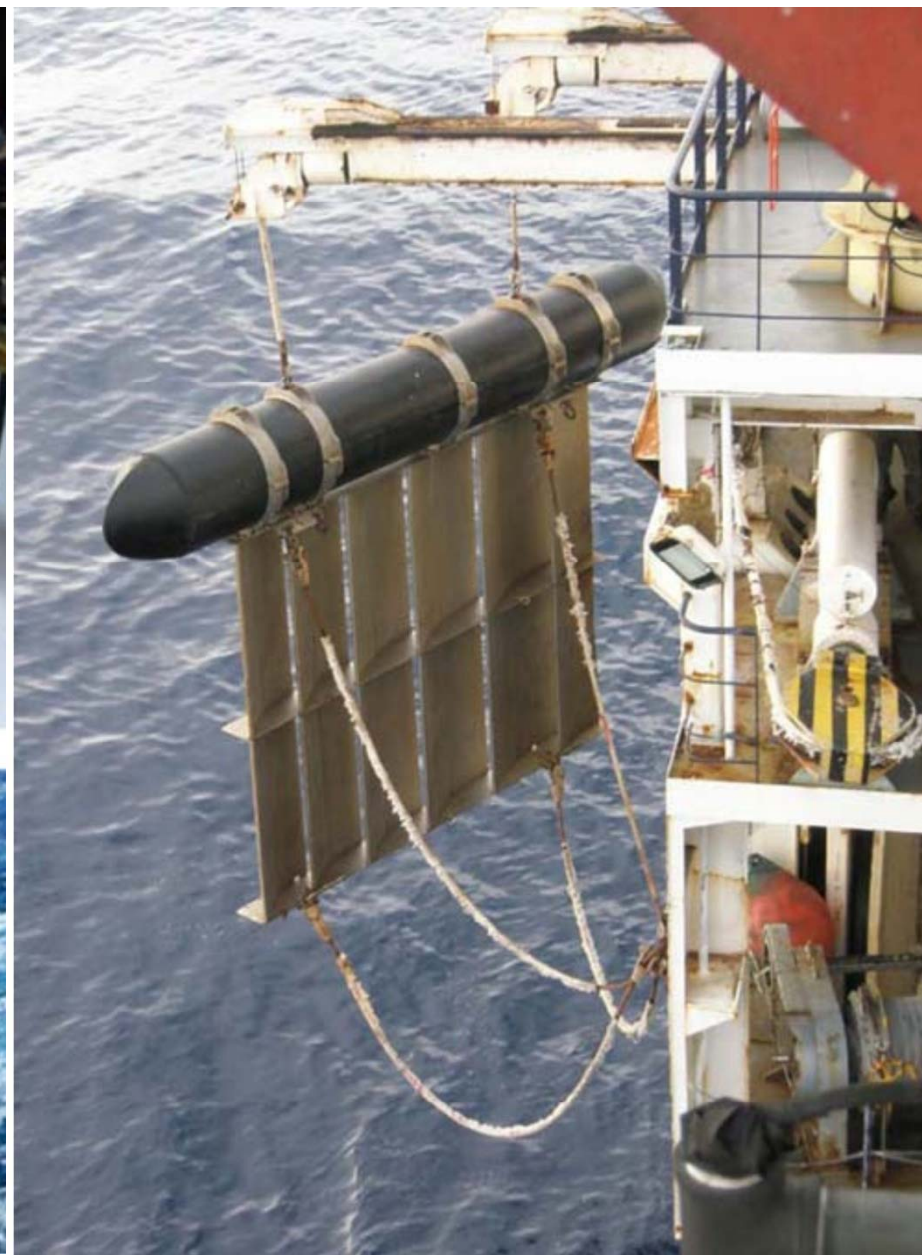
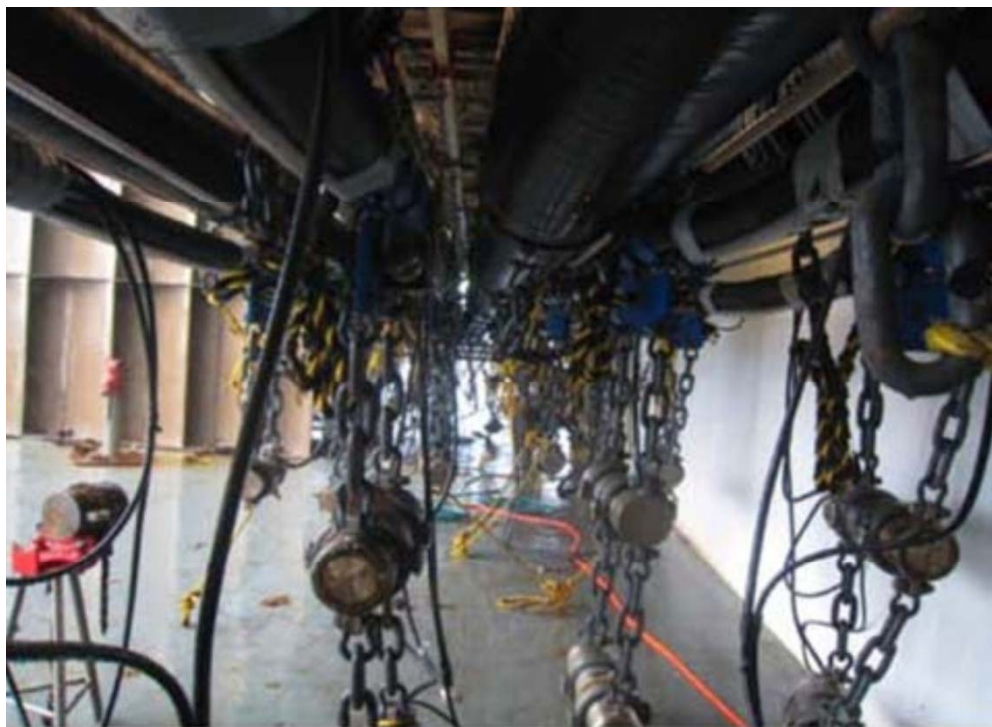


Langseth Towing Configuration

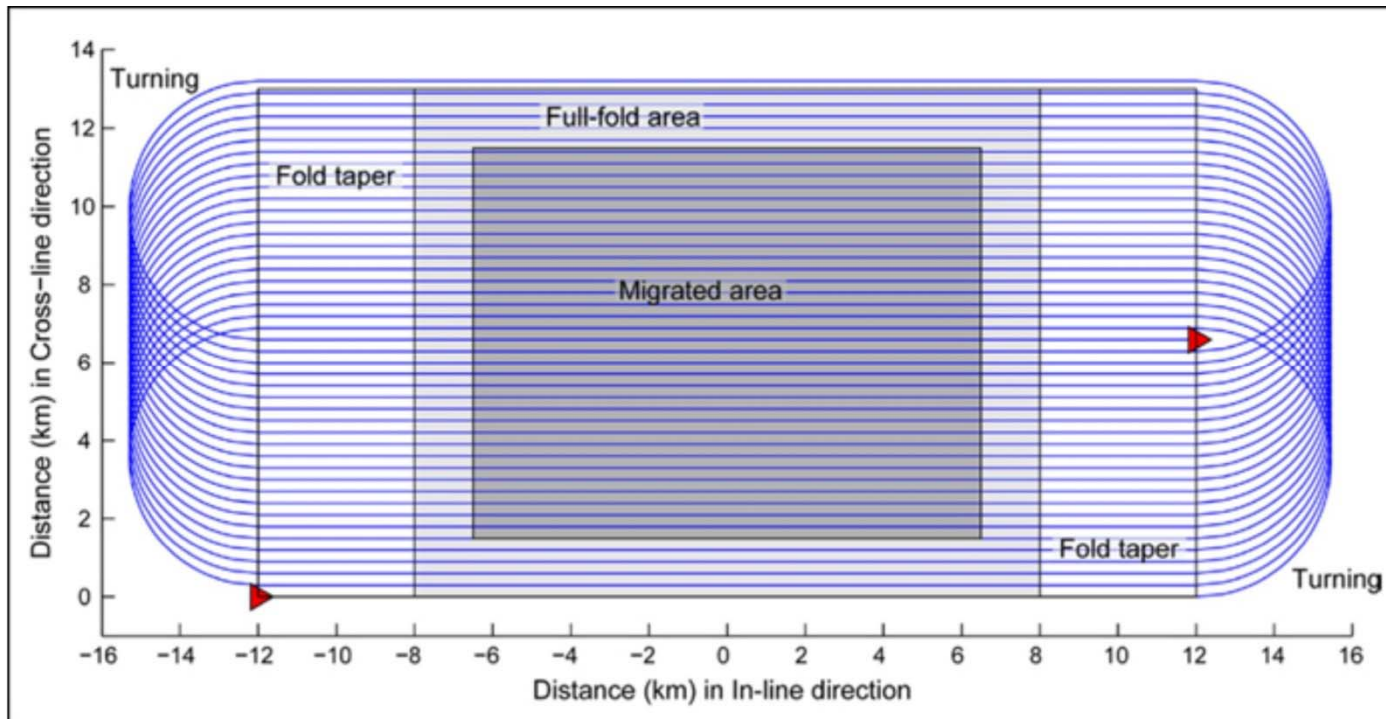
(2 Gun Arrays, 4 6-km-long streamer => 8 CMP-lines)



Acoustic Imaging Seismic Systems



Racetrack 3D Shooting Pattern



Data recording

- **Analog-Filter:** High-pass eliminates low frequency noise

Low-pass filter (Anti-aliasing-Filter) eliminates frequencies higher than the Nyquist frequency

- **Amplifier**
- **AD-converter**
- **Demultiplexer**
- **Digital drive**

Typical seismic formats:

Society of Exploration Geophysicist

SEG D: Multiplexed Data (Time-sequential format)

SEG Y: Demultiplexed Data (Trace sequential format)

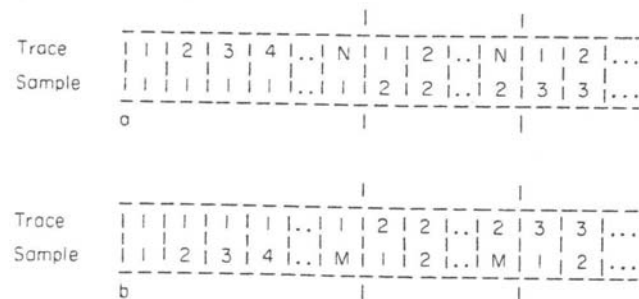


Fig. 3.1. Illustrating the different organisation of (a) multiplexed tape formats, and (b) demultiplexed tape formats.



Fig. 3.5. A schematic of the SEG Y demultiplexed format.

Tape reel Header: 3600 byte
Data record: 240 byte Trace Header
+ 4 byte / sample

Trace Header

Bytes

- 1-4 Trace sequence number within line
- 9-12 Original field record number
- 13-16 Trace number within original field record
- 29-30 Trace identification code
 - 1 = seismic data
 - 2 = dead
 - 3 = dummy
 - etc.
- 115-116 Number of samples in this trace
- 117-118 Sample interval in microseconds for this trace.

Aliasing

The seismic trace is a continuous signal, which is digitized at a specific sample rate.

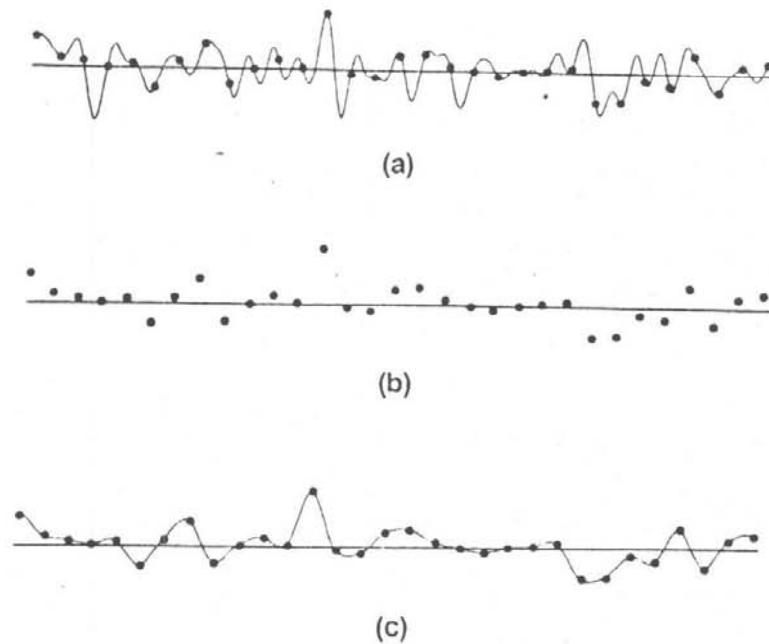


FIG. 1-5. When digitized, a continuous analog signal loses frequencies above the Nyquist frequency: (a) continuous analog signal, (b) digitized signal, (c) reconstructed analog signal. (Adapted from Rothman, 1981.)

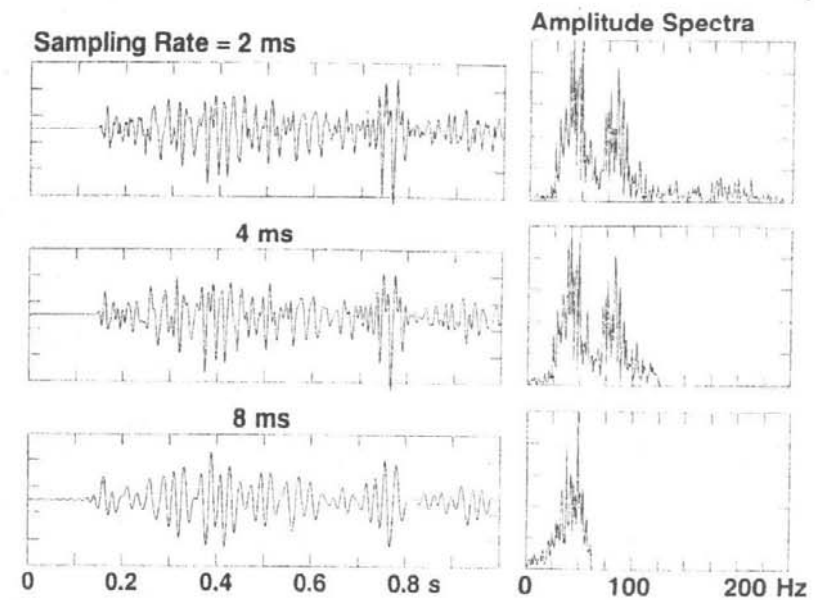


FIG. 1-6. A time series sampled at 2 ms has a Nyquist frequency of 250 Hz. Resampling to 4 and 8 ms confines the frequency band to 125 and 62.5 Hz, respectively. Note the loss of high frequencies at larger sampling intervals.

Nyquist-Frequenz (Highest frequency which can be reproduced):

$$f_{Ny} = 1/(2\Delta t)$$

Exmple: $\Delta t = 2 \text{ ms}$, $f_{Ny} = 250 \text{ Hz}$

Samplig at a sampling rate Δt allows to reproduce frequencies up to the Nyquist Freq. Such a sampling is irreversible, i.e., later resampling with shorter sampling rates will not reproduce the high frequencies.

Aliasing is
occurring in
addittion.

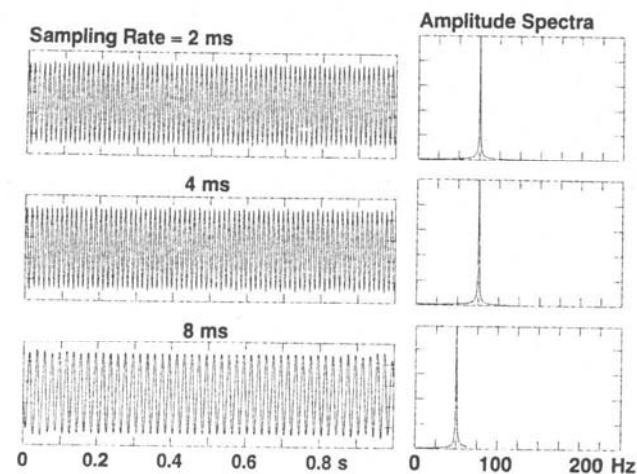


FIG. 1-8. A 75-Hz sinusoid sampled at 2 ms remains unchanged when resampled at 4 ms, but appears as a 50-Hz sinusoid when resampled at 8 ms. Hence, the latter is the alias of the original sinusoid.

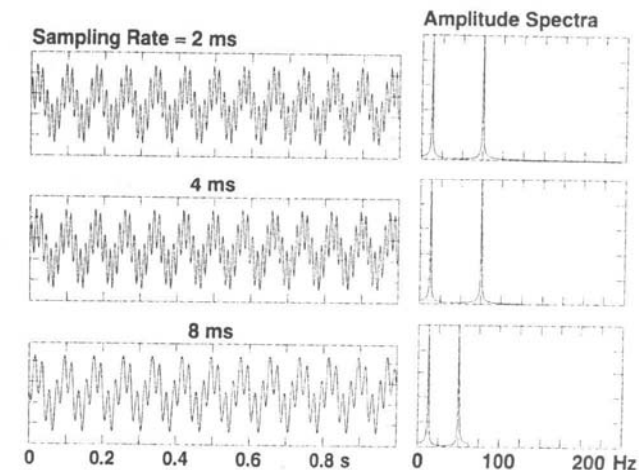


FIG. 1-10. A time series synthesized from two sinusoids at 12.5 and 75 Hz at 2-ms sampling rate remains unchanged when resampled at 4 ms. However, at 8 ms, its high-frequency component shifts from 75 to 50 Hz, while its low-frequency component remains the same.

Aliasing

Sampling a continuous signal needs to at a high rate. Aliasing occurs for all frequencies above the Nyquist-frequency.

Frequencies above the Nyquist frequency cannot be reproduced and are contaminating the frequency spectra.

Consequences of under-sampling

Limitation of frequency spectra up to the Nyquist-Frequency

Contamination of digital time series due to aliasing

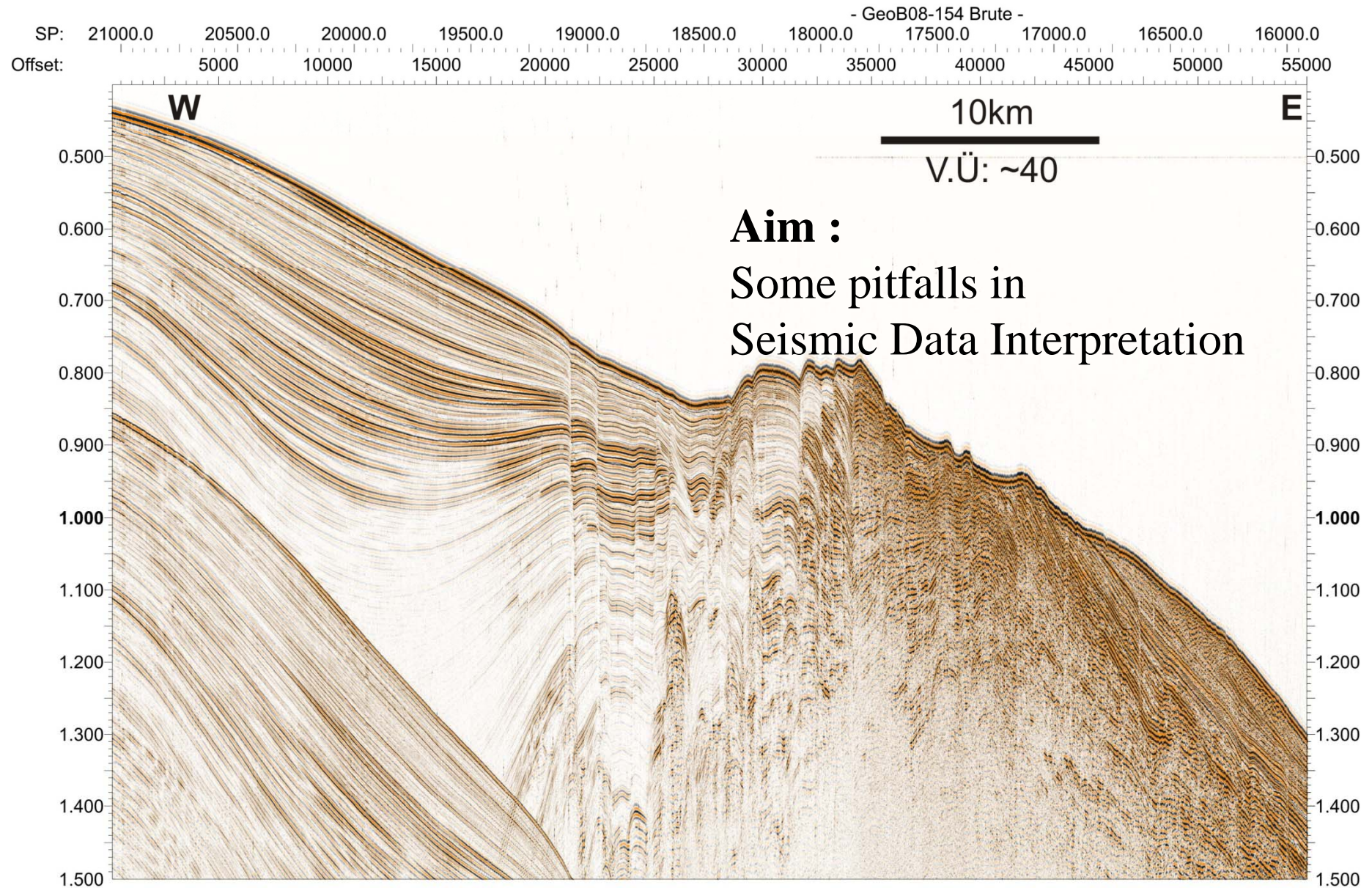
As a consequence, each recording unit includes an analog filter, which eliminates high frequencies before sampling



future ocean
KIEL MARINE SCIENCES

Acoustic Imaging

Seismic Interpretation





1. Some Basics

1.1 When do we get reflected waves?

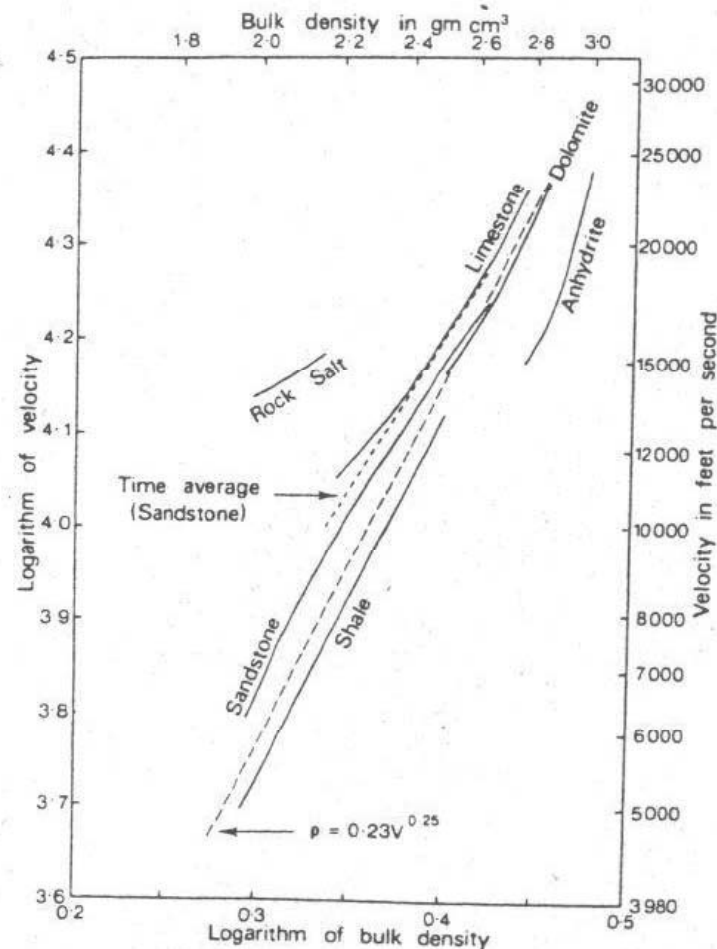


Figure 2/7 Velocity-density relationships in rocks of different lithology (after Gardner *et al.*, 1974).

Reflections (vertical incident) occur at interfaces characterized by a change of the acoustic (seismic) impedance $Z=v*\rho$

Table 7.3 Typical seismic reflection coefficients (R)

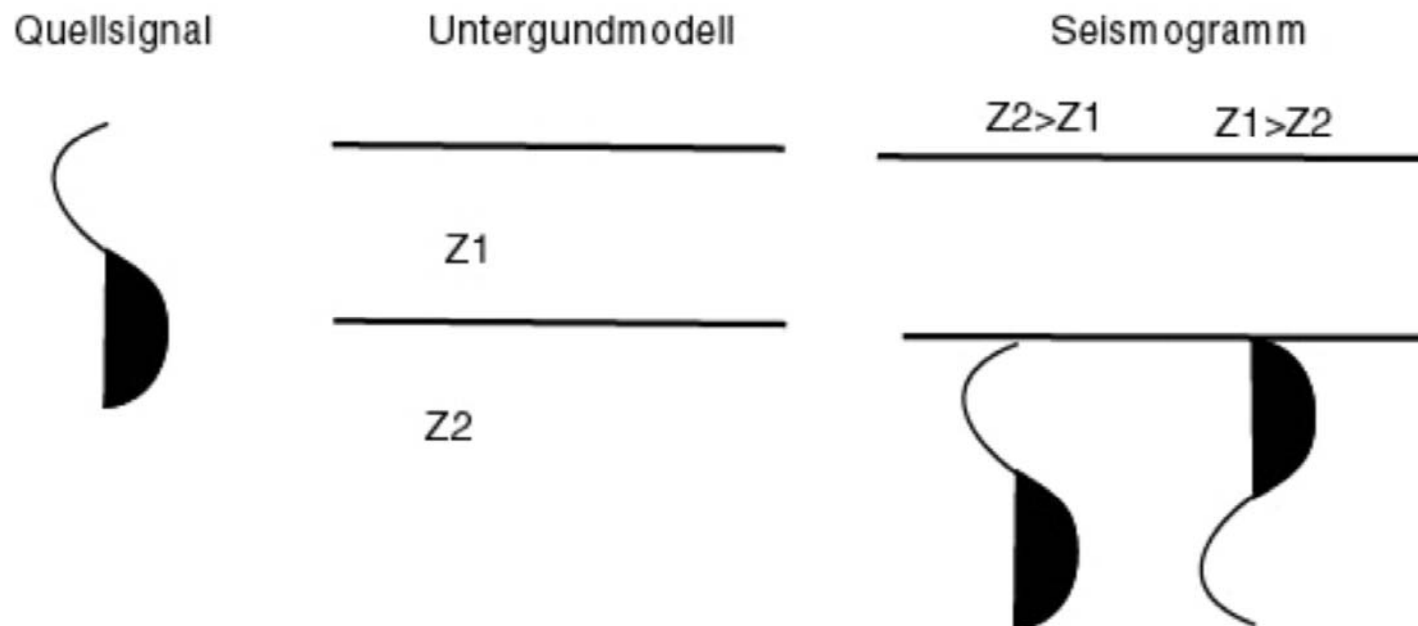
interface	Approximate R
Air over sea	1.0
Sea over limestone	0.65
Sea over boulder clay	0.45
Sea over recent sand/clay	0.3
Clays over gas sand, 500 m	-0.30
Sea-bed multiples	0.25
Sand/shale over limestone, 1500 m	0.20
10% change in acoustic impedance	± 0.05

A strong impedance contrast results in strong reflections =>

Reflection coefficient: $R = (Z_2 - Z_1) / (Z_2 + Z_1)$.

Transmission coefficient : $T = 1 - R = 2Z_1 / (Z_2 + Z_1)$
(only for vertical incident)

Reflections do show different polarities (positive or negative):





future ocean
KIEL MARINE SCIENCES

Acoustic Imaging Seismic Interpretation

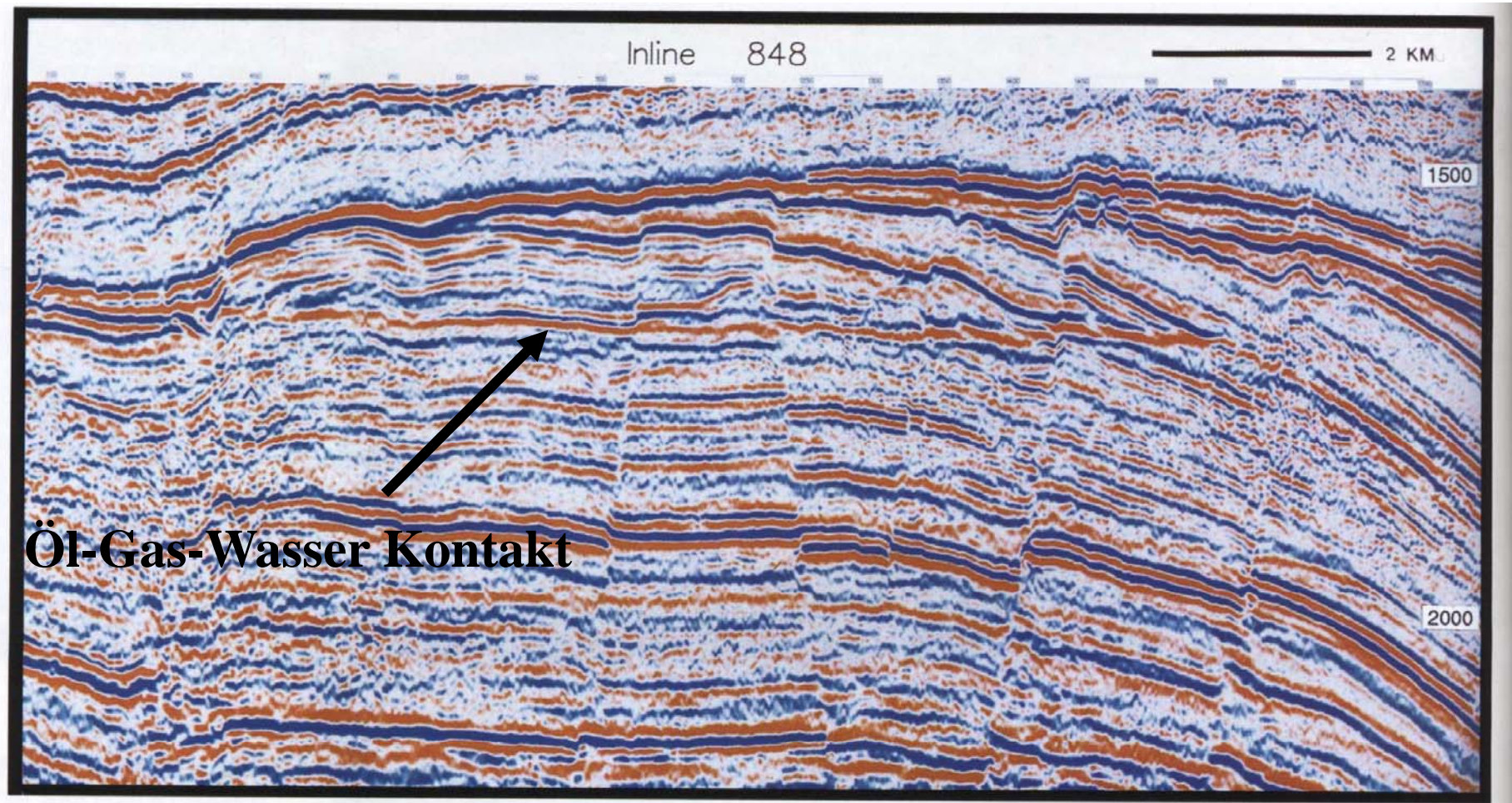


Fig. 5-17. Vertical section across Troll gas field offshore Norway. Note 7 km long flat spot at about 1700 ms. The reservoir is Jurassic in age with an average porosity of 28%. (Courtesy Norsk Hydro a.s.)

2 The real world

Central problem in ,The real World‘:

Noise, z.B background noise, multiples, diffraktions

Distortion, as we usually have time sections and not depth sections

2.1 Background Noise

Land: Wind, traffic, animals, power line ect

Water: Waves, electrical noise, Noise from other vessel and/or the survey vessel

What to do?:

Optimization of all acquisition parameters

Processing

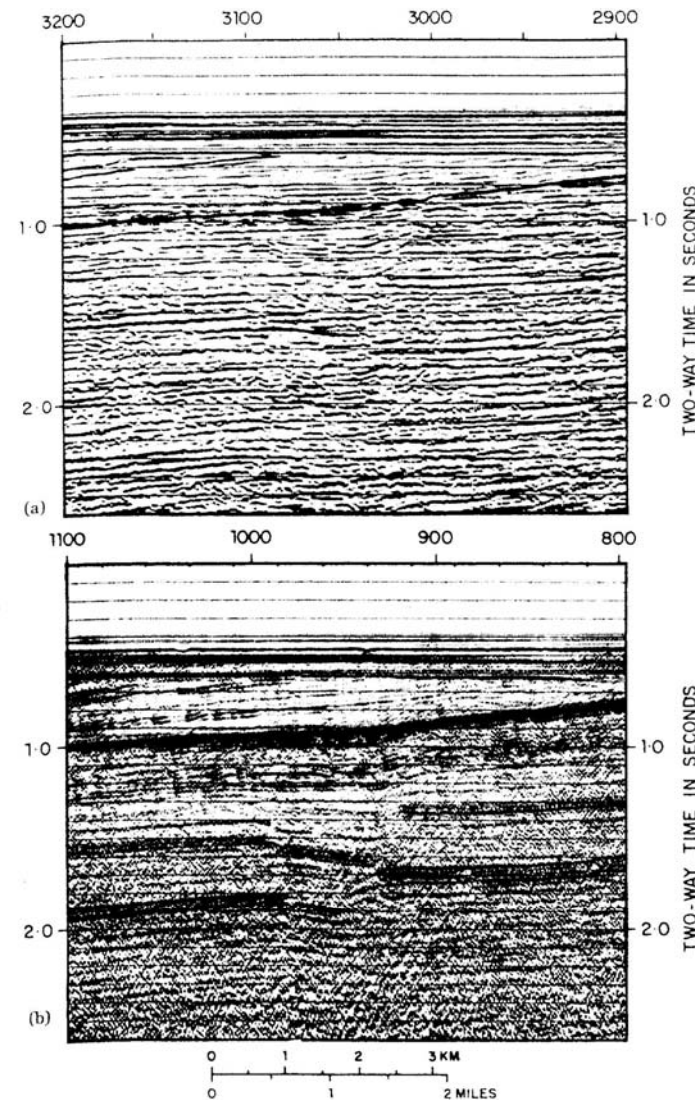


FIGURE 3.1 Two seismic profiles shot over the same location. Line (a), shot in 1982, is poorly processed, and has a very poor signal-to-noise ratio. Line (b), shot in 1980, is excellent. Reflectors A, B, and C, and the faults X and Y, so clear on line b, can only be followed with great difficulty on line a. Courtesy Norsk Hydro.

2.2 Multiples

Multiples=multiple reflections between interfaces

Long-Path-Multiples: Travel time of multiple is significantly different than the primary reflection

Short-Path-Multiples: Travel time of multiple and primary reflection varies only a bit (often occurrence of interference).

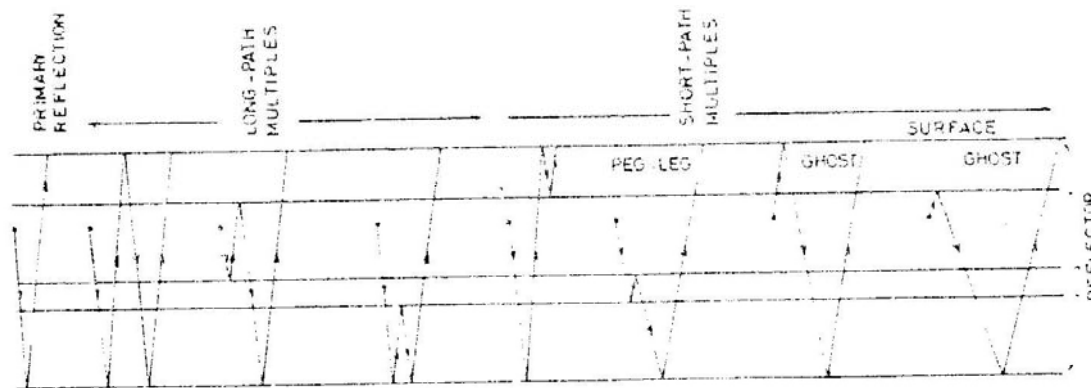


FIGURE 3.7 Common types of multiple reflections. Reprinted by permission of Birkhäuser Verlag from Al-Sadi, 1980.

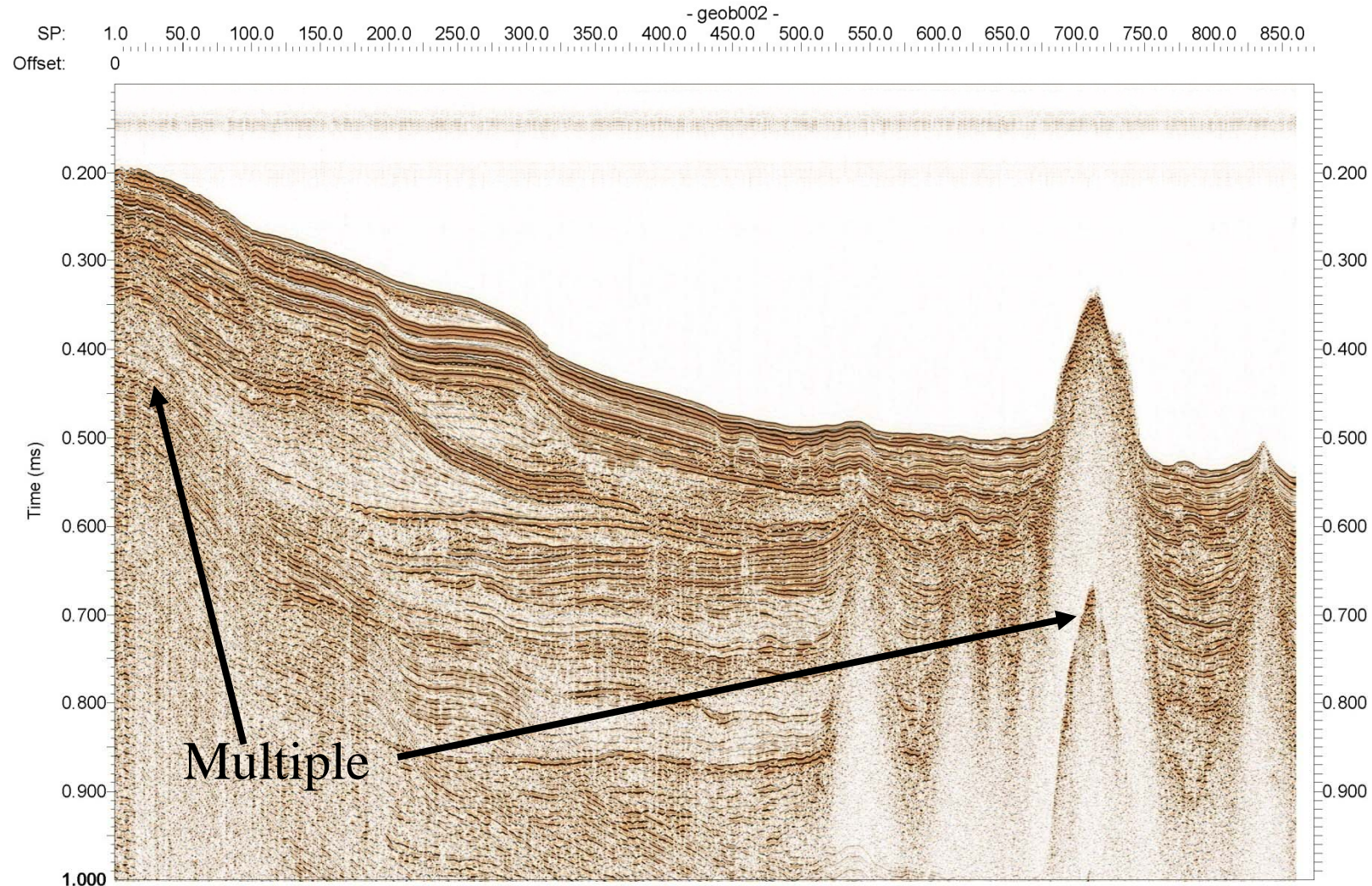


future ocean
KIEL MARINE SCIENCES

Acoustic Imaging

Seismic Interpretation

Water multiple: Multiple reflection between sea floor and water surface (twice the travel time and slope angle)





Simple Multiple: Shot/Reflector/Water-land-surface/same Reflector, receiver. Same effects as water multiple.

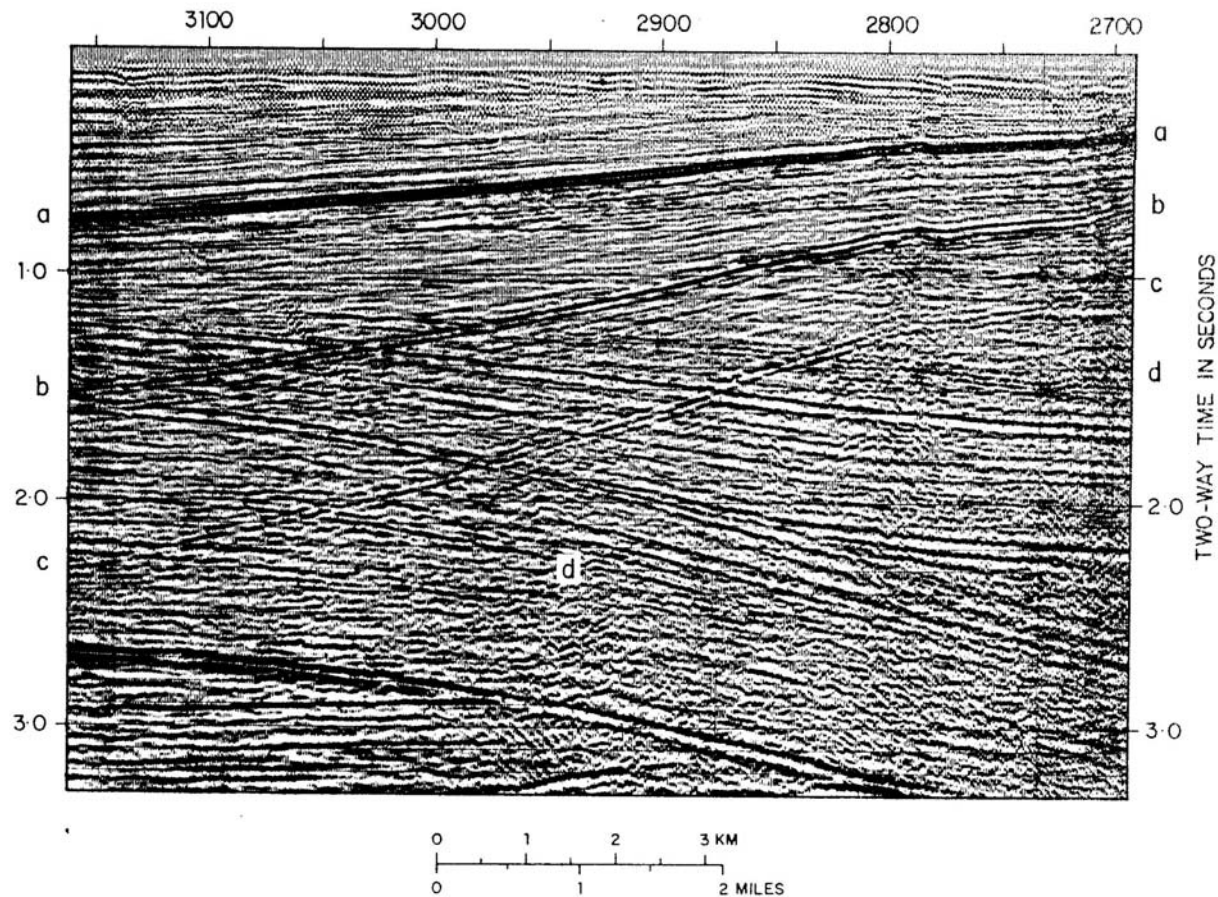


FIGURE 3.14 Seismic section showing dipping simple multiples from reflection a. Three bounces of the multiples, b, c, and d can be seen. The dip of each successive multiple increases by an amount equal to the dip of the primary reflection a. Courtesy: Merlin Profilers Ltd.

Interbed Multiple: Multiple resulting from multiple reflections in one layer.

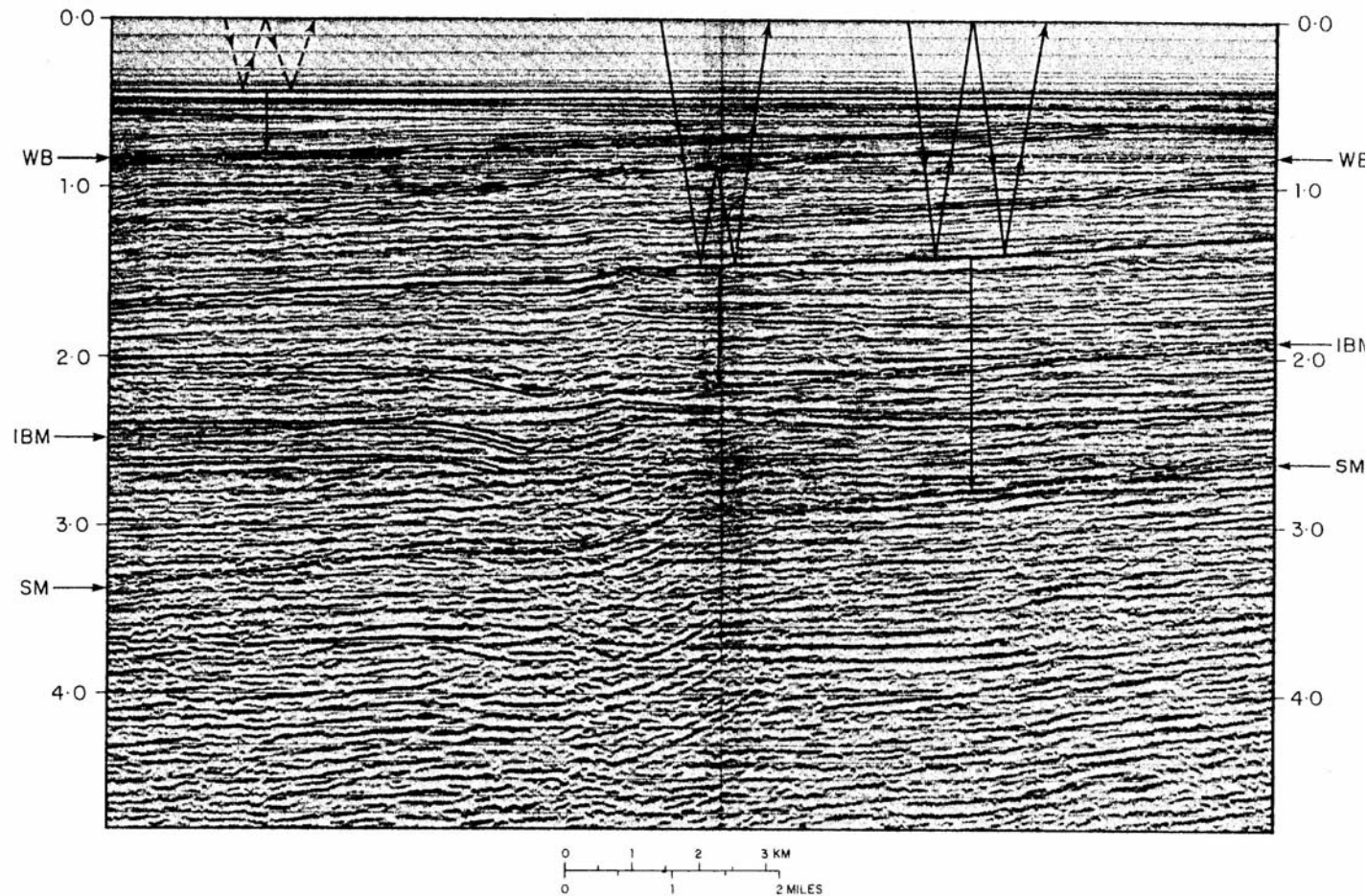


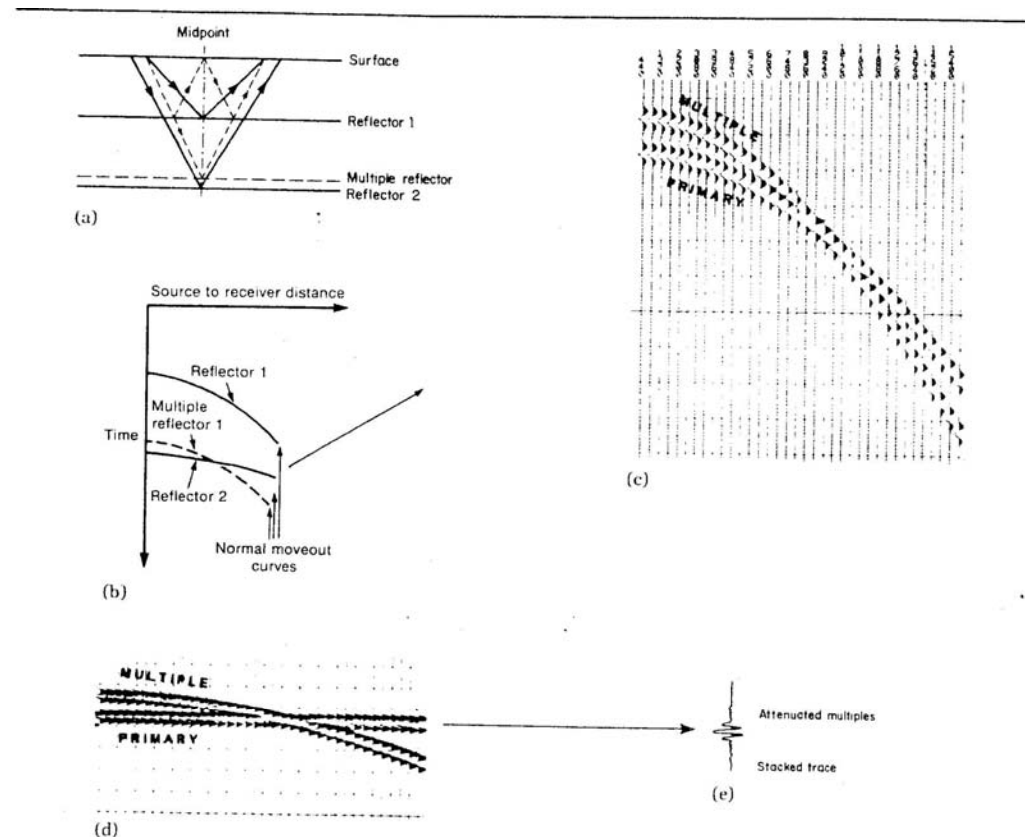
FIGURE 3.10 A seismic section with a "good" set of multiples. SM, simple multiple; WB, water-bottom multiple; IBM, interbed multiple. Courtesy Société Nationale Elf Aquitaine.

Peg Leg Multiple: one ,Extra-Reflection' between two reflectors.

Ghosts: Reflection at the surface immediately after the shot or prior to recording.

Main method for multiple suppression:
Suppression by stacking
(lower velocity than primary reflections)

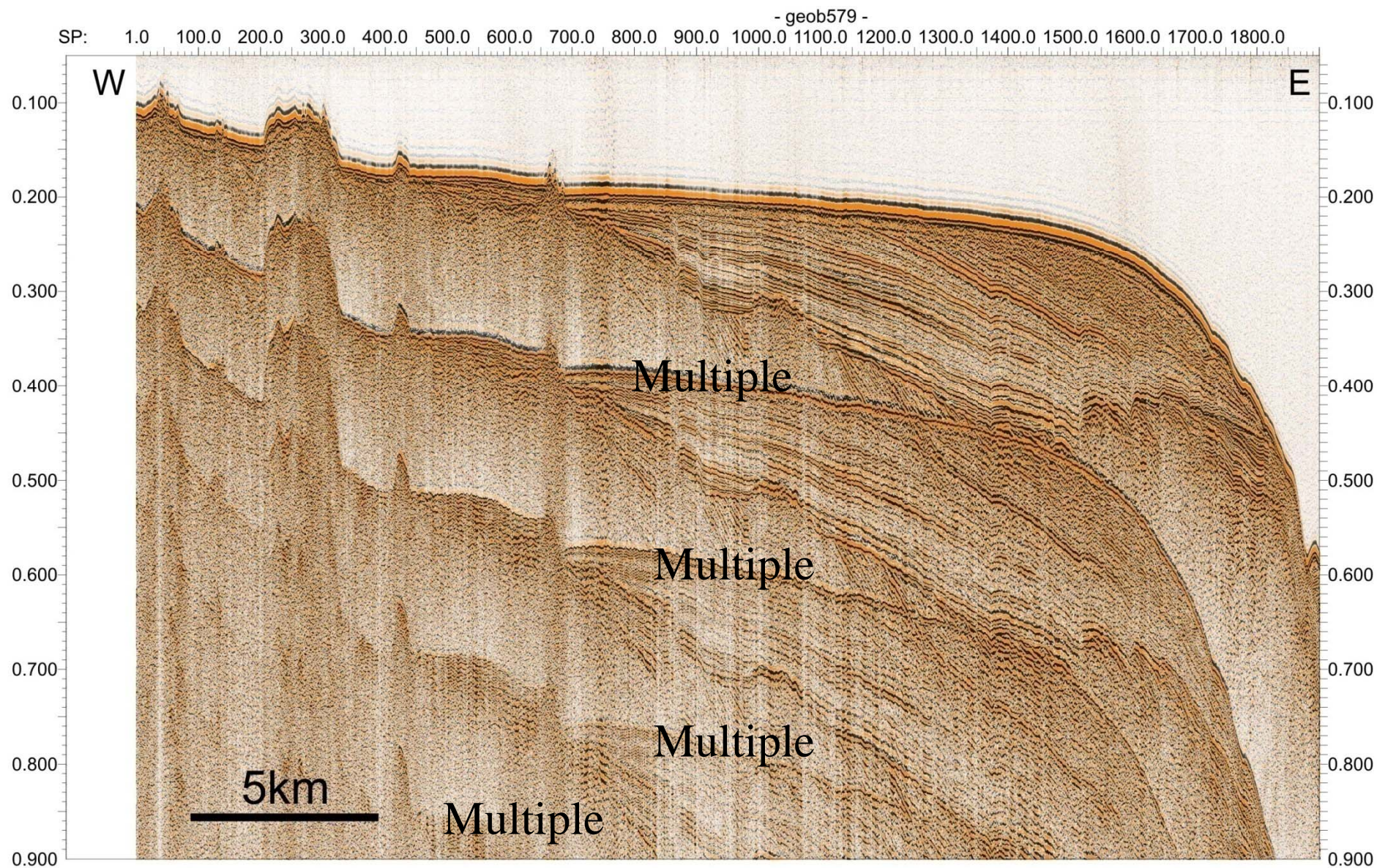
Deconvolution





future ocean
KIEL MARINE SCIENCES

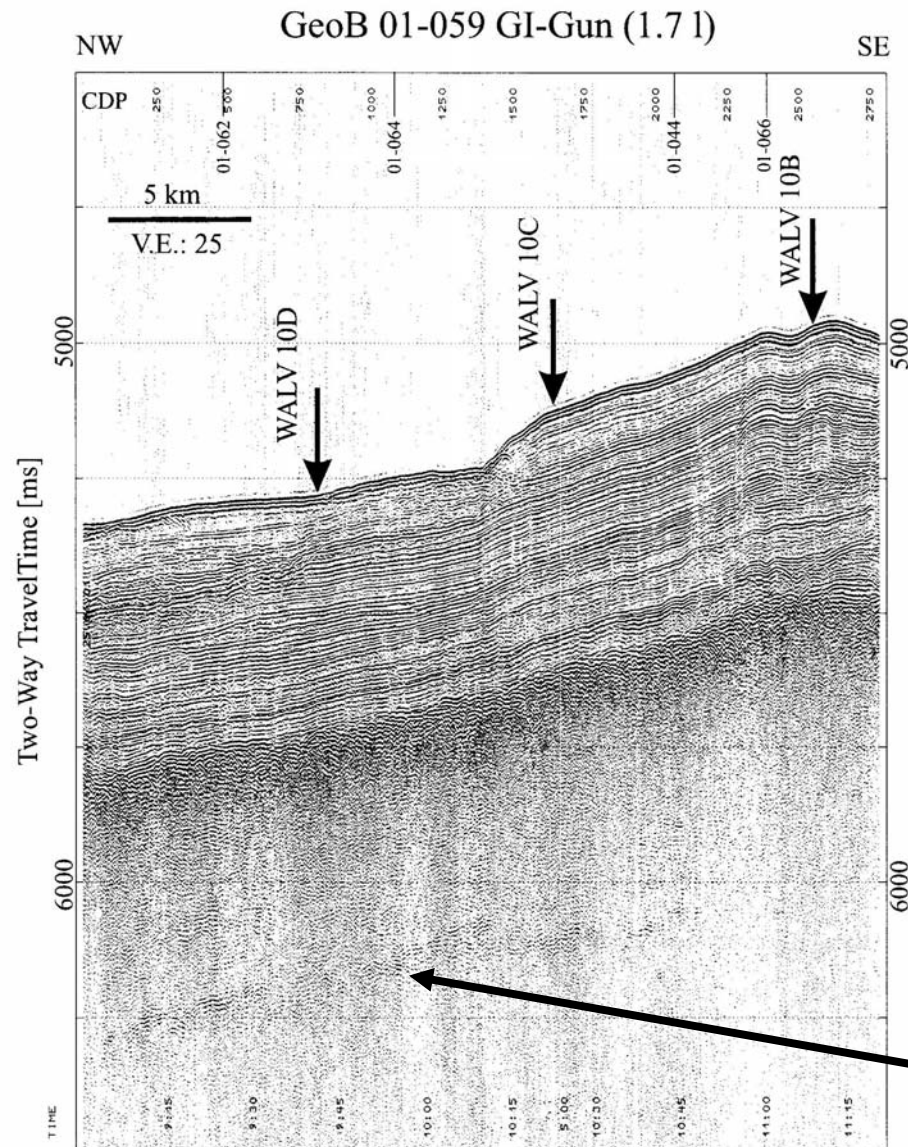
Acoustic Imaging Seismic Interpretation





future ocean
KIEL MARINE SCIENCES

Acoustic Imaging Seismic Interpretation



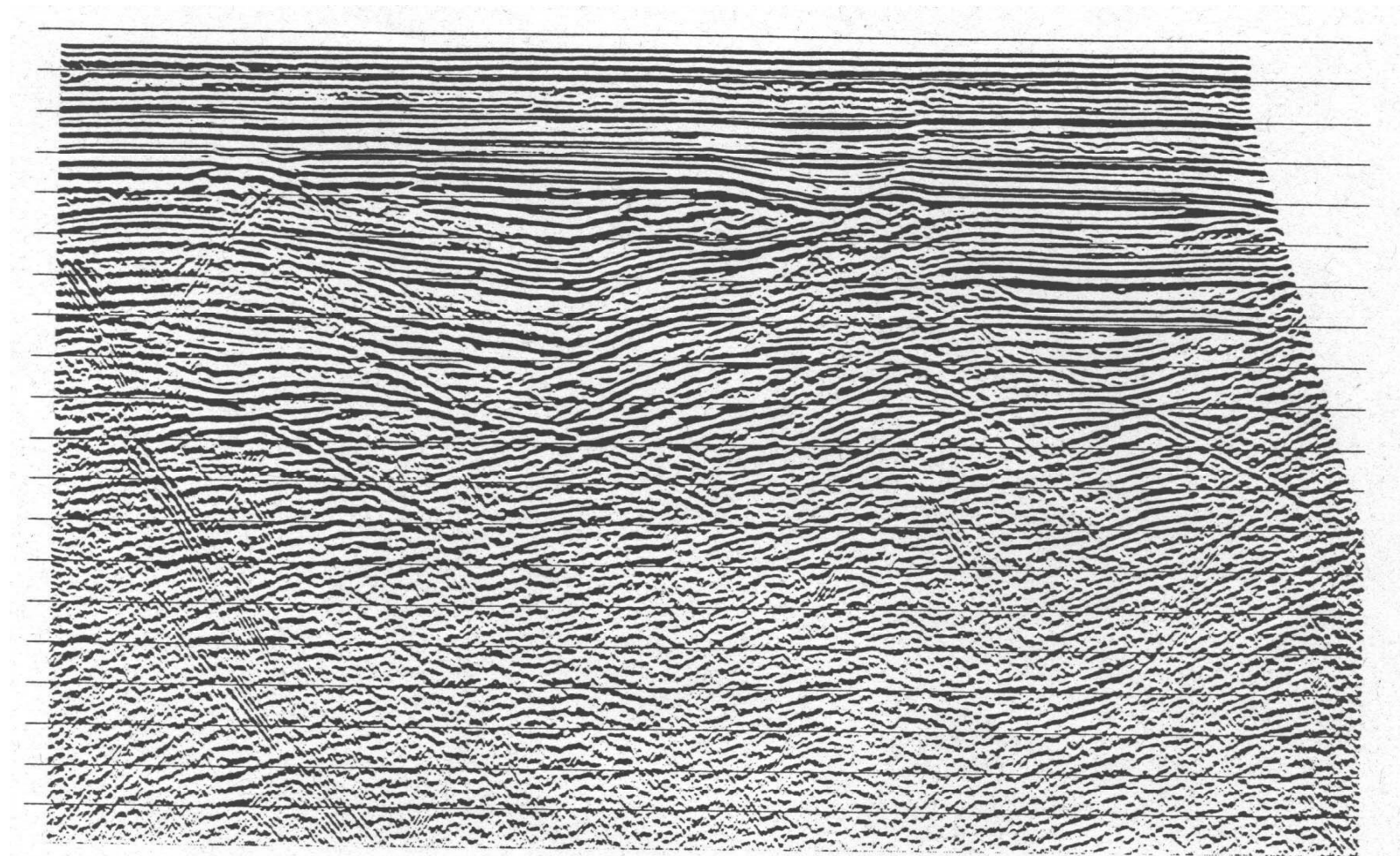
Einfache Multiple
(Meeresboden-Basement)

2.3 Diffraction

Diffraction hyperbolas develop at edges or diffraction points

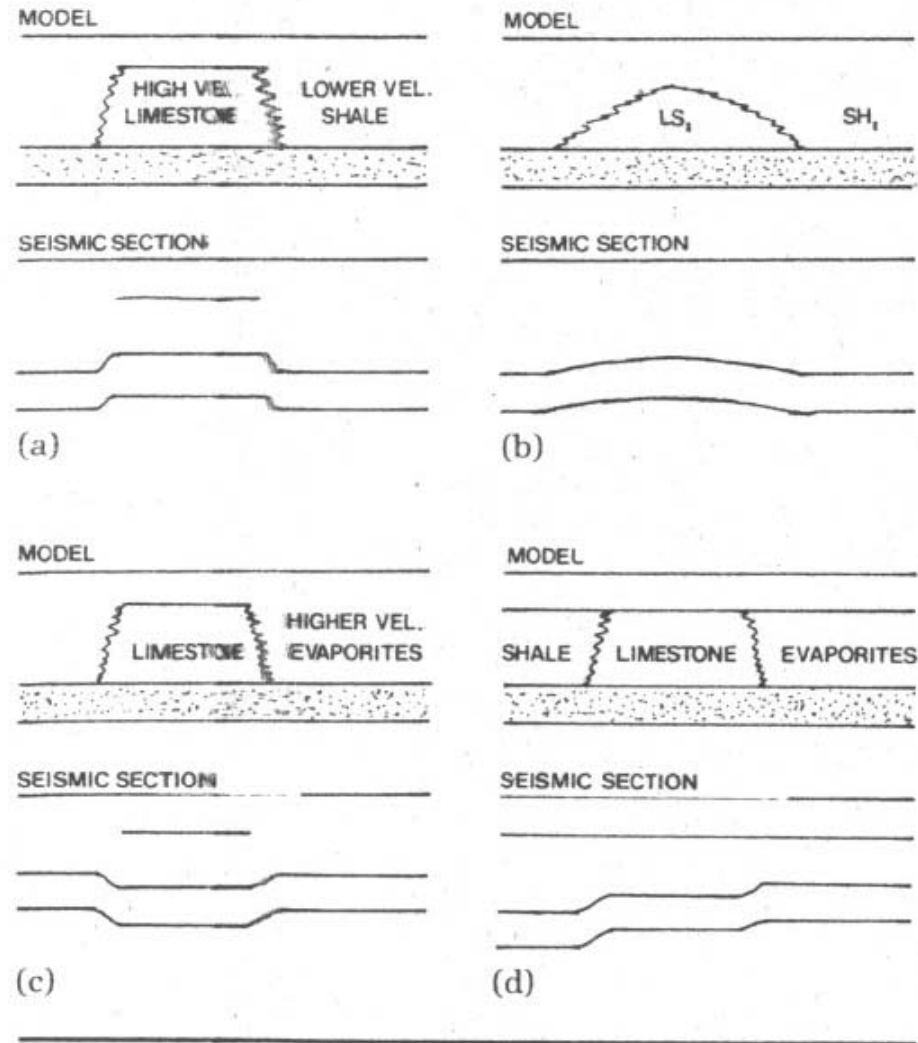
Solution: Migration

Stacked section with diffraction hyperbolas



2.4 Velocity distortion

As a result of using time instead of depth, velocity variations might result in a distortion of reflectors.



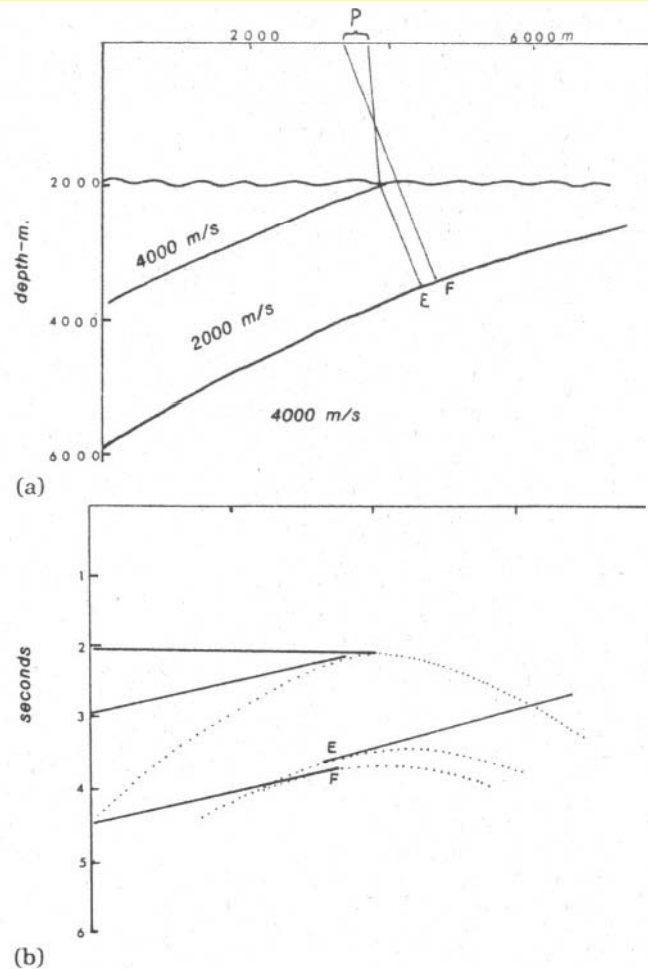


FIGURE 3.37 Distortion resulting from the focusing effects of a wedge with high interval velocity. (a) Geological model. The raypath from reflection point F just misses the high-velocity wedge. The raypath from E, however, is refracted, so that it crosses the raypath from F. (b) Seismic expression. The earlier arrival of ray E, refracted through the wedge edge, causes two reflections to be seen beneath P. Reprinted by permission of the AAPG; after Sheriff, 1982, fig. 9, p. 13.

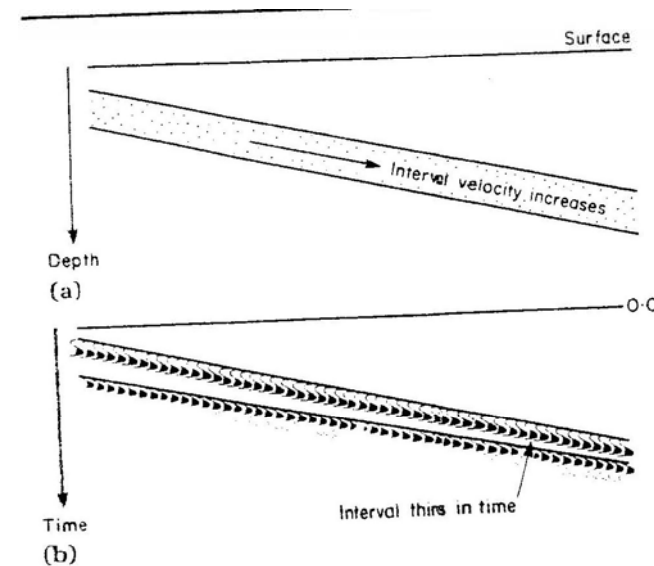


FIGURE 3.29 The effect of increasing velocity with depth on the seismic expression of a dipping unit. (a) Geological model of a thick dipping sandstone unit. The sandstone's interval velocity increases with depth due to diagenesis, but its thickness remains constant. (b) Seismic expression: The sandstone unit appears to thin. It takes less time for the seismic signal to travel through the sandstone as its interval velocity increases.

3 Seismic Stratigraphy

seismic stratigraphy (seismostratigraphy) The study and interpretation of information obtained by seismic-*reflection *profiling in order to construct subsurface *stratigraphic cross-sections. Analysis of seismic reflections on a seismic section (see SEISMIC RECORD) can identify buried stratal

surfaces that, when traced laterally and continuously, represent surfaces of synchronous deposition or their correlative *unconformity surfaces. The character of a reflection may vary as the seismic profile moves across a *facies boundary, but the continued presence of the reflection is of *chronostratigraphic significance. More detailed information regarding the age and *lithology of the subsurface strata may be gathered by means of geophysical *well logging. See also CHRONOSTRATIGRAPHIC CORRELATION CHART; and DEPOSITIONAL SEQUENCE.

stratigraphy 1. The branch of the geologic sciences concerned with the study of stratified rocks in terms of time and space. It deals with the correlation of rocks from different localities. Correlation methods may involve the use of *fossils (*biostratigraphy), rock units (*lithostratigraphy), or *geologic-time units or intervals (*chronostratigraphy). **2.** The relative spatial and temporal arrangement of rock strata.

facies 1. Sum total of features that reflect the specific environmental conditions under which a given rock was formed or deposited. The features may be lithologic, sedimentological, or faunal. In a sedimentary facies, *mineral composition, *sedimentary structures, and bedding characteristics are all diagnostic of a specific rock or lithofacies. **2.** See METAMORPHIC FACIES.

depositional sequence A discrete succession of *strata, deposited more or less continuously, and bounded at top and bottom by either an *unconformity surface or the equivalent, correlative *disconformity or conformity surfaces (see CONFORMABLE). The ancient stratal surfaces can be traced laterally by seismic *reflection *profiling. A depositional sequence is the basic, operational, *stratigraphic unit in *seismic stratigraphy. Where top and bottom boundaries can be traced to conformity surfaces a depositional sequence becomes of *chronostratigraphic significance, as it represents a specific interval of geologic time during which the particular unit was deposited. See BASELAP; DOWNLAP; ONLAP; and TOPLAP.

Conclusions based on seismic stratigraphy:

- Geological time correlation
- Identification of depositional sequences
- Thickness and depositional conditions of individual sequences
- Paleo-bathymetry
- Sedimentary history
- Relief and topography of unconformities

The following steps may be carried out:

- Seismic sequence analysis
- Sequence analysis of wells
- Calculation of synthetic seismograms for correlation between seismics and wells
- Seismic facies analysis
- Interpretation of depositional conditions and litho facies

Seismic Sequence analysis:

Depositional sequence (seismic sequence): Stratigraphic unit consisting of a sequence of individual layers, which are deposited at ‘similar’ depositional conditions. Top and base of a sequence are bounded by an unconformity or their equivalent conformity surfaces.

Types of Unconformities:

Lapouts: Lateral termination of a unit caused by non deposition.

Truncation: Lateral termination of a unit caused by erosion.



Acoustic Imaging

Seismic Interpretation

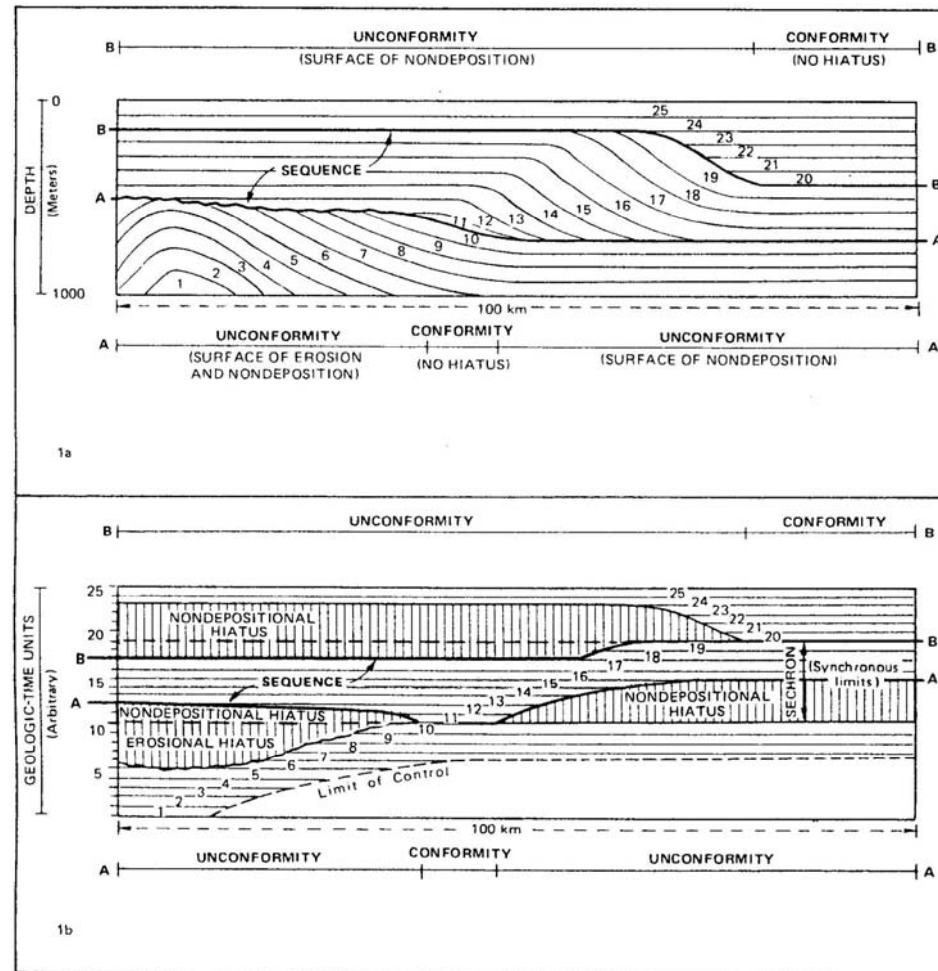


FIG. 1—Basic concepts of depositional sequence. A depositional sequence is a stratigraphic unit composed of relatively conformable successions of genetically related strata and bounded at its top and base by unconformities or their correlative conformities.

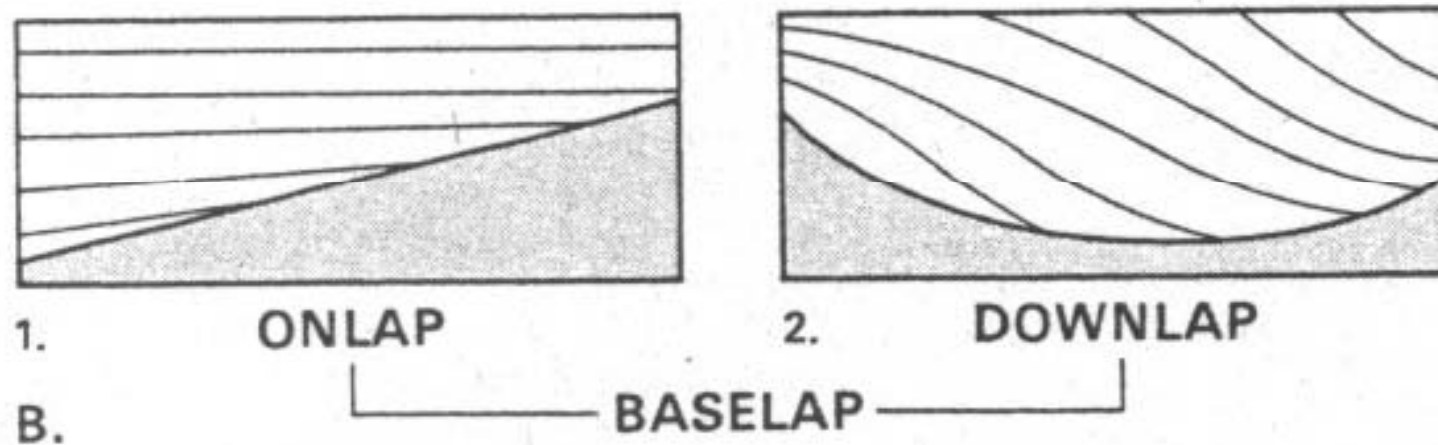
A. Generalized stratigraphic section of a sequence. Boundaries defined by surfaces A and B which pass laterally from unconformities to correlative conformities. Individual units of strata 1 through 25 are traced by following stratification surfaces, and assumed conformable where successive strata are present. Where units of strata are missing, hiatuses are evident.

B. Generalized chronostratigraphic section of a sequence. Stratigraphic relations shown in A are replotted here in chronostratigraphic section (geologic time is the ordinate). Geologic-time ranges of all individual units of strata given as equal. Geologic-time range of sequence between surfaces A and B varies from place to place, but variation is confined within synchronous limits. These limits determined by those parts of sequence boundaries which are conformities. Here, limits occur at beginning of unit 11 and end of unit 19. A sechron is defined as maximum geologic-time range of a sequence.)

Baselap: Termination against the base of a depositional unit (sequence)

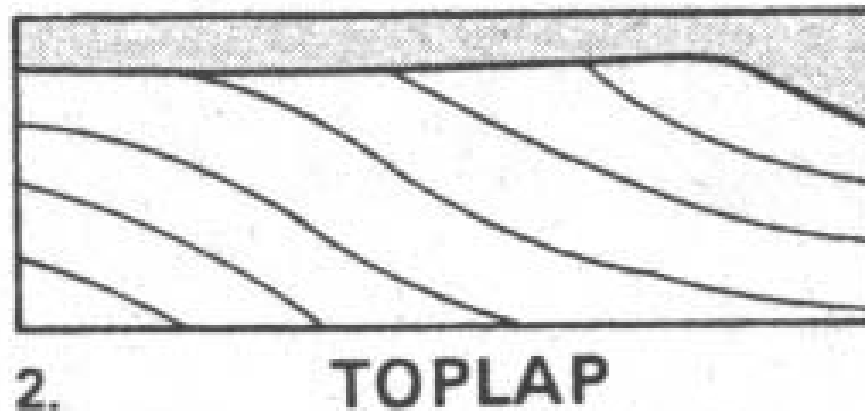
- **Onlap:** Termination of a horizontal layer against an inclined layer of an inclined layer against a more inclined layer.
- **Downlap:** Termination of a down going layer against a lower boundary.

Hiatus (Schichtlücke) caused by non deposition.
The hiatus increases in the onlap direction.



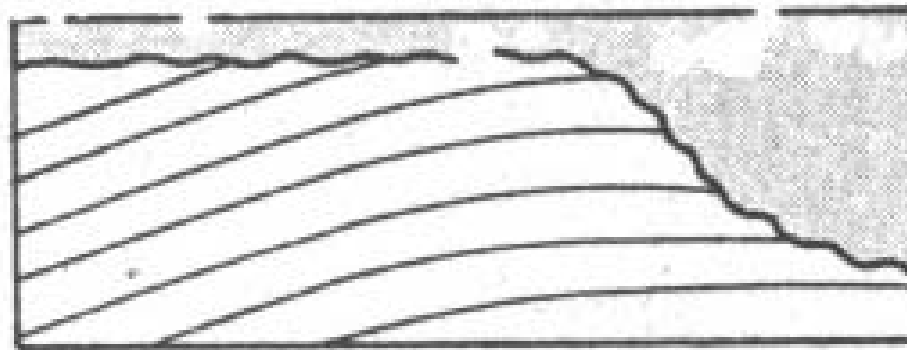
Toplap: Termination against the upper boundary of a depositional unit (sequence). Initially inclined layers, such as prograding units, are characterized by toplap. An asymptotic convergence against the upper boundary may exist but is difficult to identify in seismic data.

Hiatus caused by non-deposition



Erosional Truncation: Termination against the top of a depositional unit (sequence) caused by erosion.

It is not always easy to distinguish between truncation and toplap. The layers beneath an erosive surface often show parallel bedding, while toplap structures are sometimes characterized by asymptotic convergence against the unconformity.



1. EROSIONAL TRUNCATION

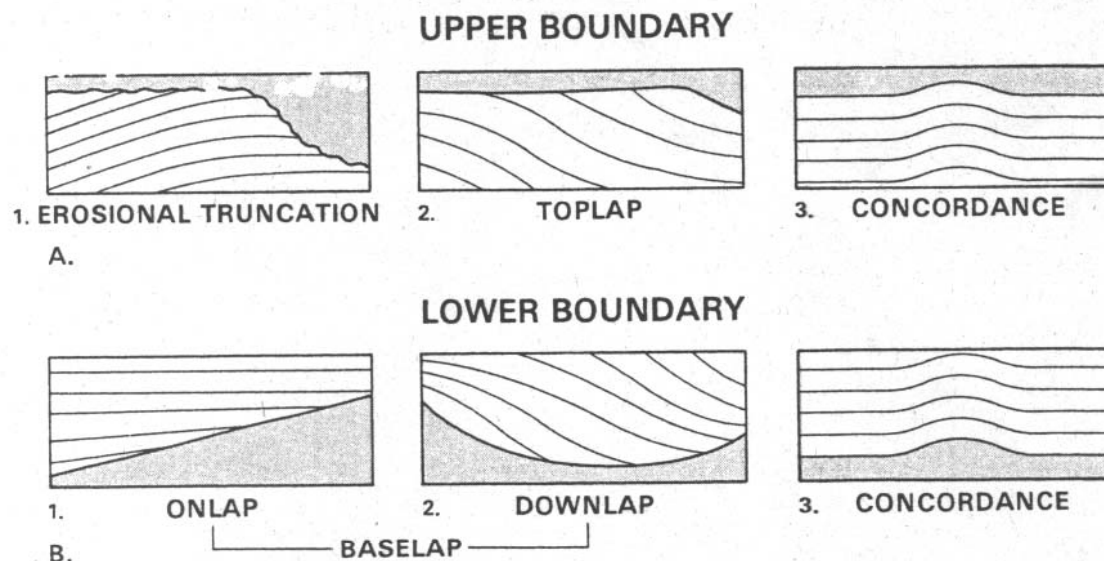


FIG. 2—Relations of strata to boundaries of depositional sequences:

A. Relations of strata to upper boundary of a sequence. **A1.** Erosional truncation: strata at top of given sequence terminate against upper boundary mainly as result of erosion (e.g., tilted strata terminating against overlying horizontal erosion surface, or horizontal strata terminating against later channel surface). **A2.** Toplap: initially inclined strata at top of given sequence terminate against upper boundary mainly as result of nondeposition (e.g., foreset strata terminating against overlying horizontal surface at base-level equilibrium where no erosion or deposition took place). **A3.** Top-concordance: relation in which strata at top of given sequence do not terminate against upper boundary.

B. Relations of strata to lower boundary surface of a sequence. **B1.** Onlap: at base of sequence initially horizontal strata terminate progressively against initially inclined surface, or initially inclined strata terminate updip progressively against surface of greater initial inclination. **B2.** Downlap: at base of sequence initially inclined strata terminate downdip progressively against initially horizontal or inclined surface (e.g., initially inclined strata terminating against underlying initially horizontal surface). **B3.** Base-concordance: strata at base of sequence do not terminate against lower boundary.

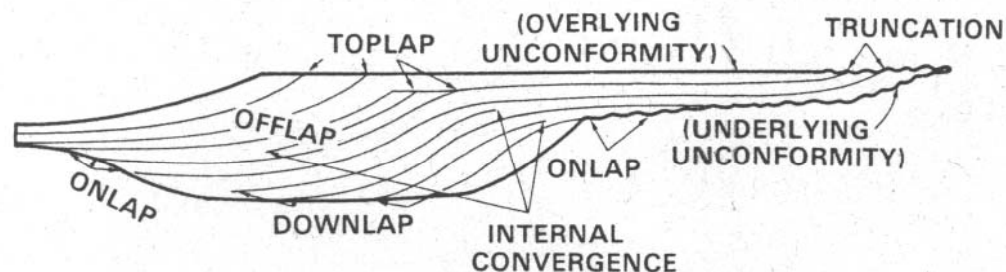


FIG. 1—Seismic stratigraphic reflection terminations within idealized seismic sequence.



Always describe terminations
above and below an
unconformity.

A hiatus usually increases in
one direction.

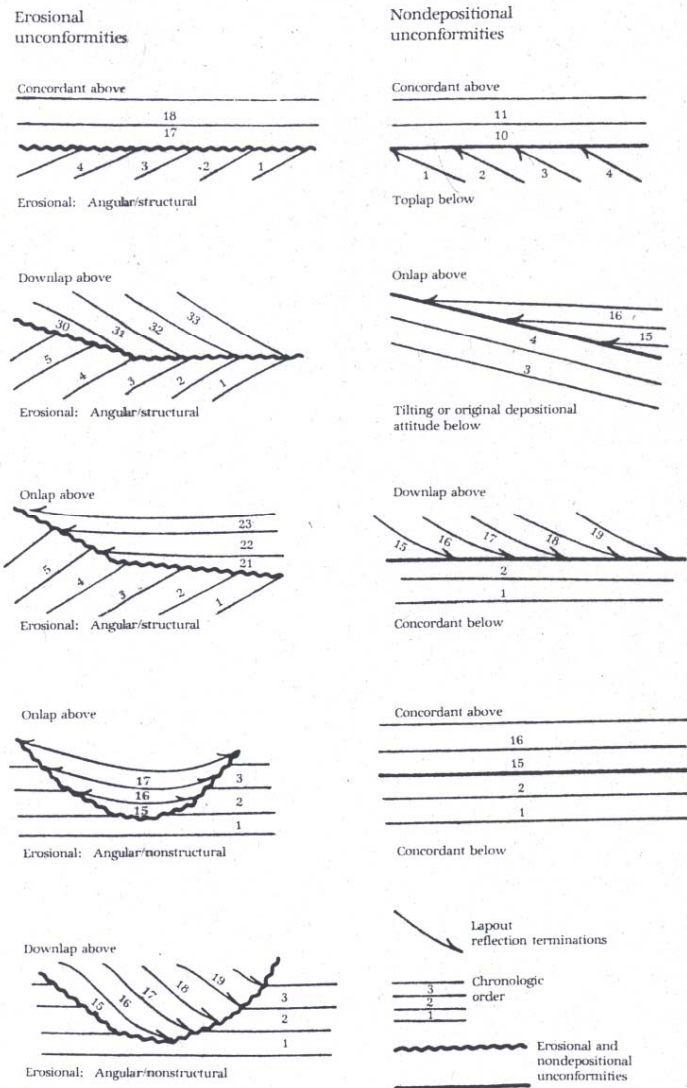


FIGURE 4.16 Seismic reflection configurations that define unconformities. Reprinted by permission of the AAPG from Brown and Fisher, 1980, fig. 46, p. 82.



Acoustic Imaging Seismic Interpretation

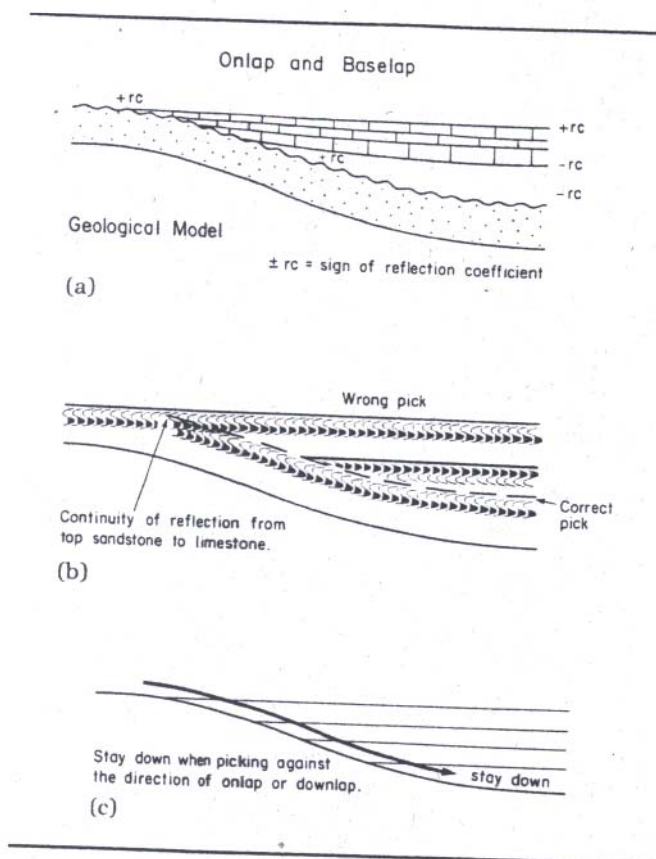


FIGURE 7.14 Picking criterion—onlap and downlap. (a) Geological model: A sandstone of intermediate acoustic impedance is onlapped by shales of low acoustic impedance, and limestone of high acoustic impedance. The reflection coefficient signs are indicated on the diagram. (b) Seismic expression: The top sand reflection, the sequence boundary defined by the onlap, changes polarity due to the varying reflection coefficients between the sandstone, limestone, and shale. The apparent continuity between the top sand and top limestone reflections is a potential trap for the unwary interpreter. (c) A general rule when following an onlapped sequence boundary is to stay down when picking against the onlap direction.

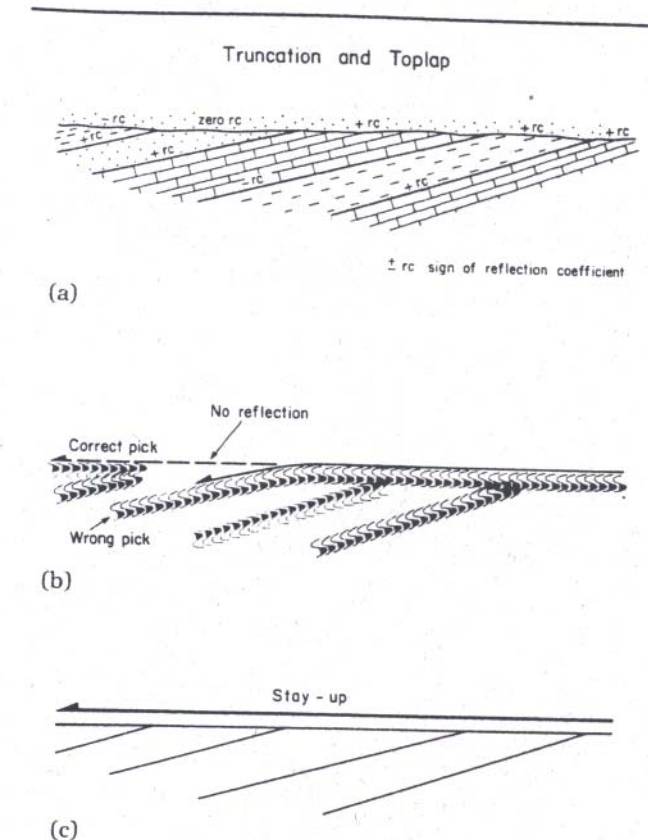
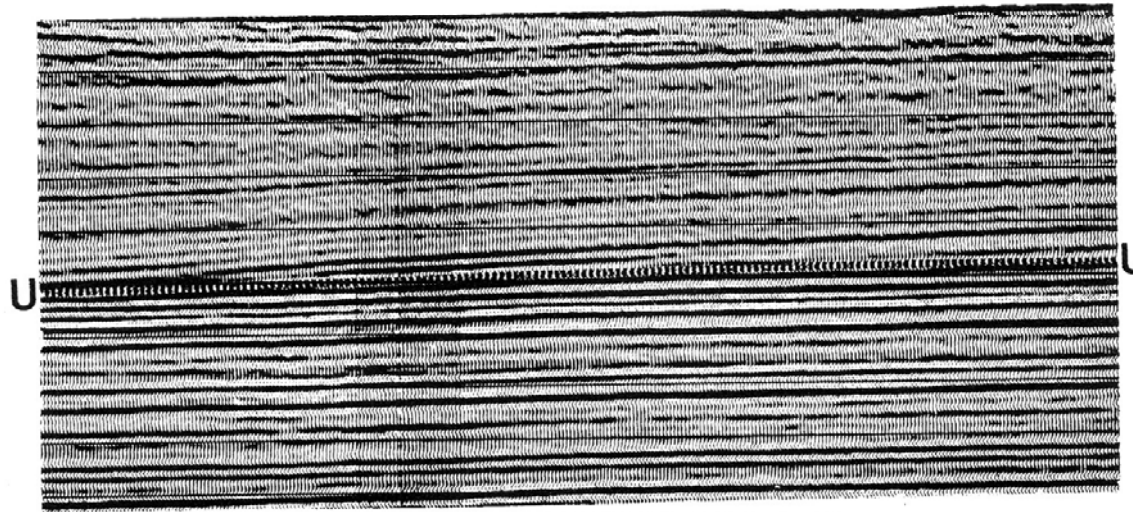


FIGURE 7.15 Picking criterion—toplap and truncation. (a) Geological model: An interbedded sequence subcrops an unconformity overlain by a sand. Signs of the reflection coefficient are indicated. There is no acoustic-impedance contrast between the sands. (b) Seismic expression: The unconformity has a positive reflection coefficient to the right, no reflection where it is subcropped by sand, and a negative reflection coefficient to the left. A potential interpretation pitfall would be to take the unconformity pick along the top limestone reflection. (c) A general rule when following a surface in the direction of truncation or toplap direction is to stay high.

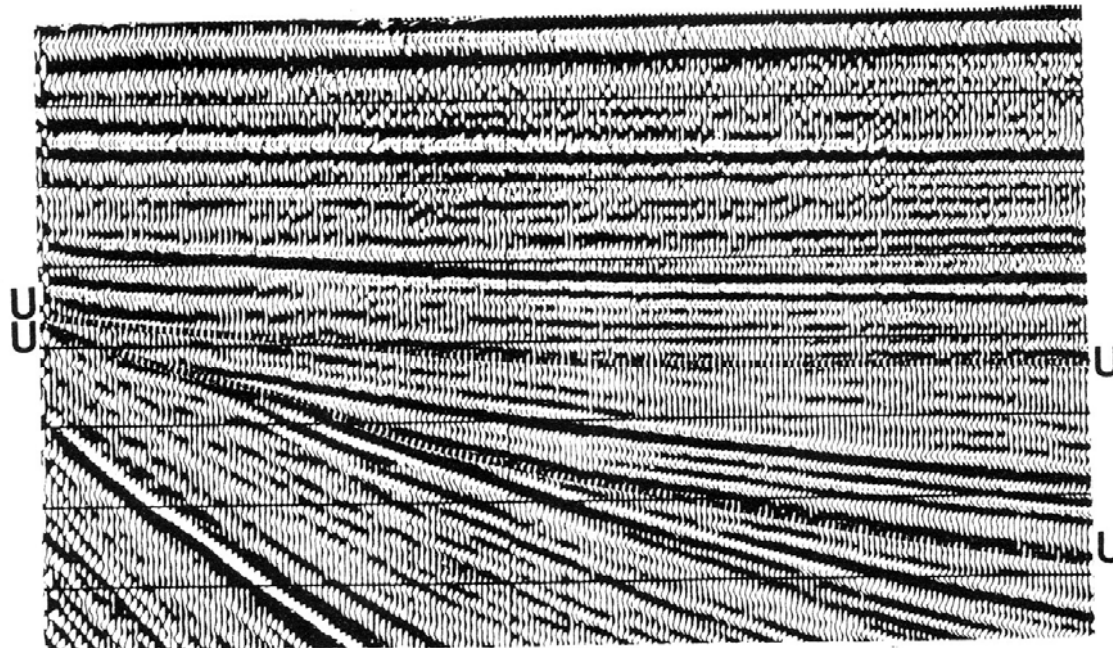


future ocean
KIEL MARINE SCIENCES

Acoustic Imaging Seismic Interpretation



Downlap
concordant



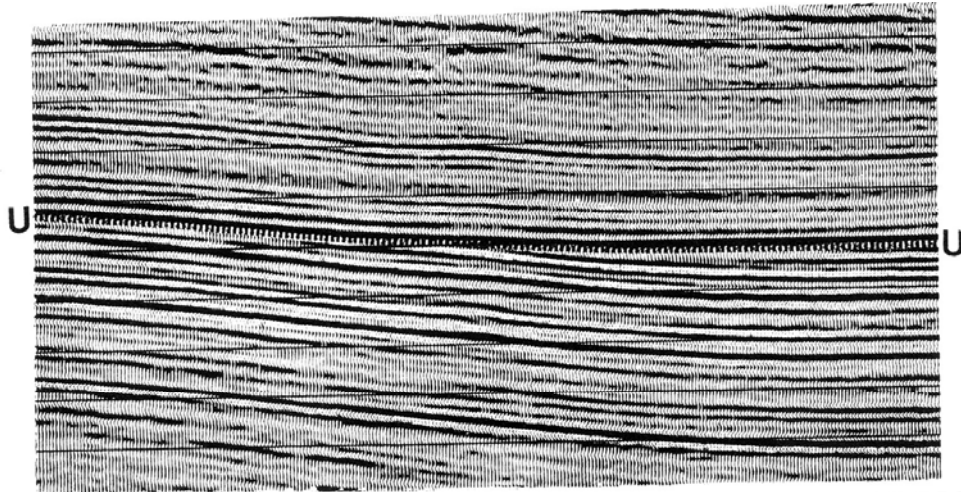
Onlap (difficult to see)
Truncation
Onlap
Truncation



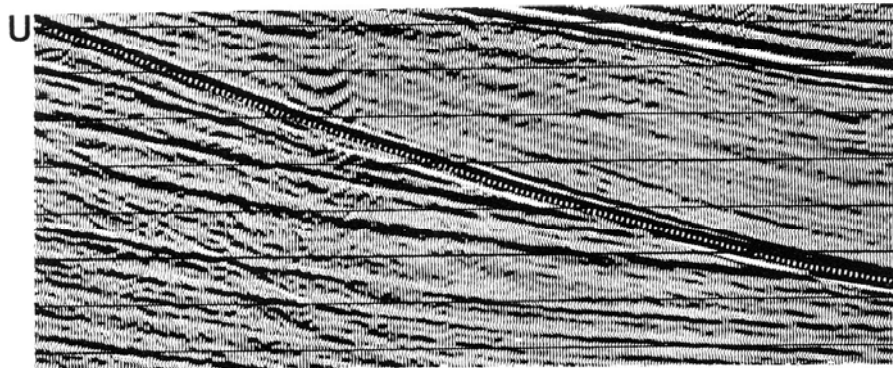
future ocean
KIEL MARINE SCIENCES

Acoustic Imaging

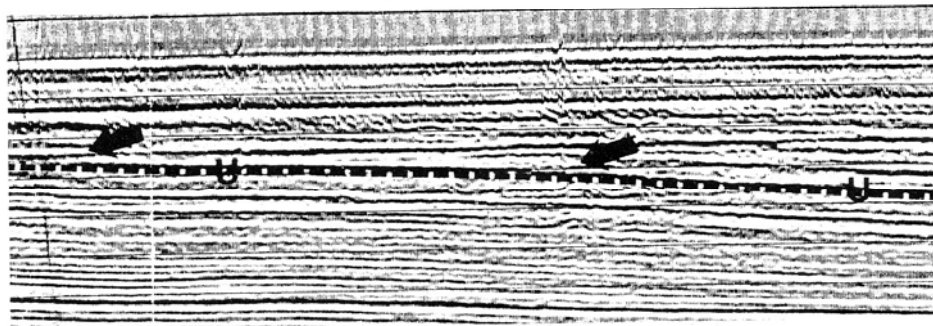
Seismic Interpretation



concordant
Toplap



concordant
Truncation



Baslap (onlap oder downlap)
concordant

Sea level fluctuations: A typical application of seismic stratigraphie

Relative rise of sea level:

- Rising sea level and stationary, subsiding or slower rising sea floor.
- Stationary sea level and subsiding sea floor.
- Falling sea level but faster subsiding sea floor.



A relative rise of sea level is indicated by coastal onlap.

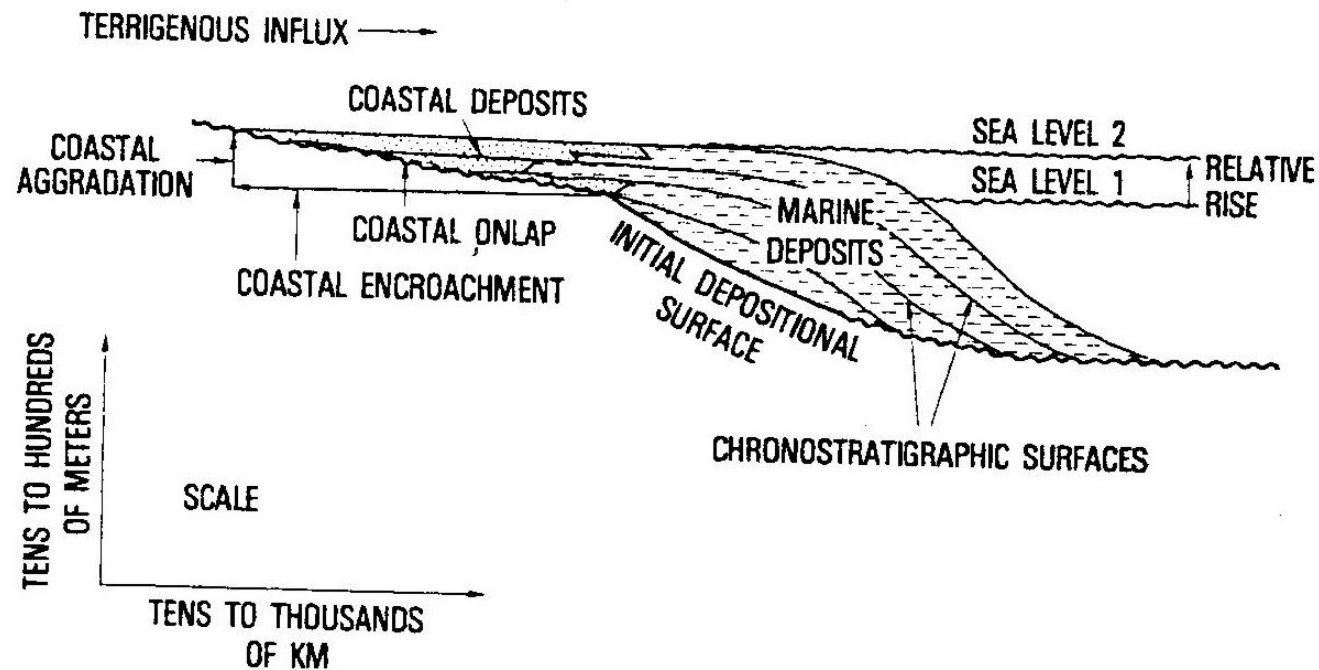


FIG. 2—Coastal onlap indicates a relative rise of sea level. Relative rise of base level allows coastal deposits of a maritime sequence to aggrade and onlap initial depositional surface.



A rising sea level does not imply a transgression!

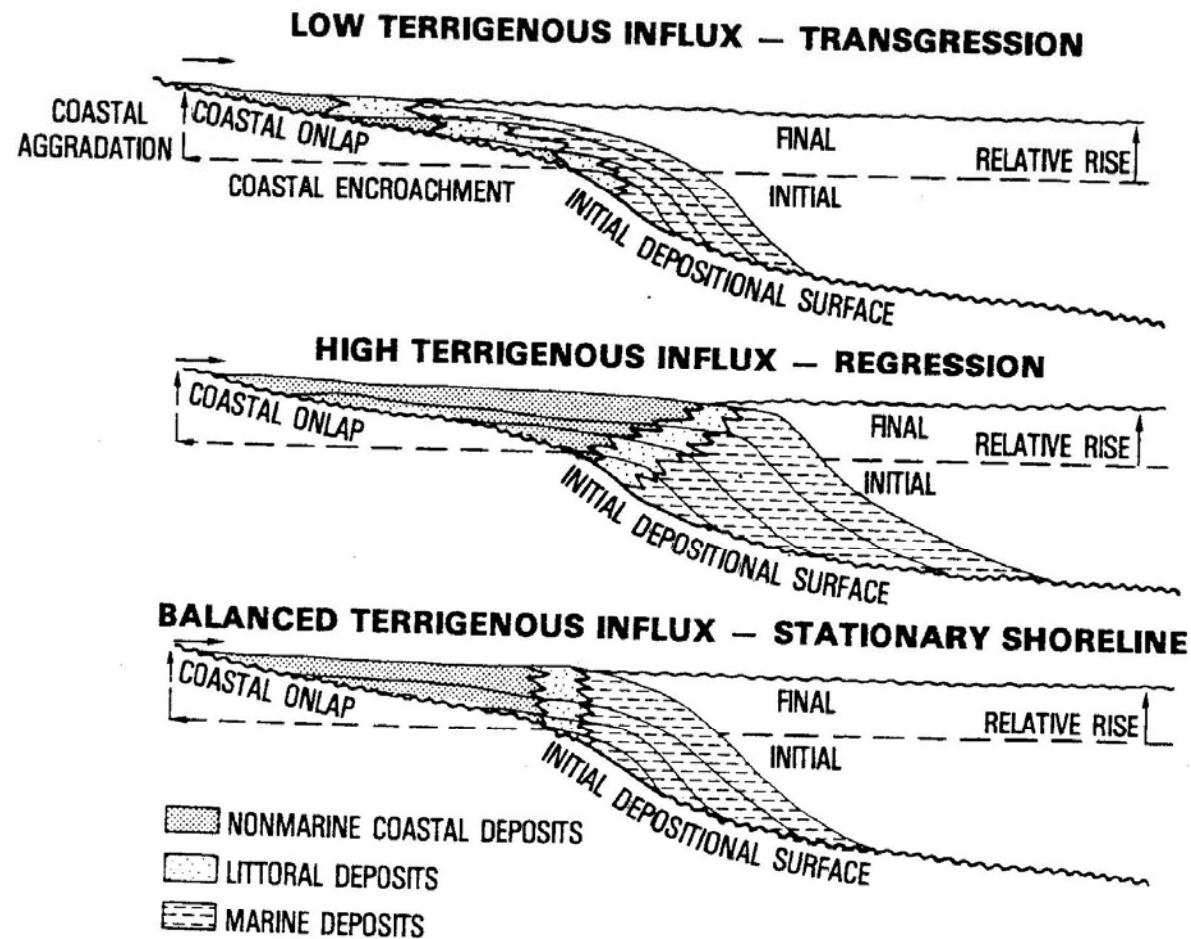


FIG. 3—Transgression, regression, and coastal onlap during relative rise of sea level. Rate of terrigenous influx determines whether transgression, regression, or stationary shoreline is produced during relative rise of sea level.

A **stationary sea level** causes prograding sequences (clinoforms) =>
Toplap

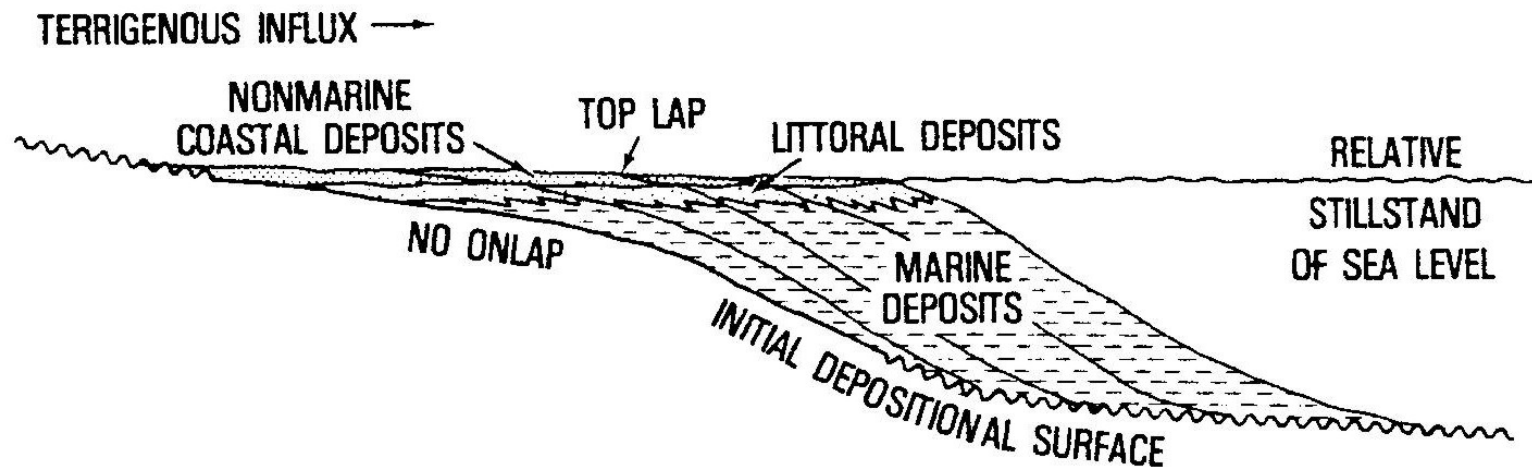


FIG. 6—Coastal toplap indicates relative stillstand of sea level. With no relative rise of base level, nonmarine coastal and/or littoral deposits cannot aggrade, so no onlap is produced; instead, by-passing produces toplap.



A falling relative sea level causes a downward shift of coastal onlaps.

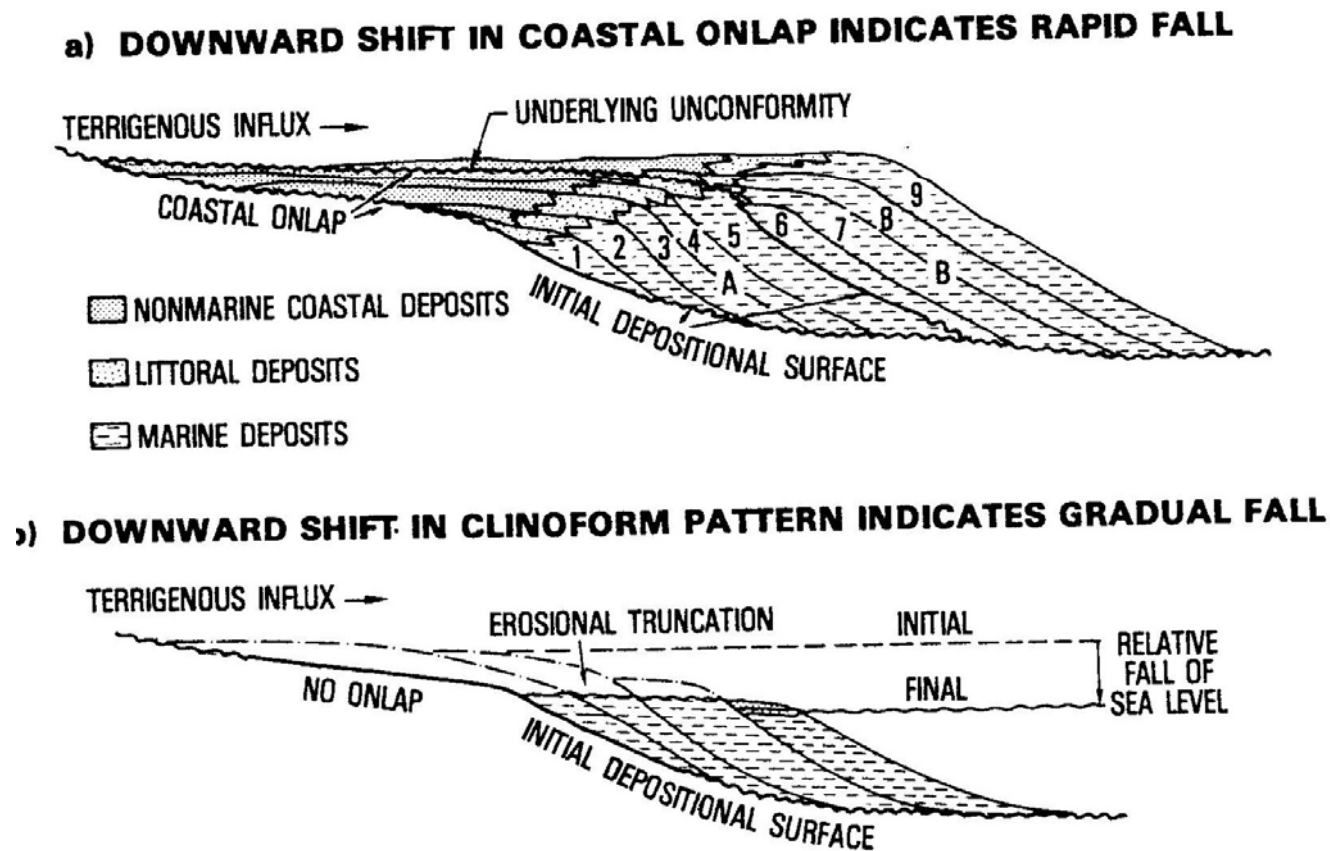


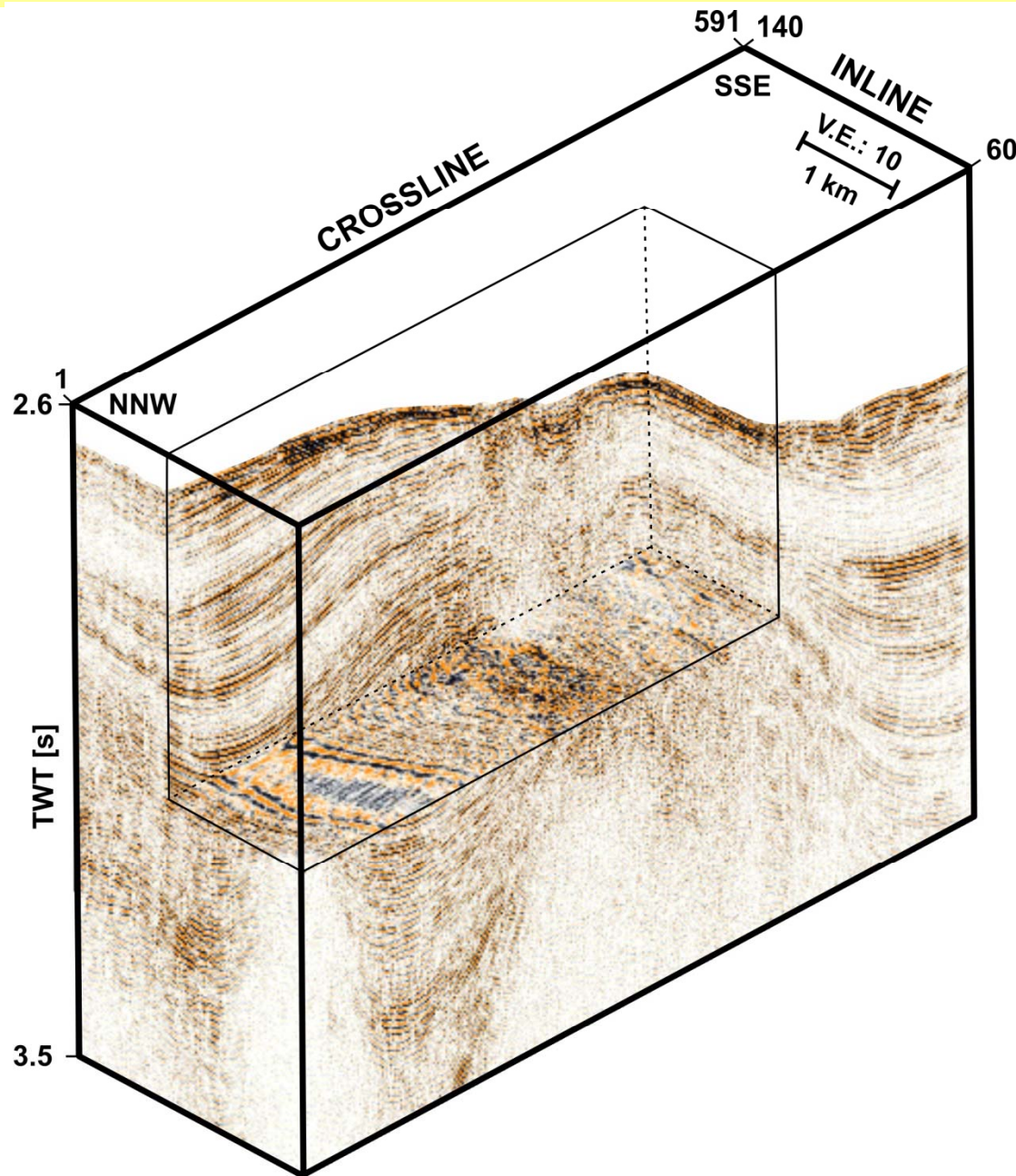
FIG. 8—Downward shift of coastal onlap indicates relative fall of sea level. With relative fall of base level, erosion is likely: deposition is resumed with coastal onlap during subsequent rise. (a) Downward shift in coastal onlap indicates rapid fall observed in all cases studied so far. (b) Downward shift in clinoform pattern (after Weller, 1960), indicates gradual fall; but has not been observed on seismic data.



future ocean
KIEL MARINE SCIENCES

Acoustic Imaging

Introduction to Kingdom



Aim:

Introduction to Kingdom Suite

Introduction in most important
program features using a real
seismic data

Interpretation of Seismic Data with Kingdom Suite

Kingdom Suite (Seismic Micro-Technology) is the market share leader for Windows-based seismic interpretation software.

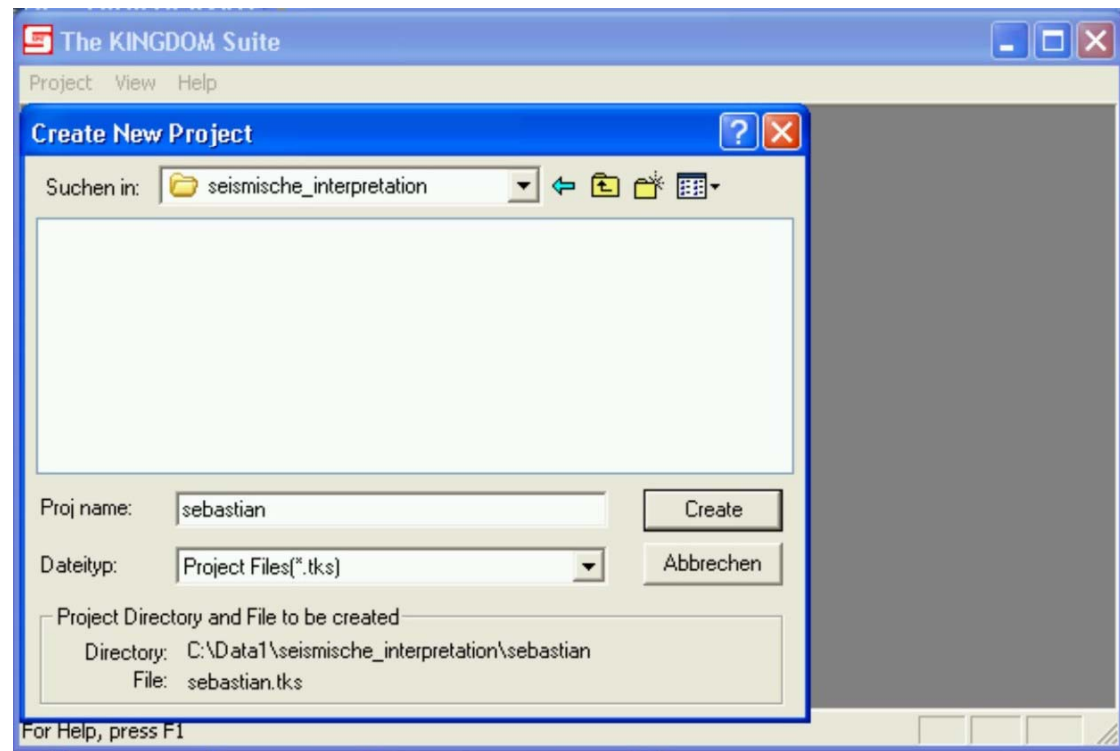
SMT Educational Gifts Program

The goal of SMT's Educational Gifts Program is to put workstation software in the classroom so those students graduating from universities are equipped for the job market with workstation experience. Our software is utilized for both teaching and research at the academic institutions shown below.

We can use Kingdom for education and research free of charge!!

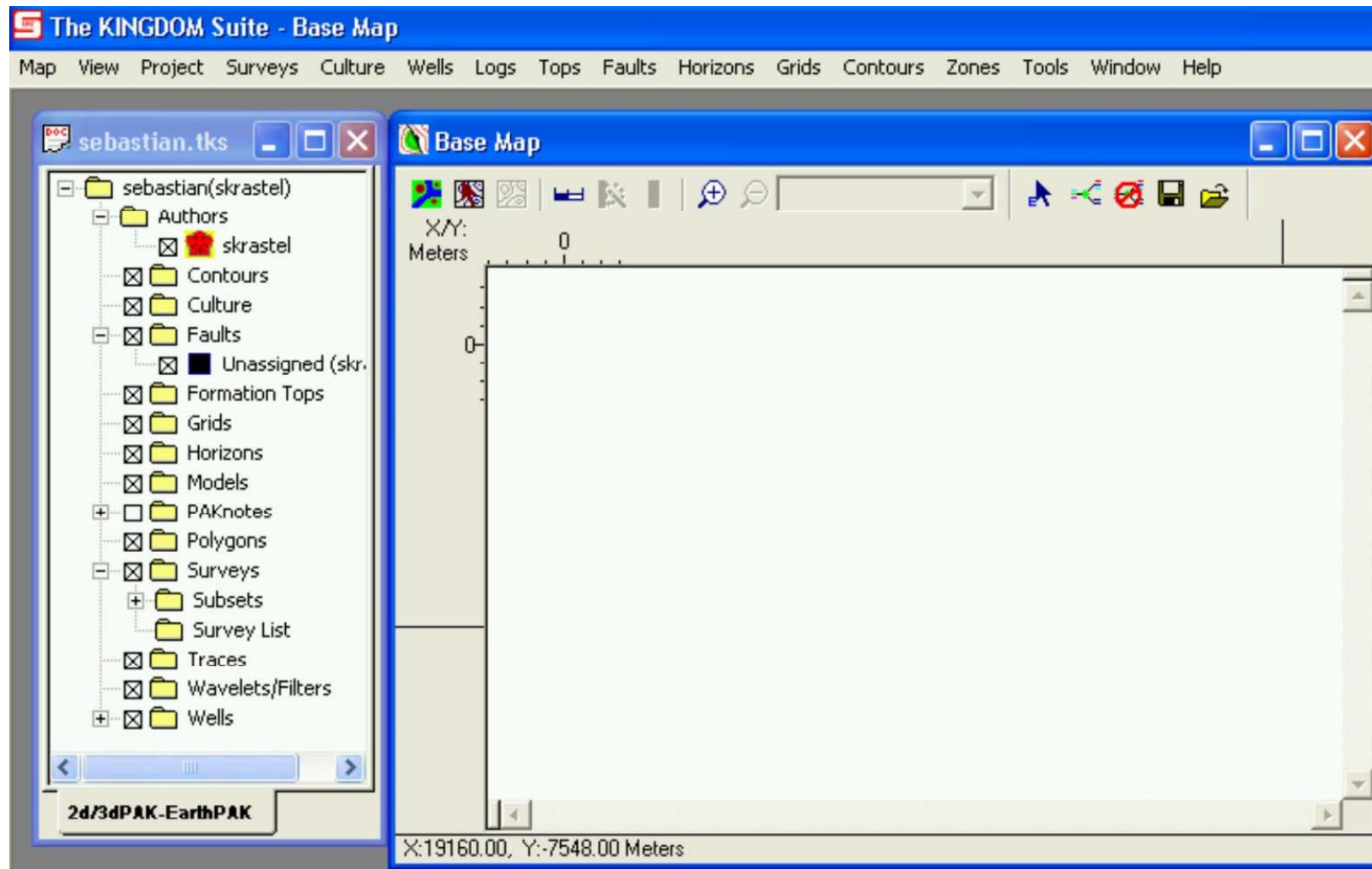
Project Management with Kingdom

Open Kingdom, Create a New Project



Use your name as Project-Author, Select any data base
Select ‚Meter‘ at the Window ‚Project Options‘ and confirm with ‚Yes‘
Do you want to use coordinate system of existing Project: No

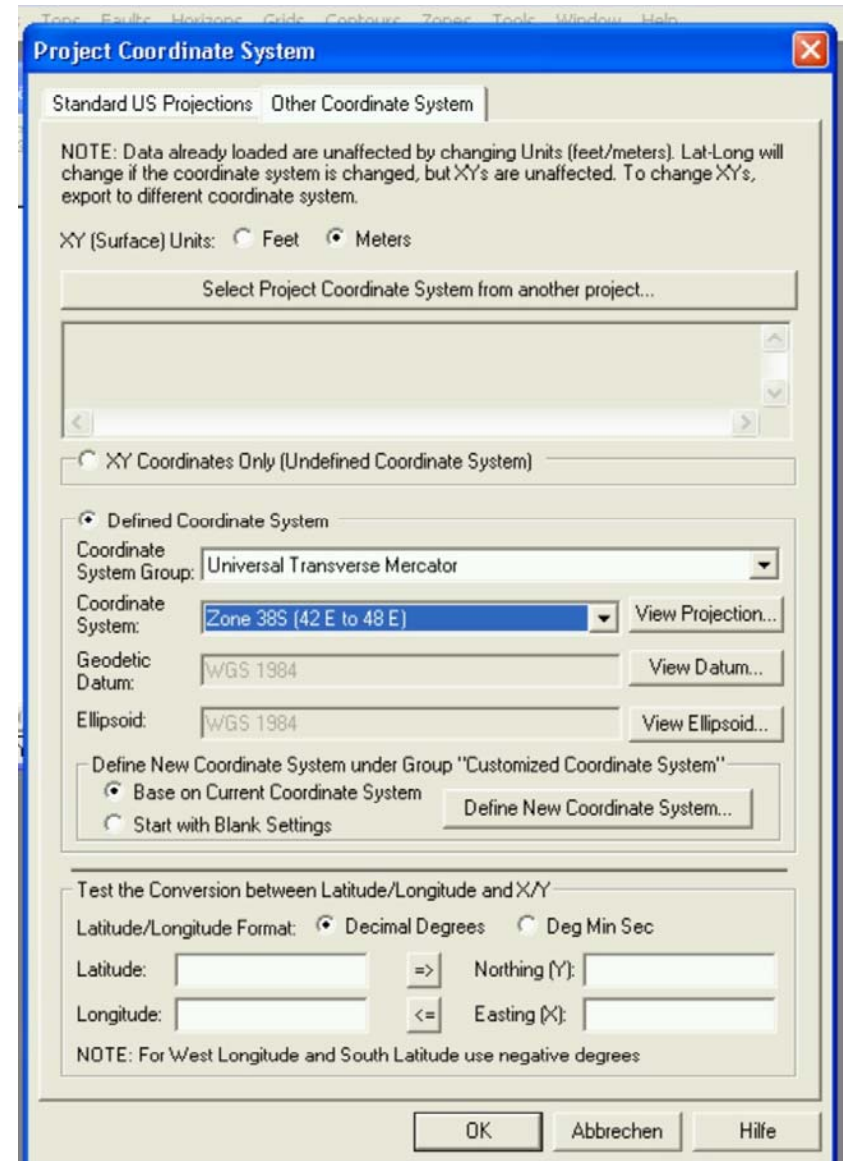
Thereafter you screen should look as below:



First of all we would like to select a projection.

Choose 'Project/xy-Projection-Method'

By default only Standard US Projections are visible. Choose Other Coordinate Systems. Select the UTM-Zone for 47N because it includes survey area. The Ellipsoid should be WGS84

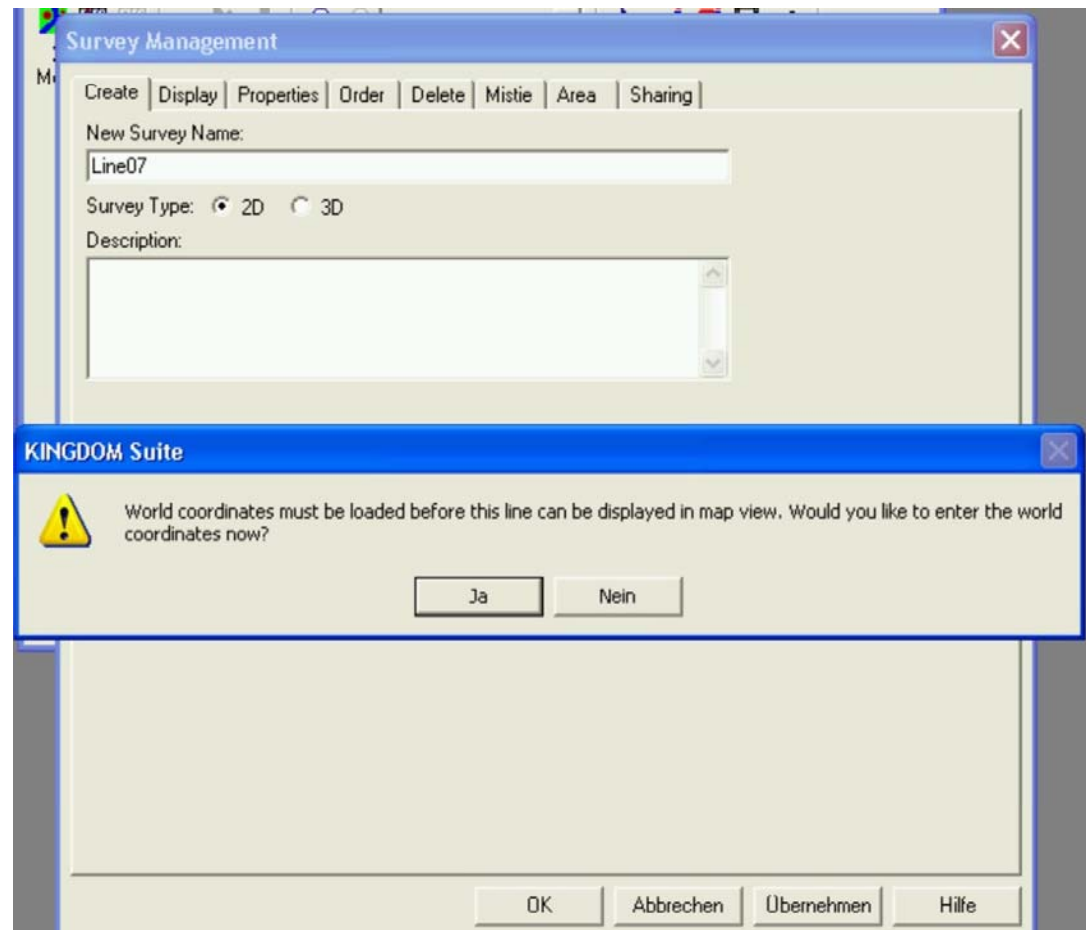


Now we want to load the processes seismic line. Each line is handled as survey by Kingdom.

Fore importing a seismic line, select ‚Survey management‘ form the menu ‚Survey‘. We want to create a new 2D-survey with the same name as the seismic line (Line 039).

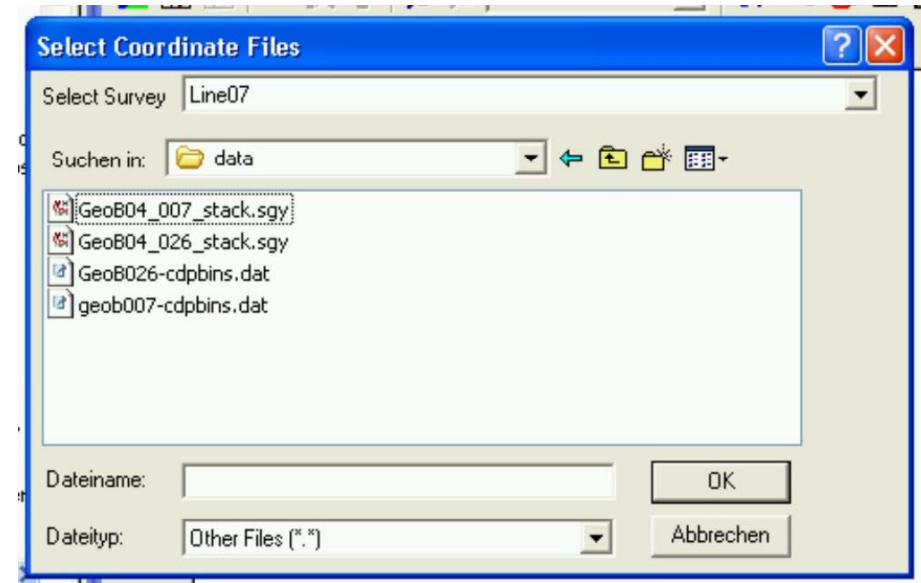
Now Kingdom would like to know, if we want to load coordinates. Answer this question with Yes.

If this question does not show up, choose
‘Surveys/Import World Coordinates/2D by File.



Select the coordinate files in the window shown to the left. The coordinate files do have the extension .Dat. Hence select *.* as file type. Select the coordinate file (here geob039_pos.dat).

Imported coordinates in meters':
answer with yes.





In this window, Kingdom would like to know, which columns should be interpreted.

The first columns represents the Shot_Point. The second column is not important. The third columns shows the longitude (in decimal degrees); the forth column the latitude.

Due to reasons I do not understand, you need to select the coordinate system again (as described above).

Shot Point Data File: C:\Data1\seismische_interpretation\data\geob007-cdpbins.d

Lines to Skip: 0

Select an Item from the Selection List to Identify a Column in File Data

File Data

	Shot		Longitude	Latitude
1	2956		42.67085	38.487732
2	2957		42.671028	38.487727
3	2958		42.671198	38.487736
4	2958		42.671364	38.487772
5	2959		42.671518	38.487829
6	2960		42.671666	38.487897
7	2960		42.671797	38.487985

Selection List

<input type="checkbox"/> Line_Name	Char
<input checked="" type="checkbox"/> Shot_Point	Float
X	Double
Y	Double
Degrees Latitude	Float
Minutes Latitude	Float
Seconds Latitude	Float
Latitude Direction (N or S)	Char
Degrees Longitude	Float
Minutes Longitude	Float
Seconds Longitude	Float
Longitude Direction (E or W)	Char
<input checked="" type="checkbox"/> Latitude Decimal Degrees	Double
<input type="checkbox"/> Latitude Decimal Direction (N or S)	Char
<input checked="" type="checkbox"/> Longitude Decimal Degrees	Double
<input type="checkbox"/> Longitude Decimal Direction (E or W)	Char

Deselect All

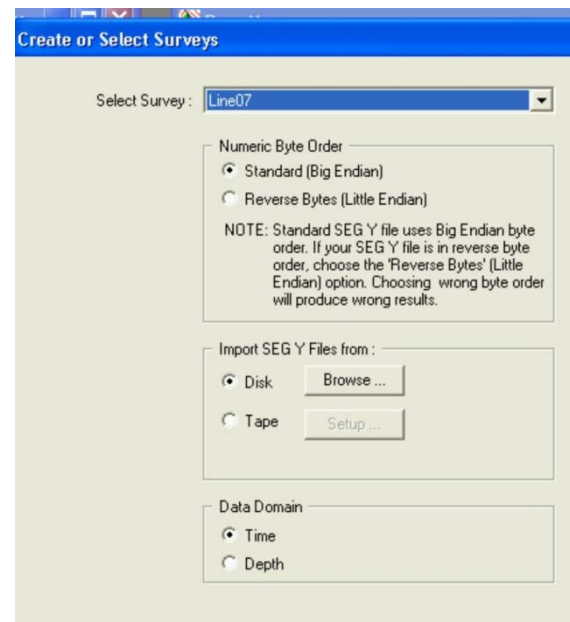
Load Template... Save Template...

OK Cancel Help

Afterwards Kingdom would like to know if you want to load SEG Y-data. Answer with ,No‘.

We will load the SEG Y-Data via the ,Survey‘ –Menu. Select ,Import SEG Y‘

Click OK for the next window. Make sure that the correct survey is selected in the window shown to the left. Click at Import SEG Y and select the SEG Y-file belonging to the selected survey.

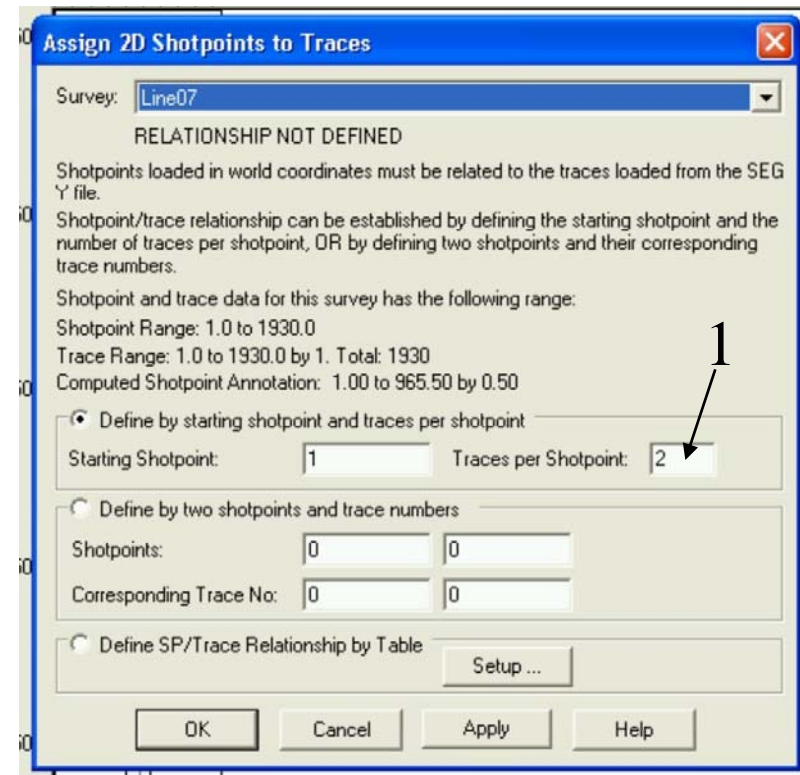


Click OK until you see the following window.

Set: ,Define by starting shot point and set ‘traces per shot‘ to 1.

Afterwards you should see your line in the base map with plenty of annotations.

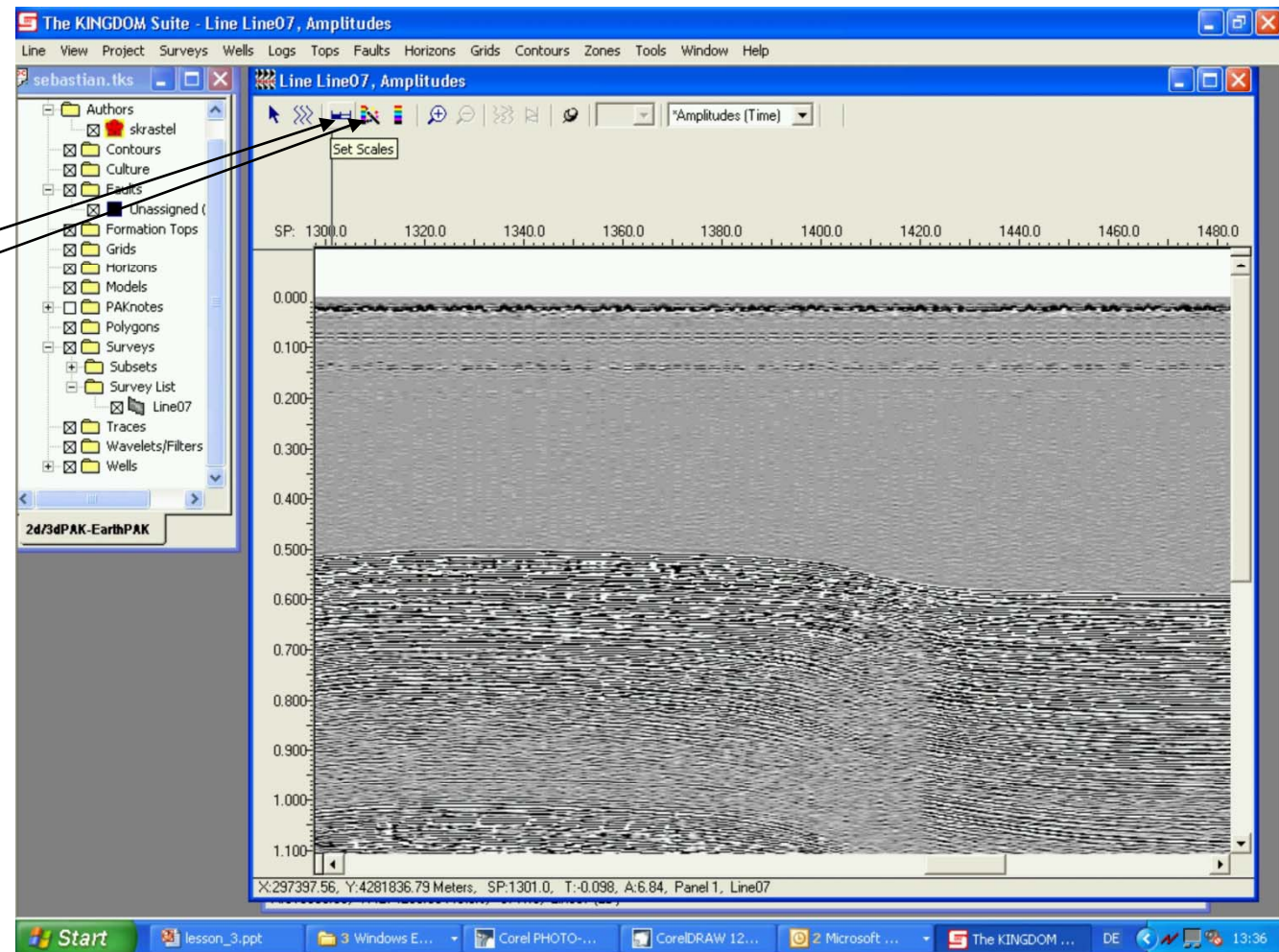
For getting ‘nicer’ annotations, click with the right-hand mouse bottom on the line in the Map-View and select ‘Survey Annotation’. Select a proper annotation. Apply annotations to all 2D-Surveys.



For Displaying the line, click with right-hand mouse button on the Map-View and select ‚Display 2D-Line‘ or double click on the line in the project-window.

The image usually needs some improvement. Try to select a proper scale, select a different capture, and vary the gain using F5 and F6.

What do we see on the line?

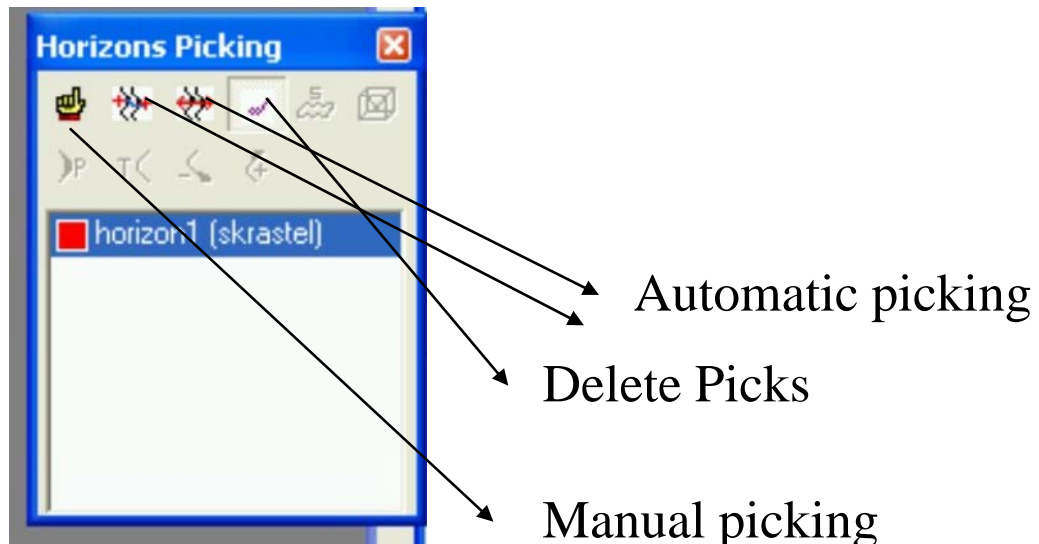


Now we want to continue with Kingdom-Project of the entire Mass Survey. Close your current Kingdom-Project and open the Kingdom-Project provided today.

Have a look at the data set. What features do you identify?

We would like to pick a few horizons. Select ,Horizon/Horizon Management‘ and name your first reflector to pick.

To ensure picking you need to set ,Horizon Picking‘ in the menu under view/toolbars. Then you should see the following window.

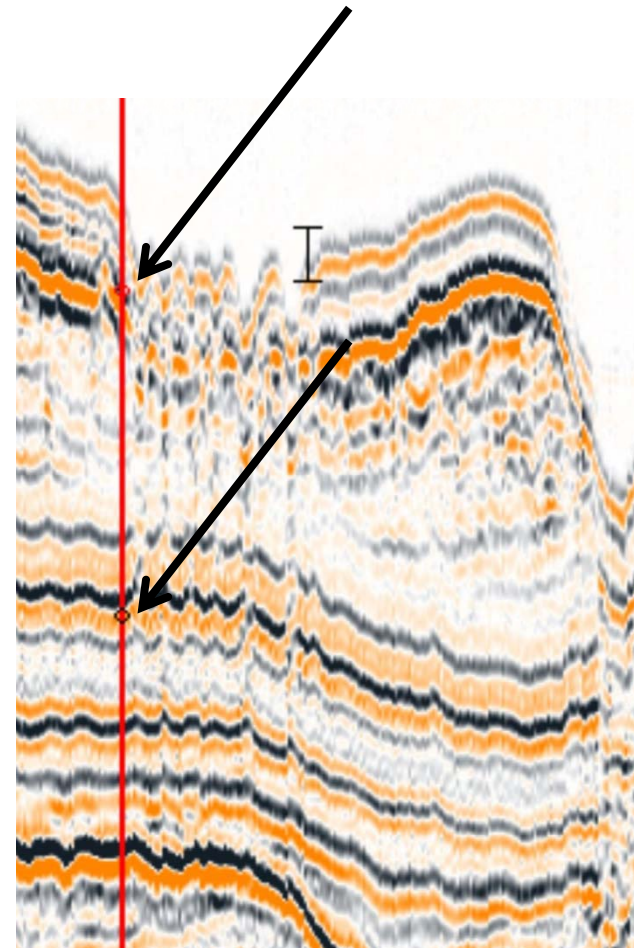


Try automatic picking (especially 2D-hunt). You can modify the parameters for automatic picking at ,Horizons/picking Parameters‘. Reduce the numbers for Length (time and depth). Also check differences between different picking modes (Peak, Trough ect)

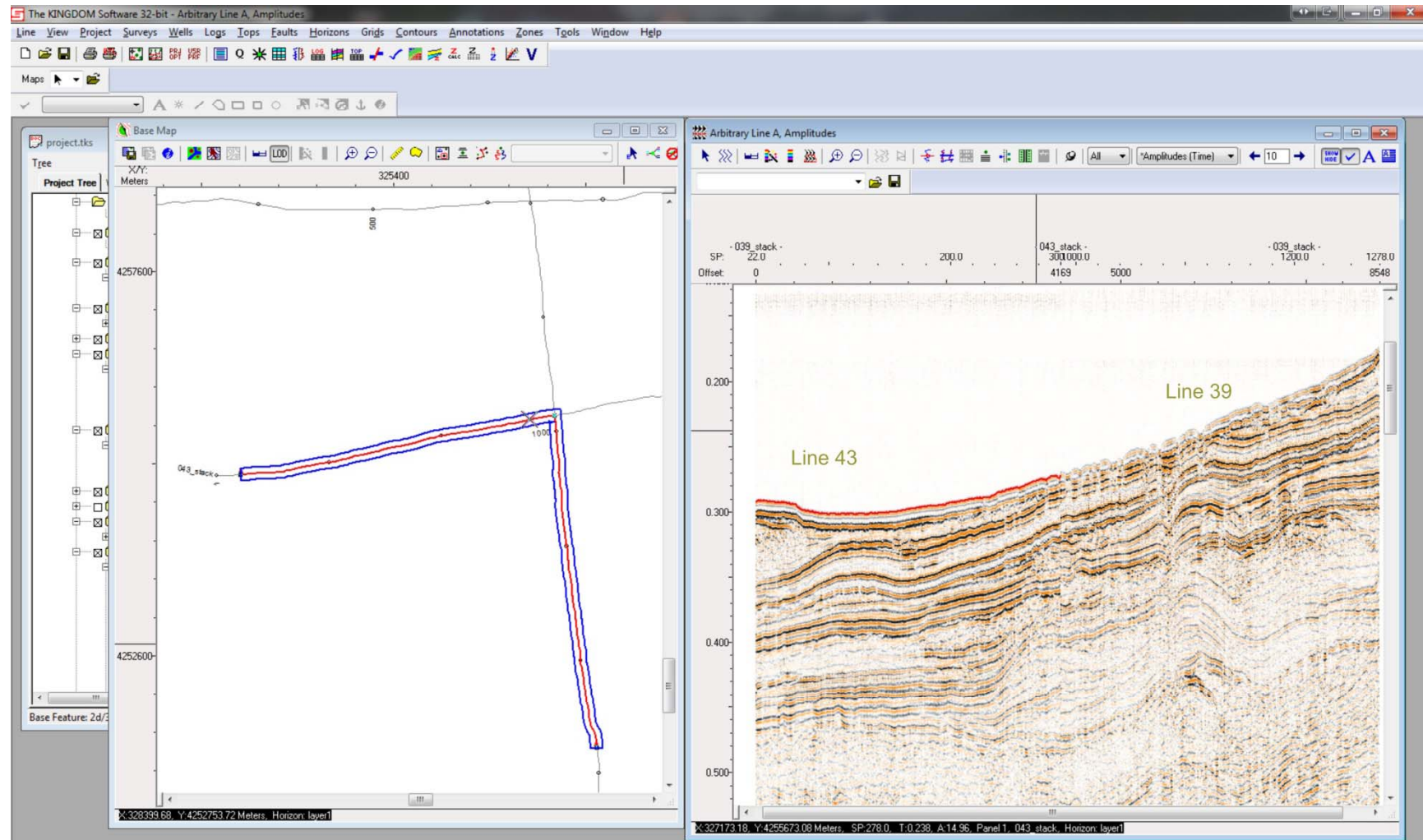
Try to pick the same reflector on all profiles.

There are numerous tools supporting correlation between profiles:

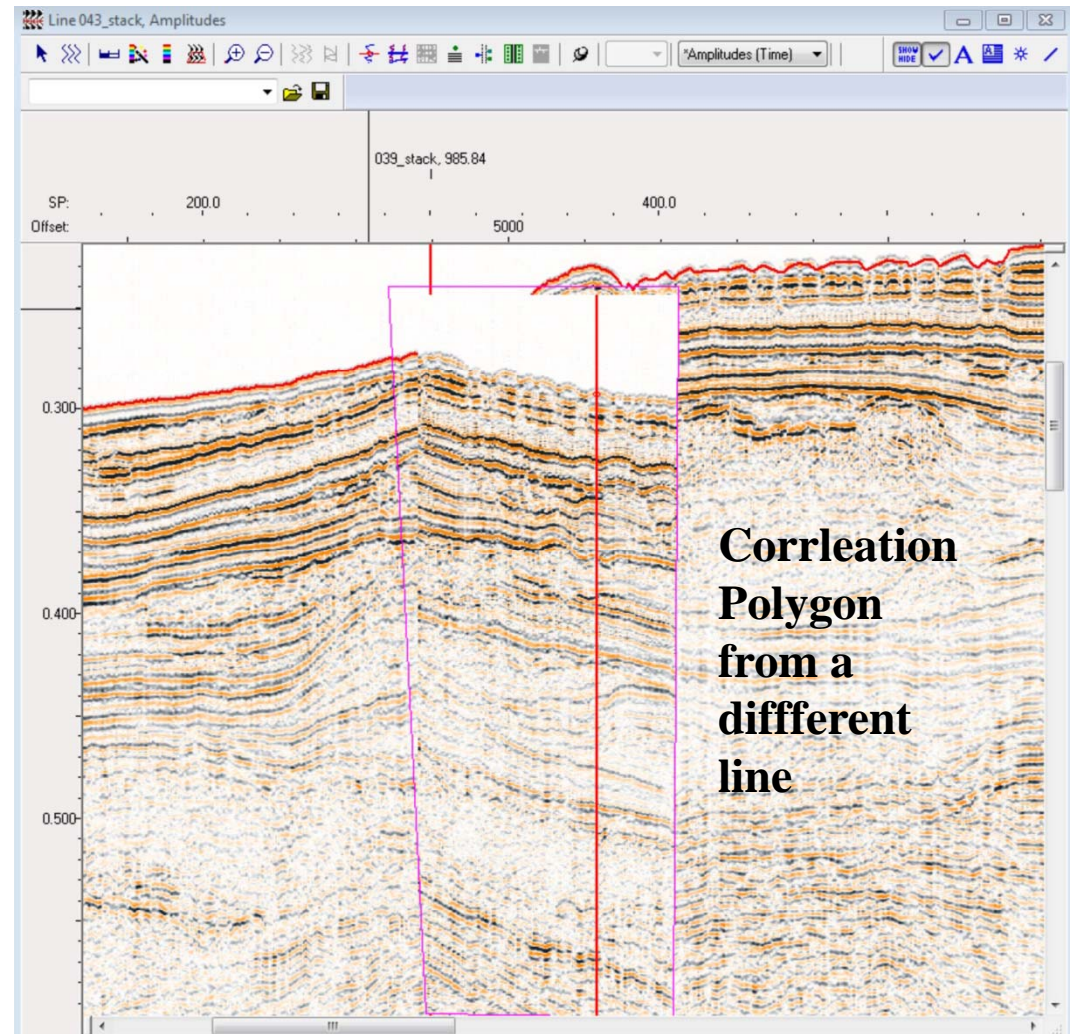
1) Picks on one line are shown as little circles at the intersection with other lines.



2) You can display crossing lines continuously by clicking the right-hand mouse button on the base map and selecting 'Digitize Arbitrary lines/Single across 2D surveys only'.

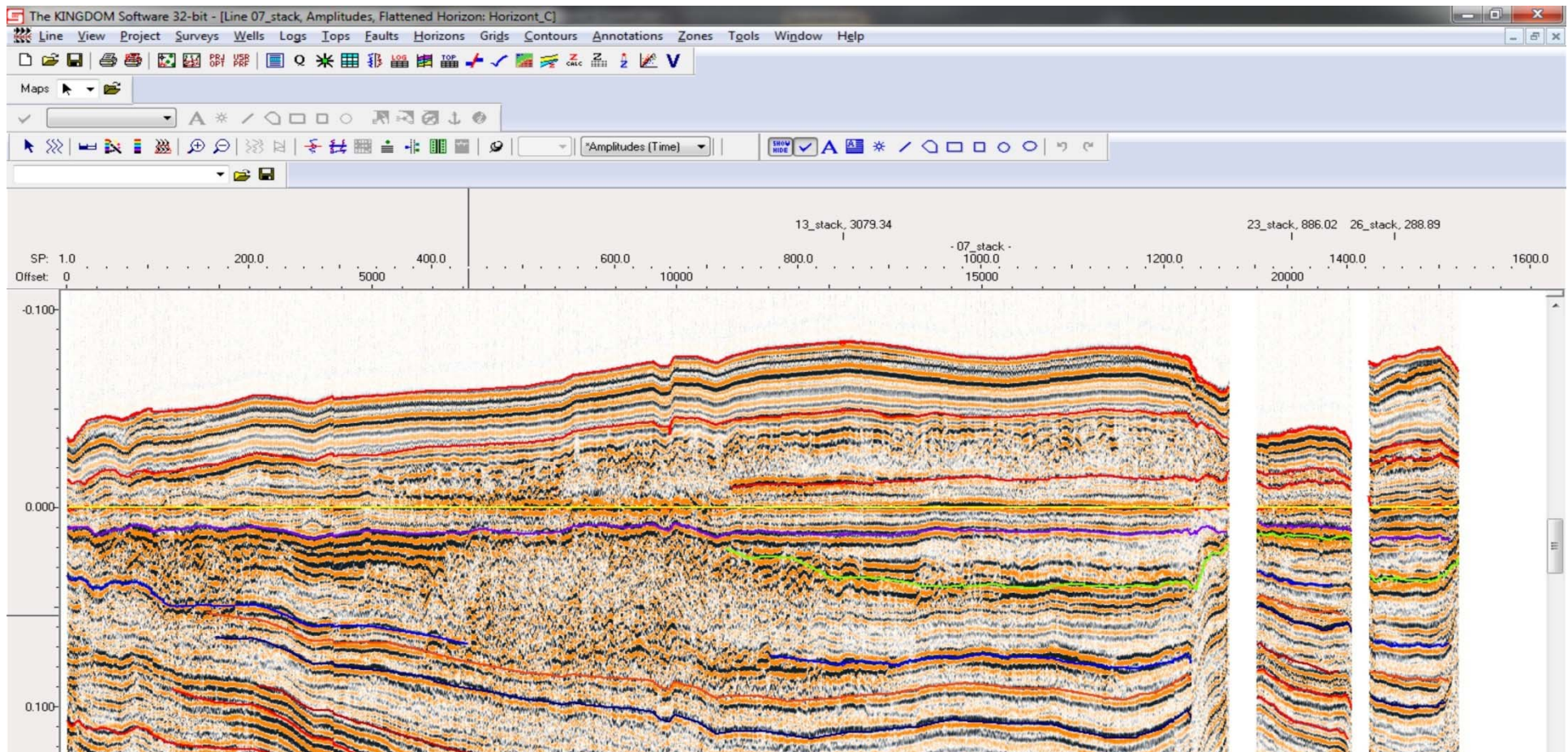


3) You can copy selected parts of a profile and paste this part to any other profile for comparison. Choose 'Tools/Correlation Polygon' and Digitize your correlation Polygon. You can move it around on the line or copy (STRG C) and (STRG V) paste it to other lines.



Some other useful features in Kingdom

Flatten horizons: Select 'Horizons/Flatten or Unflatten'. Follow the instructions.



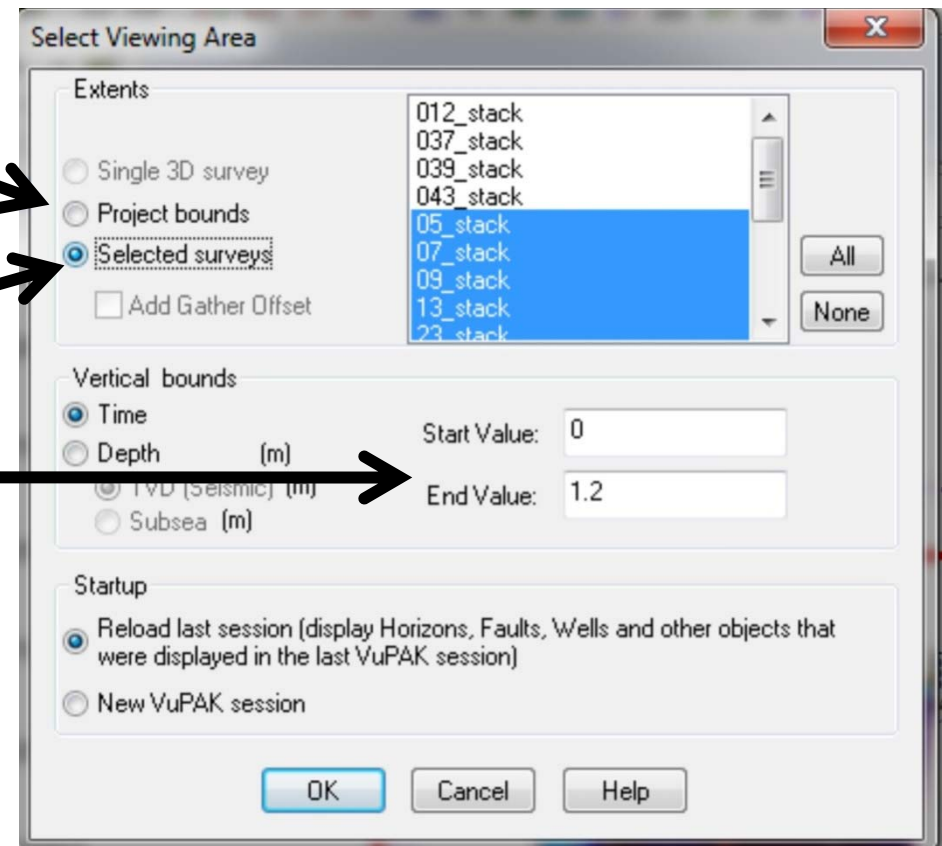
VUPak: Create 3D-Plots

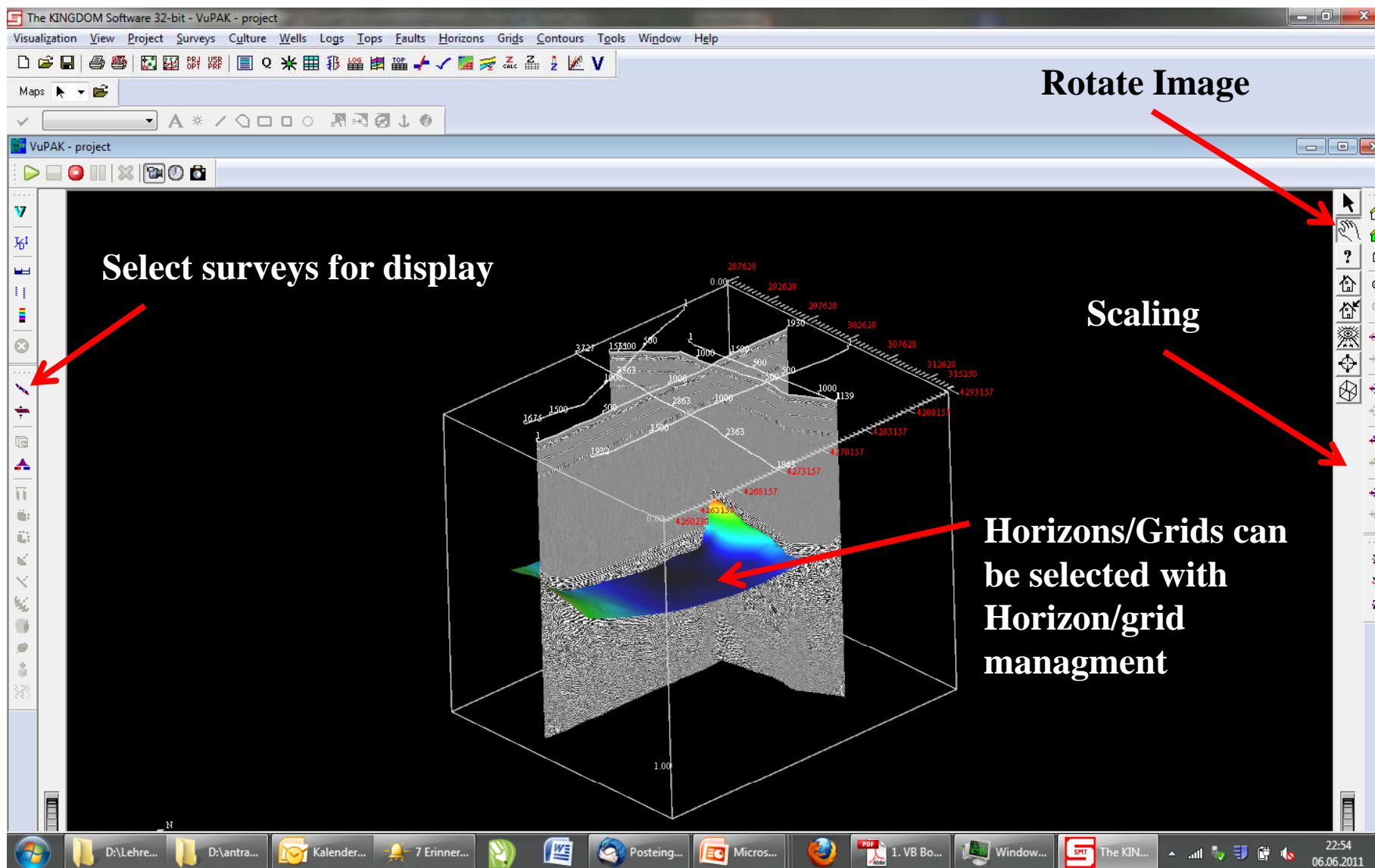
Select ,Project/VUPak‘

Select or digitize your
project bounds

Make sure to select the surveys,
Which might be displayed‘

Select the time bounds





Generic Mapping Tools (GMT)

Used since 1988 (in house software at Lamont-Doherty Earth Observatory)

1991: First official release as public domain software

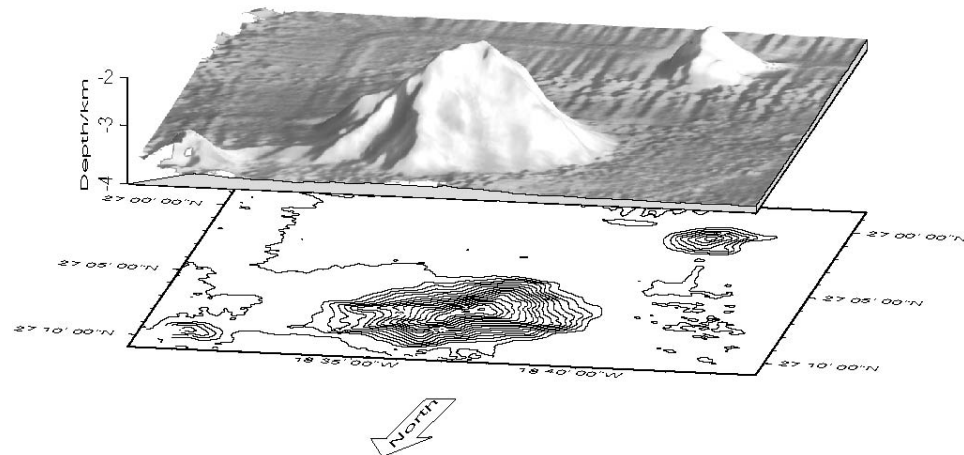
Used to manipulate columns of tabular data, time-series, and gridded data sets, and display these data in a variety of forms

Script language (same syntax as Unix)

GMT uses PostScript as output format

GMT includes more than 50 tools

Las Hijas Seamounts

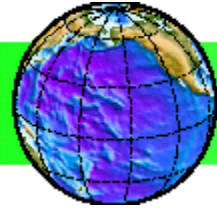




future ocean
KIEL MARINE SCIENCES

Acoustic Imaging

GMT



THE GENERIC MAPPING TOOLS

Generic

Projections, Visualization,
Filtering, Gridding

Mapping

Ca. 30 projections and
transformations

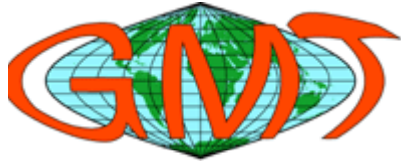
Tools

Ca. 60 commands

Operating systems: Unix, Linux, Windows

License: Public Domain, GNU General Public License

Homepage: gmt.soest.hawaii.edu



Installations for Windows

-Download von: <ftp://ftp.geologi.uio.no/pub/gmt/windows> or
https://ftp.ifm-geomar.de/users/skrastel/submarine_mapping/

- GMT_basic_install.exe (GMT-commands)
- GSHHS_highfull_install.exe (high-res coastlines)
- GMT_pdf_install.exe (PDF-documentation)
- Ghostview (Visualization of postscript)

Install all files

- Configure `/gmtfolder/share/conf/gmt.conf`

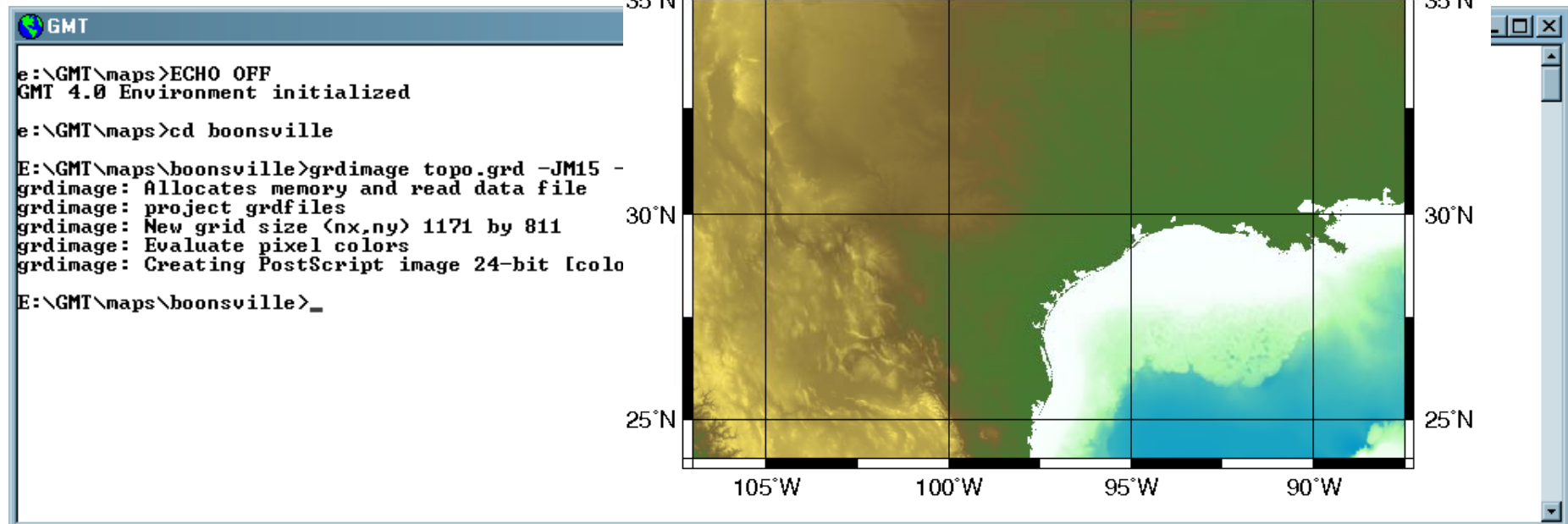
Content of gmt_folder\share\conf\gmt.conf

```
SI      <- Set to SI or US
#       $Id: gmt.conf.orig,v 1.1 2001/01/03 02:11:56 pwessel Exp $
#
#       GMT configuration file
#
#       !! MUST contain either the word SI or US
#       !! in the first 2 columns of the first record
...
```




How does it work?

- Command-line usage
- Parameters are set via option keys
- Output is *Postscript*
- Layer-principal





Programs

Plotting

grdcontour
grdimage
grdvector
grdview
psbasemap
psclip
pscoast
pscontour
pshistogram
psimage
pslegend
psmask
psrose
psscale
pstext
pswiggle
psxy
psxyz

Filtering

blockmean
blockmedian
blockmode
filter1d
grdfilter

Trends

fitcircle
grdtrend
trend1d
trend2d

Coverision / Extracting

gmt2rgb
gmtconvert
gmtselect
grd2xyz
grdcut
grdblend
grdpaste
grdreformat
splitxyz
xyz2grd

Information

gmtdefaults
gmtset
grdinfo
minmax

Gridding

nearneighbor
surface
triangulate

Sampling

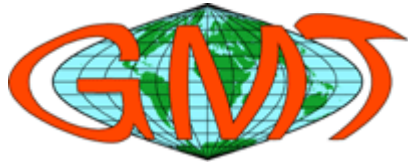
grdsample
grdtrack
sample1d

Projection and transformation

grdproject
mapproject
project

Miscellaneous

gmtmath
makecpt
spectrum1d
grd2cpt
grdclip
grdedit
grdfft
grdgradient
grdhisteq
grdlandmask
grdmath
grdvolume



Important Parameters

-J → Projectio / Scale

-R → Area/ Map area

-B → Frame annotations

-V → ,Verbose'-Mode

-O → Not the first command line of multiple postscript outputs

-K → Not the last command line of multiple postscript outputs

**Note!! A space is needed between individual parameters but no space when setting a specific parameter,
Upper and lower case letters do have different meanings !!**

The -K -O options

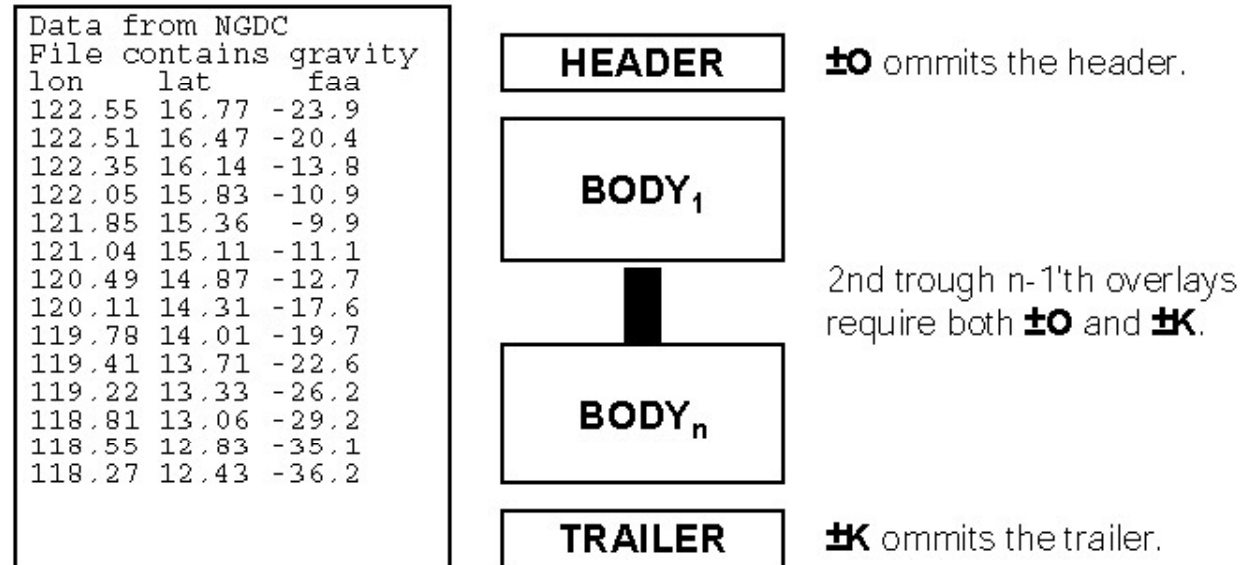


Figure 1.10: (left) Input files may have an arbitrary number of header records, specified with -H; here, we would use -H3. (right) A final *PostScript* file consists of a stack of individual pieces

The -K and -O options control the generation of *PostScript* code for multiple overlay plots. All *PostScript* files must have a header (for initializations), a body (drawing the figure), and a trailer (printing it out) (see Figure 1.10). Thus, when overlaying several **GMT** plots we must make sure that the first plot call ommits the trailer, that all intermediate calls omit both header and trailer, and that the final overlay ommits the header. The -K switch ommits the trailer which implies that more *PostScript* code will be appended later [Default terminates the plot system]. The -O switch selects Overlay plot mode and ommits the header information [Default initializes a new plot system]. Most unexpected results for multiple overlay plots can be traced to the incorrect use of these options.

Plotting a Mercator-Projected World Map

REM Every comment line needs to start with REM

REM Setting parameters. You can set the parameters here.

REM If you want to use the parameters in the comand-lines,

REM you need to embed the parameters in %Parameter% (see below)

set REGION=-180/180/-70/70

set PROJECT=M

set SCALE=25

set OUT= world_mercator.ps

REM

REM gmtset will adjust individual GMT defaults settings

gmtset DEGREE_FORMAT 3

gmtset FRAME_WIDTH 0.1c

gmtset COLOR_NAN 255/255/255

gmtset MEASURE_UNIT cm

REM

REM Now we can list our gmt-programs

REM

pscoast -J%PROJECT%%SCALE% -R%REGION% -Dl -G0/255/0 -I1/1/0/0/255 -N1 -S0/0/255 -V -K > %OUT%

psbasemap -R%REGION% -J%PROJECT%%SCALE% -Ba40f20 -O >> %OUT%

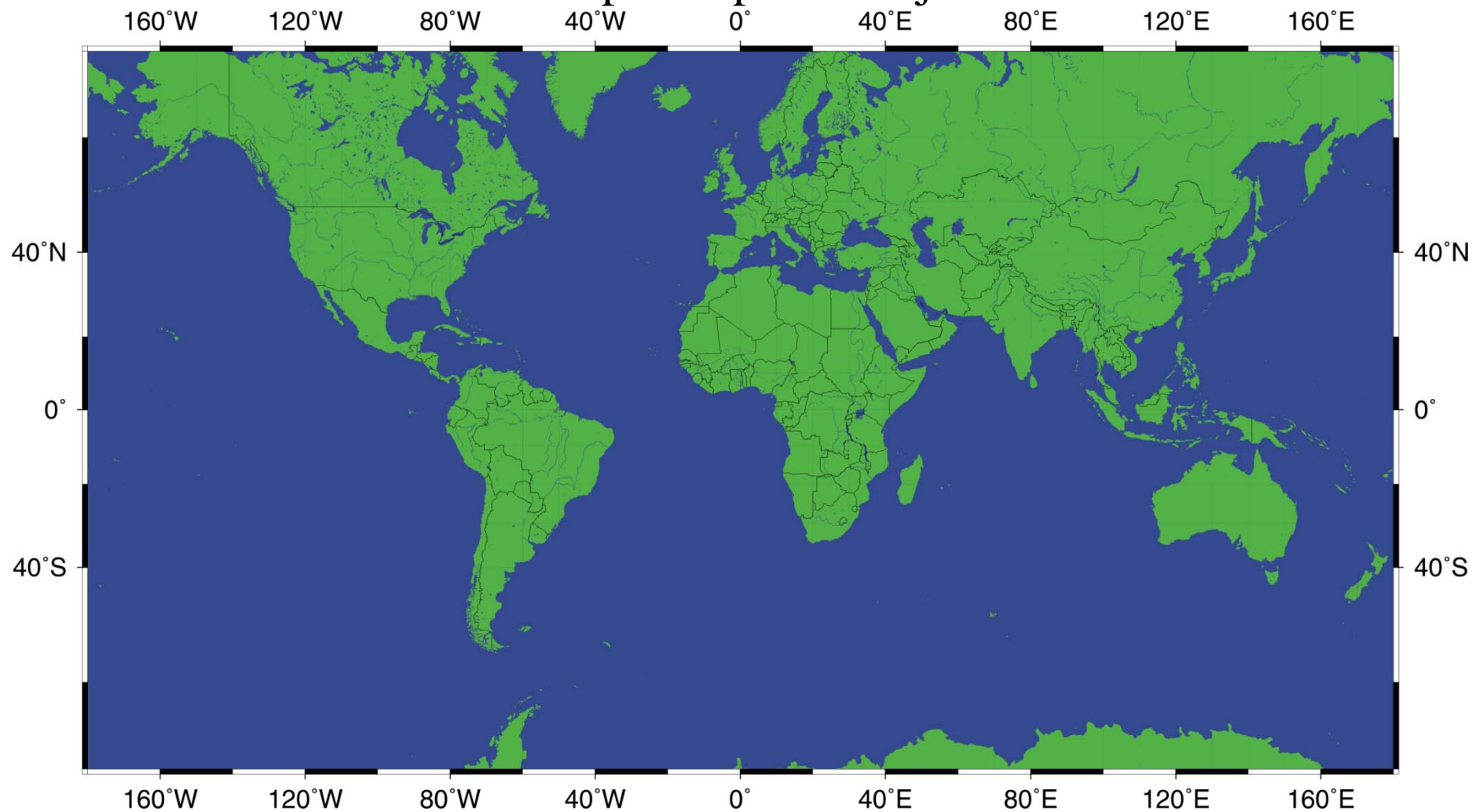


future ocean
KIEL MARINE SCIENCES

Acoustic Imaging

GMT

Output of previous job

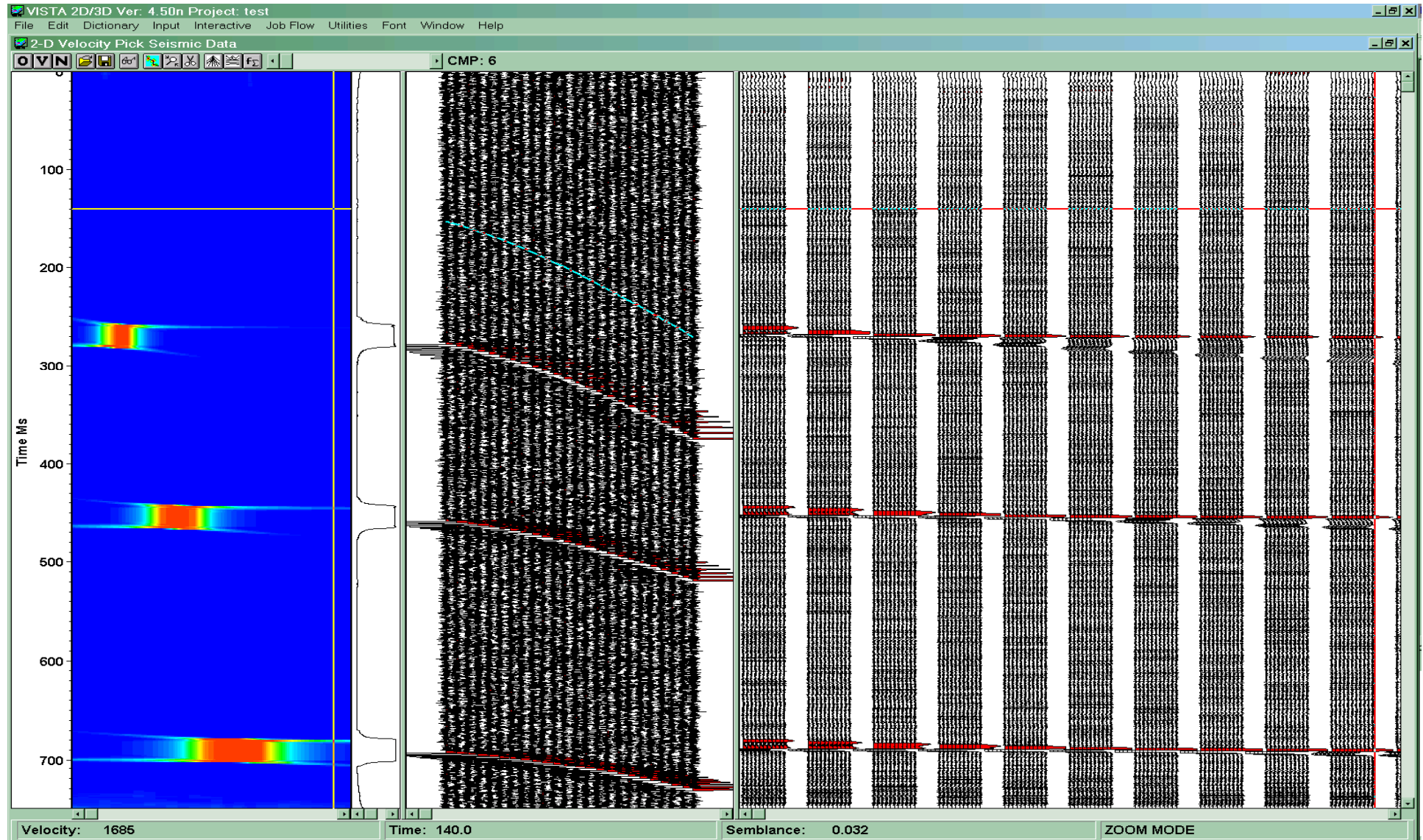




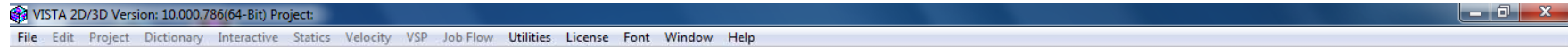
future ocean
KIEL MARINE SCIENCES

Acoustic Imaging

Seismic data processing: exercise

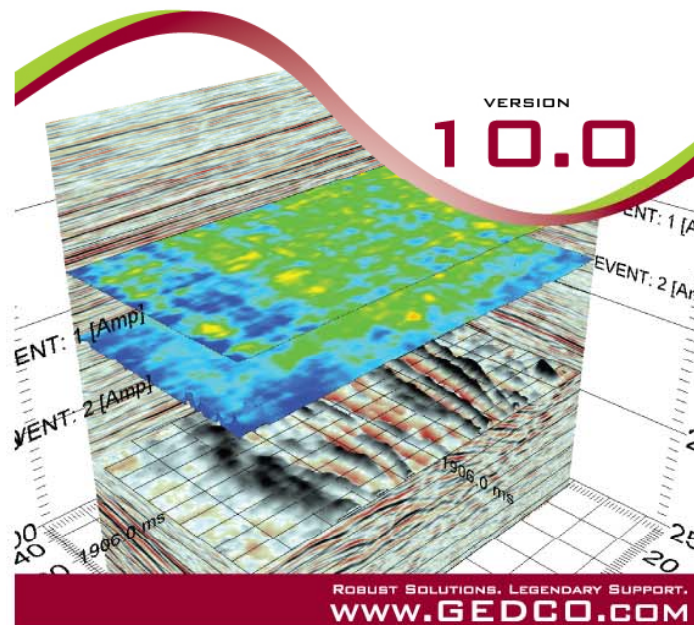


We will use Vista 2D/3D (GEDCO) , a low cost commercial software.
GEDCO provided free training licenses for this course

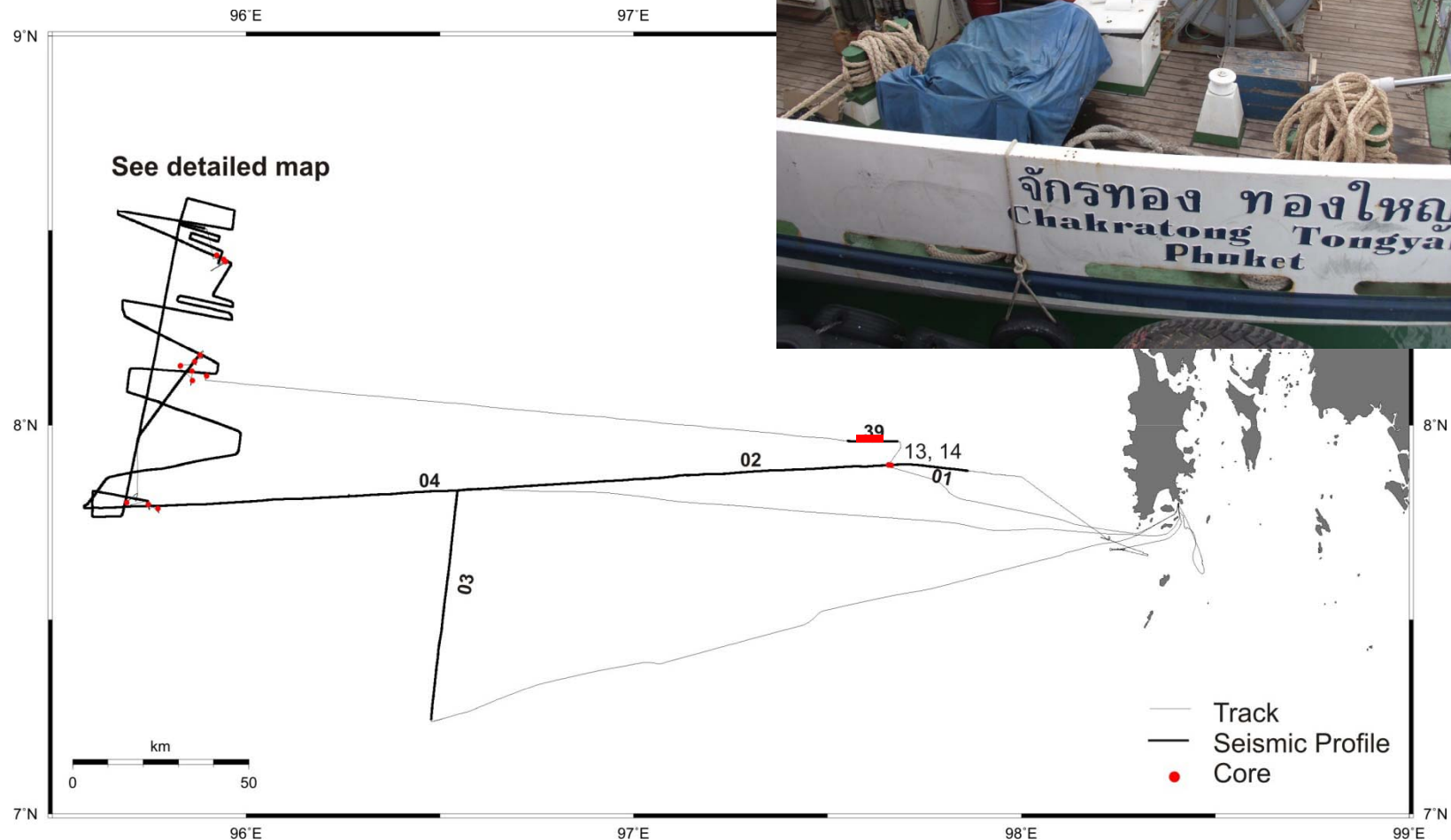


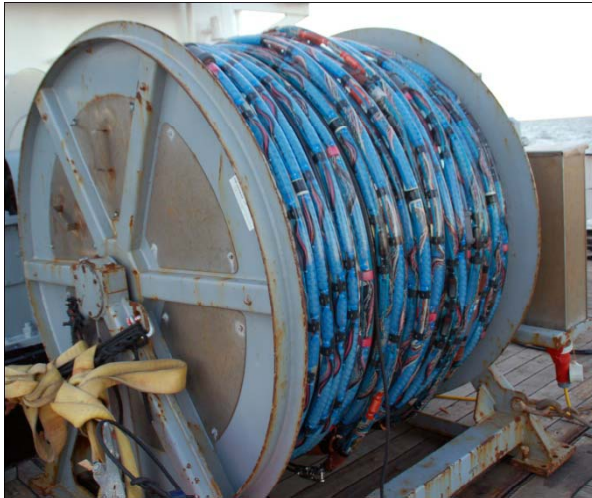
VISTA[®]

2D/3D SEISMIC DATA PROCESSING

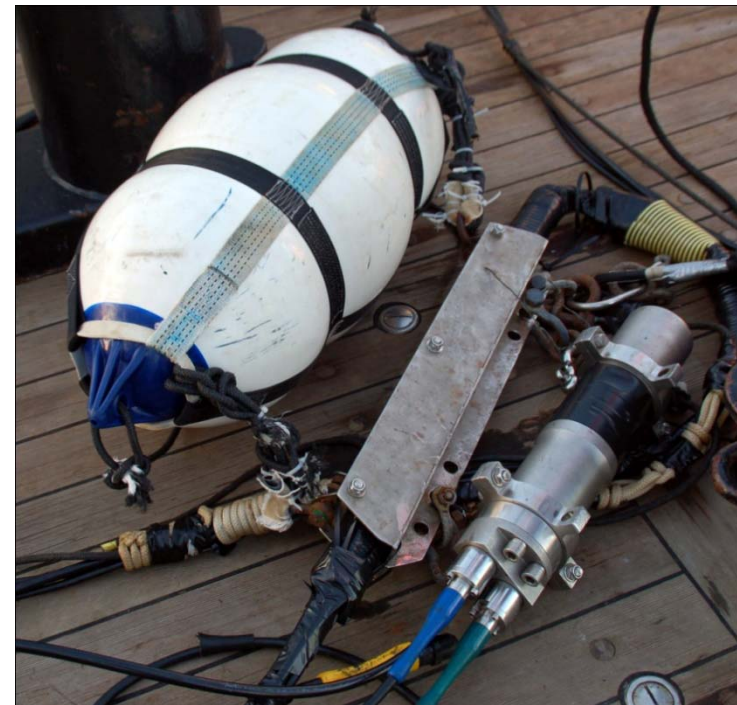


We will process data collected during Mass III-cruise early this year





Digital Streamer, 96 channels
Distance between groups: 1.56 m
2 Birds for depth control

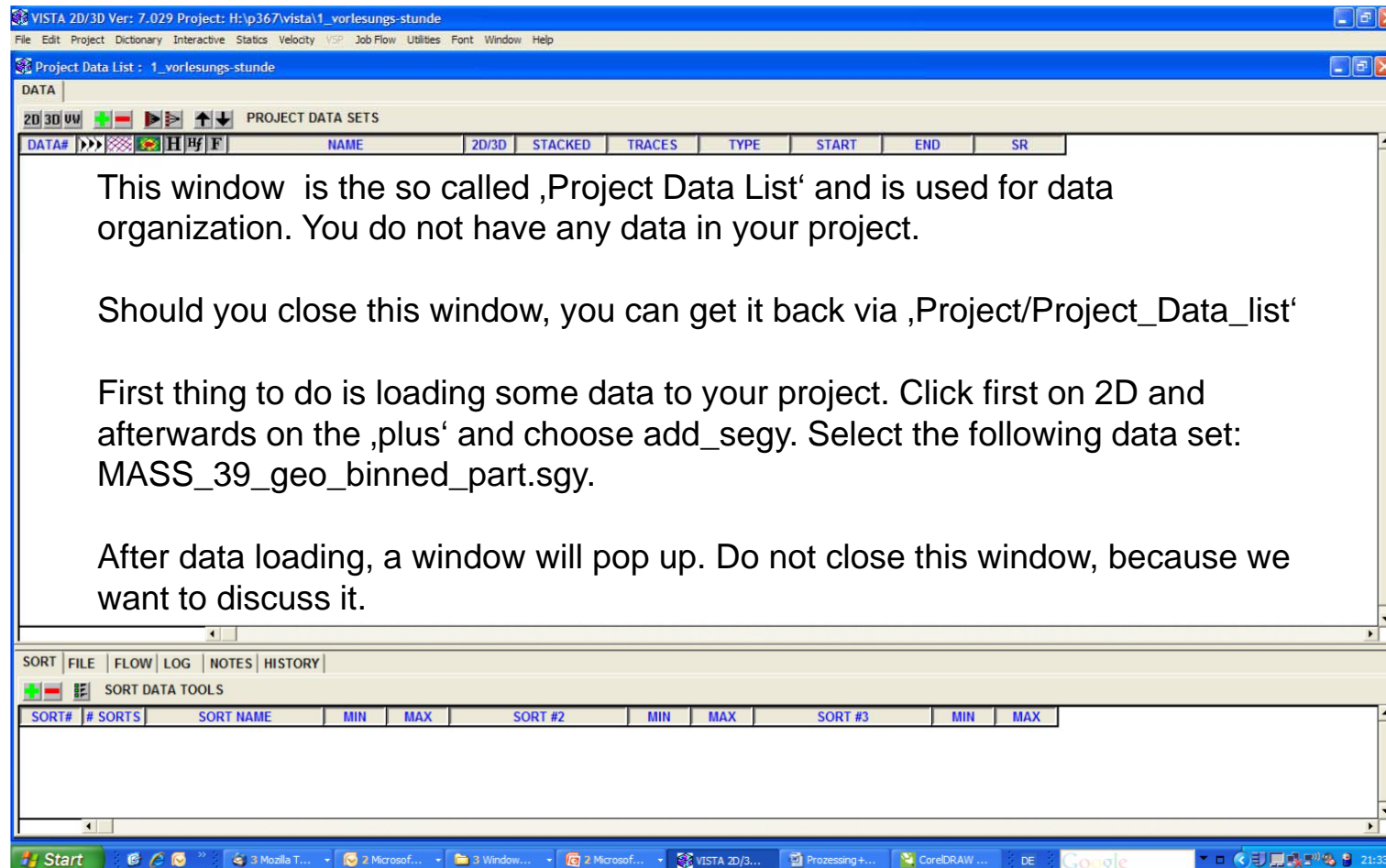


Mini GI-Gun with a a
volume of 0.1l

Training Licenses for Vista Seismic Processing

1. Open the VISTA software
2. On the menu bar, select LICENSE - OPTIONS SOFT / HARD KEY
3. Toggle on “RLM Reprise Soft Key” (make sure Sentinel Pro Key is toggled off)
4. Click LICENSE - SOFT KEY - AUTHORIZE RLM LICENSE
5. Follow Step 2 and 3 of the window (open the license folder and copy the license key to the folder, then ‘Refresh the License’)
6. It may be necessary to close Vista and open it again.

Now (hopefully) we can start to work with vista.
Open the program (if not done so far)
Create a new project. You should get this window





VISTA 2D/3D Ver: 7.029 Project: H:\p367\vista\1_vorlesungs-stunde

File Edit Project Dictionary Interactive Statics Velocity VSP Job Flow Utilities Font Window Help

Project Data List : 1_vorlesungs-stunde

DATA

2D 3D UW + - > < PROJECT DATA SETS

DATA#	NAME	2D/3D	STACKED	TRACES	TYPE	START	END	SR
1	[Z]: data_example	2-D	UNSTACKED	30880	TIME SEISMIC	0.00 ms	500.00 ms	250.00 us

The icons in front of the data set can be used for viewing the data and header information as well as the geometry processing. We will discuss them together in order to get a first impression of the data set.

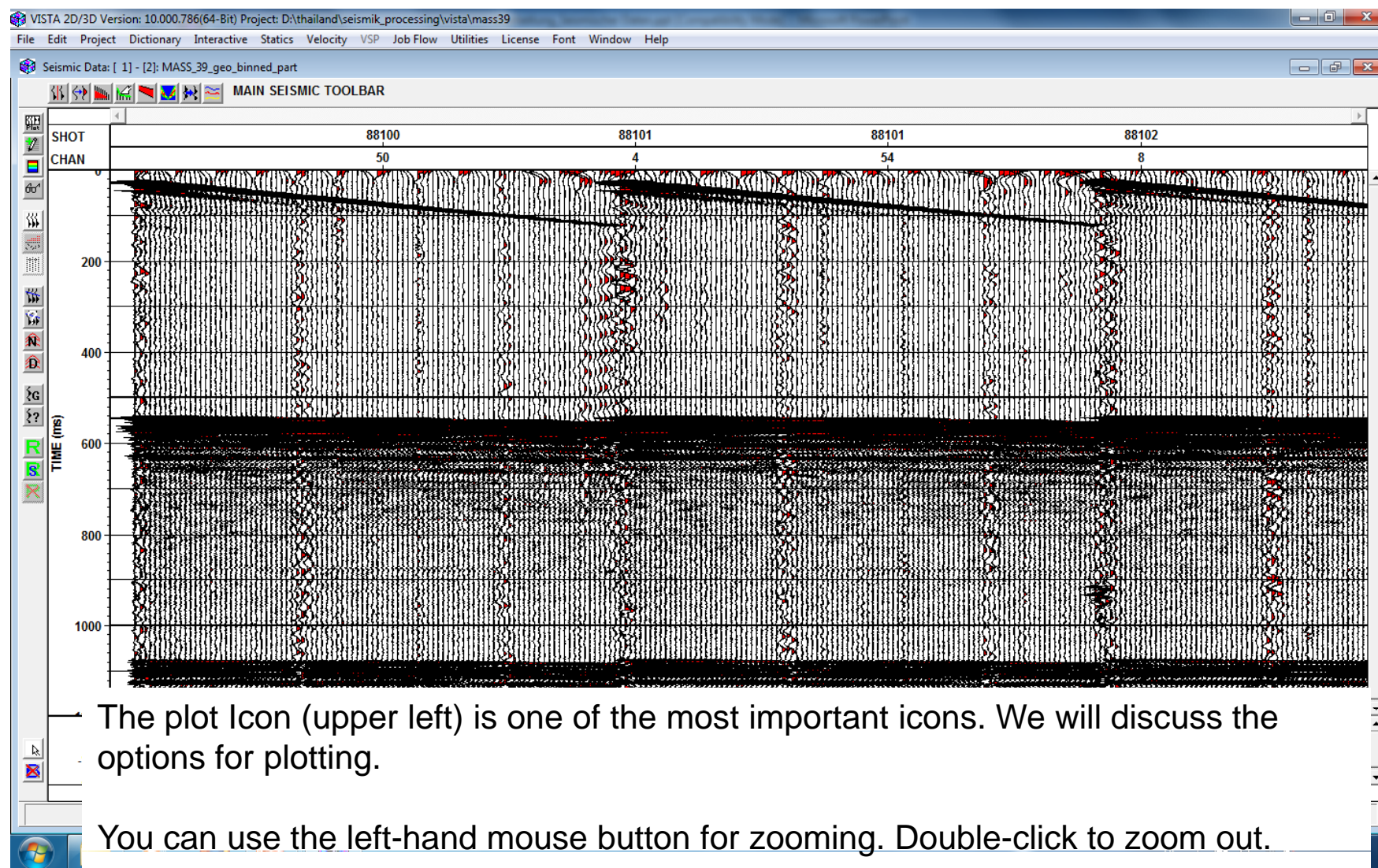
If you view the data set, you should get a smiliar picture.

SORT FILE FLOW LOG NOTES HISTORY

SORT DATA TOOLS

SORT#	# SORTS	SORT NAME	MIN	MAX	SORT #2	MIN	MAX	SORT #3	MIN	MAX
1	772	SHOT_POINT_NO	0	35124	CHANNEL_NO	0	0			
2	1	FIELD_STATION_NUMBER	0	0						
3	40	CMP_NO	1	40	OFFSET_SH_REC	-74609	0			
4	772	FIELD_RECORD_NO	1	772	CHANNEL_NO	0	0			

Start Mozilla T... 2 Microsof... 3 Window... 2 Microsof... VISTA 2D/3... Processing+... CorelDRAW ... DE Google 21:58



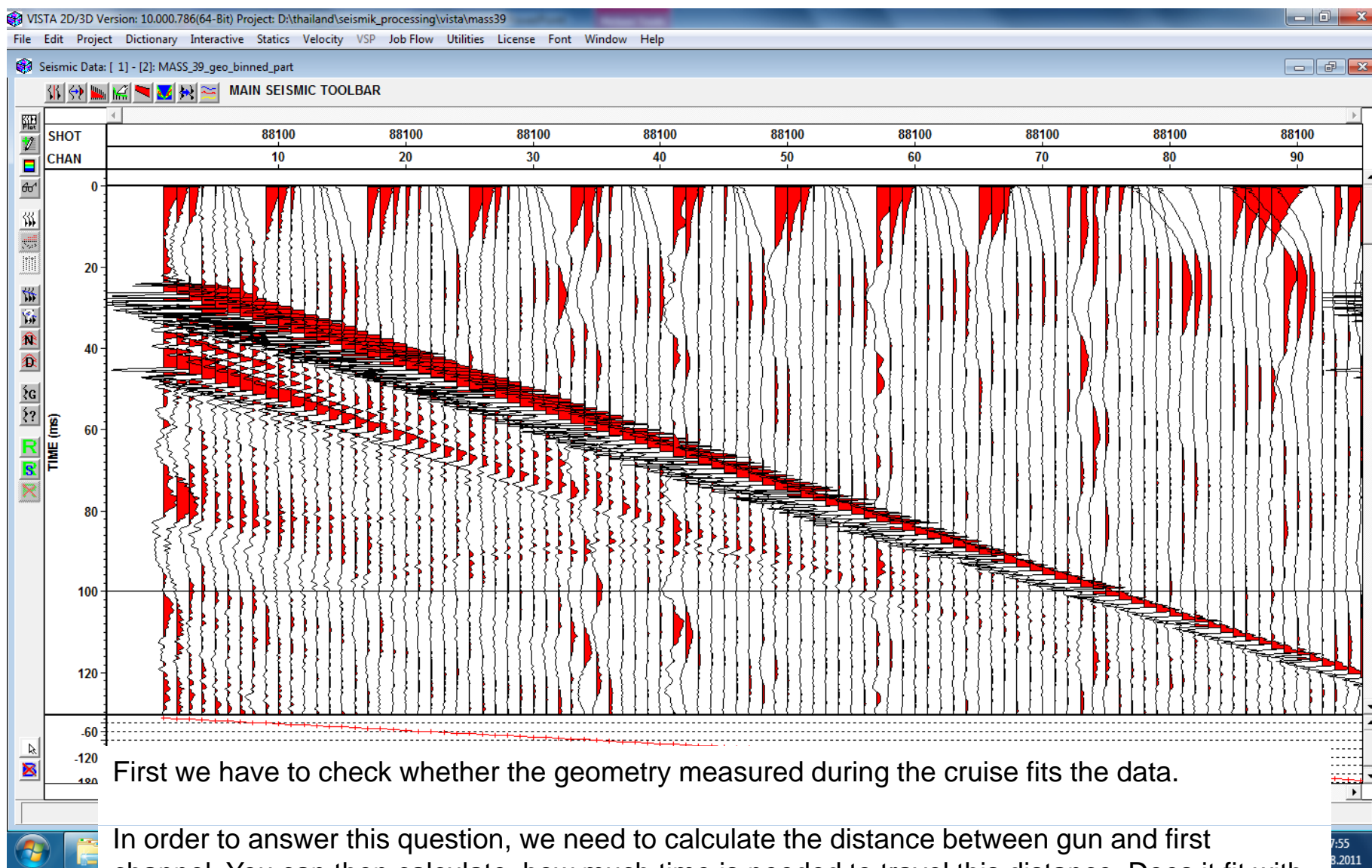
What do we see?



future ocean
KIEL MARINE SCIENCES

Acoustic Imaging

Seismic data processing: exercise



First we have to check whether the geometry measured during the cruise fits the data.

In order to answer this question, we need to calculate the distance between gun and first channel. You can then calculate, how much time is needed to travel this distance. Does it fit with the arrival time of the direct wave?

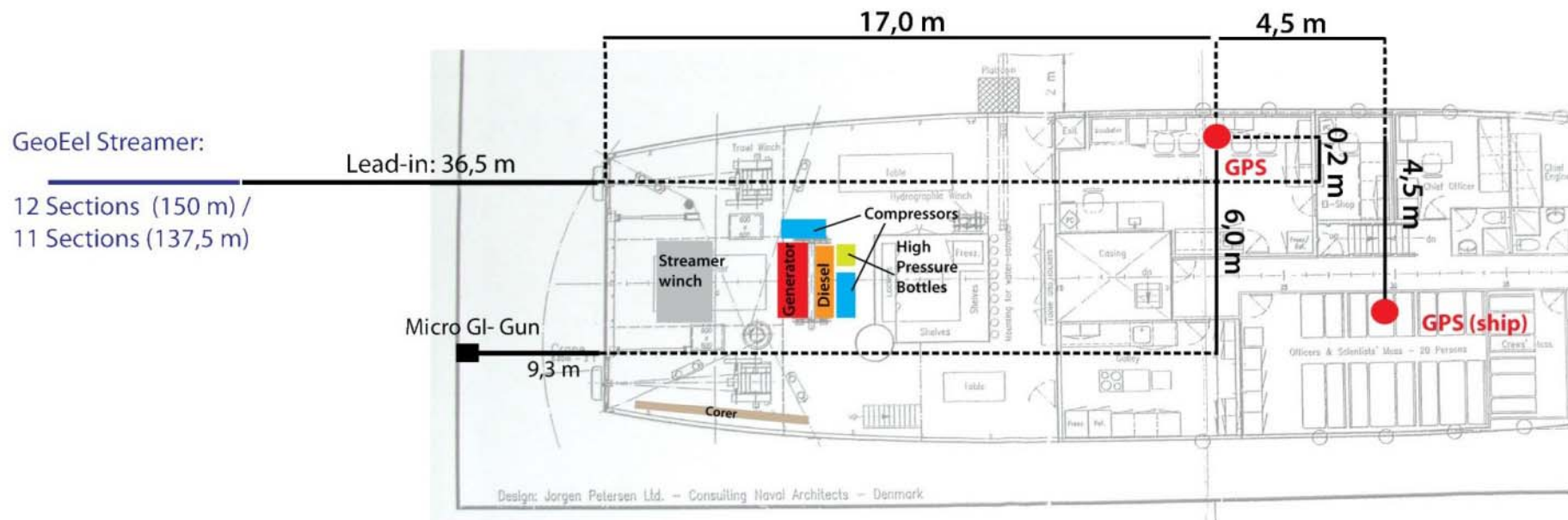


future ocean
KIEL MARINE SCIENCES

Acoustic Imaging

Seismic data processing: exercise

Geometry during data acquisition



A first important step during data processing is the creation of a so called brute stack. For a brute stack, we just use a few selected traces and stack them together (without any correction). This gives a first impression of the features on the profile.

In order to create a brute stack, open the file `brute_stack`, under ,Job Flow/Open Flow_File‘

We will discuss this flow-file. Afterwards run the job. If anything is yellow, click into the flow window with the right-hand mouse button and select ,Set all execute on‘

You might notice, that the brute stack is still relatively noisy. Noise can be suppressed by filtering. In order to get familiar with Vista Flow Files, try to include a Ormsby Filter to the previous Brute-Stack job.

Chose ,Job Flow/Vista Flow Command Window‘. A window will open with all available commands. (click with the right-hand button on any command for help). Select an ,Ormsby-Filter‘ from this window and drag and drop it to your ,Brute stack‘ Flow. Place it between the ,Select Data Icon‘ and the ,Stack Icon‘. Double-Click the new Icon and set the following filter frequencies:

Low-Trunc: 55, Low-Cut: 55, High-Cut: 800, High-Trunc: 1500. Chose a different output name (e,g, `prof39_brute_filte`). Activate the command and run the job.

We want to improve the image by changing plotting parameters.

Click on the Icon 'Seismic Plot Parameters'. Choose

- 1) Options/Display Type/Variable Density'
- 2) Set under 'Display Options' 'Max Trcs/Panel' to 1000.
- 3) Click OK. What do you see?
- 4) Try to change the color-scheme for the seismics. Right-hand click into the seismic section and choose 'Display Options/Color-Bar Options' . Try different Color Bars under List. Which one do you like most?

Before we start with the real data processing, we should check for bad channels. Open the raw data file and check some shots distributed across the profile. Do you see bad channels. If yes, I will explain how to delete them.

Next step is the setup of the geometry as preparation for the cmp-sorting. I will show you how to do it.

The CMP (Common Midpoint) Concept

Rearrangement of data from shots to CMPs

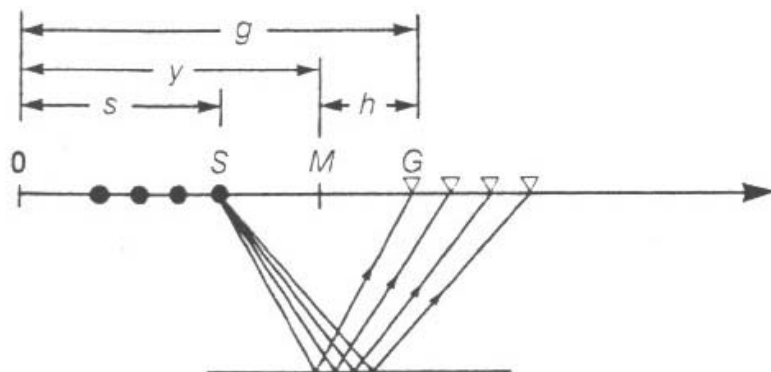


FIG. 1-40. Seismic data acquisition is done in shot-receiver (s, g) coordinates. The raypaths shown are associated with a planar horizontal reflector from a shotpoint S to several receiver locations G . The processing coordinates, midpoint-(half) offset, (y, h) are defined in terms of (s, g) : $y = (g + s)/2$, $h = (g - s)/2$. The shot axis here points opposite the profiling direction, which is to the left.

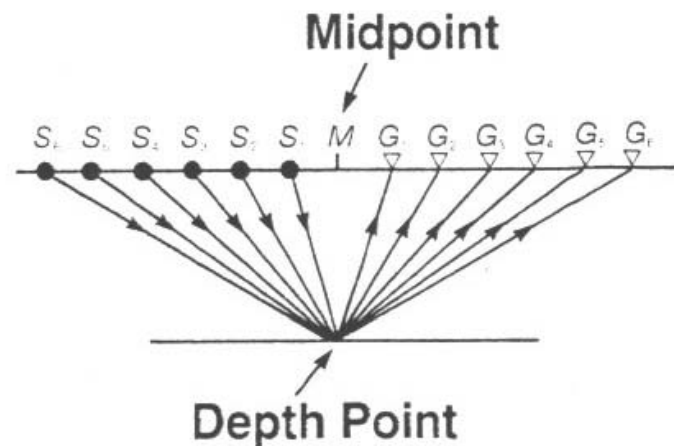


FIG. 1-41. Seismic data processing is done in midpoint-offset (y, h) coordinates. The raypaths shown are associated with a single CMP gather. A CMP gather is identical to a CDP gather if the depth point were on a horizontally flat reflector and if the medium above were horizontally layered.

Offset is the distance between shot and receiver

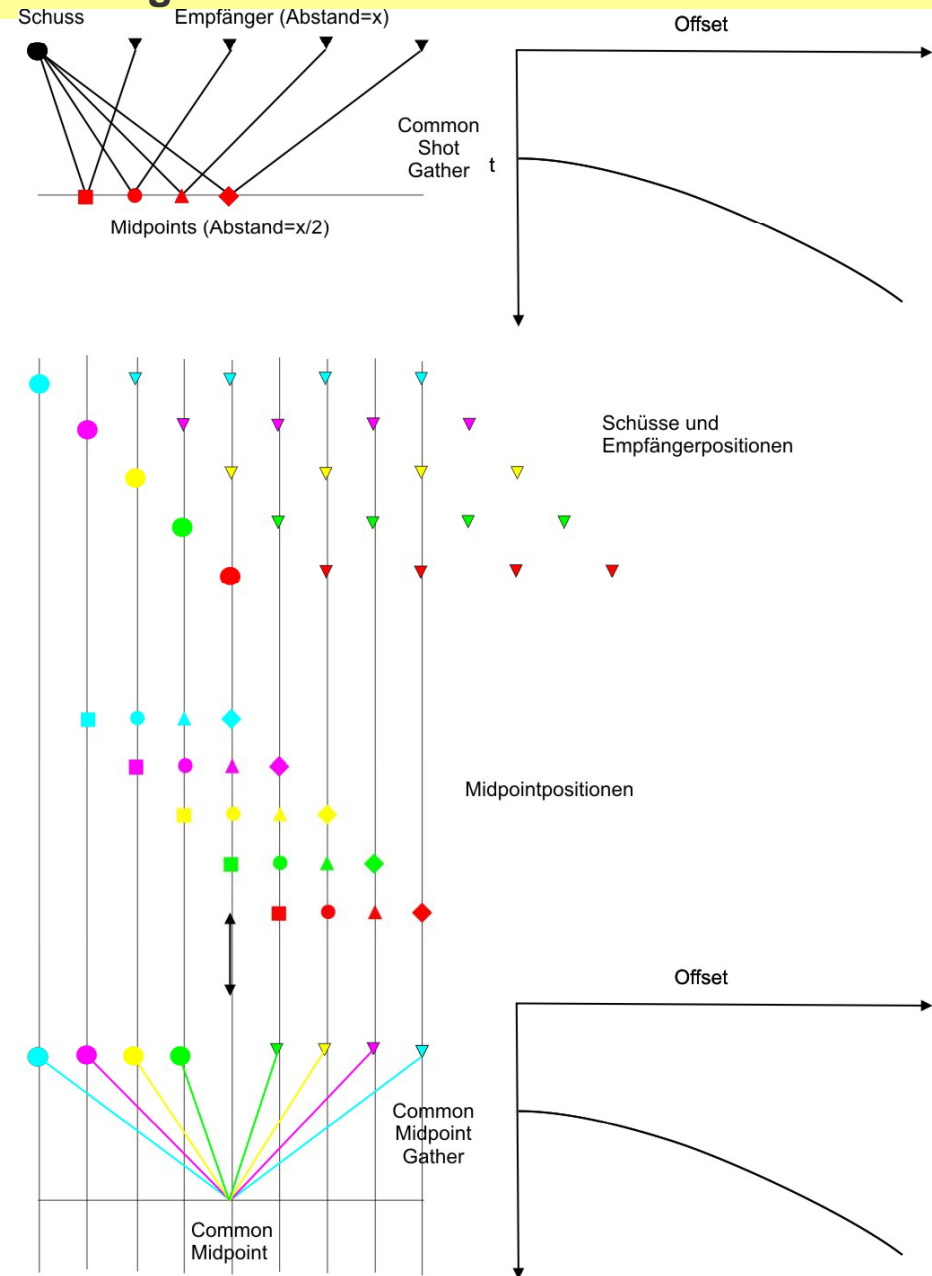
A Midpoint is the 'midpoint' between shot and receiver

Seismic data processing: exercise

A CMP-Gather (Common Midpoint) consists of all traces of shot-receiver pairs with the same midpoint.

Fold: Number of traces in a CMP-Gather

A distance x between individual receivers results in a midpoint-distance of $x/2$



Irregual Geometries (e.g. velocity variations during acquisition, no straight lines):

Binning

- Small areas (bins) are defined instead of a CMP
- Binning: Allocation of midpoints to bins
- Sort for bins

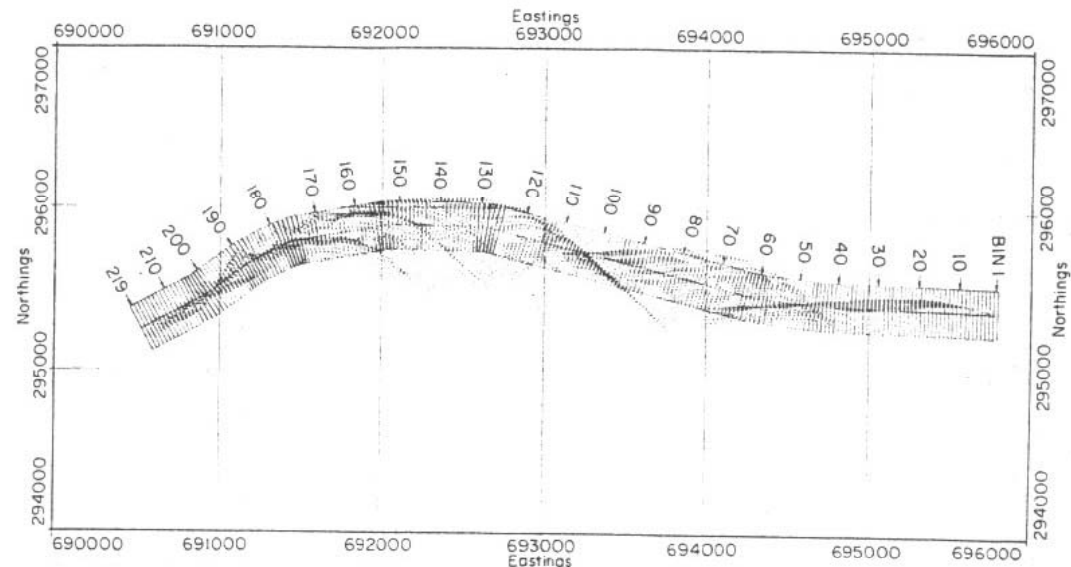


Fig. 3.92. A 'binning strategy' for the mid-point distribution of Fig. 3.91.

Required Information: Distance of Bins, Shape of Bins, Location of Bins

⇒ Allocation of midpoints to bins, Bin-Number is written to header

⇒ Sort for bins

In Vista two movies are available for binning at Vista\Vista Movies (Tutorial A 2D Geometry.avi, 2D Geometry Crooked Line.avi)

Your data files already includes all geometry information. Hence we can start with the CMP-Processing.

First step is the CMP-Sorting. You should write your own job for cmp-sorting. Open a new flow-file. You just need an input and an output. Drag and drop them to your flow-window. Select your Input file (double click on the icon and select the raw data file). In this window you can also choose the sort order. Choose CMP_NO under sort. Afterwards click OK and double-click on the output command. Choose a proper name for the output-file. You need to connect these two commands. Choose the icon with the two rings. Now you can connect commands just by drawing a line with the mouse (keep it clicked) from the input to the output.

Activate both commands. How does your output look like. How many traces do you have in a cmp-gather?

Next step is the velocity analysis. This is the most time consuming step during data processing.

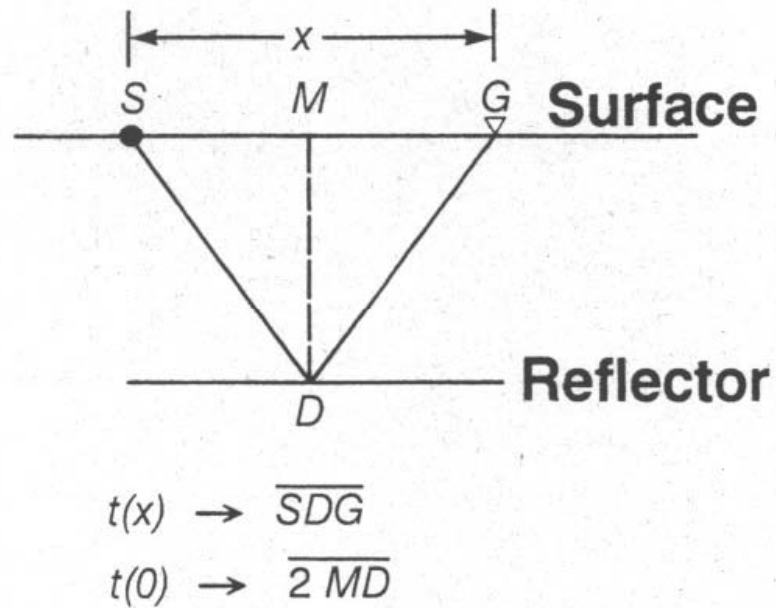


FIG. 3-4. The NMO geometry for a single horizontal reflector [refer to equation (3.1)].

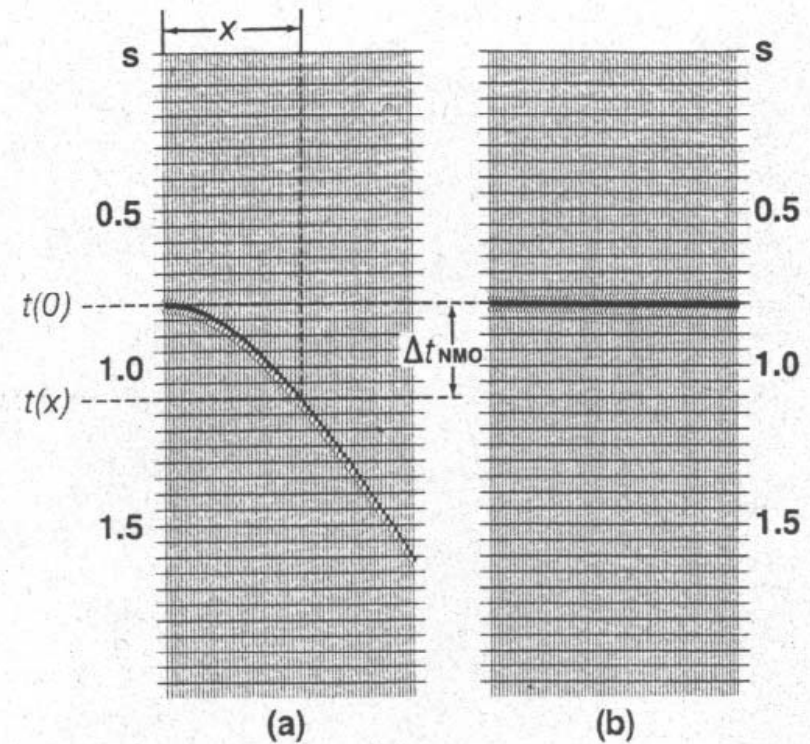


FIG. 3-6. NMO correction [equation (3.2)] involves mapping nonzero-offset traveltime $t(x)$ onto zero-offset traveltime $t(0)$. (a) Before and (b) after NMO correction.

Difference between $t(x)$ and $t(0)$ is called NMO



future ocean
KIEL MARINE SCIENCES

Acoustic Imaging

Seismic data processing: exercise

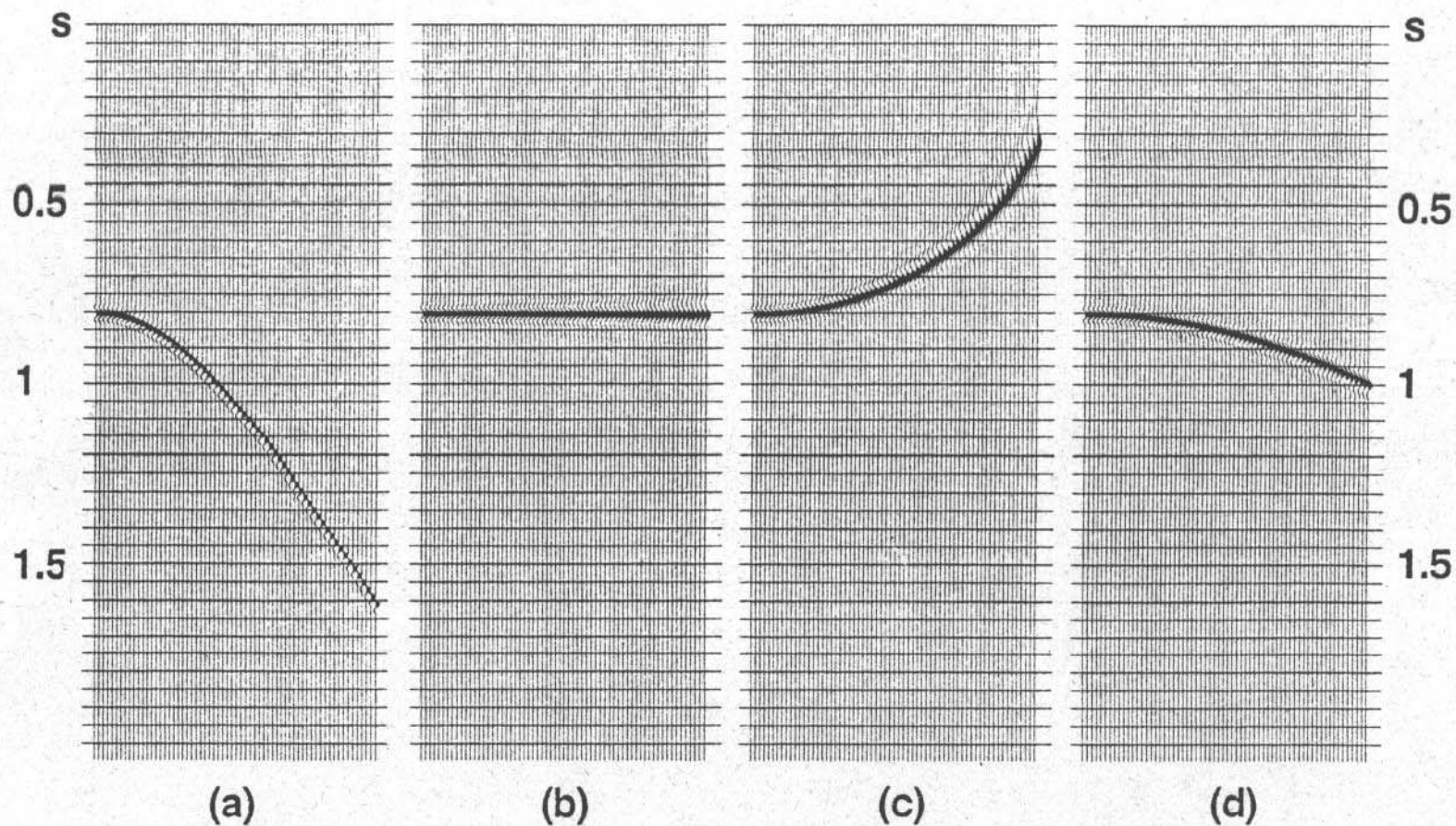


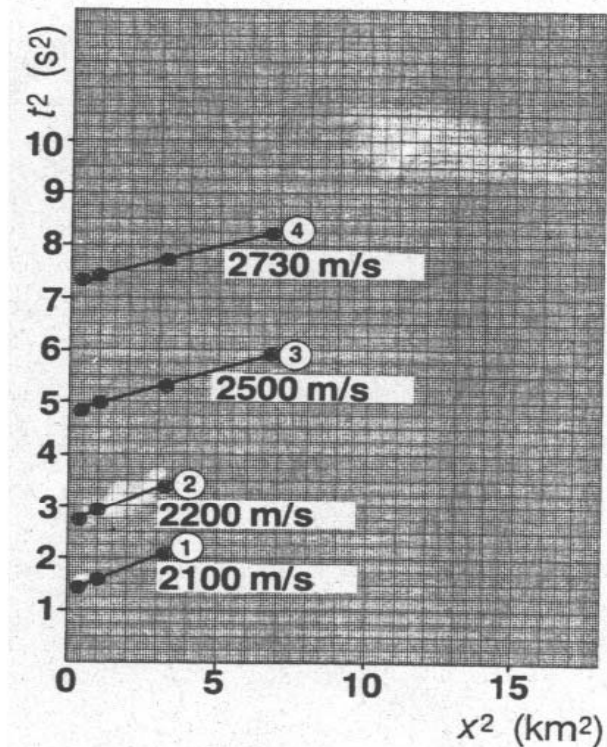
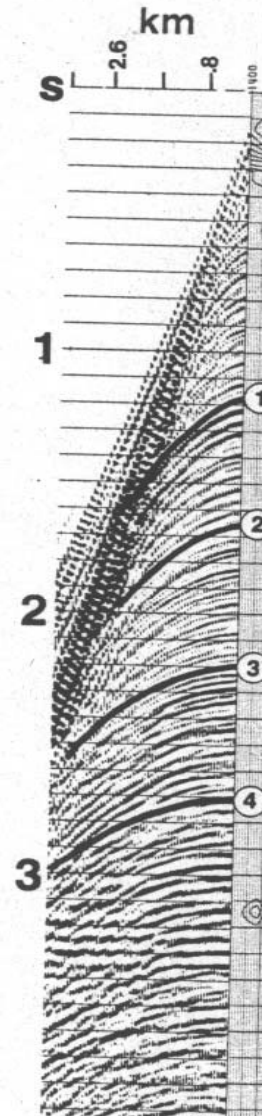
FIG. 3-8. (a) CMP gather containing a single event with a moveout velocity of 2264 m/s; (b) NMO-corrected gather using the appropriate moveout velocity; (c) overcorrection because too low a velocity (2000 m/s) was used in equation (3.2); (d) undercorrection because too high a velocity (2500 m/s) was used in equation (3.2).

Velocity-Analysis

1. t^2 - x^2 -Method

Determination of velocity from inclination of the straight line.

$$t(x)^2 = t(0)^2 + x^2 / v_{\text{NMO}}^2$$



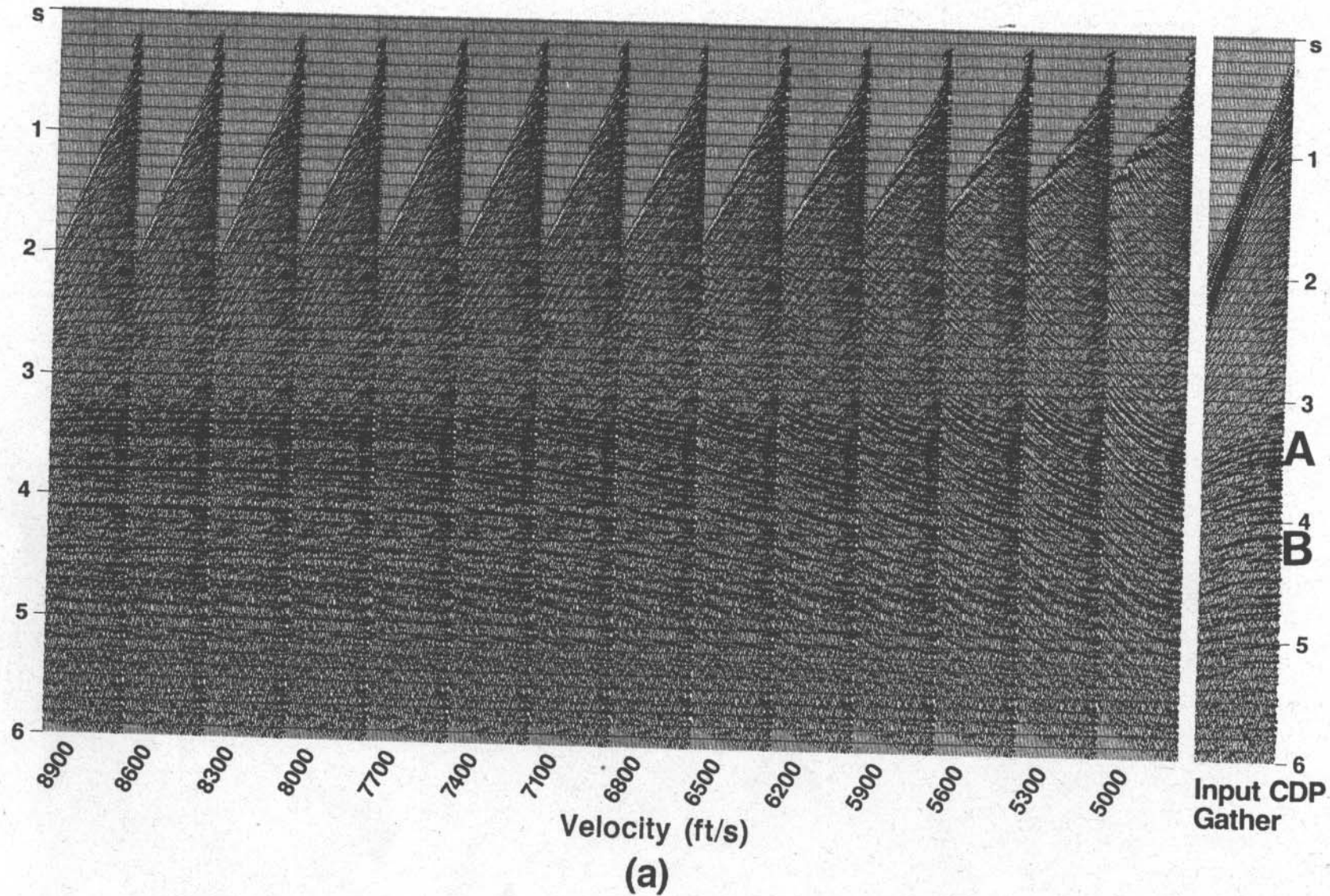


future ocean
KIEL MARINE SCIENCES

Acoustic Imaging

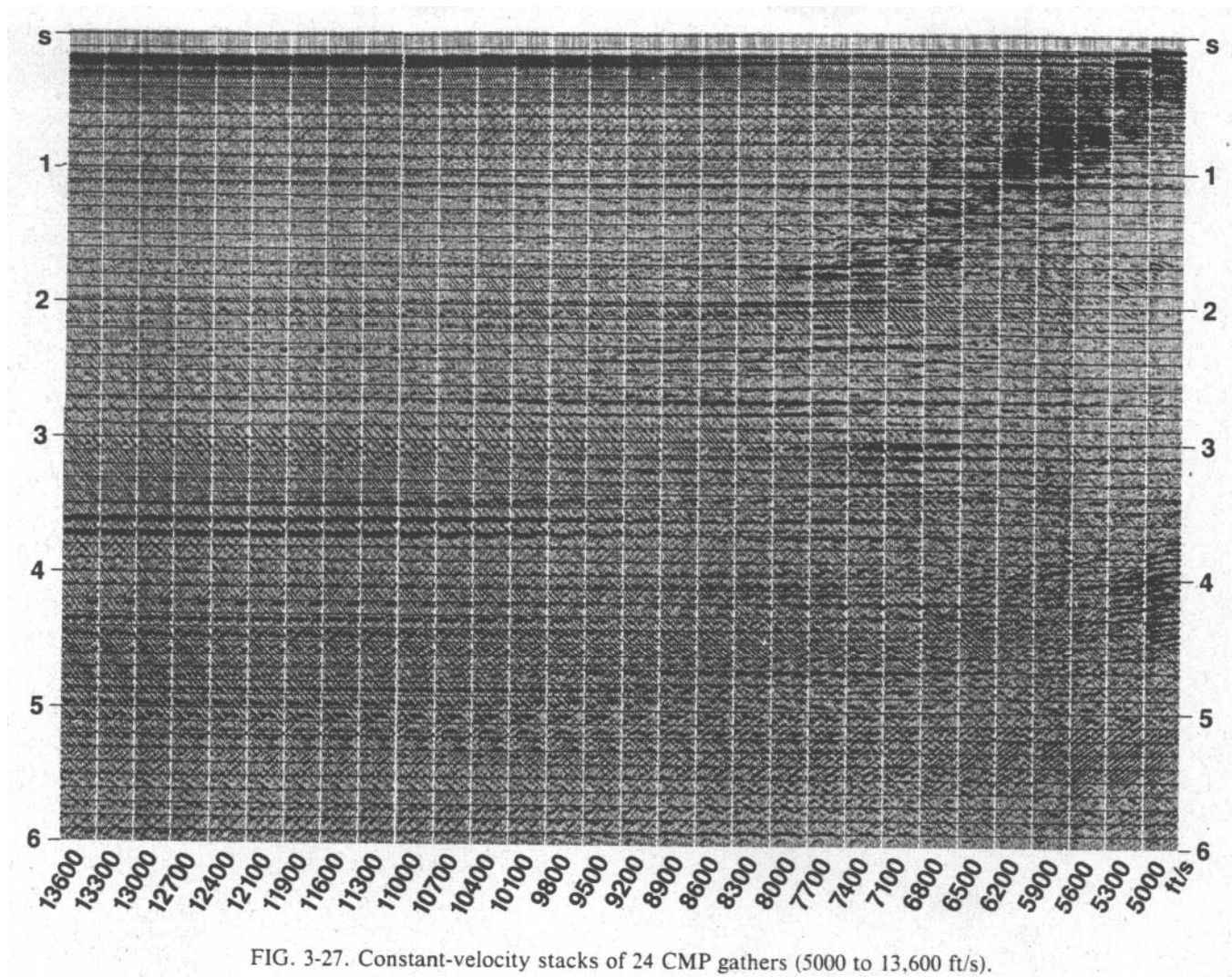
Seismic data processing: exercise

2. Correction of CMP-Gathers with constant velocities



3. Costant Velocity Stacks (CVS)

A velocity-depth model is constructed out of optimal stacking results.





future ocean
KIEL MARINE SCIENCES

Acoustic Imaging

Seismic data processing: exercise

Cross-correlation in a cmp-gather allows to determine the velocity with highest semblance.

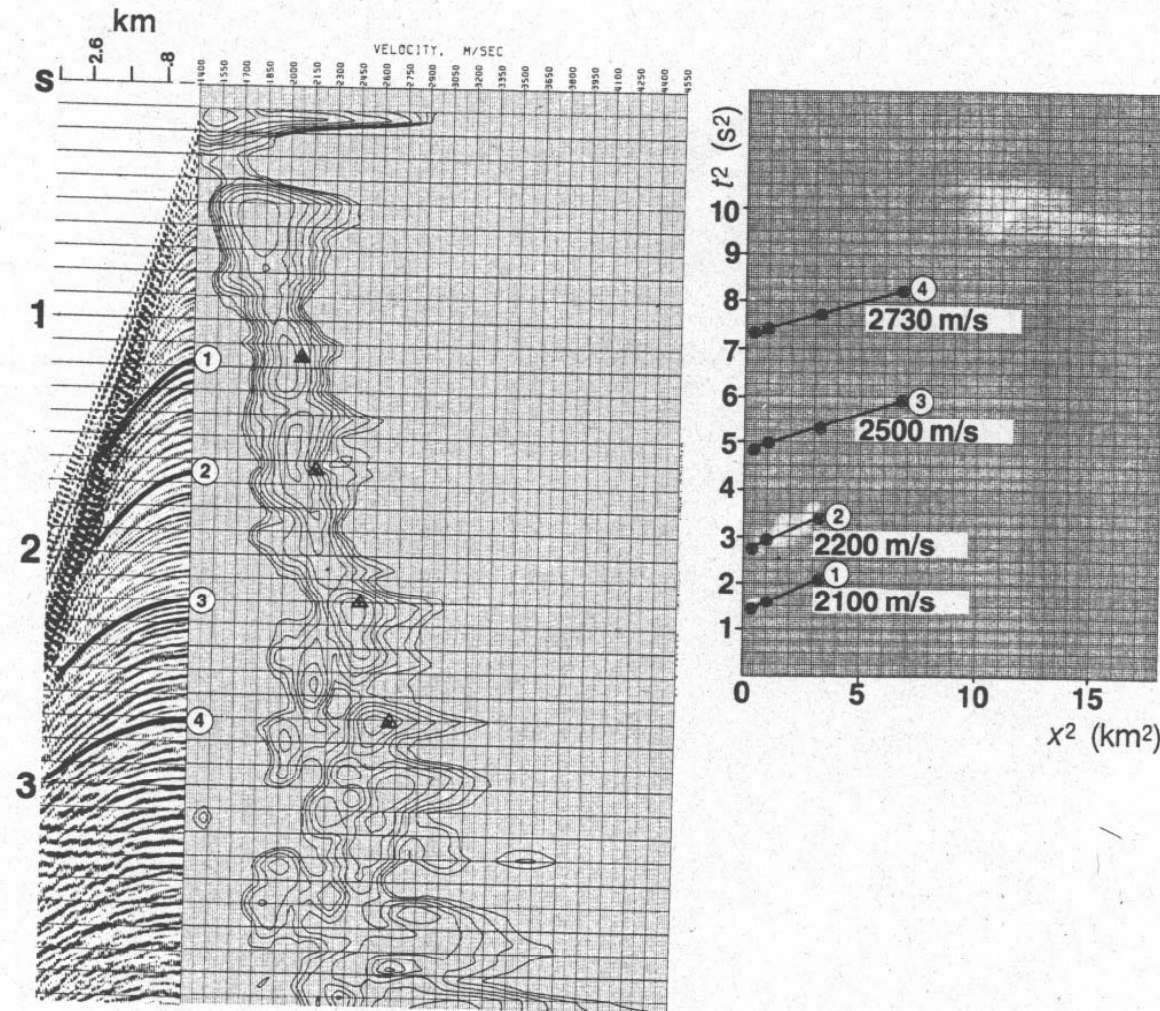
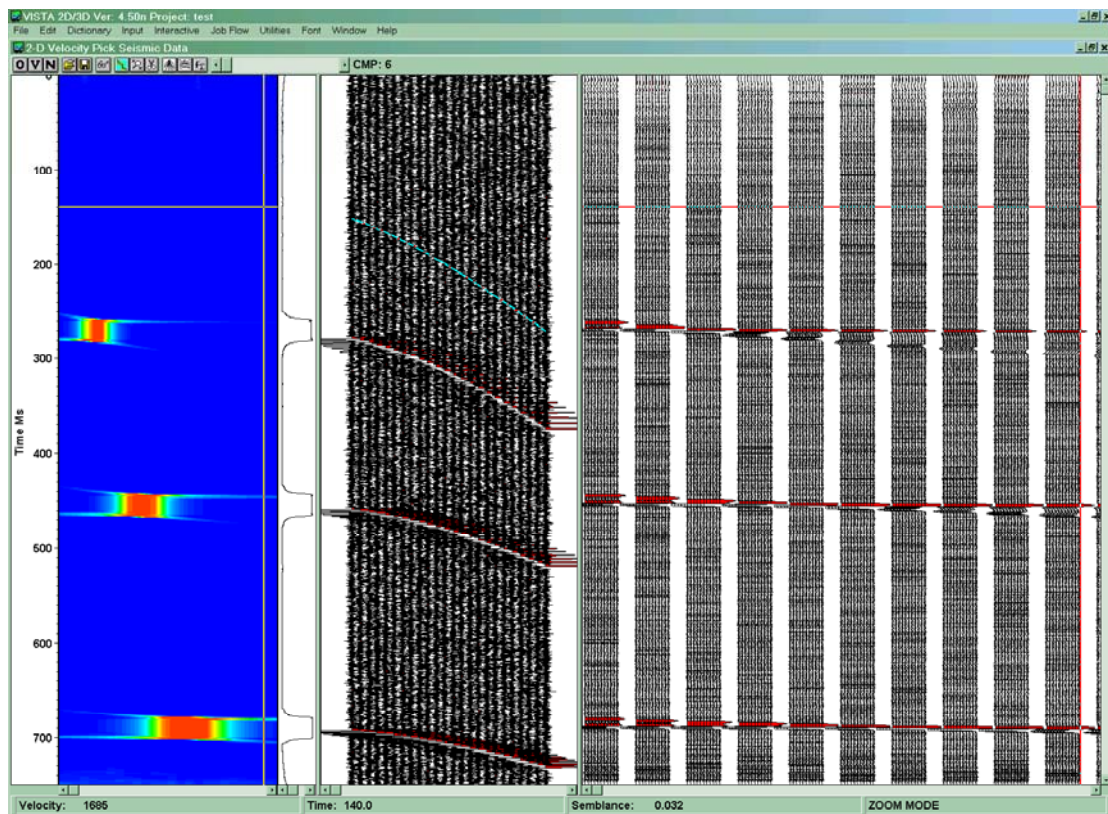


FIG. 3-24. The $(t^2 - x^2)$ velocity analysis applied to a CMP gather. The triangles on the velocity spectrum [center panel, based on equation (3.19)] represent velocity values derived from the slopes of the lines shown on the graph at the right.

The velocity analysis on real data is tricky. Hence we will start with a synthetic example, which is much easier to handle.

Load the following data set to your project. Synthetic.sgy (located in the folder synthetic).



Open the job flow ,velocity_analysis' also located in the synthetic folder. We will discuss this flow together. Afterwards run the flow. You will create three new outputs. These files will be used for the velocity analysis. Choose ,Interactive/Velocity Tools/Interactive Velocity Analysis'. Select the three new datasets in the pop-up window. You get the following window:



The left window shows the semblance. The central window the CMP-Gather and the right window Constant-Velocity Stacks. The combination can be used to create a velocity-depth profile. First we should optimize the plotting parameters. Click with the right-hand mouse button in the central window and select Gather Parameters/Plot Parameters. Choose process and select as Amplitude Scale -12. Repeat this step in the cvs-window and select CVS-Parameters/Plot Parameters. Choose -18 as amplitude scale. Afterwards we will discuss the windows.

Use this icon  for picking velocities. Pick a velocity-depth profile.

This icon  can be used to change between corrected and uncorrected gather. Try the difference.

Clicking on  opens a new window. Afterwards click on . You will see a graph of your velocities and the corresponding interval velocities.

Now we will conduct a velocity analysis with our real data set. Open the job ,Velocity_analysis_prof39' (in the job directory). Conduct the velocity analysis for all selected CMPs. Do not forget to save your velocity-depth profile as you will need it for the NMO-correction

Afterwards we need to check the quality of our velocity analysis. Therefore we want to apply the NMO-correction. Write a job for the NMO-correction. You should have horizontal arrivals after the NMO-Correction.

If the NMO-Correction looks fine, you can stack the data. Try to write a job for stacking the data. Do you see major improvements compared to the Brute Stack?

Stacking

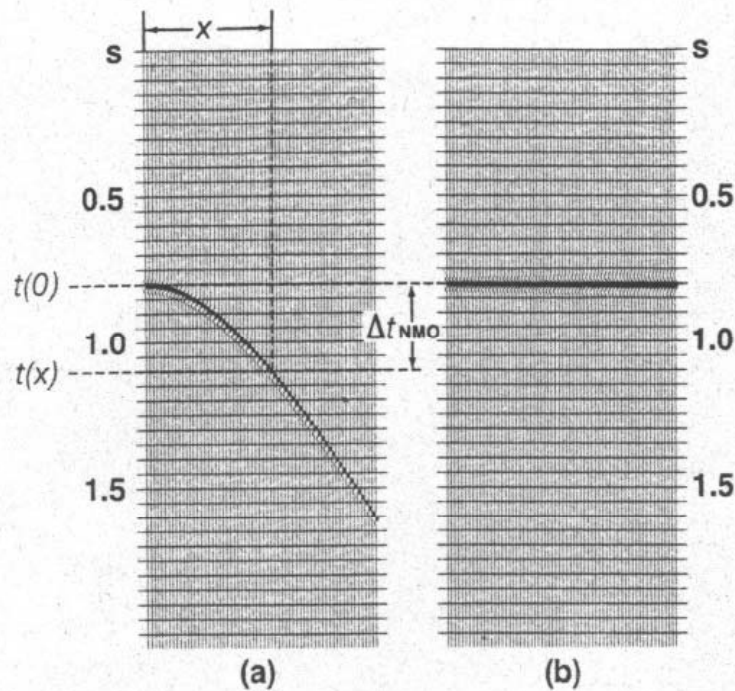


FIG. 3-6. NMO correction [equation (3.2)] involves mapping nonzero-offset traveltime $t(x)$ onto zero-offset traveltime $t(0)$. (a) Before and (b) after NMO correction.

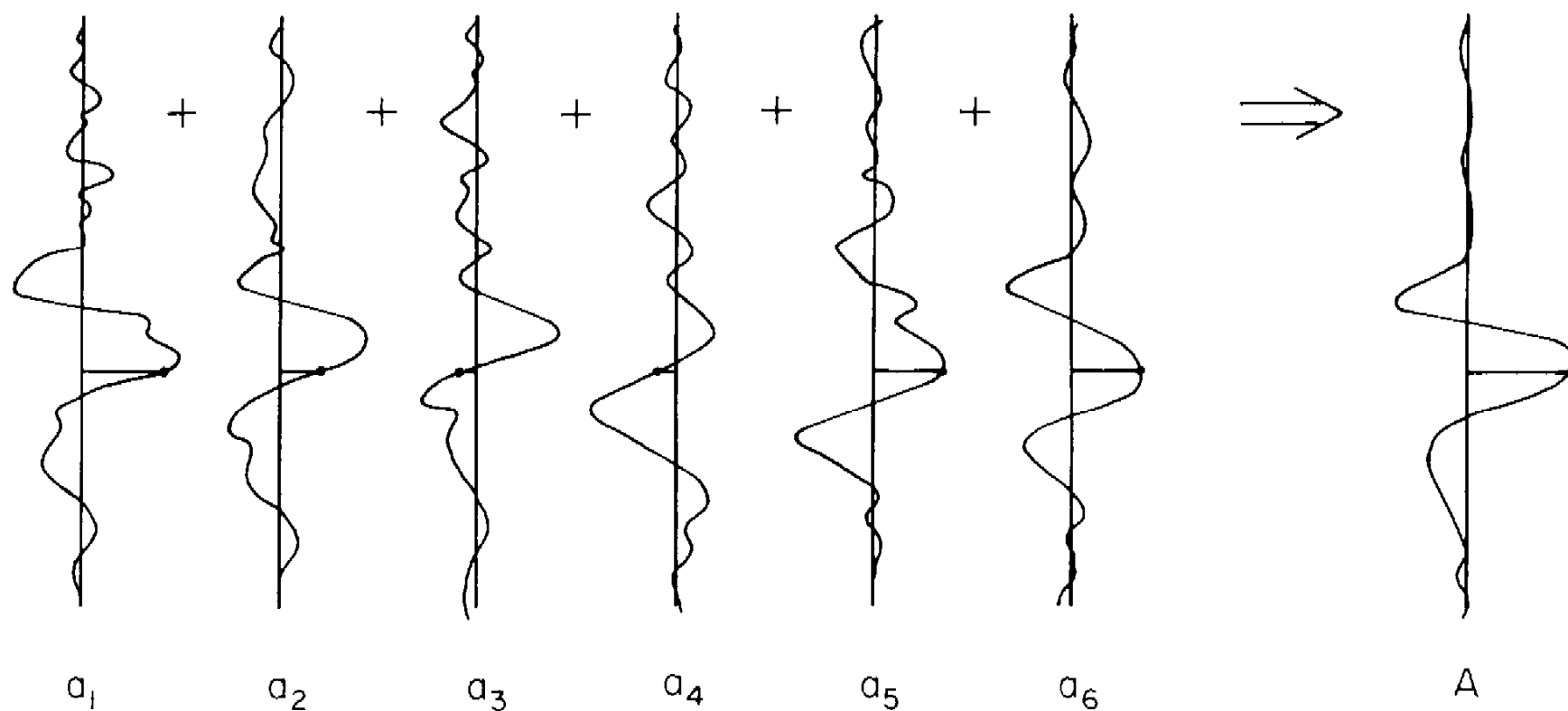
Stacking: Summation of NMO-corrected traces in a CMP-Gather.

Aim: Improvement of des S/N-ratio (Signal/Noise).

Improvement of S/N-ratio: $\sim \text{SQR}(\text{Fold})$.

Stacking

Fig. 3.39. The action of stacking.



ภาคผนวก ค

Morphodynamics and Slope Stability of the Andaman Sea Shelf Break

Annual Research Report for Year 1

(15 September 2006 – 30 September 2007)

Submitted to

National Research Council of Thailand

By

Anond Snidvongs^{1, 2}

With Contributions from:

Wilhelm Weinrebe³

Warner Brückmann³

Christian Hensen³

Pachoenchok Jintaseranee^{3, 4}

Suratta Bunsomboonsakul¹

¹ Southeast Asia START Regional Center, Chulalongkorn University, Bangkok, Thailand

² Department of Marine Science, Faculty of Science, Chulalongkorn University, Bangkok, Thailand

³ Leibniz Institute of Marine Sciences (IFM-GEOMAR), Kiel, Germany

⁴ Department of Aquatic Science, Faculty of Science, Burapha University, Chonburi, Thailand

บทคัดย่อ

เป้าหมายสำคัญของโครงการเสถียรภาพของชั้นตะกอนและการเกิดแผ่นดินถล่มใต้ทะเลบริเวณขอบไหล่ทวีปในทะเลอันดามัน คือการสำรวจเพื่อจำแนกขอบไหล่ทวีปในทะเลอันดามันตามร่องรอยการเกิดแผ่นดินถล่มในอดีตและแนวโน้มในอนาคต โดยการออกเรือครั้งที่ 1 โดยใช้เรือจักรทอง ทองใหญ่ ในช่วงเดือนพฤศจิกายน - ธันวาคม 2549 เพื่อทำการสำรวจโดยใช้เครื่องมือหังความลึกโดยใช้คลื่นเสียงสะท้อนแบบหลายความถี่ (multibeam bathymetric echosounder) และเครื่องมือศึกษาชั้นตะกอนโดยใช้คลื่นเสียงพารามิตรี (parametric sediment echosounder) ในพื้นที่สำรวจกว่า 2,000 ตารางกิโลเมตร ภายในเขตเศรษฐกิจจำเพาะของประเทศไทยด้านตะวันตกเฉียงใต้ ที่ความลึกของทะเลในช่วง 500 - 1,400 เมตร ข้อมูลที่ได้จากภาคสนามทั้งหมดกำลังทำการวิเคราะห์อยู่ แต่ ณ ปัจจุบัน ได้พบตำแหน่งที่พื้นทะเลที่มีลักษณะทางธรณีสัณฐานหรือชั้นตะกอนมีลักษณะทางเสียงที่ไม่ปกติแล้วจำนวน 34 แห่ง ซึ่งในจำนวนนี้ 30 แห่งเป็นตำแหน่งที่พื้นทะเลอาจจะมีของเหลวหรือก๊าซที่มีความหนาแน่นต่ำกว่าน้ำแทรกตัวอยู่ในชั้นตะกอน โดยที่ตำแหน่งที่พบการแทรกตัวเหล่านี้ทั้งหมดจะอยู่ในบริเวณที่มีความลึกน้ำมากกว่า 900 เมตร นอกจากนี้ยังพบเนินใต้น้ำในบริเวณด้านบนของลาดทวีปซึ่งอาจจะมีเส้นผ่าศูนย์กลางต่ำกว่า 500 เมตร และสูงจากพื้นทะเลโดยรอบกว่า 50 เมตร โดยอาจจะมีก๊าซหรือของเหลวออกมาจากเนินด้วย เนื่องจากพบการสะท้อนกลับของคลื่นเสียงจากชั้นน้ำเหนือพื้นทะเล ซึ่งสันนิษฐานว่าเกิดจากฟองก๊าซที่ลอยกระจายอยู่ในมวลน้ำ

Summary

The primary aim of the project “Morphodynamics and Slope Stability of the Andaman Sea Shelf Break” is the in situ characterization of the slope of the Andaman Shelf in terms previous slope failure and tendency to fail in the future. The first cruise of the project was conducted in November - December 2006 using the RV Chakratong Tongyai and devoted to hydro-acoustic mapping of the shelf break and the slope. A multibeam bathymetric echosounder and a parametric sediment echosounder were used to map the bathymetry and the thickness and structure of the uppermost sedimentary layer of hitherto unexplored parts of the shelf break in the Andaman Sea. An area of more than 2,000 km² in the southwestern corner of the Thai EEZ in the Andaman Sea was successfully mapped. The data covered the upper shelf break from about 500 m down to about 1,400 m in water depth. The processing of the data is still ongoing but so far 34 locations that had distinct morphologic and/or unusual sediment seismic features in this survey area were identified. Most of these (30) were attributed to areas with possible occurrence of low-density fluids or gases in the shallow sediment layers. Almost all of these fluids or gases deposits were in lower slope areas with water depth greater than 900 m. In addition, several manifestations of fluid venting were also mapped on the upper shelf edge at water depths of about 600 m. Some of these shallower vents could form mounds with diameters of up to 500 m and heights of up to 50 m. Diffuse reflections in the vicinity of the mounds and strong signals not related to seafloor reflections indicate the presence of uprising bubbles or gas flares.

Table of Content

Introduction	4
<i>Submarine Slope Stability</i>	5
<i>Types of Offshore Mass Movements</i>	5
<i>Causes of Slope Failure</i>	6
<i>Geological Setting of the Andaman Sea</i>	7
Objectives.....	7
Survey Area.....	7
Survey Instruments.....	10
<i>SEA BEAM 1050 Multibeam Echosounder</i>	10
<i>Sound Velocity and Motion Calibration of the SEA BEAM 1050</i>	11
<i>INOMAR SES 2000 Subbottom Sediment Profiler</i>	12
Survey Results.....	12
<i>Multibeam Bathymetry Survey</i>	12
<i>Subbottom Profiler Survey</i>	14
<i>Shelf Break Morphology—Indications of Slope Failures</i>	16
<i>Shallow Gas Deposits and Fluid Venting Structures</i>	19
Conclusions and Recommendations.....	21
References	23

Introduction

Since December 26, 2004 when a devastating tsunami generated by an earthquake off Sumatra hit the west coast of Thailand, claimed the lives of many people and destroyed large areas along the coast, the potential risk for future tsunami events in that area is of major concern to the Thai people and the scientific community. Besides the risk for tsunamis generated by large earthquakes along the Sunda Arc subduction zone, submarine slumping could be a potential cause for tsunamis in the Andaman Sea as it might had been in Papua

New Guinea in 1998 (Synolakis *et al.*, 2002), for example.

Little is known about the seafloor and the tectonic structure of the Thai part of the Andaman Sea, a pull-apart backarc basin between the Andaman-Nicobar-Islands, Sumatra and the west coast of the Malayan Peninsula. In contrast, the bathymetry, geology, and tectonic structure of the Indian part of the Andaman Sea is well described after recent cruises (Raju *et al.*, 2004). The eastern boundary of the central basin is formed by Mergui Ridge (Fig. 1). According to global bathymetric data sets (GEBCO 1-min) the western rim of the Mergui Ridge forms an escarpment like structure with steep slopes up to a maximum value of about 4.5° . The resolution of these datasets is very coarse and only based on satellite information or very sparse single beam soundings. Thus locally there well may exist much steeper slopes. To date no high-resolution bathymetric data by a high-resolution multibeam bathymetric survey from the Mergui Ridge is available for research and scientific communities and is critically in need to image the morphology of Mergui Ridge and slope.

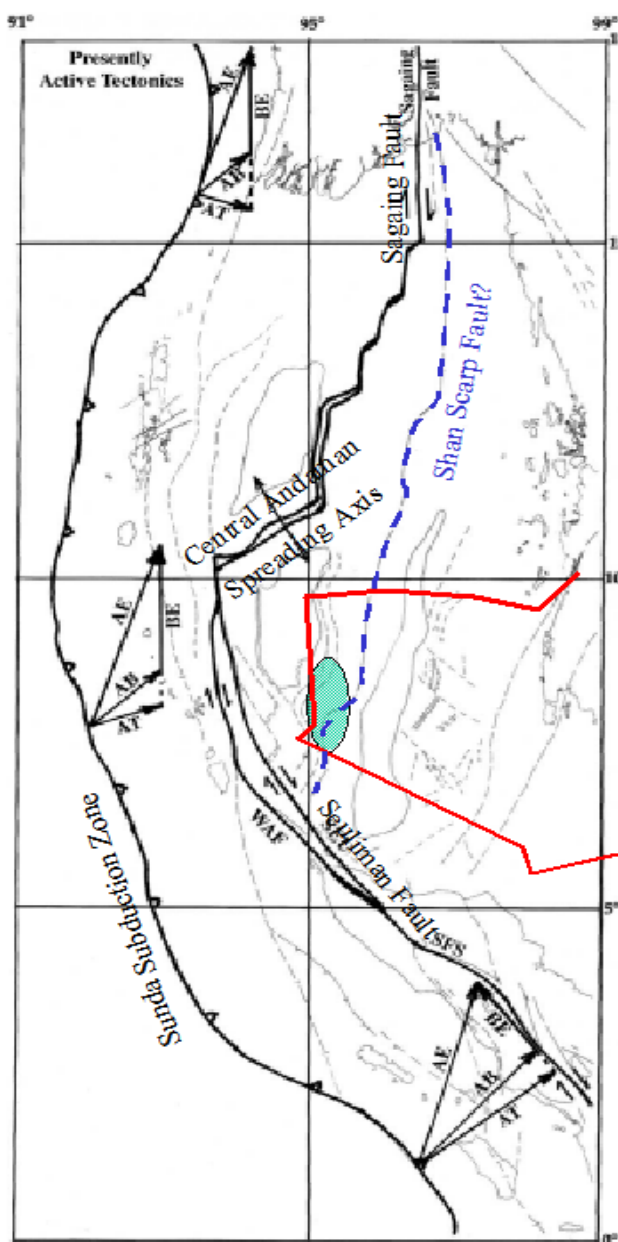


Figure 1. Presently active tectonic elements in Andaman Sea shown in heavy black lines (Curray, 2005). Possible location of Shan Scarp Fault is shown by the blue dashed line. Survey area is shown as green ellipse and EEZ of Thailand in red.

Submarine Slope Stability

Landsliding is an important geomorphic process in mountain areas where it constitutes a major natural hazard. However, submarine landslides are also surprisingly abundant on the seafloor, particularly at the continental slope and the flanks of ocean islands. Mass movements in these settings are of great interest for both fundamental scientific and the commercial interests. Improved knowledge of slope processes and depositional features is a priority goal for the energy industry, because of oil exploration and production in deep water and for protection of existing offshore infrastructure (platforms and pipelines, communication cables) against natural hazards. In addition, submarine landslides are being given increasing attention as a plausible cause of tsunamis, which can ravage coastal areas.

Landslides have been defined as the downward and outward movements, generally driven by gravity, of slope-forming materials, in which shear failure occurs. Most submarine landslides originated in unlithified sediments (e.g., Hampton *et al.*, 1996), but also at volcanic islands within volcanoclastic deposits and volcanic rocks (Watts and Masson, 1995; Urgeles *et al.*, 1999). However, on land it has been documented that slides also form in well-lithified rock by fracturing on a small scale (Brückl, 2001). Nevertheless, landslides occur particularly in environments where weak geological materials such as rapidly deposited fine-grained sediments or fractured rock are subject to strong environmental stresses such as earthquakes, large storm waves, and high internal pore pressures. They occur at locations where the downslope component of stress exceeds the resisting stress, causing movement along one or several concave to planar rupture surfaces. Slope failure can involve huge amounts of material and can move great distances. Slide volumes as large as 20,000 km³ and runout distances in excess of 100 km have been reported (Hampton *et al.*, 1996; Mulder and Cochonat, 1996).

Only a few submarine landslides in historical times, namely those that disrupted populated shoreline or offshore engineering structures, have been documented directly. In most cases an earthquake or large storm waves triggered the event. Unfortunately, even from those extreme events little is known about the state of the slope before failure. Many questions are still unanswered; e.g., had the slope already been creeping and has been accelerated because of earthquake excitation or wave loading or was it quasi-stationary before external forces acted on the slope? Most of what we know about submarine landslides is from remote sensing of features associated with slides, like rupture surfaces and displaced masses of sediment or rock (e.g., Hampton *et al.*, 1996; Mulder and Cochonat, 1996).

Types of Offshore Mass Movements

Creep and cyclic mobility are two phenomena that can cause long-term deformation of sediments and rocks without failure due to elastic and plastic deformation of material under constant load and very low deformation rate (Mulder and Cochonat, 1996). Onshore, creep deformation is well documented but offshore it is observed only at a few locations, perhaps because of difficulties to separate it from tilted blocks. However, creep may accelerate because of increase in sediment loading or wave or earthquake excitation. If the plastic deformation limit is reached, creep may change into a slide or into a plastic flow. Thus, existing creep may characterise an area prone to future failure.

Gravity driven mass movements are avalanches, slides and slumps (Mulder and Cochonat, 1996). In rock avalanches dislocation of the material is important. Energy dissipation is due to the impacts between grains or blocks. Avalanches are catastrophic large-scale events and occur in submarine environments on the flanks of volcanic islands (Watts and Mason, 1995; Urgeles *et al.*, 1999). The size and displacement of individual submarine slide blocks can be impressive. At Tenerife a giant landslide is exposed over an area of 5,000 km². It is estimated to have a length of 100 km, a width of up to 80 km, and a volume of about 1,000 km³ (Watts and Mason, 1995).

Slides and slumps are movements of coherent masses of sediments bounded on all sides by distinct failure planes. The internal structure of the removed material is largely undisturbed during the movement and displacement is limited. However, while in slides the internal structure remains undisturbed it may be distorted in slumps. The rupture surface, particularly in mechanically homogeneous material, commonly is concave upward and scoop-shaped. Accordingly, motion of the displaced mass is rotational, whereby the original seafloor is backtilted. However, if mechanical inhomogeneities such as bedding planes control failure, then the rupture surface is more or less planar, and the movement is translational. Compared to subaerial landslides, submarine slides are enormous. Subaerial slides are generally less than 20 km³ in volume, while the largest submarine slide off South Africa has a volume of 20,000 km³ (Dingle, 1977).

Postfailure evolution of a submarine landslide corresponds to the development of velocity vectors in the displaced mass. Depending on the in-place stress field, sediment properties, and morphology, the failed mass either will stop a short distance along the rupture surface or will evolve into a flow with a relatively large travel distance. Plastic flows are frequent and usually result from the movement of typically underconsolidated masses of sediments. The scarps in their source area are usually indistinct or non-observable when the failure surface is shallow. The only information on the event is provided by the shape and the nature of the deposits. The potential for limited deformation landslides to transform into sediment flows is related to the density of the slope forming material and the amount of shear strength that is lost when the slope fails. If the resulting strength will be smaller than the downslope gravitational stress, the failed sediment mass will accelerate downslope and tend to disintegrate and flow. However, only contractive sediment (i.e., sediment which tends to loose its fabric) can produce a disintegrative type of failure.

Causes of Slope Failure

Some geological environments have certain conditions, which lead to submarine slides (for a review see Hampton *et al.*, 1996). Rapid accumulations of thick sedimentary deposits, sloping seafloor and high environmental stresses are the conditions most commonly associated with such slides. However, many specific factors contribute to submarine landslides, and they occur in a diversity of environments, like fjords, active river deltas on continental margins, submarine canyon-fan systems, the open continental slope and oceanic volcanic islands. Common to all of these environments is the presence of an inclined seafloor where the force of gravity persistently acts to pull sediment or rock downslope. Continental slopes are typically 3° – 6° (Shepard, 1963) and volcanic islands have slopes often steeper than 10°, sometimes as steep as ~30° (Gee *et al.*, 2001). Thus a relatively high tendency

exists for gravitationally driven downslope movements. However, in the Mississippi Delta some mass movements occur on slopes of less than 1° (Mulder and Cochonat, 1996).

Mechanically, a landslide occurs when the downslope driving stress exceeds the resisting strength of the slope forming material. Analyses have shown that the force of gravity typically is not great enough to be the sole cause of failure on most slopes, except in some places of high tectonic steepening. In fact, the controls on most identified slides are obscure, although earthquake shaking and loading by large ocean waves is commonly speculated to be the cause. However, it has been documented for only a few events.

At river deltas the fine-grained deposits have often very high water content and are extremely underconsolidated. The same holds for continental slopes in high productivity regions, for example off Peru. Furthermore, decay of organic material forms expansive interstitial gas. Consequently, the static shear strength can be so low that these weak sediments move down the nearly flat delta surface or continental shelf under a small gravitational driving force. At the head of submarine canyons slope failure might be caused by internally derived seepage forces (Orange *et al.*, 1994). Analysis of some headless canyons indicates that increasing hydraulic-head gradient, caused by tectonic compression or from artesian sources at the canyon head, promotes slope failure and thus causes canyon growth. Moreover, the repeated loading due to waves and earthquake motion may cause a build-up of pore pressure in fine-grained sediment that at least partially support the weight of the grains, decreasing the effective stress (i.e., frictional resistance) at grain contacts and thereby decreasing the strength (Hampton *et al.*, 1996).

In overall the inclined seafloor is the primary agent to pull sediment or rock downslope by gravity. To cause a landslide, however, the downslope stress must exceed the resisting strength of slope-forming material. Geotechnical (physical) parameters of slope-forming material indicate that nearly always other factors than gravity must contribute to increase downslope stress or decrease resisting strength; pore pressure and interstitial gas are important parameters governing the slope stability. Nevertheless, generally external forces like earthquake shaking or cyclic loading by large storm waves must be involved as well.

Geological Setting of the Andaman Sea

The Andaman Sea extends from Myanmar in the north to Sumatra in the south and from the Malay Peninsula in the east to the Andaman and Nicobar islands, which form a part of the Andaman Nicobar ridge, in the west. Andaman Sea Basin presents a very complex sea floor morphology (Fig. 1). The south western part of the basin is dominated by N-S trending fault systems. The basin is dissected by a prominent valley-like feature, which corresponds to the Andaman backarc spreading center. The western part is dominated by volcanic constructs that are related to arc volcanism and backarc spreading activities, whereas the eastern part is distinctly smooth (Raju *et al.*, 2004). From the tectonic point of view, the Andaman Sea region is divided into three provinces: forearc basin, the magmatic arc and the backarc basin. The forearc basin includes West Basin, Invisible Bank and other banks further to the South. The magmatic arc corresponds to Barren-Narcondam volcanic islands, and other small volcanic constructions. The backarc region includes Alcock and Sewell Rises, East Basin, the shelf and basins to the north and east and the Central Andaman Basin (Curry, 2005).

The Andaman Sea is an active backarc basin and lies above and behind the Sunda subduction zone where convergence between the overriding Southeast Asian plate and the subducting Australian plate is highly oblique. This oblique convergence has produced a sliver plate between the subduction zone and a complex right lateral fault system. The late Paleocene collision between Indian and Asian plates with approximately normal convergence started clockwise rotation and bending of the northern and western Sunda Arc. The initial faulting, which probably started in the Eocene, extended through the outer arc ridge offshore Sumatra, through the present region of the Andaman Sea into the Sagaing Fault. With more oblique convergence due to the rotation, the rate of strike-slip motion increased and a series of extensional basins opened obliquely by the combination of back arc extension and the strike-slip motion. The chronology of the basin formation is the Mergui Basin starting at ca. 32 Ma, the conjoined Alcock and Sewell Rises starting at ca. 23 Ma, East Basin separating the rises from the foot of the continental slope starting at ca. 15 Ma and finally at ca. 4 Ma the present plate edge was formed. As a result Alcock and Sewell Rises were separated by formation of the Central Andaman Basin, and the faulting moved onshore from the Mentawai Fault to the Sumatra Fault System dissecting Sumatra (Curry, 2005). In the backarc region the current spreading centre is located in the Central Andaman Basin, which is oblique to the trench and lies between Alcock and Sewell Rises. These two seamounts are of volcanic origin and is defined by the 3,000 m boundary isobath (Curry, 2005; Raju *et al.*, 2004). Their orientation on either side of the spreading centre indicates that these seamount complexes were probably together prior to the initiation of backarc spreading (e.g., Raju *et al.*, 2004).

A complex system of short spreading rifts and transforms in the central basin of the Andaman Sea has been suggested to be the consequence of spreading with an initial slower opening rate of 1.6 cm/yr and an increase in spreading rate to about 3.8 cm/yr from magnetic anomaly 2 (2 Ma) to present (Curry *et al.*, 1979; Raju *et al.*, 2004). Current direction of spreading is NW-SE (e.g. Raju *et al.* 2004). The topographic expression of the backarc spreading center varies from a smooth sediment filled 12-15 km wide rift valley in the northeast to an 8-9 km wide rugged and shallow rift valley toward the southwestern part. The depth of the rift valley floor varies from ca. 3000 m in NE to ca. 4,000 m in the SW producing 400 to 600 m deep valley with respect to the adjacent seafloor. The sediment thickness in the Central Andaman Basin ranges from essentially zero in the southwestern part of the basin to almost 2 km in the outer edges of the northeastern end near the bend in the plate edge. In the SW, some tilted blocks resulted from basement block faulting, are devoid of sediment covers (Raju *et al.*, 2004). The spreading has been continuous, but the influx of sediment transported by turbidity currents into this basin was episodic with fluctuations in Plio-Pleistocene sea level. During Periods of lowered sea level, sediments poured off the shelf down the canyons and gullies cut into the shelf edge and slope as massive turbidity currents. Then, during rise of sea level as the river mouths retreated from the shelf edge, the sediments supply was greatly reduced and the fan valleys or turbidity channels were filled. This is the Andaman Submarine fan, extending from the continental slope of the Gulf of Muttam, offshore southern Myanmar, to East Basin, with more recently opened segment in the Central Andaman Sea (Curry, 2005).

East Basin presents a section of flat ponded sediments at least 4.6 km thick overlying an oceanic basement. The tentative limit between oceanic and continental crust runs N-S though lower continental slope to the east of East Basin. The origin of the margin in the

Andaman Sea is presumed to be an extensional margin formed by opening of the Andaman Sea along a backarc fault line known as Shan Scarp Fault. Seismic reflection image suggest down to basin listric faulting beneath the continental slope, as mentioned previously. Faulting of the shelf is also important in some of the area. Mergui Basin is an offshore extension of the North Sumatra Basin. It is a backarc basin formed by rifting, transtension and thinning of continental crust. The basic simplified structure is a sag basin formed by graben and half graben extensional faulting. The extension was in an E-W to ESE-WNW direction, but dextral sliver faulting turns this extension direction to NW-SE.

Objectives

The project has primarily aimed to assess the potential risk for tsunamis generated by submarine slumping of the Andaman Sea shelf break off the west coast of Thailand through the following tasks:

- To map the morphology of the western slope of Mergui Ridge and identify scarps, headwalls, escarpments, debris toes and other manifestations of slope failures and downslope mass transport;
- To determine the character of slope failures (creep, slide, slump) and distinguish between sequential and catastrophic events; and,
- To determine the morphodynamic and tectonic state of the area derived from high resolution bathymetry.

Survey Area

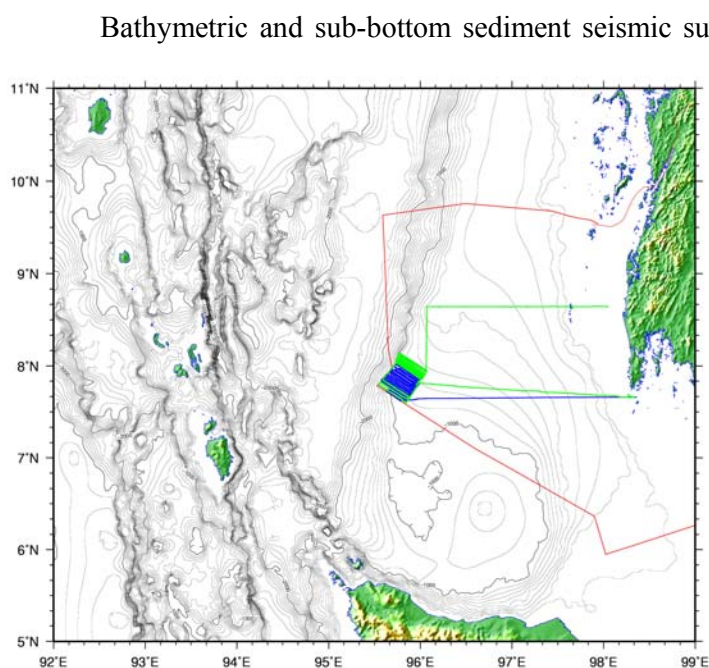


Figure 2. Survey area and tracks of leg 1 (blue) and leg2 (green). The red line denotes the boundary of the Thai EEZ. At the end of leg 2 a reference profile was surveyed towards the Similan Islands.

Bathymetric and sub-bottom sediment seismic surveys were conducted on board the R.V. Chakratong Tongyai of the Department of Marine and Coastal Resources, Ministry of Natural Resources and Environment, between 20 November – 6 December 2006 in the continental shelf margin and upper slope of the Andaman Sea shown in Fig. 2. The cruise was separated into two legs, leg 1 covered 20 – 27 November 2006 and leg 2 covered 29 November – 6 December 2006. Water depths in the survey area were ranging from 500 to 1,400 meters.

Surveys were carried out along 30 parallel tracks that were oriented roughly in the northwest-southeast direction. Tracks were about 22 nm long and about 1'

(about 1.8 nm) apart, or less, to ensure sufficient overlapping of swaths of the multibeam echosounder. The area covered by this survey cruise was about 2,000 km².

Survey Instruments

Two main survey systems used in this project were the SEA BEAM 1050 Multibeam Echosounder and the INNOMAR SES 2000 Subbottom Profiler. Both instruments were on loan from the IFM-GEOMAR in Kiel, Germany. The principles and configurations of these two systems are described below.

SEA BEAM 1050 Multibeam Echosounder

The SEA BEAM 1050 System contained two narrow beam width transducer arrays of the Type LSE 237 with a transmitter power output of 3,500 W for each transducer. The transducers were mounted over the port side of the R.V. Chakratong Tongyai using a specially constructed removable pole (Fig. 3). The transducers pinged quasi-simultaneously into 14 directed sectors. Each sectors comprised of three narrow beams at which each contained three subfans a beam width of 1.5° (Phase calculator) and a spacing of 1.25°.

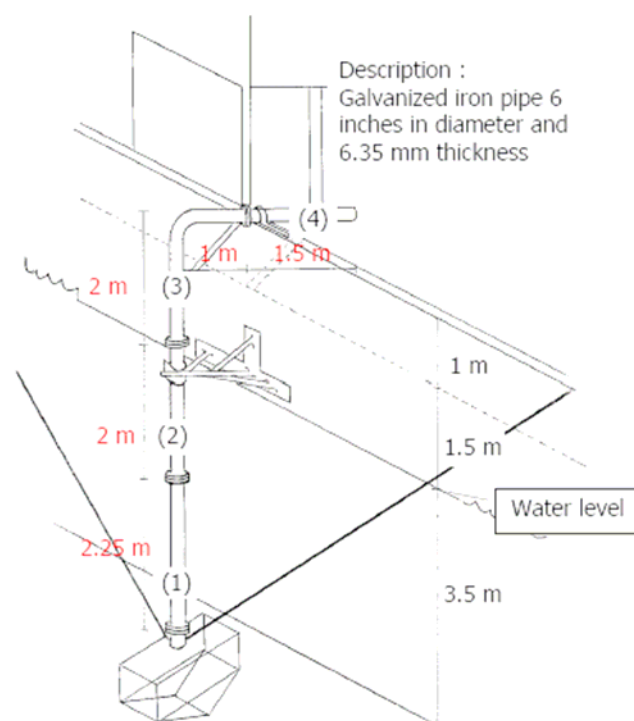


Figure 3. Multibeam transducer mounting over the port side of the R.V. Chakratong Tongyai.

Therefore the entire system comprised of 14 sectors x 3 beams x 3 subfans = 126 beams in total. The relatively high operating frequency of 50 kHz in conjunction with small size transducers offered two advantages, high coverage and narrow beam width, over one-way procedures, i.e. non-directed transmission and reception.

The IXSEA OCTANS 1000 Motion Sensor recorded the ship rolling, pitching and heaving data that were used to calculate the compensation for ship dynamic motion.

The position, speed and heading of the ship were based on a GARMIN 1000 GPS which was regularly compared with the ship main navigational GPS (FURUNO).

Schematic configuration of the SEA BEAM 1050 System on board the R.V. Chakratong Tongyai is shown in Fig. 4.

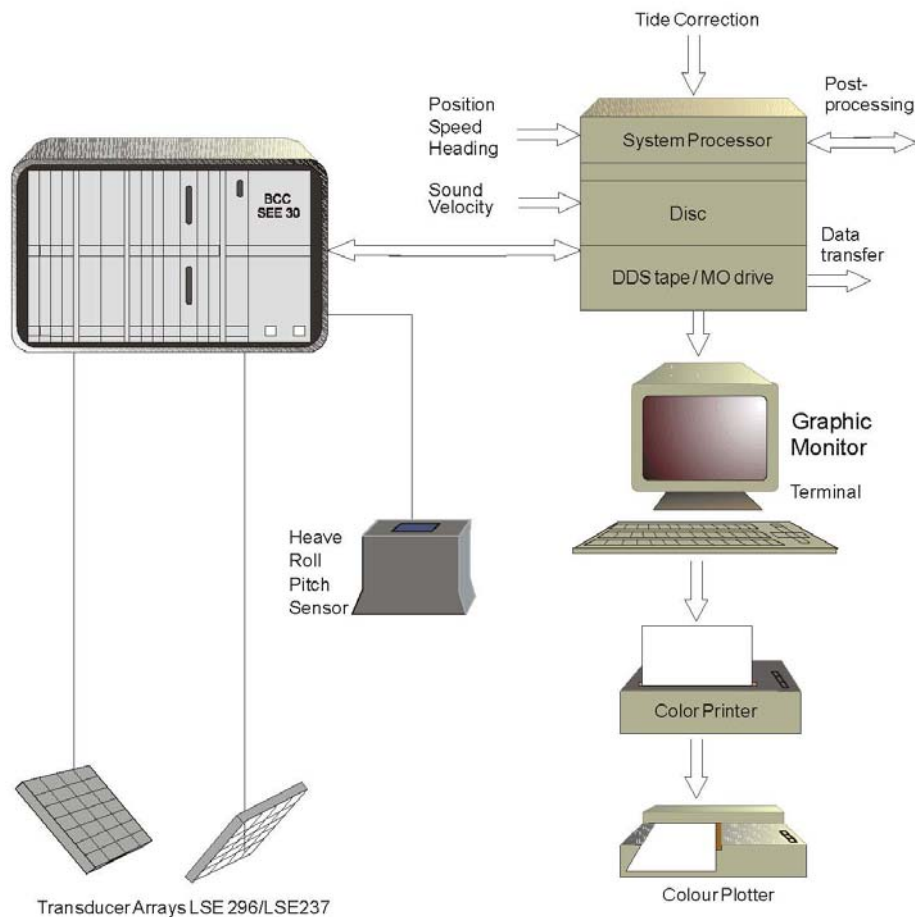


Figure 4. SEA BEAM 1050 System configuration on board the R.V. Chakratong Tongyai.

Sound Velocity and Motion Calibration of the SEA BEAM 1050

The influence of the sound velocity on the sound beam propagation in water was taken into account by using ray tracing algorithms based on the sound velocity profiles. Such profiles were calculated from the *in situ* temperature, salinity and pressure measured at positions $7^{\circ} 42.28' N$ and $98^{\circ} 23.8' E$ and $7^{\circ} 38.15' N$, $95^{\circ} 46.76' E$ using a CTD (SEA & SUN CTD48M).

Roll calibration procedure was first done on 20th November over a 2 nautical miles track near to Phuket Island with water depths of around 40 m and quite planar seafloor. The recordings of the multibeam system were processed for each direction separately. The differences in the inclination across track of both digital terrain models (DTM) were calculated. Negative value of the inclination represented the roll calibration value. As the SEA BEAM 1050 system had two transducers, one each directed towards port and starboard side of the vessel, two different bias values were applied. Values of 3.35° for the port and

2.18° for the starboard transducer had been determined. A similar roll calibration was run at the beginning of leg 2 on 29th November and the same values were retained.

INNOMAR SES 2000 Subbottom Sediment Profiler

The INNOMAR SES-2000 system utilized the parametric or non-linear sound propagation effect—a principle that when two slightly different frequency sounds were transmitted, they propagated and generated a secondary sound with lower frequency. These primary high frequencies can be used for the exact determination of the water depth while the secondary sound generated by difference of the two primary frequencies, which had a much lower frequency, could penetrate the bottom sediments down to about 15 m to give information about the sub-bottom structure and reveal any unconformities related to slope failures and instabilities.

Because the low frequency was generated from parametric propagation of the two higher frequencies, the generated sound retained the small and thus high resolution bottom footprint. This is an advantage over the use of a linear system to generate the same low frequency since the footprint will be much larger and the survey resolution would be much less.

Survey Results (Preliminary)

Multibeam Bathymetry Survey

The multibeam echo sounding data have been processed by various visualisation techniques to image for the morphology of the area in great detail. However due to the unexpected high noise level during the data acquisition and technical problems with the multibeam transducers, the processing of the data could not just follow standard routine procedures but requires special attention and specifically adapted processing algorithms which had led to a delay in the generation of final maps. The bathymetric map in Fig. 5 shows along the swathes a distinct noise pattern that was resulted from a defect in the transducer. A special algorithm to delete these erroneous depth determinations is under development and will use new data to be collected for the same area in the 2nd cruise in the late 2007 to correct for these inconsistencies.

The survey cruise covered the southwestern corner of the Thai EEZ (Fig. 2), which forms the southern end of the Mergui Ridge by a topographic rise that stretches through the central Andaman Sea in north-south direction. Water depths in the survey area varied from about 500 m on the top of the Mergui Ridge to more than 1,400 m at the southwestern edge of the area. The shelf break was pronounced and clearly visible. The top of the Mergui Ridge displayed by a smooth and gentle topography with no large distinct topographic features on its top.

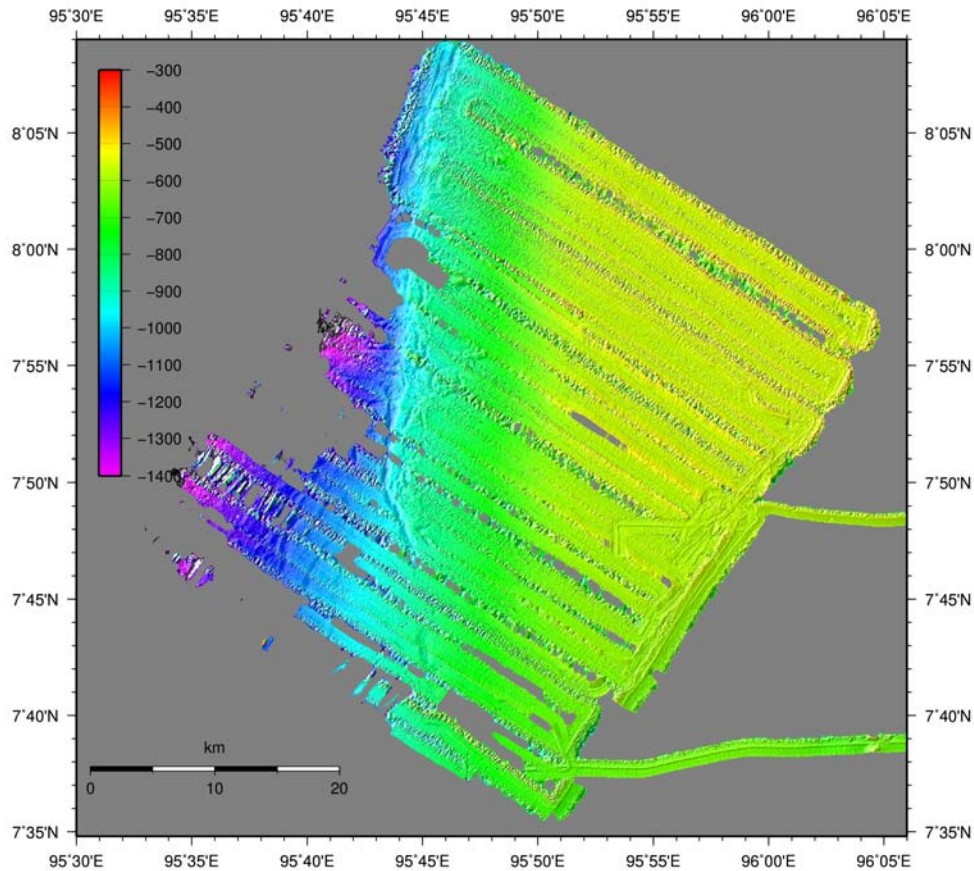


Figure 5. Preliminary results of the multibeam survey.

Parallel to the shelf edge between about 7° 50' N and 7° 55' N a small graben with a maximum width of about 100 m and a maximum depression of around 80 m (Fig. 6) was visible. The graben could be traced along the break over a distance of about 15 km. Similar structures could be found along the break at about 8° N to 8° 05' N but, however, smaller and shorter. Whether or not these grabens in any ways associated with downslope creeping of sediments remained to be further explored.

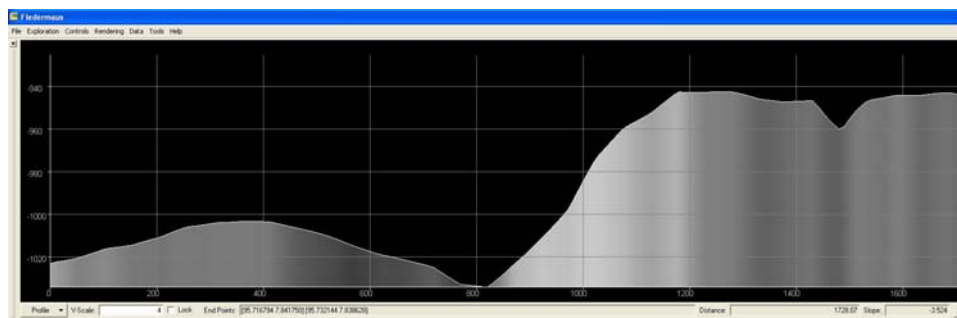


Figure 6. Depth profile crossing the graben like structure at position 7° 50' N, 95° 43' E.

Subbottom Profiler Survey

The Innomar parametric subbottom profiler SES2000 was operated during the entire cruise. Reliable records were obtained down to a water depth of nearly 1,400 m, thus this system covered the same depth range as the multibeam echosounder. Data quality was generally good down to a water depth of about 800 m, records from greater depths were degraded by weaker signals and increased noise level. Penetration of the signals into the sedimentary layers was achieved up to about 10 m with maximum values of 15 m. Over large areas the record sections were rather uniform, showing a prominent second reflecting horizon about 5 m below the seafloor (Fig. 7). In water depths greater than 850 m this second reflector was not observed. It was not possible to determine whether this reflector disappeared in greater depths, or was just not recorded due to weaker signals. Observations indicated that the thickness of this layer might be decreasing with increasing depth (Fig. 11).

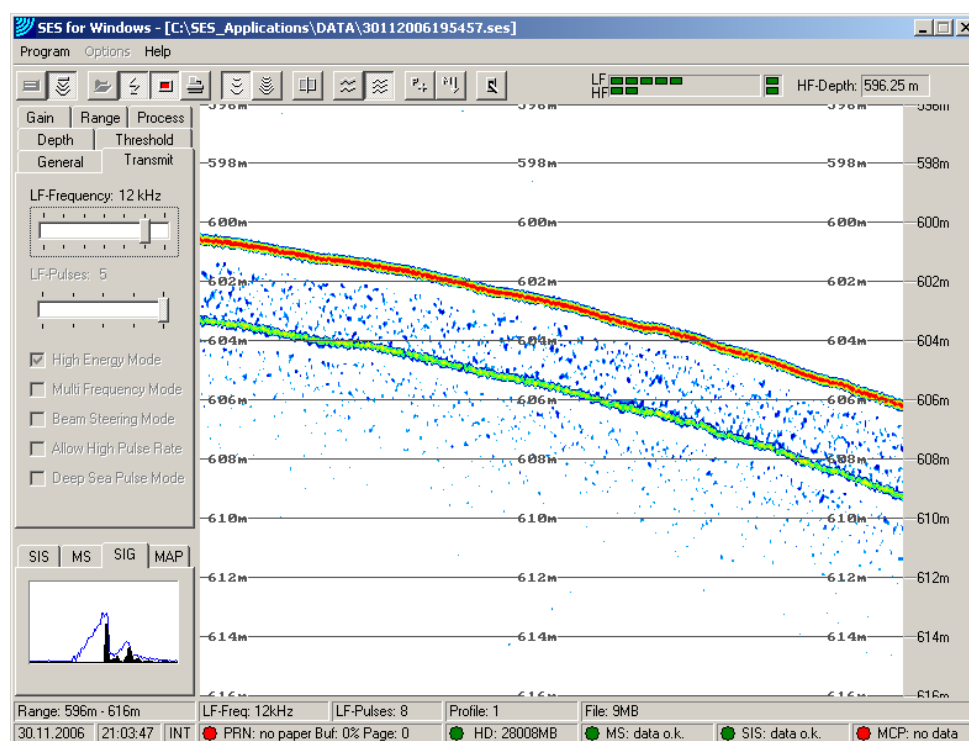


Figure 7. Subbottom profiler record showing the second reflector below the seafloor.

A remarkable number of subbottom profiler records showed reflections with negative polarity (blue areas in the records), predominantly just beneath the seafloor (Fig. 8). Negative polarity records indicated reflections from layers with less density than water, such as gas bubbles or gas layers. This might be an indication for gas bearing sediments or free gas in the sediments. Generally, the areas with negative polarity records were not continuous over large distances but often associated with morphological features. Figure 6 shows a domal uplift in 860 m water depth, just reaching the seafloor. Negative polarity records were found just below the top of the domal uplift. This observation led to a speculation of shallow gas migrating upwards and concentrating below the non-permeable seafloor.

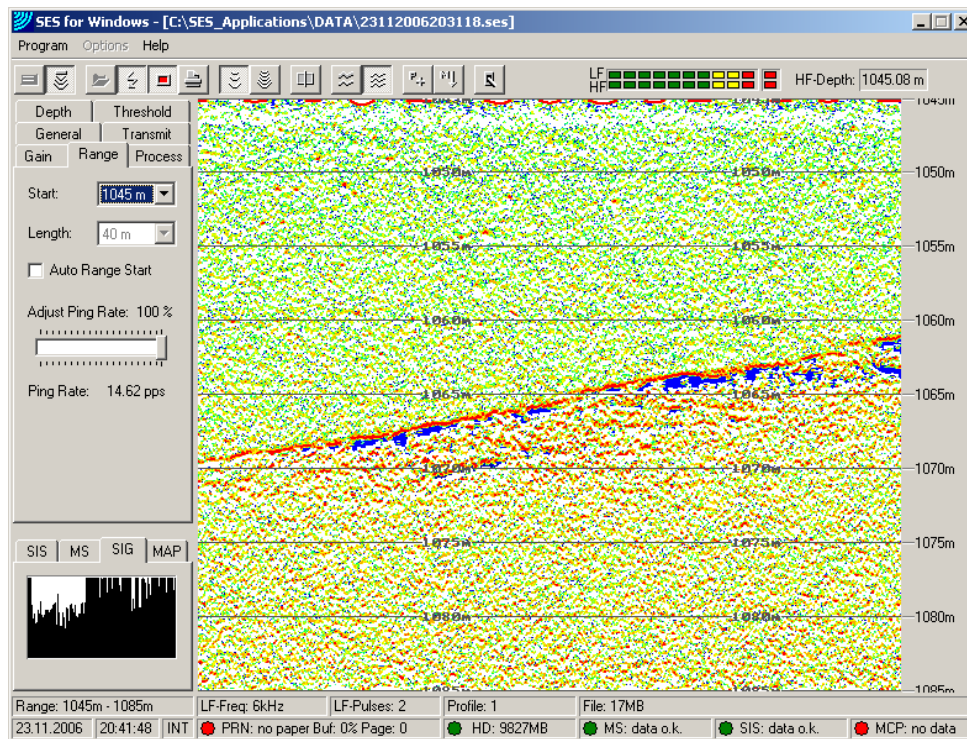


Figure 8. Subbottom profile showing reflections with negative polarity (blue)

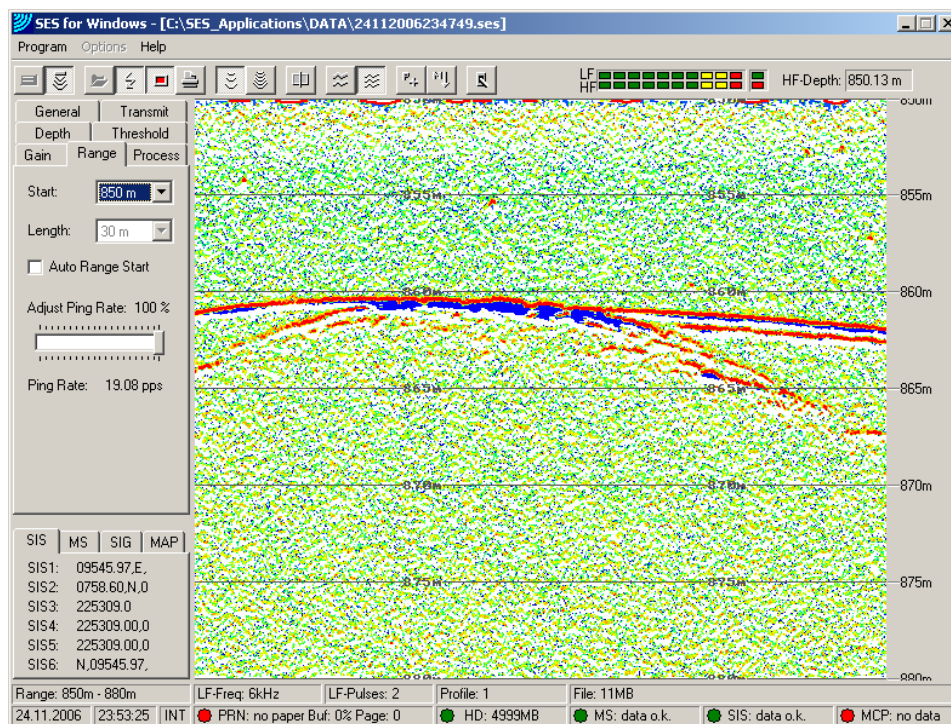


Figure 9. Subbottom profile of a mound-like structure and possible concentrations of gas below the seafloor at the top of the mound; position 7° 58.6'N, 95° 45.97'E

Shelf Break Morphology—Indications of Slope Failures

The multibeam bathymetric surveys yielded a high-resolution data set that were used to develop a morphotectonic map of the area. Indications of downslope mass transport and slope failures such as faults, scarps, headwalls, debris fields, toes of slide masses could be identified in the morphology and helped to document the current state of slope stability. Simultaneously the stratigraphies of the upper sedimentary layers were also recorded by the parametric subbottom profiler.

Generally, the survey area was characterized by a gentle and smooth morphology, as derived from the multibeam echosounder data. In Fig. 10 three different depth profiles across the slope are shown. For most upper slopes the inclination was rather constant with an angle of just 1.0° to 1.2° . In the northern part of the survey area at a water depth of about 900 m this gentle inclination was suddenly increasing to about 5° and more, while in the southern part of the survey area the inclination angle remained rather constantly gentle down to about 1,300 m, the maximum depth which was surveyed. Further processing of the data is underway to investigate the nature of the rapid increase in inclination angle and its possible roles in the nature of the slope failures.

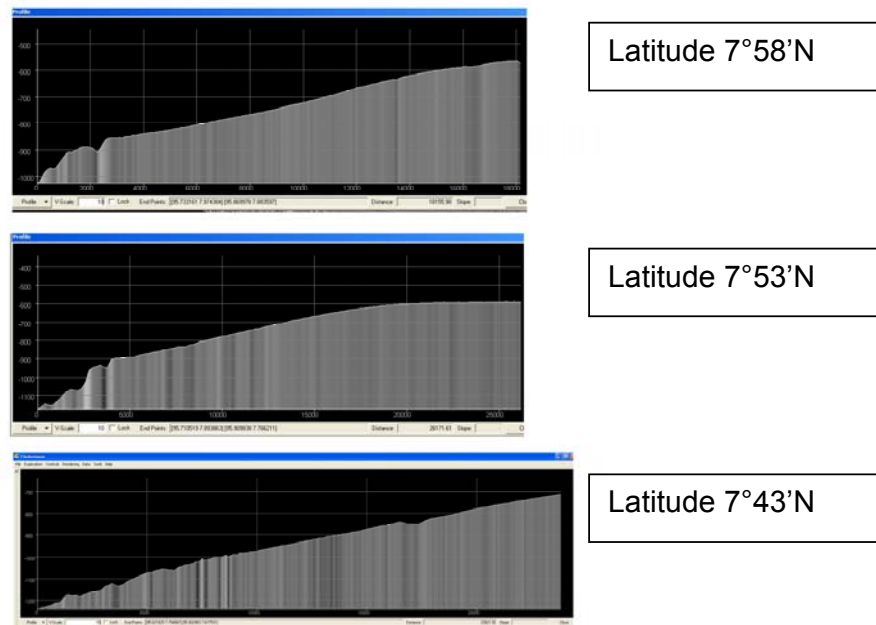


Figure 10. Depth profiles from multibeam echo sounding across the slope from north to south

In the subbottom profiler records, some weak indications of slope failures were only observed in the southern part of the survey area. Profiles derived from digitized subbottom profiler records across these structures are displayed in Figs. 11 to 15. Possible outlines of displaced masses can be traced in these Figures, and the thickness of these masses were usually not more than 10 m.

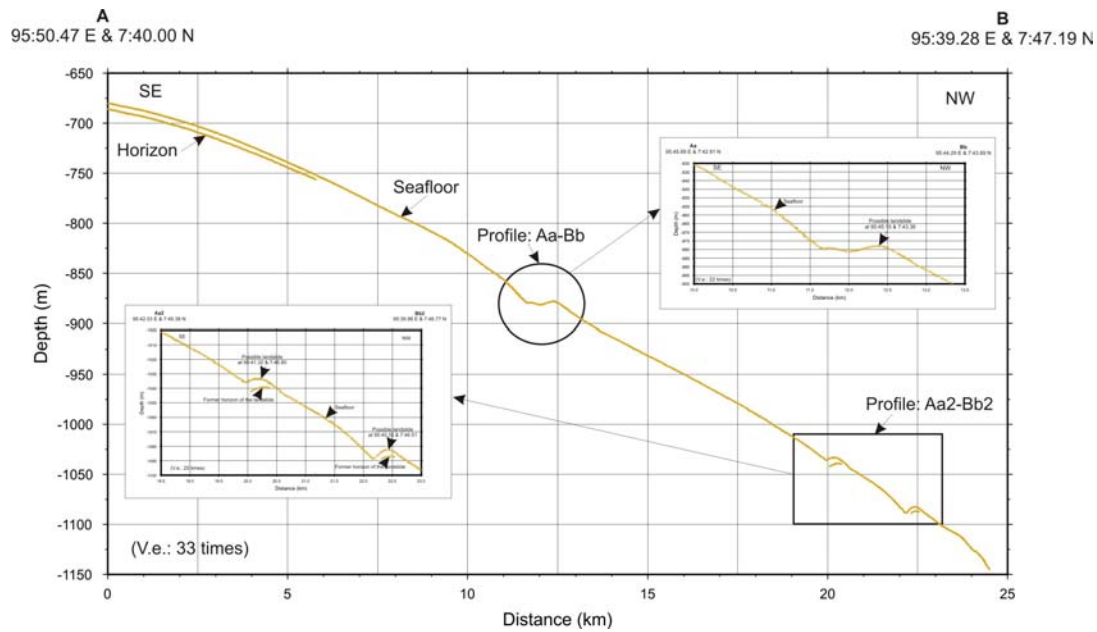


Figure 11. Depth profile based on digitized subbottom profiler records across the slope

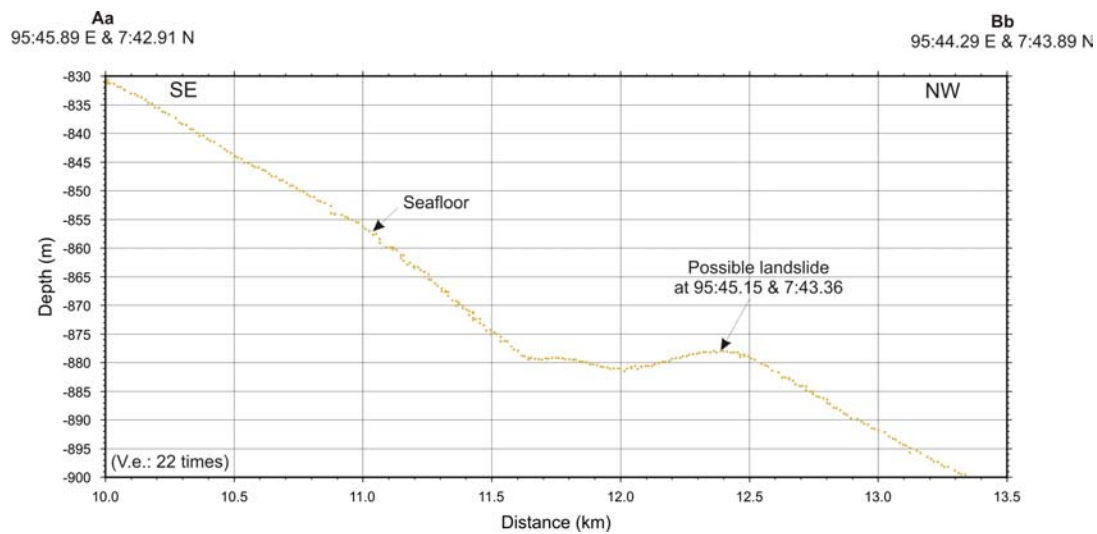


Figure 12. Depth profile Aa-Bb based on digitized subbottom profiler records across the slope (blow up of Fig. 11)

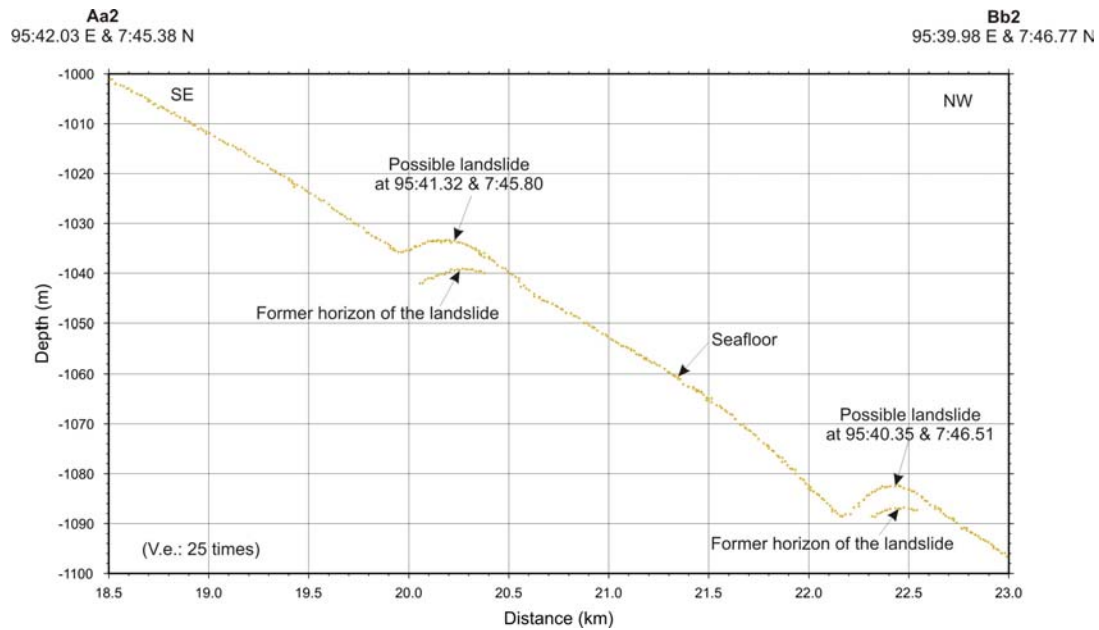


Figure 13. Depth profile Aa2-Bb2 based on digitized subbottom profiler records across the slope (blow up of Fig. 11)

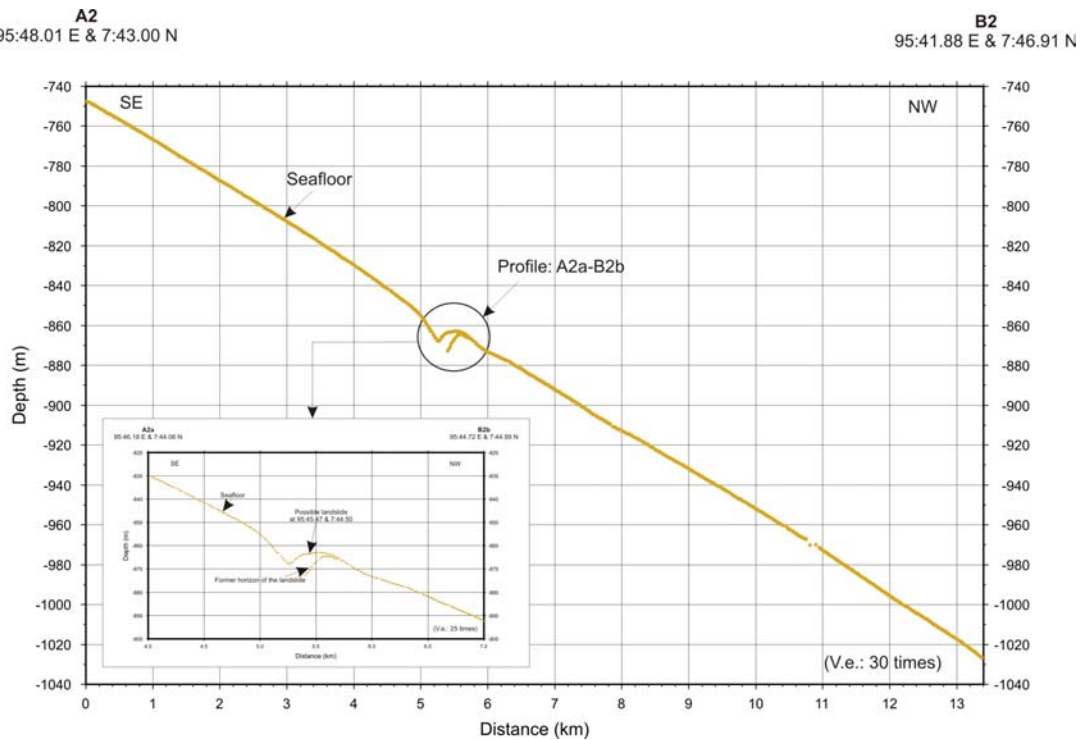


Figure 14. Depth profile based on digitized subbottom profiler records across the slope

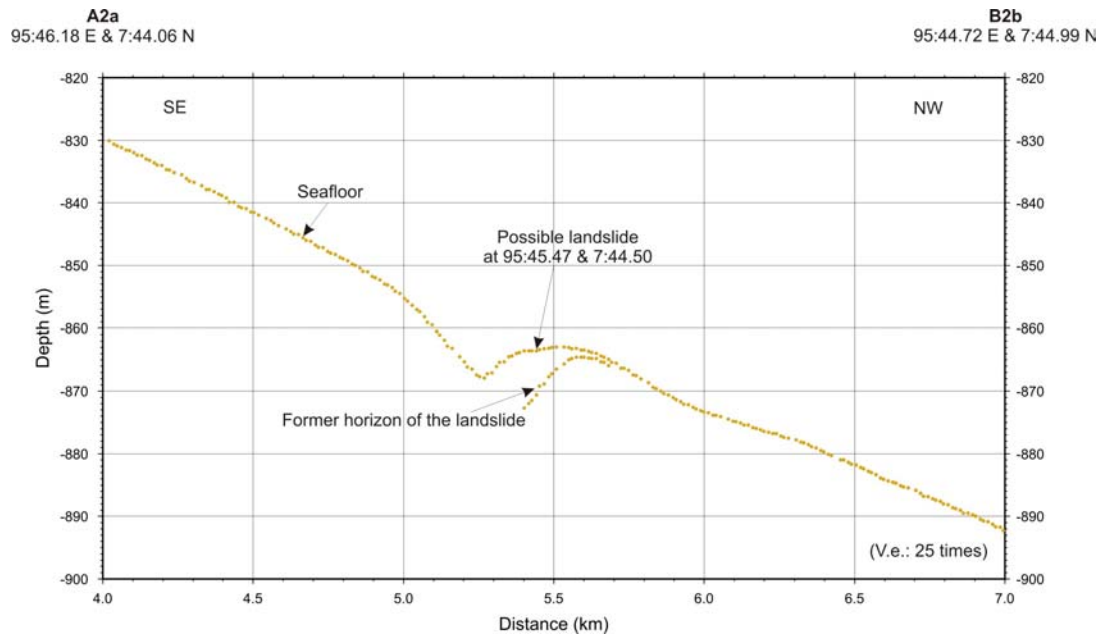


Figure 15. Depth profile A2a-B2b based on digitized subbottom profiler records across the slope (blow up of Fig. 14)

Shallow Gas Deposits and Fluid Venting Structures

Negative polarity reflections in some subbottom profiles (e.g., Fig. 9) had led to a speculation of possible shallow gas deposits in the northwestern part of the survey area. All of these observations only observed in water depths greater than 800 m.

Shallow seabed gas had been found on continental margins worldwide (Fleischer *et al.*, 2001). Biogenic methane is generated in shallow seabed sediments on continental margins by biogeochemical processes, especially in rapidly deposited muddy sediments with high organic matter content (Best *et al.*, 2006). Gassy sediments can destabilize seabed slopes (Best *et al.*, 2006) and hence initiate slope failures (Longva *et al.*, 2003). In the subbottom profiler records we found one possible slump associated with the occurrence of gassy sediments. These records had to be carefully evaluated further to assess the potential risk for slope failures.

In addition to the possible occurrence of shallow gas there were also places with very distinct and focused venting of fluids or gas. A prominent morphological feature was found at 7° 48' N, 95° 57.8' E and verified in several additional profiles that were surveyed over this area (Fig. 16). This circular domal uplift of about 35 m high with a diameter of about 200 m was also mapped by the multibeam bathymetry system. The shape of this mound resembles a mud dome or mud volcano. The seafloor at both sides was bended downwards. Acoustically transparent areas near the top and the flanks of the mound indicated the presence of fluids or gas. This assumption was supported by a number of diffuse reflections above the seafloor in the water column. In addition, indications for rising gas flares or bubbles were recorded by

the multibeam system, i.e. strong signals not related to the seafloor reflection were recorded in the vicinity of the mound.

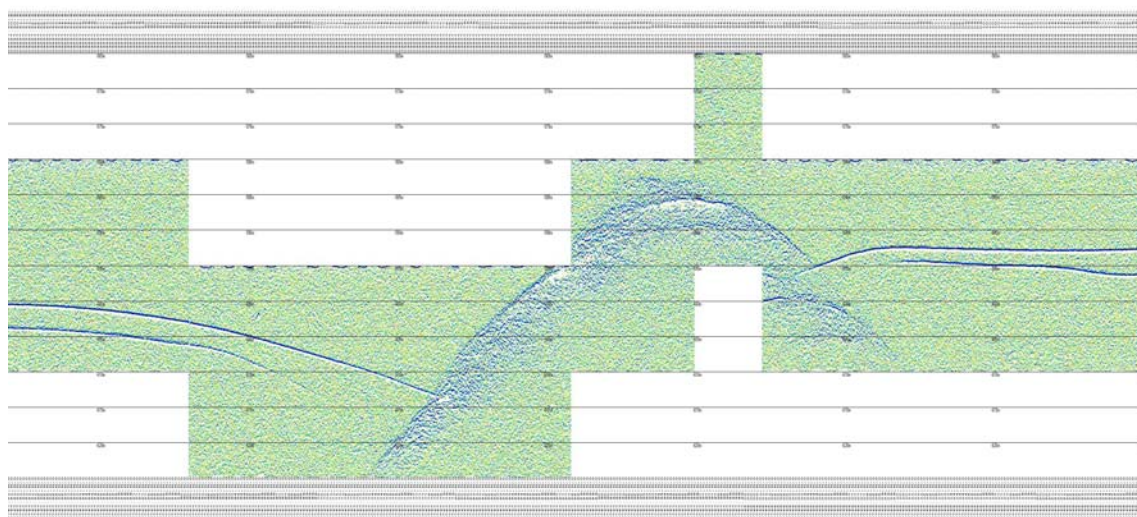


Figure 16. Subbottom profile across a possible mud dome or mud volcano.

Another example was previously shown in Fig. 9 where a hidden mound-like structure was imaged. The top of the mound just reaches the ocean floor but did not project out of the sediment layer. Negative polarity signals (blue in that figure) again indicated the presence of fluids and/or gas. However while the “hidden mud dome” shown in Fig. 9 lied in the region of observed negative polarity signals and furthermore, also with the water depth coincided with the depth of these observations, the “projected” dome in Fig. 16 fell outside of that region and was found in shallower water depth. It is not clear so far whether this feature comprised of a different modes of venting of similar biogenic shallow gas or whether a different origins of the gas were involved.

Preliminary overlaying the survey area over major tectonic features in the region (Curry, 2005) revealed that the area was possibly in the vicinity of the Shan Scarp Fault (Fig. 1). However, because this Fault is not known to be active recently and the exact location in the sea is not well located, which are so do for Ranong and Klong Marui Faults, whether these fault zones could be a geological source of heat for the dome venting remained to be inconclusive.

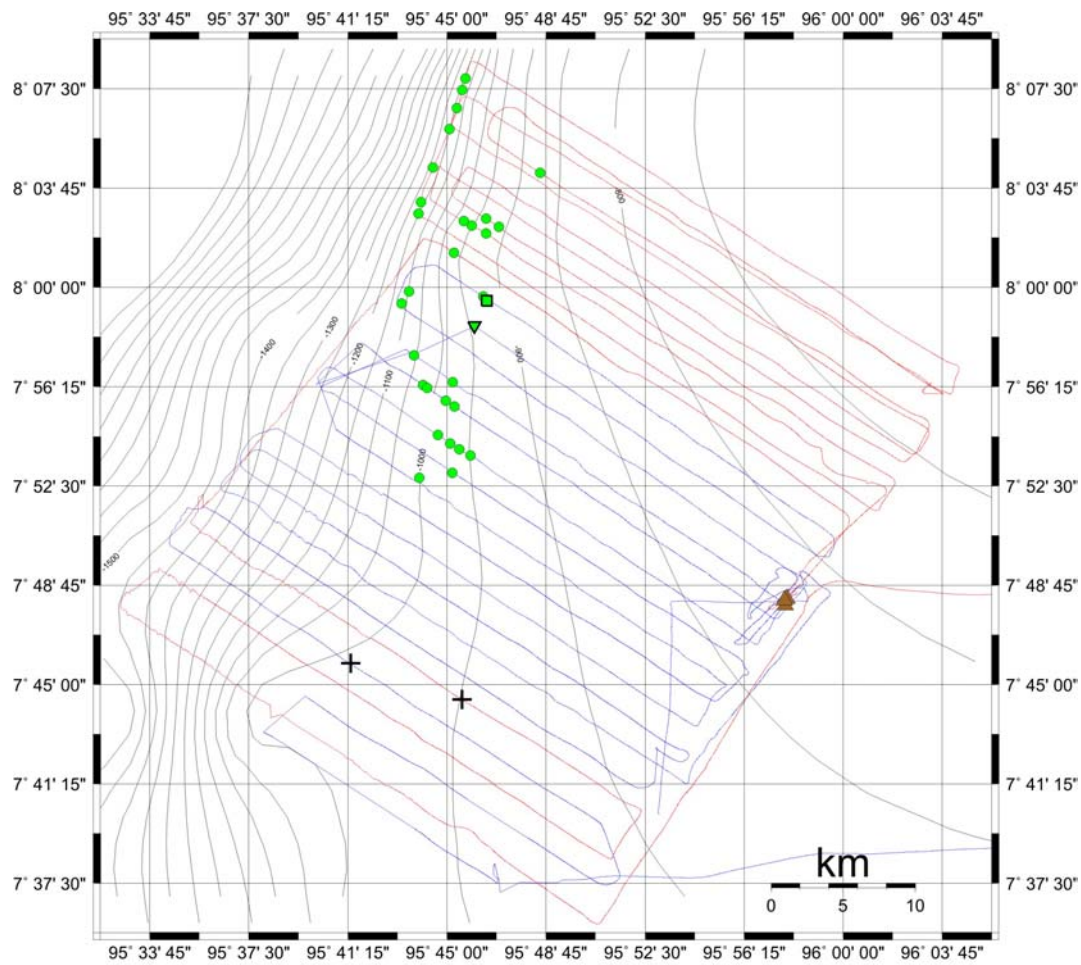
Conclusions and Recommendations

So far 34 locations that had distinct morphologic and/or sediment seismic features in the Cruise I survey area were identified (Fig. 17). The largest number (30) was attributed to areas with possible occurrence of low-density fluids or gases in the shallow sediment layers. Almost all of these fluids or gases deposits were in lower slope areas with water depth greater than 900 m. Among those locations, one was associated with possible slump and another one with a possible “hidden” mud dome.

Two possible “projected” mud domes were found along the upper slope with water depth of about 600 m. However, the possibility that these two features were the submarine rock outcrops still cannot be ruled out. Lastly, two locations with possible downslope landslide were identified in the southern part of the survey area (Fig. 17).

To verify our speculations for these features, in depth analyses of multibeam bathymetry and sediment seismic profiles are necessary. At the point, the Thai scientists were able only to process and basic visualize the data. However, to further analyze and interpret the data in terms of geodynamic and sediment geophysics the Thai team would require additional training and practice on deep-sea sedimentology and marine geo-acoustic. Such advanced training and data analysis workshop is offered by the German counterparts of this project to be held in Late January 2008 in Kiel, Germany, where 2-3 Thai marine geological scientists and apprentices engaged in this project will take a 4-weeks post-graduate level intensive program under closed supervision from German experts from IFM-GEOMAR as well as from University of Kiel.

Many of the likely to be fluids/gases deposits were located along the deepest northwestern edge of this survey area. If these were methane deposits, for example, we would expect to find more of those in the deeper areas and also possibility of having methane hydrates. About 50 km north of the survey area, there might be a submarine canyon, which could indicate an old Pleistocene river mouth that might supply large amount of ancient organics into these sediments. More survey to the north of the current area will yield very valuable information critically necessary to interpret the current data.



Legend:

- Possible deposits of fluids or gases below the seafloor in a shallow deep
- Possible slump with the occurrence of possible fluids or gases
- ▼ Possible Mud-Dome below the seafloor with deposits of fluids or gases above
- ▲ Striking Mud-Dome or Mud-Vulcano with possible deposits of fluids or gases
- + Steep slope with possible landslide

Figure 17. Seafloor structures classified based on subbottom profiler records. Depth contours in the background is from GEBCO data and not from this survey, which are under processing.

References

- Best, A. I., Richardson, M. D., Boudreau, B. P., Judd, A. G., Leifer, A., Lyons, P., Martens, C. S., Orange, D. L., and Wheeler, S. J. 2006. Shallow seabed methane gas could pose coastal hazard. *EOS Trans. Amer. Geophys. Union* 87: 213-220.
- Brückl, E. P. 2001. Cause-effect models of large landslides. *Natural Hazards* 23: 291-314.
- Curry, J. R. 2005. Tectonics and history of the Andaman Sea region. *J. Asian Earth Sci.* 25: 187-232.
- Dingle, R. V. 1977. The anatomy of a large submarine slump on a sheared continental margin (SE Africa). *J. Geol. Soc. Lond.* 134: 293-310.
- Fleischer, P. T., Orsi, H., Richardson, M. D., and Anderson, A. L. 2001. Distribution of free gas in marine sediments: A global overview. *Geol. Mar. Lett.* 21: 103-122.
- Gee, M. J. R., Masson, D.G., Watts, A.B. and Mitchell, N.C. 2001. Offshore continuation of volcanic rift zones, El Hierro, Canary Islands. *J. Volcanol. Geotherm. Res.* 105: 107-119.
- Hampton, M. A., Lee, H. J. and Locat, J. 1996. Submarine landslides. *Rev. Geophys.* 34: 33-59.
- Longva, O., Janbu, N., Blikra, L. H., and Bøe, 2003. The 1996 Finneidfjord slide: Seafloor failure dynamics. In: J. Locat and J. Mienert (eds.) *Submarine Mass Movements and Their Consequences*. New York: Springer Adv. Nat. Technol. Hazards Res. Ser., pp. 531-538.
- Mulder, T. and Cochonat, P. 1996. Classification of offshore mass movements. *J. Sedimentary Res.* 66: 43-57.
- Orange, D. L., Anderson, R. S. and Breen, N. A. 1994. Regular canyon spacing in the submarine environment: The link between hydrology and geomorphology. *GSA Today* 4: 29-39.
- Raju, K. A. K., Ramprasad, T., Rao, P. S., Rao, B. R. and Varghese, J. 2004. New insights into tectonic evolution of the Andaman basin, northeast Indian Ocean. *Earth Planet. Sci. Lett.* 221: 145-162.
- Shepard, F. P. 1963. *Submarine Geology*. New York: Harper-Collins, 557 pp.
- Synolakis, C. E., Bardet, J. P., Borrero, J. C., Davies, H. L., Okal, E. A., Silver, E. A., Sweet, S. and Tappin, D. R. 2002. The slump origin of the 1998 Papua New Guinea Tsunami. *Proc. R. Soc. Lond. A* 458: 763-789.
- Urgeles, R., Masson, D. G., Canals, M., Watts, A. B. and Le Bas, T. 1999. Recurrent large-scale landsliding on the west flank of La Palma, Canary Island. *J. Geophys. Res. B.* 104: 25,331-25,348.
- Watts, A. B. and Masson, D. G. 1995. A giant landslide on the north flank of Tenerife, Canary Islands. *J. Geophys. Res. B.* 100: 24,487-24,398.

**Morphodynamics and Slope Stability of the
Andaman Sea Shelf Break
Annual Research Report for Year 2**

By

Anond Snidvongs^{1,2}

Wilhelm Weinrebe³

Warner Brückmann³

Christian Hensen³

Pachoenchok Jintaseranee^{3,4}

Suratta Bunsomboonsakul¹

¹ Southeast Asia START Regional Center, Chulalongkorn University, Bangkok, Thailand

² Department of Marine Science, Faculty of Science, Chulalongkorn University, Bangkok, Thailand

³ Leibniz Institute of Marine Sciences (IFM-GEOMAR), Kiel, Germany

⁴ Department of Aquatic Science, Faculty of Science, Burapha University, Chonburi, Thailand

Summary

An enormous 2004 tsunami wave had demolished constructions in large areas along the Andaman Sea coast of the southwestern Thailand and caused the worst natural disaster to people life reiterate human in natural hazards. In order to assess the possible impact of future tsunami in near real time, the availability of a reliable bathymetric chart is required. In addition, such a chart allows assessing the potential of slope stability in the area. Seafloor topography of the continental shelf and upper slope of the Andaman sea within the Thai EEZ was investigated on board RV Charkratong Tongyai in November-December 2006 and October-November 2007 in the frame work of the project “Morphodynamics and slope stability of the Andaman Sea Shelf break” using an ELAC Bottomchart Mk.II 50 KHz multibeam echosounder and an INNOMAR parametric sediment profiler. The primary aim of the project was to map the hitherto unexplored parts of the western slope of Mergui Ridge and the in-situ characterization of the slope stability. An area on approximate 3,000 km² in the Andaman Sea shelf break in Thai EEZ from 500 m to 1,700 m water depth covering the outer shelf and upper slope area was successfully mapped.

As yet, one situation as it were a mud volcano and ten positions of possible mound as seen from parametric sediment profiles are studied in a smooth area above 700 m water depth. In addition twenty four anomalous features were attributed to areas with possible occurrence of low-density fluids or gases in the shallow sediment layers in lower slope areas greater than 900 m water depth. In order to generate a reliable bathymetry, various grid resolutions are evaluated in term of accuracy assessment by using histogram plots. A histogram plots of 50 m grid resolution show that 90% of whole grids obtained data at least 3 points per grid while the standard deviation of most grids is better than 0.5 % of water depth. The evaluated values are presented to indicate that a reliable high resolution bathymetric chart can be generated by 50 m grid resolution. A number of previous unknown features including three plateaus, two pockmarks as seen from the bathymetry are visually indentified above 700 m water depth, whereas, three escarpments with two possible displaced masses and more than ten gullies are identified in a slope area below 700 m depth.

To evaluate slope stability in the area, slope gradients are computed from profiles perpendicular to contours depth covering the map. On approximate between 500-700 m depth, the computed inclination angle of about 0° on average indicates a smooth area on top of the ridge. On approximate between 700-1,300 m depth in the west side of the ridge can be divided into two provinces. The computed angles are ranging 1-1.7° in the first province while the angles are ranging 3.2°-4.6° in the second province. The angles indicate slope stability in the continental slope below 700 m depth.

The entire backscatter echoes obtained with simultaneous swath bathymetry covering the area are mapped. Blanket tones covering the map are presented to indicate pattern of seafloor textures. Dark tones blanket smooth area indicates hard seafloor while light tones blanket plateaus, escarpments and gullies

indicate soft seafloor. Less information of subbottom profiles were acquired, however, surface seafloor can still be studied. Strong continuous reflections are observed on smooth area, while rough reflections are observed on slope area. The reflections indicate possible creeping of sediment from uppermost part downslope to be possible displaced mass behind escarpments.

Keyword : Andaman Sea, Mergui ridge, Thai EEZ, Bathymetry, Parametric sediment echosounder

1. Introduction

The geology and the origin of the Andaman-Nicobar Ridge was started consideration that the ridge has been formed of sediments uplifted from the deep ocean floor. The ridge extended southward as the outer arc ridge off Sumatra and Java ([Hochstetter, 1869](#)) and drifted toward to the west away from mainland and thus forms a little Andaman Island ([Sewell, 1925](#)). [Rodolfo \(1969\)](#) was a modern worker who fully understands the rifting and extensional opening of the Andaman Sea. The Andaman-Nicobar Ridge and the Indo-Burma range are composed of the sediments of the Bengal and Nicobar Fans ([Curray *et al.*, 1979](#)).

Over past three decades, several modern hypotheses about the tectonic setting of the Andaman basin and their status at a present to understanding the rifting and extensional opening of the Andaman Sea were published by many researchers ([Frerichs, 1971](#); [Curray, *et al.*, 1979](#); [Eguchi, Uyeda, and Maki, 1979](#); [Mukhopadhyay, 1984](#); [Dasgupta and Mukhopadhyay, 1993](#)). Recently, data bases on bottom penetrating echosounder and airgun seismic reflection profiles from various cruises and from oil companies were used to well describe a tectonic setting of whole Andaman basin ([Curray, 1994; 2003; 2005](#); [Raju *et al.*, 2004](#); [Khan and Chakraborty, 2005](#)). By a tectonic point of view, the basin is divided into three provinces, which are: a forearc basin includes West Basin, Invisible Bank and other banks further to the South. The magmatic arc corresponds to Barren-Narcondam volcanic islands, and other small volcanic constructions. The backarc region includes Alcock and Sewell Rises, East Basin, the shelf and basins to the north and east and the Central Andaman Basin ([Fig. 1](#)).

The Andaman Sea is an active backarc basin which probably started in Eocene (Curry, 2005). The effect of the oblique convergence has been formation of a suture plate between a subduction zones in the southwestern part of Sumatra-Java and a complex right lateral fault system in the Andaman basin. To date, seafloor topography covering Sumatra-Java subduction zones in the south of Indonesia (IFM-GEOMAR, 2005) and central of the Andaman basin in the vicinity to the Andaman Islands (Raju *et al.*, 2004) are successfully mapped. Rate of incline Sumatra-Java subduction (Acharyya, 2000; Curry, 2005) and rate of opening plate in the central Andaman basin are also studied (Raju *et al.*, 2004; Khan and Chakraborty, 2005).

The central Andaman basin, the swath mapping and magnetic gathering of the area was carried out (Raju, *et al.*, 2004). The data revealed several morphotectonic features and divided the central basin into a complex western part comprising arc-parallel seamount chains, N-S-trending fault systems and a relatively smooth eastern part. High-resolution reconstruction of Benioff zone depth-dip angle trajectory for Burma-Java subduction margin were published (Khan and Chakraborty, 2005). The result also reveals that the basin is much young spreading phase recorded towards north of 78 Lat. is possibly the result of late Miocene–Pliocene trench retreat and follow-up trans-current movement along Sagaing and Sumatran fault system with NW-SE pull-apart extension. In addition, the position of strike-slip fault which is called a Shan Scarp Fault (SSF) continue from Burma in vicinity of the northern of Thailand was investigated, however, position of the fault in vicinity of the Andaman Sea shelf break near the Mergui Ridge has not been exactly known (Richter, *et al.*, 1993; Polachan and Racey, 1993; Curry, 2005). Really implication that the basin has not been fully surveyed and poorly known in morphodynamics of anomalous features.

Over past decade, one arc minute global digital atlas (GDA) of ocean floor topography derived from ship soundings and satellite altimetry was developed and distributed to provide the most accurate data set of major oceans topography publically available for geoscientists and oceanographers for current essentially understanding of features covered by the sea (GEBCO, 1997). A global map of horizontal gradients that has been produces can reveal all of the intermediate and large-scale structures of the ocean basins (Smith and Sandwell, 1997). By the way, the global seafloor topography can be completely charted in 5 years by satellite altimetry, whereas ship sounding surveys would take more than 200 years (Sandwell, *et al.*, 2006). To date, 30 arc-second global digital bathymetry data is available. However, grid that has been obtained from many sources of data set believed to be reliable essentially in deep ocean but its accuracy and completeness cannot be guaranteed, because most of areas of the oceans have not been fully surveyed. Moreover, the chart does not include detailed bathymetry for shallow shelf water (The GEBCO_08 Grid, 2008).

Recently when the devastating 2004 tsunami wave which is generated by the north Sumatra earthquake had destroyed large area and kills many people along the coast of the southern Thailand. A reliable bathymetry in the area is a

major requirement. However, no available bathymetry derived from a high resolution hydroacoustic echodata in the western part in vicinity to Thailand and Burma for scientific community. This paper purpose a new reliable bathymetry of the Andaman Sea shelf breaks in Thai EEZ and the prominent features as seen from the bathymetric chart. In addition, detailed information as seen from the map can be utilized for asses slope stability which could probably a cause of local tsunami in the area.

To map a high resolution bathymetry of Andaman Sea in Thai EEZ, the Natural Research Coucil of Thailand and the German Research Foundation (NRCT-DFG) cooperation research in the frame work of “Morphodynamic and slope stability of the Andaman Sea Shelf break” is commenced in 2006. The primary aim of the project is to characterize a high resolution bathymetry derived from multibeam bathymetric echodata and to determine morphodynamic and tectonic state of southeastern part of the Andaman Sea of Thai EEZ. The map is successfully usefull for characterization of seafloor topographic features and to be a basemap for further visual planning of investigation and measurement.

The aim of this paper is to chart a new high resolution bathymetric map derived from a multibeam bathymetric echodata of southeastern part of the Andaman Sea of Thai EEZ, and to determine morphodynamic and tectonic state of the basin that can be linked to bathymetric features which will be the topic of discussion for the next separated publication.

2. Methodology

2.1 A survey area and tentative planning for investigation

An area of investigation is in the southwestern part of the Andaman Sea of Thai EEZ, the western part of Mergui ridge and Mergui Terrain. By a territorial claim under a law of the sea, the Andaman Sea is a sea surface area of combination of own five countries which are Indonesia, Malaysia, Thai, India and Burma. Prior to survey planning in March 2006, to avoid an unexpected political problem for exclusive economic zone of such a country, it was really importance that a boundary of Thai EEZ in the Andaman Sea had to be taken into account. By this respect, the boundary of Thai EEZ was determined following to EEZ Claims of Thailand ([The Royal Gazette, 1988](#)).

Prior to survey-track planning, a bathymetric chart of Thai EEZ derived from 1 arc minute GEBCO global digital bathymetry ([IOC, IHO and BODC, 2003](#)) was evaluated mainly on basis of a high slope area which it was potentially for submarine landslide occurring following a given well description in an inclination angle leading to submarine landslides ([Hampton, Lee and Locat, 1996](#)). By roughness interpretation from the chart, an area composed with a narrow-stripe with approximately of about 50 km width has been seen from the global map and slope gradients in term of inclination angel with maximum on approximate 4.5° in the area has been computed. Due to steep-slope gradient

variability with in the area, the survey tracks were tentatively planed perpendicular to the slope contour lines. The spacing between adjacent swathes coverage was planed to realize approximately of about 10% and coverage of the entire area.

2.2 Hydroacoustic equipments

The equipments consisted of the hydroacoustic survey systems which are the ELAC Bottomchart Mk.II 50 KHz multibeam echosounder (SEA BEAM 1050 multibeam echosounder) with an accessory of the Sea&Sun CTD48M-sound velocity probe and IXEA OCTANS 1000 motion sensor, and an INNOMAR SES 2000 “medium” parametric sediment echosounder.

The SEA BEAM 1050 multibeam echosounder hydroacoustic survey system of the L-3 Communications ELAC Nautik GmbH (<http://www.elac-nautik.de/>) comprising two transducer arrays type LSE 237 which are installed on board at port and starboard side are used to record echoes in medium water up to 3,000 m water depth by manufacture. Such transducer consists of 126 narrow beams with of 1.5° resolutions in widths. A transmitter power output of 3,500 W for such transducer is normally operated. In addition, real time records of ship rolling, pitching and heaving are obtained by a motion sensor which is an accessory. A GPS signal receiver was use for record ship navigations along the survey tracks. During in the surveys, the transducers were operated at regular frequency of 50 kHz. The swath width of the multibeam echosounder can be operated in the sea up to 120° with maximum 126 individual beams. The IXSEA OCTANS 1000 Motion Sensor of the IXSEA SAS manufacturer (<http://www.ixsea.com/en/>) was used to record data of ship rolling, pitching and heaving in real time. The records were used to calculate the real time compensation for ship dynamic motion. A GPS-receiver of the GARMIN Ltd. (<http://www.garmin.com/garmin/cms/site/us>) was used to get ship position information along surveys.

The Sea&Sun CTD48M-sound velocity probe of the Sea&Sun Technology GmbH (<http://www.sea-sun-tech.com/home.html>) is usually used onboard for self-recording of conductivity, temperature, and depth data along profile of water column. The records can be downloaded from the data logging through a standard RS232 interface and were then used for calculation speed of sound propagation in water column along its profile.

The INNOMAR SES-2000 “medium” single beam hydroacoustic survey system of the Innomar Technologie GmbH (<http://www.innomar.com/>) utilized the parametric or non-linear sound propagation effect a principle that when two slightly different frequency sounds were transmitted, they propagated and generated a secondary sound with lower frequency. These primary high frequencies can be used for the exact determination of the water depth while the secondary sound generated by difference of the two primary frequencies, which had a much lower frequency, could penetrate the bottom sediments down to about

15 m to give information about the subbottom structure beneath the seafloor and reveal any unconformities related to slope failures and instabilities

2.3 Design, Constructions and Attachment of equipments on the research vessel

Really importance that the Thai research vessel namely RV Chakratong Tongyai of the Department of Marine and Coastal Resources (PMBC), Ministry of Natural Resources and Environment Thailand, has no moon pool available for attachment of hydroacoustic transducers mobile bracket, thereby, constructions like over-side-arm in shape had to be designed, constructed, and attached onboard in order to hold the frame of multibeam echosounder and a transducer of parametric sediment echosounder during the surveys. Two constructions like inverted-L in shape were sketched carefully following a manufacturing design sample of the L-3 Communications ELAC Nautik GmbH (<http://www.elac-nautik.de/>).

Basically, such construction was divided into two connecting pipes which were a horizontal short-arm pipe and a vertical long-arm pipe. The short pipe had to be horizontally attached and fixed to the deck of ship, whereas the long pipe had to be attached vertically at the end position of such as short pipe. The Galvanized-iron pipe 6 inches in diameter and 4 inches in diameter were selected to be a construction for mounting the multibeam transducer and single beam parametric transducer, respectively. The making processes of constructions were done at Phuket province and the attachments of them were done at the pier of PMBC prior to cruise surveys.

Attachment of equipments on the research vessel, the SEA BEAM 1050 transducer was mounted to a mobile bracket and then attached the bracket to the end of its 6 inches in diameter vertical long-pipe. The pipe was attached to its short-pipe which was installed over the port side of the research vessel. It is really importance that the bracket had to be positioned at the end of the long pipe below the keel of the ship between survey period to avoid unexpected noises or small bubbles probably generated by the wave during the survey.

Whereas the INNOMAR SES 2000 transducer was mounted at the end of its 4 inches in diameter and then attached the pipe to its short-arm which was installed over the starboard side of the research vessel. During transit from the pier at Phuket island to the research area, the transducers can be hoist up and fixed outside the water to allow for a higher ship speed. While during survey time at sea, the transducer had to be placed in a fixed position in the water using U-shape clamp which was installed beside the vessel very close to surface water level. The communication cable from both transducers can be passed inside their pipe hole through the end of the short pipe and direct to control unit box in laboratory. The acquired echoes can be real time seen on screen in laboratory.

3. Data collection and processing

3.1 Erroneous noise and optimum ship speed determination and roll calibration

To determine systematically erroneous noises occurring and optimal ships speed for surveying, multibeam echodata were recorded during transit to the area of investigation in the first cruise. An interesting was that the multibeam data acquisition during the determinations revealed higher erroneous noise level. It was realized that the noise can probably be generated by tiny bubbles of waviness under the window of transducers due to dimension of transducer pole and the wires which held the pole in the U-shaped clamp. The noise can also probably be generated by strong vibrations of ship engine which obviously were transferred to the transducer along the steel construction of the poles and due to the clamp which is installed near to the main engine.

Data quality was significantly improved by releasing tension of the wires. Soundings when the vessel was at position and the engine slowed down were definitely better. A speed of 3 to 4 knots was determined as an optimum of ship speed between data quality and mapping yield. However, data quality was not really good but just acceptability. The noise level was still quite high limiting the maximum achievable depth to around 1,000 m and the maximum swath width to around 90° instead of 120°.

To improve the quality of data acquisition in the second cruise, the dimension of transducer pole of multibeam echosounder was adjusted which are; the short-arm which was fixed over the deck was reduce for 20 cm from the first cruise installation and the long-arm which hold the transducer was extend for 0.5 m long beneath the keel of ship. Moreover, the shape of clamp was changed from U-shape to V-shape and added a rubber sheet to absorb an oscillatory vibration from wavy.

Roll calibration procedure in the first cruise in leg1 was done over many a 2 nautical miles track back and forth in vicinity of Phuket Island on a quite planar seafloor at water depths of about 40 m. The recordings of the multibeam system were processed for each direction separately. The differences in the inclination across track of both digital terrain models (DTM) were calculated. Negative values of 3.35° for the port and 2.16° for the starboard transducer had been determined from leg1 in the first cruise. A similar procedure of roll calibration as well as in leg1 was done in the beginning of leg2 in the second cruise. Values of 1.66° for the port and 2.11° for the starboard transducer had been determined from the second cruise over many a 2 nautical miles track in the same area of roll calibration from the first cruise. The position, speed and heading of the ship were detected base on a GARMIN 1000 GPS which was regularly compared with the ship navigation.

3.2 Sound velocity profile

In order to achieve high quality bathymetric data, detailed sound speed information along water column is essentially to be known. To estimate influence of the sound velocity on the sound beam propagation in sea water and to calibrate the sound velocity for data acquisition, two CTD profiles were investigated. The first CTD profile was continuously measured at shallow water from surface down to 40 m water depth in approximation, whereas, and the last CTD profile was continuously measured from surface down to 643 m water depth in approximation during the transit of ship to survey area in the first cruise.

The profiles were located on 7°42.28' N, 98°23.8' E which named CTD1-1 and 7°38.145' N, 95°46.764' E which named CTD1-2, respectively. A commercial The supplied Standard Data Acquisition Software package “SST-SDA” for Win95 to XP of the Sea&Sun Technology GmbH was used to download the records from data logging on board and displayed the sound velocity profile on a screen. After that all profiles were plotted using a commercial software Grapher 5.0 of Golden Software, Inc. U.S.A. to publish. Two profile plots of CTD1-1 and CTD1-2 show in Fig.2. Resemblance of CTD profiles can be seen in the same positions in the second cruise. Then the acquired data from station CTD1-2 were applied during the surveys.

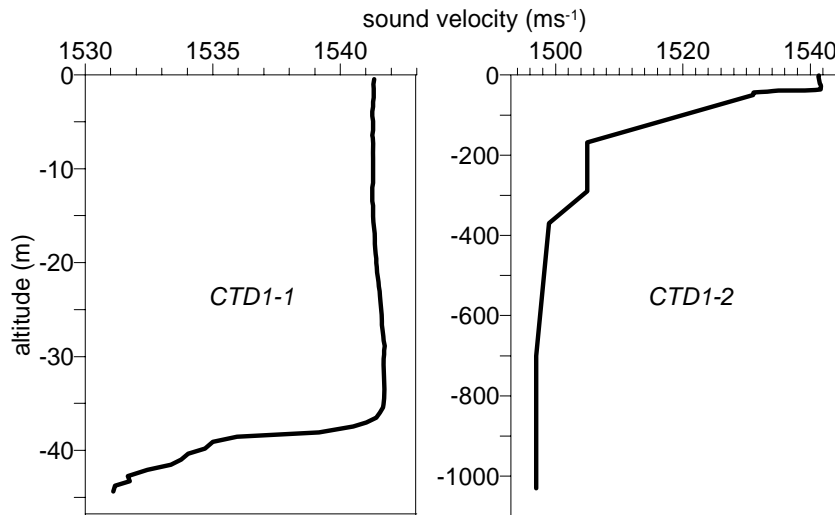


Figure 2. Water sound velocity profiles plots at position 7°42.28'N, 98°23.8'E (CTD1-1) and 7°38.145'N, 95°46.764'E (CTD1-2).

3.3 Bathymetric survey and echodata processing

Acquired multibeam echoes were obtained from two cruise surveys on board RV Chakratong Tongyai at water depth ranging from 500-1,700 m. The first cruise was separated into two legs, leg 1 covered 20-27 November 2006 and leg2 covered 29 November-6 December 2006. The second cruise was conducted on 6-15 November 2007. An area on approximate 3,000 km² was successfully surveyed consisting of more than 60 parallel tracks of about 30 km length (Fig. 3).

During the surveys, difference GPS was planned to get position information of ship to keep the ship on the track, unfortunately, GPS signal from the bridge was unavailable in laboratory. Therefore, positions of ship for hydroacoustic system were measured by a new installation of a GPS signal receiver over the ceiling of laboratory. The L3 communications ELAC Nautik online software Hydrostar 3.5.3 was used for data acquisition during surveys.

The fixed beam angle of 1.5° due to the manufacturer generates the footprint size of the pre-formed beams which is approximately 13 m at 500 m water depth and which is approximately 44.5 m at 1,700 m water depth corresponding to a center beam. The investigation was performed at slow ship speed which it was about 4 knots in average during surveys by take into accounts, to provide sufficient data points density in the along track direction to be generated a high resolution bathymetry. The along track point spacing is approximately 10 m and a dense line spacing is approximately about 100 m with a ping rate interval on approximate 6-7 seconds.

Most of pre-cleaning processes of the multibeam echodata acquisition were done onboard. Basically, recorded echoes were revealed on screen and erroneous points were generally rejected from main records. Roll bias at port and starboard sides which were determined between the transits, heave and pitch records and also positions of the ship were required in processing to generate depth. Then the first plot of each single track was map basis for further post-cleaning processes. Post-cleaning processes were done by taken into account using a powerful command of MB-System under GNU public license software (Caress and Chayes, 2004).

Generic Mapping Tool (GMT) under GNU public license software (Wessel and Smith, 1998) was used for generating and presentation of whole cleaned-echodata as digital terrain model (DTM). In this respect, 2D and 3D view of contours and relief color-shades charts of the entire area were mapped for visual interpretation of anomalous features in difference prospective views. An interactive 3D perspective view can also be visualized using a commercial software Fledermaus of the IVS 3D and software the Global mapper 10.

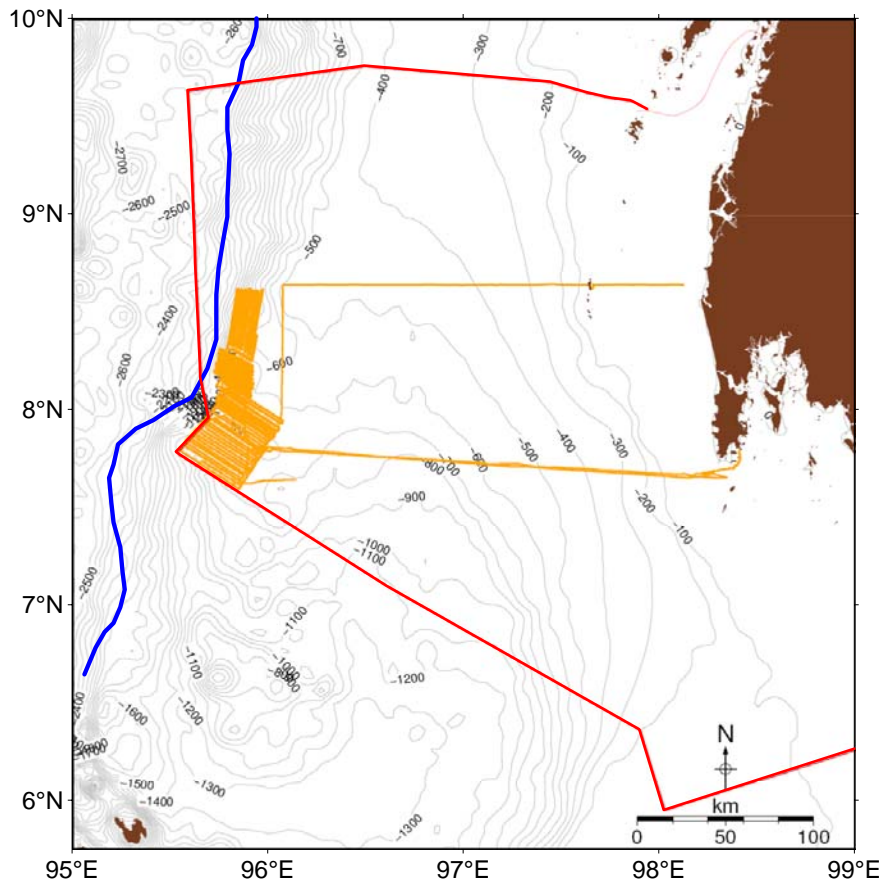


Figure 3. Show an area of investigation in this study. Contourline in this map show in 100 m interval. Land show in darkbrown. Orange lines show ship track surveys. Boundary of Thai EEZ shows by red line. A digitize of an approximate situation of Shan Scarp Fault (SSF?) which is derived from [Curry \(2005\)](#) shows by a solid blue line

3.4 Parametric sediment echosounder survey and data processing

The INNOMAR SES2000 parametric sediment echosounder was operated continuously during the cruises simultaneously to multibeam surveys. In the first cruise of investigation echoes were continuously recorded along 30 profiles in each of about 22 nm in length in northwest-southeast direction as well as along several additional short lines perpendicular to the main profiles. However, in the second cruise the echosounder data was recorded along 20 profiles in north-south direction due to strong wave propagations mainly in north-south direction. As with the multibeam system also the parametric sediment echosounder suffered from the noise generated by strong vibrations of the engine and amplified by the long free arm of the pole holding the transducer over the starboard side of the vessel. However, data quality was generally acceptable. The maximum water depth surveyed was about 1,700 m. Generally, the penetration of the signals into the sea bottom was on the order of 5 to 10 m, a maximum penetration of 15 m was achieved.

An INNOMAR SES for windows (or SESWIN) software was used for data collection. Because the low frequency was generated from parametric propagation of the two higher frequencies, the generated sound retained the small and thus high resolution bottom footprint. This is an advantage over the use of a linear system to generate the same low frequency since the footprint will be much larger and the survey resolution would be much less. The ISE 2.9.2 software of Innomar Technologie GmbH, was used for display data acquisition of parametric echosounder profiles. To process the data, raw data were converted and revealed an operating range of each profile using SES Convert software of Innomar and were grouped basically by operating range of the data. Grouped data were exported to SGY format using a commercial VISTA 2D3D Seismic Processing software of the Geophysical Exploration & Development Corp and then imported to a generated flow algorithm under a commercial KINGDOM software of the Seismic Micro-Technology, Inc to process and display subbottom profiles along ship track surveys. To compare anomalous feature between multibeam bathymetry and parametric profiles, the multibeam bathymetry must be imported to the KINGDOM software as basemap.

4. Result

4.1 Assessment of data accuracy

Really importance is that the acquired echoes which were recorded along leg1 in the first cruises provided 79.82% of good beam in average, whereas from leg2 provided 69.03% while the second cruise provided 72.44%. The results involve a new concerning with respect to stability of the research vessel during survey periods which is become a major priority concerning in measurement of a good data set for next investigation. However, the bathymetry must be generated by using this echodata set. First of all, assessment of data accuracy must be evaluated.

To generate a new reliable bathymetry in the area, accuracy assessments from various grid resolutions were evaluated. A sequence of 30m, 40m, 50m, and 60m grid resolution were processed. First of all, a number of data points which obtained per individual grid are needed to be known in whole grids. It is therefore helpful to know some information about the density and regularity of data points which were obtained in such grid. The second, standard deviations for individual grid need to be computed to helpful about variation and therefore accuracy of data points (Beyer, Rathlau, and Schenke, 2005b). Histogram plots to show relation between a number of data points per grid and frequency of the data set were presented to reveal dense of data point for all of the various grid resolutions. Whereas, histogram plots between a standard deviation in % of water depth were used for the presents of all of accuracy of those grids. A number of data points per grid and the standard deviation in every grid cells are computed and generated histogram plots. Overall accuracy includes an accuracy of measurement and grid

deficiency derived from DTM. Summary results of computed accuracy show in [Table 1](#).

The results from the table reveal a regular acquisition of a number of data points per each grid resolution in sequence which is a 30 m, 40 m, 50 m and 60 m grid quantitative. Accuracy assessments from different grid resolutions are evaluated in term of dense data points per grid and standard deviation ([Fig 4](#)).

Accumulated data achieve in term of a relation plot between a number of data points per grid and percent frequency show that 56% of a 30 m grid size obtained more than 3 data points per grid while between 80-90 % of larger grid size obtained the similar data points per grid. It is found that the difference of median for 5 m can be compared to standard deviation for 0.4% of water depth. The accumulated data acquired from a relation plot between standard deviation in percent of water depth and percent frequency show that 78% of 30 m grid cell obtained standard deviation better than 0.5 % of water depth, whereas, 80% of 40 m grid and 77% of 50 m grid cell obtained standard deviation better than 0.5% of water depth and 74% of 60 m grid cell obtained standard deviation better than 0.5% of water depth.

Although, good statistic values which were computed from 50 and 60 m grids qualities supported by statistic values that a reliable high resolution bathymetry in this investigation area can be accepted to generate by both grid resolutions, however, a computed standard deviation of a 50 m grid size show higher values of about 77% while a computed standard deviation of a 60 m grid size show lower values of about 74%. The value implied that a high resolution bathymetry in the investigation area could be generated by a 50 m grid resolution.

The primary aim of the MASS project focuses on a mapping of a new bathymetric chart derived from a high resolution bathymetry data of southeastern of the Andaman Sea (or on the southwestern of Mergui Ridge) of Thai EEZ. To generate a new map in this area following the accuracy assessment which is derived above, bathymetric data acquisition can be processed and then generated by 50 m grid quality. Furthermore, a terrain model is applied for generating a shade relief of a high resolution bathymetric chart. Sea floor topography of an investigation area derived from the model is revealed in great detail. Overall in the past, no high resolution bathymetry in this area is publically available. Therefore, the chart which is shown in this publication becomes the first implication of a new reliable bathymetric map of the western part of Mergui Ridge ([Fig. 5](#)).

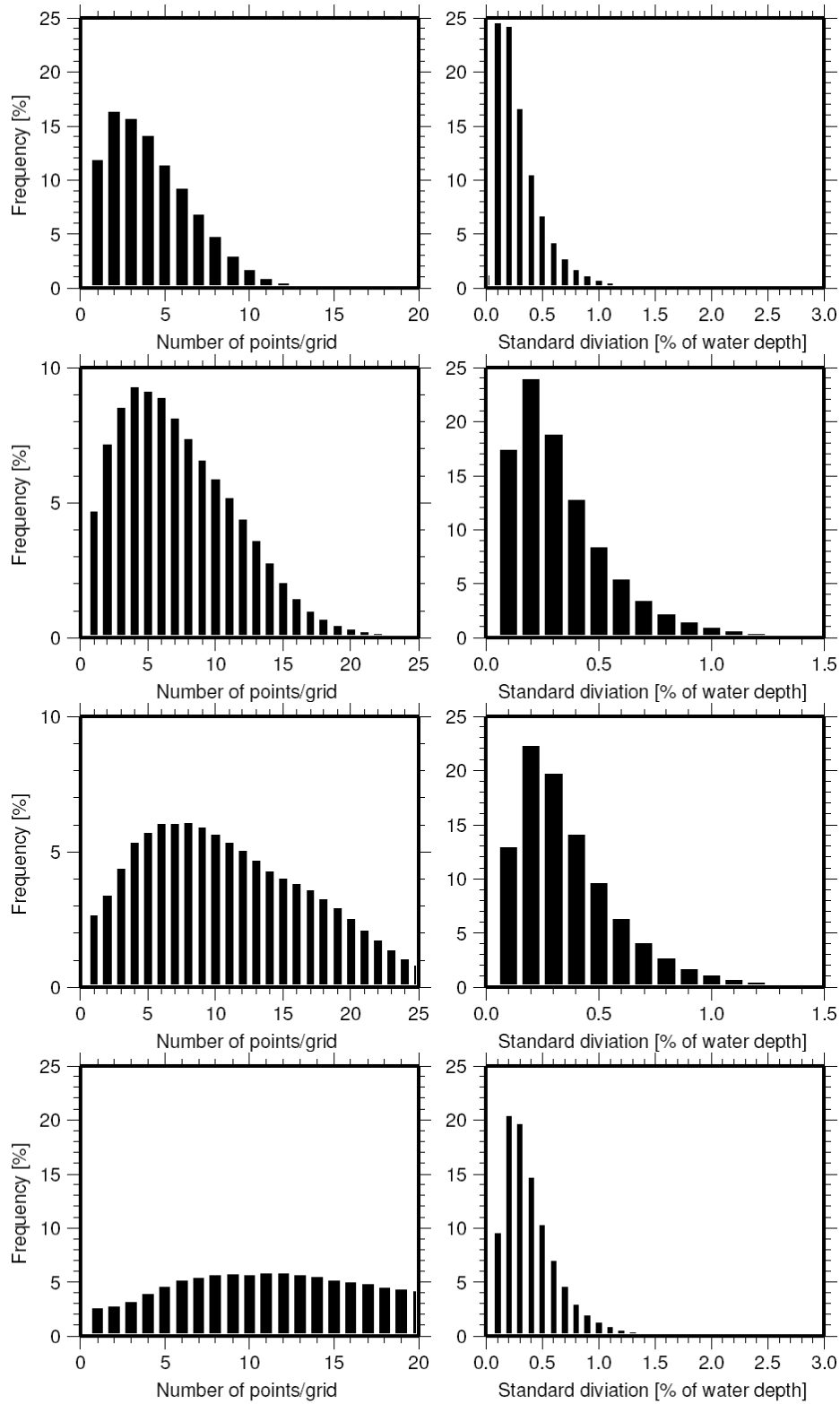


Figure 4. Show cumulative plots in percent frequency of a number of data points per grid (left), standard deviation and standard deviation in percent of water depth (right) for 30m, 40m, 50m, and 60m grid resolutions, respectively.

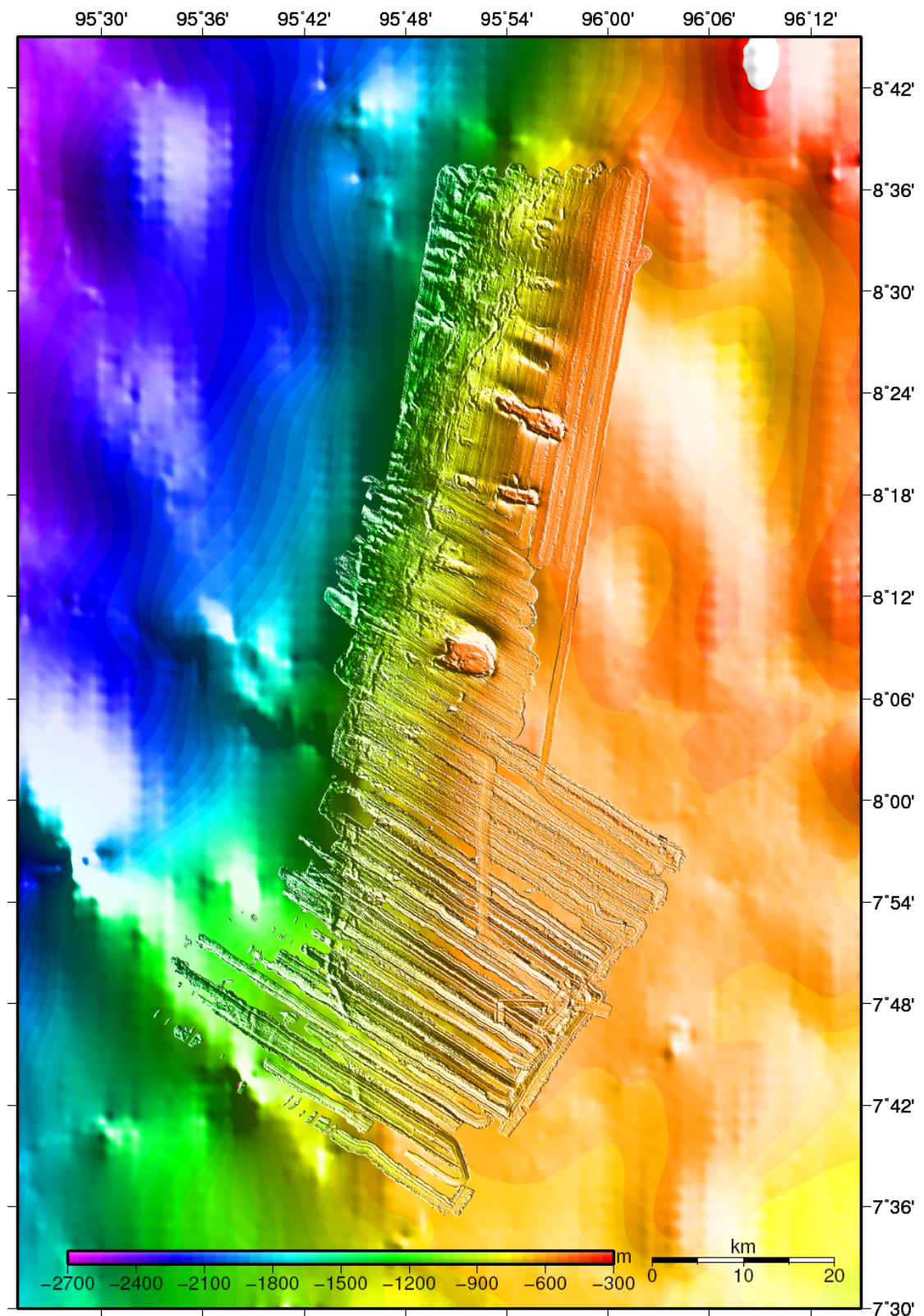


Figure 5. A color-code shade relief bathymetry map of the southwestern slope of Mergui Ridge of Thai EEZ overlaid on GEBCO 30-arc second digital global bathymetry.

To evaluate a good of fit between a high resolution bathymetry and global digital bathymetric dataset available worldwide, a high resolution bathymetry was totally compared to digital global bathymetric dataset which are GEBCO1-min, ETOPO1, and GEBCO30-sec, respectively. The entire data obtained in the same area are extracted from a reliable bathymetry and those of global digital bathymetry, respectively. Spatial analysis in term of correlation (R^2) and error in term of root mean square error (RMSE) are use for spatial evaluation in term of a goodness of fit of a couple areas (Table 2). A value of 33.43 ± 188.22 reveals a big difference between MASS50 and GEBCO1, while a value of 92.47 ± 63.32 which is evaluated from a comparison between MASS50 and ETOPO1 and a value of 95.17 ± 50.70 which is evaluated from a comparison between MASS50 and GEBCO30-sec indicate high correlation between both global bathymetries.

Table 1. Statistic values of various grid resolution show a number of data points per grid and standard deviation.

Grid resolution	30 m	40 m	50 m	60 m
percent of grids obtained at least 3 data points per grid	56	80	90	90
percent of grids obtained standard deviation better than 0.5 % of water depth	78	80	77	74

Table 2. Spatial analysis in term of R^2 and RMSE show a goodness of fit between a high resolution bathymetry by 50 m grid quantity (MASS50) and digital global bathymetries which are GEBCO1-min, ETOPO1, and GEBCO30-sec, respectively.

Spatial analysis	MASS50-GEBCO1	MASS50-ETOP01	MASS50-GEBCO30
SST	5.78E+10	5.78E+10	5.78E+10
SSE	3.85E+10	4.35E+09	2.79E+09
R^2	33.43	92.47	95.17
RMSE	188.22	63.32	50.70

4.2 Slope inclination angle

To evaluate seafloor stability in the area, one possibility can be use for assessment stability in the area is slope inclination angel (Hamton, Lee, and Locat, 1996). Many profiles perpendicular to slope contour lines are drawn on the bathymetry. Depth records in every 100 m along each profile are extracted to show characteristic of the profile and slope gradients are computed. Characteristic of profiles are shown by Fig. 6. Inclination angle computed from ~500-700 m depth is on average $\sim 0^\circ$ indicates a smooth area on top of the ridge. West side of the ridge can be divided into two provinces. The first province is about 700-1,300

m depth with slopes $\sim 1\text{-}1.7^\circ$. The second province is about 1,300-1,700 m depth with slope $\sim 3.2^\circ\text{-}4.6^\circ$ indicates tendency of slope stability in the area.

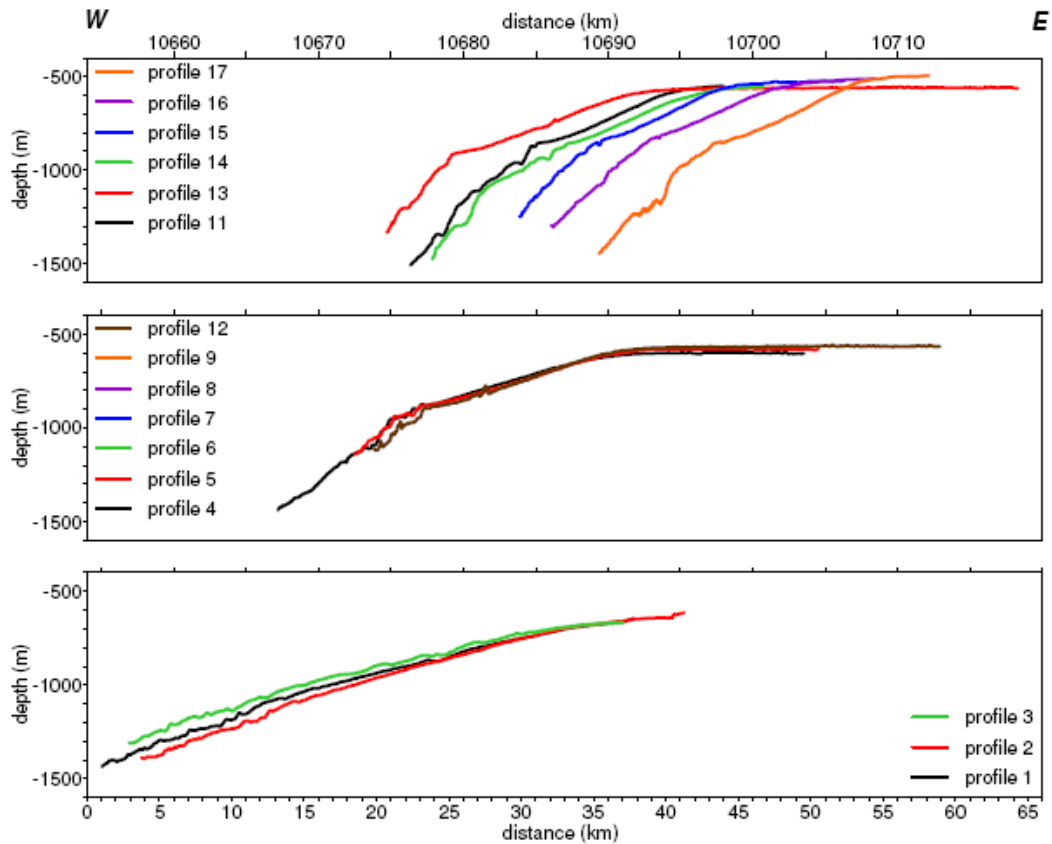


Figure 6. Plots of relation between distance and depth show slope cover the south, the middle, and the north of the research area. The profiles are presented to indicate tendency of slope stability in the area.

4.3 Morphology of the Andaman Sea in Thai-EEZ

Interpretation by visualization and by determination from many cross section profiles parallel to slope in near W-E direction reveal that an investigated area can be characterized into a flat top like of high region coverage in the eastern part and a slope like of low region coverage in the western part.

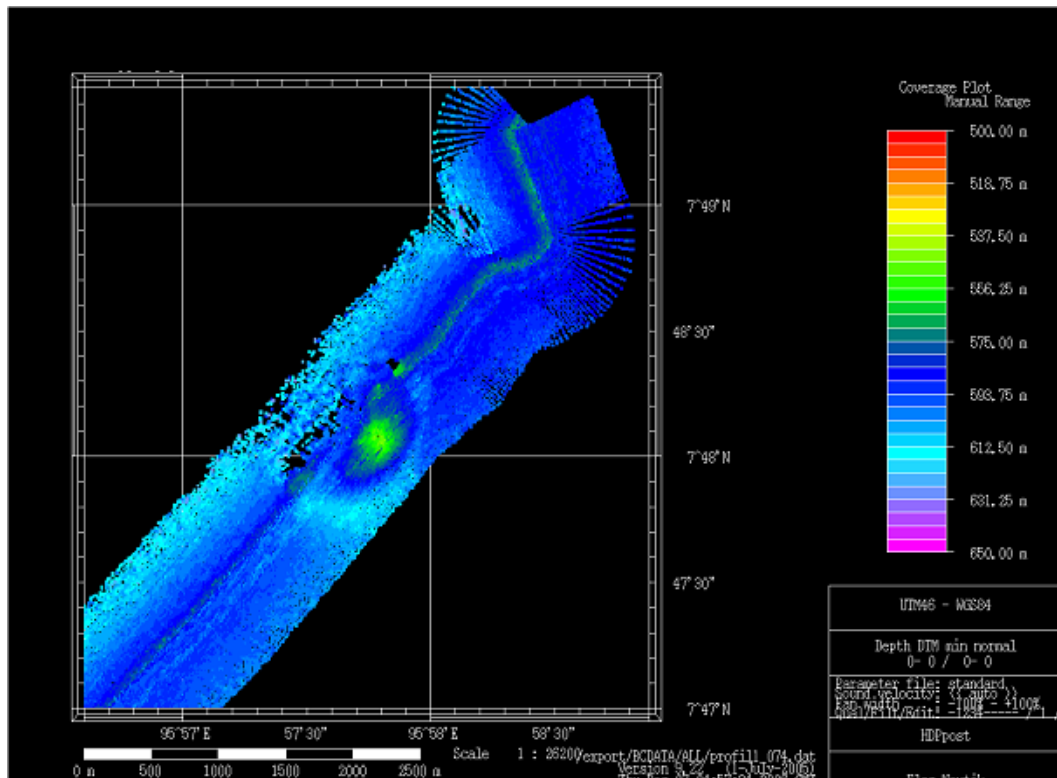
4.3.1 Characterization on a flat top area

A flat top area is characterized on the Mergui Ridge at the northeastern part in the upper most area with approximate 500 m depth continue to the southern end of the area of about 700 m depth. An inclination angle is computed from many cross section profiles cover the area. An average angle of about 0° indicates that the area is rather a smooth or a gently plain topography. Most of area has no large distinct topographic features on its top.

4.3.1.1 Mounds and mudvolcano

By literatures, mud volcanism is widely distributed onshore and has attracted the attention of geologists for over 200 years. Work on onshore mud volcanoes has delineated their tectonic settings, activity and products (mud as well as fluids), the mechanisms of formation, and their importance for petroleum prospecting (Goubkin and Fedorov, 1938; Yakubov et al., 1971; Higgins and Saunders, 1973; Hedberg, 1974; 1980; Barber et al., 1986; Rakhmanov, 1987; and many others). However, a comprehensive study of submarine mud volcanoes has become possible only in the last decades due to the wide use of side scan sonar and the increased accuracy of the positioning of bottom samplers.

An embankment can be observed on the area from the chart. A situation of the embankment locates at 95°57.8' E and 7°48' N. The embankment is characterized as a prominent feature shaped a mound or volcano like structure. Shape of the feature is nearly to a circular form. Dimension of the form is about 35 m high with about 500 m in diameter. The characterization of the feature which could possibly be identified as a volcano is supported by a raw swaths bathymetry named profil1_074.xse from the first cruise (Fig. 7). Regarding to a parametric sediment profiles, a detailed structure that reveal a mud volcano like structures (M-01) is locates at 95°57.75' E and 7°48.19' N. (Fig. 8). In addition, many positions of possible mounds (M-02 to M-10) and one position of possible sediment bank (B-01) behind the mounds can be seen from subbottom profiles (Table 3).



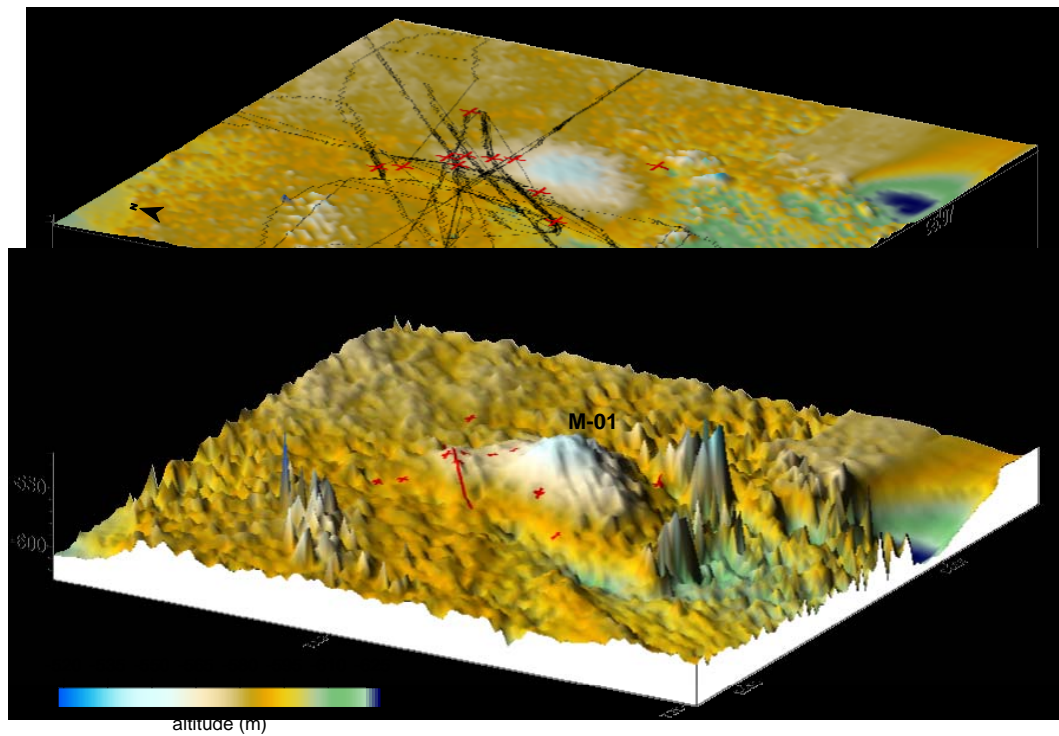


Figure 7. Swaths bathymetry covers a volcano like structure.

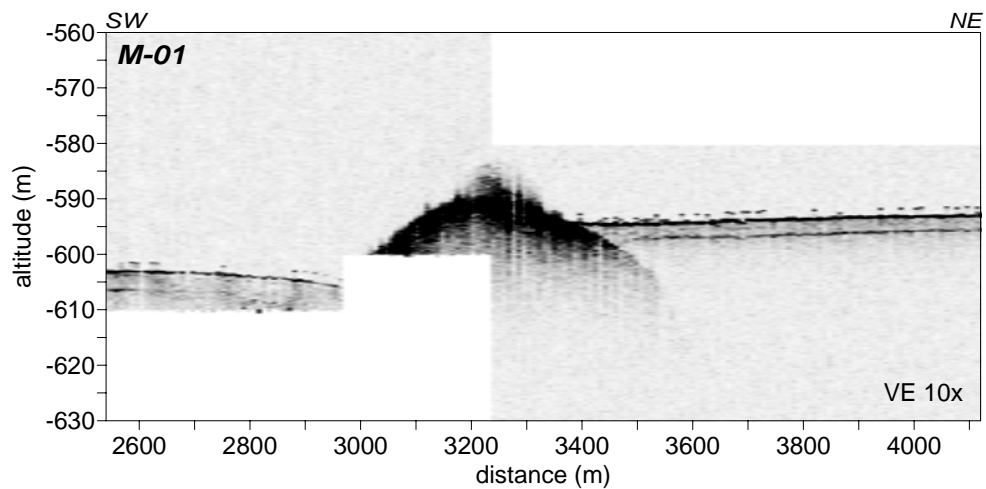


Figure 8. A parametric sediment profiles show volcano like structure.

Table 3. Situations of prominent features which are identified as a mud volcano (M-01) and many positions of mounds (M-02-M-10) and position of sediment bank (B-01)

Positions	Name	Filename
95°57.75' E, 7°48.19' N	M-01	#02122006_021548
95°57.77' E, 7°48.22' N	M-02	#02122006_091042
95°57.80' E, 7°48.16' N	M-03	#02122006_091042
95°57.71' E, 7°48.26' N	M-04	#02122006_062750

95°57.69' E, 7°48.29' N	M-05	#02122006_062750
95°57.79' E, 7°48.20' N	M-06	#26112006_052255
95°57.81' E, 7°48.13' N	M-07	#26112006_084409
95°57.71' E, 7°48.03' N	M-08	#02122006_062750
95°57.62' E, 7°47.95' N	M-09	#02122006_105626
95°57.90' E, 7°47.94' N	M-10	#24112006_105735_111209
95°57.96' E, 7°48.29' N	B-01	#02122006_091042

4.3.1.2 Plateau

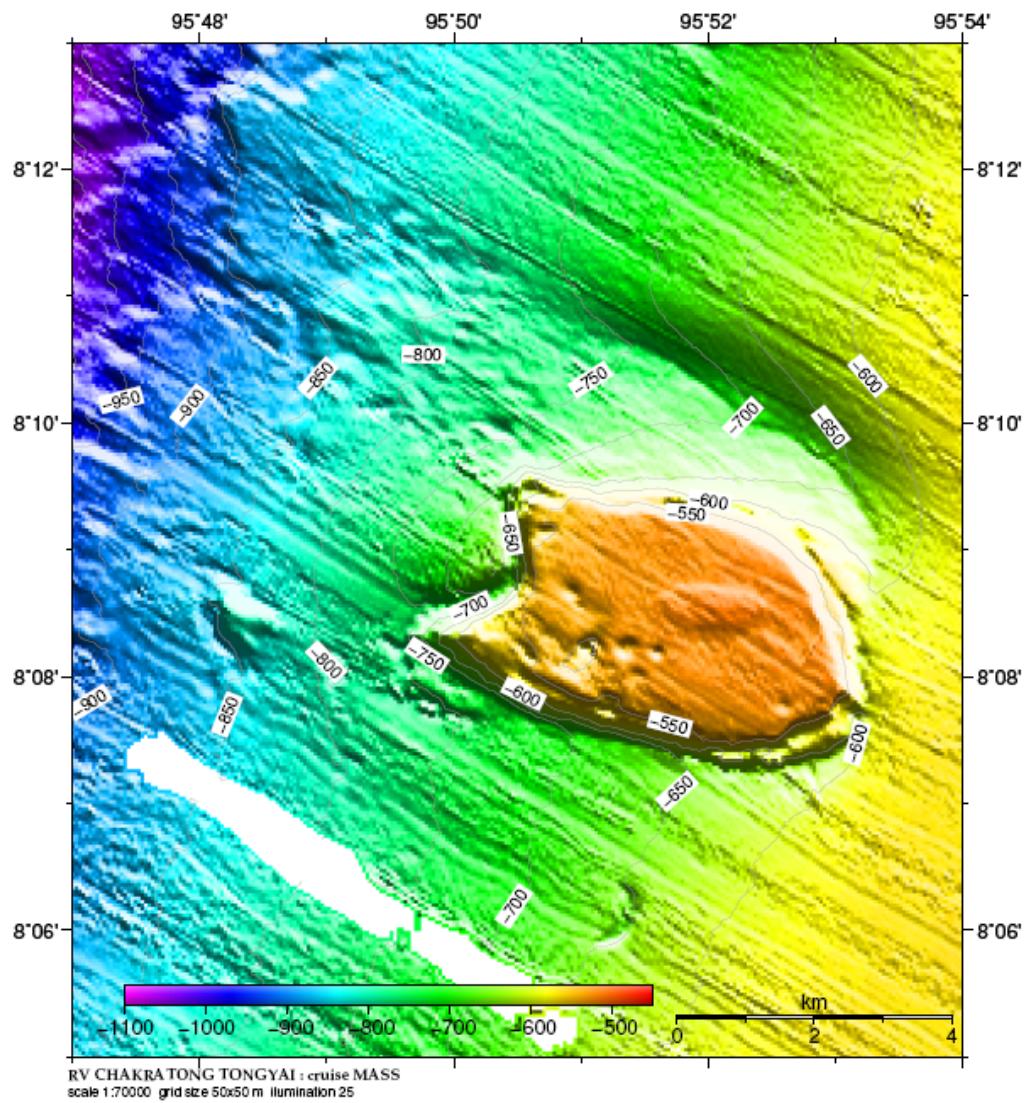
An oceanic plateau (also submarine plateau) is a large, relatively flat submarine region that rises well above the level of the ambient seabed. While many oceanic plateaus are composed of continental crust, and often form a step interrupting the continental slope, some plateaus are undersea remnants of large igneous provinces. These were formed by the equivalent of continental flood basalts such as the Deccan Traps in India and the Snake River Plain in the Pacific Northwest of the United States. Geologists believe that igneous oceanic plateaus may well represent a stage in the development of continental crust as they are generally less dense than oceanic crust while still being denser than normal continental crust.

Density differences in crustal material largely arise from different ratios of various elements, especially silicon. Continental crust has the highest amount of silicon (such rock is called felsic). Oceanic crust has a smaller amount of silicon (mafic rock). Igneous oceanic plateaus have a ratio intermediate between continental and oceanic crust, although they are more mafic than felsic.

However, when a plate carrying oceanic crust subducts under a plate carrying an igneous oceanic plateau, the volcanism which erupts on the plateau as the oceanic crust heats up on its descent into the mantle erupts material which is more felsic than the material which makes up the plateau. This represents a step toward creating crust which is increasingly continental in character, being less dense and more buoyant. If an igneous oceanic plateau is subducted underneath another one, or under existing continental crust, the eruptions produced thereby produce material that is yet more felsic, and so on through geologic time.

Three conspicuous feature shaped so-called plateaus are observed from the map at central of an investigation area at water depth about 550 meters (Fig. 9). The first biggest plateau with approximate dimension 4km × 6km × 160m is revealed at position 95°51'30" E and 8°08'30" N. The middle which is the smallest plateau with approximate dimension 2km × 4km × 100m is observed at position 95°54'30" E and 8°18' N. The last plateau with approximate dimension 2km × 8km × 160m is observed at 95°55'30" E and 8°22'30" N. Very interesting is that moat can be observed around the plateaus. Appearing of moat indicates a movement of sediment around the plateaus. Detailed analyses need more

information from subbottom profiles, backscatter map, and also sediment textures in the area.



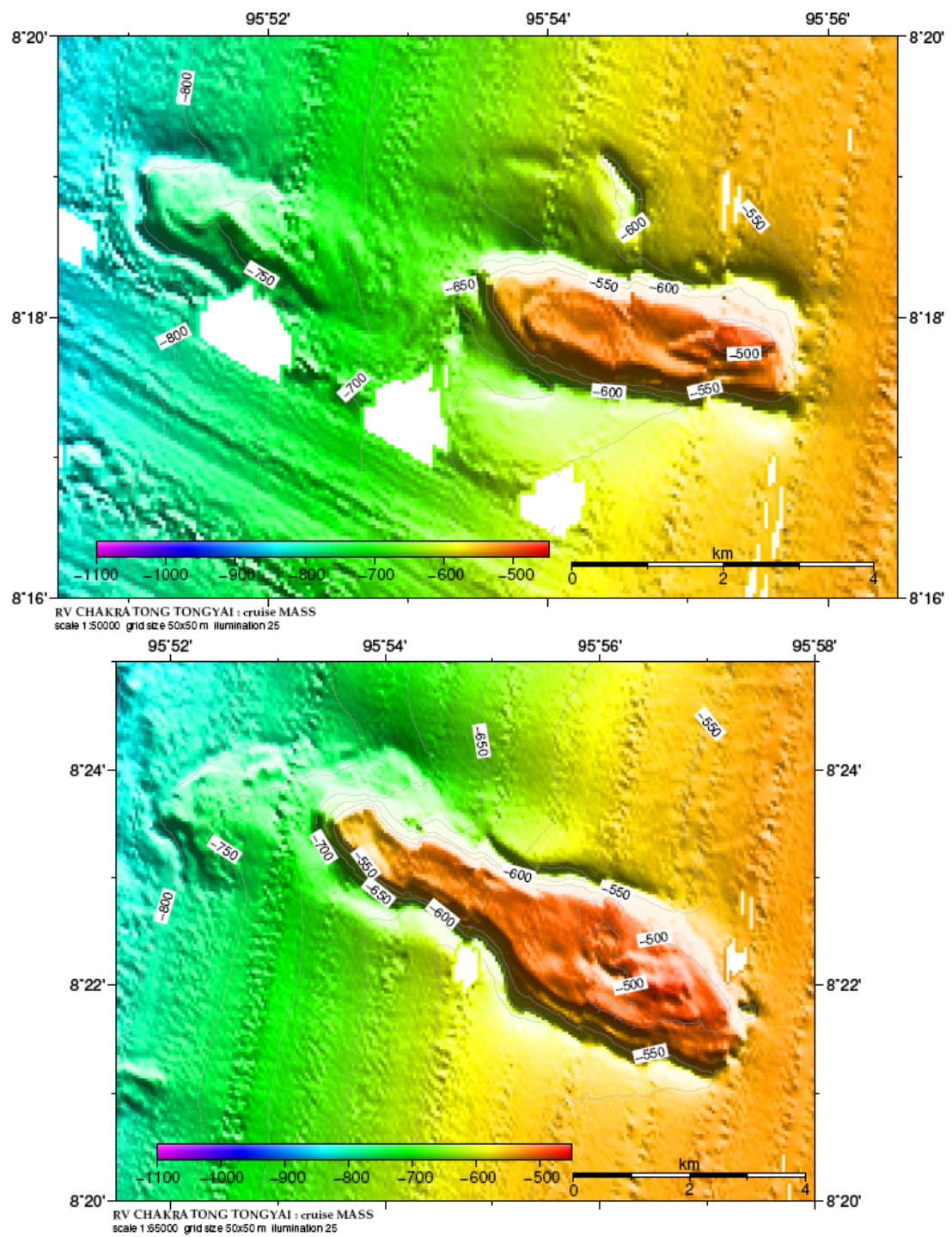


Figure 9. Color code shade relief seafloor topography show three prominent features which are identified as plateaus.

4.3.1.3 Pockmark

Pockmarks include isometric cone- to saucer shaped depressions on the seafloor varying in size from 1 m to more than a few hundred meters across with depths of less than 1 to more than 10 m. They were described and named for the first time in 1970 as morphological features formed on the continental shelf off Nova Scotia, Canada (King and McLean, 1970) and then observed and reported in many places all over the world ocean (e.g. Hovland and Judd, 1988). They occur in areas of fluid discharge, and need fine-grained sediments to support their structure and long existence. Nowadays it is widely accepted that pockmarks originated by expulsion of gas from over pressured shallow gas pockets, dispersing the sediment into the water column (Hovland and Judd, 1988) or by intensive continuous fluid discharge.

At the northern end side of the plateau which is observed at the central of the bathymetry, a feature which it could probably be characterized as a pockmark (Fig. 10) can be remarked with approximate dimension $1\text{km} \times 0.25\text{km} \times 40\text{m}$ at situation $95^{\circ}54'35''$ E and $8^{\circ}18'45''$ N

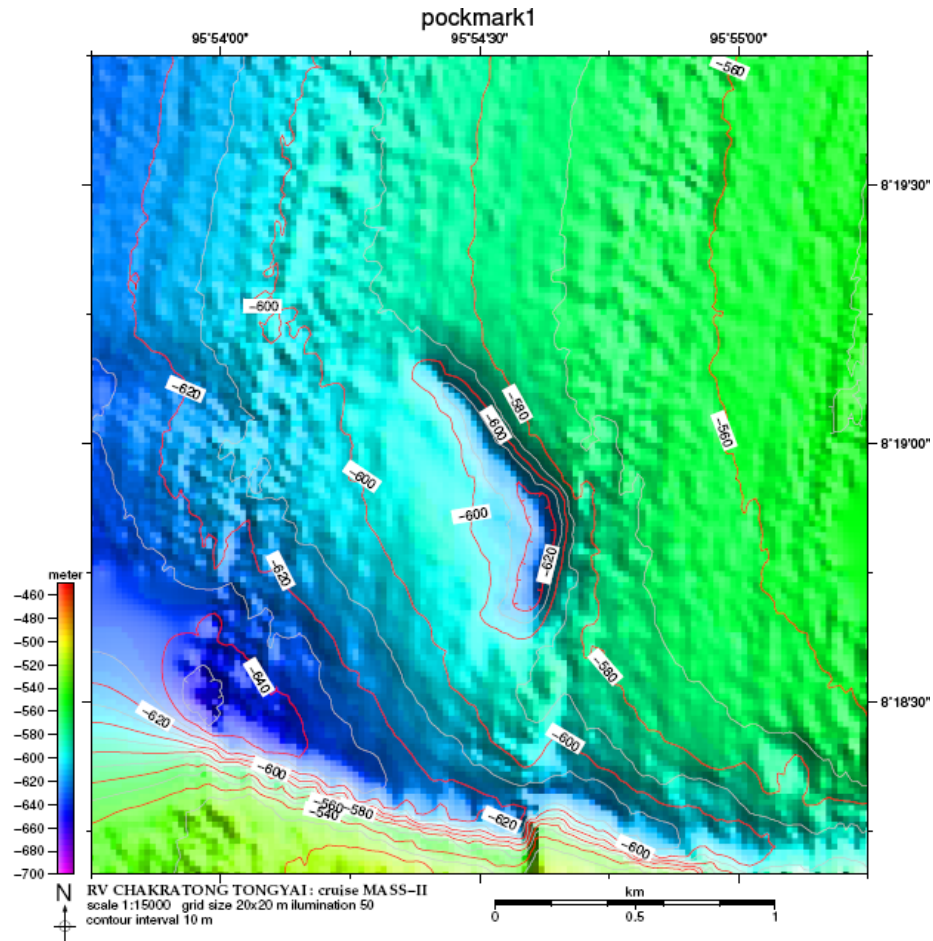


Figure 10. Color code shade relief seafloor topography show a prominent feature which is identified as a pockmark.

4.3.2 Characterization of a slope area

A low region slope in W-E direction in the west side of the ridge can be divided into two provinces. The first province is about 700-1,300 m depth with slopes $\sim 1-1.7^\circ$. The second province is about 1,300-1,700 m depth with slope $\sim 3.2^\circ-4.6^\circ$ indicates tendency of slope stability in the area. Many prominent features can be observed from the area, which are escarpments, displaced masses, and gullies.

4.3.2.1 Escarpments, displaced masses and gullies

In geomorphology, an escarpment is a transition zone between different physiogeographic provinces that involves a sharp, steep elevation differential, characterized by a cliff or steep slope. Usually escarpment is used interchangeably with scarp. But some sources differentiate the two terms, where escarpment refers to the margin between two landforms, while scarp is synonymous with a cliff or steep slope. The surface of the steep slope is called a scarp face. Scarps are generally formed by one of two processes: either by differential erosion of sedimentary rocks, or by vertical movement of the Earth's crust along a fault.

Two escarpments which are common on inclined areas of the seafloor where weak geologic materials reside are observed from the bathymetry at about 900 m depth. Dimension of the escarpments are about 5 km long and approximately 70 m high (Fig 11). The area reveals a number of escarpments which are probably generated by supporting of creeping sediment from the upper flat area flowing downslope to the area. A prominent feature which could possibly be identified as a trace lie along over a distance of about 30 km and parallels to a shelf edge from about $95^\circ 44' \text{ E}$ and $7^\circ 47' \text{ N}$ to $95^\circ 45' \text{ E}$ and $7^\circ 59' \text{ N}$ at water depth about 1,000 meters. Unfortunately, no detailed information of subbottom profiles in between the escarpment because of problem of current supply from the ship. However, remaining of some subbottom profiles can be use for presentation of detail information of displaced masses behind the escarpments. Four situations of displaced mass are observed from parametric profiles at the first escarpment which are profiles name S1-1, S1-2, S1-3 S1-4. Whereas, one situation is observed from another escarpment which is profile name S2-1 (Fig 12-16).

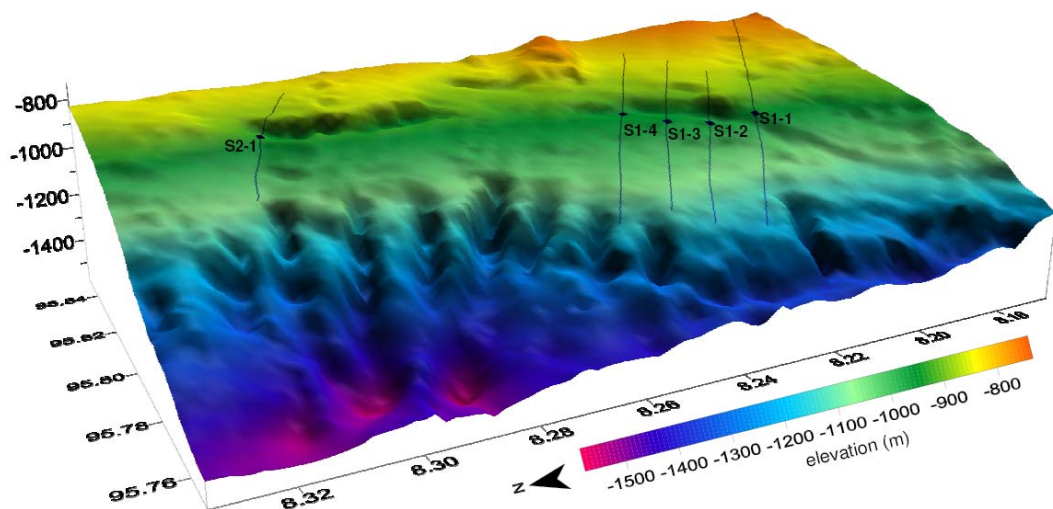


Figure 11. A 3D color code relief shade of escarpment shows two positions which can be identified as escarpments. Behind the escarpment are displaced mass. Solid blue lines show situations of subbottom profiles across the escarpments.

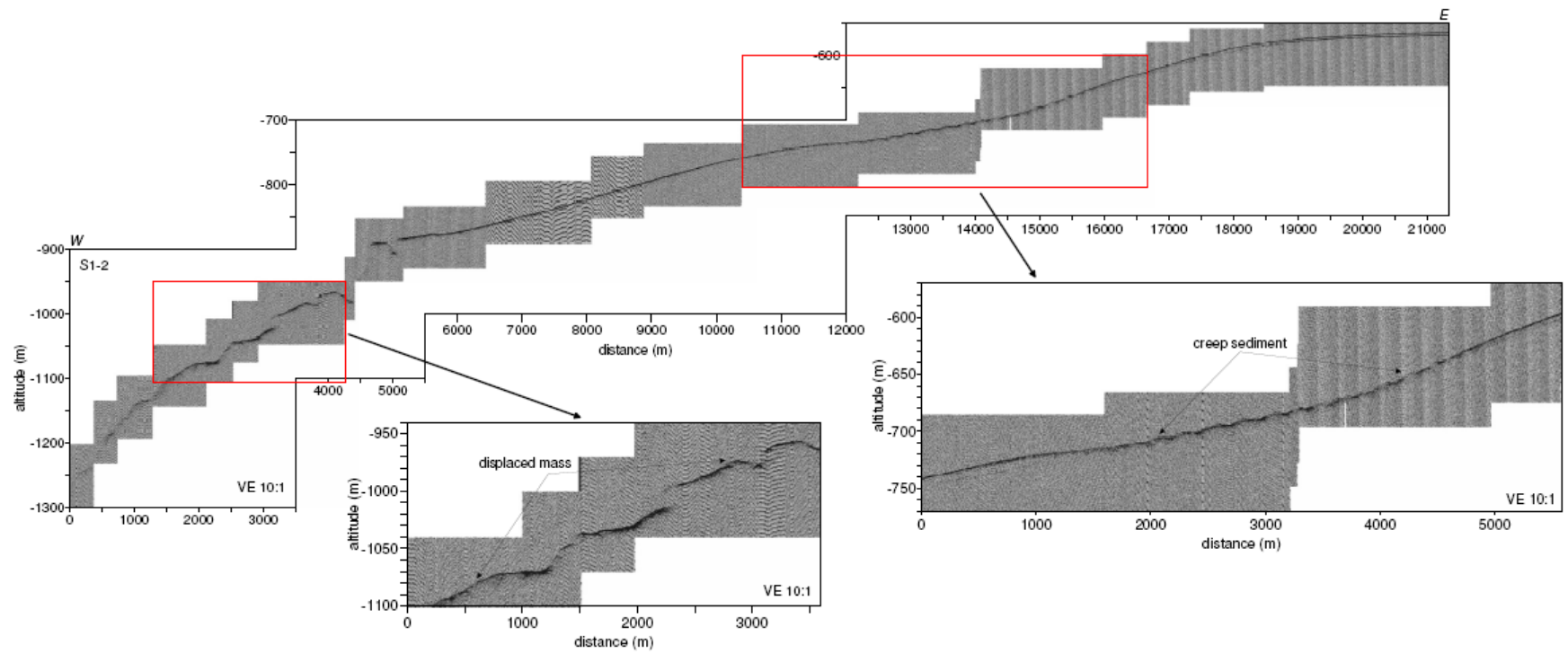


Figure 13. Shows detailed information of subbottom profile name S1-2.

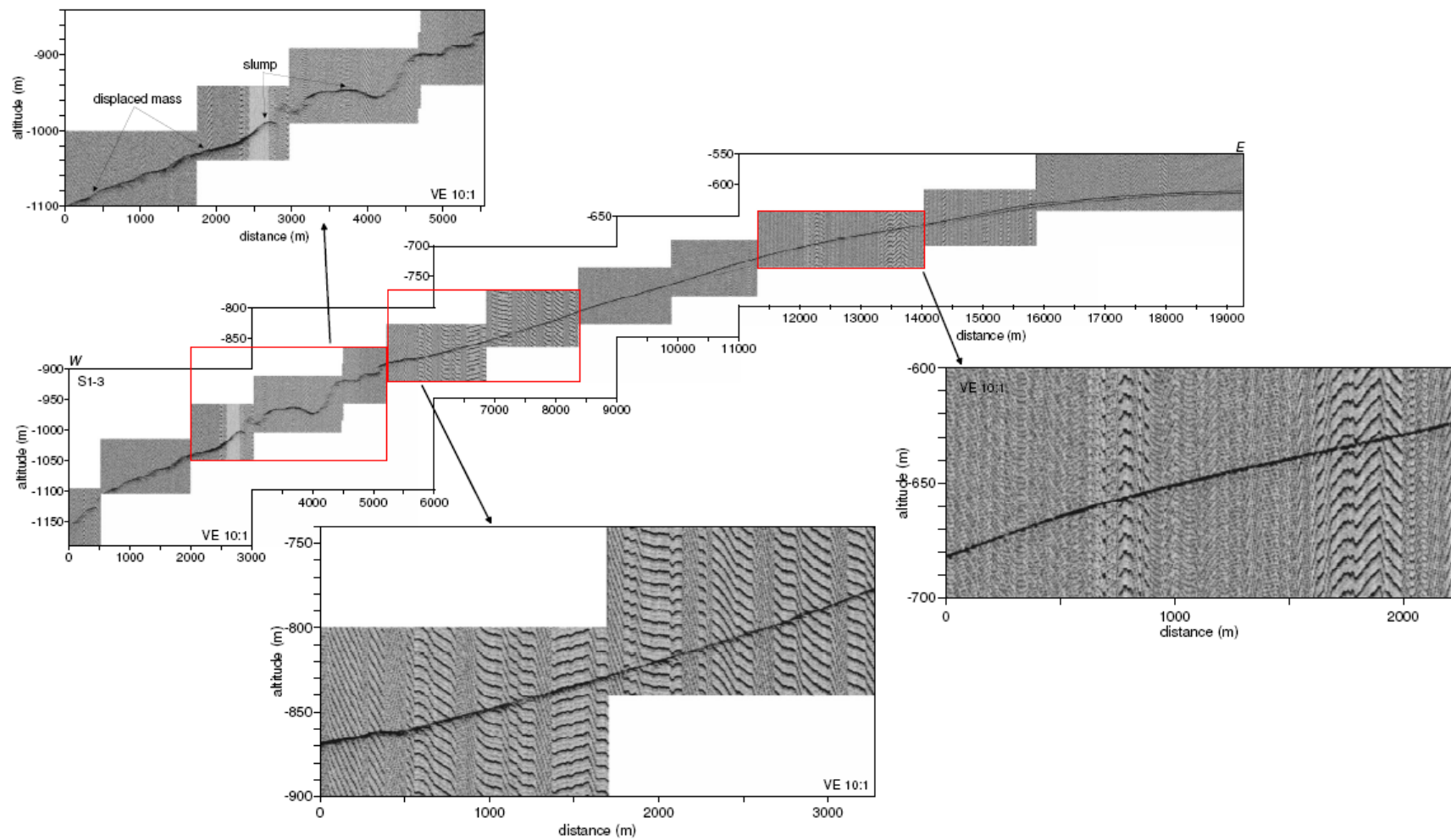


Figure 14. Shows detailed information of subbottom profile name S1-3.

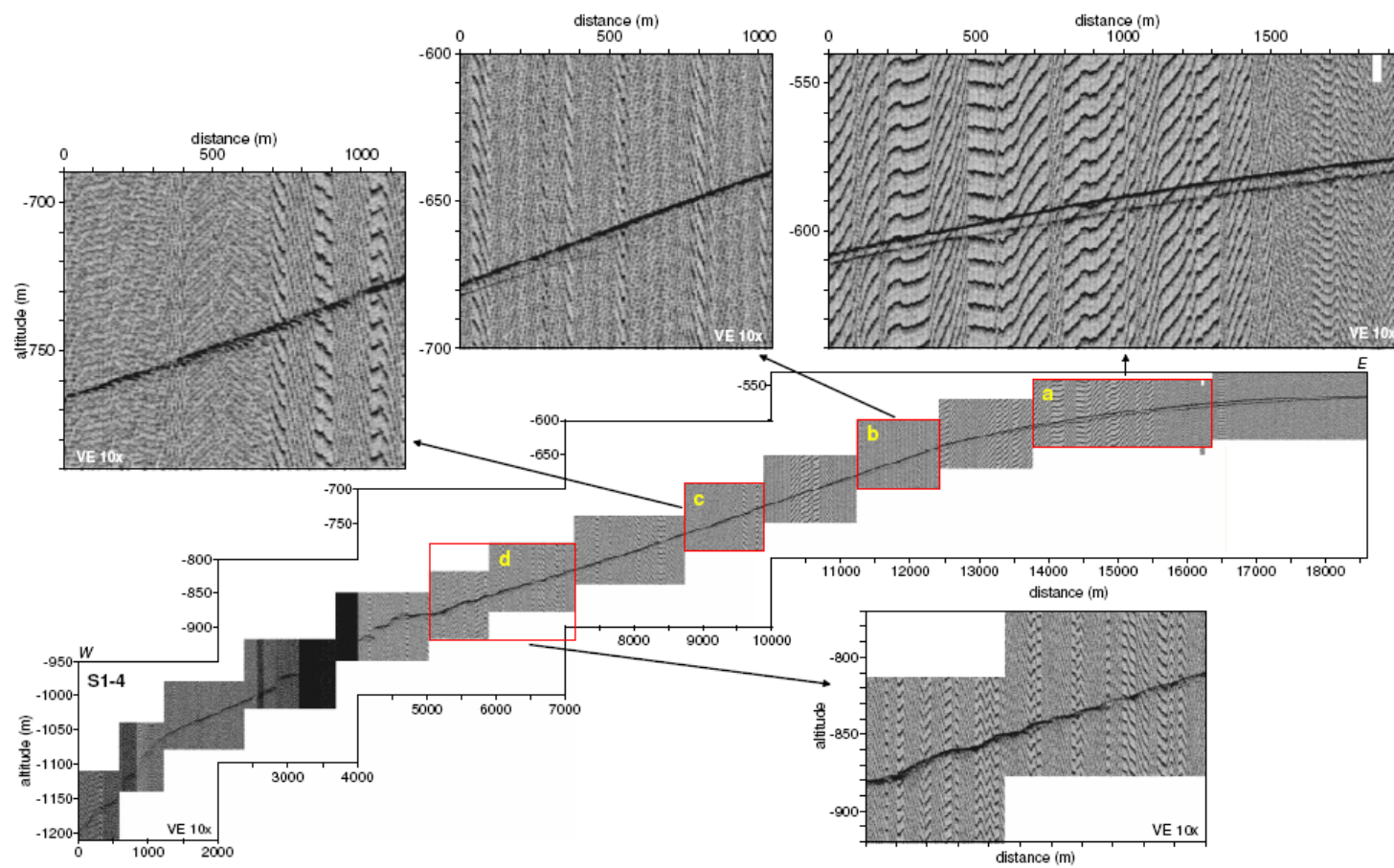


Figure 15. Shows detailed information of subbottom profile name S1-4.

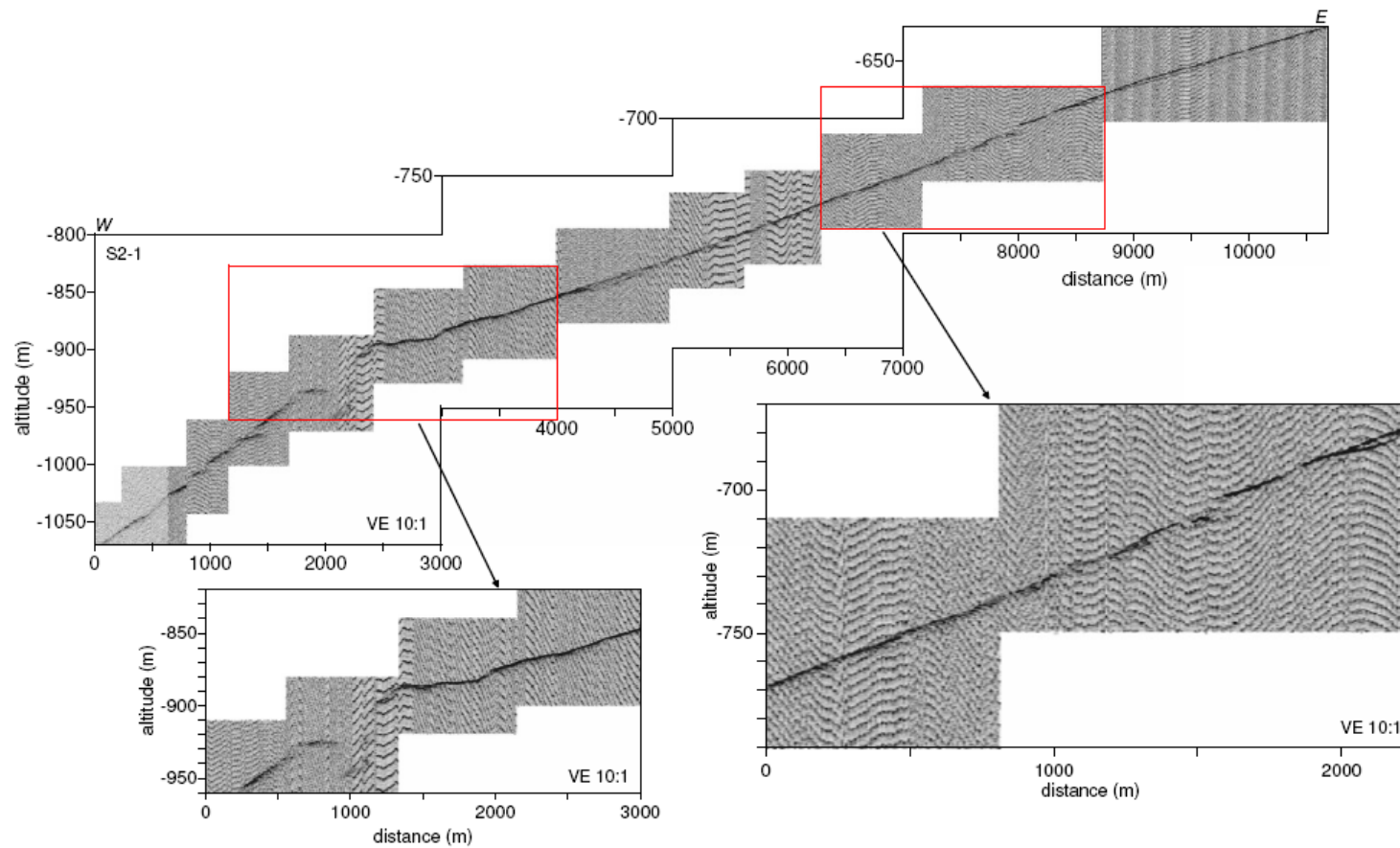


Figure 16. Shows detailed information of subbottom profile name S2-1.

The second province is about 1,300 m depth down to 1,700 m with an approximate slope range of about 3.2° to 4.6°. More than ten features which could possibly be identified as gullies are revealed at an slope area between about 8°10' N and 8°34' N at the water depth ranging between 1,000-1,500 m continuously to northward.

4.3.3 Backscatter map

The use of multibeam echo sounders for bathymetric purposes start in the seventies with system (e.g. the SEABEAM system) strictly designed to improved bathymetric mapping efficiency by measuring simultaneous depths inside a fan narrow acoustic beam. De moustier showed the interest of reflectivity measurements as a function of incident angle ([De moustier 1986; 1991](#)), making clear that a multibeam echo sounder could be available tool in seafloor characterization in spite of the limiting capabilities of the system.

The entire backscatter obtained with simultaneous swath bathymetric echodata covering the area is mapped ([Fig. 17](#)). By visual interpretation, the area which are presented by tones can be divided into three provinces, which are; (1) smooth area are blanketed by light tones, (2) area of prominent features are blanketed by dark tones, and (3) between both area are blanketed by moderate tones. This texture pattern is interpreted to indicate distribution of sediment-grained size. However, interface roughness influence which causes high reflectivity levels must be taken into account for interpretation. In addition, more information related to transportation of mass in the area is important to be known.

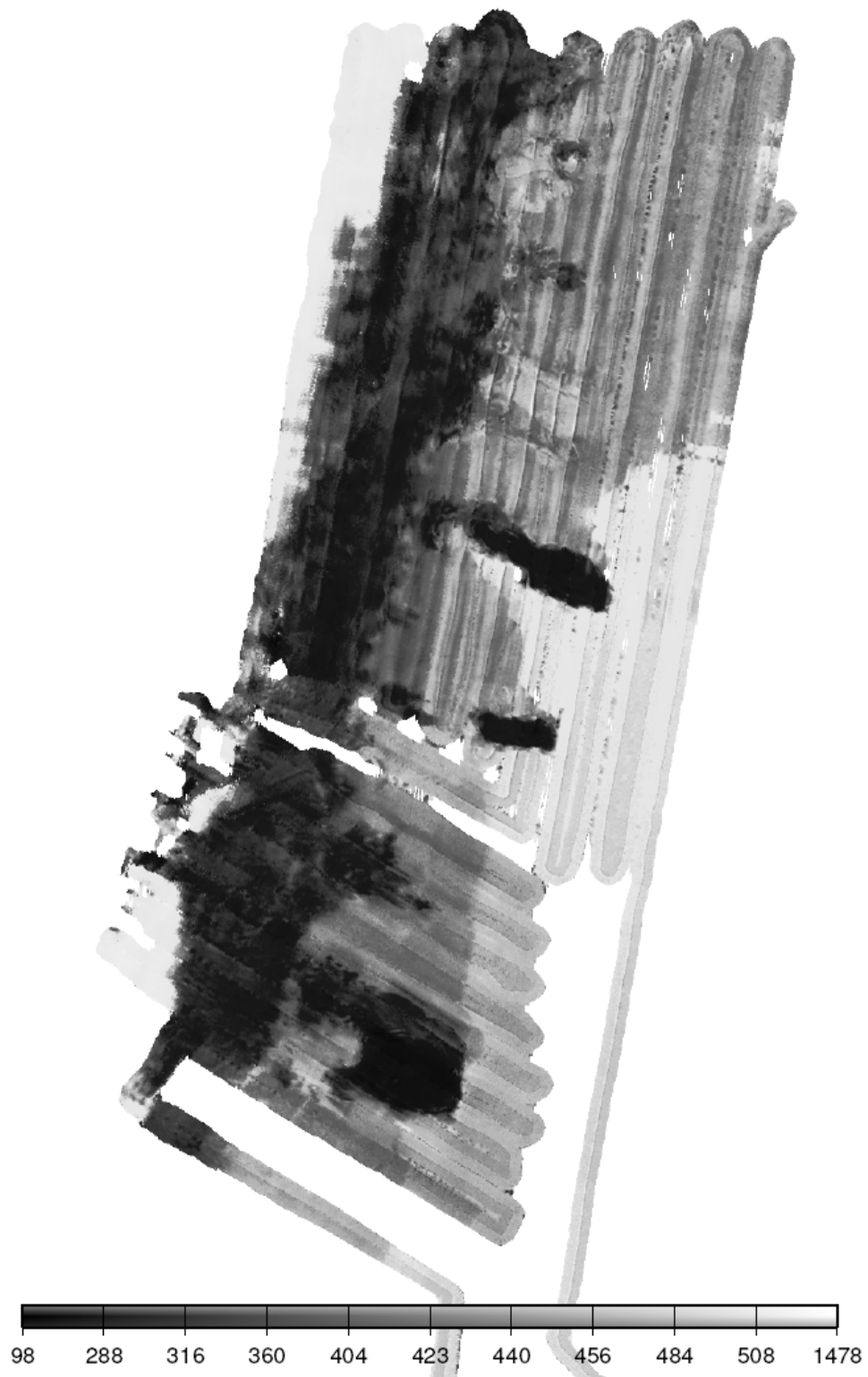


Figure 17. Show backscatter map covering prominent features and slope area.

4.3.4 Shallow gases

An area with gathering of conspicuous characteristics of gas is studied from parametric sediment profilers. Ten positions of possible mound and one position of possible mud volcanoes are observed at water depth vary about 850-950 meters. Twenty-four positions of possible occurrence of shallow gas are observed at water depth ranging about 850-950 meters (Fig. 18). Fourteen positions of possible slump are observed at water depth ranging about 850-950 meters. The positions of those shallow gases are summarized in Table 4. In addition, almost of prominent morphologies resemble as slope failures were only distinguished in the southern part of the survey area. Twelve positions of possible mass movement are observed at western part of Mergui ridge and the water depth approximately about 800 m and further downslope. The thickness of these masses was usually not more than 10 m.

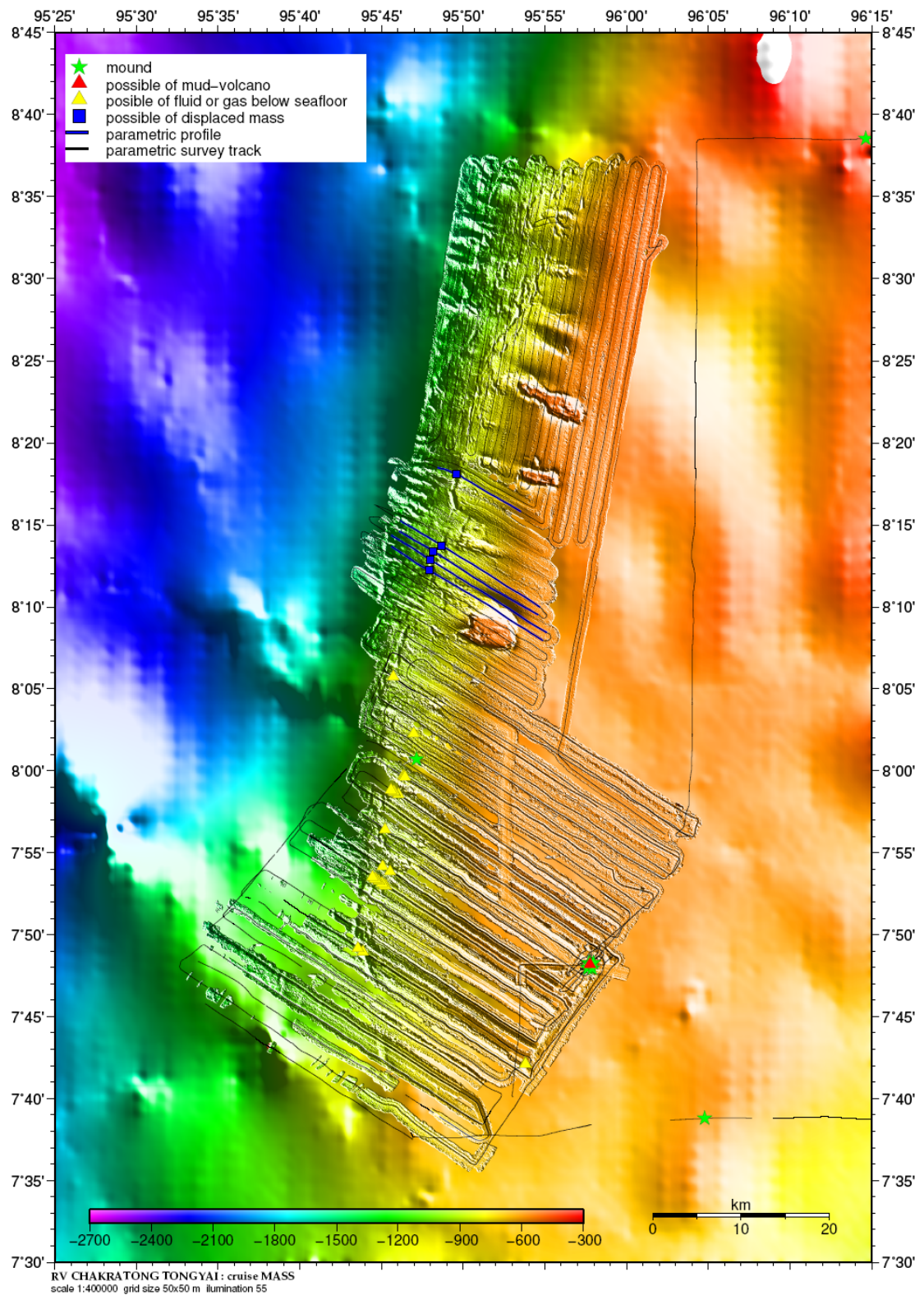


Figure 18. Show positions of possible mounds, mud volcano, displaced masses, and fluids/gases beneath seafloor which are observed from subbottom profiles. SBP tracks of surveys show by black lines.

Table 4. *Show positions of possible shallow gases/fluids beneath seafloor.*

Number	Longitude	Latitude
1.	95°53.81' E,	7°42.11' N
2.	95°53.80' E,	7°42.12' N
3.	95°53.79' E,	7°42.12' N
4.	95°43.87' E,	7°48.95' N
5.	95°43.55' E,	7°49.17' N
6.	95°45.27' E,	7°52.98' N
7.	95°45.18' E,	7°53.04' N
8.	95°45.04' E,	7°53.14' N
9.	95°44.84' E,	7°53.27' N
10.	95°44.69' E,	7°53.37' N
11.	95°44.59' E,	7°53.43' N
12.	95°44.44' E,	7°53.53' N
13.	95°46.44' E,	7°59.61' N
14.	95°46.38' E,	7°59.65' N
15.	95°46.32' E,	7°59.69' N
16.	95°45.72' E,	8°05.73' N
17.	95°57.80' E,	7°48.13' N
18.	95°46.03' E,	7°58.56' N
19.	95°45.80' E,	7°58.70' N
20.	95°45.74' E,	7°58.74' N
21.	95°45.58' E,	7°58.84' N
22.	95°45.22' E,	7°56.42' N
23.	95°45.07' E,	7°54.16' N
24.	95°45.53' E,	7°53.85' N

6. References

- Amante, C. and B. W. Eakins. (2008). ETOPO1 1 Arc-Minute Global Relief Model: Procedures, Data Sources and Analysis, National Geophysical Data Center, NESDIS, NOAA, U.S. Department of Commerce, Boulder, CO, August 2008.
- Archarya, S.K. (2000). Break up of Australia-India-Madagascar Block, opening of the Indian Ocean and continental accretion in southeast Asia with special reference to the characteristics of the Peri-Indian collision zones. *Gondwana Research*. 3(4) : 425-443.
- Bathymetric Chart of the Oceans (GEBCO); British Oceanographic Data Centre, Birkenhead.
- Becker, J. J., D. T. Sandwell, W. H. F. Smith, J. Braud, B. Binder, J. Depner, D. Fabre, J. Factor, S. Ingalls, S-H. Kim, R. Ladner, K. Marks, S. Nelson, A. Pharaoh, G. Sharman, R. Trimmer, J. vonRosenburg, G. Wallace, P. Weatherall. (2009). Global Bathymetry and Elevation Data at 30 Arc Seconds Resolution: SRTM30_PLUS, revised for Marine Geodesy, January 20, 2009.
- Beyer, A., R. Rathlau, and H.W. Schenke. (2005b). Multibeam bathymetry of the Håkon Mosby Mud Volcano. *Marine Geophysical Researches*. 26, 61-75.
- Caress, D.W., and D.N. Chayes. (2004). MB-System, Version 5, Open source software distributed from <http://www.ldeo.columbia.edu/MB-System/> and <http://www.mbari.org/data/mbsystem/>, 2003-2004.
- Curry, J.R., D.G. Moore, L.A. Lawver, F.J. Emmel, R.W. Raitt, M. Henry, R. Kieckhefer. (1979). Tectonics of the Andaman Sea and Burma, *the American Association of Petroleum Geologists*, 189–198.
- Curry, J.R. (1989). The Sunda Arc: A Model for Oblique Plate Convergence, *Netherlands Journal of Sea Research*, Vol. 24. 131-140.
- Curry, J.R. (1994). Sediment volume and mass beneath the Bay of Bengal. (1994). *Earth and Planetary Science Letters*. 125;371-383.
- Curry, J.R., Emmel, F.J., Moore, D.G., (2003). The Bengal Fan: morphology, geometry, stratigraphy, history and processes. *Marine and Petroleum Geology* 19, 1191–1223.
- Curry, J.R. (2005). Tectonics and history of the Andaman Sea region, *Journal of Asian Earth Science*, Vol.25. 187-232.
- Dasgupta, S., and M. Mukhopadhyay. (1993). Seismicity and plate deformation below the Andaman arc, northeastern Indian Ocean, *Tectonophysics*, Vol. 225. 529-542.
- De Moustier, C. (1986). Beyond bathymetry mapping acoustic backscattering from the deep seafloor with sea beam, *JASA* 79(2), 316-331.
- De Moustier, C. (1991). Angular dependence of 12 kHz seafloor acoustic backscatter, *JASA* 90(1), 522-531.
- Eguchi, T., S. Uyeda, and T. Maki. (1979). Seismotectonics and Tectonic History of the Andaman Sea, *Tectonophysics*, Vol 57. 35-51.

- Frerichs, W.E. (1971). Paleobathymetric Trends of Neogene Foraminiferal Assemblages and Sea floor Tectonism in the Andaman Sea Area, *Marine Geology*, Vol. 11, 159-173.
- GEBCO. (1997). General Bathymetric Chart of the Oceans (Data from GEBCO Digital Atlas), Sheet 97.3, bathymetric contours. IOC, IHO and BODC, Supporting Volume to the GEBCO Digital Atlas, published on behalf of the Intergovernmental Oceanographic Commission (of UNESCO) and the International hydrographic Organization as part to the General.
- Hampton, M.A., H.J. Lee, and J. Locat. (1996). Submarine Landslides. *Reviews of Geophysics*. 34. 33-59.
- Hochstetter, F. Von. (1869). Geology and physical geography of Nicobar Islands. *Records Geological Survey of India* 2 (Pt 3).
- Innomar Technologie GmbH. (2005). SES-2000 Parametric Sediment Echo Sounder. Operator's Manual (November 2005). 40 pp.
- IOC, IHO and BODC. (2003). Centenary Edition of the GEBCO Digital Atlas, published on CD-ROM on behalf of the Intergovernmental Oceanographic Commission and the International Hydrographic Organization as part of the General Bathymetric Chart of the Oceans, British Oceanographic Data Centre, Liverpool, U.K
- Khan, P.K., and P.P. Chakraborty. (2005). Two-phase opening of Andaman Sea a new seismotectonic insight, *Earth and Planetary Science Letters*, Vol. 229. 259-271.
- L-3 Communications ELAC Nautik GmbH. (2003). Shallow and Medium Water Multibeam SEA BEAM 1000. Technical Handbook-TH 44 301 8004 E. 40 pp.
- L-3 Communications ELAC Nautik GmbH. (xxxx). SEA BEAM 1050-Multibeam Sonar. <http://www.elac-nautik.com>
- Mukhopadhyay, M. (1984). Seismotectonics of Subduction and Back-Arc Rifting Under the Andaman Sea, *Tectonophysics*, Vol. 108. 229-239.
- Polachan, S., and A. Racey. (1993). Lower Miocene larger foraminifera and petroleum potential of the Tai Formation, Mergui Group, Andaman Sea, *Journal of Southeast Asian Earth Science*, Vol. 8. 487-496.
- Raju K.A. K., T. Ramprasad, P.S. Rao, B.R. Rao, and J. Varghese. (2004). New insights into the tectonic evolution of the Andaman basin, northeast Indian Ocean, *Earth and Planetary Science Letters*, Vol. 221. 145-162.
- Richter, B., Fuller, M., Schmidtke, E., Tin Myint, U., Tin Ngwe, U., Mya Win, U., Bunapas, S. (1993). Paleomagnetic results from Thailand and Myanmar: implications for the interpretation of tectonic rotations in Southeast Asia. *Journal of Southeast Asian Earth Sciences* 8, 247-255.
- Rodolfo, K.S. (1969). Sediments of the Andaman Basin, Northeastern Indian Ocean, *Marine Geology*, Vol. 7, 371-402.
- Schmidt, V., D.N. Chayes, and D.W. Caress. (2004). The MB-System Cookbook, <http://www.mbari.org/data/mbsystem/mb-cookbook> and <http://www.ldeo.columbia.edu/MB-System/mb-cookbook>, Version 1.1, 2004.

- Sandwell, D.T., W.H.F. Smith, S. Gille, E. Kappel, S. Jayne, K. Soofi, B. Coakley, and L. Geli. (2006). Bathymetry from space: Rationale and requirements for a new, high-resolution altimetric mission. *C. R. Geoscience*. 338 : 1049–1062.
- Sewell, R.B.S. (1925). The geography of the Andaman Sea basin. *Asiatic Society of Bengal*. 9: 1–26.
- Smith, W.H. F. and D.T. Sandwell. (1997). Global Sea Floor Topography from Satellite Altimetry and Ship Depth Soundings. *Science*. Vol .277. 1956-1962.
- The GEBCO_08 Grid. (2009). version 20090202, <http://www.gebco.net>
- The Royal Gazette (1988). The EEZ Claims of Thailand according to The Royal Gazette. V. 105(120), 231-234 (26 July 1988).
- Wessel, P. and W.H.F. Smith. (1998). New improved version of generic mapping tools release, EOS Trans. Amer. Geophys. U. 79 (47), 579.

ภาคผนวก ง

Final report MASS III

Julia Schwab, Sebastian Krastel and Felix Gross

1 Acquisition and processing of new acoustic and core data

1.1 Bathymetry

In addition to already existing bathymetric data of the continental slope, that were acquired during the previous MASS cruises in 2006 and 2007, it was planned to use a multibeam echo sounder system (*Seabeam 1050 Multibeam Echosounder*) in order to achieve new bathymetric data from previously unsurveyed areas.

1.1.1 Multibeam configuration

For the multibeam transducers a holding construction was built that had been used also during the previous MASS cruises onboard of Chakratong Tongyai in 2006 and 2007 (Fig. 1). Construction of the poles was done at the pier of the PMBC. This time the multibeam was deployed on the starboard side of the vessel (Fig. 1). The holder construction consisted of:

- the holding arm pipe between multibeam transducer and the second arm pipe
- the second straight pipe arm
- the elbow holding arm pipe between the second arm pipe and the starboard pipe
- the starboard fixed pipe (Fig 1)

By using flanges and screws the construction could be moved from the vertical position where transducers are in the water (during measurement) to a horizontal position with transducers fixed to the ship's side (during transit).

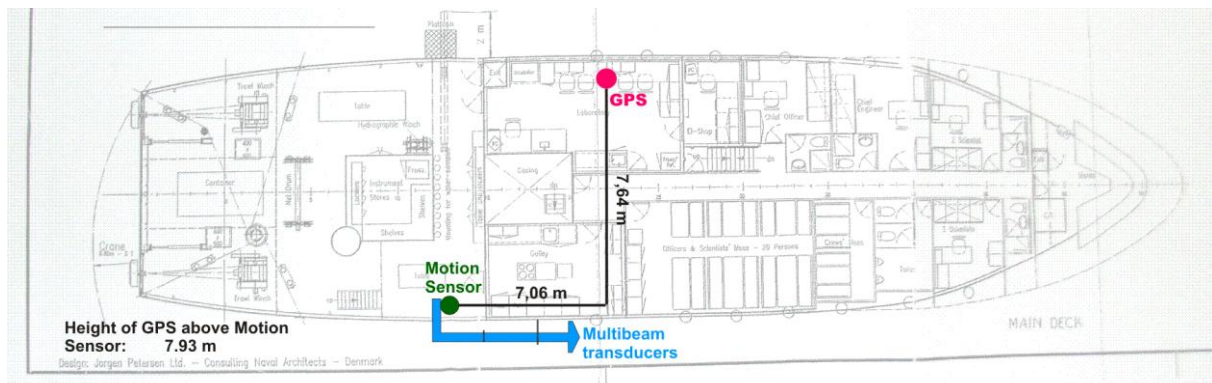


Figure 1. GPS and multibeam configuration onboard RV Chakratong Tongyay (from Krastel, 2011)

1.1.2 Results of multibeam data acquisition

The holder construction bent shortly after roll calibration was finished due to high ship speed (see Krastel 2011 for more detailed information). With the deformed pole it was not possible to collect bathymetry data anymore. For a more detailed description of the acquisition of the data refer to the cruise report.

1.2 High resolution multichannel seismic profiling

A high-resolution multichannel seismic survey was carried out during the MASS III-cruise on RV Chakratong Tongyai with the objective to resolve sedimentary structures along the continental margin west of Thailand. A micro-GI Gun was used to transmit a seismic signal. The reflections from the seafloor and deeper geological structures have been recorded with a digital Geometrics GeoEel150 m long streamer which was towed behind the vessel. Configuration during the seismic survey is documented on Figure 2.

1.2.1 Data acquisition and system components

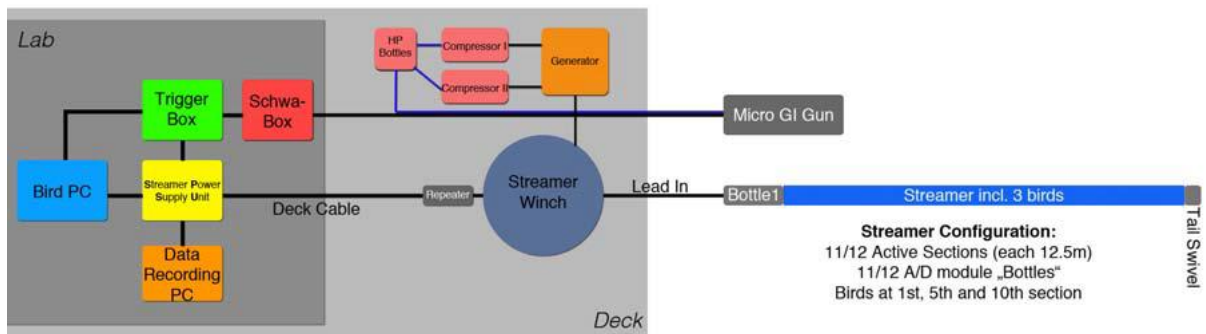


Figure 2. Configuration of multichannel seismic system components (from Gross, 2012)

Seismic source

During seismic surveying a Micro-GI Gun (Fig. 11) was used (Generator 0.1L, Injector 0.1L). During seismic profile MASS 001 profile only the Generator was shot due to problems with one of the compressors. From the second profile on the GI-mode was applied and the Injector was triggered with a delay of 20 ms after the Generator-signal for depressing the bubble signal. The Micro-GI Gun was towed about 0.5 m below the water surface. Shooting range was adjusted to the water depth, varying between 5 and 6 seconds. The gun was shot at an air pressure of ca. 120 bars and was working without problems during the whole seismic survey.

Streamer-system

A digital streamer (Geometrics GeoEel) was used for recording the seismic signals. The first active streamer section was towed 36.5 m behind the stern of the ship. During the cruise 11 respectively 12 sections were used, each with a length of 12.5 m, resulting in a total streamer length of 137.5 m / 150 m. Each section contains 8 channels (channel spacing 1.56 m) and each channel consists of two hydrophones. One AD digitizer module belongs to each active section. These AD digitizer modules are small Linux computers built in a water resistant housing. Communication between the AD digitizer modules and the recording system in the acquisition laboratory was realized via TCP/IP. A repeater was located between the deck cable and the tow cable (lead-in) to ensure connectivity. The SPSU (streamer power supply

unit) manages the power supply and communication between the recording system and the AD digitizer modules. The recording system is described below. Three birds were attached to the streamer (Fig. 2). Designated streamer depth was 3 m. A small buoy was attached to the tail swivel. Leakage problems at the beginning of the survey resulted in removing two sections of the streamer. After checking those sections onboard one sections was again attached to the streamer between seismic profile 11-003 and 11-004.

Bird Controller

Three Oyo Geospace Bird Remote Units were attached at the streamer (Fig. 1). All RUs have adjustable wings. The RUs are controlled by a bird controller in the acquisition laboratory. Controller and RUs communicate via communication coils nested within the streamer. A twisted pair wire within the deck cable connects controller and coils. Operating depth of the birds was set to 3 m. Automatic depth position scanning during the survey was switched off because this might cause noise in the recorded data. The birds worked reliable during the whole cruise keeping the streamer in the designated depth and therefore ensured good quality of the recorded seismic data.

Data acquisition systems

Geometrics GeoEel software was used for recording incoming data from the streamer. The analogue signal was digitized in the AD digitizers with 4 kHz. The data were recorded as multiplexed SEG-D. One SEG-D file was generated per shot. Data were recorded with delay but the delay was not written to the header. The delay was adjusted manually, depending on the water depth. The acquisition computer allowed online quality control by displaying shot gathers, a noise window, and the frequency spectrum of each shot. The cycle time of the shots is displayed as well. The software also allowed online NMO correction and stacking of data for displaying stacked sections. Parameters such as shot time and shot position were saved to log files. Data were converted to SEG-Y file while being at sea. During acquisition of seismic profile 01 to profile 03, problems with the GPS occurred, which was represented by missing GPS times for several shots – the Baud rate of the GPS device was too low

(4000). This problem was solved by using the system time of the computer from profile 04. The system time was synchronized on a regular basis.

Trigger unit

A custom trigger unit, (SchwaBox) was used during the cruise. This device generates triggers (TTL) at arbitrary combinations for controlling seismic sources, acquisitions systems, and bird controllers. In addition, the SchwaBox was connected to a gun amplifier unit. The trigger scheme was adjusted to the water depth during the survey. The trigger system worked very reliable during the entire cruise.

1.2.2 Seismic data processing

Standard processing methods were applied in order to improve data quality. The processing was carried out with the commercial software Vista Seismic Processing 9.0 by Gedco. Additionally WinGeoapp, a software tool written by Hanno Keil (University of Bremen), was used for setting up the geometry. A workflow of the processing method used is shown in Figure 3.

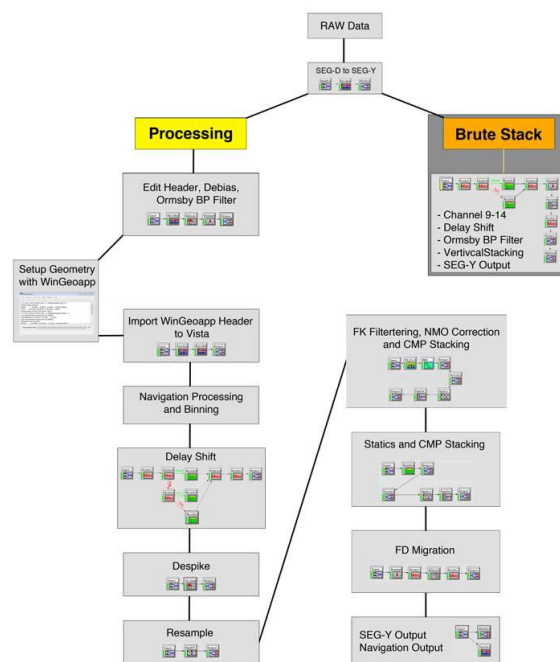


Figure 3. Processing workflow applied for MASS III seismic data (processed with Vista Seismic Processing Software (from Gross, 2012))

Pre-processing

1 During pre-processing the dataset was prepared for further processing steps. The
2 collected SEG-D dataset was converted to SEG-Y format. Each profile was stored as
3 a single SEG-Y dataset. During SEG-Y conversion a header was created for each
4 profile and checked for potential errors. A wide Ormsby Band Pass filter was set to
5 reduce and cut interfering noise. Low-pass was set to 15/30 Hz and high-pass to
6 800/1200 Hz.

8 **Navigation processing with WinGeoapp**

9 The vessel position was recorded via GPS during the cruise. The navigation data
10 were stored in NMEA-format (National Marine Electronics Association standard file
11 system for navigation data). These files record UTC year, day, hour, second, and
12 position of the vessel. To set up the geometry of the streamer and its navigation the
13 custom tool WinGeoapp (Hanno Keil, University of Bremen), was used. It compiles all
14 navigation/NMEA data for each channel and the position of the GI-Gun. With this
15 information the header of the SEG-Y files was updated for correct positioning of each
16 shot and each channel. As WinGeoapp uses an algorithm, that plots each channel of
17 the streamer in relation to the cruise track, it was possible to enhance quality of
18 positioning accuracy, especially in curves and changes of the course direction.

20 **Binning**

21 For stacking of the data (carried out with Vista Seismic Processing Software) all
22 midpoints were assigned to a "bin" (small area according to the midpoint between
23 source and receiver). To ensure a high signal to noise ratio after data stacking a
24 minimum fold of 20 traces per bin was applied. With a bin size of 2 m (inline) it was
25 possible to guarantee a high horizontal resolution in respect to sampling (Fig. 4). This
26 enhanced especially the resolution at sharp boundaries like escarpments or small-
27 scale structures.

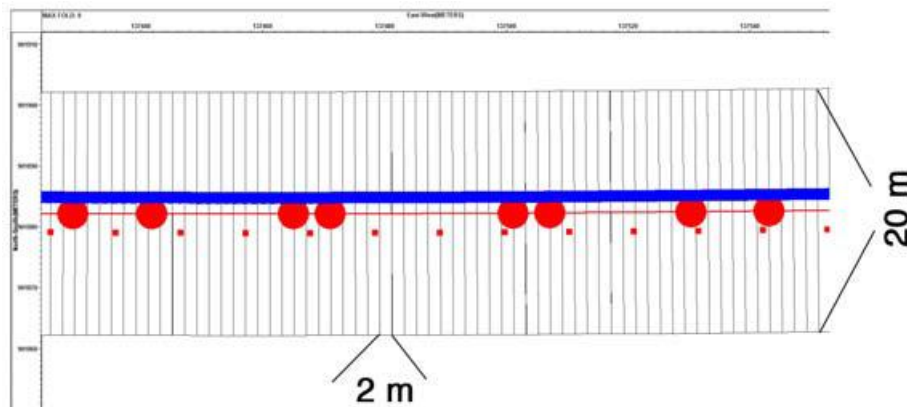


Figure 4. Setup Geometry and Bins in the Vista Geometry module – Blue line = Receiver/Streamer, Red line = Midpoints, Small red dots = shot points, Big red dots = calculated crooked line (from Gross, 2012)

Data despiking

A despiking module was applied to reduce spikes from the dataset. Spikes are high amplitude noise signals, created by electrical disturbances in the cables between streamer and vessel, faulty hydrophones or unwanted acoustic sources like breaking waves and noise from the ship running along the streamer. The despiking filter was applied to NMO corrected and CMP sorted data. It reduced the impact of spikes on the data quality by adjusting the amplitudes of channels with unusual amplitude characteristics. This adjustment was carried out by calculation of the standard deviation of the amplitudes of five neighboring channels within a 50 ms windows, and comparison to the maximum amplitude of each of these 5 traces. If the amplitude of a track varied more than 1.5 times the standard deviation, the data content was reduced to 1.5 times the standard deviation. This filtering was applied subsequently to the complete dataset.

FK-filter

The FK filter was applied to further eliminate unwanted noise signals in the dataset. Unwanted data can result from coherent linear noise / ground roll, guided waves and side scattered energy (Yilmaz, 1987). For most of the profiles a “standard” FK (frequency, wave number) filter was used by setting up a fan-shaped filter to eliminate unwanted energy. The unwanted noise was treated as a coherent linear noise and a side scattered energy, which was especially observed when crossing the structural highs in the working area.

Spherical divergence

Spherical divergence correction was calculated for each channel in order to eliminate the effect of unwanted amplitude variations due to increasing attenuation of the sound wave amplitudes with increasing distance from the source.

Normal move out correction

Due to varying offsets in a CMP-gather, the recorded travel times differ for each channel. A dynamic time correction for each shot-receiver pair has to be carried out in order to create a zero offset section.

As no reliable velocity model for the area was available, the NMO correction was carried out with the mean water velocity of 1500 m*s⁻¹. An additional velocity analysis was resigned due to the length of the streamer in relation to the water depth. For the working area in most parts NMO and residual statics are in the same range and no reliable velocity picking can be carried out. Additionally strong lateral and vertical variations in velocities due to bunched lithology in the working area may have led to a vertical distortion of the data.

CMP stack

CMP stacking was carried out for the traces within individual bins, which were assigned to 2 m x 20 m. As each bin contains traces with similar CMP position and comparable seismic information, all NMO corrected CMP gathers were stacked. This resulted in an amplification of the signal to noise ratio

Static module

For several profiles the "static module" was used to recalculate residual statics. The static module in Vista Seismic Processing offers an iterative correlation of the first-bricks of a CMP and their alignment to each other. After the static module was applied, the resulting data were compared with the uncorrected CMP stack in order to preclude distortions.

Migration

In order to correct the vertical reflection time of reflection events and to enhance resolution of the seismic data, "migration" was the final processing step (see Figure 5 for an example of improvement of data quality).

In case of a dipped reflector the first reflection is not origination from the point directly beneath the source, instead the spherical spread out acoustic wave front is first interfering with some part of the reflector upslope of this position. Therefore, two way travel time (TWT) between source and receiver is smaller, which results in a misinformation for depth and inclination of the reflector. Reflectors in the seismic section are imaged with reduced inclination and at greater depth than in reality. These aberrations occur at many geological structures. Sharp edges and diffraction points result in diffraction hyperboles. (Yilmaz, 1987). Migration of seismic data aims to correct for the dislocation of seismic reflectors. Diffraction hyperbolae will collapse in their apex. Inclined reflectors will be steepened and shifted in up-dip direction. Synclines will get reworked and all "bowties" will be deleted. Anticlines will be straightened which results in elimination of crossing reflectors.

The seismic dataset was time migrated and "FD Migration" (finite difference migration) was applied, which means that a differential solution of the wave equation with the help of finite elements is applied (Yilmaz, 1987)

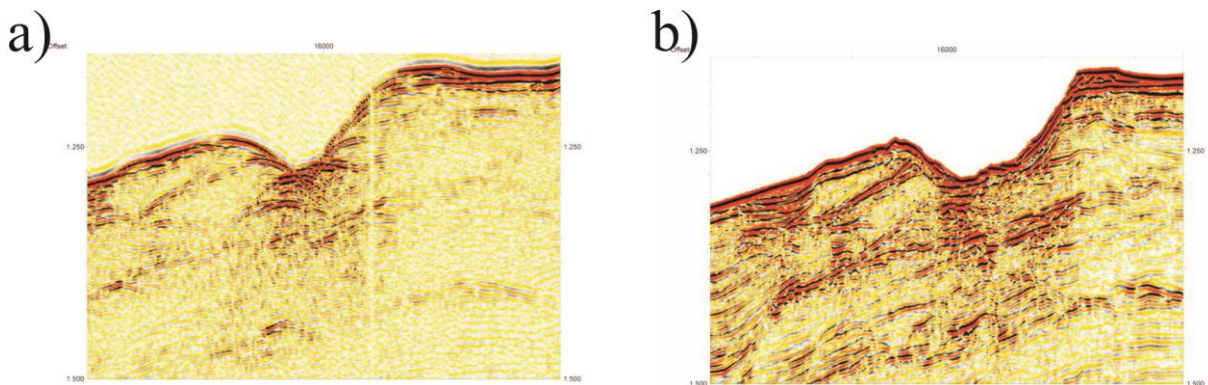


Figure 5. a) Brute stack of an extract of Profile 14 using only 6 channels (BP filter and stack), b) Full processed extract of Profile 14 using 96 channels (FD migrated, geometry setup, FK filtering, NMO, static module, CMP stacking) (from gross, 2012)

1.3 Sediment sampling

A mini-gravity corer was used to take samples from different environments. Three main areas were chosen for sampling stations. These areas are:

- an assumed mass wasting area in the northern part of the bathymetric map
- the area around a large platform
- a deeper part of the continental slope

Table 1: List of Mini Gravity Corer Stations (Krastel et al.2012)

Station Number	Core Number	Date	Time	Lat (at surface)	Long (at surface)	Depth	Recovery
MASS III-001 ¹⁾	1	19.01.11	2:24	8°25.48	95°56.66	573.3	187 cm
MASS III-002 ¹⁾	none	19.01.11	3:45	8°25.30	95°56.95	555.6	empty
MASS III-002 ¹⁾	none	19.01.11	7:39	8°25.47	95°57.08	551.1	empty
MASS III-002 ¹⁾	1	19.01.11	8:26	8°25.31	95°35.58	591.2	123 cm
MASS III-003 ¹⁾	none	19.01.11	9:45	8°26.04	95°55.57	689.7	empty
MASS III-003 ¹⁾	none	19.01.11	11:16	8°25.89	95°55.61	687.9	empty
MASS III-004 ¹⁾	1	20.01.11	3:04	7°49.49	95°43.17	982.2	empty
MASS III-005 ¹⁾	1	20.01.11	7:57	7°48.10	95°44.89	857.8	empty
MASS III-006 ¹⁾	1	20.01.11	9:16	7°47.32	95°46.28	822.2	30 cm
MASS III-005 ¹⁾	2	20.01.11	10:51	7°48.33	95°44.80	857.8	fragments
MASS III-007 ¹⁾	1	21.01.11	1:48	8°11.97	95°52.96	597.8	142cm
MASS III-007 ²⁾	2	21.01.11	2:59	8°10.97	95°52.88	604.4	157cm
MASS III-008 ²⁾	1	21.01.11	3:56	8°09.95	95°52.06	686.7	empty
MASS III-008 ²⁾	1a	21.01.11	4:59	8°09.91	95°52.10	682.2	empty
MASS III-009 ²⁾	1	21.01.11	5:55	8°09.23	95°49.88	714.5	91cm
MASS III-010 ²⁾	1	21.01.11	6:55	8°06.92	95°51.74	632.2	150cm
MASS III-010 ¹⁾	2	21.01.11	7:31	8°06.41	95°51.52	628.9	50cm
MASS III-011 ²⁾	1	21.01.11	8:22	8°08.40	95°51.64	512.2	empty
MASS III-012 ²⁾	1	21.01.11	9:15	8°07.61	95°53.91	557.9	empty
MASS III-012 ²⁾	2	21.01.11	9:43	8°07.27	95°53.76		125cm
MASS III-013 ²⁾	1	22.01.11	2:03	7°53.90	97°39.47	353.3	empty
MASS III-013 ²⁾	2	22.01.11	2:34	7°53.66	97°39.36	354.5	empty
MASS III-014 ²⁾	1	22.01.11	3:24	7°53.81	97°39.91	313.3	empty

¹⁾ Archived in core repository of IFM-GEOMAR in Kiel

²⁾ Archived in core repository of Chulalongkorn University, Bangkok, Thailand

The used mini gravity corer is able to take cores up to 2 m length. Its top weight counts 250 kg. The installed winch on RV Chakratong Tongyai offered a total cable length of 2000 m. Hydraulic problems of the winch made an accurate use nearly impossible. As no device for measurement of rope tension was available coring was complicated further. Due to a missing dynamic positioning system on RV Chakratong Tongyai it was not possible to maintain the position of the vessel during corer deployment. Strong currents resulted in drift velocities of up to 1.5 knots, which made

the accuracy of the real position of the cores very hard to estimate. Widespread sandy environments anticipated the penetration of the sediment corer and no sediment recovery was possible in several cases (Table 1). Consequently, adversely to originally planned, sediment cores could not be acquired at locations crucial for slope stability analysis such as the areas off Mergui ridge. Therefore age dating of mass transport deposits was not possible. In total, 9 cores were retrieved from 14 stations (Table 1).

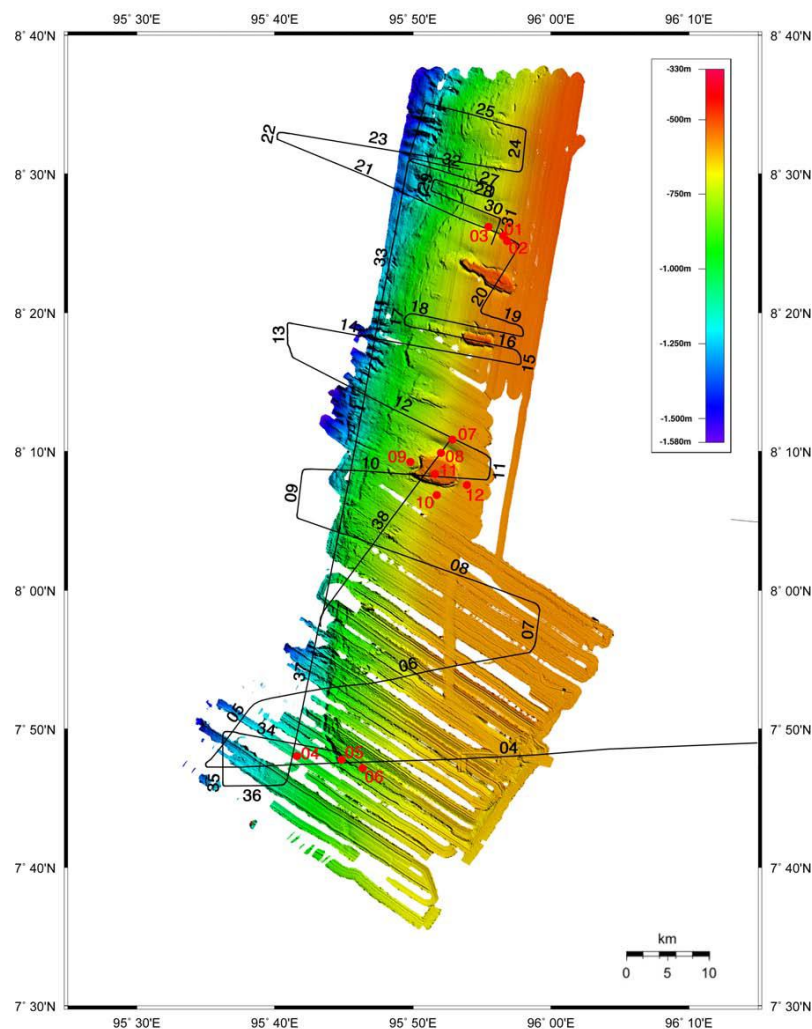


Figure 6. Overview map of seismic profiles and core locations of MASS III cruise (from Krastel, 2011). The bathymetry has been taken from Jintasaerane et al. (2012).

2 Quantification of individual mass wasting events

The general architecture of the background sedimentary units and the distributions and dimensions of mass transport deposits (MTDs) were deduced from the seismic dataset. MTDs were interpreted according to their external geometries and internal reflector characteristics. Lens- or wedge-shaped bodies showing a chaotic to transparent seismic facies were classified as MTDs. Precise measurements of volumes and areal extents of MTDs were not possible from our dataset, as spacing between profiles is relatively large, ranging between about 1 km and 7 km. Therefore, the geometries of the MTDs had to be interpolated over long distances of up to 7 km. An isopach grid was calculated, based on interpreted horizons of top and base for each MTD, using a constant sound velocity of 1500ms⁻¹. Subsequently, volume and areal extent was deduced from the isopach grid. Values are summarized in Table 2. The values in Table 2, however, have to be regarded only as rough estimations due to the uncertainties mentioned above and due to the fact that the lateral boundaries of the MTDs are not present in our dataset, except for one MTD close to the sea floor, where boundaries

Table 2. Measured properties of identified MTDs in the working area (Schwab et al. (2012))

MTD	interpolated areal [km ²]	maximum thickness of MTD [m]	approx volume MTD [km ³]	Depth of shallowest of point from surface [m]
A1	70	56	1.3	1130
A2	27	36	0.3	1280
A3	33	55	0.8	1350
A4	69	166	3.0	1210
B1	24	91	1.0	1850
B2	10	46	0.3	1950
B3	43	135	3.0	1570
B4	53	150	3.4	1710

B5	27	125	1.5	2020
C1	23	76	0.7	1480
C2	46	89	2.6	1420
C3	45	90	2.1	1550
C4	32	62	1.0	1530
C5	22	72	1.0	1560
D1	40	75	0.9	880
D2	33	234	4.0	830
D3	585	62	14.0	640

Seventeen individual mass transport deposits (MTDs) were identified in the three different environments described above. Four MTDs are located in the southern basin area (MTD A1–A4), ten MTDs in the northern part (MTD B1–B5 and MTD C1–C5), and three MTDs on Mergui Ridge (MTD D1–D3). The positions of the MTDs, their boundaries and minimum areal extents, as far as they were traceable on the dataset, are illustrated on Fig.7. The MTDs identified within the basin sediments (A1–A4, B1–B5, C1–C5) are generally characterized as lens- or wedge-shaped bodies, partially with a hummocky surface. They reveal internal chaotic to transparent reflector characteristics.

3 Characterization of slope failures

We did not classify the single mass transported deposits in detail. Classification of landslides based on single, wide spaced 2d-lines is difficult, because the 3d-geometry of the deposits could be established based on the available dataset, and detailed internal structures are not imaged in sufficient detail. We therefore decided to describe all deposits of gravitational mass wasting events with the general terms "mass transport deposit" and "landslide", irrespective of the process of formation. A further classification would be very speculative at the moment.

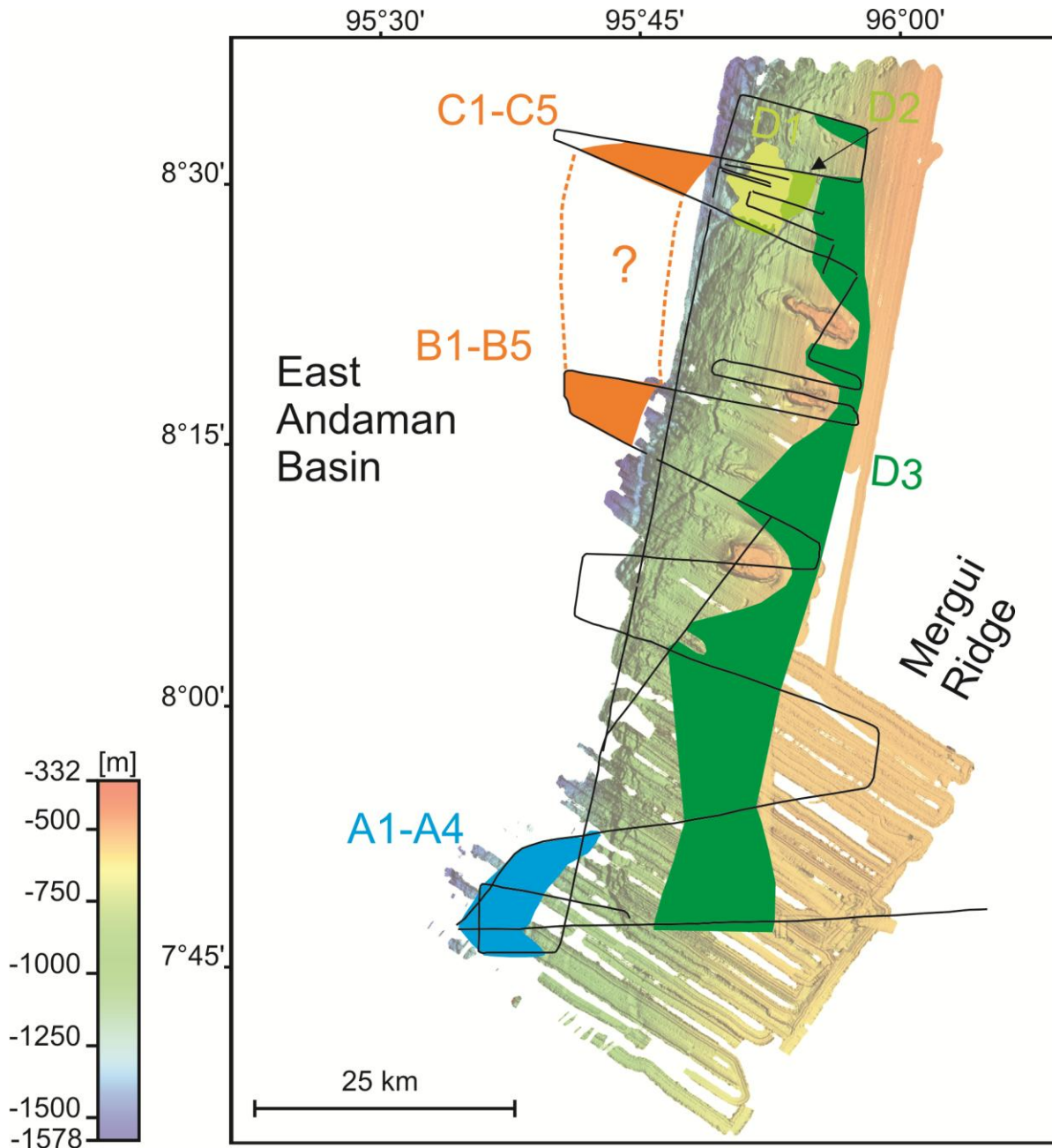


Figure 7. Map of locations and areal extent of MTDs identified in the working area

4 Determination of sedimentary properties

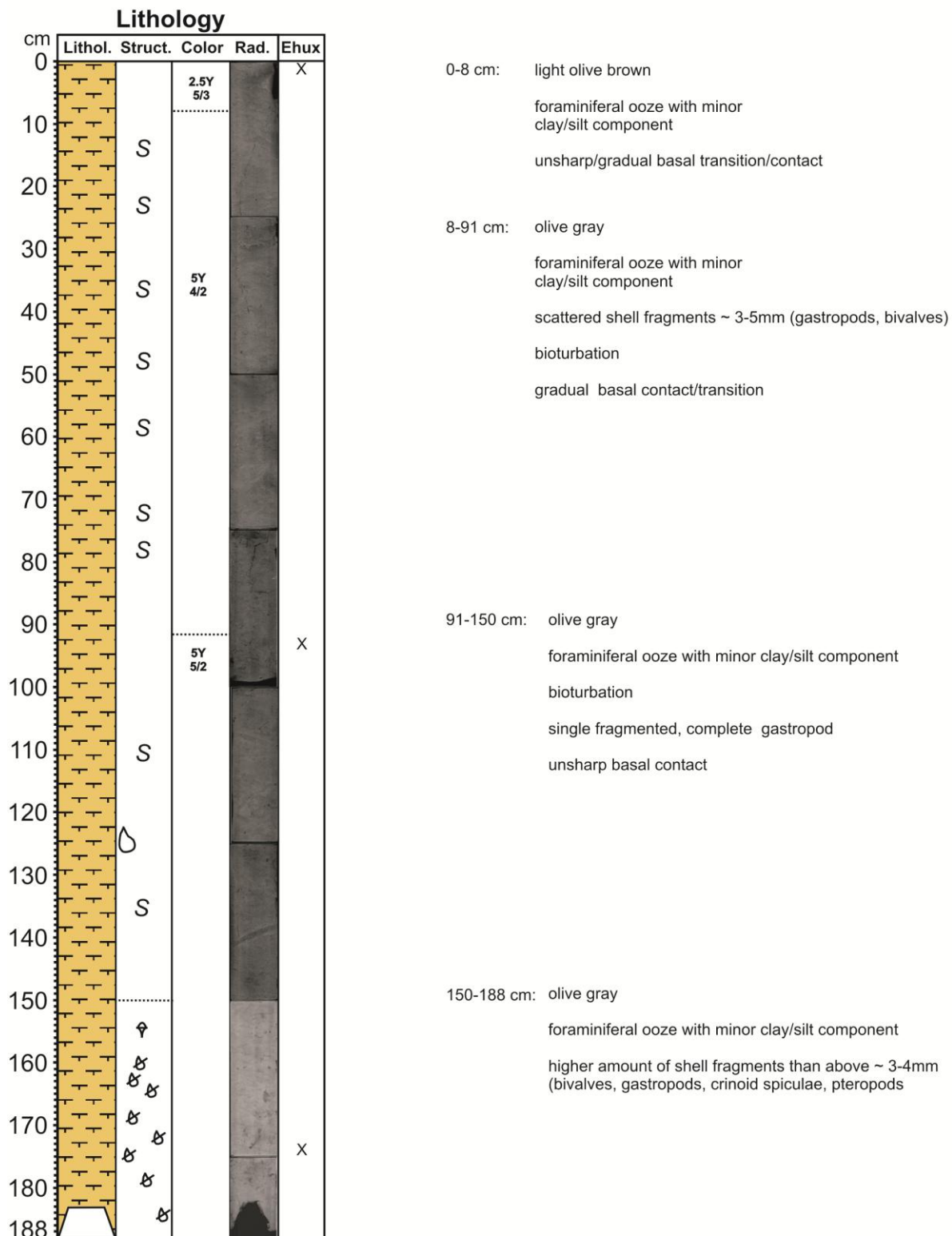
4.1 Core description and radiographs

To date, the cores MASS III 001-1, MASS III 002-1, MASS III 006-1 and MASS III 007-1 (Figs. 8, 9, 10) were split and visually described (see core descriptions). The

1 archive halves were photographed and sediment samples for qualitative analysis of
2 sediment components were taken from the working halves
3 To gain a better overview on the sedimentary structures radiography samples were
4 taken. According to the usual sampling method, plastic cases of the width of the core
5 diameter (length 25 cm, thickness 0.4 cm) were pressed into the sediment surfaces
6 and slices of the sediment surface were cut off the surface. For conservation the
7 slices are kept in the plastic cases and are sealed with plastic foil. Digital X-ray
8 radiographies were obtained by a standard medical X-ray apparatus.

MASS III 001-1

Date: 19.01.11 Pos: 8°25.48'N 95°56.66'E
Water Depth: 573 m Recovery: 188 cm

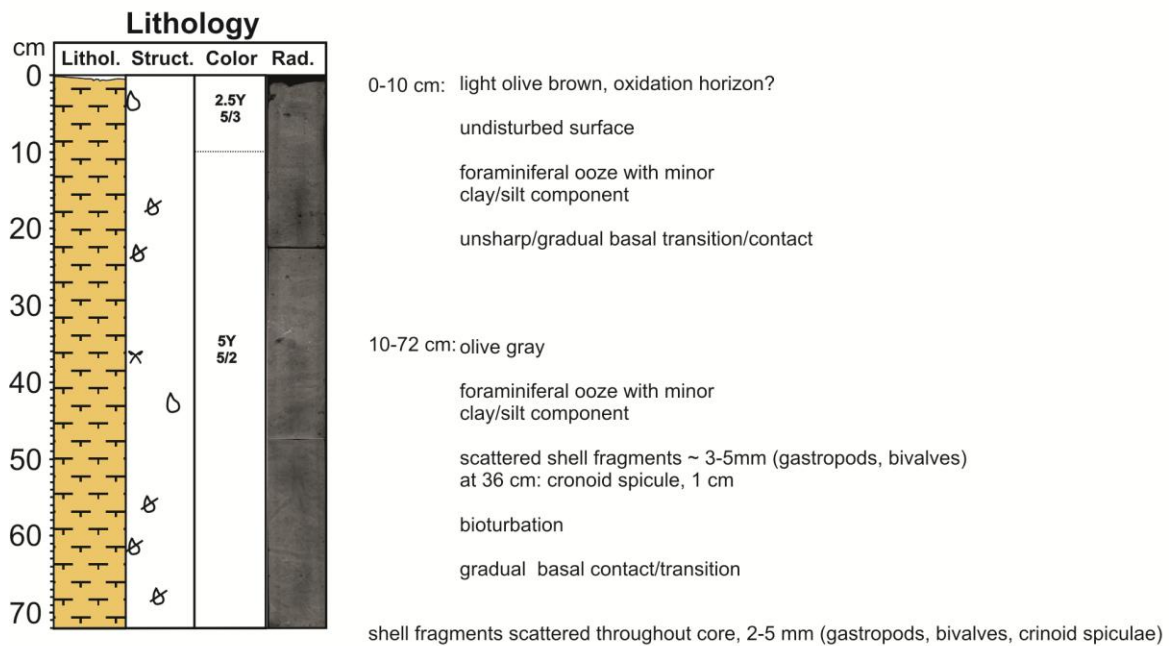


1
2

Figure 8. Visual core description and radiographic images of core MASS III 001-1

MASS III 002-1

Date: 19.01.11 Pos: 8°25.31'N 95°35.58'E
Water Depth: 602 m Recovery: 72 cm



MASS III 006-1

Date: 20.01.11 Pos: 7°47.12'N 95°46.33'E
Water Depth: 822 m Recovery: 25.5 cm

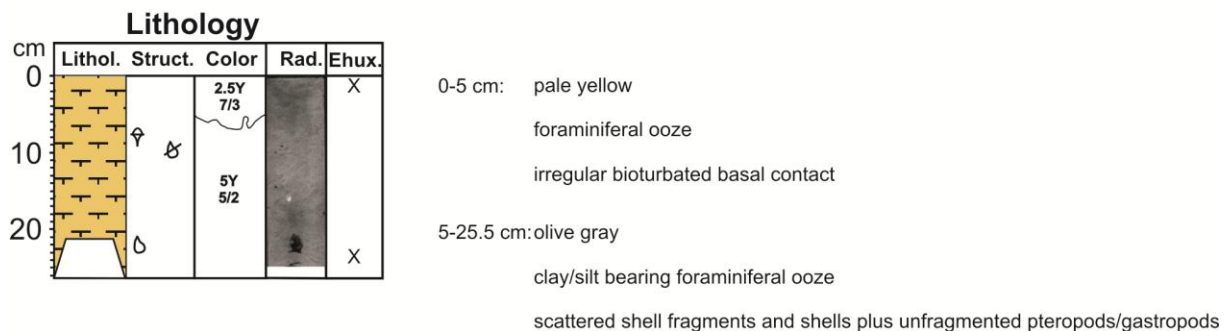


Figure 9. Visual core description and radiographic images of core MASS III 002-1 and MASS III 006-1

4.2 Physical properties of sediment samples

MSCL

Magnetic susceptibility and gamma-ray attenuation were measured in order to gain insight in fluctuations of sediment composition and bulk density. For measurement of these parameters a GEOTEK Multi Sensor Core Logger at GEOMAR, Kiel was used.

The working halves of cores MASS III 001-1 and 007-1 were analyzed at a sampling distances of 1 cm. Results of the susceptibility and gamma ray measurements are shown Figures 11 and 12.

MASS III 007-1

Date: 21.01.11 Pos: 8°10.84'N 95°52.88'E
Water Depth: 595 m Recovery: 125 cm

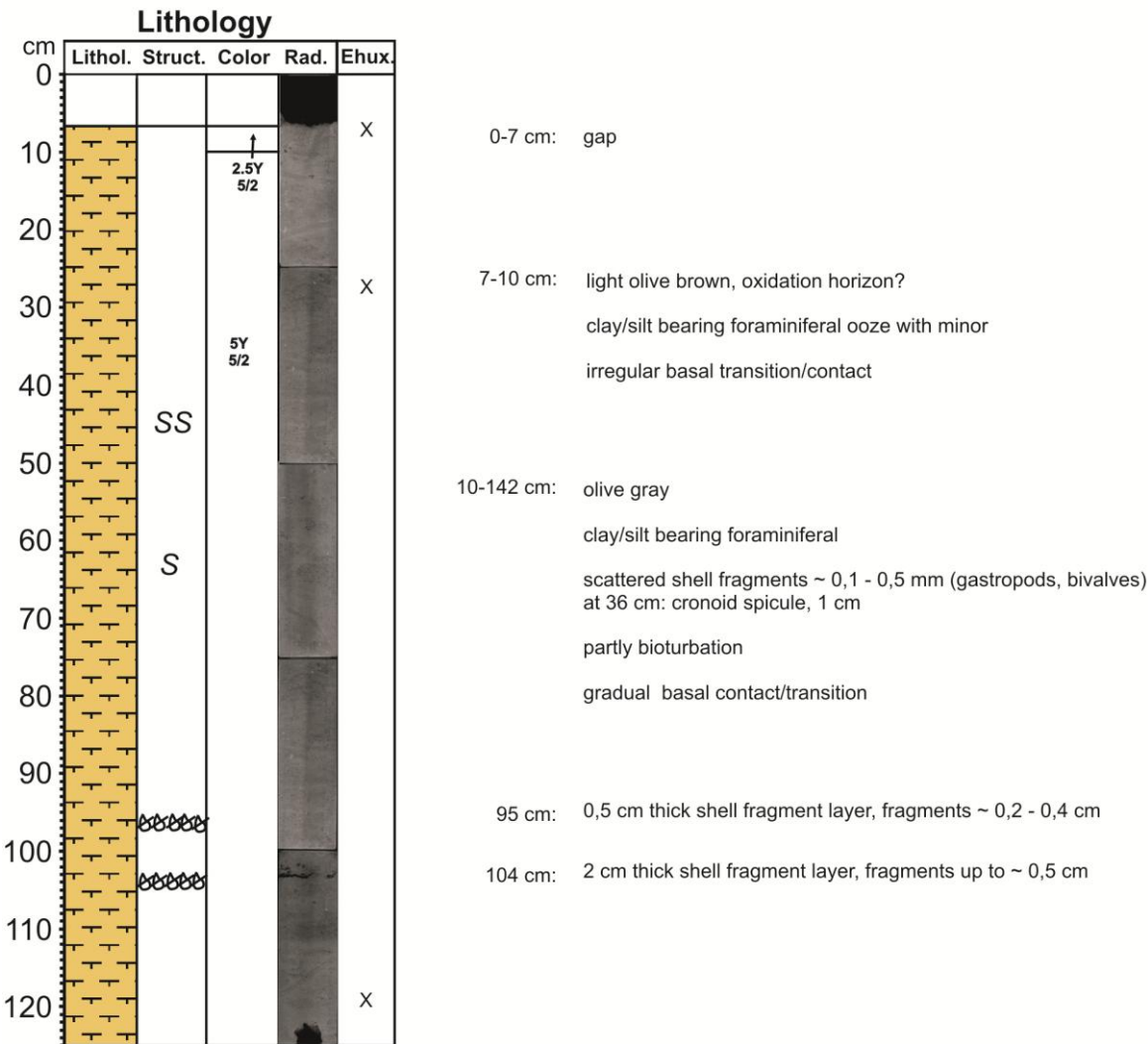


Figure 10. Visual core description and radiographic images of core MASS III 007-1

XRF

The X-ray fluorescence method was used to determine changes in relative abundances of elements contained in the sediment. For these measurements an Aavatech XRF core scanner, located at the Geoscience Faculty of University of Kiel was used. Cores MASS III 001-1, MASS III 002-1, MASS III 006-1 and MASS III 007-1 were analyzed every 10 mm with generator settings of 10 kV, 30 kV and 50 kV.

Examples for these measurements are shown in Figures 11 and 12. Ratios of K/Al, Ti/Ca, Ba/Ti and Si/Ca are plotted for cores MASS III 001-1 and MASS 007-1.

Scanning electron microscope (SEM)

In order to get an estimate of the age of the sediments retrieved in the cores, several samples from cores MASS III 01, 02, 06 and 10 were examined for coccoliths that can be used as biostratigraphic markers (*see table and core descriptions*). Samples for coccolithophore analyses were prepared with a combined filtration/dilution technique. A small amount of sediment was suspended in tap water and ultrasonicated for 15 to 30 s. Then a small amount of the suspension was filtered on a polycarbonate membrane filter (0,4 µm pore size). After drying the membranes for 24 h a small piece was mounted on a stub and sputtered with gold/palladium. The samples were then examined with a CamScanCS44 scanning electron microscope at the Institute of Geosciences, University of Kiel.

4.3 Sediment types and age estimations

Due to the above described problems with the sampling, most cores that were retrieved are very short (below 1 m) and are located on top of Mergui Ridge (see fig. X). and could therefore not be considered so far for slope stability analyses or absolute age dating of mass transport deposits (MTD). Most cores reveal a quite uniform lithologies with mostly bioturbated foraminiferal ooze of uniform olive green colouring throughout the cores. The XRF and MSCL measurements as well as the radiographic photographs show very uniform properties for all cores examined so far.

All samples that have been examined with the scanning electron microscope (see core descriptions) contained the coccolith *E. Huxleyi*. The first appearance date of *E. huxleyi* has been dated to 294 kyr by Vey and Peleo-Alampa (1993) and it has been the dominant species within coccolith assemblages since 73 000 yrs (Thierstein et al. 1977), This indicates that all of the surficial sediments on top of Mergui Ridge that have been retrieved by the sampling generally are younger than 268 kyr or even 73000 yrs and therefore are of Pleistocene origin.

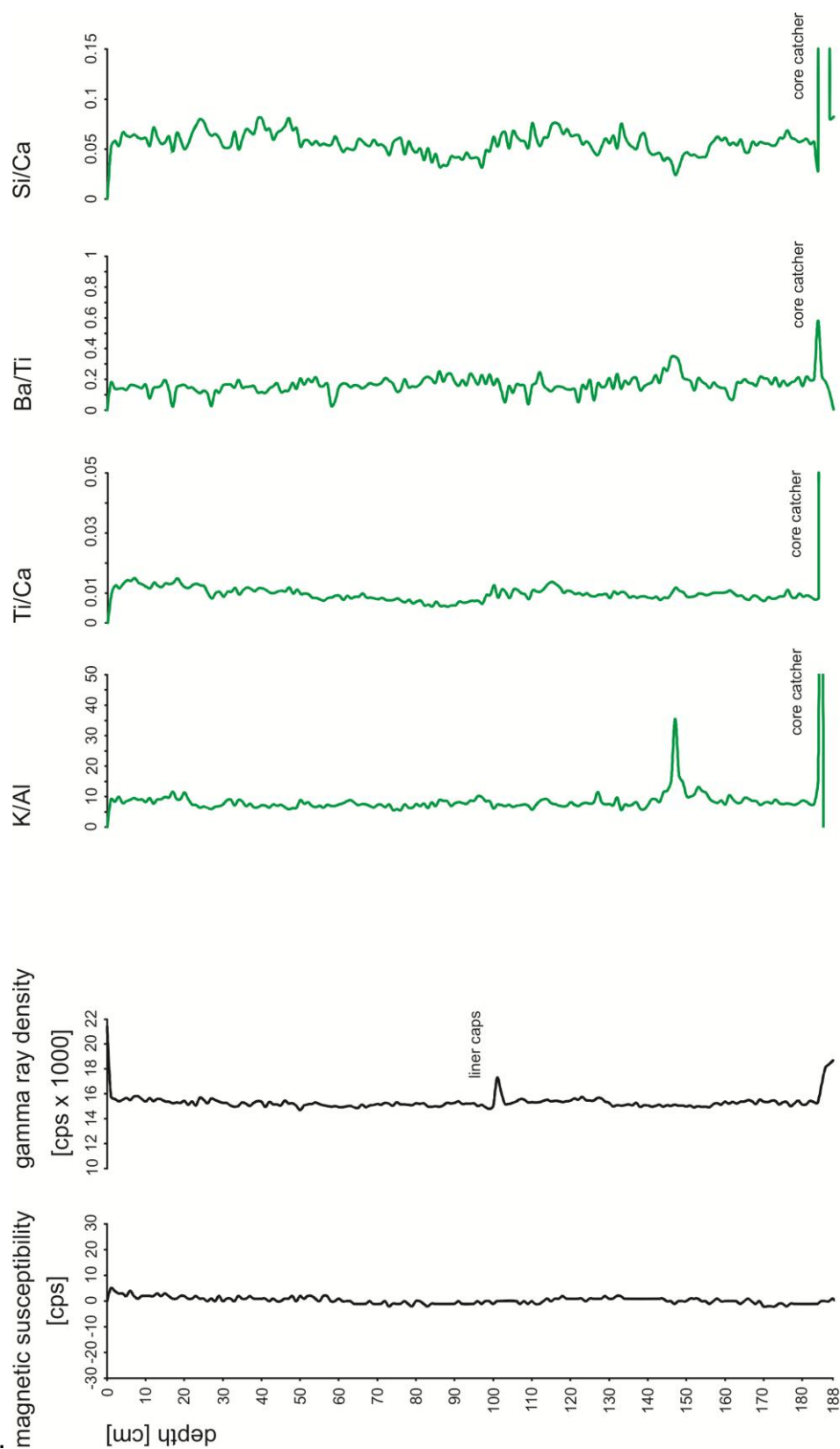
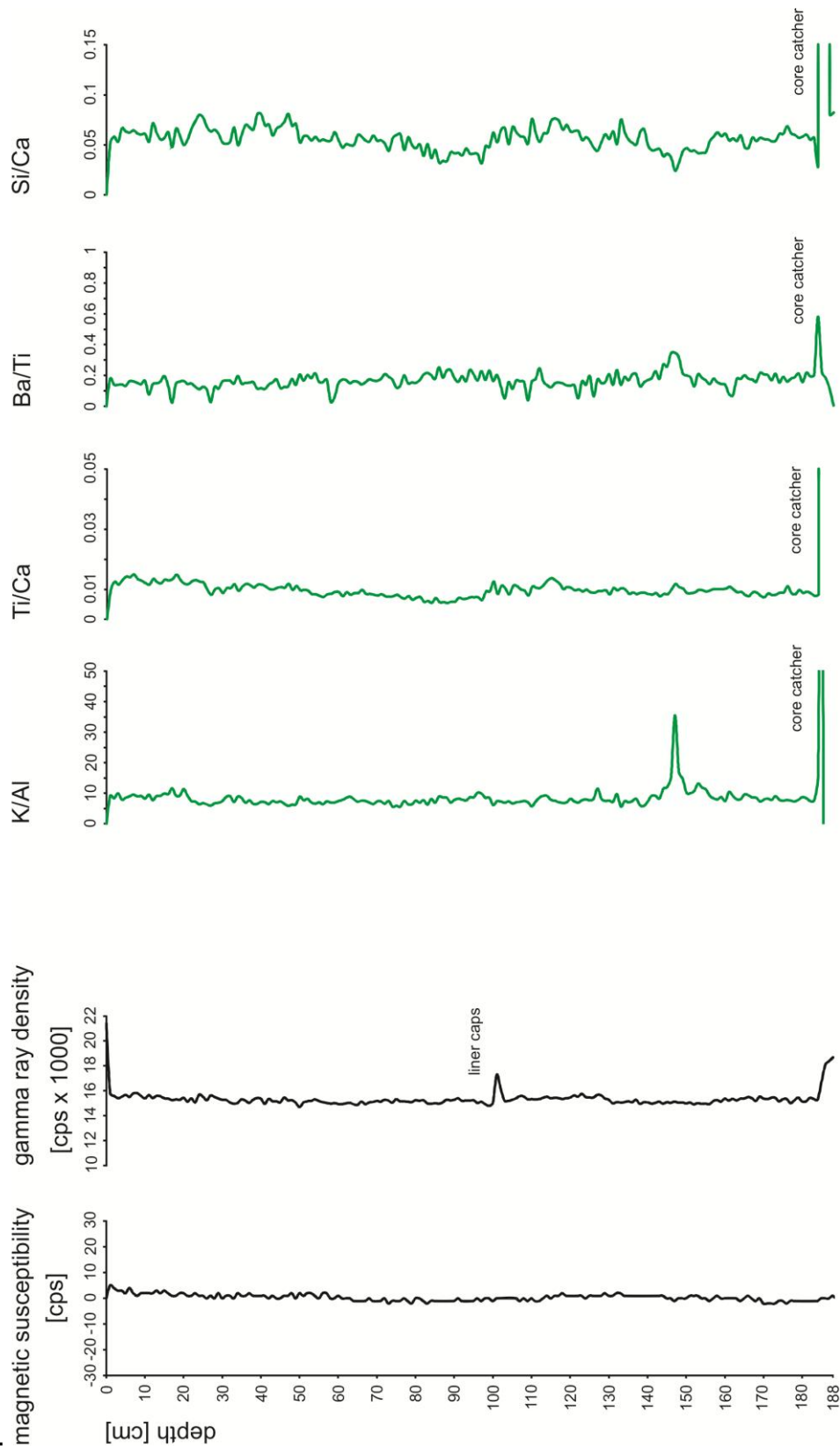


Figure 11. Results of the susceptibility and gamma ray measurements as well as Ratios of K/Al, Ti/Ca, Ba/Ti and Si/Ca for core MASS III 001-1

1



2 **Figure 12. Results of the susceptibility and gamma ray measurements as well as Ratios of**
 3 **K/Al, Ti/Ca, Ba/Ti and Si/Ca) for MASS III 007-1**

4.3.1 Carbonates

Core MASS III - 011 was taken on top of one of the plateaus (Table 1, Fig. 6) in water depths around 500 m. The core did not penetrate into sediments but a few hard rock fragments were recovered in the core catcher (Fig. 13). The fragments have diameters of up to 4.5 cm in size, but most samples are smaller than 2 cm. The colors vary from dark greyish over brownish yellow to light grey. The composition of these assumed biogenous rock samples is heterogeneous. Small clasts are cemented by a fine grained matrix. Some rounded components can be observed in the samples, too. Furthermore some vegetal incrustations on some of the fragments have been observed. Especially sample MASS III – 011-A exhibits a fractional coverage of benthic organic matter, which is determined at a sharp boundary. All descriptions of these samples have been done with the help of pictures, taken on-board, as the samples are stored at Chulalongkorn University, Bangkok, Thailand.

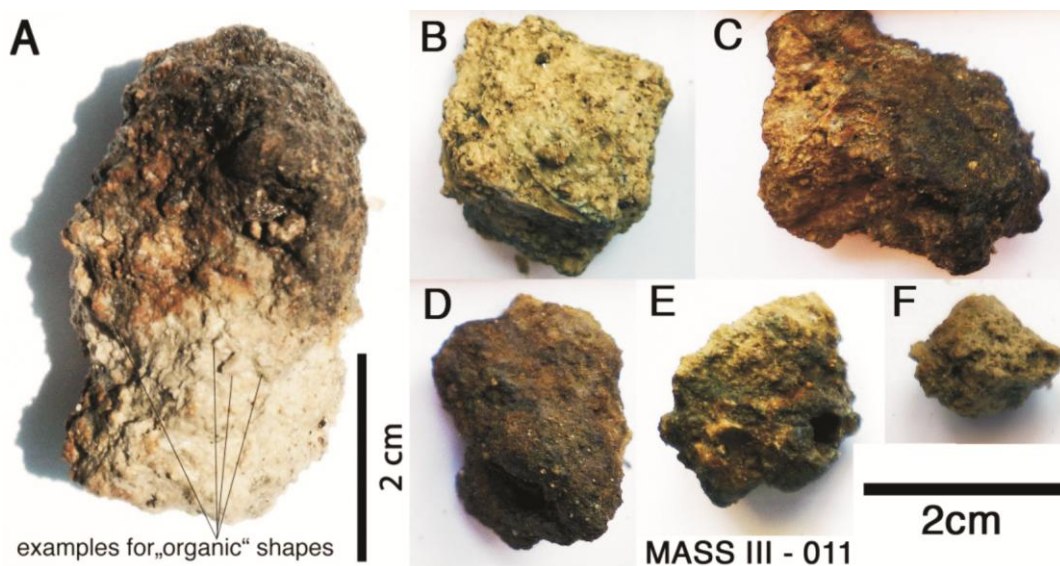


Figure 13. Examples of biogenic (carbonate) nodules retrieved from sampling at station MASS III 011 (from Gross, 2012)

5 Age determination of mass-wasting events and Frequency of slope failures

Approximate time intervals between individual slide events (A1–A4, B1–B5, C1–C5) have been established for the MTDs in the southern and northern East Andaman Sea settings (see Fig. 7 for locations). For the southern working area (A1–A4) they range between 940 ka and 1.19 Ma; for the northern working area between 220 ka and 1.47 Ma (B1–B5) and 370 and 950 ka (C1–C5), respectively (Table 3). For the MTDs on Mergui Ridge (D1–D3), no calculation of recurrence intervals have been established as information on sedimentation

Table 3. Calculated minimum time intervals between slide events, based on constant sedimentation rates of 10cm/ka (from Rodolfo, 1969)

Interval between MTDs	Maximum thickness of undisturbed sediment between MTDs [m]	Calculated time interval [ka]
A1-A2	94	940
A2-A3	91	910
A3-A4	119	119
B1-B2	39	390
B2-B3	22	220
B3-B4	96	960
B4-B5	147	1470
C1-C2	47	470
C2-C3	95	950
C3-C4	37	370
C4-C5	48	480

6 Analysis of near-surface gas hydrates and fluid seepage

In the seismic data some features indicating the presence of fluids and near surface gas hydrates have been identified, in addition to the features that have already been described by Jintasaerane et al. (2012).

An unusual high content of terrestrial organic carbon has been reported for these sediments (Keller and Richards, 1967, Colin et al. 1999, Bird et al., 2008, Ramaswamy et al. 2008,), which may be favorable of formation of gas within the drift deposits. Jintasaerane et al. (2012) reported gas-charged sediment at the Mergui Ridge slope area from subbottom profiler data. A possible bottom simulating reflector (BSR) was identified in the southern working area (Fig. 15c). Several possible gas migration pathways are imaged on our seismic data as vertical zones of acoustic transparency (Fig. 16).

7 Correlation of recent (small-scale) failure events with regional seismicity

A correlation of seismic events with slope failures has not been possible yet, due to the lack of precise absolute age dating of failures.

8 Determination of the current state of the slope

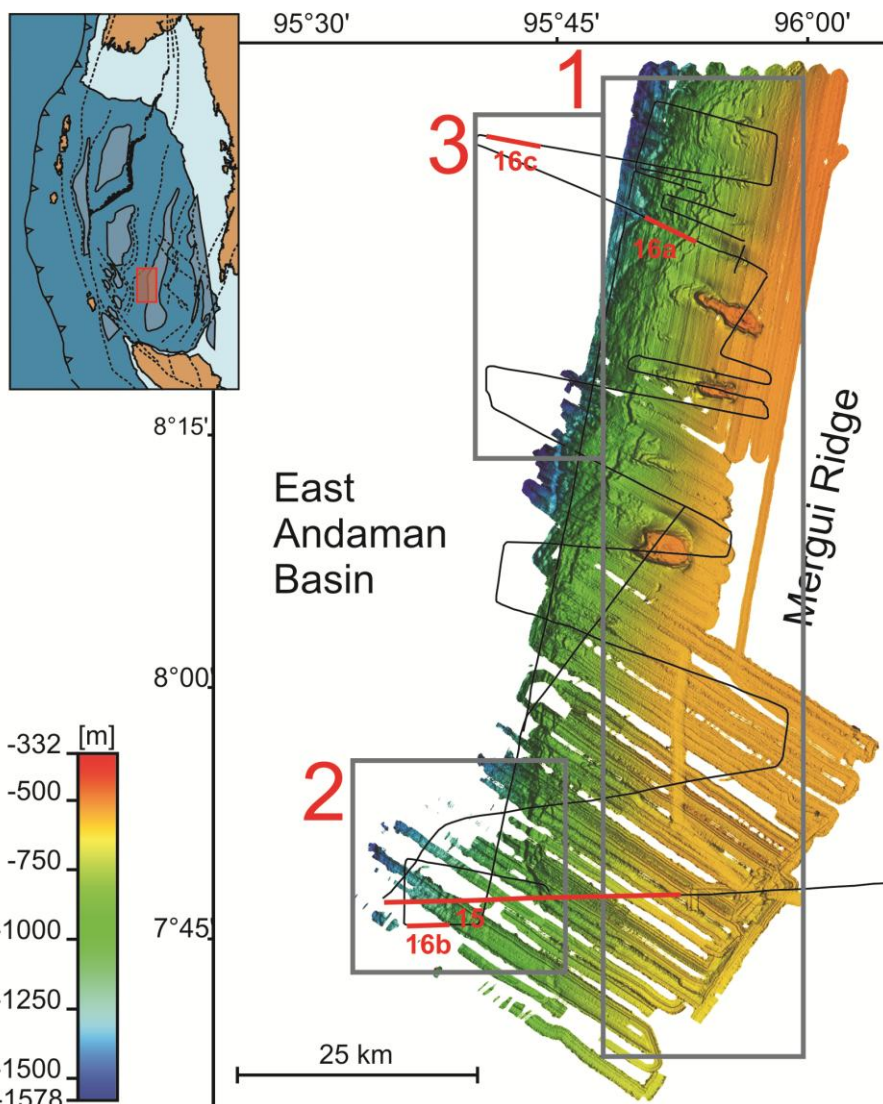
8.1 General architecture of the slope

The investigated area is located at the transition from the Mergui Ridge/outer shelf area to the deep sea environment of the East Andaman Basin, and seismic profiles acquired run closed to or across this basin-ridge transition (see Fig. 14 for profile locations). Water depths are increasing from east (Mergui Ridge) to west (East Andaman Basin) from about 300 m to about 2200 m. The western flank of Mergui Ridge forms the slope of the East Andaman Basin. Slope gradients of the basin-ridge transition are generally lower in the southern working area with values of about 1.5°. Towards the north, slope angles at the edge of the Mergui Ridge are considerably

higher, and reach, up to 12°. Downslope of the flank of the Mergui Ridge, the basin area is deepening towards north.

Based on the architecture of the basin-ridge transition, we differentiated three settings in the working area:

- Mergui Ridge in the western part of the working area (location of MTDs D1 - D3)
- Basin sediments of the East Andaman Basin in the southern working area (location of MTDs A1-A4)
- Basin sediments of the East Andaman Basin in the northern working area (location of MTDs B1 - B5 and C1 - C5)



1 *Figure 14. Locations of the three defined settings in the working area (dark grey boxes),*
2 *Mergui Ridge (1), East Andaman Basin south (2) and East Andaman Basin north (3), and*
3 *locations of profiles shown in figures 15 and 16 (red lines)*
4

1) Mergui Ridge:

Mergui Ridge forms the eastern boundary to the east Andaman Basin. We identified three main seismic units that make up Mergui Ridge. Their main characteristics are:

- MR1 is the oldest Mergui Ridge unit. It shows continuous parallel reflectors of variable amplitude, and in the northern part towards its top a reflection pattern of transparent patches, alternating with chaotic, high amplitude areas. MR1 is overlying the acoustic basement at the western flank of Mergui Ridge. It has a wedge-shaped geometry. The thinning of this unit towards the east and its reflector characteristics indicate deposition in a hemipelagic environment. Deformation of MR1 is caused by numerous faults throughout the working area.
- MR2 overlies comprises high-amplitude, subparallel reflectors.
- MR3 is characterized by parallel reflectors of variable amplitude with good lateral continuity. This unit is tapering out towards the east.

Based on its architecture and state of deformation we interpret the oldest unit (MR 1) as sediments of an older slope (see Schwab et al. 2012). Its sediments were deposited in a hemipelagic environment, and we speculate that they correspond to synrift sequences of Late Oligocene/Early Miocene age, that have been described (Polachan 1991, Curray 2005, Jha et al. 2010; Morley et al. 2011,). The two younger units MR2 and MR3, which are unconformably overlying MR1 are not tectonically deformed but influenced by bottom currents (see Schwab et al. 2012) which is indicated by marginal valley and a depositional tail around the morphological highs, which are characteristic indicators for sediment transport as outlined by Hernandez-Molina et al. (2008).

2) East Andaman Basin south:

In the southern working area sediments of the East Andaman Basin are overlying the older Mergui Ridge units. We differentiated three units:

- SB1 is the oldest basin fill unit. It exhibits a disturbed acoustic character with reflectors of varying amplitude and continuity. Towards its landward termination, the oldest basin fill unit SB1 is directly overlying MR1/MR2 sediments (Fig 15).

- SB2 is overlying SB1. It shows packages of well stratified, continuous to sub-continuous parallel reflectors of weak - to - moderate amplitudes, separated by pronounced reflectors of high amplitude. Towards its upslope edge SB1 onlaps against MR1 /MR 2 and it is confined by a moat (Fig 15a). Sediment waves are a characteristic feature of this up to 300 m thick unit (Fig 15). Narrow vertical zones of low amplitude, crossing several reflectors, are evident within SB2, (Fig 16a). These features may present fluid migration pathways. At one location, a possible bottom simulating reflector (BSR) has been identified at subsurface depths around 80 m (15c).
- HU is the youngest unit in the southern working area. It is deposited on top of SB2 and shows very regular, parallel, high-amplitude reflectors, with amplitude strengths increasing towards the seafloor. Based on its reflector characteristics, it is interpreted as a hemipelagic deposit, which is undisturbed in most parts. Sediment waves have a topographic expression in this unit Towards the surface, a few zones with small scale faulting are evident within HU. (16c).

The sediments in the southern working area fulfill typical criteria of drift deposits (see Schwab et al. 2012) and may be correlated to drift deposits west of the working area that have been described by Jha et al. (2011)

3) East Andaman Basin north:

In the northern working area (see Fig. 14 for location) we differentiated two units within the basin sediments that are overlying the Mergui Ridge units:

- NB onlaps the Mergui Ridge unit MR1. Several bodies, characterized by transparent/low amplitude chaotic reflections are alternating with sediments imaged as high-amplitude reflections within NB. Deformation of NB sediments is evident from numerous normal faults, dissecting the entire basin fill into blocks and leading to a rather disturbed appearance of NB. We did not correlate the lower units in the southern working area (SB1, SB2) and the lower unit in the north (NB). No seismic lines for direct lateral correlation are

1 available. Although these units show similar characteristics, such as high
2 amplitude reflectors alternating with low-amplitude packages, a clear
3 correlation is not possible due to the disturbed character of NB and the lack of
4 an internal boundary within NB, corresponding to the boundary between SB1
5 and SB2.

- 6 • HU is overlying NB with a thickness of up to 200 m. It is, like in the south a
7 hemipelagic unit characterized by parallel and fairly continuous/sub-
8 continuous reflectors. The seismic character of this unit is very similar to the D
9 HU is quite undisturbed, in contrast to the unit NB below it. However, some
10 faults are cutting through HU to the surface. Along one of these faults the
11 seafloor is displaced by about 20 m (Fig. 16c). Seaward of this fault, the
12 sediments show a wavy pattern (Fig. 16c). Vertical transparent zones,
13 interpreted as potential gas migration pathways are present in the seismic unit
14 HU (Fig. 16c)

15
16 The East Andaman Basin sediments in the northern working area, especially the
17 older deposits of seismic unit NB, exhibit features of tectonic deformation, such as
18 the presence of numerous faults. Although the youngest basin unit HU exhibits an
19 overall undisturbed character, a few faults cut through this unit in the northern
20 working area. This pattern is in agreement with the description of recent deformation
21 due to activity of fault zones near the working area, such as Mergui Fault (Morley et
22 al. 2011)

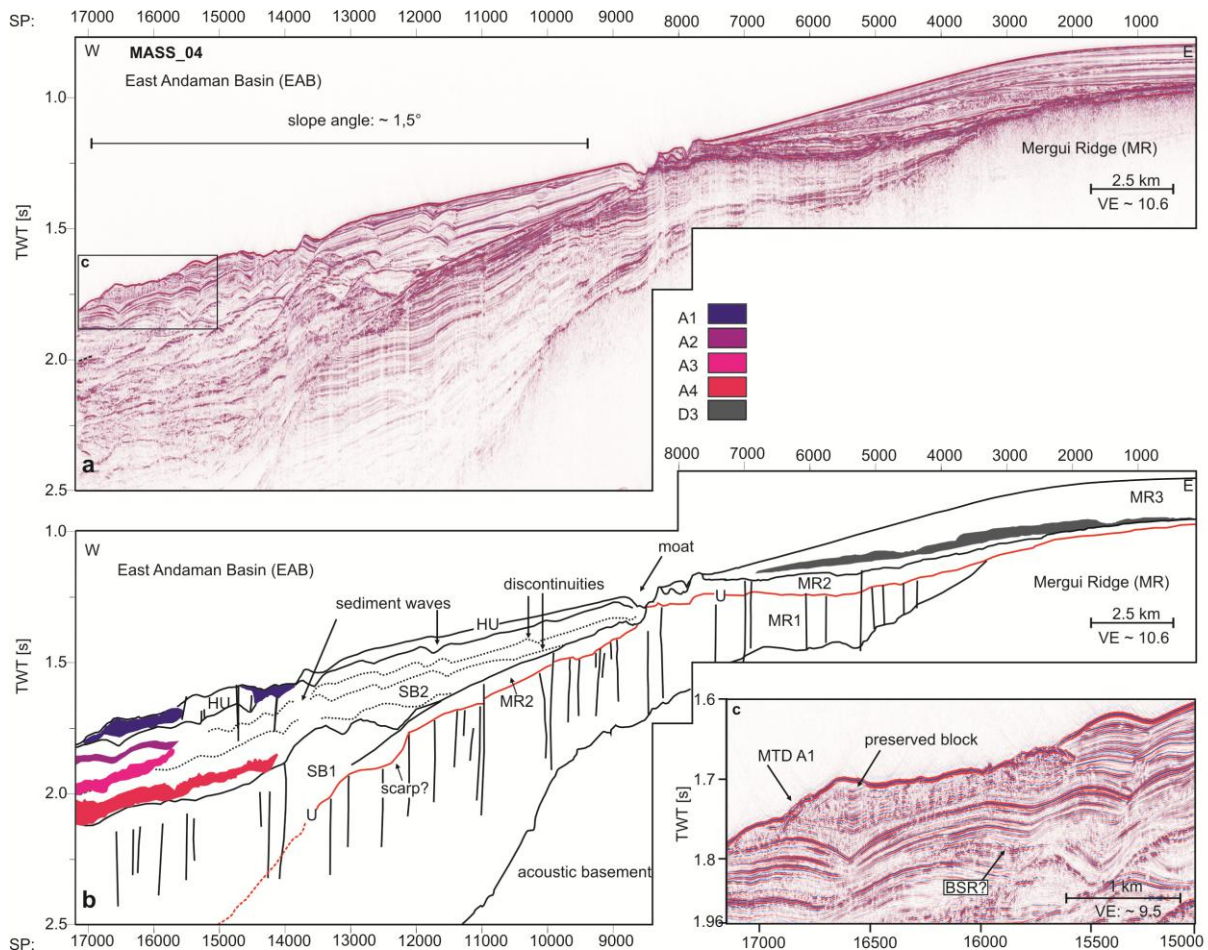


Figure 15. a, b) Example profile across the basin-ridge transition from Schwab et al. (2012) with the seismic units of Mergui Ridge in the east and East Andaman Basin sediments in the west. Moreover, MTDs are present in the basin sediments. c) Close-up of an area where a possible BSR has been identified in the upper parts of the sedimentary column

8.2 Main influences on slope stability

The seismic dataset shows that the slope generally has been unstable, with recurrent failure events. Timing between individual failures is rather long as described in chapter 5 (see also Schwab et al., 2012). However, several locations with sediment that may be unstable and fail in the future have been detected (Fig. 16). We find that the most important preconditioning factors are migrating fluids, instability of drift deposits and ongoing tectonic activity that produces deformation and generates earthquakes that are the most likely the final trigger for the destabilization of the sediments:

1 **Instable drift deposits**

2 Drift deposits are present in the southern working area. Generally drift deposits are
3 described to be prone to instability and failure due tend to be prone to liquefaction
4 during seismic loading due to good sorting of their particles and resulting high
5 porosity. High sedimentation rates in drift deposits may result in rapid loading and
6 development of excess pore pressure. The development of excess pore pressure is
7 further facilitated by gas migration, fueled by high organic matter input from
8 productive water masses along continental margins. (Laberg and Camerlenghi,
9 2008). Migrating fluids can cause build-up of excess pore pressure in upper sediment
10 layers, a process which is well known to be capable for destabilizing slope sediments
11 (Vorren et al., 1998; Stigall and Dugan, 2010).

12 Sediment building drift deposits in the southern working area contains terrigenous
13 material from the Ayeyawady River and/or the Malacca Strait. Off the ridge,
14 sedimentation rates are high (10 cm/ka, Rodolfo, 1969). An unusual high content of
15 terrestrial organic carbon has been reported for these sediments (Keller and
16 Richards, 1967, Colin et al. 1999, Bird et al., 2008, Ramaswamy et al. 2008), which
17 may be favorable of formation of gas within the drift deposits. Therefore we consider
18 that build-up of excess pore-pressure due to migrating fluids and instability of drift
19 deposits was an important pre-conditioning factor for the failure events in the
20 southern working area (MTDs A1 - A4).

21

22 **Tectonic influence: subsidence and fault controlled failures**

23 Tilting of the slope due to subsidence of a margin can act as a preconditioning factor
24 for slope failure (Masson et al. 2010). The Mergui Ridge underwent subsidence since
25 the onset of rifting in the Central Andaman Basin in Late Miocene (Kamesh Raju,
26 2005) due to dextral movement along EAFZ in Late Miocene (Jha et al. 2010) and/or
27 due to thermal contraction (Morley, et al. 2011). Jha et al. (2010) described large
28 scale subsidence as a cause for the formation of mass flows west of our working
29 area. These deposits may be correlatable to our seismic unit SB1 (see above).
30 Recent subsidence rates from the shelf area of the Malacca Strait are in the range of
31 0.25 mm/a (Lin et al. (2010). This value is relatively small compared to areas with
32 recent extension, for example the Corinth Basin with a subsidence rate of 1 mm/a

(Lykousis et al. 2007). In addition, subsidence rates tend to decrease after termination of rifting (Prosser, 1993). Therefore, subsidence and steepening may still play a role for slope stability but its influence became probably smaller since the onset of rifting that created the large mass flows described by Jha et al. (2010).

The presence of faults has been suggested to act as controlling or preconditioning factor for slope failures (Dillon 1993, Hampton 1996, Anasetti et al. 2012). Large parts of the basin fill sediments in the northern working area are tectonically deformed. The MTDs C1 - C5 and B1 - B5 are located in this environment and we consider fault activity as one of the main reasons for slope failures in our working area. Episodic slope failure due to episodic fault activity has been described by Reicherter et al. (2011) to result in slide deposits interbedded in well stratified layers. A similar pattern can be observed for the MTDs in the northern working area (B1 - B5 and C1 - C5). Moreover, the MTDs B1 - B5 seem to occur in stratigraphic depths similar to those of C1 -C5. This would imply laterally contemporaneous failures in the northern working area. We therefore suggest that episodic fault activity was important for weakening the sediments along the slope.

Tectonic deformation may also play a role in development of MTDs on top of/at the edge of the Mergui Ridge (D1 - D3), where sedimentation rates are low and oversteepening probably is not a preconditioning factor for slope failure. Surficial MTD D1 and buried MTD D2 are both located at the edge of the Mergui Ridge. Tectonic deformation of the top parts of unit MR1 may have caused the development of unstable blocks that were subsequently dislocated. Internal structures of these blocks are still preserved, therefore run out distances of blocks seem to be small.

To conclude, weakening of the sediments due to tectonic activity is considered as a main pre-conditioning factor for slope failure, especially at the basin-ridge transition.

8.3 Final trigger mechanism

An important factor for the formation and recurrence of submarine landslides is the presence of a final trigger leading to the failure of potentially unstable sediments (e.g. Masson et al. 2006). Seismic activity is common along the Sunda trench and also within the Andaman Sea (Lay et al. 2005; Ornthammarath et al. 2011; Khan 2012). Neotectonic activities have been reported from many structures in the Andaman Sea such as the modern spreading centre (Kamesh Raju et al., 2004), the Sagaing Fault

(Wang et al., 2011), the Andaman Arc (Radhakrishna et al., 2008), or the West Andaman Fault (Kamesh Raju et al., 2007). Ongoing tectonic activity is also documented in our data as faults reaching the surface. Therefore, earthquakes are likely final triggers for slope failures.

8.4 Possible locations of future slope failures and their tsunamigenic potential

Three locations of possible future slope failures were identified in our data set (Fig. 16)

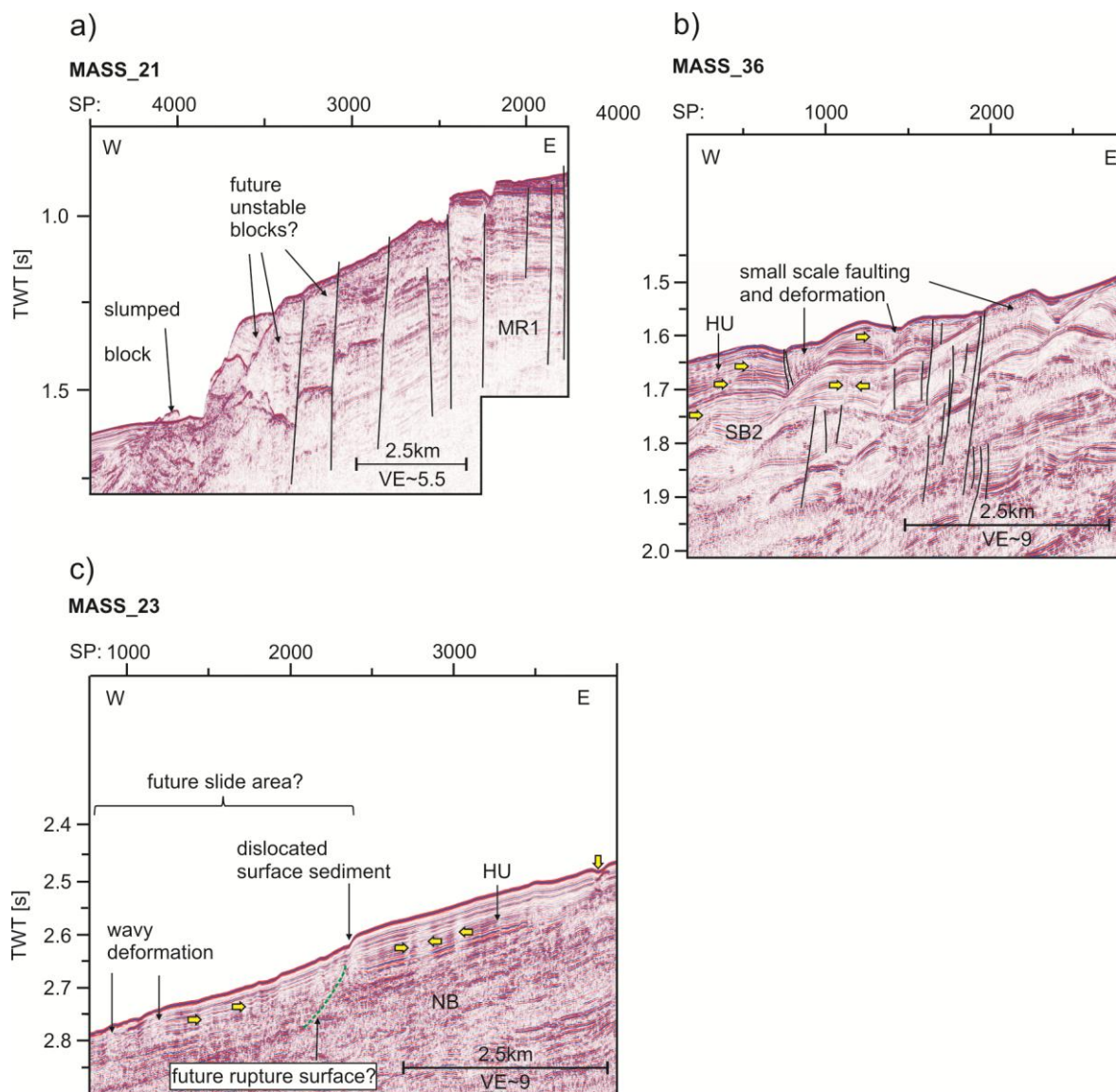


Figure 5. a) Possible locations of future slope failures from the Mergui Ridge setting (MASS_23), the East Andaman Basin in the southern working area (MASS_36) and the East Andaman Basin in the northern working area. a) Seismic profile from the edge of

1 *Mergui Ridge. Several faults, marked by black lines, cut to the surface and indicate recent*
2 *deformation and dislocation of blocks. A small slumped block may indicate that some*
3 *failure already occurred. b) Profile MASS_36 shows drift sediments from the southern*
4 *working area. Fluid migration pathways are imaged in these sediments as transparent*
5 *narrow vertical zones (yellow arrows). Small scale faulting and deformation of the upper*
6 *sedimentary layers may indicate future failure of the drift deposits. c) Seismic profile*
7 *MASS_23 reveals numerous vertical transparent features interpreted as pathways for fluids*
8 *(yellow arrows), and a fault dislocating the sea floor (green dotted line), that might act as*
9 *future rupture surface. Wavy deformation of the surficial sediments downslope of this fault*
10 *may indicate remobilization of the sediment (from Schwab et al. 2012).*
11

12 **1) Mergui Ridge:**

13 Figure 16a shows a profile where faults cut through the seafloor. As fault reactivation
14 and deformation in the region seems plausible, these deformed back rotated blocks
15 may fail in the future. Moreover, a slumped block is located basinward of this
16 deformed area, which may indicate, that some disintegration and failure already
17 occurred. Masson et al. (2006) suggest that thick slide blocks with a steep headwall
18 (rotational slides) might be particularly effective in tsunami generation even without
19 large displacements. Therefore, future slope failures at this location in relatively
20 shallow water depths between 700 m and 1100 m may definitively be tsunamigenic.
21 Regarding MTD D3 which is also located on Mergui Ridge, we cannot reconstruct
22 initiation or evolution of this MTD, as outlined above. However, we can infer that a
23 potential future failure of the same dimensions at the same water depths of about
24 500-700 m definitely falls in the range of tsunamigenic landslides.
25

26 **2) East Andaman Basin south:**

27 An area in water depths shallower than 1000 m close to MTD A1 in the southern
28 working area may be prone to future failures (Fig. 16c). Widespread sediment waves
29 in combination with small scale faulting and indications for fluid migration pathways
30 suggest a potentially unstable slope. Jintasaeranee et al. (2012) described numerous
31 small scale failures in this area. Therefore we conclude that future failures in this
32 area are likely. A failure of significant volume of this part of the slope may be
33 tsunamigenic. However, the area comprises large structural complexity and ongoing
34 tectonic activity. Slope failures from areas with regular seismic activities are expected
35 to be small in size, due to frequent triggers in the form of earthquakes, hence not
36 leaving sufficient time to accumulate large amounts of material for voluminous slides

(Völker et al. 2009). Therefore we would rather expect several small failures of individual sediment packages instead of voluminous failures. Hence, we consider the tsunami hazard, emerging from this area as low.

3) East Andaman Basin north:

Figure 16c shows an enlargement of the topmost sediment layers of profile MASS_23 in the northern working area. A listric fault cuts and dislocates parts of the superficial sediment of unit NB2. This fault may be interpreted as possible future failure surface. Downslope of the surface expression of the fault, the sediment is deformed and destabilization may be indicated by the wavy deformation patterns visible on the seismic data. Migrating fluids may further contribute to future slope instability. However, within the northern working area all MTDs as well as the area of potential future slope failure are situated well below 1000 m water depth. Consequently, future slides in the northern part of the East Andaman Basin area may occur but probably do not pose a tsunami hazard.

To sum up, the same setting that induced slope failures in the past may also lead to slope failure in the future, but only a few slides show volume and depth values typical for tsunamigenic slides. However, it has to be taken into account that our volume estimations are minimum values, as the lateral boundaries of the MTDs in most cases are not covered by the seismic dataset. Moreover, we cannot exclude a correlation between the stacked MTDs in the northern working area, as the settings where they occur show great similarity regarding characteristics, amount and architecture of the MTDs. This implies that more slides than outlined above may have triggered tsunamis in the past. However, even then their number would be small as suggested by the time intervals between the slides.

References

Anasetti, A., Winkelmann, D., Krastel, S., Bialas, J., and Brückmann, W.: The BGR slide off Costa Rica: Preconditioning factors, trigger, and slide dynamics, in: Submarine mass movements and their consequences, edited by: Yamada, Y., Kawamura, K., Ikehara, K.,

- 1 Ogawa, Y., Urgeles, R., Mosher, D., Chaytor, J., and Strasser, M., Advances in natural and
2 technological hazards research, Springer, Netherlands, 289-299, 2012.
- 3 Bird, M. I., Robinson, R. A. J., Win Oo, N., Maung Aye, M., Lu, X. X., Higgitt, D. L., Swe,
4 A., Tun, T., Lhaing Win, S., Sandar Aye, K., Mi Mi Win, K., and Hoey, T. B.: A preliminary
5 estimate of organic carbon transport by the Ayeyarwady (Irrawaddy) and Thanlwin (Salween)
6 rivers of Myanmar, Quatern. Int., 186, 113-122, doi: 10.1016/j.quaint.2007.08.003, 2008.
- 7 Colin, C., Turpin, L., Bertaux, J., Desprairies, A., and Kissel, C.: Erosional history of the
8 Himalayan and Burman ranges during the last two glacial-interglacial cycles, Earth Planet.
9 Sc. Lett., 171, 647-660, 1999.
- 10 Curray, J. R.: Tectonics and history of the Andaman Sea region, J. Asian Earth Sci., 25, 187-
11 232, 2005.
- 12 Dillon, W. P., Risch, J. S., Scanlon, K. M., Valentine, P. C., and Huggett, Q. J.: Ancient
13 crustal fractures control the location and size of collapsed blocks at the Blake escarpment, east
14 of Florida, in: Submarine landslides: Selected Studies in the U.S. Exclusive Economic Zone,
15 edited by: Schwab, W. C., Lee, H. J., and Twichell, D. C., U.S. Geological Survey Bulletin,
16 54-59, 1993.
- 17 Gross, F.: Contourites, slope stability and submarine mass wasting at the Shelf Break of West
18 Thailand, Andaman Sea, Master Thesis, University of Kiel, 2012
- 19 Hampton, M. A., Lee, H. J., and Locat, J.: Submarine landslides, Reviews of Geophysics, 34,
20 33-59, doi: 10.1029/95rg03287, 1996.
- 21 Hernández-Molina, F. J., Maldonado, A., and Stow, D. A. V.: Abyssal plain contourites, in:
22 Contourites, Developments in Sedimentology, edited by: Rebesco, M., and Camerlenghi, A.,
23 Elsevier, Amsterdam, Netherlands, 345-378, 2008.
- 24 Jha, P., Ros, D., degli Alessandrini, A., and Kishore, M.: Speculative petroleum system and
25 play model of East Andaman Basin from regional geology and basin evolution concepts:
26 Addressing the exploration challenges of an extreme frontier area, 8th Biennial International
27 Conference and Exposition on Petroleum Geophysics, Hyderabad, India, P-261, 2010.

- 1 Jha, P., Ros, D., and Kishore, M.: Seismic and sequence stratigraphic framework and
2 depositional architecture of shallow and deepwater postrift sediments in East Andaman Basin:
3 An overview, GeoIndia 2011, Greater Noida, New Dheli, India, January 12-14, 2011.
- 4 Jintasaeranee, P., Weinrebe, W., Klaucke, I., Snidvongs, A., and Flueh, E. R.: Morphology of
5 the Andaman outer shelf and upper slope of the Thai exclusive economic zone, *J. Asian Earth*
6 *Sci.*, 46, 78-85, doi. 10.1016/j.jseaes.2011.11.003, 2012.
- 7 Krastel, S.: RV Chakratong Tongyai Fahrtbericht / Cruise Report MASS-III Morphodynamics
8 and Slope Stability of the Andaman Sea Shelf Break (Thailand), *Berichte aus dem Leibniz-*
9 *Institut für Meereswissenschaften an der Christian-Albrechts-Universität zu Kiel*, 43, 2011
- 10 Kamesh Raju, K. A., Ramprasad, T., Rao, P. S., Ramalingeswara Rao, B., and Varghese, J.:
11 New insights into the tectonic evolution of the Andaman Basin, northeast Indian Ocean, *Earth*
12 *Planet. Sc. Lett.*, 221, 145-162, 2004.
- 13 Kamesh Raju, K. A.: Three-phase tectonic evolution of the Andaman Backarc Basin, *Curr.*
14 *Sci. India*, 89, 2005.
- 15 Kamesh Raju, K. A., Murty, G. P. S., Amarnath, D., and Kumar, M. L. M.: The West
16 Andaman Fault and its influence on the aftershock pattern of the recent megathrust
17 earthquakes in the Andaman-Sumatra region, *Geophys. Res. Lett.*, 34, L03305, doi:
18 10.1029/2006gl028730, 2007.
- 19 Keller, G. H., and Richards, A. F.: Sediments of the Malacca Strait, Southeast Asia, *J.*
20 *Sediment. Res.*, 37, 102-127, doi: 10.1306/74d7166d-2b21-11d7-8648000102c1865d, 1967.
- 21 Khan, A.: Seismogenic sources in the bay of bengal vis-à-vis potential for tsunami generation
22 and its impact in the northern bay of bengal coast, *Natural Hazards*, 61, 1127-1141, doi:
23 10.1007/s11069-011-9970-x, 2012.
- 24 Laberg, J. S., and Camerlenghi, A.: The significance of contourites for submarine slope
25 stability, in: *Contourites, Developments in sedimentology*, edited by: Rebesco, M., and
26 Camerlenghi, A., Elsevier, Amsterdam, Nertherlands, 537-556, 2008.

1 Lay, T., Kanamori, H., Ammon, C. J., Nettles, M., Ward, S. N., Aster, R. C., Beck, S. L.,
2 Bilek, S. L., Brudzinski, M. R., Butler, R., DeShon, H. R., Ekström, G., Satake, K., and
3 Sipkin, S.: The great Sumatra-Andaman earthquake of 26 December 2004, *Science*, 308,
4 1127-1133, doi: 10.1126/science.1112250, 2005.

5 Lin, Y.-n. N., Sieh, K., and Stock, J.: Submarine landslides along the Malacca Strait-Mergui
6 Basin shelf margin: Insights from sequence-stratigraphic analysis, *J. Geophys. Res.*, 115,
7 B12102, doi: 10.1029/2009jb007050, 2010.

8 Lykousis, V., Sakellariou, D., Moretti, I., and Kaberi, H.: Late Quaternary basin evolution of
9 the Gulf of Corinth: Sequence stratigraphy, sedimentation, fault-slip and subsidence rates,
10 *Tectonophysics*, 440, 29-51, doi: 10.1016/j.tecto.2006.11.007, 2007.

11 Masson, D. G., Harbitz, C. B., Wynn, R. B., Pedersen, G., and Lovholt, F.: Submarine
12 landslides: Processes, triggers and hazard prediction, *Philos. T. R. Soc. A*, 364, 2009-2039,
13 doi: 10.1098/rsta.2006.1810, 2006.

14 Masson, D. G., Wynn, R. B., and Talling, P. J.: Large landslides on passive continental
15 margins: Processes, hypotheses and outstanding questions, in: *Submarine mass movements*
16 *and their consequences*, edited by: Mosher, D. C., Moscardelli, L., Baxter, C. D. P., Urgeles,
17 R., Shipp, R. C., Chaytor, J. D., and Lee, H. J., *Advances in natural and technological hazards*
18 *research*, Springer, Netherlands, 153-165, 2010.

19 Morley, C. K., Charusiri, P., and Watkinson, I.: Structural geology of Thailand during the
20 Cenozoic, in: *The geology of Thailand*, edited by: Barber, A. J., and Ridd, F. D., *Geological*
21 *Society of London*, London, United Kingdom, 539-571, 2011.

22 Ornthammarath, T., Warnitchai, P., Worakanchana, K., Zaman, S., Sigbjörnsson, R., and Lai,
23 C.: Probabilistic seismic hazard assessment for Thailand, *B. Earthq. Eng.*, 9, 367-394, doi:
24 10.1007/s10518-010-9197-3, 2011.

25 Polachan, S., Praditnan, S., Tongtaow, C., Janmaha, S., Intarawijitr, K., and Sangsuwan, C.:
26 Development of cenozoic basins in thailand, *Marine and Petroleum Geology*, 8, 84-97, doi:
27 10.1016/0264-8172(91)90047-5, 1991.

- 1 Polachan, S., and Racey, A.: Stratigraphy of the Mergui Basin, Andaman Sea: Implications
2 for petroleum exploration, *J. Petrol. Geol.*, 17, 373-406, doi: 10.1111/j.1747-
3 5457.1994.tb00147.x, 1994.
- 4 Prosser, S.: Rift-related linked depositional systems and their seismic expression, *Geological*
5 *Society, London, Special Publications*, 71, 35-66, doi: 10.1144/gsl.sp.1993.071.01.03, 1993.
- 6 Radhakrishna, M., Lasitha, S., and Mukhopadhyay, M.: Seismicity, gravity anomalies and
7 lithospheric structure of the Andaman Arc, NE Indian Ocean, *Tectonophysics*, 460, 248-262,
8 doi: 10.1016/j.tecto.2008.08.021, 2008.
- 9 Ramaswamy, V., Rao, P. S., Rao, K. H., Thwin, S., Rao, N. S., and Raiker, V.: Tidal
10 influence on suspended sediment distribution and dispersal in the northern Andaman Sea and
11 Gulf of Martaban, *Mar. Geol.*, 208, 33-42, doi: 10.1016/j.margeo.2004.04.019, 2004.
- 12 Rodolfo, K. S.: Sediments of the Andaman Basin, northeastern Indian Ocean, *Mar. Geol.*, 7,
13 371-402, 1969.
- 14 Schwab, J. M.; Krastel, S.; Grün, M.; Gross, F.; Pananont, P.; Jintasaeranee, P.,
15 Bunsomboonsakul, S.; Weinrebe, W.; Winkelmann, D.: Submarine mass wasting and
16 associated tsunami risk offshore western Thailand, Andaman Sea, Indian Ocean, *Nat. Hazards*
17 *Earth Syst. Sci* 12 (8), 2609–2630, (2012)
- 18 Thierstein, H., Geitzenauer, K., Molfino, B. & Shackleton, N. Global synchronicity of late
19 Quaternary coccolith datum levels Validation by oxygen isotopes. *Geol* 5, 400 (1977).
- 20 Völker, D., Weinrebe, W., Behrmann, J. H., Bialas, J., and Klaeschen, D.: Mass wasting at the
21 base of the south central Chilean continental margin: The Reloca slide, *Adv. Geosci.*, 22, 155-
22 167, doi: 10.5194/adgeo-22-155-2009, 2009.
- 23 Wang, Y., Sieh, K., Aung, T., Min, S., Khaing, S. N., and Tun, S. T.: Earthquakes and slip
24 rate of the southern Sagaing Fault: Insights from an offset ancient fort wall, lower Burma
25 (Myanmar), *Geophys. J. Int.*, 185, 49-64, doi: 10.1111/j.1365-246X.2010.04918.x, 2011.

- 1 Wei, W., Peleo-Alampay, A., 1993. Updated Cenozoic Nannofossil Magnetobiochronology.
- 2 In: Young, J. (Ed.), Newsletter of International Nannoplankton Association (INA) 1993, pp.
- 3 15-17.

- 4 Yilmaz, O.: Seismic data processing: Investigations in Geophysics, Vol 2, Society of
- 5 Exploration, 526 pp., 1987.

ภาคผนวก ง